AD-A082 015 ADVISORY GROUP FOR AEROSPACE RESEARCH AND DEVELOPMENT--ETC F/G 20/14
TERRAIN PROFILES AND CONTOURS IN ELECTROMAGNETIC WAVE PROPAGATI--ETC(U)
DEC 79 A W BIGGS

UNCLASSIFIED AGARD-CP-269 NL

1 OF 4
AD
A082015

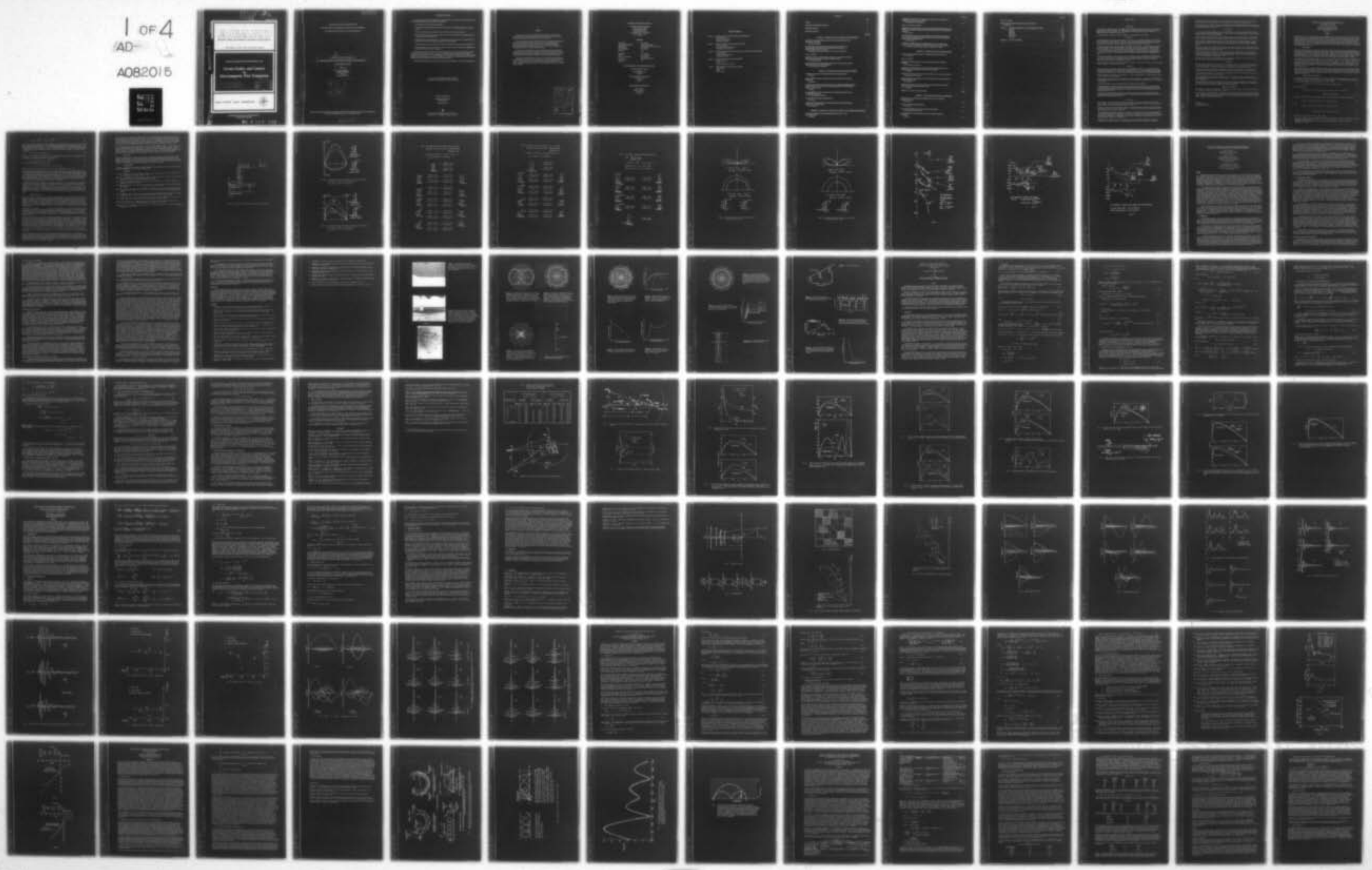

AGARD-CP-269

AGARD-CP-269

AGARD

ADVISORY GROUP FOR AEROSPACE RESEARCH & DEVELOPMENT

7 RUE ANCELLE 92200 NEUILLY SUR SEINE FRANCE

AGARD CONFERENCE PROCEEDINGS No. 269

Terrain Profiles and Contours in Electromagnetic Wave Propagation

NORTH ATLANTIC TREATY ORGANIZATION

DISTRIBUTION AND AVAILABILITY
ON BACK COVER

(14) AGARD-CP-269

NORTH ATLANTIC TREATY ORGANIZATION

ADVISORY GROUP FOR AEROSPACE RESEARCH AND DEVELOPMENT

(ORGANISATION DU TRAITE DE L'ATLANTIQUE NORD)

(9) AGARD Conference Proceedings No.269

(6) # TERRAIN PROFILES AND CONTOURS IN ELECTROMAGNETIC WAVE PROPAGATION.

Edited by

(10) Albert W. Biggs
University of Kansas
Lawrence
Kansas 66045, USA

(11) Dec 79

(12) 370

Papers and Discussions presented at the Specialists' Meeting of the Electromagnetic Wave Propagation Panel held in Spåtind, Norway, 10–14 September 1979.

400043

LB

THE MISSION OF AGARD

The mission of AGARD is to bring together the leading personalities of the NATO nations in the fields of science and technology relating to aerospace for the following purposes:

- Exchanging of scientific and technical information;
- Continuously stimulating advances in the aerospace sciences relevant to strengthening the common defence posture;
- Improving the co-operation among member nations in aerospace research and development;
- Providing scientific and technical advice and assistance to the North Atlantic Military Committee in the field of aerospace research and development;
- Rendering scientific and technical assistance, as requested, to other NATO bodies and to member nations in connection with research and development problems in the aerospace field;
- Providing assistance to member nations for the purpose of increasing their scientific and technical potential;
- Recommending effective ways for the member nations to use their research and development capabilities for the common benefit of the NATO community.

The highest authority within AGARD is the National Delegates Board consisting of officially appointed senior representatives from each member nation. The mission of AGARD is carried out through the Panels which are composed of experts appointed by the National Delegates, the Consultant and Exchange Programme and the Aerospace Applications Studies Programme. The results of AGARD work are reported to the member nations and the NATO Authorities through the AGARD series of publications of which this is one.

Participation in AGARD activities is by invitation only and is normally limited to citizens of the NATO nations.

The content of this publication has been reproduced directly from material supplied by AGARD or the authors.

Published December 1979

ISBN 92-835-1345-2

Printed by Technical Editing and Reproduction Ltd
Harford House, 7–9 Charlotte St, London, W1P 1HD

THEME

This Symposium addressed the propagation problems which are connected with terrain profiles and contours. Specifically examined were theoretical aspects, methods of digital terrain mapping, and terrain effects on antenna characteristics.

Future communication and data transmission involving, for example low-flying aircraft, as well as remotely piloted vehicles, will make extensive use of digital terrain maps. Depending upon frequency of operation, characteristics of terrain near terminals or communication links may be utilized to provide some protection against intentional and unintentional interference from other transmitting sources.

Interpretation of experimental data requires understanding of features that influence performance of sensor and antenna. Theoretical contributions include time-harmonic and transient scattering from statistically rough ground and smoothly varying properties. Effects of ground foliage and of atmospheric conditions on the received signal are also relevant.

Analytical methods include full wave solutions, ray techniques and modal techniques, with an assessment, when possible, of errors incurred as the result of approximations. When solutions are purely numerical, they were accompanied by physical interpretation of the results. Contributions on the inverse problem of constructing terrain features from measured data are included.

PROGRAM AND MEETING OFFICIALS

CHAIRMAN: Professor A.W.Biggs
The University of Kansas
Space Technology Center
Raymond Nichols Hall
2291 Irving Hill Drive – Campus West
Lawrence, Kansas 66045
USA

MEMBERS

Dr K.Becker
Universität des Saarlandes
Fachrichtung 12
Elektrotechnik
6600 Saarbrücken
Germany

Dr L.Felsen
School of Engineering
Polytechnic Institute of New York
Farmingdale
N.Y. 11735
USA

Mr L.Hoivik
NDRE
Division for Electronics
P.O. Box 25
N-2007 Kjeller
Norway

Dr J.H.Blythe
GEC – Marconi
Great Baddow
Chelmsford, CM2 8HN
UK

ELECTROMAGNETIC WAVE PROPAGATION PANEL

CHAIRMAN: Dr H.J.Albrecht
FGAN
Wachtberg-Werthhoven
Germany

DEPUTY CHAIRMAN: Dr J.Aarons
L.G. Hanscom Field
Bedford
USA

HOST NATION COORDINATOR

Dr T.R.Larsen
NDRE, P.O. Box 25
N-2007 Kjeller
Norway

SESSION CHAIRMEN

Session I – TERRAIN EFFECTS ON ANTENNA CHARACTERISTICS
Dr Klaus D.Becker
Universität des Saarlandes
Saarbrücken, Germany

Session II – PROPAGATION EFFECTS IN TERRAIN MAPPING
Dr Leopold B.Felsen
Polytechnic Institute of New York
Farmingdale, New York, USA

Session III – THEORETICAL ASPECTS OF SCATTERING AND EMISSION FROM TERRAIN
Dr John H.Blythe
GEC Marconi Electronics Ltd
Chelmsford, Essex, UK

Session IV – METHODS OF DIGITAL TERRAIN MAPPING
Dr Hans J.Albrecht
FGAN
Wachtberg-Werthhoven, Germany

Session V – MEASUREMENT OF TERRAIN PARAMETERS
Mr Lars Hoivik
NDRE
Kjeller, Norway

CONTENTS

	Page
THEME	iii
PROGRAM AND MEETING OFFICIALS	iv
SESSION CHAIRMEN	v
TECHNICAL REVIEW	ix
	Reference

SESSION I – TERRAIN EFFECTS ON ANTENNA CHARACTERISTICS

THE EFFECTS OF STRATIFIED GROUND ON CHARACTERISTICS OF THE INVERTED L ANTENNA
by E.Niver and A.Hizal — 1

THE EFFECTS OF RE-RADIATION FROM HIGH RISE BUILDINGS AND TRANSMISSION LINES UPON THE RADIATION PATTERN OF MF BROADCASTING ANTENNA ARRAYS
by J.S.Belrose, W.Lavrench, J.G.Dunn, C.W.Trueman and S.J.Kubina — 2

Paper 3 is cancelled

SURFACE FIELDS AND RADIATION PATTERNS OF A VERTICAL ELECTRIC DIPOLE OVER A RADIALLY VARYING GROUND SYSTEM
by C.Teng and R.J.King — 4

TERRAIN EFFECTS ON LOG-PERIODIC ANTENNA CHARACTERISTICS USING THE SINGULARITY EXPANSION METHOD
by K.D.Rech and K.J.Langenberg — 5

SESSION II – PROPAGATION EFFECTS IN TERRAIN MAPPING

THEORIES OF GROUND WAVE PROPAGATION OVER MIXED PATHS
by R.H.Ott — 6

HIGH-FREQUENCY SIGNAL PROPAGATION AND SCATTERING IN GUIDING CHANNELS
by L.B.Felsen — 7

GROUND WAVE PROPAGATION OVER IRREGULAR, INHOMOGENEOUS TERRAIN: COMPARISONS OF CALCULATIONS AND MEASUREMENTS AT FREQUENCIES FROM 121 kHz to 50 MHz
by R.H.Ott — 8

AN EXPERIMENTAL STUDY OF SURFACE WAVE PROPAGATION ON A LOW PERMITTIVITY MEDIUM
by J.Appel-Hansen and R.J.King — 9

MULTIPATH ANALYSIS OF ILS GLIDE PATH
by T.Breien — 10

AIRBORNE MEASUREMENTS OF ELECTROMAGNETIC WAVE REFLECTIONS FROM LAND AND SEA WATER
by A.L.Johnson — 11

SESSION III – THEORETICAL ASPECTS OF SCATTERING AND EMISSION FROM TERRAIN

SCATTERED RADIATION FIELDS FROM ROUGH SURFACES – FULL WAVE SOLUTIONS
by E.Bahar — 12

Reference

THEORETICAL ASPECTS OF TRANSIENT RADIATION AND SCATTERING IN LOSSLESS TWO MEDIUM HALF SPACES
by M.Döbrich and K.J.Langenberg 13

Papers 14, 15 and 16 are cancelled

THEORETICAL DISTRIBUTION FUNCTIONS OF MULTIPATH PROPAGATION AND THEIR PARAMETERS FOR MOBILE RADIO COMMUNICATION IN QUASI-SMOOTH TERRAIN
by R.W.Lorenz 17

ON THE INFLUENCE OF SURFACE STATISTICS, GROUND MOISTURE CONTENT AND WAVE POLARISATION ON THE SCATTERING OF IRREGULAR TERRAIN AND ON SIGNAL POWER SPECTRA
by K.J.Hortenbach 18

THEORETICAL MODELLING AND EXPERIMENTAL DATA MATCHING FOR ACTIVE AND PASSIVE MICROWAVE REMOTE SENSING OF EARTH TERRAIN
by J.A.Kong, L.Tsang, M.Zuniga, R.Shin, J.C.Shiue and A.T.C.Chang 19

SESSION IV – METHODS OF DIGITAL TERRAIN MAPPING

SOME OF THE PROBLEMS IN DIGITAL TERRAIN MODEL CONSTRUCTION
by G.B.Thersby 20

Paper 21 is cancelled

AZIMUTH BEAMWIDTH EFFECT ON RADAR SENSED TERRAIN HORIZON PROFILES
by G.E.Carlson and P.W.Sapp 22

BIOLOGICAL AND GEOPHYSICAL FACTORS OF ELECTROMAGNETIC WAVE PROPAGATION AND THEIR USE IN DIGITAL DATA BANKS
by E.R.Küsters 23

PREDICTION OF RADAR COVERAGE AGAINST VERY LOW ALTITUDE AIRCRAFT
by J.R.Delaney and M.L.Meeks 24

RADIO NETWORK AND RADIO LINK SURVEYS DERIVED BY COMPUTER FROM A TERRAIN DATA BASE
by C.E.Dadson 25

VHF/UHF PATH-LOSS CALCULATIONS USING TERRAIN PROFILES DEDUCED FROM A DIGITAL TOPOGRAPHIC DATA BASE
by F.H.Palmer 26

SESSION IV – ROUND TABLE DISCUSSION RTD

SESSION V – MEASUREMENT OF TERRAIN PARAMETERS

ELECTRIC FIELD COMPONENTS IN PRESENCE OF A SEA-SEA BOTTOM INTERFACE AT ELF
by G.Tacconi 27

RADAR ALTIMETER MEASUREMENTS
by F.Thomsen 28

A LASER PROFILOMETER FOR DIGITAL TERRAIN MAPPING
by B.Rubin and M.W.Fitzmaurice 29

AN EXPERIMENTAL INVESTIGATION OF MULTI-PATH SCATTERING AT L-BAND
by P.Lewis 30

Reference

Paper 31 is cancelled

DIFFRACTION PHENOMENA DURING MULTIPATH FADING
by H.G.Giloi — 32

Appendix A: QUESTIONS, COMMENTS, AND DISCUSSIONS ON PAPERS — A-1
Session I — A-1
Session II — A-3
Session III — A-6
Session IV — A-11
Round Table — A-14
Session V — A-20

Appendix B: LIST OF ATTENDEES — B-1

TECHNICAL REVIEW

1. INTRODUCTION

This meeting was sponsored by the Electromagnetic Wave Propagation Panel and was held at the Spatind Mountain Hotel in Spatind, Norway. The meeting began on Monday, September 10, and continued with daily meetings through Friday, September 14. The Program for the meeting was excellently prepared by a committee chaired by Professor Albert W. Biggs.

The purpose of this review is to present a summary of the highlights of the meeting.

2. SESSION I

The first paper in this session was presented by Dr. A. Hizal. He described a method for calculating current distributions for inverted "L" antennas. The reflection coefficient approximation was combined with a Hallen type integral equation in the calculations. Although the antenna base was very close to the surface of the ground, the results were in good agreement with those of J.R. Wait.

The second paper described some experimental measurements of the effects of re-radiation from high rise buildings and power lines. Wire grid models, on a copper ground plane, represented these structures with scale factors of 300 (buildings) and 600 (power lines with associated towers). A building with a 300 foot height and an area of 100 by 100 feet was modeled by a wire grid with a 12 inch height and an area of 4 x 4 inches. Power line models were radiated with 516 MHz sources which represented MF stations at 860 kHz (CJBC). Numerical modeling by the method of moments agreed with experimental results.

The third paper presented results obtained from the compensation theorem (Monteath) and integral equation (Hufford) with the surface impedance concept. The antenna was a conventional vertical dipole with a radial wire ground system. The applicability of the surface impedance concept was discussed at some length in the session and round table discussions.

The last paper of this session described the terrain effects on a log periodic antenna. Results included transient responses to impulsive excitation.

3. SESSION II

The first paper of this session introduced the surface impedance concept again. The limitations of the surface impedance boundary condition were not described by R.H. Ott in his presentation, but these omissions were introduced by L. Felsen during subsequent discussions. Programs WAGNER, MODKED, BURANT, and ZWEI are available for the integral equation, mode-match, layered media, and knife edge algorithms.

The second paper was an excellent presentation by L. Felsen on guided waves. He described hybrid formulations in terms of rays and modes.

R. Ott presented the third paper with theoretical results obtained with an integral equation method for irregular and inhomogeneous terrain. The data points for his computer program seemed to be a limitation of this method.

The fourth paper described an experimental modelling system to simulate surface wave propagation.

The fifth paper described a new theoretical method for rough surface scattering. The terrain is modeled as a set of plane wedges. The mathematical method, known as the Uniform Theory of Diffraction (UTD), resolves the scattered signal as a reflected signal (geometrical optics) and a diffracted signal (dependent on wedge shape). Measurements and results were in close agreement. This method complements that of R. Ott.

The last paper in this session related to multipath fading from land and sea reflections. The link from airplane to satellite was described in terms of direct, reflected, and diffuse scatter paths. Continuous multipath fading was encountered over water, while sporadic multipath fading was encountered over land.

4. SESSION III

The first paper in this session was a theoretical analysis of the scattered radiation fields from rough surfaces. The model was developed from local modal expansions and asymptotic series expansions. The source and observer were away (above) from the surface.

Transient radiation fields from multipole sources in lossless media were described in the second paper. Results were similar to those of similar problems. The major contribution was the development of computer programs with Fast Fourier Transforms.

The third paper was an excellent study on the different distribution functions of multipath propagation across small and medium cities, open areas, and forests. The functions considered were the Weibull distribution, the Nakagami-m distribution, and the "Suzuki distribution", which was a mixture of Rayleigh and log-normal distributions. Measurements in the regions mentioned above were correlated with the three distribution functions for the best fit.

Ground moisture, surface statistics, and wave polarization were parameters included in a model for scattering from irregular terrain in the fourth paper in this session. Comparisons were made for

Gaussian and natural terrain statistics. Complex reflection coefficients were used for arbitrarily oriented surfaces, and varying ground moisture contents were coupled with these comparisons.

The last paper in this session introduced a theoretical model for remote sensing with radar imagers and microwave radiometers. Volume scattering was included with two layer media (snow on soil, alfalfa above moist ground, and layers of snow).

5. SESSION IV

The first paper described two methods for terrain data storage. Several aspects were identified with respect to the user and the software designer. These aspects included ground heights, surface culture, accuracies required, and data bank formats.

Terrain avoidance systems for low flying airplanes were discussed in the second paper. These systems include an azimuth-scanning, forward-looking, monopulse radar to sense the terrain horizon profile.

The third paper included vegetation parameters in data banks for 150 x 95 meter segments. The radar clutter data bank classified soil cover as large cities, villages, various forests, farms, swamps, fresh water, and sea water. These data points can be combined with different microwave propagation models.

Related radar studies were found in the fourth paper with radar coverage against low flying airplanes. Refraction, diffraction, and multipath (reflection) limits were evaluated. Experimental results demonstrated the validity of the model described.

The fifth paper described a method for calculating mobile radio coverage areas with computers and topographical data bases. The elements of the method included a terrain data base, radio path calculations, and presentation of results in a format comprehensible to the user. Storage and coding of terrain data was achieved with negligible errors.

The last paper in this session incorporated a digital topographic data base for extracting terrain profiles. These were used to calculate VHF/UHF path losses.

6. SESSION V

The first paper, presented by A.W. Biggs for G. Tacconi, was a study of extremely low frequencies with source and receiver at varying ocean depths. Frequencies of 2, 6, and 14 Hz were introduced into analytical formulations. Attenuation results compared favorably with experimental results.

A radar altimeter in a satellite was analyzed for ice and snow covered regions in the second paper. The theoretical formulations did not include depolarization and scattering by the rough surface.

The third paper described a laser profiler for the NASA Space Shuttle. Anticipated results were presented for snow-ice, land, and ocean surfaces.

Some experimental results of multi-path scattering at L-Band were included in the fourth paper. P. Lewis made holographic records of the scattered signal. The computer processing confirmed the experimental measurements.

The last paper was an excellent description of knife edge diffraction and fading in forested areas. Scintillation fading due to small inhomogeneities were also presented. Measurements and theoretical results provide useful prediction data for line-of-sight relay links.

7. ROUND TABLE DISCUSSION

The round table discussion was guided by H. Albrecht, who was the chairman. He was capable assisted by F. Palmer, J. Belrose, L. Høivik, and L. Felsen.

The best aspects of the meeting were the extensive and valuable comments from the participants during this round table discussion, during the discussion periods, and after the formal presentation of each paper. Several stimulating discussions were the results of capable leadership by the session chairman and by the high calibre of the participants.

A.W. Biggs
University of Kansas
Lawrence, Kansas USA

THE EFFECTS OF STRATIFIED GROUND ON CHARACTERISTICS OF THE INVERTED L ANTENNA

Edip Niver* and Altunkan Hızal
Electrical Engineering Department
Middle East Technical University
Ankara, Turkey

SUMMARY

Characteristics of an inverted L antenna over a homogeneous moist ground, a poor ground and a two-layered ground consisting of a frozen layer of earth above a moist earth are studied numerically using an integral equation formulation. The feed of the antenna is elevated from the base of the antenna to avoid the discontinuity in the current at the feed and to increase the accuracy of the reflection coefficient approximation used in the formulation. The current distributions are calculated by solving a Hallen's type integral equation. The input admittance and radiation patterns are calculated as a function of the length of the horizontal section. The results showed that the inverted L antenna studied possess useful impedance and radiation characteristics.

1. INTRODUCTION

Previously, King and Harrison (1969) solved bottom-fed inverted L antenna above perfectly conducting ground using a transmission line analogy. Also, Simpson (1971) formulated and solved the antenna considered by King and Harrison (1969) by integral equation method. Egashira and Taguchi (1978) obtained an integral equation solution to an umbrella type top loaded vertical antenna. In all these integral equation formulations the common feature is the position of the feed and the perfectly conducting ground. Here, the interest is on the effect of the imperfect ground on the characteristics of the inverted L antenna.

The inverted antenna considered is shown in Fig.1. It consists of the vertical structure of length h, feed at h_o from the base and of the horizontal top loading element of length ℓ. The elevated feed avoids the difficulty in the modelling of the feed in the presence of an imperfect ground. Moreover, the elevated feed antenna may possess certain advantages such as decreased sensitivity of the input impedance to the changes in the ground parameters. Hızal (1974) investigated the elevated feed vertical antennas over imperfect ground.

The current distribution, the input admittance and the radiation pattern of such antennas will be studied by an integral equation approach. For this purpose a Hallen's type integral equation derived by Niver (1979) is used for the inverted L antenna. In this integral equation the effect of the ground is taken into account by a reflection coefficient approximation which is appropriate for the individual Hertzian elements of the antenna.

2. INTEGRAL EQUATION FORMULATION

The vertical and horizontal structures are described by different coordinate systems as (x,y,z) and (u,v,w) and their corresponding surfaces as S_1 and S_2, respectively. The integral equation corresponding to δ-gap excited antenna confined to surface S_1 is (Niver, 1979)

$$\int_L I(s')\Pi_1(z,s')ds' + Q_1 \cos(k_o z) + Q_2 \sin(k_o z) = -j\frac{V}{60}\sin k_o|z-h_o| \tag{1}$$

and on surface S_2 is

$$\int_L I(s')\Pi_2(u,s')ds' - Q_1 \sin(k_o h)\sin(k_o u) + Q_2 \cos(k_o h)\sin(k_o u) + Q_3 \cos(k_o u)$$

$$= -j\frac{V}{60}\cos k_o|h-h_o|\sin(k_o u) \tag{2}$$

where $k_o = (\varepsilon_o\mu_o)^{1/2}$ and V is the applied voltage. The kernels of these equations are given by

$$\Pi_1(z,s') = G(z,s')\hat{z}\cdot\hat{s}' + \int_0^z \cos k_o(\zeta - z)\,\bar{\nabla}_{tz}\cdot G(\zeta,s')\hat{s}'\,d\zeta \tag{3}$$

and

$$\Pi_2(u,s') = G(u,s')\,\hat{u}\cdot\hat{s}' + \int_0^u \cos k_o(\zeta - u)\,\bar{\nabla}_{tu}\cdot G(\zeta,s')\,\hat{s}'d\zeta$$

$$+ \sin(k_o u)\int_0^h \sin k_o(\zeta - h)\bar{\nabla}_{tz}\cdot G(\zeta,s')\,\hat{s}'\,d\zeta \tag{4}$$

where $\bar{\nabla}_{tz} = \hat{x}\frac{\partial}{\partial x} + \hat{y}\frac{\partial}{\partial y}$ and $\bar{\nabla}_{tu} = \hat{v}\frac{\partial}{\partial v} + \hat{w}\frac{\partial}{\partial w}$

The Green's function, using the reflection coefficient approximation, is given by (Niver and Hızal, 1978)

*Presently with the Department of Electrical Engineering, Polytechnic Institute of New York, Brooklyn, N.Y. 11201

$$G(s,s') \approx \frac{e^{-jk_o r^+}}{r^+} - \cos 2\alpha \, R(\theta) \frac{e^{-jk_o r^-}}{r^-} \tag{5}$$

where r^+ is the distance from the Hertzian element at s' along the center of the antenna to the field point at s on the surface of the antenna. r^- is the corresponding distance from the geometrical image of the Hertzian element to the field point. α is the angle between the horizontal direction and the direction along which the Hertzian element is directed. θ is the angle between r^- and the vertical direction. $R(\theta)$ is the Fresnel reflection coefficient for the polarization parallel to the plane of incidence. which is expressed by

$$R(\theta) = (\cos\theta - K_e)/(\cos\theta + K_e) \tag{6}$$

where K_e is the effective surface impedance of the ground normalized by the intrinsic impedance of the free-space. For a homogeneous ground it can be shown that

$$K_e = K_1 = u_1/\varepsilon_{r1} = (\varepsilon_{r1} - \sin^2\theta)^{1/2}/\varepsilon_{r1} \tag{7}$$

For a two-layered homogeneous ground K_e becomes

$$K_e = K_1\,(K_2 + jK_1 \tan k_o u_1 d)/(K_1 + jK_2 \tan k_o u_1 d) \tag{8}$$

where K_2 is given by an expression similar to (7) with the replacement of ε_{r1} by ε_{r2}.

The reflection coefficient approximation in various forms is widely used in applications. Miller et al (1972) and Hızal (1974) have applied it to vertical antennas over homogeneous and inhomogeneous grounds. It is found that this method yields sufficiently accurate results for the current distributions within 10% of the exact results at some small fraction of the computer time (~ 1%) required for the rigorous treatment. Sarkar and Strait (1975) concluded that the reflection coefficient approximation for evaluation of self and mutual impedances of wire antennas with assumed current distributions is accurate within 10% of the rigorous Sommerfeld approach if the height of the antenna elements above ground are no less than $0.7|\sqrt{\varepsilon}|\lambda$, where ε is the complex dielectric constant of the ground.

In numerical solution,method of moments is used where the unknown current distribution I(s') is expanded in subsectional parabolic basis functions (Chang and Wait, 1970). Vertical and horizontal sections are modelled by N_v and N_h number of segments. Equations (1) and (2) are matched at N_v+1 and N_h+1 points, respectively. Assuming the continuity of the axial current at the junction $I(z=h) = I(u=o)$ holds. This procedure results in $(N_v + N_h - 1)$ unknowns where the condition that current vanishes at the ends of the antenna is taken into account. These unknown coefficients in the expansion of the current distribution together with the constants Q_1, Q_2 and Q_3, which are also unknown, form (N_v+N_h+2) linear algebraic equations.

3. NUMERICAL RESULTS

A computer program is developed to evaluate the current distribution along the inverted L antenna. As a check it is used to solve the inverted L antenna placed on perfectly conducting plane. A very satisfactory agreement is obtained for the previously reported results for such an antenna of $\lambda/4$ length (King and Harrison, 1969 and Simpson, 1971) fed from the end. The end fed geometry is treated by appropriate modification in the computer program and equations (1) and (2). Moreover, the results for an inverted L antenna, with a very small horizontal section, placed on an imperfect ground are compared with those for a vertical antenna of the same dimensions placed on the same ground. A good agreement is obtained between the two results.

The effects of top loading for half and quarter wave vertical antennas placed above homogeneous ground are studied by two computer programs: one is based on equations(1) and (2) for the inverted L antenna and the other is for the vertical antenna which is based on a reduced form of (1). The results for the current distributions are shown in Figs. 2 and 3. It is seen that bending the vertical antenna into an inverted L type has little effect on the shapes of the current distribution but their levels are greatly influenced.

Additional results concerning the effects of adding horizontal top sections to vertical antennas are shown in Table 1 for half-wave and in Table 2 for quarter-wave antennas, respectively. In these tables results of top loading effect are compared with vertical antennas fed at the same position but having no top loading elements. The antenna length is an important factor, as for short antennas (~ $\lambda/4$) the top loading acts to increase capacitive susceptance whereas for longer antennas (~ $\lambda/2$) it decreases the susceptance. Additionally, as observed in linear antennas, the current distribution of the half-wave inverted L antenna converges rapidly during the numerical solution for the antenna model of few segments but in the case of $\lambda/4$ antenna more segments are necessary to obtain a stable solution. Hence 8 segments (N_v = 6, N_h = 2) for $\lambda/2$ antenna and 16 segments (N_v = 12 , N_h = 4) for $\lambda/4$ antenna are used. Also, the computation time increases as the radius of the antenna decreases. This is due to the rapid variation of the integrands of (1) and (2).

It is also observed from Tables 1 and 2 that the effect of the horizontal section is to increase the radiation conductance in all cases. However, as the feed is lowered towards the base of the antenna the radiation conductance decreases. The input impedances are also indicated in Tables 1 and 2. It is seen that the radiation resistances decrease with top loading. If such antennas are to be fed by 50-75 ohms transmission lines for matching purposes the position of the feed and the length of horizontal section can be adjusted to obtain the desired input resistance.

A quarter-wave vertical antenna considered in Table 2 is also studied when it is placed over a frozen layer of earth above a semi-infinite moist earth. The thickness of the frozen earth is assumed to be 1 m. The shapes of the current distributions are similar to those for a homogeneous earth so only the results for the admittances and the impedances are given in Table 3. The behaviour of the results with loading is similar to that for the homogeneous moist earth presented in Table 2. Moreover, the effect of the frozen layer of earth is to increase the impedance values slightly. The impedance variations are more clearly shown in Figs. 6, 7 and 8.

The radiation patterns of the inverted L antenna in two principal planes are shown in Figs.4 and 5 for the half and quarter wave antennas, respectively. It is seen that the radiation density for the half-wave antenna (Fig.4) increases with loading towards the wide angle side of the inverted L section. Also, an overall increase in the radiation density is observed for all angles. For the quarter-wave antenna (Fig.5) the patterns seem to be symmetrical with respect to the vertical section with the increased radiation as the horizontal length decreases, which is the opposite effect of that for the half-wave antenna.

4. CONCLUSIONS

Inverted L antenna could be an alternative solution to shorten the physical height of vertical antennas above the ground without a significant sacrifice in its radiation and impedance characteristics. The parameters to be altered for various applications might be the length of the horizontal section, the feed location, the antenna elevation and the total length of the antenna. The effect of the ground on the input impedance of the antenna may be reduced by elevating the feed above the ground.

5. ACKNOWLEDGEMENT

The authors acknowledge the Department of Computer Engineering of the Middle East Technical University for providing the computing time in the IBM 370/145 computer.

REFERENCES

Chang, D.C., and Wait, J.R., 1970 *"Theory of a vertical tubular antenna located above a conducting half-space"*, IEEE Trans. Ant. Prop., AP-18, 182-188.

Egashira, S., and Taguchi, M., 1978, *"Hallen type integral equation for antenna composed of straight wires"*, 1978 Int. Symp. on Ant. and Prop., sendai, Japan, 129-132.

Hızal, A., 1974, *"Current distribution and impedance of monopole antenna on lossy ground"*, Int. J. of Electronics (England), 37 , 49-60.

King, R.W.P., and Harrison, C.W., 1969, *"Antennas and waves, a modern approach"*, The MIT Press, Cambridge, Massachusetts

Miller, E.K., Poggio, A.J., Burke, G.J., and Selden, E.S., 1972,*"Analysis of wire antennas in the presence of a conducting half-space. Part I. The vertical antenna in free-space"*, Can. J. of Physics, 50, 879-888.

Niver, E. 1979, *"A numerical study of oblique and inverted L wire antennas above stratified ground'*, Ph.D. Dissertation, Dept. of Elect. Eng., Middle East Technical University, Ankara, Turkey.

Niver, E., and Hızal, A., *"Current distribution and admittance of an oblique antenna above a stratified ground"*, Int. Conf. on Ant. and Prop. (London), IEE , 169 , 341-344. (1978)

Sarkar, T.K., and Strait, B.J., 1975, *"Analysis of arbitrarily oriented thin wire antenna arrays over imperfect ground planes"*, Tech. Rept. TR-75-15 , Syracuse Univ., New York.

Simpson, T.L., 1971, *"The theory of top-loaded antennas: Integral equations for the currents"*, IEEE Trans. Ant. Prop. AP-19, 186-190.

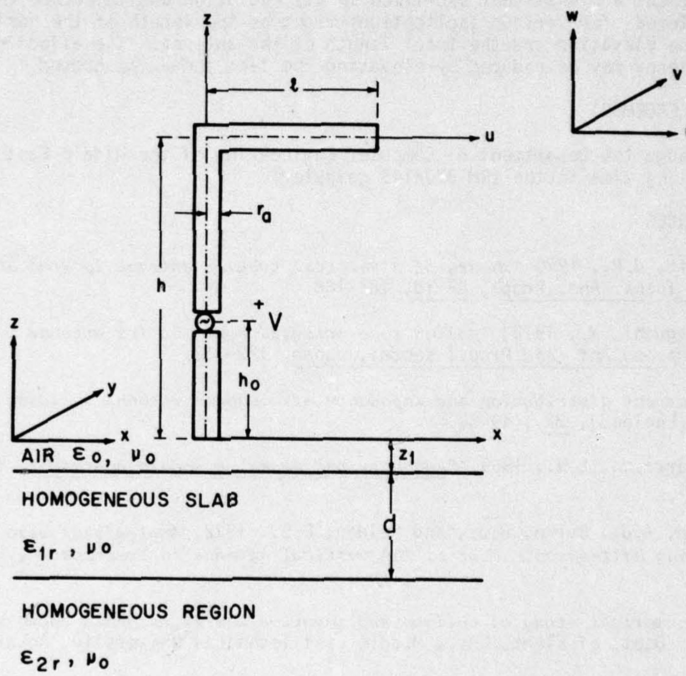

Figure 1 Geometry of the inverted L antenna above two-layered earth.

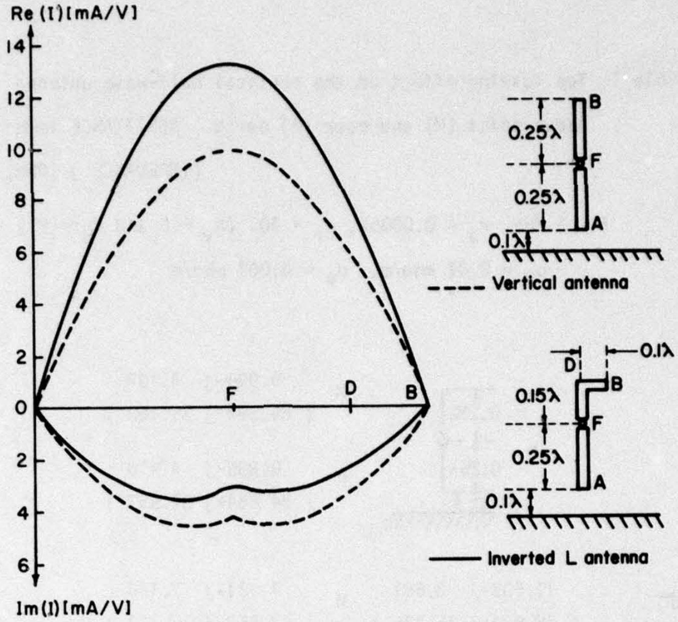

Figure 2 Current distributions for half-wave antenna* above moist earth.
*f = 3 MHz, $r_a = 0.0005\ \lambda$, ($N_v = 12$ and $N_h = 4$)
Moist earth ($\epsilon_r = 10$, $\sigma = 0.01$ mho/m)

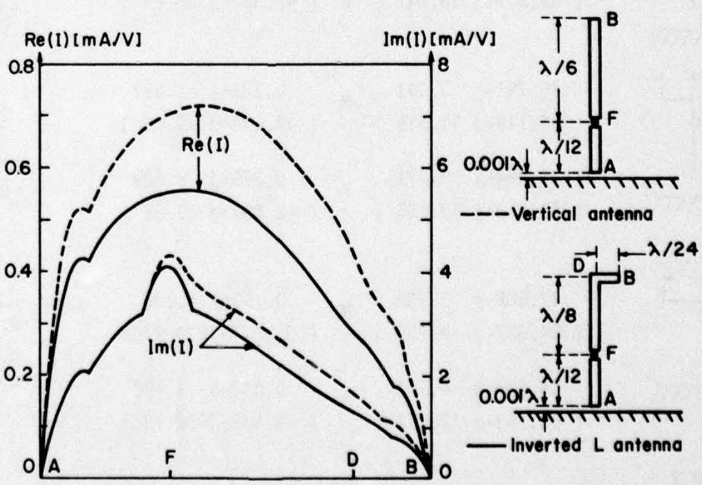

Figure 3 Current distributions for quarter-wave antenna* above moist earth.
*f = 3 MHz, $r_a = 0.005\ \lambda$, ($N_v = 12$ and $N_h = 4$)
Moist earth ($\epsilon_r = 10$, $\sigma = 0.01$ mho/m)

Table 1 Top loading effect on the vertical half-wave antenna above moist (M) and poor (P) earth ADMITTANCE [mmho] (IMPEDANCE) [Ohm]

$f = 3$ MHz, $r_a = 0.0005\lambda$, $\varepsilon_r = 10$, ($N_v = 6$ and $N_h = 2$)

$\sigma_M = 0.01$ mho/m, $\sigma_P = 0.001$ mho/m

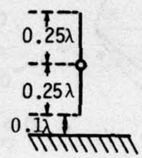		M	9.994-j 4.107 (85.594+j 35.180)	
		P	9.835-j 4.410 (84.654+j 37.957)	
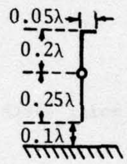	11.503-j 3.661 (78.934+j 25.126)	M	7.121+j 7.426 (67.263-j 70.151)	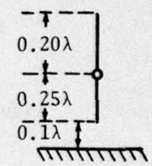
	11.411-j 4.068 (77.749+j 27.722)	P	7.370+j 7.597 (65.783-j 67.808)	
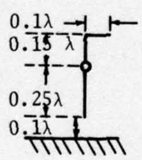	13.437-j 3.081 (70.701+j 16.214)	M	1.313+j 4.909 (50.870-j190.09)	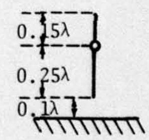
	13.450-j 3.639 (69.277+j 18.747)	P	1.302+j 4.971 (49.322-j188.23)	
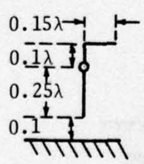	15.791-j 3.001 (61.119+j 11.615)	M	0.288+j 2.527 (44.644-j390.59)	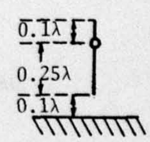
	15.984-j 3.771 (59.263+j 13.985)	P	0.279+j 2.539 (42.851-j389.02)	
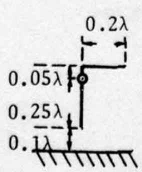	17.682-j 3.139 (54.827+j 9.735)	M	0.050+j 1.188 (35.877-j839.97)	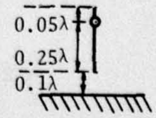
	18.229-j 4.143 (53.163+j 11.857)	P	0.048+j 1.190 (34.139-j838.79)	
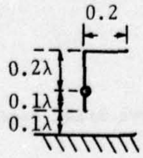	6.800-j 0.530 (146.16 +j 11.405)	M	0.132+j 2.036 (31.815-j489.02)	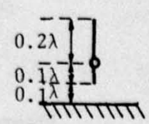
	6.977-j 0.890 (140.62 +j 17.904)	P	0.123+j 2.038 (29.508-j488.69)	

Table 2 Top loading effect on the vertical $\lambda/4$ antenna*
above moist (M) and poor (P) earth ADMITTANCE [mmho]
(IMPEDANCE) [Ohm]

*$f = 3$ MHz, $r_a = 0 \cdot 005\lambda$, $\varepsilon_r = 10$, ($N_v = 12$ and $N_h = 4$)

$\sigma_M = 0.01$ mho/m, $\sigma_P = 0.001$ mho/m

	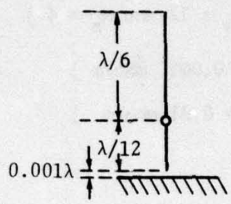	M	0.708+j 4.212 (38.827-j230.84)	
		P	0.452+j 3.926 (28. 96-j251.37)	
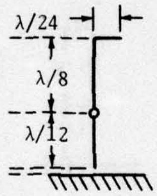	0.554+j 4.052 (33.144-j242.26)	M	0.383+j 3.559 (29.938-j277.71)	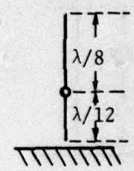
	0.358+j 3.798 (24.650-j260.96)	P	0.241+j 3.347 (21.409-j297.20)	
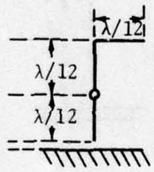	0.498+j 4.645 (22.840-j212.80)	M	0.193+j 3.680 (14.272-j270.93)	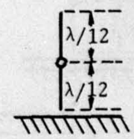
	0.310+j 4.369 (16.198-j227.69)	P	0.117+j 3.541 (9.358-j282.03)	
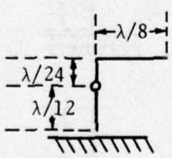	0.470+j 5.015 (18.535-j197.64)	M	0.073+j 2.303 (13.777-j433.72)	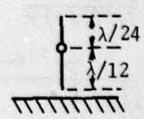
	0.285+j 4.690 (12.919-j212.40)	P	0.041+j 2.238 (8.365-j446.58)	
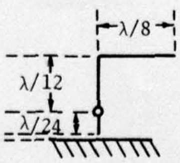	0.398+j 3.969 (25.919-j249.44)	M	0.149+j 2.526 (23.348-j394.45)	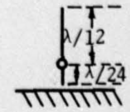
	0.214+j 3.632 (16.215-j274.32)	P	0.075+j 2.361 (13.481-j422.96)	

Table 3 The inverted L antenna* placed above two-layered earth ADMITTANCE [mmho] (IMPEDANCE) [Ohm]

*f =3 MHz, r_a = 0.005λ , (N_v = 12 and N_h = 4)

Frozen earth (ε_{r1} = 5, σ_1 = 0.001 mho/m)

Moist earth (ε_{r2} = 10, σ_2 = 0.01 mho/m)

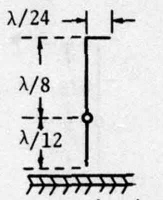	0.681+j 3.939 (42.668-j246.48)	0.447+j 3.481 (36.333-j282.59)	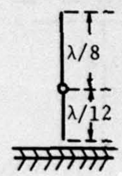
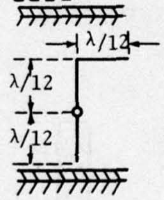	0.675+j 4.546 (31.945-j215.19)	0.237+j 3.635 (17.894-j273.88)	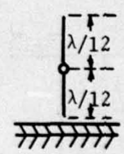
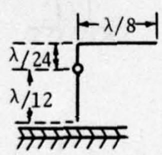	0.676+j 4.928 (27.336-j199.15)	0.093+j 2.283 (17.956-j437.16)	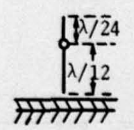
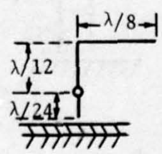	0.562+j 3.864 (36.887-j253.43)	0.202+j 2.477 (32.779-j401.02)	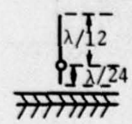
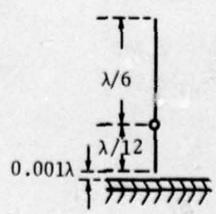		0.785 j 4.084 (45.413-j236.11)	

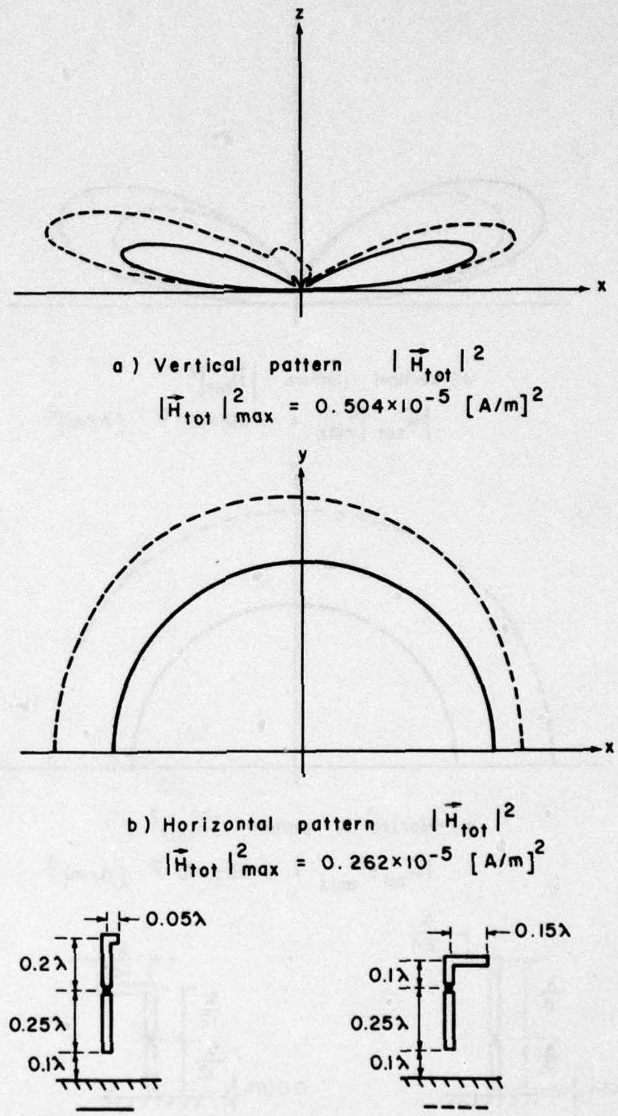

Figure 4 Radiation patterns for the half-wave inverted L antennas above moist earth.

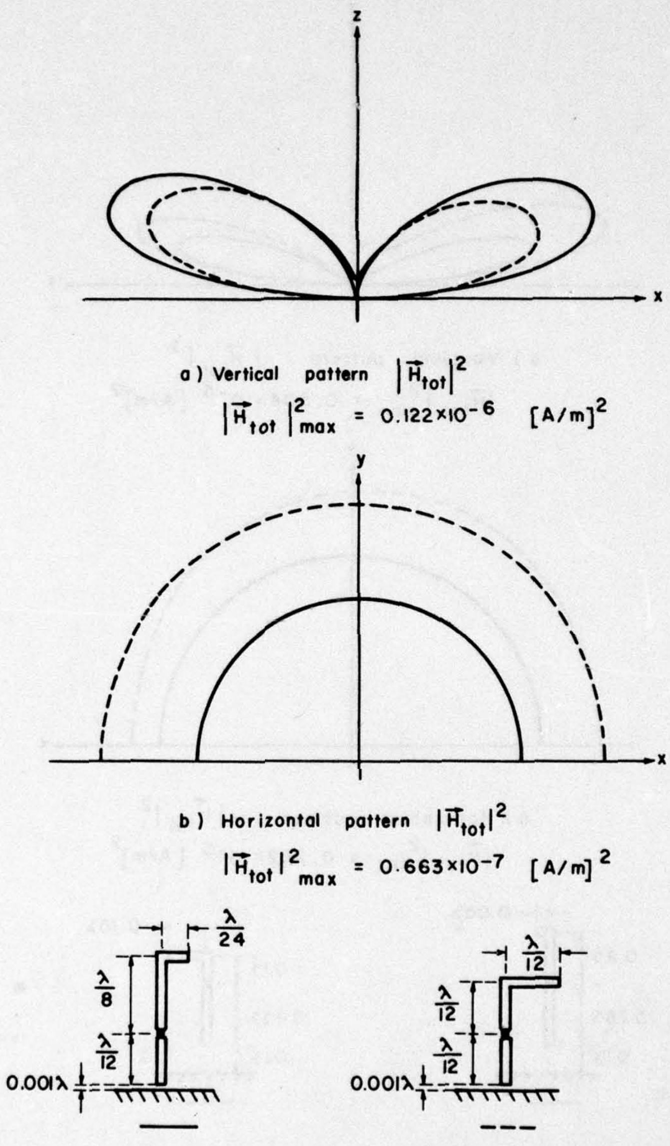

Figure 5 Radiation patterns for the quarter-wave inverted L antennas above moist earth.

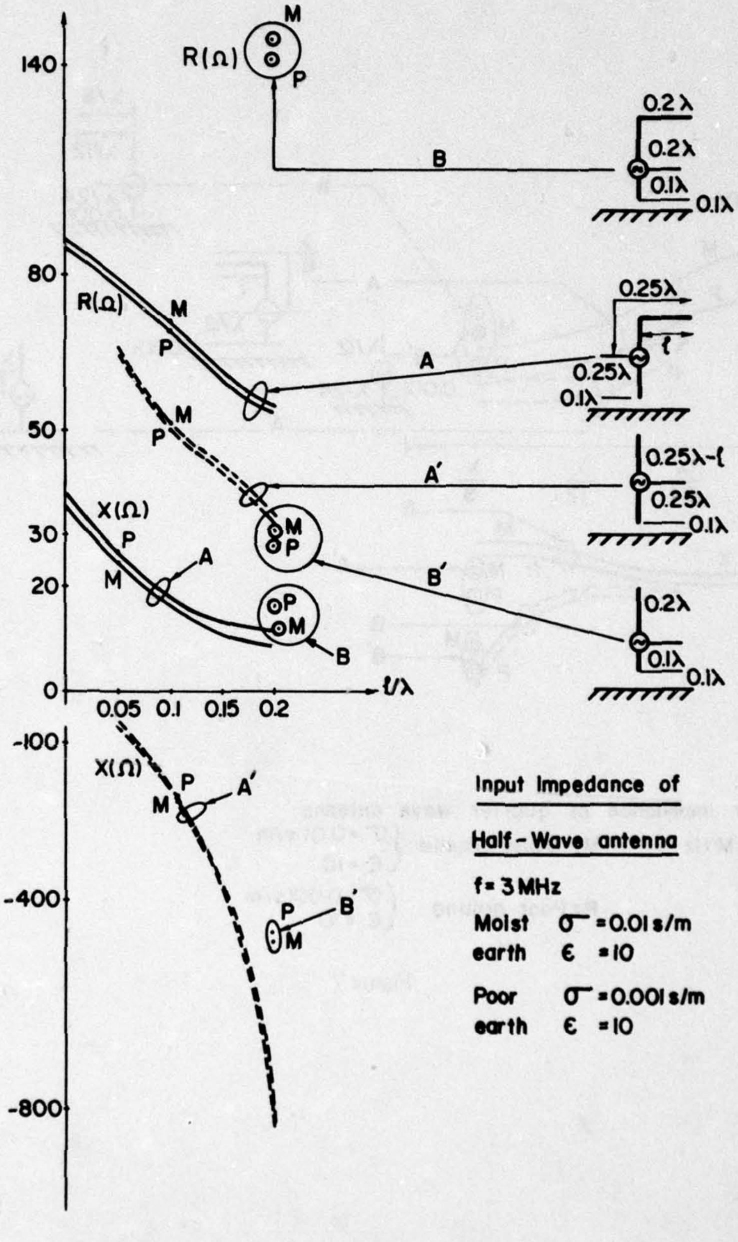

R(Ω)
M
P
140
0.2λ
0.2λ
B
0.1λ
0.1λ
80
R(Ω)
M
P
0.25λ
ℓ
A
0.25λ
0.1λ
50
M
P
0.25λ-ℓ
A′
0.25λ
0.1λ
X(Ω)
P
M
30
A
M
P
20
B′
P
M
0.2λ
0.1λ
0.1λ
B
0
ℓ/λ
0.05
0.1
0.15
0.2
-100
X(Ω)
P
A′
M
-400
P
B′
M
-800
Input Impedance of
Half-Wave antenna
f = 3 MHz
Moist σ = 0.01 s/m
earth ε = 10
Poor σ = 0.001 s/m
earth ε = 10

Figure 6

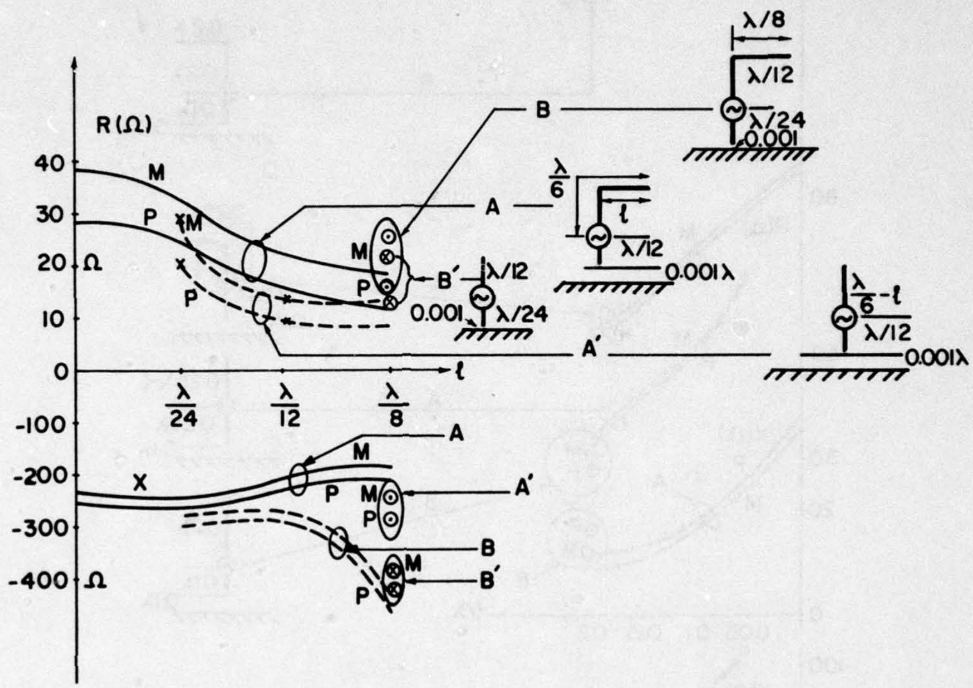

Input impedance of quarter wave antenna

f = 3 MHz **M = Moist ground** $\begin{cases} \sigma = 0.01\ s/m \\ \epsilon = 10 \end{cases}$

P = Poor ground $\begin{cases} \sigma = 0.001 s/m \\ \epsilon = 10 \end{cases}$

Figure 7

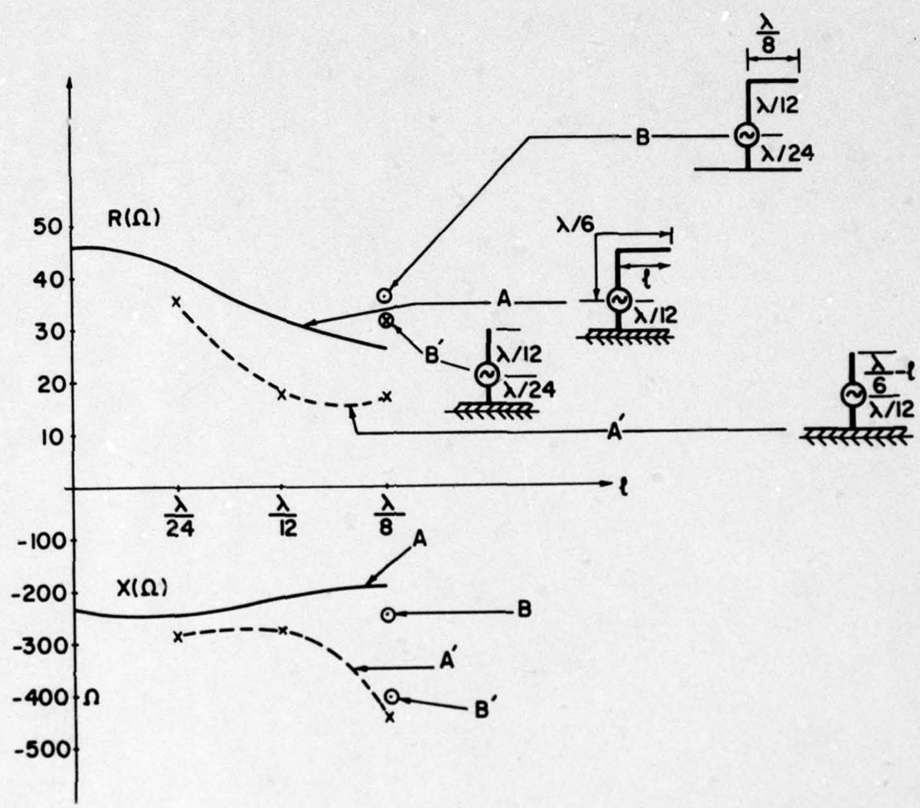

Input impedance of quarter wave antenna over a two layered earth

1st layer: frozen earth $\epsilon = 5$, $\sigma = 0.001$ s/m

Bottom layer: moist earth $\epsilon = 10$, $\sigma = 0.01$ s/m

Figure 8

THE EFFECTS OF RE-RADIATION FROM HIGHRISE BUILDINGS AND TRANSMISSION LINES UPON THE RADIATION PATTERN OF MF BROADCASTING ANTENNA ARRAYS

John S. Belrose
Communications Research Centre
Department of Communications
Ottawa, Canada

W. Lavrench and J.G. Dunn
Electromagnetic Engineering Section
Division of Electrical Engineering
National Research Council
Ottawa, Canada

C.W. Trueman and S.J. Kubina
Electromagnetics Laboratory
Department of Electrical Engineering
Concordia University/Loyola Campus
Montreal, Canada

SUMMARY

Many MF broadcasting directional arrays have been designed to a close tolerance in order to provide an adequate service and, at the same time, meet international treaty limits and domestic regulations with respect to permissible levels of radiation in particular directions, which could cause interference to listeners in the broadcast coverage area of an adjacent station operating on the same frequency. With population growth and the encroachment of "civilization" on once isolated transmitting sites, re-radiation from tall buildings, power lines and other structures can result in distortion of the pattern, and in difficulty with maintaining an adequate null in the directional pattern to minimize interference. If the re-radiator is extended, e.g., a power line, and close to the transmitting antenna, even the main beam can be adversely affected, and as well the pattern of an omni-directional antenna.

This paper describes experimental measurements employing antenna modelling techniques on the re-radiation from model highrise buildings and power lines, constructed using scale factors of 300 and 600 respectively. It is found that highrise buildings having typical cross-sectional dimensions of 100 x 100 feet and 100 x 400 feet in full scale are resonant in the middle of the MF broadcast band (about 1000 kHz) if the building height is 176 feet. Since this is a typical height for a highrise building, re-radiation can be strong, and, depending on the requirements, buildings located ten or more wavelengths (3 kilometers) from the MF broadcasting array could affect the far-field pattern. High voltage power transmission lines (500 kV systems) typically employ towers of height 177 feet spaced about 900 feet. The towers are electrically connected at their tops by a "sky wire" which forms the "ground" for the three phase power system. The towers, the connecting sky wires and their image in the ground therefore form loops which fortuitously are 2λ resonant at about 860 kHz, and in fact, the 3λ and 4λ resonances also fall within the broadcast band. A long power line can be thought of as a system of over-coupled, staggered tuned loops, and if the resonant frequency of the power line is that of a nearby broadcast station, the effects of re-radiation on the pattern of the MF broadcast antenna could be large.

Numerical modelling by the method of moments has given good agreement with experiment although it is difficult to calculate the re-radiation from extended structures like power lines. It is also important to realize that the experimental and numerical modelling work to date represent a worst case situation, since the "earth" is perfectly conducting and the structures employed are either insulated from or connected to it. An important part of the research, yet to be undertaken, is to establish the relation between results presented here, and the real world situation; and as well to investigate ways and means of reducing the effects of re-radiation.

1. INTRODUCTION

This problem has been of concern to broadcasters, broadcast consultants and to the Broadcast Spectrum Engineering Methods and Standards Division of the Telecommunications Regulatory Service for some time. While various researchers have attacked the problem in different ways, including full scale experimental studies as well as experimental and numerical modelling, little has been published on the subject and the significance of work that has been published (or is available) is difficult to assess.

Prestholdt [1] discussed the effects of re-radiation from television towers and other structures upon direction antennas, and suggested ways of reducing these effects. Alford and French [2] modelled power transmission lines, excited them, and investigated ways to reduce the radiation from them. Flood and Field [3] carried out an experimental study of backscatter from conducting objects having large cross-sectional dimensions with respect to the wavelength. King [4] has demonstrated that inductive loading can reduce the re-radiated field in the equatorial plane of a parasitic monopole re-radiator ... such detuning techniques were the basis of a U.S. patent by Alford and Jasik [5] in 1952.

In spite of the apparent extent of this early work, the importance and magnitude of re-radiation effects on the directional and omni-directional patterns of broadcast antenna arrays were more of a question of hearsay than experimental fact. A great deal of attention has been given to detuning techniques [2,4,5,6 and 7], and little attention to clearly establishing the magnitude of the problem, and to developing predictive techniques to estimate pattern distortion. Some exceptions are the work of Jones and Hicks [8] who were concerned with re-radiation effects of power lines; and A.D. Ring & Associates [9] who tried to calculate the backscatter from buildings of various shapes, by calculating the backscatter from an "equivalent ellipsoid", and then employing methods given by Crispen and Maffet [10].

Most of the early work was concerned with backscatter from conducting objects, and thus in order to derive the effects of this re-radiation, on pattern distortion, it is necessary to assume that the structure(s) behave as isotropic hemispherical sources. It is clear that there was a need for a fresh approach to the problem: (1) by experimental modelling of practical situations that more closely relate to the problem, viz. the effect of re-radiation on pattern distortion; and (2) by numerical modelling employing the tools of present day electromagnetics, such as wire grid modelling and method of moment analysis which have been developed for computer analysis.

The work reported here was started in June 1977. A considerable amount of experimental data employing antenna modelling techniques has been amassed (Belrose [11]), measuring null filling as well as scalloping of the main beam due to re-radiation from thin towers, buildings of various cross-section and height and power lines with and without skywires (the "ground wire" connected to the top of the towers), and with and without power carrying wires, for various distances from the broadcast array.

A particular example, of interest to Ontario Hydro and the Canadian Broadcasting Corporation, concerns the EHV (500 kV) power lines recently constructed that run near to the CBL/CJBC AM broadcast station near Hornby, Ontario (Figure 1). This situation has been modelled (Figure 2) and the pattern distortion measured. Hydro Quebec lines are reportedly affecting the directional pattern of an AM station near Shawinigan Falls, Quebec; and new power lines proposed for installation by Calgary Hydro, will run near to directional antennas in Edmonton and Calgary. It is clear, therefore, that there was a real requirement for research work in this area, c.f. Elder [12].

A first report of our work, on measurements made in an anechoic chamber, at the University of Toronto, was given by Balmain and Belrose [13]. This present report gives some results that more closely match full scale situations measured on an outdoor antenna pattern range, as well as some of the results so far obtained by numerical modelling.

2. THE EXPERIMENTAL TECHNIQUE

The experimental measurements were made employing an outdoor ground level antenna pattern range, a wire grid about 70 feet by 200 feet in size containing at one end a flush mounted 20 foot diameter turntable (Figure 2). Scale model frequencies of 300 and 600 MHz were used, which is the scale factor for a broadcast frequency of 1 MHz. The smaller scale factor was used to study re-radiation due to monopoles and buildings, the larger scale factor to measure re-radiation effects due to power transmission lines ... so that as many hydro towers as possible could be mounted on the turntable.

Two types of "broadcasting arrays" have been modelled to illuminate the object(s) whose scatter characteristics are under investigation. In situations where the scatter results in "null filling" of the directional array, a two-element array was used to produce a figure-of-eight pattern with minimum approaching -40 dB. After the source of re-radiation is placed in the vicinity of the array, the signal appearing at azimuths of the original minima is assumed to be caused by the structure(s) under test. An example is given in Figure 3, which shows the modified pattern (solid line) which is to be compared with the original pattern (broken line) caused by re-radiation from a single building located in the main beam of the antenna array. The registration is relative signal strength on a dB scale. The height of the re-radiator is 12 inches (300 feet, in full scale for a scale model frequency of 300 MHz), and the distance from the array is 2 meters (2000 feet in full scale). The building had a uniform cross-section of 4 x 4 inches (100 x 100 feet).

The second type of transmitting antenna used was a single vertical radiator. This produces an omni-directional pattern which is useful to measure the amount of scalloping produced by nearby objects. The curves in Figure 4 show the modified pattern (solid line) which is to be compared with the omni-directional pattern (dashed line) for a building 2 meters (2000 feet) from the antenna. The registration is relative field strength on a linear scale. In this case, the building was of height 10 inches (250 feet) and had a cross-sectional dimension of 4 x 16 inches (100 x 400 feet) with the wide side of the building facing the antenna. Since the signal at a given distance from an omni-directional monopole antenna, in the absence of re-radiators, is constant in phase and amplitude, the scalloped pattern gives some information on the phase, as well as the amplitude of the re-radiated signal.

In situations where the scatter signal is to be measured directly, the direct signal from the omni-directional antenna, with no re-radiator present, can be cancelled out, by introducing a signal directly into the receiver, and adjusting its amplitude and phase to "null out" the received direct signal. After the source of re-radiation is placed in the vicinity of the array, the signal appearing at all azimuths is assumed to be caused by the structure(s) under test. The system gain is adjusted so that the omni-directional field before cancellation is full scale on the record. The scatter field is therefore read directly as a fraction of the omni-directional field strength. An example of this kind of record is shown in Figure 5 which is the situation of re-radiation caused by a power line, the geometry for which is sketched in Figure 6. The scalloping of the omni-directional pattern, for this same situation is given in Figure 7.

Further detail on this power line model will be given below. For the present, our purpose is to note that the effects of re-radiation from tall buildings and power lines can be large, and that the effects are readily measurable on the NRC antenna pattern range and that these effects need to be taken into account when predicting the pattern of AM broadcast arrays.

Re-Radiation From Towers and Buildings

Measurements have been made for grounded monopoles of height ranging from 2 inches to 34 inches (50-900 feet full scale for a scale model frequency of 300 MHz), and for buildings of heights to 16 inches (400 feet). Buildings having two cross-sectional dimensions have been studied: 4 x 4 inches (100 x 100 feet), and 4 x 16 inches (100 x 400 feet). The effects due to two or more buildings have also been measured. Some of the results obtained are shown in Figures 8, 9 and 10. These diagrams illustrate some

important facts so far obtained.

In Figure 8, we show the signal scattered into the null of the figure-of-eight antenna pattern for monopoles of various heights (curve 1), and for buildings (curves 2, 3 and 4). The geometry was the same for all these measurements. The single building or the monopole was located in the maximum of the antenna pattern, at a distance of 2 meters (2000 feet) from the antenna array. We note that the thin monopole exhibits a sharp resonance at about 0.24λ, and that the buildings scatter more strongly for heights less than this, but for greater heights, there is no sharp decrease in the scatter signal. The various curves for buildings (curves 2, 3 and 4) are for: a building of square cross-section 4 x 4 inches (100 x 100 feet) curves 2; a building of rectangular cross-section 4 x 16 inches (100 x 400 feet), with the wide side towards the array (curve 3) and with the narrow side towards the array (curve 4). There seems to be very little difference between buildings having these cross-sections. The increase of scatter for the taller buildings with the narrower dimension towards the array is very likely brought on by the fact that, although the centre of the building is at a constant distance in all cases, the near face of the building is closer in the broadside orientation. A series of patterns were also measured for various angular positions of a 10 inch (250 feet) building. No significant variations in scatter level were noted, other than a small gradual increase as the narrow side of the building came to face the array.

A building height of 0.18λ has a physical height of 176 feet at 1 MHz, and since this is a typical height for highrise buildings, such structures are resonant at broadcast frequencies.

The curve in Figure 9 shows the measured scatter signal, as described above, for a resonant building height 8 inches (200 feet in full scale) located in the main beam of the antenna at various distances (measured in wavelengths) from the antenna array. It will be noted that if the effects due to a building are to be such as to not cause a null filling >-35 dB, the building must be at a distance of >10λ (>3 kilometers from the antenna array for a broadcast frequency of 1 MHz).

If there is more than one building, the resultant pattern distortion is like that for a multi-element antenna array; where all structures must be considered as a part of the antenna system: which comprises the broadcast array and each of the parasitically excited re-radiators.

The various structures, monopoles and buildings, modelled in our study were grounded, since this is the situation in real life. Although the efficiency of the "grounding" of a large structure, like a highrise building is unknown, it is likely to be reasonably well grounded, since water pipes, the ground wire of the electrical wiring, sewer pipes, etc. are grounded. The steel work is however probably not so well grounded. The earlier work of Flood and Field [3] considered insulated base re-radiators, and their results for monopoles show resonance at λ/2 and λ, instead of λ/4 and 3/4λ heights as we have observed for grounded re-radiators, see Figure 10.

Re-Radiation from Power Lines

The effect of high voltage power lines on the directional pattern of broadcast stations is much more complicated. EHV power lines (500 kV systems) typically employ towers of height 177 feet spaced 900 feet in Eastern Canada. Power lines in the prairies typically employ shorter towers (110 feet) but longer spans (1300 feet), but the net effect is the same for reasons which we shall see. The towers are electrically-connected at their tops by a "skywire" which forms the "ground" for the three phase power system. Fortuitously, the towers, the connecting skywires and their image in the ground, form "loops" which are 2λ resonant in the middle of the broadcast band (about 860 kHz for the power line studied). The 3λ and 4λ resonances also fall within the broadcast band (at frequencies of about 1130 and 1455 kHz). A long power line can therefore be thought of as a system of over-coupled, stagger-tuned loops, and if the resonant frequency of the power line is that of a nearby broadcast station, the effects of re-radiation on the pattern of the MF broadcast antenna could be large.

We have already given results for a particular situation: the broadcast station at Hornby, Ontario, operates on frequencies of 740 and 860 kHz, employing a single 645 foot radiator. A high voltage line (Figure 1) passes within 1470 feet (1.28 distant at 860 kHz) of this broadcast array. The photograph in Figure 2 shows the Hornby site modelled on the antenna pattern range, but the results given in this paper are for a simpler situation (only one power line having towers uniformly spaced (Figure 6)). The curves in Figures 5 and 7 show measured results at 516 MHz (CJBC at 860 kHz). For comparison, we show in Figure 11 the scalloped pattern at 444 MHz (CBL at 740 kHz).

Measurements have been made, mainly at the two frequencies noted above, for various situations: towers alone, skywires insulated, skywires connected to all towers, skywire insulated from some of the towers, power lines with skywires and as well, power carrying wires. A few measurements were made for tower spacings of λ and λ/2.

The effects observed can be summarized as follows: (1) for the Hornby situation modelled, the effect of the transmission line is markedly different at the two frequencies. Whereas at 444 MHz, no violent departure in pattern circularity was found for any wire arrangement, the results at 516 MHz indicate that the ground wire has a very prominent effect. At 444 MHz, the ripple in the pattern is about 2-3 dB. At 516 MHz, the average ripple is of the order of 4-5 dB for situations where the ground wires do not appear to be contributing to the scatter signal. When the ground wires are in place (at 516 MHz), and connected to all towers, four significant minima are produced in the pattern. These are of the order of 6-7 dB below the original circular pattern; (2) addition of power carrying wires produces no significant change in the patterns; (3) markedly different results are obtained for closely spaced towers (λ/2 spacing).

Initial Theoretical/Computational Approach to the Problem

Computation of re-radiation carried out in support of this work from thin towers, buildings, and power lines has given some quantitative agreement with measurement, but there is much work yet to be done. All computations have used some version of the method of moments. Some early results of Chugh (14] based

on the work of Jordan and Balmain [15], Harrington [16] and Richmond [17] calculated the modified patterns for a figure-of-eight directional pattern when thin monopoles were placed at various distances in the direction of the maximum of the pattern. The electric field strength in the null direction was shown to have two peaks (Figure 12), corresponding to heights of about 0.225 and 0.77 wavelengths for any distance from the broadcast array (compare with the experimental measurements in Figure 10). The second peak is usually higher than the first peak by about 1.5 to 2 dB depending upon the distance of the tower. The electric field strength decreases with an increase in distance of the tower from the broadcast array. In order to have a field of less than -40 dB in the null direction, a tower of any height should be located at a distance of more than 24 wavelengths from the broadcast array. The re-radiation from very thick monopoles (buildings) cannot be calculated by this simple analysis.

Balmain [18] employing the work of Richmond [19,20] has calculated re-radiation from both buildings and power lines that is in good agreement with results measured by him [13,21] in an anechoic chamber, at the University of Toronto.

The discussion which follows, and results given in the present paper employ computational techniques, and computer software and hardware developed at Concordia University.

The geometry of the truss-like power line towers with their four crossarms (Figure 13), pair of "skywires" and 6 sets of four wire bundle "phase wires" must be simplified considerably in order to be tractable for numerical computation. The simplest possible model is arrived at by: (1) noting that in the measured patterns, the phase wires have little effect and so can be omitted; (2) arguing that the pair of skywires is electrically equivalent to a single wire which is much fatter than the actual skywires because its diameter accounts for the separation of the actual wires; and (3) replacing the tower by a single wire of diameter comparable to the tower cross-sectional size.

A less oversimplified tower model is the A-frame model [18] of Figure 14, which relates to the tower profile as shown in Figure 13. The radiation patterns obtained with these models are discussed below.

The current on the wires of the antenna and the power line model is found by a numerical solution of Pocklington's Integral Equation [22], which states the boundary condition that the total axial electric field is zero at any point on any of the wires of the antenna. The total electric field is broken into two constituents, which are the excitation field and the secondary field due to the currents on the wires. Thus, the integral equation states that at any point on any wire, the secondary field, expressed as an integral of the current on the wires, plus the excitation field, equals zero. The system is excited at the base of the antenna. The integral equation is solved by the "moment method" [22], by expanding the current of each wire as a sum of suitable basis functions multiplied by unknown complex coefficients. A matrix equation is derived by enforcing the integral equation at a set of discrete points on the wires ("point matching"). The "Antenna Modelling Program" (AMP, [23]) has been used for the work reported here. AMP divides each wire into a user-specified number of segments and represents the current as the sum of a constant plus a cosine plus a sine function, with three unknown complex coefficients. Two of these are chosen such that the current and the charge density are continuous across segment boundaries. This leaves one unknown coefficient per segment, which is chosen to satisfy the integral equation by point matching. At wire junctions, Kirchoff's Current Law is enforced. The cost in CPU time of running the AMP computer program rises sharply with the number of unknown current coefficients, particularly for large problems where the amount of core memory available cannot accommodate the complete coefficient matrix, and so it is necessary to spool parts of the problem in and out of memory. Thus, it is advantageous to keep the number of current amplitudes as small as possible.

The task of the tabulation and punching onto cards of the rectangular coordinates of the endpoints of all the wires in a multi-tower power line model is a formidable one and is prone to human error. To overcome this difficulty and also to make easy any change in the model's parameters (number of towers, tower height, spacing, etc.), a "model generator program" is written, which computes from the basic parameters of the model, the endpoint coordinates of all the wires, and writes a data file called "AMPIN" in format suitable for input to the AMP program. To change the tower separation, for example, only one card in the "model generator program" need be altered, although this changes most of the wire endpoint data in the file "AMPIN". A run of "AMP" produces an output file called "AMPOUT" which contains the complex current amplitude at the centre of each segment on each wire of the antenna, and also the radiation pattern. Hand-plotting of this data is tedious and does not lend itself to quick comprehension of the significance of the result of a particular run. To alleviate this difficulty, the "AMPOUT" file is spooled over a high speed line to a minicomputer equipped with storage-type CRT graphics. Programs are written on the mini which display the current or the radiation pattern on the CRT screen rapidly. Digitizing and storing the measured patterns on the minicomputer's disc makes direct comparison with the measured pattern easy. Because the same set of graphics commands drives either the CRT screen or a CALCOMP plotter, figures such as Figure 15 are readily produced.

The validity of the numerical model is being established by comparison of the results with the patterns measured on the NRC antenna pattern range. The radii of the wires in the model were chosen heuristically for best agreement with the measurements. Thus, Figure 15 compares the measured H-plane pattern of the antenna and power line with that computed using the "A-frame tower", at 860 kHz. For the A-frame model the tower wires were chosen as two meters in radius, and the skywires were made four meters.

The computer program was used to find the H-plane pattern for power line models using 5, 7, 9, 11 and 13 towers, in order to determine how many towers must be represented to obtain a satisfactory radiation pattern. It was found that using more than 9 towers does not change the H-plane pattern significantly from that with 9 towers. Thus Figure 15 compares the computed patterns with a 9-tower power line with patterns measured using a 13-tower power line model.

An indicator of the degree of departure of the pattern from isotropic ("scalloping") is given by the ratio of the maximum value of the pattern to its minimum value, or max-to-min ratio. If the max-to-min ratio is plotted as a function of frequency, as in Figure 16, then the "resonance" of the power line

shows up as a broad peak. Thus the measured data has a resonance at about 860 kHz, with a "bandwidth" of about 100 kHz.

The computed curves in Figure 16 were obtained by calculating the H-plane pattern at a number of individual frequencies over the range of interest, and finding the maximum and minimum value of each pattern. It is evident that the resonant frequency of the "single wire tower" model is too low, whereas the "A-frame tower" model quite nicely reproduces the measured curve.

Once the computational model has been validated, useful parametric studies can be undertaken. For example, guidelines specifying the necessary separation of the power line from the broadcast tower can be expressed in terms of the scalloping effect. By running the AMP program for a number of different separation distances with all the other parameters constant, the "scalloping" expressed as max-to-min ratio is readily graphed as a function of the separation of the power line, as shown in Figure 17 at 860 kHz. Thus to guarantee that a "scalloping" of less than 2 dB will affect the radiation pattern, a separation of about 5100 feet (4-1/2 wavelengths) is required.

Further work is being carried out to try to refine the computational model to predict the "fine details" of the radiation pattern more accurately. Corrective measures are being investigated which "detune" the power line by shifting the resonant frequency out of the broadcast range or, by use of quarter wave stubs, prevent current flow on it.

CONCLUSIONS

We have shown that large structures such as radio masts, buildings, and power lines can be resonant at MF broadcast frequencies, and therefore re-radiation from such structures could significantly alter the directional pattern of the broadcast station. Numerical modelling by the method of moments has given good agreement with experiment although it is difficult to calculate the re-radiation from extended structures like power lines. It is also important to realize that the experimental and numerical modelling work to date represent a worst case situation, since the "earth" is perfectly conducting and the structures employed are either insulated from or connected to it. An important part of the research, yet to be undertaken, is to establish the relation between results presented here and the real world situation where imperfectly conducting structures are uncertainly connected to an imperfectly conducting earth; and as well, to investigate ways and means of reducing the effects of re-radiation.

REFERENCES

1. Presthold, O.L., *The effects of re-radiation from television towers and other structures upon directional antennas,* Proc. of 1958 NAB Broadcast Engineering Conference, 1958.

2. Alford, A. and E. French, *Some Observations Concerning the Re-radiation of Radio Frequency Energy from Power Line and Transmission Towers,* Andrew Alford Consulting Engineers, Boston, Mass., 6 August 1966.

3. Flood, D.P. and J.C. Field, *Experimental Study of the Backscattering from Conducting Objects in the Range of One-quarter to One Wavelength,* AFCRL Report 64-541, April 1964.

4. King, R.W.P., *Reduction of re-radiated field in equatorial plane of a parasitic antenna,* IEEE Trans. A&P, pp. 376-379, May 1972.

5. Alford, A. and H. Jasik, *Antenna Detuning System,* U.S. Patent No. 2,611,871, 23 September 1952.

6. Alford, A., *Re-radiation from tall guyed towers located in a strong field of a directional AM station,* IEEE Trans. on Broadcasting, BC-23, pp. 97-106, December 1977.

7. Chen, K.M. and V. Kiepa, *The minimization of backscattering of a cylinder by central loading,* IEEE Trans. A&P, pp. 576-582, September 1964.

8. Jones, D.E. and R.L. Hicks, *Effects of power lines on radiation patterns of broadcast antennas,* Ontario Hydro Research Quarterly, 23, No. 4, pp. 7-13, 1971.

9. Ring, A.D. and Associates, *The Calculation of Re-radiation or Scatter at Standard Broadcast Frequencies from Buildings and Similar Structures,* Washington, D.C., 14 May 1972.

10. Crispin, J.W. and A.L. Maffet, *Radar Cross Section Estimation for Simple Shapes,* Proc. IEEE, August 1965.

11. Belrose, J.S., *The Effects of Re-radiation from Highrise Buildings, Transmission Lines, Towers and Other Structures Upon AM Broadcasting Directional Arrays,* Interim Progress Reports 1-6 for the Working Group on Re-radiation Problems in AM Broadcasting, 1977-1979 (unpublished).

12. Elder, J.G., *Re-radiation: Assessment and Correction,* The Broadcaster, pp. 36-37, January 1979.

13. Balmain, K.G. and J.S. Belrose, *AM Broadcast Re-radiation from Buildings and Power Lines,* Proc. International Conference on Antennas and Propagation, London, England, pp. 268-272, 1978.

14. Chugh, R.K., *Analytical Model for Scattering Pattern Calculated from an Array of Thin Towers,* in above-mentioned Interim Reports No. 2 and 3, 1978 (unpublished).

15. Jordan, E.C. and K.G. Balmain, *Electromagnetic Waves and Radiating Systems,* p. 336, Prentice-Hall of Canada Ltd., Toronto, 1968.

16. Harrington, R.F., *Matrix methods for field problems*, Proc. IEEE, 55, pp. 136-149, 1965.

17. Richmond, J.H., *Digital computer solutions of the rigourous equations for scattering problems*, Proc. IEEE, 53, pp. 796-804, 1965.

18. Balmain, K.G., *Analysis of Re-radiation of AM Broadcast Signals*, Final Report on DOC/DSS Contract OSU78-00146, University of Toronto, 1979.

19. Richmond, J.H., *Radiation and Scattering from Thin-wire Structures in the Complex Frequency Domain*, NASA Report CR-2396, 1974.

20. Richmond, J.H., *Computer Programs for Thin-wire Structures in a Homogeneous Conducting Media*, NASA Report CR-2399, 1974.

21. Balmain, K.G., *The Effects of Re-radiation on AM Broadcast Signals*, Final Report on DOC/DSS Contract OSU77-00288, University of Toronto, 1978.

22. Mittra, R. (editor), *Computer Techniques in Electromagnetics*, Pergamon Press, 1973.

23. Antenna Modelling Program Engineering Manual, MB Associates Report No. IS-R-72/10, 10 July 1972.

FIGURE 1. Photograph of the CBL/CJBC transmitter site showing one branch of the 500 KW power line (six power line towers spaced approximately 900 feet can be seen). The 645 foot antenna tower can be seen on the left in the background.

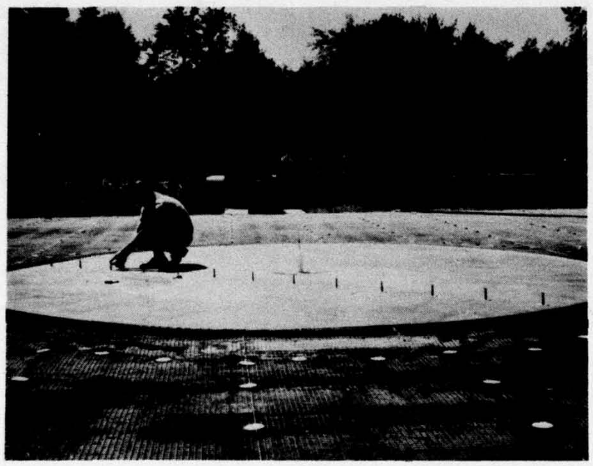

FIGURE 2(a)

FIGURE 2. Photograph of power line models on the NRC antenna pattern range; (a) showing simplified modelled power line (i.e. single line with uniformly spaced towers) on turntable. The boom for measuring the vertical pattern can be seen lying along the rear edge of the ground screen; and (b) showing the actual CBL/CJBC model. The styrofoam block surrounding the antenna model is to stabilize the monopole in the wind. Model scale factor was 600.

FIGURE 2(b)

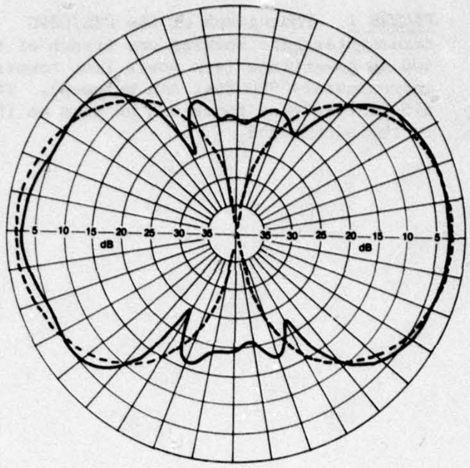

FIGURE 3. Measurement of modification of the figure-of-eight pattern caused by re-radiation from a single building (original pattern is shown by the broken line). The building is of height 12 inches (300 feet at full scale for a model scale factor of 300), cross-sectional dimension 4 x 4 inches (100 x 100 feet), at a distance of 2 meters (2000 feet) from the array.

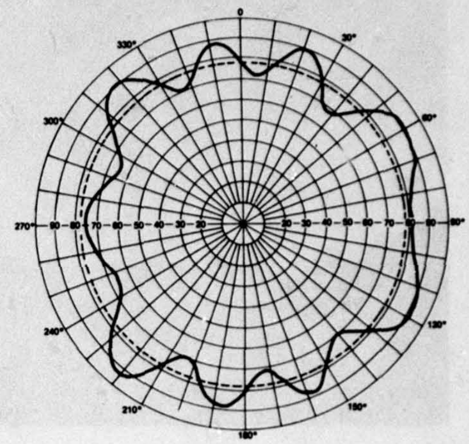

FIGURE 4. Measurement of modification of the omni-directional pattern caused by re-radiation from a single building (original pattern is shown by the broken line). The building is of height 10 inches (250 feet), cross-sectional dimension 4 x 16 inches (100 x 400 feet), at a distance of 2 meters (2000 feet). The wide side of the building is toward the antenna.

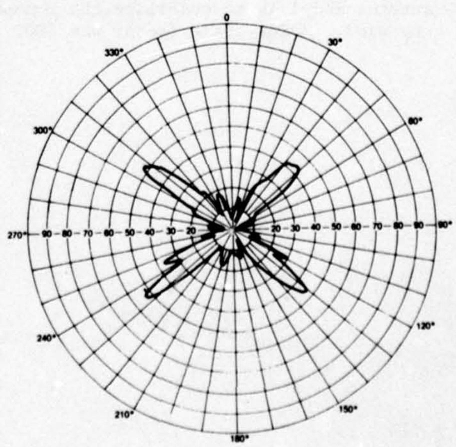

FIGURE 5. Scatter pattern of Hornby model at 516 MHz (CJBC 860 kHz) caused by a modelled 500 KV power line (see Figure 6 which shows the geometry). The ground wires are connected to all towers, and as well three power wires are attached. The omni-directional pattern which has been cancelled out was adjusted initially for full scale deflection.

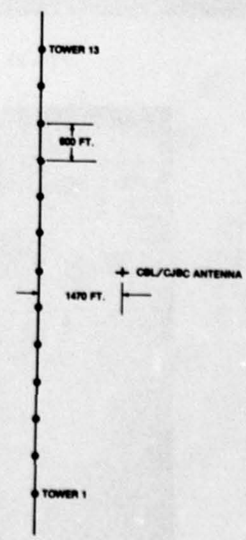

FIGURE 6. The CBL/CJBC Hornby, Ontario model (simplified geometry).

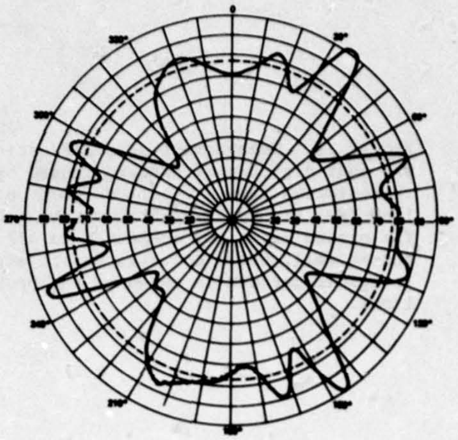

FIGURE 7. Measurement of modification of the figure-of-eight pattern caused by re-radiation from a modelled power line (simplified model as sketched in Figure 6). Ground wire connected to all towers, frequency 516 MHz (CJBC 860 kHz).

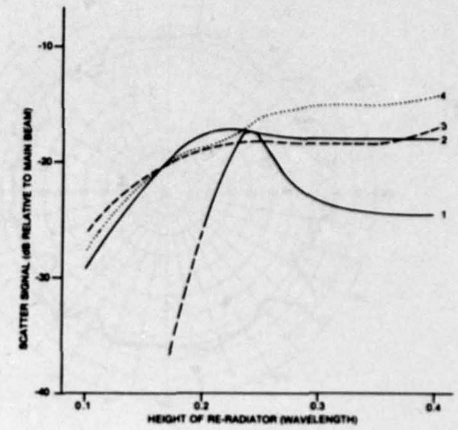

FIGURE 8. Scatter signal in the null direction relative to the main beam signal strength: caused by a thin monopole (curve 1) and for buildings (curves 2, 3 and 4). See text for details.

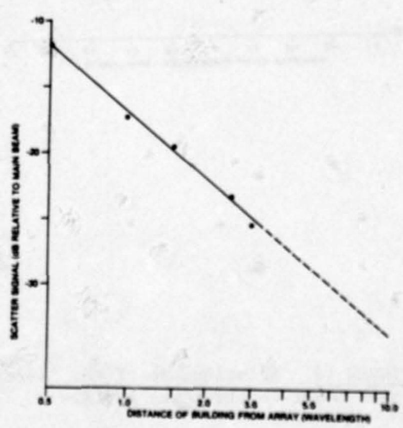

FIGURE 9. Scatter signal in null direction caused by a single building in the main beam, as a function of distance from the array.

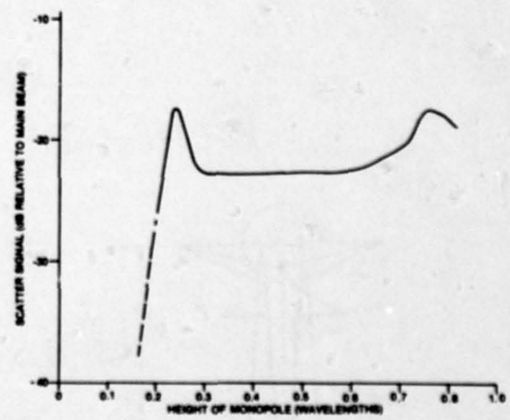

FIGURE 10. Scatter signal in null direction caused by a thin monopole in the main beam, as a function of the height of the monopole.

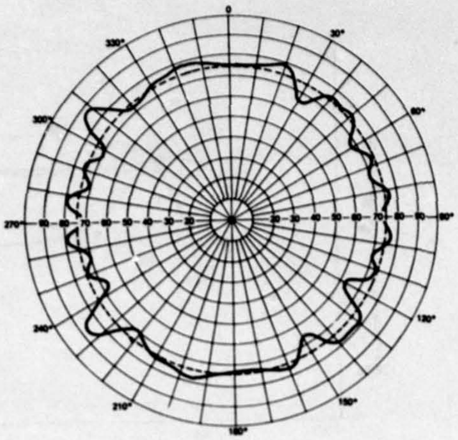

FIGURE 11. Measurement of modification of the omni-directional pattern caused by re-radiation from a modelled 500 KV power line (see Figure 6 which shows the geometry). The ground wires are connected to all towers, and as well, three power wires are attached (original pattern is shown by the broken line).

FIGURE 12. Calculated scatter signal into the null direction caused by a thin monopole of various heights and distance from the antenna array (after Chugh).

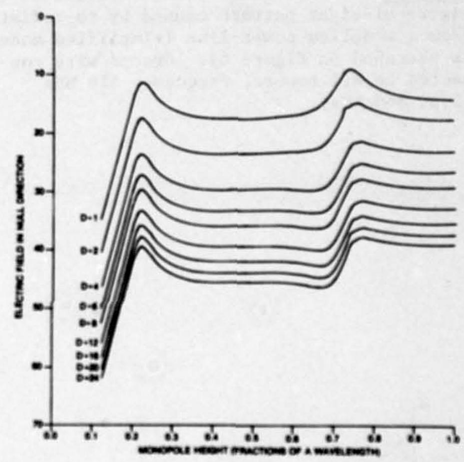

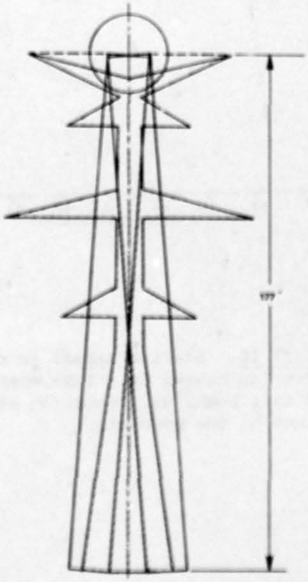

FIGURE 13. Relationship of the "A-frame" tower model to the tower profile.

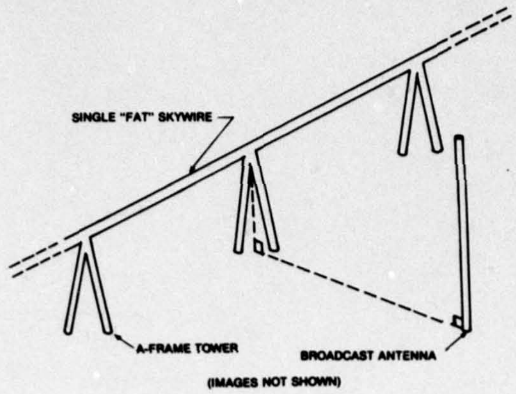

FIGURE 14. "A-frame" tower model.

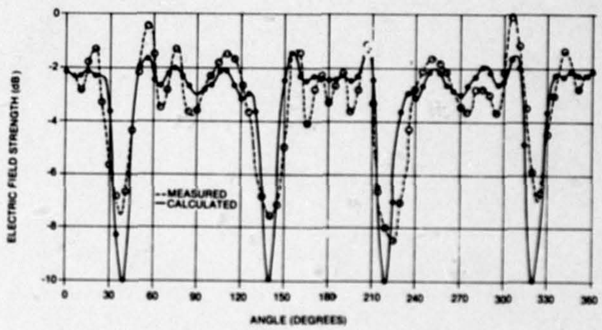

FIGURE 15. Calculated modification to omni-directional pattern caused by a power line, compared with measured curve.

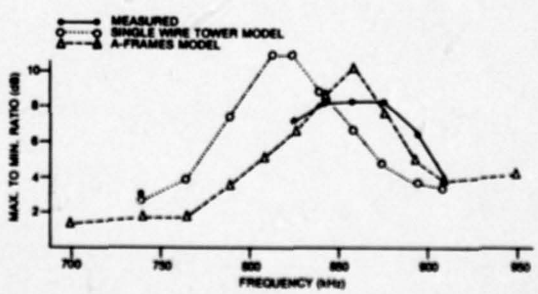

FIGURE 16. Calculated resonant frequency of a power line (177 foot towers uniformly spaced at 900 feet, ground wires connected to all towers), compared with measured resonant frequency.

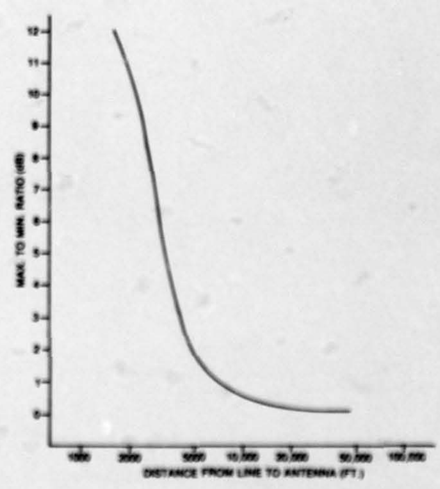

FIGURE 17. The max-to-min ratio (scalloping of omni-directional pattern) as a function of distance from the antenna to the transmission line, computed for the "A-frame" model using 9 towers.

SURFACE FIELDS AND RADIATION PATTERNS OF A VERTICAL ELECTRIC DIPOLE OVER A RADIALLY VARYING GROUND SYSTEM

C. Teng
The MITRE Corp., Bedford, MA 01730

and

R. J. King
Dept. of Electrical and Computer Engineering
University of Wisconsin, Madison, WI 53706

Summary

EM propagation over and radiation from radially varying ground systems are studied by numerical methods using the compensation theorem integral formulation. The source is taken to be a vertical electric dipole (VED) situated either on or above an azimuthally symmetric plane ground system having an assumed surface impedance profile which can vary arbitrarily in the radial direction.

Because the formulation is based on the surface impedance concept, it can be applied to a variety of ground systems configurations having a radius greater than about one wavelength. Particular attention is given to conventional HF radial-wire systems laid on both well and poorly conducting earth, and to HF ground systems near a sloping beach.

For one-section radial-wire ground systems, the radiation patterns were found to be independent of increasing radial length if the magnitude of the composite surface impedance is within 90% of the surface impedance of the underlying ground. It is also found that the radially varying feature tends to suppress high-angle lobes which are otherwise present with highly conducting ground systems, especially if the surrounding ground is poorly conducting. Suitable combinations of VED height, and the length and number of radials tend to enhance the low-angle radiation, as does the use of compound radial-wire systems.

A land-sea beach on which the water depth gradually increases is shown to have little effect on the radiation pattern compared to that for an abrupt coastline.

1. INTRODUCTION

Over-the-horizon propagation at HF has prompted renewed interest in the theory and design of antenna ground systems giving improved radiation patterns and efficiency. Cost and size usually dictate that the ground system is radially and/or azimuthally nonuniform, e.g., radial-wire systems. Additional non-uniformity results at the system termination (either gradual or abrupt).

Here, we are chiefly concerned with determining the effects on the radiation characteristics of a vertical electric dipole (VED) by a nonuniform ground plane on which the amplitude and/or argument of the surface impedance $Z_S'(\rho)$ varies arbitrarily in the radial direction, but is azimuthally symmetric. The formulation is couched so that it can be applied to a wide variety of ground systems from LF through HF, and admits to such configurations as a nonuniform ground system on land near a beach.

For background, some of the major contributions which have been helpful are mentioned. Hufford [1952] developed a scalar integral equation using the free space Green's function in Green's second identity for the Hertzian potential of an elevated VED above an irregular earth. G. de Jong [1975] used a similar approach with a different Green's function, forming a two-dimensional integral equation for the attentuation function of a VED over a nonuniform flat earth. Rafuse and Ruze [1975] studied low-angle radiation from vertically polarized antennas over a radially uniform flat earth. Their sky-wave solution is obtained as the sum of the direct dipole radiation and the radiation from a system of equivalent electric and magnetic currents as specified by the Sommerfeld attenuation function. Wait [1963; 1967a,b; 1969], Anderson [1963], King [1969], Wait and Spies [1970a,b], and Cho and King [1976a,b] have used the electromagnetic compensation theorem to develop solutions of radiation fields and surface waves for various impedance profiles.

The compensation theorem is also used here. It is particularly well suited for application of the plane wave surface impedance, an economical and convenient means for accounting for complex configurations. This combination has proved accurate in mixed-path groundwave theory, and often useful in cases where use of the plane wave surface impedance is clearly violated, e.g, near abrupt boundaries [King and Wait, 1976]. This success is chiefly a consequence of the fact that integral equations tend to smooth errors in the integrand.

The compensation theorem yields a two-dimensional integral equation which can be used to find the electromagnetic field anywhere in the free space region, except very near the VED source. The first step in the solution is to set the observation point on the surface and reduce the integral equation to one dimension in ρ. We then proceed to numerically find the magnetic field $H_\phi'(\rho)$ on the surface, and then insert $H_\phi'(\rho)$ back into the original two-dimensional integral to obtain the radiation pattern. Several nonuniform surface impedance profiles are studied to show their effect.

2. FORMULATION

An elemental VED with current moment $I_1\ell_1$ is located at $\rho = 0$ and $z = h_1$, and a horizontal magnetic dipole (HMD) with current $k_2\ell_2$ located at ρ and $z = h_2$ is used as a test receiving antenna as shown in Fig. 1. The $z = 0$ plane is the surface S and the medium for $z > 0$ is free space. The unspecified medium for $z \leq 0$ determines the surface impedance profile

$$Z_s'(\rho) = \eta_0\,\Delta'(\rho), \tag{1}$$

where $\Delta'(\rho)$ varies radially in magnitude and/or argument, with no dependence on ϕ.

Let $\bar{E}_1$, $\bar{H}_1$, $\bar{E}_2$ and $\bar{H}_2$ be the electric and magnetic fields for the VED (source 1) and the HMD (source 2) when the surface is homogeneous with a constant surface impedance $Z_s = \eta_0\Delta_0$. Let $\bar{E}_1'$ and $\bar{H}_1'$ be the unknown fields of the VED when the surface impedance for $\rho \leq b$ is changed to $Z_s'(\rho)$. In the above, $\Delta'(\rho)$ and Δ_0 are surface impedances normalized by η_0 ($= 120\pi$). As the problem is azimuthally symmetric, it is TM to ρ and so we choose a ϕ-directed HMD test source to find $H_{1\phi}'$ due to the VED.

The electromagnetic compensation theorem as first given by Monteath [1951] was later generalized by Mittra [1961]. As applied to the present problem, it can be stated as

$$\int_S (\bar{E}_1'\times\bar{H}_2 - \bar{E}_2\times\bar{H}_1')\cdot\bar{n}\,dS = \int_R [\bar{J}_2\cdot(\bar{E}_1'-\bar{E}_1) - \bar{M}_2\cdot(\bar{H}_1'-\bar{H}_1)]\,dv \tag{2}$$

where the volume R includes only source 2 and $\bar{n}$ is normal to S. The unprimed fields are known while the primed fields are to be found. Invoking the surface impedance, the relations for the tangential fields are:

$$\bar{n}\times\bar{E}_1 = -Z_s\,H_{1\phi}\,\bar{a}_{1\phi} \tag{3}$$

and

$$\bar{n}\times\bar{E}_1' = -Z_s'\,H_{1\phi}'\,\bar{a}_{1\phi}$$

In the present problem, $\bar{M}_2 = k_2\ell_2\delta(P-P_2)\,\bar{a}_{1\phi}$ and $\bar{J}_2 = 0$, where P_2 is the location of source 2. Then, substituting (3) into (2) gives

$$H_{1\phi}'(\rho,h_1,h_2,\Delta') = H_{1\phi}(\rho,h_1,h_2,\Delta_0) + \frac{\eta_0}{k_2\ell_2}\int_S (\Delta'-\Delta_0)H_{1\phi}'(\rho_1,h_1,0,\Delta')[\bar{a}_{1\phi}\cdot\bar{H}_2]\,dS \tag{4}$$

where $\Delta' = \Delta'(\rho_1)$, and $H_{1\phi}$ can be expressed in the form [King, 1969]:

$$H_{1\phi}(\rho,h_1,h_2,\Delta_0) = \frac{jkI_1\ell_1}{4\pi}\left[\cos\psi_d\,\frac{e^{-jkd}}{d} + \Gamma(\psi_r)\cos\psi_r\,\frac{e^{-jkR_r}}{R_r} + (1-\Gamma(\psi_r))F(\rho,h_1,h_2,\Delta_0)\cos\psi_r\,\frac{e^{-jkR_r}}{R_r}\right], \tag{5}$$

where

$$F(\rho,h_1,h_2,\Delta_0) = 1 - j(\pi w)^{1/2}e^{-w}\,\mathrm{erfc}(jw^{1/2}) \tag{6}$$

is the Sommerfeld attentuation function, in which $w = \dfrac{-jkR_r}{2\cos^2\psi_r}(\sin\psi_r + \Delta_0)^2$ is the numerical distance. The suppressed time factor is $\exp(j\omega t)$. Also, $\sin\psi_r = (h_1+h_2)/R_r$, $\cos\psi_r = \rho/R_r$ and $\cos\psi_d = \rho/d$ where $R_r = [\rho^2 + (h_1+h_2)^2]^{1/2}$, $d = [\rho^2 + (h_1-h_2)^2]^{1/2}$ and $\Gamma(\psi_r) = \dfrac{(\sin\psi_r - \Delta_0)}{(\sin\psi_r + \Delta_0)}$ is the TM_ρ Fresnel reflection coefficient. Eq. (5) assumes that $\rho > \lambda$ as the induction and higher order terms are neglected, and that $|\sin\psi_r + \Delta_0|^2 \ll 1$. At the integration point Q located on S [King 1969; King and Wait, 1976],

$$\bar{H}_2 = \frac{jkk_2\ell_2}{4\pi\eta_0}\sin\psi_2\,\frac{e^{-jkr_2}}{r_2}\,.$$

$$[1 + \Gamma(\psi_2) + (1-\Gamma(\psi_2))F(\rho_2,h_2,0,\Delta_0)]\,\bar{a}_{2\phi} \tag{7}$$

where $\sin\psi_2 = h_2/r_2$, $\sin\psi_1 = h_1/r_1$,

$\cos\psi_2 = \rho_2/r_2$, $\cos\psi_1 = \rho_1/r_1$,

$$\Gamma(\psi_2) = \frac{(\sin\psi_2 - \Delta_0)}{(\sin\psi_2 + \Delta_0)},$$

$r_2 = (\rho_2^2 + h_2^2)^{1/2}$, $\quad \rho_2 = (\rho^2 + \rho_1^2 - 2\rho\rho_1\cos\phi_1)^{1/2}$,

$r_1 = (\rho_1^2 + h_1^2)^{1/2}$,

$$\phi_2 = \phi_1 + \alpha - \frac{\pi}{2} \quad \text{for } 0 \le \phi_1 \le \pi$$

$$= \phi_1 - \alpha - \frac{\pi}{2} \quad \text{for } \pi \le \phi_1 \le 2\pi,$$

$$\tan \phi_2 = \frac{(\rho - \rho_1 \cos \phi_1)}{(\rho_1 \sin \phi_1)},$$

$$\sin \phi_2 = \frac{(\rho - \rho_1 \cos \phi_1)}{\rho_2}$$

Again, (7) is under the restrictions that $\rho_2 > \lambda$ and $|\sin \psi_2 + \Delta_o|^2 \ll 1$. It is also assumed in (7) that the $TM_{\rho 2}$ wave is dominant.

From Fig. 1, we have

$$\bar{a}_{1\phi} \cdot \bar{a}_{2\phi} = \cos \alpha = \frac{(\rho_1^2 + \rho_2^2 - \rho^2)}{2\rho_1\rho_2} \tag{8}$$

Now cast the unknown field in the form

$$H'_{1\phi}(\rho, h_1, h_2, \Delta') = H_{1\phi}(\rho, h_1, h_2, \Delta_o)\, F'(\rho, h_1, h_2, \Delta') \tag{9}$$

where F' is an attenuation function in excess of that for propagation over Δ_o.

Substituting (7), (8), and (9) into (4),

$$F'(\rho, h_1, h_2, \Delta') = 1 + \left[\frac{jk}{2\pi H_{1\phi}(\rho, h_1, h_2, \Delta_o)}\right] \int_S (\Delta' - \Delta_o) \frac{e^{-jkr_2}}{r_2} \cdot$$

$$\left[\frac{\sin \psi_2 \cos \alpha}{\sin \psi_2 + \Delta_o}\right] [\sin \psi_2 + \Delta_o\, F(\rho_2, h_2, 0, \Delta_o)]\, H_{1\phi}(\rho_1, h_1, h_2, \Delta_o)\, F'(\rho_1, h_1, 0, \Delta')\, dS$$

$$\text{for } \Delta_o \ne 0. \tag{10}$$

For the special case where $\Delta_o = 0$, this reduces to

$$F'(\rho, h_1, h_2, \Delta') = 1 + \left[\frac{jk}{\pi X}\right] \int_S \Delta' \frac{\rho_1\, e^{-jk(r_1 + r_2)}}{r_1^2\, r_2} \sin \psi_2 \cos \alpha\, F'(\rho_1, h_1, 0, \Delta')\, dS \tag{11}$$

after using (5), where

$$X = \cos \psi_d \frac{e^{-jkd}}{d} + \cos \psi_r \frac{e^{-jkR_r}}{R_r}$$

The following is based on the two-dimensional Fredholm integral equations (10) and (11), where the integration only extends over the perturbed portion of S, i.e., over $0 \le \rho \le b$ where Δ' differs from Δ_o. The procedure, as explained in Sec. 3, is to first put the HMD test source on the perturbed S by setting $h_2 = 0$, and solve (10) or (11) for $F'(\rho, h_1, 0, \Delta')$. (Using (9), this gives the field $H_{1\phi}(\rho, h_1, 0, \Delta')$ on S.) This result is then inserted back into (10) or (11) to give $F'(\rho, h_1, h_2, \Delta')$ by numerical integration; using (9) again, the radiation pattern can be found, as explained in Sec. 4.

3. SOLVING FOR $H'_{1\phi}$ ON THE PERTURBED SURFACE ($h_2 = 0$).

Following an earlier approach [King, 1969], the two-dimensional surface integration in (10) or (11) is approximately reduced to one-dimension by a stationary-phase integration which requires $k\rho \gg 1$. Here we assume that: (a) the induction fields can be neglected, as is the case if $k\rho \gg 1$, (b) $F'(\rho_1, h_1, 0, \Delta')$ depends strongly upon the surface within a narrow Fresnel zone and neglects the effects outside of the Fresnel zone; this is true for $h_1 \ll \rho$. (c) any surface waves reflected from surface impedance discontinuities are negligible, and (d) $F'(\rho_1, h_1, 0, \Delta')$ varies slowly with ρ_1. On the surface we construct an elliptic cylindrical (u,v) coordinate system in which (see Fig. 2)

$$dS = \rho_1 \rho_2\, du\, dv$$
$$\rho_1 = \rho(\cosh u + \cos v)/2 \tag{12}$$
$$\rho_2 = \rho(\cosh u - \cos v)/2$$

where $-\infty < u < \infty$ and $0 \le v \le \pi$. After converting the integrands of (10) and (11) into elliptic coordinates [see Teng, 1978], the u-integration is evaluated approximately by the stationary phase method

about the region $u \doteq 0$, assuming $\rho > \lambda$. Here, the Taylor series expansion for $\cosh u \doteq 1 + u^2/2$ for $u \ll 1$ is used and k is allowed to have a small negative imaginary part to secure convergence. Substituting $\sin \phi_2 \doteq 1$, $\cos \alpha \doteq -1$, $\cos \phi_1 \doteq 1$, and $\cos \varphi \doteq 1$ into the resulting reduced one-dimensional integral equation and changing it back into circular cylindrical coordinates gives

$$F'(\rho) = 1 - \int_0^\rho F'(t) g(\rho,t) \phi(\rho,t)\, dt \tag{13}$$

where, for brevity,

$$F'(\rho) = F'(\rho, h_1, 0, \Delta'), \quad \phi(\rho,t) = [t(\rho - t)]^{-1/2},$$

and

$$g(\rho,t) = \left(\frac{jk}{\pi}\right)^{1/2} \frac{R^2}{\rho^{3/2}} \cdot \frac{(\Delta'(t) - \Delta_0)\, t^{5/2}}{(h_1^2 + t^2)[t + (h_1^2 + t^2)^{1/2}]^{1/2}} F(\rho - t, 0, 0, \Delta_0) \cdot$$

$$\frac{h_1 + (h_1^2 + t^2)^{1/2} \Delta_0 F(t, h_1, 0, \Delta_0)}{h_1 + R\,\Delta_0\, F(\rho, h_1, 0, \Delta_0)} \cdot \frac{h_1 + R\Delta_0}{h_1 + (h_1^2 + t^2)^{1/2} \Delta_0}\, e^{jk[R - \rho + t - (h_1^2 + t^2)^{1/2}]} \text{ (general case)}, \tag{14}$$

$$= 0 \quad \text{for } t = 0 \text{ (special case)},$$

$$= \left(\frac{jk}{\pi}\right)^{1/2} (\Delta'(\rho) - \Delta_0)\rho/(\rho + R)^{1/2} \quad \text{for } t = \rho \quad \text{(special case)}.$$

When $\Delta_0 = 0$,

$$g(\rho,t) = \left(\frac{jk}{\pi}\right)^{1/2} \Delta'(t) \frac{R^2}{h_1^2 + t^2} \frac{t^{5/2}}{\rho^{3/2}[t + (h_1^2 + t^2)^{1/2}]^{1/2}} e^{jk[R - \rho + t - (h_1^2 + t^2)^{1/2}]}$$

and when $h_1 = 0$,

$$g(\rho,t) = \left(\frac{jk\rho}{2\pi}\right)^{1/2} \frac{\Delta'(t) - \Delta_0}{F(\rho, 0, 0, \Delta_0)} F(\rho - t, 0, 0, \Delta_0) F(t, 0, 0, \Delta_0).$$

In the above $R = (\rho^2 + h_1^2)^{1/2}$, and $F(0,0,0,\Delta_0)$, $F(\rho,0,0,0)$, $F(t,0,0,0)$ and $F(\rho - t,0,0,0)$ are all equal to unity.

When identical special cases are examined, (13) reduces to the same integral equations as obtained by King [1969]. These serve as a partial check on the numerical solution of (13). For example, if $\Delta'(t)$ is constant and $b \to \infty$, (13) has been shown to give (6).

Note that (13) is a Volterra integral equation of the second kind having weakly singular kernels such as $t^{-1/2}$ and $(\rho - t)^{-1/2}$. To obtain an approximate numerical solution, the integration can be replaced by a numerical quadrature procedure. However, the integrand is unbounded at $t = 0$ and ρ, so standard methods are not applicable. In such cases, the technique of product integration is often used. In the following, the generalized trapezoidal rule [Linz, 1969] was used to solve (13). More details of the integration procedures using both the trapezoidal and Simpson's rules are given in Teng [1978].

If the range of integration $[0,\rho]$ is divided into $(n-1)$ subintervals, d_1 $(=0)$, $d_2, d_3, \ldots, d_n (=\rho)$, then (13) becomes

$$F(d_n) = 1 - \sum_{i=1}^{n} W_{ni}\, F(d_i) g(d_n, d_i) \tag{15}$$

where the weights are

$$W_{ni} = I(n, i, i+1) - J(n, i, i-1) \tag{16}$$

and

$$I(n,i,i+1) = (\sqrt{d_{i+1}(d_n - d_{i+1})} - \sqrt{d_i(d_n - d_i)} - (\frac{d_n}{2} - d_{i+1}) [\sin^{-1}(\frac{d_n - 2d_i}{d_n}) - \sin^{-1}(\frac{d_n - 2d_{i+1}}{d_n})])/(d_{i+1} - d_i)$$

$$J(n,i,i-1) = (\sqrt{d_i(d_n - d_i)} - \sqrt{d_{i-1}(d_n - d_{i-1})} - (\frac{d_n}{2} - d_{i-1}) [\sin^{-1}(\frac{d_n - 2d_{i-1}}{d_n}) - \sin^{-1}(\frac{d_n - 2d_i}{d_n})])/(d_i - d_{i-1})$$

while

$$I(n,i,i+1) = 0 \quad \text{for } i = n$$
$$J(n,i,i-1) = 0 \quad \text{for } i = 1$$

Generation of the weights using (16) is the chief advantage of this numerical procedure. In (15), $F(d_n)$ is obtained if $F(d_i)$, $i = 1,2,\ldots,n-1$, is known. Thus, starting from $F(d_1) = F(0) = 1$, we proceed in a stepwise fashion to determine each $F(d_n)$, $n = 2,3,\ldots,N$.

The numerical solution of (13) is then

$$F(d_n) = \frac{1 - \sum_{i=1}^{n-1} W_{ni}\, F(d_i) g(d_n,d_i)}{1 + W_{nn}\, g(d_n,d_n)} \tag{17}$$

4. SOLVING FOR $H'_{1\phi}$ ABOVE AND BEYOND THE PERTURBED SURFACE

To find the field above and beyond the perturbed surface S, we need to perform a two-dimensional numerical integration of (10) or (11) over a circular region of radius b. Note that this two-dimensional integration cannot be carried out with the stationary phase method unless $(h_1 + h_2) \ll \rho$.

For the observation points beyond the perturbed portion of S ($\rho > b$) and the source VED above the surface ($h_1 > 0$), there are no singularities in the integrand. A two-dimensional Gaussian quadrature formula can be used to give reasonable accuracy in the range $0 \le \psi \le \frac{\pi}{2}$. But when the VED is placed on the surface ($h_1 = 0$) the integrand contains a ρ_1^{-1} factor and extra precautions must be taken. We split the integral in (10) into two parts as follows:

$$\int_S I\, F'(\rho_1,h_1,0,\Delta')\, dS = \int_0^{\delta}\int_0^{2\pi} I\, F'(\rho_1,h_1,0,\Delta')\rho_1 d\phi_1 d\rho_1 + \int_{\delta}^{b}\int_0^{2\pi} I\, F'(\rho_1,h_1,0,\Delta')\, \rho_1 d\phi_1 d\rho_1 \tag{18}$$

where δ is a small positive constant, $F'(\rho_1,h_1,0,\Delta')$ is finite and azimuthally symmetric, and I represents the remaining known factors in the integrand. Examining the integrand for small ρ_1 and $h_1 = 0$, we find that the first integral on the right-hand side of (18) becomes

$$\int_0^{\delta}\int_0^{2\pi} I\, F'(\rho_1,0,0,\Delta')\, \rho_1 d\phi_1 d\rho_1 = -\int_0^{2\pi}\left(\int_0^{\delta} \frac{jk}{2\pi}[\Delta'(\rho_1)-\Delta_0] \cdot F(\rho_1,0,0,\Delta_0)\frac{r}{\rho} F'(\rho_1,0,0,\Delta')\ d\rho_1\right) \cos\phi_1\, d\phi_1 . \tag{19}$$

As the ρ_1 integration is finite and independent of ϕ_1, the above integral is zero for $\rho \neq 0$ (i.e. $\psi \neq \frac{\pi}{2}$) due to the ϕ_1 integration of $\cos\phi_1$. In the case where $\rho = 0$ or $\psi = \pi/2$, $H_{1\phi}$ and $H'_{1\phi}$ are both zero as seen from (5) and (9). Thus, only the second part of (18) contributes and there is really no singularity problem.

To perform the two-dimensional integration we divide the perturbed portion of S ($\rho \le b$) into several concentric annuli and apply a quadrature procedure in each annulus to construct a composite rule. Imagine the innermost annulus to be infinitesimal disc ($0 \le \rho_1 \le \delta$) and compute only the second part of (18).

Peirce's [1957; Stroud, 1971] method for numerical integration over a planar annulus was chosen for use here. The basic formula is

$$I = \int_0^{2\pi}\int_R^1 f(r,\theta)\, r\, dr\, d\theta = \sum_{j=1}^{m+1}\sum_{i=1}^{4(m+1)} C_j\, f(r_j,\theta_i) \tag{20}$$

The procedure can be stated as a theorem·

Theorem If it is required that (20) have accuracy $n = 4m+3$, $m = 0,1,\ldots$, in $r\cos\theta$ and $r\sin\theta$, using the minimum number of evaluation points which are intersections of concentric circles (radius r_j) and rays emanating from the origin (angle θ_i), then it is both necessary and sufficient for the existence of a unique set of real weights C_j that

1) $\theta_i = \dfrac{\pi i}{2(m+1)}$,

2) $r_j^2 = v_j$ are the m+1 zeros of $P_{m+1}(v)$, which is the Legendre polynomial orthogonalized on $R^2 \le v \le 1$ with leading coefficient one,

$$3)\ C_j = \frac{\pi}{4(m+1)\, P'_{m+1}(v_j)} \int_{R^2}^1 \frac{P_{m+1}(v)}{v-v_j}\, dv \tag{21}$$

where $j = 1,2,\ldots,m+1$, $i = 1,2,\ldots,4(m+1)$, and $P'_{m+1}(v_j) = \left.\dfrac{d}{dv} P_{m+1}(v)\right|_{v = v_j}$.

The weights C_j are positive and their sum is the area of the annulus.

Note that $P_{m+1}(v)$ in (21) is orthogonolized on $[R^2,1]$ instead of the usual $[-1,1]$. In order to use the tabulated formulas and data in the mathematical handbooks for Legendre polynomials $P_{m+1}(u)$ orthogonalized on $u \in [-1,1]$, we apply a linear transformation to $v \in [R^2,1]$ by using

$v = \frac{1}{2}(1-R^2)u + \frac{1}{2}(1+R^2) = r^2$. Then (21) becomes

$$C_j = \frac{\pi(1-R^2)}{8(m+1)\,P'_{m+1}(u_j)} \int_{-1}^{1} \frac{P_{m+1}(u)}{u-u_j}\,du \tag{22}$$

and

$$r_j = v_j^{1/2} = [\tfrac{1}{2}(1-R^2)u_j + \tfrac{1}{2}(1+R^2)]^{1/2}, \tag{23}$$

where u_j are the (m+1) zeros of $P_{m+1}(u_j)$.

Let there be n annuli bounded by $\rho_1 = x_k$ and $\rho_1 = x_{k+1}$ where $k = 1,2,\ldots,n-1$. Also let $x_1 = 0$ and $x_n = b$, measured in free space wavelengths. The x_k's are arranged so that $\Delta'(\rho_1)$ varies continuously within each annulus but can be discontinuous at an annulus boundary. Best accuracy is obtained if small intervals are chosen between annuli in regions where $\Delta'(\rho_1)$ changes rapidly.

The integral in (10) can now be written

$$\int_0^{2\pi}\int_0^{b} I\,F'(\rho_1,h_1,0,\Delta')\rho_1\,d\rho_1\,d\phi_1$$

$$= \sum_{k=1}^{n-1} \int_0^{2\pi}\int_{x_k}^{x_{k+1}} I\,F'(\rho_1,h_1,0,\Delta')\rho_1\,d\rho_1\,d\phi_1$$

$$= \sum_{k=1}^{n-1} x_{k+1}^2 \int_0^{2\pi}\int_R^{1} [I\,F'(\rho_1,h_1,0,\Delta')]\Big|_{\substack{\rho_1 = s x_{k+1}\\ \phi_1=\theta_i}} s\,ds\,d\phi_1$$

where $R = x_k/x_{k+1}$.
Applying the basic integration formula (20) to each of the above integrals, a composite rule results and (10) becomes

$$F'(\rho,h_1,h_2,\Delta') = 1 + \sum_{k=1}^{n-1} x_{k+1}^2 \sum_{j=1}^{(m+1)} \sum_{i=1}^{4(m+1)} C_j \,.$$

$$[I\,F'(\rho_1,h_1,0,\Delta')]\Big|_{\substack{\rho_1 = x_{k+1} r_j\\ \phi_1 = \theta_i\,.}} \tag{24}$$

Once the value for $F'(\rho_1,h_1,0,\Delta')$ is found as explained in Sec. 3, $F'(\rho,h_1,h_2,\Delta')$ can be determined by (24) and the problem is solved. A 64-point 15th-degree formula (i.e., m=3) was found to be satisfactory here.

One interesting fact derived from (24) is that by setting $h_2 = 0$ and $\rho = r_j x_{k+1}$ for $1 \le k \le n-1$ and $1 \le j \le m+1$, we can get a system of $(n-1)(m+1)$ simultaneous linear equations with $F'(r_j)$ on the perturbed surface as unknowns. The direct Gaussian elimination LU method or an indirect method (e.g., iteration, successive overrelaxation, or Newton's method, etc.) can be used to solve this system of equations. This gives a numerical method for solving a two-dimensional integral equation. It is a two-dimensional equivalent of the one-dimensional Nyström method [Atkinson, 1976]. An analysis of error estimation for two-dimensional integration is given in Teng [1978].

5. VERIFICATION OF THE FORMULATION AND NUMERICAL SOLUTIONS

To check the formulation and the numerical procedures, some special case studies were chosen for comparision with the results of other workers. Since it is not possible to give details here, we must be content to make general comments, and refer the interested reader to Teng [1978]. Several combinations of h_1, Δ_o and Δ' (= const.) were considered for propagation over uniform ground. It was generally found that the results are accurate when $\Delta_o = 0$ and $|\Delta'|^2$ is small compared to unity. This is consistent with known groundwave theory [e.g., see Sec. 3.4 of King and Wait, 1976]. In all cases studied, the phase was found to be quite accurate, but the accuracy in the magnitude decreases for $\Delta_o \neq 0$ and $|\Delta'|^2$ not small. The assumption $h_1 \ll \rho$ or $\sin\psi_r \ll 1$ may be relaxed or waived; this too is consistent with known theory and experimental results [King et al., 1973].

Radiation patterns were checked against some known special cases such as low-angle radiation from a dipole near an abrupt coastline as computed by Anderson [1963], and the low-angle radiation of a dipole over an exponentially tapered dielectric ground as computed by Wait and Spies [1970a]. The present formulation, however, is not restricted to computing low-angle radiation.

6. NUMERICAL EXAMPLES: HF RADIAL-WIRE GROUND SYSTEMS

As the formulation is based on the surface impedance, it can be applied to a variety of ground system configurations for which $b > \lambda$. Particular attention is given to conventional HF radial-wire systems laid on various types of earth and to HF ground systems near a sloping beach. The VED is located either at or above the ground system center.

6.1. Simple HF Radial-Wire Ground Systems on a Homogeneous Earth

Let the wires of radius r_a be located at the interface between free space (μ_0, ϵ_0) for $z > 0$, and the homogeneous earth $(\mu_0, \epsilon, \sigma)$ for $z < 0$. The equivalent shunt impedance of a radial-wire grid is given by Wait [1962]

$$Z_{grid} = j \frac{2\pi\rho}{N} \left[\frac{\eta_0}{\lambda} \left(f_0 \, \ell n \left(\frac{\rho}{Nr_a}\right) + \Delta_f\right) + Z_i\right] \quad (25)$$

where f_0 and Δ_f are functions of the angle of incidence as well as the electrical constants of earth and wires, Z_i is the internal impedance of the wires, N is the number of radial wires, ρ is the distance from the origin, and $\left(\frac{2\pi\rho}{N}\right)$ is the interwire distance, d, at ρ. The composite surface impedance is then assumed to be the parallel combination of Z_{grid} and the surface impedance of the earth, Z_e. Hence

$$\eta_0 \Delta'(\rho) = \frac{Z_{grid} \cdot Z_e}{Z_{grid} + Z_e}, \text{ for } \rho < b. \quad (26)$$

For typical earth, the angular dependence of Z_e is quite weak, making that of $Z'(\rho)$ quite weak also, even though that of Z_{grid} is more pronounced [Teng, 1978].

Two types of homogeneous lossy earth were studied: well conducting earth ($\epsilon = 15\epsilon_0$, $\sigma = 10^{-2}$ S/m) and poorly conducting earth ($\epsilon = 5\epsilon_0$, $\sigma = 10^{-4}$ S/m). At 10 MHz, these correspond to $\Delta_0 = Z_e/\eta_0$ = 0.204 exp (j24.1°), and 0.400 exp (j0.77°) respectively. For comparison, a perfectly conducting disc was also considered. In the following numerical examples, B and S No. 6 (r_a = 2.06 mm) radial copper wires are used. The normalized surface impedance profile is then $\Delta'(\rho)$ as given by (26) for $\rho \le b$ and Δ_0 for $\rho > b$. The typical behavior of $\Delta'(\rho)$ is shown in Fig. 3 for the two earth types, f = 10 MHz and N = 120. Fig. 4 shows the corresponding magnetic field, H_ϕ^t, on the ground system as calculated using (17), (9) and (5) with $h_2 = h_1 = 0$. The source height h_1 was taken as zero unless stated otherwise.

To illustrate and compare the effects of simple radial-wire systems and the conducting disc, the H_ϕ radiation patterns are shown in Figs. 5–8. The radiation pattern for a constant Δ_0 plane (corresponding to a lossy homogeneous earth) is also shown on each figure for comparison. It is

$$1/2 \cos\psi \,(1 + \Gamma_{||}) = \frac{\sin\psi \cos\psi}{\sin\psi + \Delta_0} \quad (27)$$

which vanishes at $\psi = 0$. To account for the surface wave contribution near $\psi = 0$, use (5). All of the patterns shown are normalized by the H_ϕ radiation field on a perfectly conducting plane at the radiation distance R, i.e., by the factor $jkI_1\ell_1/2\pi R$ (where R is chosen as 5000λ). Because of the large number of parameters, the results of only a few cases were chosen to illustrate certain features.

Effects of ground system size and underlying earth

(i) Low-angle radiation is enhanced by using either a radial-wire ground system or a conducting disc of any size, relative to a homogeneous earth. This is because more power is reflected into the upper space by the former configurations, and is particularly true for the disc if $b > 2\lambda$, or when the underlying earth is poorly conducting. Short radial-wire systems ($b < \lambda$) having $N > 120$ are nearly as effective as a conducting disc for both earth types (Fig. 5).

(ii) There is no first side lobe when the wire system is over well conducting earth, whereas for poorly conducting earth the first side lobe can be significant if $1 < b/\lambda < 4$.

(iii) The radiation patterns are generally quite broad. Typically, the -3 dB beamwidth (BW) is 43°– 48°, the -10 dB BW is 71°– 73°, and -20 dB BW is 84°– 86°. One exception is the system with $b = 2\lambda$ and N = 120 over poorly conducting earth (Fig. 6b), in which case the main lobe - 3 dB BW is 23°, the -10 dB BW is 36°, and -20 dB BW is 43°, but other major lobes appear at 65° and 82°.

(iv) The radially varying feature of radial-wire systems tends to eliminate the higher angle side lobes compared to the disc systems at the expense of low-angle radiation for $b > 2\lambda$.

(v) Conversely, conducting disc systems for which $\lambda < b$ tend to have a strong beam near the zenith (ψ = 90°), especially if the earth is poorly conducting (Figs. 6-8). This could be useful for close range sensing using ionospheric reflections, but is generally undesirable for lower angle sensing. Presumably, this is due to the impedance mismatch at the edge. Such mismatches are less severe for radial-wire systems.

(vi) The low-angle radiation for a radial-wire system may actually exceed that of a disc for $1 < b/\lambda < 2$ (Fig. 6). Clearly, the conducting disc is not always the preferred ground system, even aside from the cost factor.

(vii) For N = 120, the radiation patterns are nearly identical for all $b > 3\lambda$ if the earth is well conducting (e.g., compare Figs. 7a and 8a). Although not shown, the same is concluded for all $b > 4\lambda$ and poor earth. As a general rule, we have found that the largest effective value of b is that where

$|\Delta'(\rho = b)|$ is 90% of $|\Delta_0|$. These values are marked on Fig. 3 for N = 120. Making b larger than this has little effect on the radiation pattern if N is fixed. We have also found that the largest effective value of b increases in proportion to N, which is not very surprising, since $\Delta'(\rho)$ varies approximately as (ρ/N) if $|Z_{grid}| << |Z_e|$ (see (25), (26) and Fig. 3).

Effect of the Number of Radials N

(viii) Fig. 9 shows that the low-angle radiation is improved by increasing the number of radials, N. Although these curves are for $b = 10\lambda$, they also apply to all b equal to or greater than the largest effective radius as explained in (vii) above.

Effect of VED height, h_1

(ix) The radiation pattern was found to be insensitive to small heights, i.e., $h_1 < 0.1\lambda$, but some reduction in the main beam angle can be achieved if the VED is raised so that the h_1/λ is comparable to or greater than unity, in agreement with Gustafson et al. [1966]. But this can result in undesirable multiple lobes at higher angles, e.g., for $h_1 = 2\lambda$, $b = 2\lambda$ and N = 120, the radiation pattern has four major lobes (Fig. 10).

Table 1 lists the angles (ψ) and relative levels of the main beam and first side lobe vs. h_1/λ for $b = 2\lambda$, N = 120 and both well and poorly conducting earth. For well conducting earth, we see that the center position (ψ_0) of the main beam lobe decreases as h_1/λ increases from zero (this case shown in Fig. 6a) to 0.5; ψ_0 increases in the vicinity of $h_1/\lambda = 1$, and then rapidly decreases to 7° at $h_1/\lambda = 2$ (this case is shown in Fig. 10). Meanwhile, for $h_1/\lambda > 0.5$, the first side lobe level becomes comparable to that of the main beam, and its position (ψ_1) also rapidly decreases between $1 < h_1/\lambda < 2$. Thus, if $h_1/\lambda = 0.3$ is chosen, ψ_0 is lowered to 17° without creating a very significant side lobe.

If the earth is poorly conducting, the first side lobe level is comparable to that of the main beam even when $h_1/\lambda = 0$ (see Fig. 6b). As h_1/λ increases to 0.25, the first lobe level decreases at a faster rate than does the main lobe, being least at $h_1/\lambda = 0.25$. The main lobe position, ψ_0, decreases to 17° at $h_1/\lambda = 0.2$, increases slightly in the vicinity of $h_1/\lambda = 0.25$, and begins another decreasing cycle for $h_1/\lambda > 0.25$. If the earth is poorly conducting, the position of the first lobe, ψ_1, is generally lower than that for well conducting earth until $h_1/\lambda = 2$.

6.2 Compound Radial-wire Systems

We have seen that N and the earth parameters (ε,σ) determine the largest effective radius, beyond which the interwire separation, $d(= 2\pi\rho/N)$ is too great to have any significant effect on the pattern. Thus, for a given system radius, b, it is important that N be large enough that $|\Delta'(\rho = b)| \cong 0.9\ |\Delta_0|$, as deduced under (vii) above. But near the center where the radials converge, $|\Delta'(\rho)| << |\Delta_0|$, and so the number of radials canbe reduced in the interest of economy. This suggests the use of so-called compound radial-wire ground systems in which there are N_1 radials for $0 < \rho < a$ and N_2 radials for $a < \rho < b$, with $N_1 < N_2$ as shown in the inset of Fig. 11.

We have not yet completed our study of such compound systems, but some significant results are shown in Fig. 11. Noteworthy is the fact that the patterns at low angles for ($a = 0$, $b = 4\lambda$) and ($a = \lambda$, $b = 4\lambda$) are nearly identical. Thus, 120 fewer radials one wavelength long are required in the latter case. Also noteworthy is the fact that the additional 240 radials extending from $2 < \rho/\lambda < 4$ contribute significantly, as seen by comparing the ($a = \lambda$, $b = 2\lambda$) and the ($a = \lambda$, $b = 4\lambda$) cases. Actually, the largest effective radius for N = 240 and well conducting earth is 6λ (not shown). As it turns out, the pattern for this case in the range $0 < \psi < 20°$ is the same as when $b = 4\lambda$, but the pattern is enhanced somewhat for $20° < \psi < 40°$. Thus, for low-angle applications, the ($a = \lambda$, $b = 4\lambda$) case would probably be preferred.

6.3 HF Radial-Wire Ground System Near a Sloping Beach

Given the constitutive parameters of the land and sea, their surface impedances are easily calculated, but the surface impedance of a sloping beach is not known exactly. A sloping beach (Fig. 12) is similar to the problem of wave propagation in the direction of increasing wedge depth studied by King and Hustig [1971]. According to those experiments, backscattering due to a wedge (or sloping beach) is expected to be small. Since sea water is quite conductive and has a high dielectric constant, the refracted wave entering the water from the air is essentially vertically propagating. Considering the large losses of the water, as well as that at the water-ground bottom, higher order internal reflections or diffraction modes should be negligible. Therefore, the surface impedance in the sloping beach region can be calculated approximately by using an overburden of uniform depth equal to the local depth $h(\rho)$, and simple parallel-stratified media theory should suffice.

Note that this method is only expected to work when the depth is increasing in the direction of wave propagation. If the wedge depth is decreasing, it may not apply, but reciprocity does apply [King and Hustig, 1971]. Consequently, if the transmitting pattern can be found for a transmitter on land, its receiving pattern is identical for a transmitter over the sea. Moreover, for small h_1, the grazing surface impedance can be used in our formulation, whereas for large h_2 of a transmitting antenna over the sea, the angular dependence of Z_s should be taken into account.

Fig. 13 shows the normalized surface impedance profile for a 3° sloping beach at 10 MHz. The electrical properties of the sea bottom and the ground near the sloping beach are assumed to be $\varepsilon = 15\varepsilon_0$, $\sigma = 10^{-2}$ S/m, and for the sea water, $\varepsilon_s = 80\varepsilon_0$, $\sigma_s = 4$ S/m. We observe that the wave does not "see" the sea bottom beyond about 0.15λ from the coastline where the normalized surface impedance settles to that of the sea.

Figs. 14a and b show the radiation pattern of a VED when placed 0.5λ and λ to the left of the coastline, respectively. The pattern for a homogeneous sea and an abrupt coastline without sloping beach are also shown for comparison. The sloping beach is found to have little effect on the radiation

pattern compared to that of an abrupt coastline at HF. This is reasonable considering the effective beach transition is only about 0.15λ. We expect there is even less effect on the radiation pattern at lower frequencies or steeper slopes, since the beach then becomes more like an abrupt coastline. For example, at 10 KHz (VLF) the transition is about 0.01λ, at 100 KHz (LF) it is about 0.02λ, and at 1 MHz (MF) it is about 0.06λ for a 3° slope.

Fig. 14b shows that as the source moves away from the coastline, the radiation field at low angles ($0° \leq \psi \leq 65°$) is decreased. Note also that in the homogeneous sea pattern the surface wave portion of (5) gives a significant amount of grazing angle radiation, whereas there is an infinitesimally small amount in the uniform land pattern due to its greater loss. Low-angle launching can be further improved by adding a radial-wire ground system on the earth beneath the VED, as shown in Fig. 15. In this case, the pattern is slightly better than that of the homogeneous sea at low angles.

7. OTHER APPLICATIONS

The results shown in these examples can be directly applied to other frequencies or problems having the same impedance profiles ($\Delta'(\rho)$ and Δ_o), where all distances are measured in wavelengths.

These studies indicate that some degree of radiation pattern manipulation is possible by adjusting the ground system parameters for a given underlying earth. Adjustment of the VED height appears to hold particular promise; using a stacked array of dipoles with arbitrary currents gives additional flexibility, including the possibility of steering the pattern electronically. Wait [1970] studied this problem for the case where $\Delta'(\rho)$ is uniform for $0 < \rho < b$.

Because the formulation uses the surface impedance, it can be adapted to other configurations such as stratified media or buried ground systems. Particular examples are radial-wire ground systems laid on ice over a highly conducting sea, and to ground systems covered with ice or snow.

Teng [1978] has used the present formulation to study surface wave antennas excited by a VED source. By varying the surface reactance profile, the antenna length and the source height, the antenna's directivity, beamwidth and sidelobe level can be optimized.

It is expected that this work will find other applications in the design of more efficient radiating systems having more nearly optimized radiation patterns, particularly at HF.

REFERENCES

Andersen, J. B., 1963, "The radiation field from a vertical dipole on an inhomogeneous ground," in Electromagnetic Theory and Antennas, E. C. Jordan (ed), 1099-1112, Pergamon Press, N.Y.

Atkinson, K. E., 1976, A Survey of Numerical Methods for the Solution of Fredholm Integral Equations of the Second Kind, Soc. for Ind. and Appl. Math.

Cho, S. H. and King, R. J., 1976a,"Radiation from a finite sinusoidally modulated reactance surface (SMRS)," Radio Sci.11(6), 561-570.

Cho, S. H. and King, R. J., 1976b,"Numerical solution of nonuniform surface wave antennas," IEEE Trans. Antennas Propagation, AP-24(4), 483-490.

Gustafson, W. E., Chase, W. M. and Balli, N. H., 1966, "Ground system effect on HF antenna propagation," U.S. Navy Electronics Lab Report No. 1346.

Hufford,G.,1952,"An integral equation approach to the problem of wave propagation over an irregular terrain," Quart. J. Appl. Math., 9(4), 391-404.

de Jong,G.,1975,"Electromagnetic wave propagation over an inhomogeneous flat earth (two-dimensional integral equation formulation)," Radio Sci. 10(12), 925-933.

King, R. J., 1969, "Electromagnetic wave propagation over a constant impedance plane," Radio Sci. 4(3), 255-268.

King, R. J. and Hustig, C. H., 1971, "Microwave surface impedance measurements of a dielectric wedge on a perfect conductor," Can. J. Phys. 49(7), 820-830.

King, R. J. and Wait, J. R., 1976, "Electromagnetic Groundwave Propagation Theory and Experiment" in Symposia Mathematica, 18, Academic Press, London.

King, R. J., Cho, S. H., Jaggard, D. L. and Sokolov, V., 1973, "Height-gain experimental data for groundwave propagation: 1, Homogeneous Paths," Radio Science, 8(1), 7-15.

Linz, P., 1969, "Numerical methods for Volterra integral equation with singular kernels," SIAM J. Numer. Anal. 6(3), 356-374.

Mittra, R., 1961, "A vector form of compensation theorem and its application to boundary value problem," AFCRL 575, University of Colorado, Boulder.

Monteath, G. D., 1951, "Application of compensation theorem to certain radiation and propagation problems," Proc. Inst. Elec. Eng., 98, Pt. IV, 23-31.

Peirce, W. H., 1957, "Numerical integration over the planar annulus," J. Soc. Indust. Appl. Math. 5(2).

Rafuse, R. P. and Ruze, J., 1975, "Low-angle radiation from vertically polarized antennas over radially heterogeneous flat ground," Radio Sci. 10(12), 1011-1018.

Stroud, A. H., 1971, Approximate Calculation of Multiple Integrals, Prentice Hall, Englewood Cliffs, N.J.

Teng, C., 1978, Groundwave Propagation and Radiation Patterns of a Vertical Electrical Dipole over a Radially Varying Surface Impedance Plane, Ph.D. Thesis, University of Wisconsin.

Wait, J. R., 1962, "Effective impedance of a wire grid parallel to the earth's surface," IRE Trans. Antennas Propagation, AP-10, 538-542.

Wait, J. R., 1963, "The theory of an antenna over an inhomogeneous ground plane," in Electromagnetic Theory and Antennas, E.C. Jordan (ed), 1079-1098, Pergamon Press, N.Y.

Wait, J. R., 1967a, "Pattern of a linear antenna erected over a tapered ground screen," Can. J. Phys., 45(9), 3091-3101.

Wait, J. R., 1967b, "On the theory of radiation from a raised electric dipole over an inhomogeneous ground plane," Radio Sci. 2(9).

Wait, J. R., 1969, "Characteristics of antennas over lossy earth," in Antenna Theory, R. E. Collin and F. J. Zucker (ed), McGraw-Hill, N.Y., Pt. 2, Ch. 23.

Wait, J. R., 1970, "Elevation steering of the pattern of a vertical array of vertically polarized elements over a ground screen," IEEE Trans. on Antennas and Propagation, AP-18(1), 105-107.

Wait, J. R. and Spies, K. P., 1970a, "Integral equation approach to the radiation from a vertical antenna over an inhomogeneous ground plane," Radio Sci., 5(1), 73-79.

Wait, J. R. and Spies, K. P., 1970b, "On the radiation from a vertical dipole with an inductive wire-grid ground system," IEEE Trans. Antennas Propagation, AP-18(4), 558-560.

This research was supported by the National Science Foundation Research Grant ENG75-16174 and the University of Wisconsin Research Committee.

Table 1. Positions and relative levels of main beam and first side lobe for a simple radial-wire ground system vs. VED height. ($b = 2\lambda$, $N = 120$, $f = 10$ MHz).

VED HEIGHT (h_1/λ)	Well Conducting Earth $\varepsilon = 15\varepsilon_o$, $\sigma = 10^{-2}$S/m				Poorly Conducting Earth $\varepsilon = 5\varepsilon_o$, $\sigma = 10^{-4}$S/m			
	MAIN BEAM		FIRST SIDE LOBE		MAIN BEAM		FIRST SIDE LOBE	
	ANGLE (ψ_0)	LEVEL	ANGLE (ψ_1)	LEVEL	ANGLE (ψ_0)	LEVEL	ANGLE (ψ_1)	LEVEL
0 (Fig. 6)	27°	0.733			24°	1.03	64°	1.03
0.1	25°	0.701			18°	0.955	64°	0.875
0.2	21°	0.637	81°	0.046	17°	0.92	64°	0.72
0.25	19°	0.599	82°	0.053	22°	0.88	48°	0.185
0.3	17°	0.560	63°	0.086	21°	0.838	48°	0.302
0.4	14°	0.488	56°	0.270	18°	0.738	48°	0.554
0.5	12°	0.431	51°	0.464	16°	0.631	48°	0.771
1	28°	0.681	64°	0.363	10°	0.47	30°	0.49
2 (Fig.10)	7°	0.628	29°	0.638	7°	0.8	30°	0.49

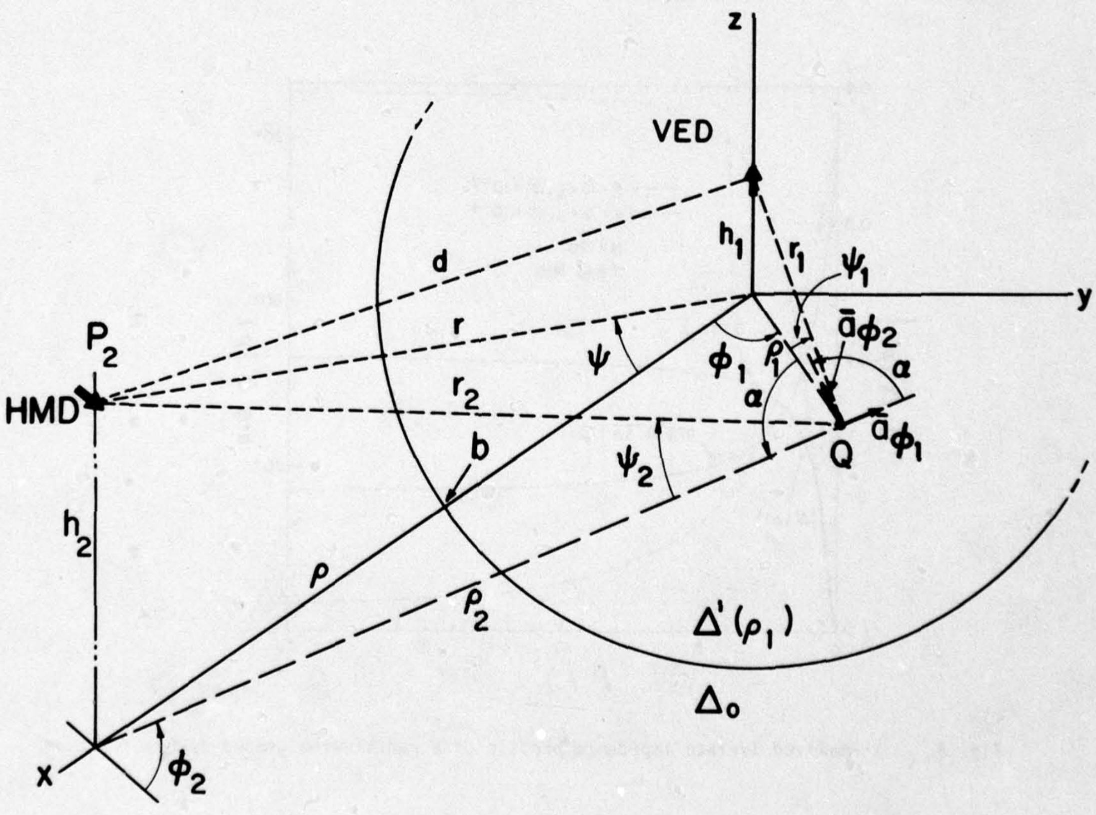

Fig. 1. Geometry of a VED over a radially varying surface impedance plane.

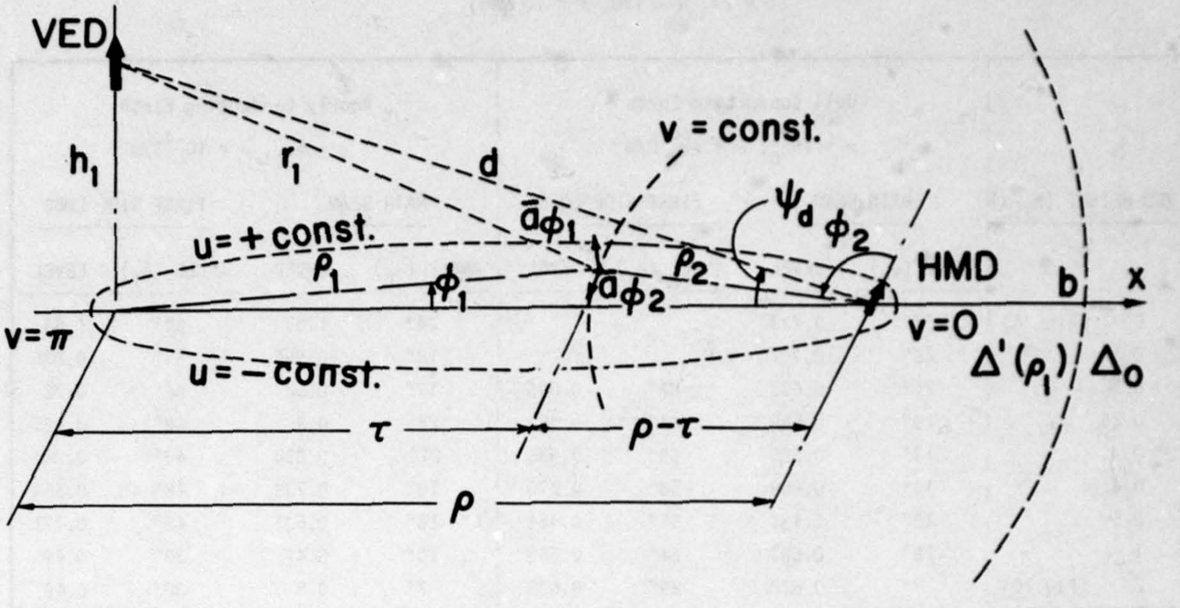

Fig. 2. The transmitting-receiving antenna pair superimposed on an elliptic cylindrical coordinate system.

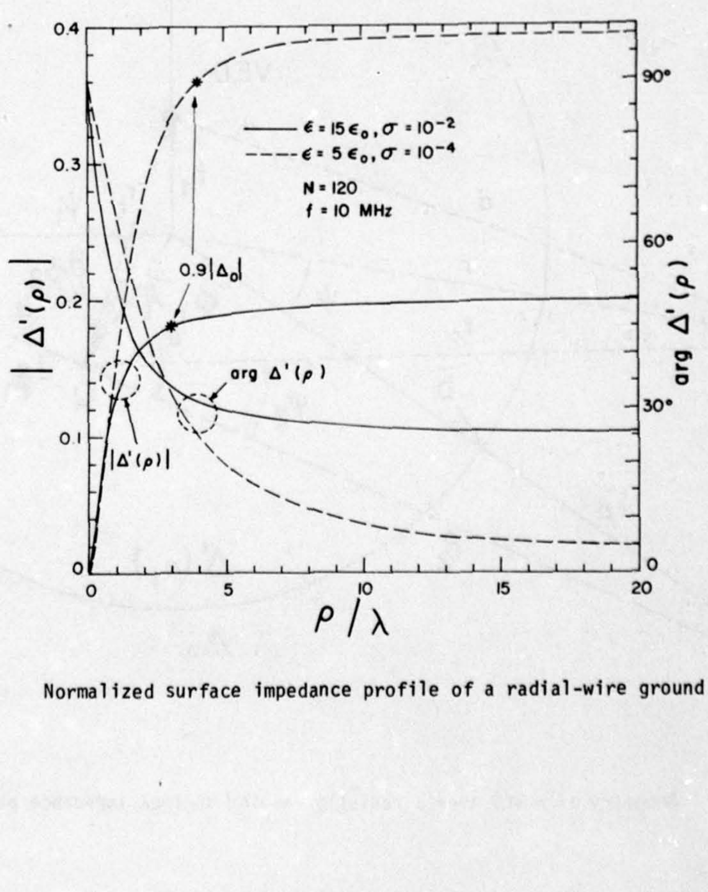

Fig. 3. Normalized surface impedance profile of a radial-wire ground system.

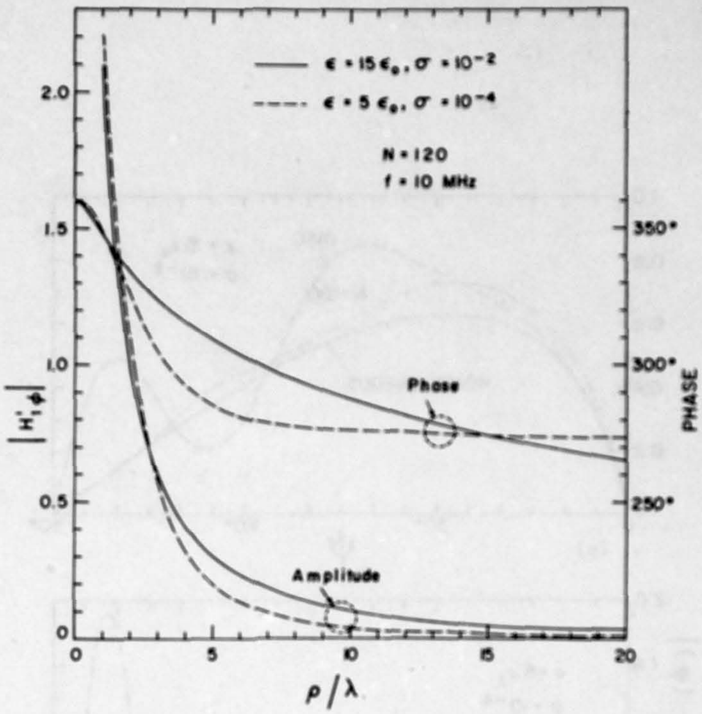

Fig. 4. Magnetic field of a VED on the surface of a radial-wire ground system. Amplitude is normalized by $k\, I_1 \ell_1 / 4\pi$.

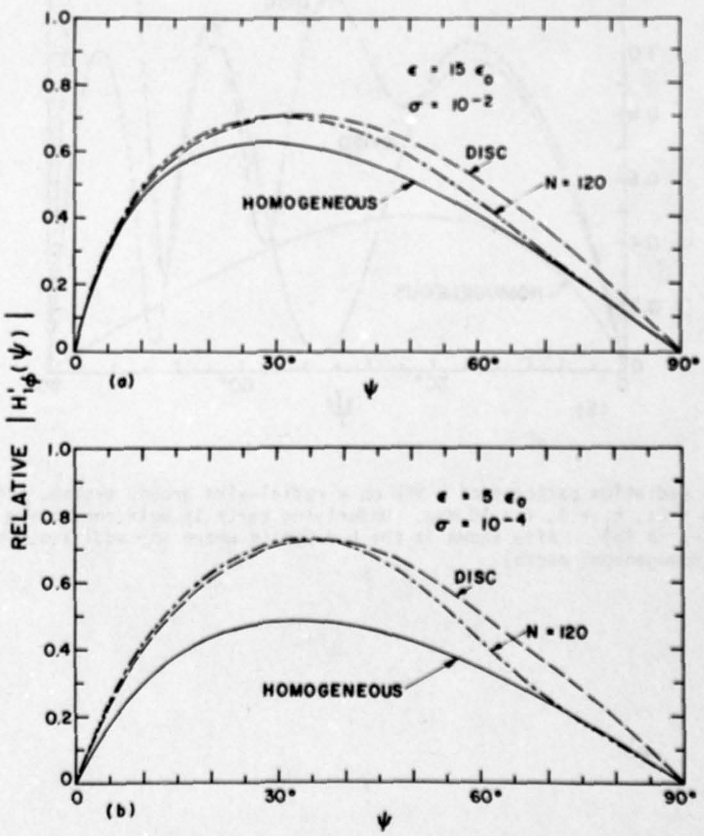

Fig. 5. Vertical radiation patterns of a VED on a radial-wire ground system, and on a conducting disc. $b = \lambda$, $h_1 = 0$, $f = 10$ MHz. The underlying earth is well conducting in (a) and poorly conducting in (b). Also shown is the $b = 0$ case where any additional ground system is absent (homogeneous earth).

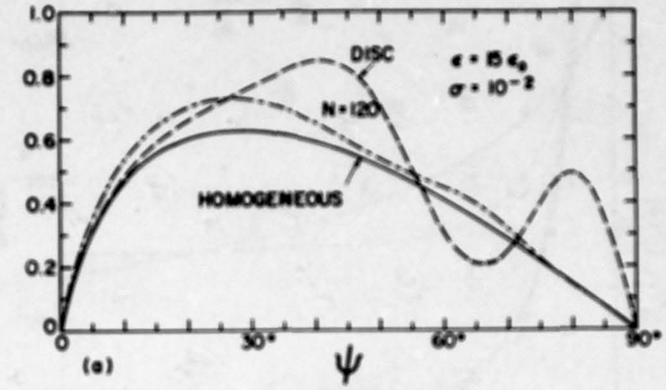

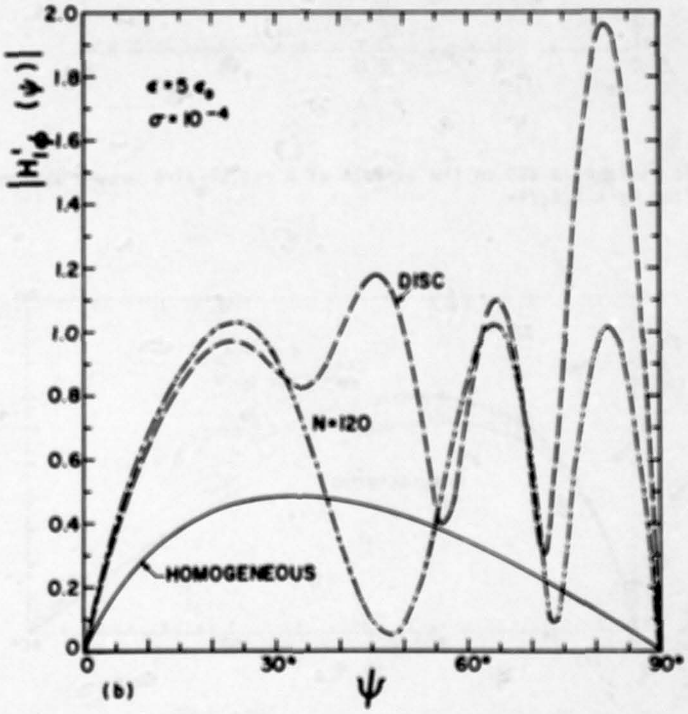

Fig. 6. Vertical radiation patterns of a VED on a radial-wire ground system, and on a conducting disc. $b = 2\lambda$, $h_1 = 0$, $f = 10$ MHz. Underlying earth is well conducting in (a) and poorly conducting in (b). Also shown is the $b = 0$ case where any additional ground system is absent (homogeneous earth).

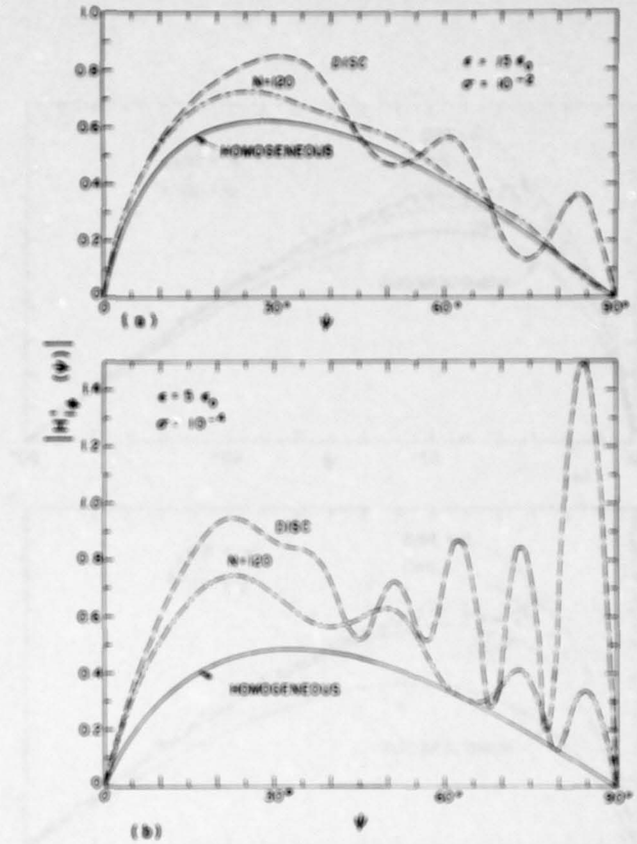

Fig. 7. Vertical radiation patterns of a VED on a radial-wire ground system and on a conducting disc. $b = 3\lambda$, $h_1 = 0$, $f = 10$ MHz. Underlying earth is well conducting in (a) and poorly conducting in (b).

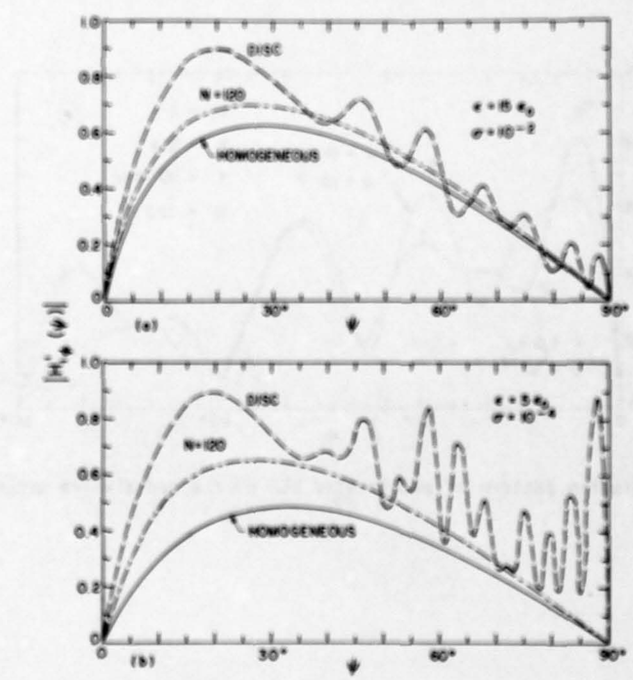

Fig. 8. Radiation patterns of a VED on a radial-wire ground system, and on a conducting disc. $b = 7.5\lambda$, $h_1 = 0$, $f = 10$ MHz. Underlying earth is well conducting in (a) and poorly conducting in (b).

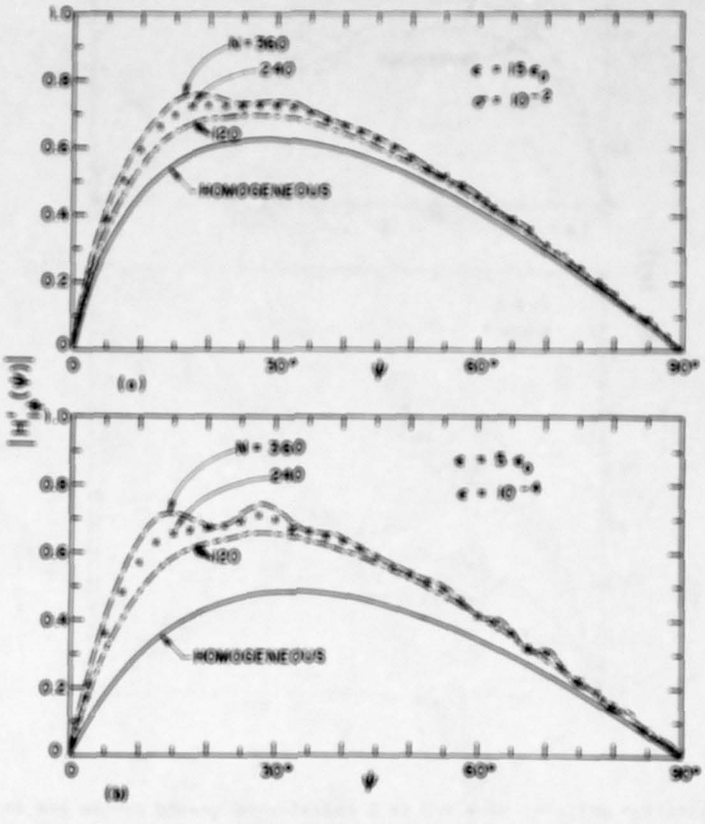

Fig. 9. Radiation patterns of a VED on a radial-wire ground system. $b = 10\lambda$, $h_1 = 0$, $f = 10$ MHz. Underlying earth is well conducting in (a) and poorly conducting in (b).

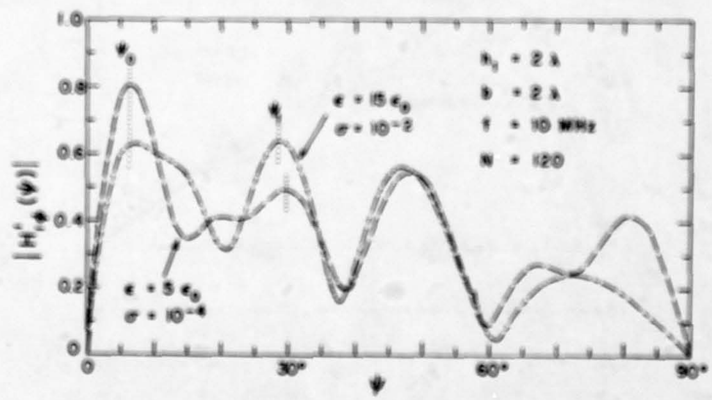

Fig. 10. Radiation pattern of an elevated VED over a radial-wire ground system.

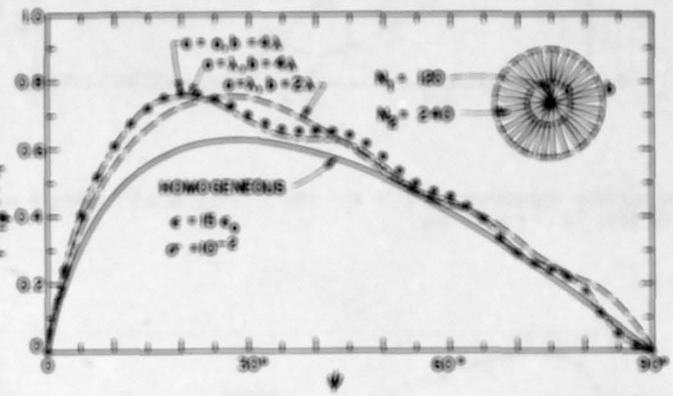

Fig. 11. Radiation patterns for a VED on a compound radial-wire ground system overlying well conducting earth. $h_1 = 0$, $f = 10$ MHz.

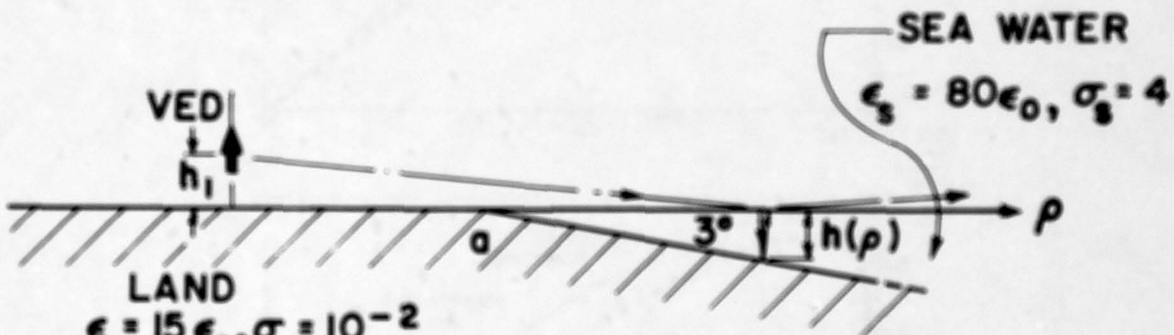

Fig. 12. Geometry for a VED on land near a sloping beach. The earth beneath the VED may be covered with a radial-wire ground system.

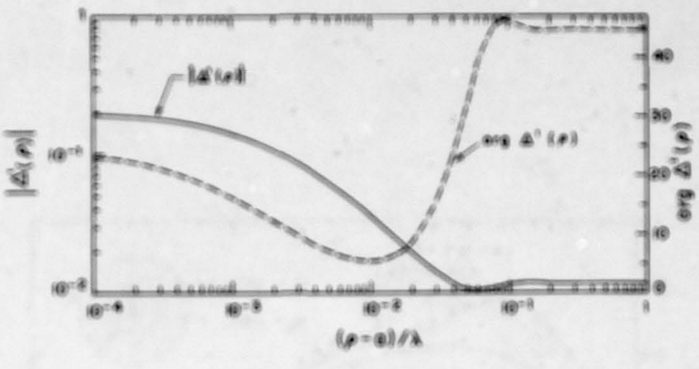

Fig. 13. Normalized surface impedance profile for the sloping beach having a well conducting bottom as shown in Fig. 12. f = 10 MHz.

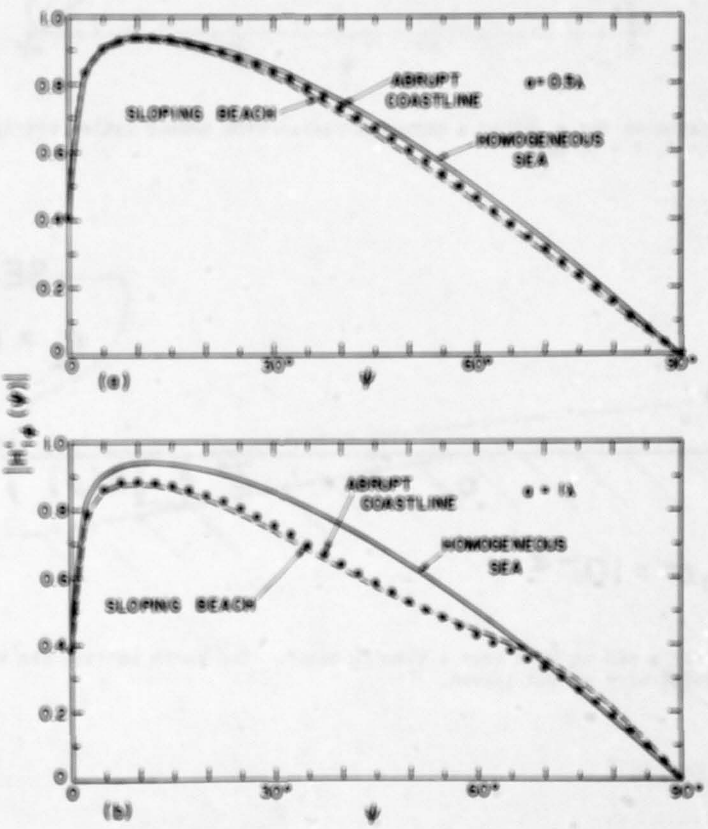

Fig. 14. Vertical radiation patterns for a VED on land near a sloping beach. $h_1 = 0$, $f = 10$ MHz. In (a), the VED is situated on the land at a = 0.5λ from the sea. In (b), a = 1λ. For comparison, the patterns for an abrupt coastline and for no land (homogeneous sea) are also shown.

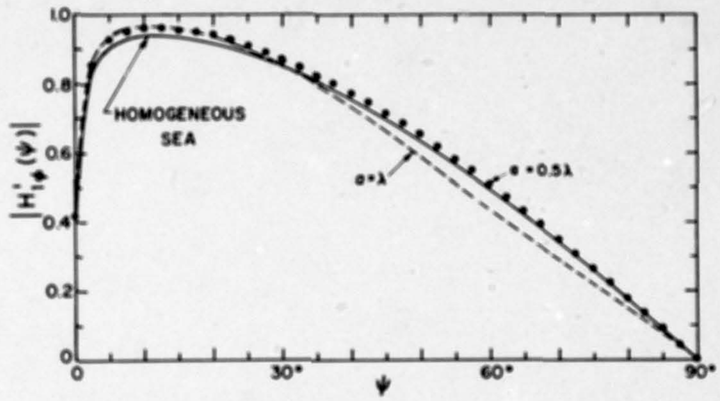

Fig. 15. Vertical radiation patterns for a VED on a radial-wire ground system (N = 120) near a sloping beach. The ground system overlies well conducting land and extends up to the sea (a = b). For comparison, the pattern for a VED on a homogeneous sea (no land) is also shown. $h_1 = 0$, $f = 10$ MHz.

TERRAIN EFFECTS ON LOG-PERIODIC ANTENNA CHARACTERISTICS

USING THE SINGULARITY EXPANSION METHOD

K.D. Rech/K.J. Langenberg

Theoretische Elektrotechnik
Universität des Saarlandes
D-6600 Saarbrücken, FRG

SUMMARY

A verticalLPDA is investigated with SEM in free space, over a lossy ground and over a perfectly conducting halfspace using Nortons approximation for the Sommerfeld integrals. The influence of the feedingnetwork and of the mutual coupling of the elements as well as the influence of antenne thickness on the natural resonances is studied. The modes of the LPDA are presented and the current in frequency and time domain is computed in free space. Dependent on the ground parameters and the antenna height we show the pole migration in the complex frequency plane and determine the appropriate modes. Starting from the free space current distribution we compute the transient farfields of the vertical LPDA over ground for various ground parameters and antenna heights.

1.0 INTRODUCTION

Aspects of system reliability in military and professional domain and scientific insight in the physical process have stimulated transient investigations in the electromagnetic domain. The question of receiving and transmitting of electromagnetic pulses, the dispersion characteristics of currents on antennas and scattering objects and the resulting fields got one main topic of investigation during the last decade. New methods were developed. Especially SEM (BAUM, C.E.,1978) has proven to be physically enlightening.

A widespread antenna for receiving and transmitting of electromagnetic signals in the frequency range from to 5 MHz till 1 GHz is the LPDA. In frequency domain this antenna was analyzed with approximate analytical methods by CHEONG and KING et al. (CHEONG, W.M./ KING, R.W.P., 1967). Investigations over ideal conducting earth were done numerically by IMBRIALE for a horizontal LPDA (IMBRIALE, W.A., 1975) and the time domain behavior of this LPDA was studied with a fourier-extension method for a limited bandwidth by DEADRICK (DEADRICK, F.J., 1977).

Pure time domain investigations started in the early seventies. First, there were analytical approximations developed on the basis of a phenomenological description of the wave propagation on the antenna structure (KNOP, C.M.;1970; WIGGINS, C.M., 1974; STARK, W.J., 1977). In 1973 SOLMAN investigated the LPDA with a time stepping procedure. LANGENBERG gave in 1978 a first approximate analytical description of the LPDA with a HALLEN SEM approximation neglecting the mutual coupling of the elements and the influence of the transmission line (LANGENBERG, K.J., 1978).

In this paper we present a systematic SEM analysis of the complete LPDA. We study the influence of the mutual coupling of the elements and the influence of antenna thickness on the pole location. Further we look at the poles of the antenna dependent on the distance of the antenna over perfectly conducting and lossy ground. We compute the appropriate modes and study their behavior under variation of height and earth parameters. The transient current distribution is calculated in frequency domain with subsequent fourier inversion or with SEM. Starting from this current distribution we investigate the far field of the antenna in free space, over lossy and perfectly conducting ground.

2.0 MATHEMATICAL FORMULATION

2.1 Geometry

The geometry of the antenna under concern is shown in Fig.1. It consists of N straight wire elements of length L_n and radius a_n parallel to the z-axis. The elements are arranged center-symmetric to the ρ-axis in a form that the tips of the elements touch the legs of a triangle with apex angle α. The length ratio of successive elements is denoted by τ and the ratio of element spacing and element half-length is σ. The single elements are connected in the center by a two wire transmission line which is crossed in between each two elements. This transmission line is terminated at the longest element with its characteristic impedance Z_0 and fed at the smallest element by a matched generator. In the case of a ground plane the antenna is situated vertically at a height h_0 about this plane.

2.2 Feeding Network

The feeding network of the LPDA consists of a ladder network (Fig. 2) where the boxes represent the transmission lines. I_n are the currents which are flowing into the antennas and U_n are the voltages at the antenna feed points. R_{source} is the generator impedance, which equal to Z_0. V_{source} is the generator voltage . In the following γ is the propagation constant and s is the complex frequency.

(1) $$\gamma = \frac{s}{j \cdot c} \quad ; \quad s = \sigma + j\omega$$

The network analysis results in the following admittance matrix equation.

(2)

$$I_N\left(\frac{\Delta l}{2}\right) + \left(\frac{\cosh\gamma d_N}{-Z_0 \sinh\gamma d_N} + \frac{\cosh\gamma d_{N-1}}{-Z_0 \sinh\gamma d_{N-1}} + \frac{Z_L}{Z_0 \sinh\gamma d_N}\,\frac{1}{Z_0\sinh\gamma d_N + Z_L\cdot\cosh\gamma d_N}\right)U_N + \frac{1}{-Z_0\sinh\gamma d_{N-1}}U_{N-1} = 0$$

$$I_{N-1}\left(\frac{\Delta l}{2}\right) + \frac{1}{-Z_0\sinh\gamma d_{N-1}}U_N + \left(\frac{\cosh\gamma d_{N-1}}{-Z_0\sinh\gamma d_{N-1}} + \frac{\cosh\gamma d_{N-2}}{-Z_0\sinh\gamma d_{N-2}}\right)U_{N-1} + \frac{1}{-Z_0\sinh\gamma d_{N-2}}U_{N-2} = 0$$

$$I_2\left(\frac{\Delta l}{2}\right) + \frac{1}{-Z_0\sinh\gamma d_2}U_2 + \left(\frac{\cosh\gamma d_2}{-Z_0\sinh\gamma d_2} + \frac{\cosh\gamma d_1}{-Z_0\sinh\gamma d_1}\right)U_2 + \frac{1}{-Z_0\sinh\gamma d_1}U_1 = 0$$

$$-R_{source} I_1\left(\frac{\Delta l}{2}\right) + \frac{R_{source}}{Z_0\sinh\gamma d_1}U_2 + \left(\frac{\cosh\gamma d_1\, R_{source}}{Z_0\sinh\gamma d_1} + 1\right)U_1 = V_{source}$$

The antenna elements themselves are described in frequency domain (exp(+jωt)) by a pocklington type integral equation. For free space and perfectly conducting half space we use the exact Greens function and in the case of lossy half space we use Nortons approximation (NORTON, K.A., 1937) of the Sommerfeld integrals. The integral equqtions were solved with the method of Galerkin with sinusoidal subsectional base and test functions. A brief overview over the integral equation the different kernels and the numerical treatment is given in the following sections.

2.3 Integral Equations

2.3.1 Free Space

The pocklington integral equations for a coupled system of wire structures with voltage feed is given by

(3)

$$\left\{\frac{d^2}{dz^2} - s^2\right\}\cdot\left\{\int_{-\frac{L_j}{2}}^{\frac{L_j}{2}} I_j(z')\cdot K^{(1)}(z,z')\,dz' + \sum_{\substack{i=1\\ i\neq j}}^{N}\int_{-\frac{L_i}{2}}^{\frac{L_i}{2}} I_i(z')\,K^{(2)}(z,z')\,dz'\right\} + 4\pi\varepsilon s\frac{U_j}{\Delta l} = -4\pi\varepsilon s\,E_z^{inc}(z)$$

Where the first integral represents the contribution of an isolated antenna and the sum over the integrals represents the contributions of the interacting antennas. The kernel in the first integral is the complete surface current kernel. In the case of the interacting antennas the current is thought to be concentrated on the axis of the antenna, so we can apply a thin wire kernel.

(4)

$$K^{(1)}(z,z') = \frac{1}{2\pi}\int_0^{2\pi}\frac{e^{-\frac{s}{c}R}}{R}\,d\varphi\;; \qquad R^2 = (z-z')^2 + 4a^2\sin^2\varphi$$

$$K^{(2)}(z,z') = \frac{e^{-\frac{s}{c}R_{ji}}}{R_{ji}}\;; \qquad R_{ji}^2 = d_{ij}^2 + (z_j - z_i)^2 + a^2$$

2.3.2 Perfectly Conducting Half Space

In the presence of a perfectly conducting half space the kernels of the integral equation have to be altered. There must be added a second part to the Greens function representing the contributions reflected from the surface.

(5)

$$K^{(1)}(z,z') = \frac{1}{2\pi}\int_0^{2\pi}\frac{e^{-\frac{s}{c}R}}{R}\,d\varphi + \frac{e^{-\frac{s}{c}R_r}}{R_r}\;, \qquad R_r^2 = (z+z')^2 + a^2$$

$$K^{(2)}(z,z') = \frac{e^{-\frac{s}{c}R_{ji}}}{R_{ji}} + \frac{e^{-\frac{s}{c}R_{jir}}}{R_{jir}}\;, \qquad R_{jir}^2 = d_{ij}^2 + (z+z_j)^2 + a^2$$

Again we omitted the surface integration because the distance R_r of source and observation point is large in comparison to the distance R.

2.3.3 Lossy Ground

The extension of the integral equation to the lossy ground case can be accomplished rigorously for the vertical antenna. There has to be added to the kernel (5) the appropriate Sommerfeld integral (NORTON. K.A., 1937)

(6)

$$V = 2 \int_0^\infty J_0(\lambda d)\, e^{-\mu(s+s')} \frac{\mu_E}{\varepsilon_E \cdot \mu + \mu_E} \frac{2}{\mu}\, d\lambda$$

$$\mu^2 = \lambda^2 + \frac{s^2}{c^2}$$

$$\mu_E^2 = \lambda^2 - \varepsilon_E \frac{s^2}{c^2}$$

$$d^2 = \begin{cases} a^2 & \text{for source and observation point on the same antenna} \\ d_{ij}^2 + a^2 & \text{else} \end{cases}$$

ε_E is the complex permittivity of ground

$$\varepsilon_E = \varepsilon_r + \frac{\sigma_E}{s\,\varepsilon_0}$$

ε_r is the relative dielectric constant and σ_r is the conductivitiy of the lossy ground.

There is one serious drawback. The computation of Sommerfeld integrals for transient investigations wastes computer time. However LPDAs are normally operated at frequencies of more than 5 MHz so they can be elevated at a height of one half or more wavelengths above ground. Therefore we can use an approximate formulation if we restrict our attention to antennas which are elevated at a height h_0 corresponding to the lowest resonance of the longest element of the antenna array. The Norton approximation was shown to be valid all over the $(z+z')/\lambda$, $(\rho+\rho')/\lambda$ plane exept in the region $(z+z')/\lambda<1,(\rho+\rho')/\lambda<1$ (BRITTINGHAM J.N., MILLER, E.K., OKADA, J.T., 1978). For lower frequencies which are always included in transient analysis, the relative antenna height gets smaller in comparison to the wavelength, but now the antenna is operated below its resonance region. The antenna system is a bad radiator. No serious influence on the current on the antenna must be feared.

At the operating height specified before, the kernel (6) can be approximated by

(7)

$$V = \left\{ (1 - R_v) F - 1 + R_v \right\} \cdot e^{-\frac{s}{c} R_r}$$

$$R_v = \frac{\varepsilon_E \cos\Theta - \sqrt{\varepsilon_E - \sin^2\Theta}}{\varepsilon_E \cos\Theta + \sqrt{\varepsilon_E - \sin^2\Theta}}$$

$$F = 1 - j\sqrt{\pi \cdot P'}\, e^{-P}\, \mathrm{erfc}\left(j\sqrt{P}\right)$$

$$P = \frac{-s R_r}{c \sin^2\Theta} \cdot \left\{ \cos\Theta + \frac{\sqrt{\varepsilon_E - \sin^2\Theta}}{\varepsilon_E} \right\}^2$$

2.4 Numerical Solution

For the numerical solution of the integral equation we use the moment method with subsectional base functions. We segmented each element of the antenna in N_T segments. The inner segments of all elements are of equal size. The segments at the tips are of different lengths. Therefore we had to employ sinusoidal functions of the form

(8)

$$w_m(z) = \frac{\sin + \frac{\ell^3}{c}\left(\Delta z_{ml} - (z_m - z)\right)}{\sin + \frac{\ell^3}{c}\, \Delta z_{ml}} \left\{ U(z - (z_m - \Delta z_{ml})) - U(z - z_m) \right\}$$

$$\frac{\sin + \frac{\ell^3}{c}\left(\Delta z_{mu} - (z - z_m)\right)}{\sin + \frac{\ell^3}{c}\, \Delta z_{mu}} \left\{ U(z - z_m) - U(z - (z_m + \Delta z_m)) \right\} \; ; \; m = 1, \dots M$$

where U_z is the Heavyside function and Δz_{ml} and Δz_{mu} are the lengths ofthe lower respectively upper segments .

This type of test function which satisfies the homogeneous differential operator in (3) reduces the integrodifferential equation to a system of M integral expressions which have proven to give very stable results independent of the type of base functions. After two integrations by part we get the following expression for equation (3)

(9)

$$\frac{\gamma s}{c \sin \frac{\gamma s}{c} \Delta z_{ml}} \cdot \left\{ \cos \frac{\gamma s}{c} \Delta z_{ml} \cdot \underline{A}(z_m) - \underline{A}(z_m - \Delta z_{ml}) \right\}$$

$$- \frac{\gamma s}{c \sin \frac{\gamma s}{c} \Delta z_{mu}} \left\{ - \cos \frac{\gamma s}{c} \Delta z_{mu} \, \underline{A}(z_m) + \underline{A}(z_m + \Delta z_{mu}) \right\}$$

$$+ 4\pi \varepsilon s U_j \frac{\sin \frac{\gamma s}{c} \frac{\Delta z_{ml}}{2}}{\sin \frac{\gamma s}{2} \Delta z_{ml}} \left\{ \delta\left(\frac{M}{2} - m\right) + \delta\left(\frac{M}{2} + 1 - m\right) \right\} = \int_{z_m - \Delta z_{ml}}^{z_m + \Delta z_{mu}} E_z^{inc}(z)\, w_m(z)\, dz \quad ; \; m = 1, \dots M$$

$$\delta(0) := 1$$

$A(z_m)$ is a vector potential type expression:

(10)

$$\underline{A}(z_m) = \int_{\frac{L_j}{2}}^{\frac{L_j}{2}} I_j(z')\, k^{(1)}(z_m, z')\, dz' + \sum_{\substack{i=1 \\ i \neq j}}^{N} \int_{-\frac{L_i}{2}}^{\frac{L_i}{2}} I_i(z')\, k^{(2)}(z_m, z')\, dz'$$

As base functions we apply sinusoidal function in (10) and obtain a matrix equation of the form :

(11) $$\underline{\underline{Z}}\, \underline{I} = \underline{U}$$

$\underline{Z}$ is a impedence matrix as displayed in Fig. 3. $\underline{I}$ is the vector of the unknown currents on the antenna and voltages on the feeding network. $\underline{U}$ is the excitation matrix containing the incident field integrals and the excitation voltage of the feederline. There exists an other way to formulate this problem (IMBRIALE, W.A., 1975) which avoids the additional feeder and coupling matrices. But as we want to treat the problem as a whole because of our interest in the SEM pole shifting by the feeder system , we use a formulation which enlarges the rank of the matrix by the number of elements of the antenna.

2.5 SEM-Representation

All quantities in (11) are functions of the complex frequency s and the solution of (11) can be represented by (BAUM, C.E., 1978)

(12) $$I(s) = \sum_i \beta_i \frac{\langle O_i, U(s) \rangle}{s - s_i} M_i + G(s)$$

s_i are the natural resonances, M_i are the mode vectors, O_i are the coupling vectors and β_i are the normalisation constants. G(s) is an entire function, which has proven to be 0 for finite antenna structures in free space and over perfectly conducting ground. However in the case of lossy ground there are problems with the branchcut.

The natural resonances s_i are the zeros of

(13) $$\det \underline{\underline{Z}}(s_i) = 0$$

and the mode and coupling vectors are solutions of the following equations:

(14) $$\underline{\underline{Z}}(s_i)\, \underline{M}_i = 0 = \underline{\underline{Z}}^T(s_i) \cdot \underline{O}_i$$

The normalisation constant β_i can be computed by

(15) $$\beta_i = 1 / \left(\underline{O}_i\, \underline{\underline{Z}}'(s_i)\, \underline{M}_i \right)$$

$Z'(s_i)$ is the derivative of Z in s.

The time behaviour of (12) can be obtained by Laplace inversion.

(16)

$$\underline{I}(t) = \sum_i \beta_i \cdot \underline{M}_i \cdot f_i(t)$$

If the excitation function $U(s)$ has only single poles as singularities $f_i(t)$ can be represented by a sum of damped exponentials.

$$f_i = \sum_{m_i} a_{m_i} \exp(s_{m_i} t) \tag{17}$$

By convolution we can get from (16) the results for arbitrary excitation.

In the following we normally use a Gaussian excitation of the form:

$$u(t) = A_0 \exp(-a^2 (t-t_0)^2) \tag{18}$$

This bandlimiting function allows us to restrict our SEM investigation on a short range in the complex frequency plane. High frequencies are strongly damped by the fast declining Gauss function.

3.0 NUMERICAL RESULTS

3.1 LPDA in Free Space

The antenna under concern has five elements. The apex angle α is 27.12°, τ is 0.795 and σ is 0.1. The length of the largest element is 2 m. The transmission line impedance has 50 Ω (parameters of Solman, 1973). Our analysis was carried out on the basis of SEM in frequency and time domain. We try to discern the diffrent influences acting on the natural resonances as the coupling effects and geometric effects. We study the modes of the LPDA, compute the frequency response of the current and show the time behaviour of the current for step and Gaussian excitation and give some idea of the transient farfield.

In Fig. 4 we have shown the poles of the LPDA in a strip of width 2 and length 26 in the normalised left upper half of the complex frequency plane. The poles (black dots) are situated in groups which are circled by dashed lines. These pole groups are denoted by n = 1, n = 3 and n = 5. The first group of poles n = 1 can be identified by comparison with the single element poles in free space (small circles) as the basic resonances of the LPDA elements. The higher groups can be identified in the same manner. The LPDA poles are shifted left of the poles of the single elements in free space. This shifting can be explained by two effects:

1. The loading of the antennas in free space through the feeding network shifts the poles far to the left (crosses). Energy floats back from the antenna to the feeder network. This is computed by omitting the mutual coupling matrices in Fig. 3.
2. The undamping of the elements by the mutual coupling of the elements through space. Additional energy is coupled from element to element. This is computed with the whole matrix.

The influence of antenna thickness is shown in Fig. 5. For thicker antennas the poles have a stronger radiation damping. But on the other hand the radiation coupling is intensified. This can be stated by comparison of the first pole group in Fig 4 and the corresponding group in Fig. 5.

Real and imaginary part of the normalized modes of the LPDA are shown in Fig. 6 and Fig. 7 for group 1 respectively group 3 in the right half of the elements. The modes of group 1 are of the form of a half cosine and the resonant element carries the largest amplitude. The other elements especially the direct neighbours are coupled and thus they have a smaller current mode distribution. The phases of the modes are related to element N so the modes of the shorter elements show real and imaginary parts which reflect the phase shifting by the feeding network. The modes of group 3 show a three quarter period of cosine. For the shortest element there can be observed that the resonance of this element nearly coincides with another resonance of the longest element which carries therefore the second largest current mode distribution.

The normalized input current of the single elements are shown in Fig. 8 for the frequency domain. There can be observed deformations of the well known free space antenna input characteristics which are caused by the neighbouring elements. We have displayed two curves , one based on the element lengths as used by Solman for his numerical computations and a second one which is based on Solman 's τ value. These two geometries show significant differences in the current distribution.

In time domain the resulting normalized input currents for step excitation are shown in Fig. 9. As we used only three modes the currents are of a very oscillatory structure. However if we apply a Gaussian excitation as proposed by Solman in 1973 we get the results of Fig. 10 which agree very well with the results of Solman for the appropriate antenna lengths.

The farfield of the LPDA in free space is displayed in Fig. 11. For $\Theta = 90^{\circ}$ it shows the characteristic chirplike signal. If the aspect angle is changed , the signal gets more and more distorded.

3.2 LPDA over Lossy and Perfectly Conducting Ground

For our numerical computations on lossy and perfectly conducting earth we look at a vertically polarised LPDA which is elevated at half a wavelength (2 m) respectively one wavelength (4 m) above ground. (Wavelength relative to the lowest resonance of the LPDA in free space.) We investigate here the case of a lossy ground $\varepsilon_r = 9$, $\sigma_r = 0.01$ and a perfectly conducting surface.

The pole migration is displayed in Fig. 12 and Fig. 13. For pole 1 and 5 of the first group we find for the chosen antenna height an undamping effect which depends on the ground parameters and on the antenna position. In the case of perfectly conducting earth this effect is the greatest. A different situation is found in Fig. 14. This is the first pole of group two which corresponds to the unsymmetric modes. These modes are not excited in the symmetric transmitting antenna case in free space. These poles migrate in different directions because the unsymmetric modes are strongly excited dependent on the distance of the antenna to the earth. The modes corresponding to the poles Fig. 12 and Fig. 13 are very similar to those in free space and differ only in amplitude but not in shape if the antenna height and the ground parameters are changed, Fig. 15.1 and 15.2. The modes of group two however show great unsymmetry depending on the surrounding, Fig. 15.3.

The transient farfields of the LPDA over ground are computed on the basis of the current distribution in free space. This is a reasonable assumption for the chosen antenna heights as computations in frequency domain and the aforementioned investigations have shown. For $\Theta = 90^{\circ}$ the transient farfield of a vertical LPDA over perfectly conducting ground shows the same behaviour as in free space. The direct and reflected signal add in phase. The LPDA over lossy ground shows in this direction only minor amplitude variations. The direct and indirect ray arrive at the same time but the reflected ray is convoluted with the reflection coeficient of the Norton approximation. For $\Theta = 45^{\circ}$ and about 10° the transient farfield shows greater influence of ground which originates in the different travel time of direct and indirect rays and the more complicated contributions of the single elements. In the broadside direction the direct and the reflected field are nearly seperated, Fig. 16 and Fig. 17.

4.0 CONCLUSION

On the basis of a Pocklington integral equation formulation we have studied the problem of a vertical LPDA in free space over lossy ground in frequency and time domain with the aid of a SEM representation.

We investigated the poles dependend on coupling and antenna thickness and we discussed the modes, currents and farfields in free space. The influence of lossy and perfectly conducting ground on antenna poles and modes was shown for several characteristic parameter choices. The influence of ground on the farfield was also studied.

5.0 REFERENCES

BAUM, C.E., 1978, "The singularity and eigenmode expansion method", "Electromagnetic scattering", ed. USLENGHI, P.L.E., Academic Press

BRITTINHAM, J.N., MILLER, E.K., OKADA, J.T., 1978, "An improved model for studying conducting objects near lossy half spaces ", LLL, UCRL -52423

CHEONG,W.M., KING, R.W.P., 1967, "Arrays of unequal and unequally -spaced dipoles", Radio Sci. 2, No.11 , pp.1315

DEADRICK, F.J., 1977, "Computer modeling of a log periodic dipol antenna", LLL, UCRL-52372

HIZAL, A., 1974, "Currentdistribution and impedance of monopole antenna on lossy ground", Int. J. Electronics, 37, No.1, pp.49

IMBRIALE, W.A., 1975, "Application of the method of moments to thin wire elements and arrays", "Numerical and asymptotic techniques in electromagnetics", ed. MITTRA, R. , Springer

KNOP, C.M., 1970, IEEE Trans. Ant. Prop., AP 18, pp.807

KUO,W.C., MEI, K.K., 1978, "Numerical approximations of the Sommerfeld integral for fast convergence", Radio Sci. 13, No.3, pp.407

LYTLE, R.J., LAGER, D.L., 1974, "Numerical evaluation of Sommerfeld integrals", LLL, UCRL-51688

LANGENBERG, K.J., RECH, K.D., BOLLIG, G., 1978, "Time domain response of logarithmic periodic dipole antennas", IEE, Con. Pub. No. 169, Antennas and Propagation, pp.160

MILLER, E.K., et al, 1972, "Analysis of wire antennas in the presence of a conducting half space", Can. J. of Physics, 50, pp.879

NORTON, K.A., 1937, "The propagation of radio waves over the surface of the earth and in the upper atmosphere", Proc. IRE, 25, No.9, pp.1203

RUSSEGGER,M., 1976, "Einschwingverhalten bei logarithmisch-periodischen Dipolantennen", Diss. TU Braunschweig, FRG

SOLMAN, F.J., 1973, "Time domain responseof wire antenna arrays", Ph.D. Diss.,Purdue Uni., Lafayette, Indiana

STARK, W. J., 1977, "Transient response of a log periodic antenna...", Harry Diamond Labs, HDL-Tr-1792, Adelphi/MD

WIGGINS, C.M., YU, J.S., 1974, "Radiation field compression by dispersive broadband antennas", Rome air development center, Griffis Air Force Base, NY, RADC-TR-74-104

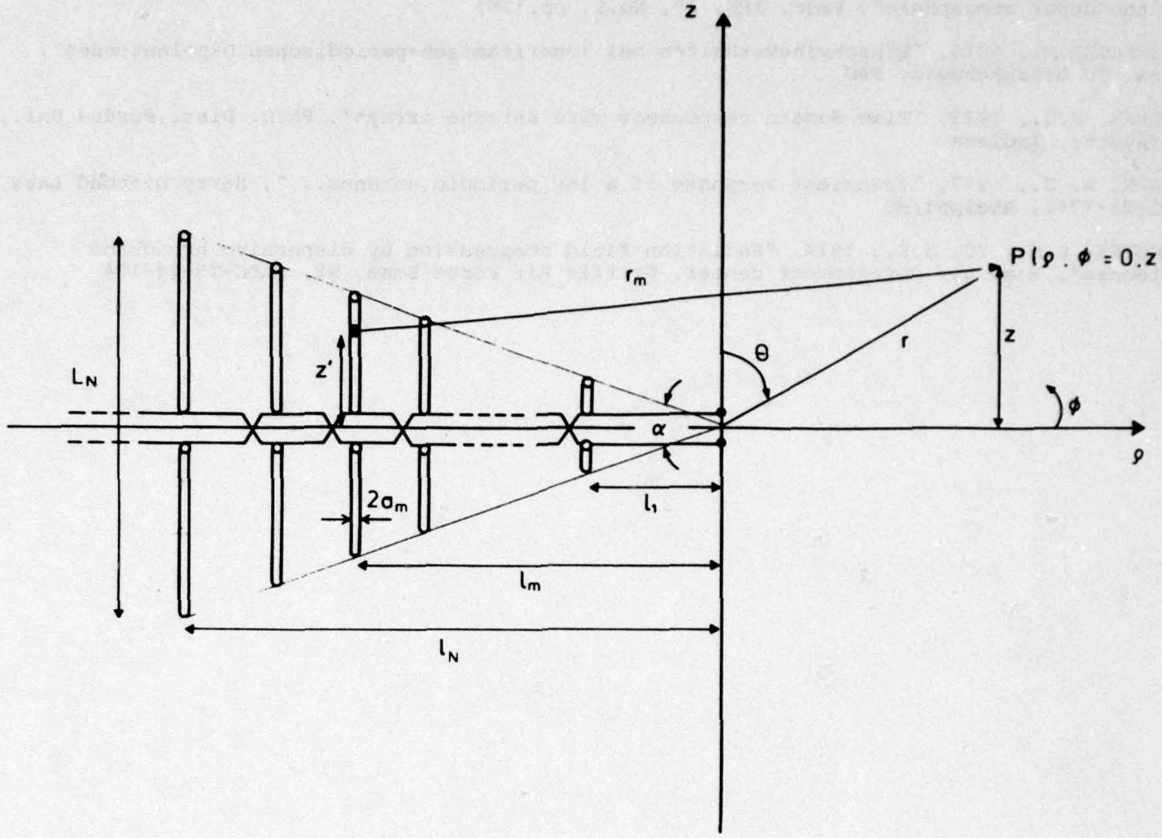

Fig. 1 Geometry of LPDA

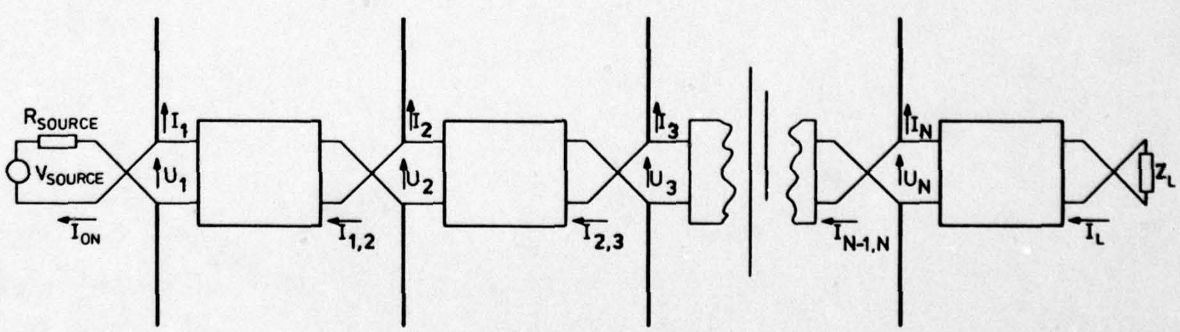

Fig. 2 Ladder Network

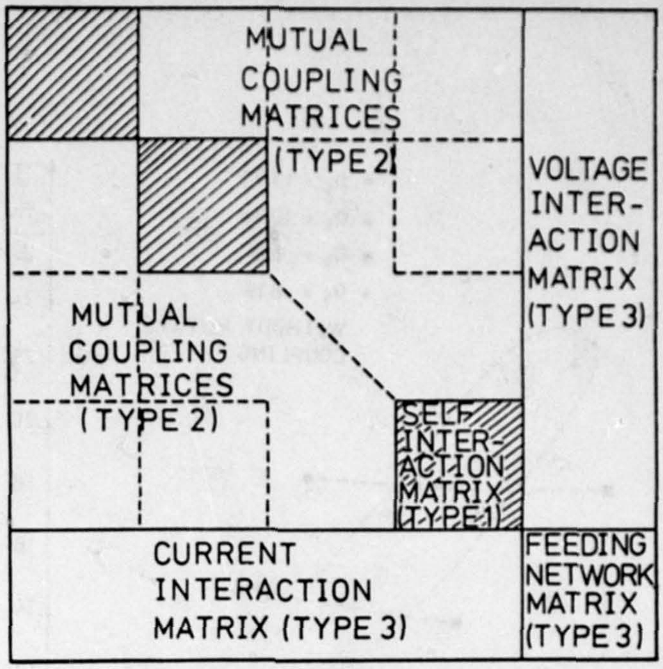

Fig. 3 Impedance Matrix

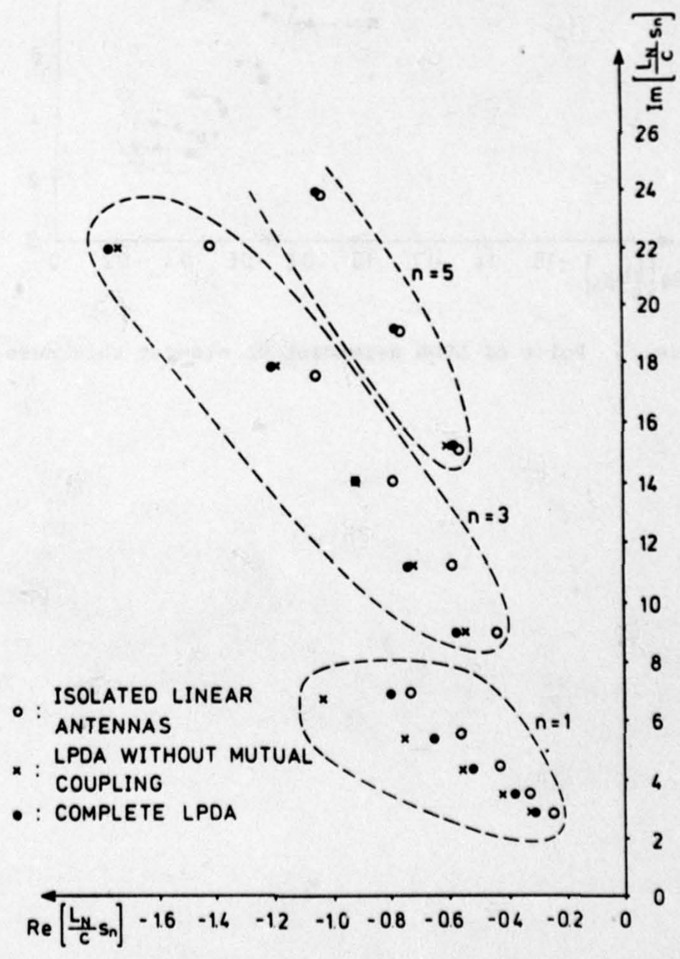

Fig. 4 Poles of LPDA, element coupling, simple elements in free space

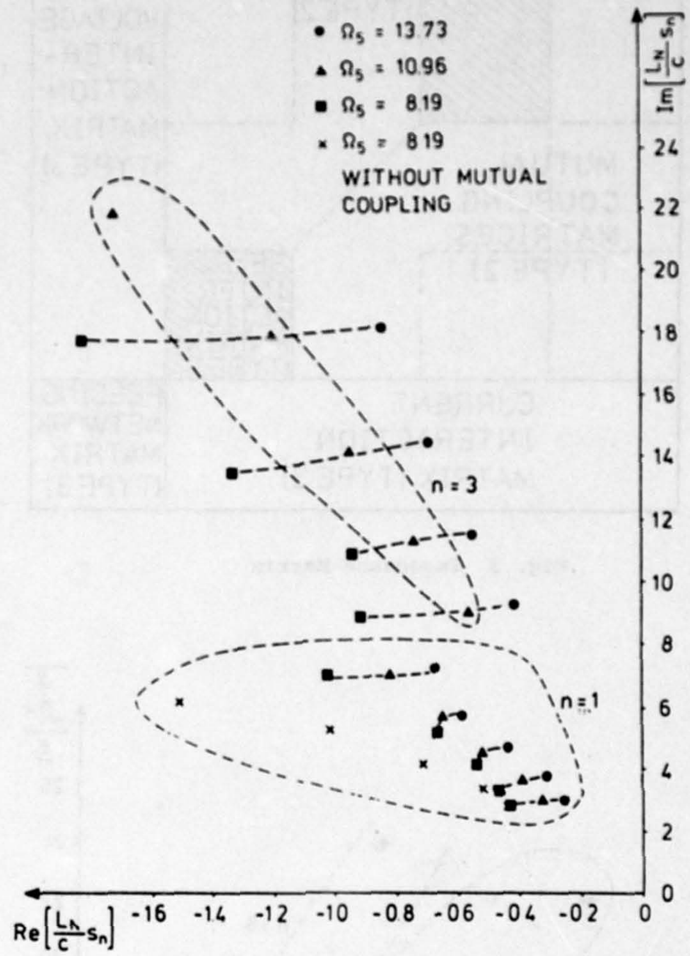

Fig. 5 Poles of LPDA dependent on element thickness

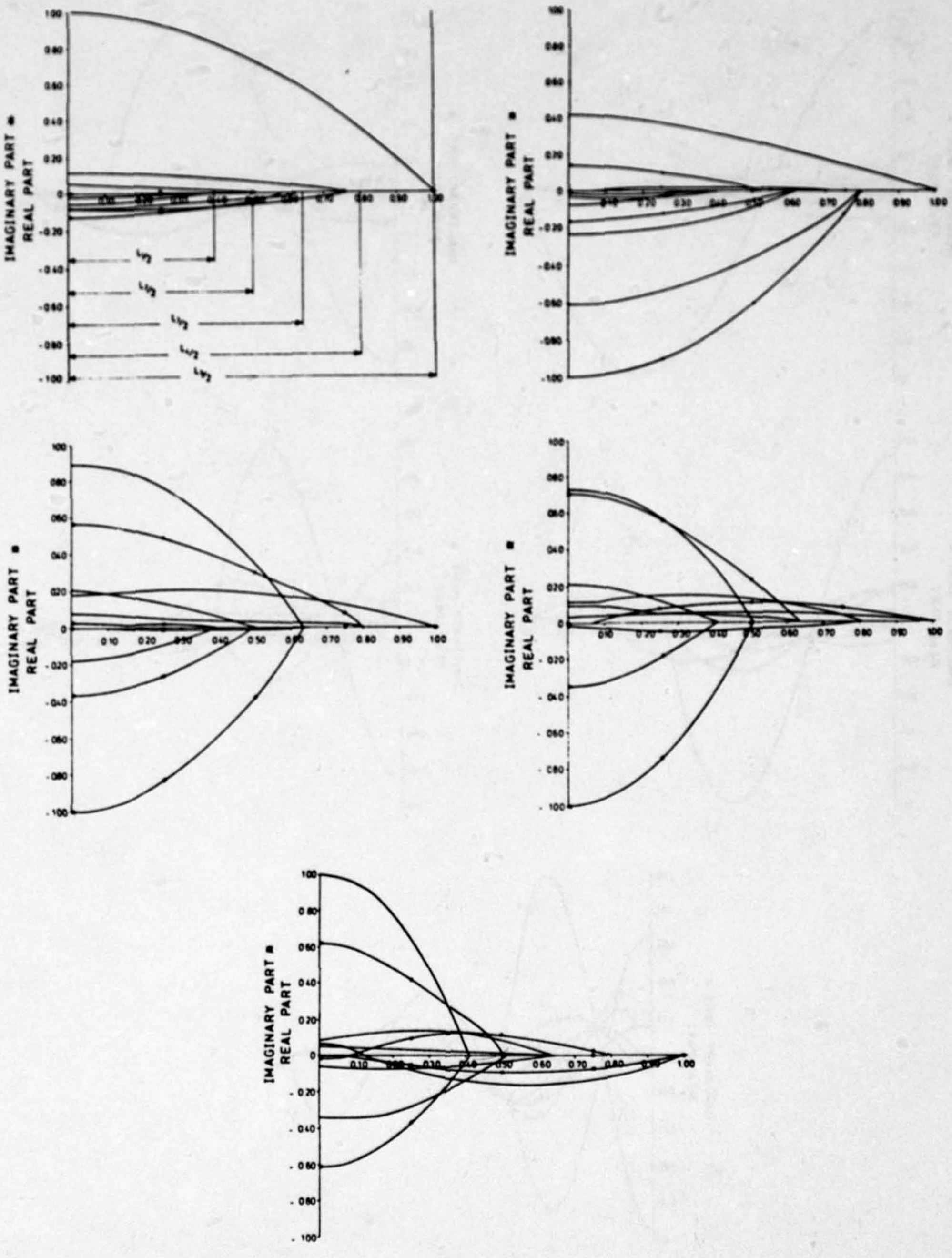

Fig. 6 LPDA modes of group 1

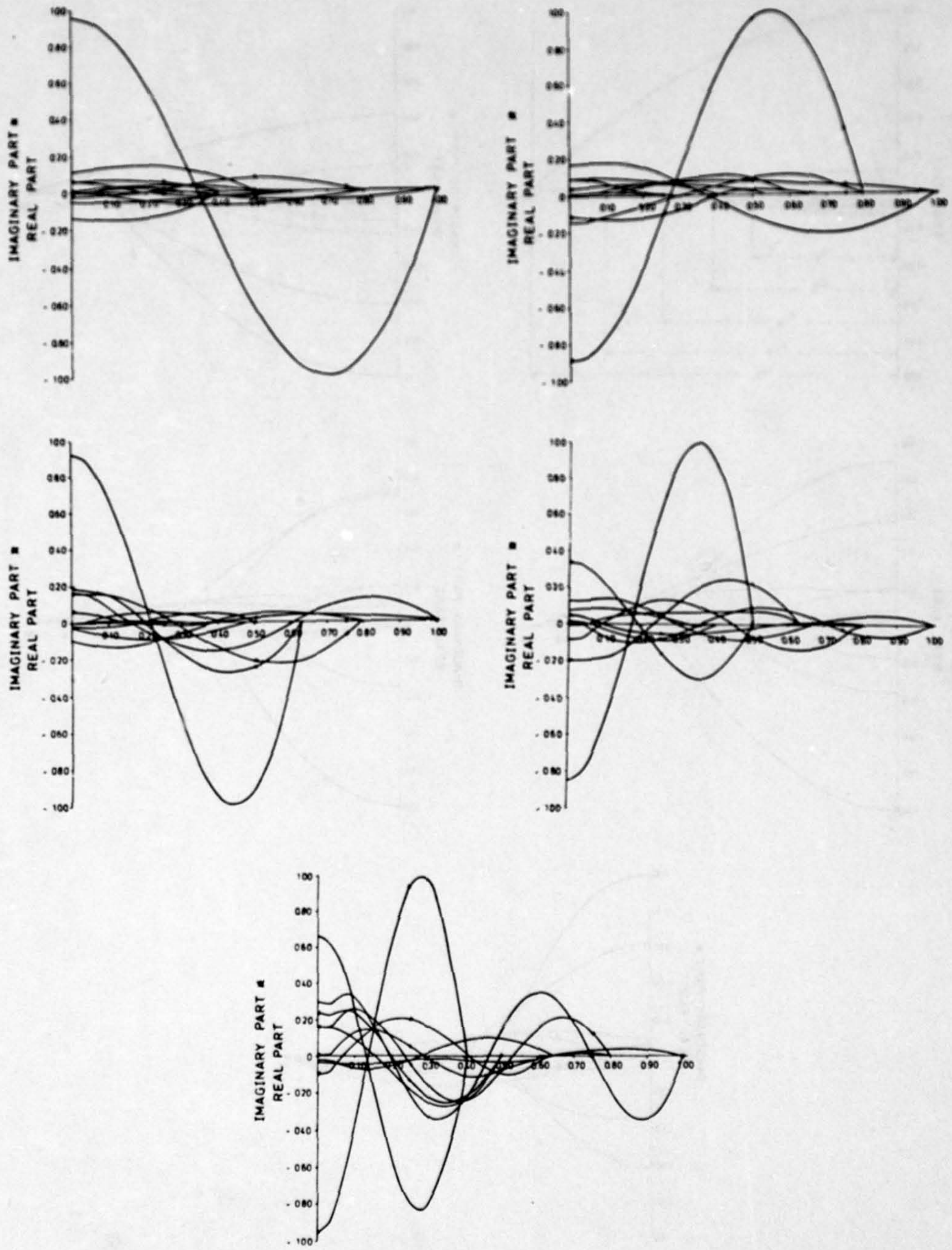

Fig. 7 LPDA modes of group 2

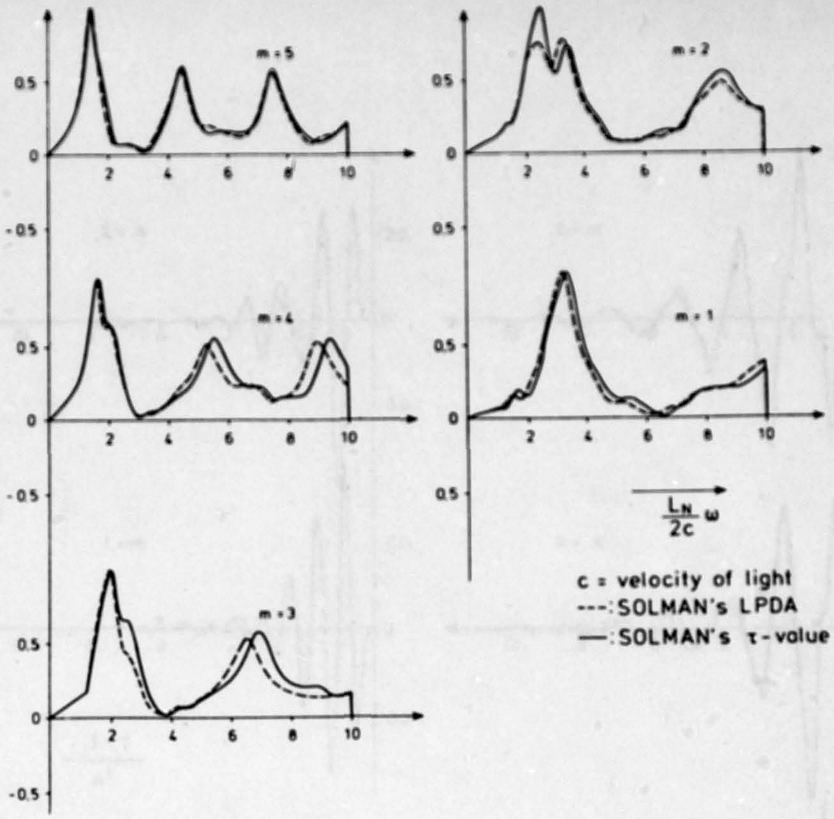

Fig. 8 Input current of the elements in frequency domain

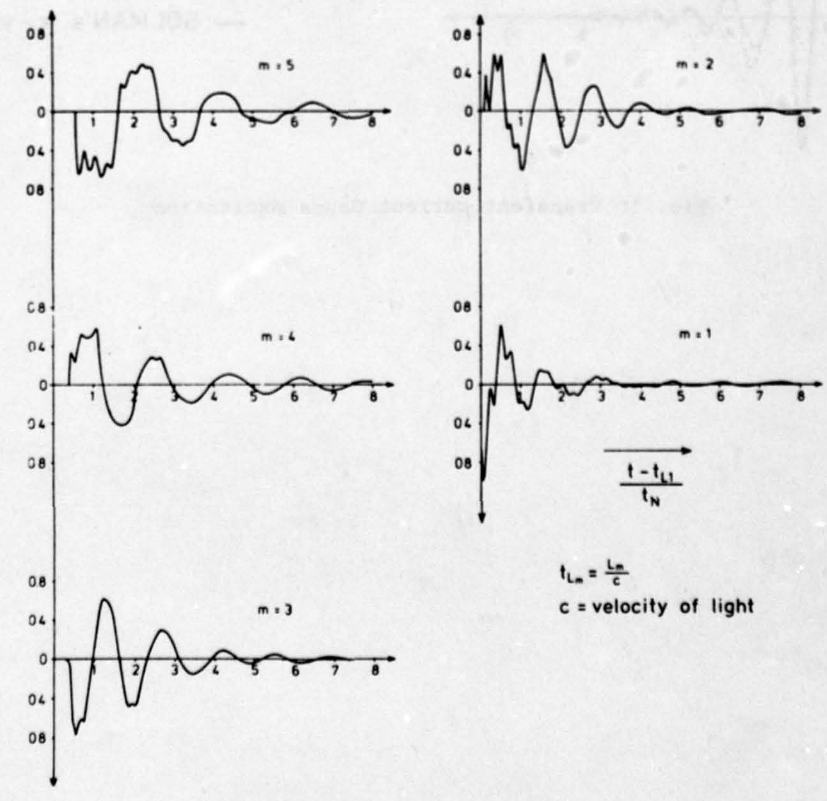

Fig. 9 Transient current, step excitation

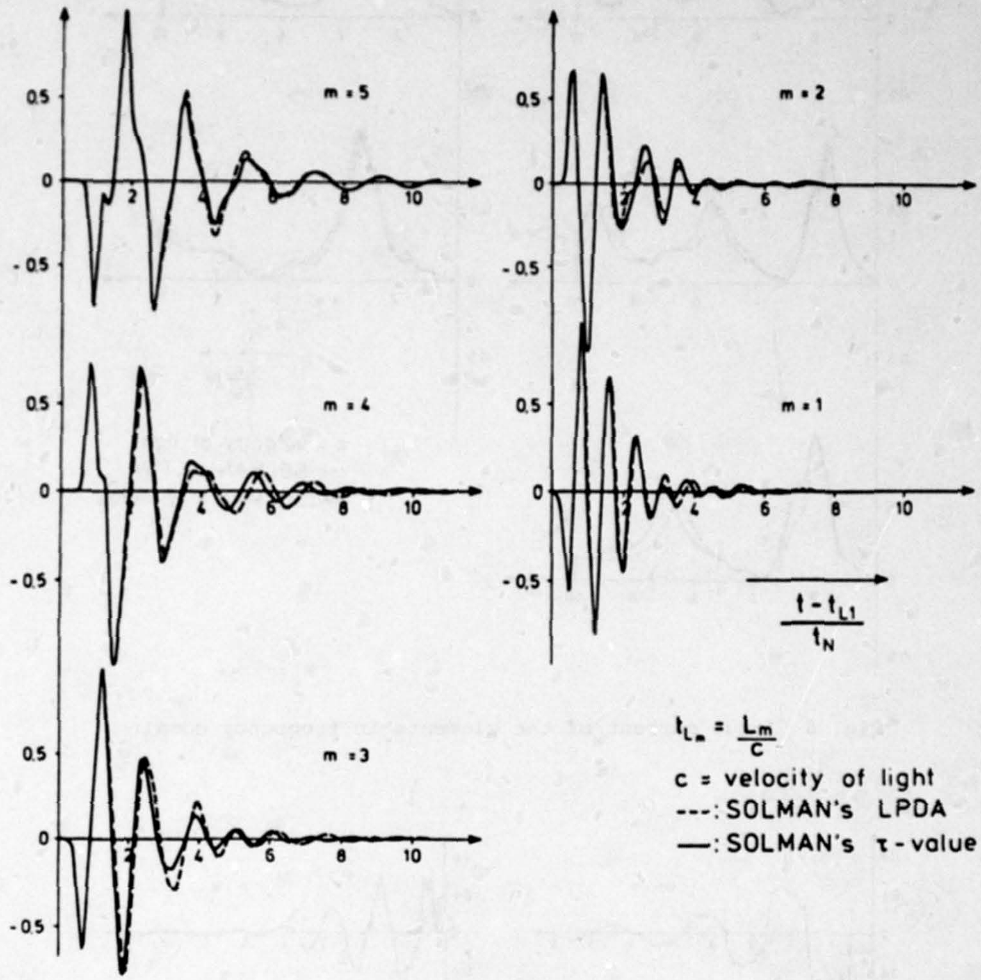

Fig. 10 Transient current, Gauss excitation

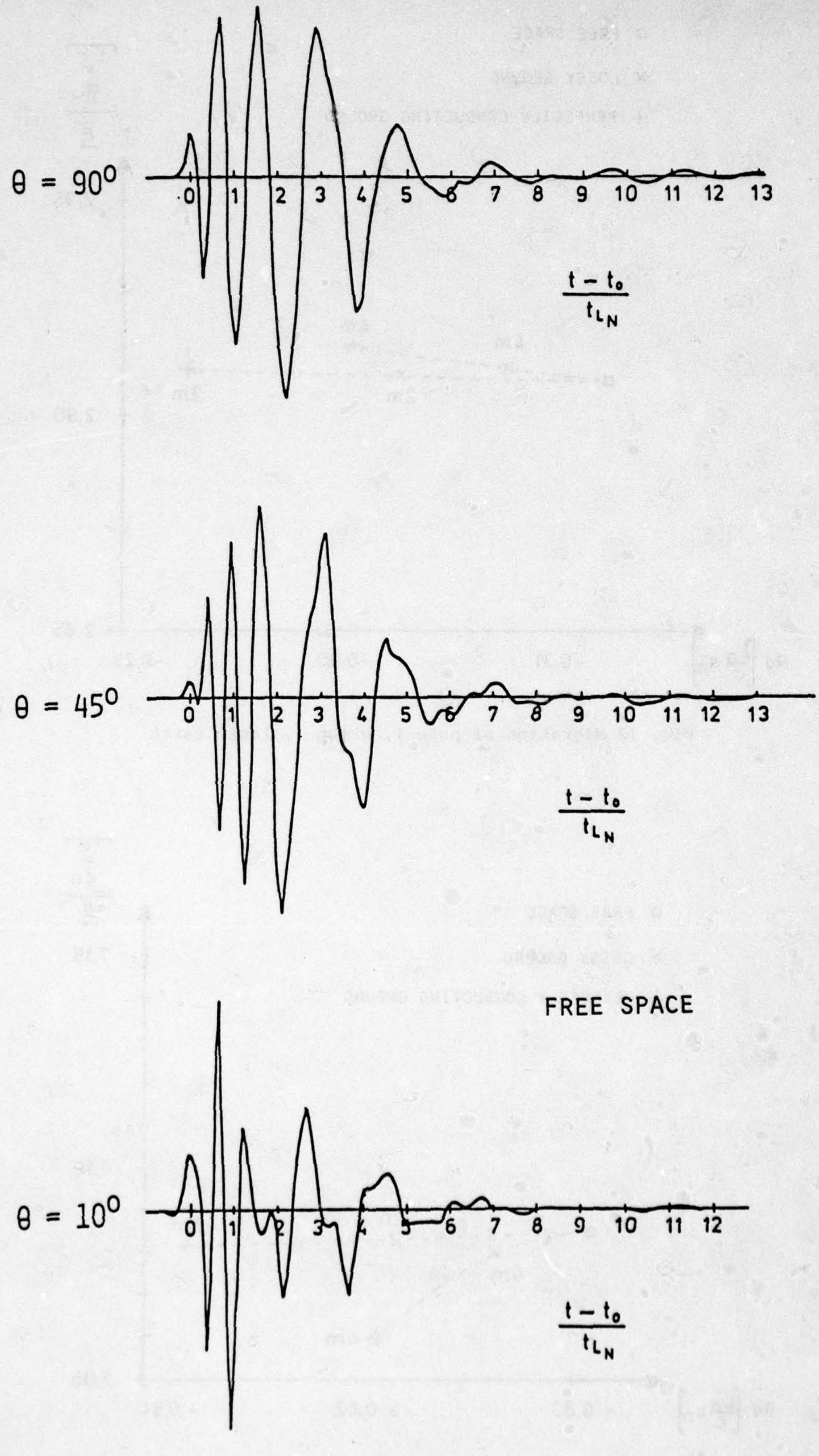

Fig. 11 Transient field of LPDA in free space, Gauss excitation, $\theta = 90^{\circ}, 45^{\circ}, 10^{\circ}$

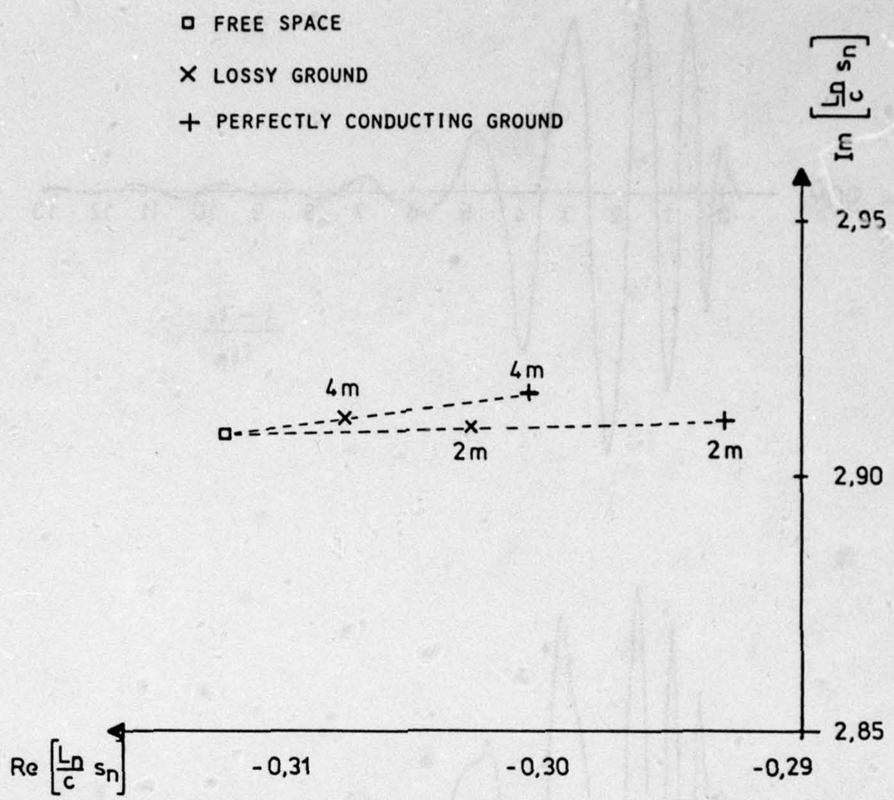

Fig. 12 Migration of pole 1, group 1, lossy earth

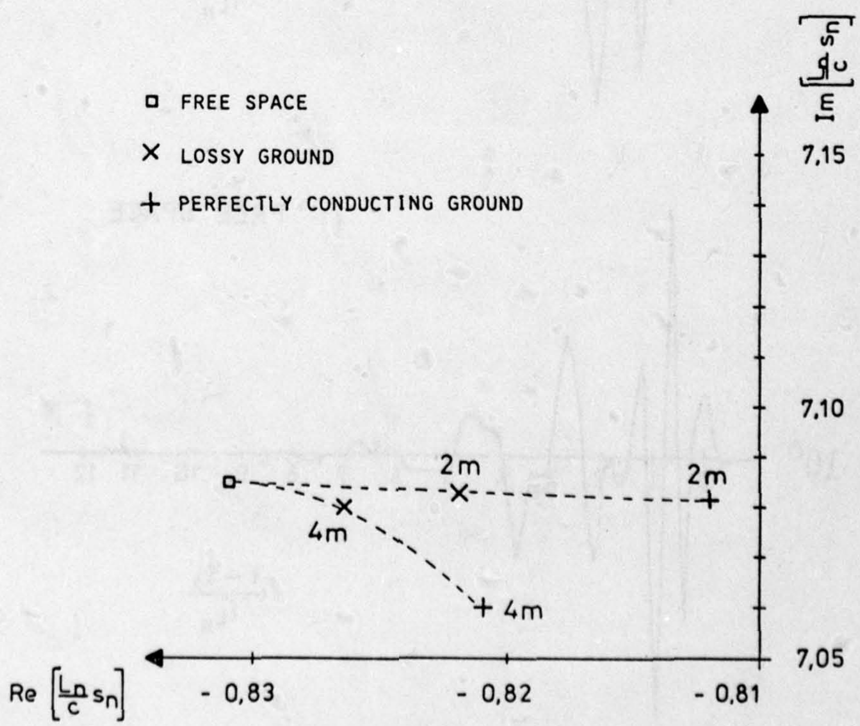

Fig. 13 Migration of pole 5, group 1, lossy earth

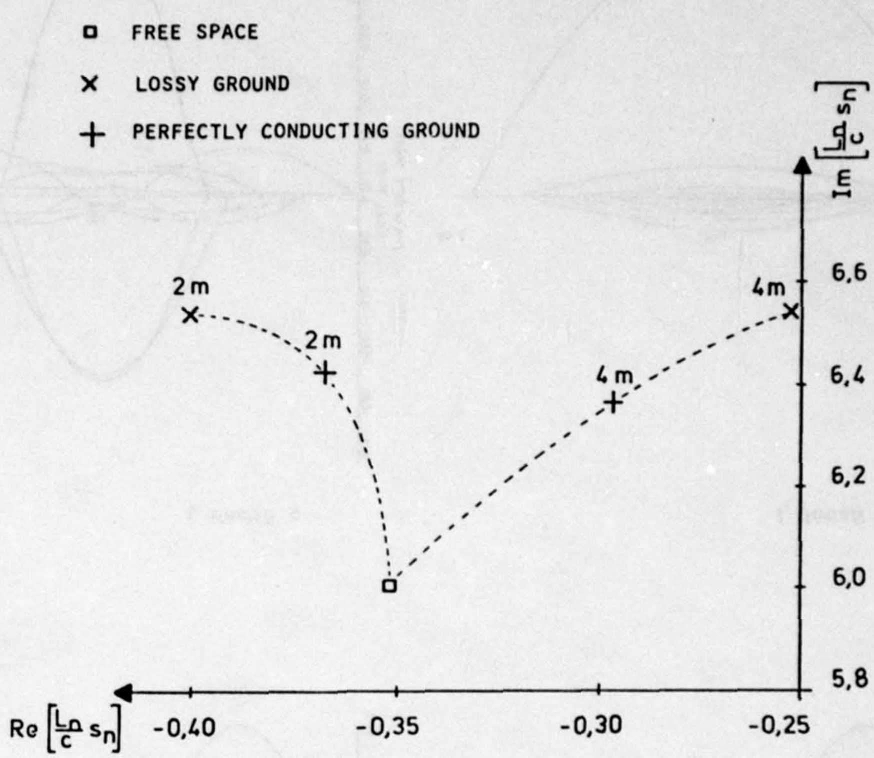

Fig. 14 Migration of pole 1, group 2, lossy earth

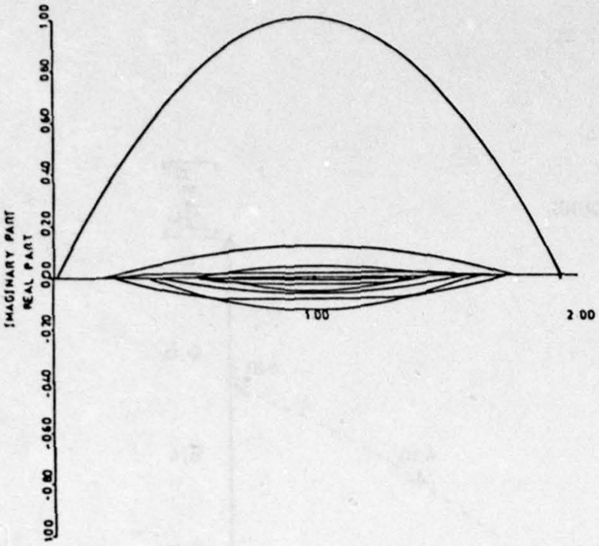

1 group 1

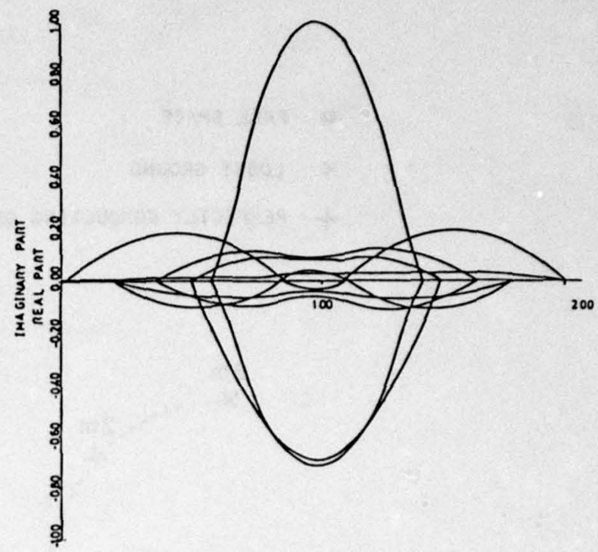

5 group 1

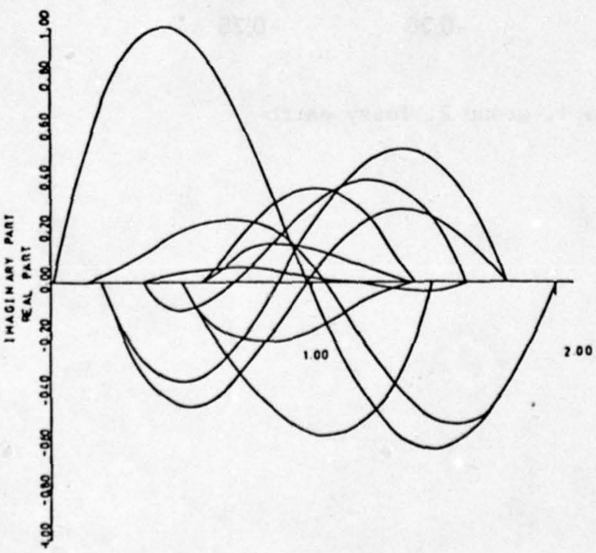

1 group 2
2 m height

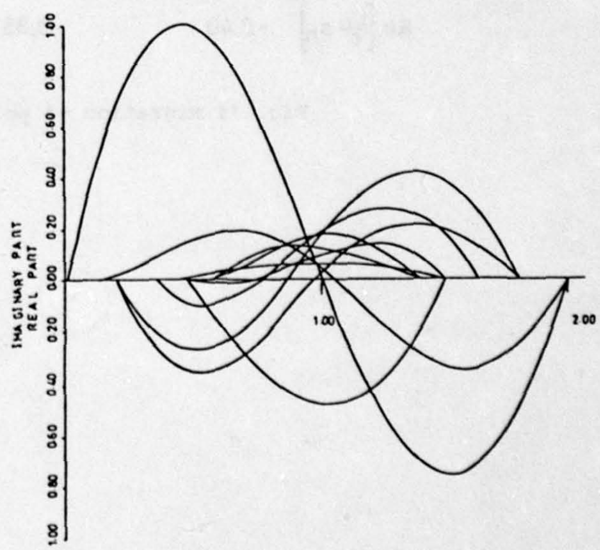

1 group 2
4 m height

Fig. 15 Modes , 1-1 group 1, 2-5 group 1, 3-1 group 2

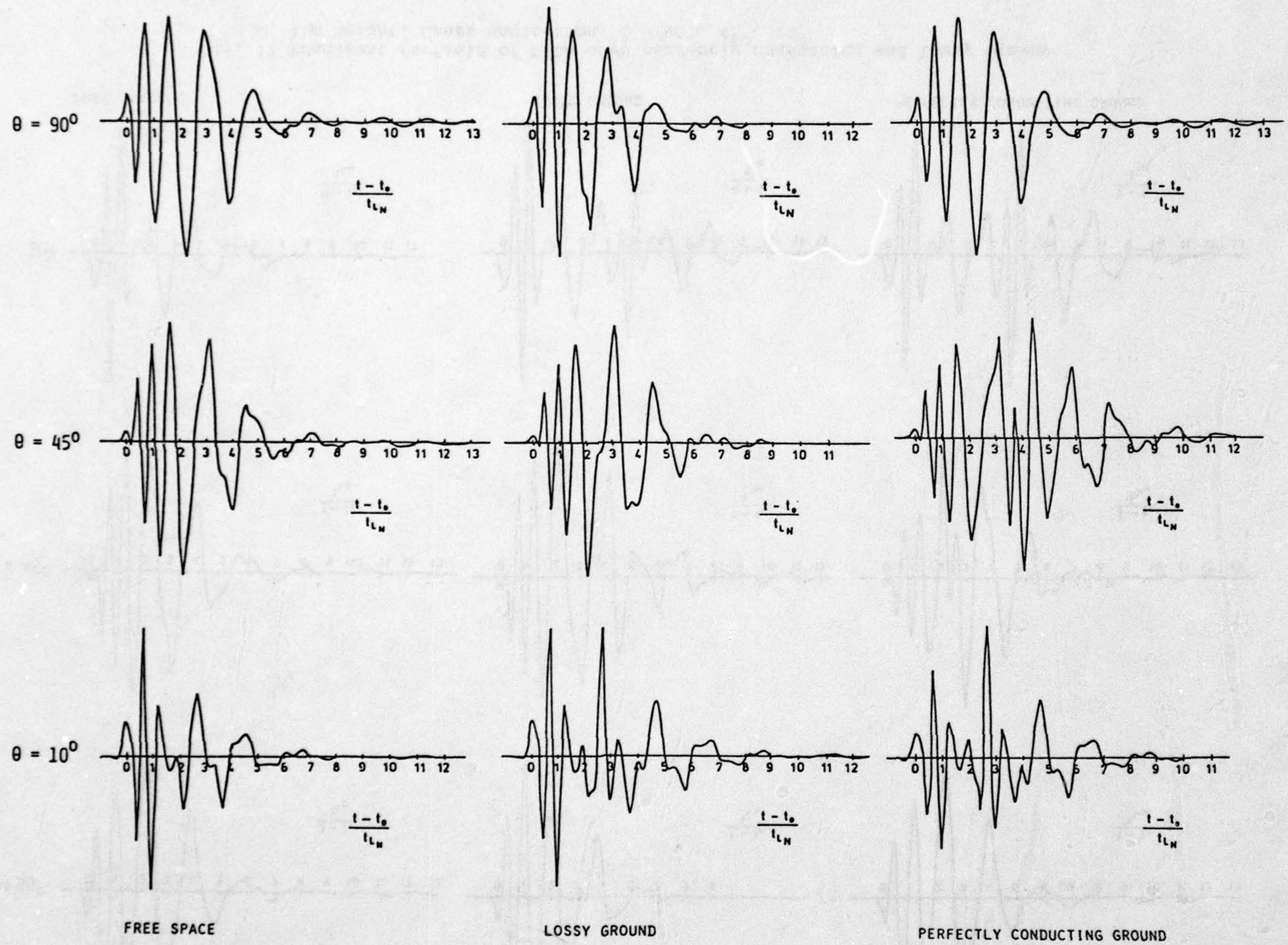

Fig. 16 Transient farfield of LPDA over perfectly conducting and lossy ground
2 m height, Gauss excitation, $\theta = 90^\circ, 45^\circ, 10^\circ$

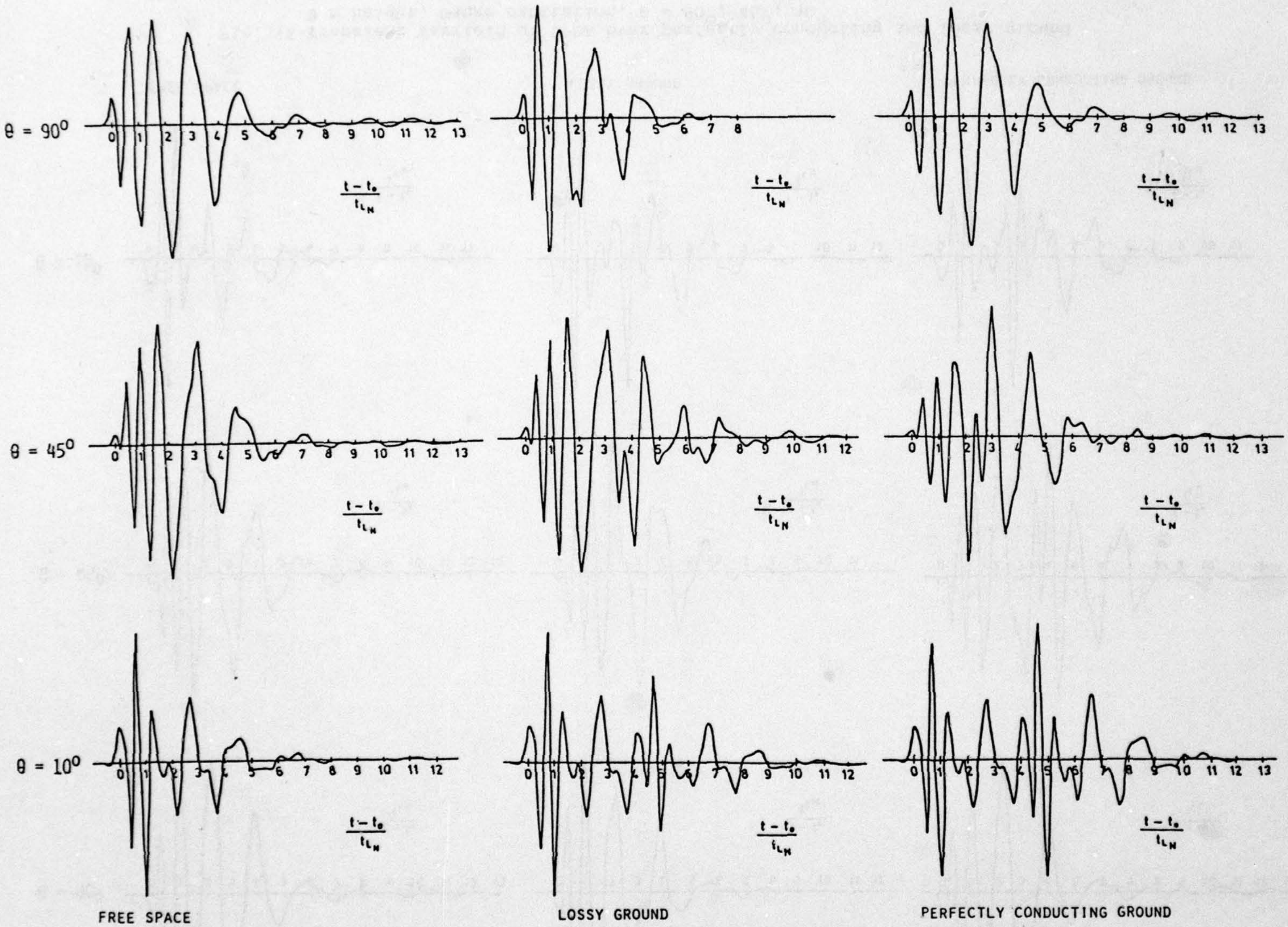

Fig. 17 Transient farfield of LPDA over perfectly conducting and lossy ground 4 m height, Gauss excitation, $\Theta = 90^{\circ}, 45^{\circ}, 10^{\circ}$

THEORIES OF GROUND WAVE PROPAGATION OVER MIXED PATHS

R. H. OTT
U. S. Department of Commerce
National Telecommunications and Information Administration
Institute for Telecommunication Sciences
Boulder, Colorado 80303 USA

SUMMARY

A review is given of some common techniques for predicting the field of a dipole transmitter over an irregular, inhomogeneous terrain profile. The effects of the atmosphere are not included except to modify the degree of "earth bulging" by the appropriate earth's radius. Some of the topics included are the impedance boundary condition, the integral equation and mode-match methods for field strength predictions, for a simple knife-edge obstacle on a spherical earth, the double-knife-edge diffraction formula for field strength predictions, and the fields of dipoles in layered media for calculating the transmission through forest-covered and vegetated media.

1. Introduction

In this paper we review four analytical methods for calculating the strength of an electromagnetic wave as it propagates along the surface of the earth such that its characteristics are influenced primarily by the profile and electrical properties of the earth. The effects of sky-wave contamination will not be included Since the terrain profile and electrical properties of the earth are the primary influence on the field, a solution for the wave equation in a region having an irregular boundary and a surface with a homogeneous boundary condition is required.

Rytov (1940) appears to have given the most general derivation of the impedance boundary condition and its restrictions in terms of the depth of penetration of the field within the conductor, and the restrictions associated with the surface curvature. His derivation is interpreted here in terms of subsequent treatments.

The first analytical method reviewed for predicting the field strength for propagation over irregular terrain is the integral equation formulation introduced by Feinberg (1944-46) and made suitable for numerical evaluation by Hufford (1952). Refinements to Hufford's integral equation were made by Ott (1970). This method has found widespread use for either polarization for frequencies up to about 30 MHz assuming normal ground constants. Recently, Monteath (1978) used the method to predict field strengths over a 300 km path from Crowborough, England toward Paris, France at 1 MHz.

The second method is called the mode-match technique (Wait, 1968a). Here the incident wave is represented as a sum of "creeping" waves and upon striking an obstacle are converted to propagating modes through the use of a scattering coefficient. This method has application at HF and VHF where there is a single terrain feature near the middle of a path that produces an effective obstacle gain.

The third method is based upon the fields for a source and/or observer located over or in an N layered earth model (Wait, 1967) having a diagonal tensor conductivity in each layer and has found application in calculating the transmission through a forest-covered or vegetated media at VHF frequencies (Ott and Wait, 1973).

The fourth method using knife-edge diffraction, has found widespread use for communication links using radio or television where the wavelength is small compared with the major ground irregularities (Furutsu, 1956, Millington et al., 1962, Wilkerson, 1966). We consider a case where double knife-edge diffraction provides excellent predictions for some recent measurements at 9.6 and 28.8 GHz.

2. The Impedance Boundary Condition

The vector form for the impedance boundary condition is

$$\underline{E}_{tang.} = \underline{E} - (\underline{e}_n \cdot \underline{E})\underline{e}_n = \frac{Z_o}{\sqrt{\eta}} \underline{e}_n \times \underline{H} \quad , \tag{1}$$

where $(\underline{E},\underline{H})$ is the field in the region outside the surface and $\underline{e}_n$ is the outward directed unit normal, $Z_o = 120\pi$ ohms, and

$$\eta = \varepsilon_r - \frac{i\sigma}{\omega\varepsilon_o} \quad , \tag{2}$$

with $\exp(i\omega t)$ time dependence, ε_r the relative dielectric constant and σ the conductivity. For example, in the case of a planar surface and vertical polarization (TM) (1) gives

$$E_x = -\frac{Z_o}{\sqrt{\eta}} H_y \quad , \tag{3}$$

and in conjunction with Maxwell's equation

$$H_y = \frac{1}{ik_o Z_o} \frac{\partial E_x}{\partial z} \quad , \tag{4}$$

one obtains

$$\frac{\partial H_y}{\partial z} = \frac{-ik_o}{\sqrt{\eta}} H_y \quad , \tag{5}$$

which is the scalar form of the impedance boundary condition.

We now give a derivation for the impedance boundary condition on a spherical surface. The derivation is given in the appendix of a paper on magneto-telluric fields by Wait (1962). Wait uses non-uniform transmission line theory to solve the scattering of a plane wave by a spherically stratified sphere. The surface impedance is defined by

$$Z = -\frac{E_\theta}{H_\phi} \text{ at } r = a \; , \tag{6}$$

where E_θ and H_ϕ are the exact solutions for the boundary value problem. For our immediate discussion, the stratified nature of the sphere is not necessary and the surface impedance then equals the characteristic input impedance of the transmission line and is given by

$$Z = \frac{Z_o}{\sqrt{\eta}} \frac{I'_\nu(\gamma a)}{I_\nu(\gamma a)} \quad , \tag{7}$$

where

$$\gamma = [i\omega\mu_o(\sigma + i\omega\varepsilon)]^{1/2} \quad , \tag{8}$$

and $I_\nu(r)$ is a solution to the radial portion of the wave equation after using separation of variables and ν is an eigenvalue that can be interpreted as the azimuthal wave number. Using the Debye approximation for the modified Bessel functions in (7); i.e.,

$$I'_\nu(\nu\xi) \sim \frac{1}{\sqrt{2\pi\nu}} \frac{(1+\xi^2)^{1/4}}{\xi} e^{\nu\eta} \quad , \tag{9}$$

and

$$I_\nu(\nu\xi) \sim \frac{1}{\sqrt{2\pi\nu}} \frac{e^{\nu\eta}}{(1+\xi^2)^{1/4}} \quad , \tag{10}$$

where

$$\eta = \int \frac{\sqrt{1+t^2}}{t} dt \quad , \tag{11}$$

we find

$$\frac{I'_\nu(\nu\xi)}{I_\nu(\nu\xi)} \sim (1 + \frac{1}{\xi^2})^{1/2} \quad , \tag{12}$$

or

$$Z = \frac{Z_o}{\sqrt{\eta}} [1 + \frac{\nu^2}{(\gamma a)^2}]^{1/2} \quad , \tag{13}$$

where $\xi = \gamma a/\nu$. Now, the greatest contribution to the scattered field occurs when $\nu \simeq k_o a$ and substituting (2) and (8) into (13) gives

$$\Delta = \frac{Z}{Z_o} = \frac{\sqrt{\eta - 1}}{\eta} \simeq \frac{1}{\sqrt{\eta}} \tag{14}$$

in agreement with (5). Note that the effects of curvature contained in the radius of the sphere; i.e., a, cancel in (13) when one substitutes $\nu = k_o a$.

A paper translated by Rosich (1977) and entitled "Perturbation method of skin-effect computations" (Rytov, 1940) appears to be the most detailed examination of the impedance boundary condition and its limitations. Rytov applies the perturbation method to the solution of Maxwell's equations, neglecting the displacement current, in curvilinear orthogonal coodinates (α,β,γ) in which the surface of the conductor is the surface $\gamma=\gamma_o$. The smallness parameter in the perturbation method is the skin-depth

$$d = \sqrt{\frac{2}{\omega\mu_o\sigma}} \quad , \tag{15}$$

and Rytov obtains solutions to Maxwell's equations (plus the boundary conditions) on the surface $\gamma=\gamma_o$ which are correct through terms of order d^2. Unfortunately Rytov uses CGS units. He points out that for the case of a non-flat surface, curvature terms can be ignored provided tne radius of curvation at the point in question is larger than the skin-depth given in (15). For radio propagation over irregular terrain having $\sigma = 0.001$ mho/m and $\mu_o \simeq 4\pi \times 10^{-7}$ Henrys/m and f = 30 MHz, (15) gives d ≃ 3m. Most terrain irregularities will be much larger than 3m and curvature effects can thus be ignored. For a spherical surface, as in the preceding derivation, Rytov shows that the curvature terms in the two orthogonal directions cancel for all possible values of conductivity and/or frequency.

To conclude this section we give Mitzner's (1967) and Rosich's (1977) refinement to the impedance boundary condition quoted by Leontovich (1948). Mitzner assumes $\varepsilon_r \ll \sigma/\omega\varepsilon_o$ and

obtains (for a flat surface)

$$Z_c = \frac{Z_o}{\sqrt{\eta}} = e^{i\pi/4} \frac{\omega\mu_o d}{\sqrt{2}} . \tag{16}$$

He then states that the correction to (16) for the case of non-planar surfaces is

$$Z = Z_c(1-p) \quad , \tag{17}$$

where

$$p = \frac{-i}{2k_c} \left(\frac{1}{p_1} - \frac{1}{p_2} \right) \quad , \tag{18}$$

and p_1 and p_2 are the two principal radii of curvatures in the two orthogonal directions and that

$$k_c = (1-i)/d . \tag{19}$$

From (16), (17), (18) and (19) Mitzner's "Leontovich" result is

$$Z = \frac{Z_o}{\sqrt{\eta}} \left[1 - \frac{e^{-i\pi/4}}{2\sqrt{\omega\mu_o\sigma}} \left(\frac{1}{p_1} - \frac{1}{p_2}\right) \right] \tag{20}$$

which is not in exactly the same form as Leontovich's result due to the use of (19). If instead of (19) we use Rosich's (1977) substitution of

$$k_c = k_o\sqrt{\varepsilon_r} \quad , \tag{21}$$

we obtain Leontovich's result (except for Leontovich's error of omission of a factor of 2 in the denominator of the second term)

$$Z = \frac{Z_o}{\sqrt{\eta}} \left[1 + \frac{i}{2k_o\sqrt{\varepsilon_r}} \left(\frac{1}{p_1} - \frac{1}{p_2}\right) \right] . \tag{22}$$

This assumes no inhomogenity in σ.

3. Analytical Methods for Field Strength Predictions Over Irregular, Inhomogeneous Terrain

3.1 Integral Equation Formuation

In this section the mathematical formulations for the various methods will not be given since they are rather well described in the appropriate references. The integral equation is a scalar approach and is most useful when the terrain is ridge-like so it can be approximated as two-dimensional. *In this case the TE and TM modes decouple and the* scalar approach is applicable. Instead discussion of the intended use of each method together with a comparison of actual measured data taken on a real path will be given.

The integral equation method was first developed by Feinberg (1944-1946) using an impedance boundary condition on the plane z=o and was correct to first order smallness in the parameter ζ, the height of the surface above the z=o plane. Following this lead, Hufford (1952), in a very elegant work, derived the integral that most authors use in their related developments (e.g. Ott, 1970, 1971. Monteath 1978), used Waits development of the compensation theorem to develop a similar integral equation. Millington (1949) in his original work used the compensation theorem as a basis for a perturbation approach.

The integral equation method is usually numerically efficient for frequencies up to about 30 MHz, for path lengths as long as 500 km, and for normal ground constants and either polarization. Recently Ott et al. (1979) show several comparisons of predictions based upon an algorithm called PROGRAM WAGNER with measured field strengths as observed in nine different parts of the U.S. from 120 kHz to 50 MHz. With the exception of one extremely rugged portion of terrain in the Colorado mountains and at a frequency of 20 MHz the algorithm provided accurate, numerically efficient predictions. The algorithm has been used in sufficiently many applications to test its validity and efficiency to be incorporated in a general prediction procedure for site selection of proposed transmitting stations.

The detail that can be obtained by using the method can be seen by examining figure 1. There predictions using the algorithm PROGRAM WAGNER (based upon the integral equation method) are compared with measurements by Kissick et al., (1978) for a path profile shown in the lower portion of figure 1 near Dry Lake, Nevada. This path crossed a high mountain range followed by a broad flat valley in southeastern Nevada. As shown in the table in figure 1, relatively large changes in the ground conductivity were expected between the mountain and valley. The values for conductivity were obtained from geological maps identifying the soil type and by then using the tables developed by Lytle (1974). The "recovery" effect occurring after going over the two ridges near x = 9 km and x = 44 km are clearly reproduced by the predictions. The computational time required to run the predictions in figure 1 was 96 sec. on a CDC 6600 computer. 4/3 effective earth's radius was assumed. The choice of ground constants to be used in the integral equation method may in some cases require measurement of these parameters using, for example, the four electrode type measurement.

3.2 Mode-Match Technique (Mode-Conversion Propagation)

The mathematical formulation for the mode-match technique is given by Wait (1968) The technique has its greatest utility in cases where there is a knife-edge like obstruction somewhere near midpath in "beyond the horizon" radio propagation conditions (Wait, 1968b). The attenuation function is given by

$$Q = \left\{ \sum_m \sum_n \frac{w(t_m)}{N_m^{1/2}} e^{-ix_o t_m} S_{n,m} e^{-i(x-x_o)t_n} \frac{w(t_n)}{N_n^{1/2}} \right\} \Big/ \sum_m \frac{e^{-ixt_m}}{t_m} \qquad (23)$$

with $x = (ka/2)^{1/3}(d/a)$, $x_o = (ka/2)^{1/3}(d_o/a)$ the "dimensionless" distances from the source to the observer and from the source to the knife-edge respectively and both source and observer are on the surface. In (23), $S_{n,m}$ are the mode conversion coefficients with a mode of mode m incident on the knife-edge converted to a mode of order n on the shaded side of the knife-edge. Also, in (23)

$$N_m = (t_m - q^2)\ [w(t_m)]^2 \qquad (24)$$

where w(t) is an Airy function and where t_m is a solution to

$$w'(t) = q\ w(t) \qquad (25)$$

with

$$q = -i\left(\frac{ka}{2}\right)^{1/3} \frac{1}{\sqrt{\eta}} \qquad (26)$$

A difficulty arises in summing the double series in (23) if $x \ll 1$ or $x_o \ll 1$ since in these cases the convergence of the series with n or m is very slow. The ratio of the $n^{\underline{th}}$ term of the summand in (23) to the $n^{\underline{th}}$ partial sum of (23) was used as the convergence criterion (the convergence ratio). Two examples give some insight into the convergence properties of (23). First, requiring the convergence ratio to be less than 10^{-5} and a value for $x \simeq 0.01$ required about 600 terms for the residue series (the denominator in (23)).

$$\sum \frac{e^{-ixt_m}}{t_m - q^2}$$

Second, in (23) requiring the converge ratio to be less than 0.5×10^{-3} and a value for $x_o = 0.03$ required 3757 terms, and still the $n^{\underline{th}}$ partial sum was not within one significant figure of the correct value. This second example indicates that the inclusion of the mode conversion coefficients slow the convergence of the residue series. For this reason it is not numerically efficient to try to calculate the attenuation function in (23) for the frequency and path geometry shown in figure 1.

An additional difficulty arises with the mode-match technique if more than one knife-edge is present along the path because in this case the mode conversion coefficients are given by (Wait, 1968a)

$$S^{(j)}_{n,m} \propto \int_{y_j}^{\infty} w(t_n - y)\, w(t_m - y)\, dy \qquad (27)$$

where the y_j is the height of each knife-edge. This requires additional time consuming numerical integration.

However, the mode-match technique is a useful method for estimating the effect of obstacle gain created by a single knife-edge near midpath, say at 100 MHz for path lengths of about 50 km. Wait and Conda (1959) gave an "early" discussion of obstacle gain and comparison with experimental microwave model data.

3.3 Fields of a Dipole in a Layered Half-space ("Lateral" Wave Propagation)

In the frequency range from 30 MHz to 300 MHz, the predominant component of the field is the so-called lateral wave (Tamir, 1966), for propagation through forest-covered media or dense vegetation.

Consider a vertical electric dipole (VED) located in one of the layers of an N-layered earth where each layer has a complex, tensor conductivity given by

$$[\sigma] = \begin{bmatrix} \sigma_{nn} & 0 & 0 \\ 0 & \sigma_{hn} & 0 \\ 0 & 0 & \sigma_{vn} \end{bmatrix} \qquad (28)$$

with $\sigma = g + i\omega\varepsilon$ and g and ε are the real conductivity and real permittivity respectively.

For the VED the fields can be derived from an electric Hertz vector that has only a z component Π_z. A subscript o is added when referring to region z>0, and a subscript n is used for region n where n = 1,2,3,...N. From an earlier analysis (Wait, 1967a, King and Wait, 1976), it follows that (for z>0)

$$\Pi_{oz} = \frac{Ids}{4\pi i\varepsilon_o\omega} \int_0^\infty \left[e^{-u_o|z-h|} + R_{11}(\lambda) e^{-u_o(z+h)} \right] \frac{\lambda}{u_o} J_o(\lambda\rho)d\lambda \;,$$

where

$$R_{11}(\lambda) = \frac{K_o Z_1}{K_o+Z_1} \;,\; K_o = \frac{u_o}{i\varepsilon_o\omega} \;,\; u_o = (\lambda^2-k_o^2)^{1/2} \;,\; k_o = \omega/c,$$

$$Z_1 = K_1 \frac{Z_2+K_1\tanh v_1h_1}{K_1+Z_2\tanh v_1h_1} \;,\; K_n = \frac{v_n}{g_{hn}+i\varepsilon_{hn}\omega} = \frac{v_n}{\sigma_{hn}} \;,$$

$$Z_2 = K_2 \frac{Z_3+K_2\tanh v_2h_2}{K_2+Z_3\tanh v_2h_2} \;, \tag{29}$$

...

$$Z_n = K_n \frac{Z_{n+1}+K_n\tanh v_nh_n}{K_n+Z_{n+1}\tanh v_nh_n} \;,\; n = 1, 2, 3, \ldots N-1$$

$$Z_{N-1} = K_{N-1} \frac{K_N+K_{N-1}\tanh v_{N-1}h_{N-1}}{K_{N+1}+K_N\tanh v_{N\,1}h_{N-1}} \;,$$

$$v_n = (\lambda^2\kappa_n + \gamma_n^2)^{1/2} \;,\; \kappa_n = \sigma_{hn}/\sigma_{vn} \;,\; \gamma_n^2 = i\sigma_{hn}\mu_o\omega \;.$$

For z > 0

$$E_{o\rho} = \frac{\partial^2\Pi_{oz}}{\partial\rho\partial z} \;,\; E_{oz} = k_o^2 + \frac{\partial^2}{\partial z^2}\Pi_{oz} \;,\; H_{o\phi} = -i\varepsilon_o\omega \frac{\partial\Pi_{oz}}{\partial\rho} \;.$$

In the limiting case z = 0, we deduce that

$$E_{o\rho} = \frac{Ids}{4\pi i\varepsilon_o\omega} \int_0^\infty e^{-u_oh} [1 - R_{11}(\lambda)]\lambda^2 J_1(\lambda\rho)d\lambda \;.$$

Ott and Wait (1973) obtained asymptotic results for the VED within the second layer and the vertical electric field in the air. The dominant far-field approximation to (29) is

$$E_{oz} \simeq \frac{i\mu_o\omega Ids}{2\pi\rho} e^{-ik_o\rho} \bar{g}_v^{(2)}(h)(1 + ik_oz\Delta)W(p) \;, \tag{30}$$

where

$$\bar{g}_v^{(2)}(h) = g_v^{(2)}(h)\Big|_{\lambda = k_o} \;,$$

$$W(p) \simeq -1/(2p) \;,$$

$$p = -ik_o\rho\Delta^2/2 \;, \tag{31}$$

$$\Delta = Z_1/Z_o\Big|_{\lambda= k_o} \;,\; Z_o = \sqrt{\mu_o/\varepsilon_o} \simeq 120\pi$$

Higher order terms in the asymptotic expansion of (31) yield

$$E_{oz} \sim \frac{i\omega\mu_o Ids}{2\pi\rho} e^{-ik_o\rho} \bar{g}_v^{(2)}(h)W(p) \quad x$$

$$x \left\{ 1 + ik_oz\Delta + \frac{3}{2p} - \frac{3z}{\Delta\rho} - \frac{3ik_oz^2}{2\rho} + \frac{k_o^2z^3}{2\rho} \right\} . \tag{32}$$

The term (3/2)p agrees with Wait (1964). In (32) Z is the height of the observer. This is entirely consistent with the formulas for the single slab quoted by Wait (1967b and 1968)

In figure 2 we show a comparison of theory, as described in Ott and Wait (1973) report, with a set of Jansky-and-Bailey-measured data selected at random. The predicted and measured basic transmission loss, defined as

$$\text{Basic Transmission Loss} = -20 \log_{10}|2E_z/E_o| + 20 \log_{10}(2k_o\rho \tag{33}$$

is plotted versus frequency in figure 2. At 20 MHz, the predicted and measured values differ by about 3 dB. As the frequency increases above 20 MHz, the difference between theory and measured basic transmission loss increases to about 18 dB at 50 MHz. From 50 MHz to 300 MHz, the difference between theory and measured basic transmission loss remains constant and equal to about 18 dB. It is interesting that the theory predicts the greater loss. A possible explanation for the discrepancy between theory and measured data in figure 2 may be the measured data were taken with the receiving antenna located on a tower in a partial clearing. At low frequencies, a partial clearing would be indistinguishable to the wave from the jungle itself. As the frequency is increased, the transition from jungle to clearing is more abrupt. As the frequency is increased still further, the loss will increase at a constant rate corresponding to one term in the residue series representation for the field strength, E_z. That is, for sufficiently high frequencies, and $z = h = 0$,

3.4 Knife-Edge Diffraction

When a radio wave propagates with a wavelength small compared to the major ground irregularities a useful method for predicting the path loss is to replace the terrain profile with equivalant knife edges, for which a treatment in terms of Fresnel integral is well established. In this section we show the application double knife-edge attenuation coefficient to some recent measurements at 9.6 and 28.8 GHz taken on a path near Monterey, California (Violette and Haakinson, 1979). When one of the ridges is in sight we use the Wilkerson approximation (1966) while when both ridges obstruct the path we use the "EMP" approximation (Wilkerson, 1966). The Wilkerson approximation is closely related to the double knife-edge diffraction formulas developed by Millington, et al. (1962). Typically the method is applicable to diffraction angles between ± 100 mrad and propagation distances between 1 and 100 km and in the VHF to UHF frequency band. In figures 3 and 4 we show a comparison of Wilkerson's double knife-edge attenuation coefficient with recent measured data. The excellent agreement between predictions and observations especially in the "lit" region where the lobe structure at 28.8 GHz in the measured data is reproduced by the theory lends confidence to the method.

4. Concluding Remarks

We have attempted to briefly show the use of various analytical methods for predicting the path loss of a radio wave as it encounters various types of terrain obstacles and profiles. The methods are only useful to engineers when a numerically efficient computer algorithm is available for prediction purposes. At the Institute for Telecommunication Sciences in Boulder, Colorado, there exists computer algorithms for the methods outlined in this paper; i.e.,

1) Integral equation formulation algorithm (PROGRAM WAGNER)
2) Mode-match technique algorithm (PROGRAM MODKED)
3) Layered media algorithm (PROGRAM BURANT)
4) Knife-edge diffraction algorithm (PROGRAM ZWEI)

These computer programs are available upon request by contacting Dr. R. H. Ott at the address shown on page 8-1.

5. References

Feinberg, E. (1944-1946), On the propagation of radio waves along an imperfect surface, Jour. Phys., USSR, 8, 317-330, 9, 1-6, 10, 410-418.

Furutsu, K. (1956), On the multiple diffraction of electromagnetic waves by spherical mountains, J. Radio Res. Lab., Japan, 3, No. 14, 331-390.

Hufford, G. A. (1952), An integral equation approach to the problem of wave propagation over an irregular terrain, Quart. J. Appl. Math., 9(4), 391-404.

King, R. J., and J. R. Wait (1976), EM Ground Wave Propagation-Theory and Experiment, Symposia Mathematics, Vol. VXIII, Academic Press.

Kissick, W. A., E. J. Haakinson, and G. H. Stonehocker (1978), Measurements of LF and MF radio propagation over irregular, inhomogeneous terrain, NTIA Report No. 78-12, Boulder, Colorado 80303.

Leontovich, M. A. (1948), Diffraction, refraction and reflection of radio waves, thirteen papers by V.A. Fock, Introduction by V. I. Smirnov, appendix by M.A Leontovich, editor N-A. Logan, Assoc. editor, P. Blacksmith, Jr., Antenna Lab., Air Force Cambridge Research Labs, Beford, Mass., report No AFCRC-57-102, NTIS No. AD1172776, June, 1957.

Lytle, R. J. (1974), Measurement of earth medium electrical characteristics: Techniques, results and applications, IEEE Trans. GeoScience and Electronics, GS-12, pp.81-101.

Millington, G., R. Hewitt, and F. S. Immirzi (1962a), Double knife-edge diffraction in field-strength predictions, Proc. IEE Monograph No. 507E., 109, pt. C., pp.419 429.

Mitzner, K. M. (1967), An integral equation approach to scattering from a body of finite conductivity, Radio Science, Vol. 2., (New Series), No. 12, Dec., pp. 1459-1470.

Monteath, G. D. (1978), Computation of ground wave attenuation over irregular and inhomogeneous ground at low and medium frequencies, BBC Research report, BBC RD 1978/7 March.

Ott, R. H. (1970), An alternative integral equation for propagation over irregular terrain, Radio Sci., 5, No. 5, pp. 767-771, May.

Ott, R. H. (1971), An alternative integral equation for propagation over irregular terrain, 2, Radio Science, 6, No. 4, pp. 429-435.

Ott, R. H. and J. R. Wait (1973), Excitation mechanisms for transmission through forest-covered and vegetated media, U. S. Army Communications Command Tech. Report No. ACC-ACO-8-73, NTIS No. AD-771915.

Ott, R. H., L. E. Vogler and G. A. Hufford (1979), Ground wave propagation over irregular, inhomogeneous terrain: Comparisons of calculations and measurements, U. S. Department of Commerce, NTIA Report 79-20.

Rosich, R. K. (1977), Electromagnetic scattering from periodic rough surfaces, thesis for Ph.D., University of Colorado, available from University Microfilms, Ann Arbor, Michigan, 48104, #78-8930.

Rytov, S. M. (1940), Perturbation method of skin-effect computations, Soviet Physics-J. Expt. and Theor. Phys., 10(2), 180-189.

Tamir, T. (1967), On radio-wave propagation in forest environments, IEEE Trans. Ant. Prop. AP-15, No. 6, Nov., 806-817.

Violette, E. J., and E. J. Haakinson (1979), Private Communication.

Wait, J. R., and A. M. Conda (1959) Diffraction of EM waves by smooth obstacles for grazing angles, J. Res., NBS, Vol. 63D, No. 2, Sept., Oct., 181-187.

Wait, J. R. (1962), Theory of Magneto-Telluric Fields, Jour. of Res., National Bureau of Standards, D. Radio Propagation, Vol. 66D, No. 5, Sept.-Oct., pp. 509-541.

Wait, J. R. (1967a), Radiation from dipoles in an idealized jungle environment, Radio Sci. 2, No. 7, 747-750. (Note, in eq. (1) replace $R_{||}(\lambda)\exp(u_o(Z+h))$ with $R_{||}(\lambda)\exp(-u_o(Z+h))$.

Wait, J. R. (1967b), Asymptotic theory for dipole radiation in the presence of a lossy slab lying on a conducting half space, IEEE Trans. Ant. Prop. AP-15, No. 5, 645-648. (Note that $r_{||}$ and $r_{\perp}$, as defined on p. 647, have a missing minus sign.

Also, in eq. (6), the plus sign between the two fractions within the braces (i.e., the fractions with exponential functions in the numerator) should be replaced with a minus sign. Also, the factor λ/u_o in (13) only is spurious.)

Wait, J. R. (1968a), Diffraction and scattering of the electromagnetic groundwave by terrain features, Radio Science, Vol. 3 (New Series), No. 10, Oct., pp.995-1003.

Wait, J. R., and K. P. Spies (1968b), Radio propagation over a cylindrical hill including the effect of a surmounted obstacle, IEEE Trans. on Ant. and Prop., Vol. AP-16, No. 6, Nov., pp. 700-705.

Wilkerson, R. E. (1966), Approximation to the double knife-edge attenuation coefficient, Radio Science, Vol. 1 (New Series), No. 12, Dec., pp. 1439-1443.

FIGURE CAPTIONS

1. Path profile (lower portion) and received signal (in dB above 1 μV/m for 1 kw effective radiated power) for Dry Lake, Nevada path. Crosses denote measured 2.5 min. averages. The table in upper right-hand corner shows the values for conductivity and relative dielectric constant as a function of distance.

2. Basic transmission loss versus frequency for propagation through a jungle.

3. Comparisons of double knife-edge attenuation coefficient with measured data near Monterey, California at 9.6 GHz.

4. Comparisons of double knife-edge attenuation coefficient with measured data near Monterey, California at 28.8 GHz.

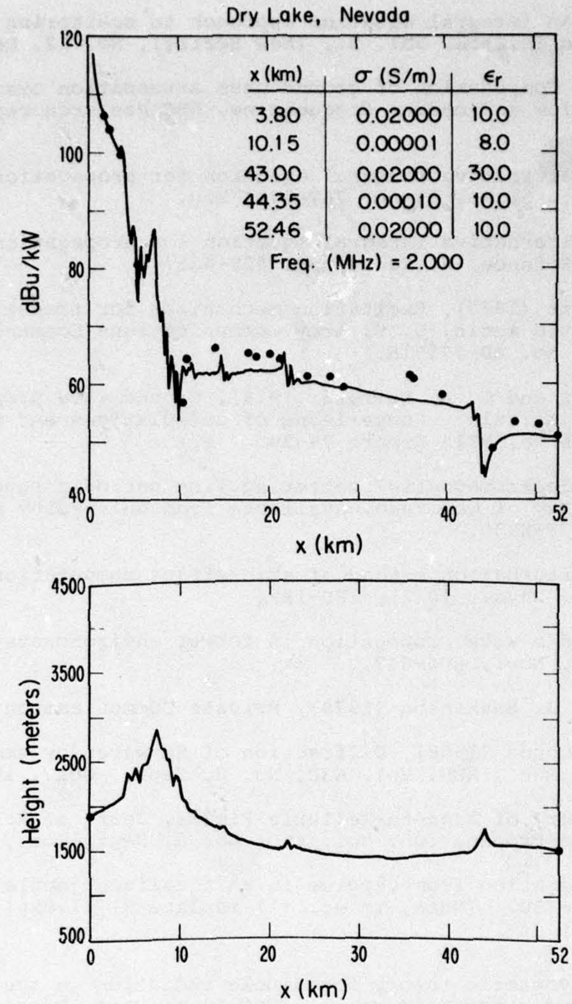

Figure 1

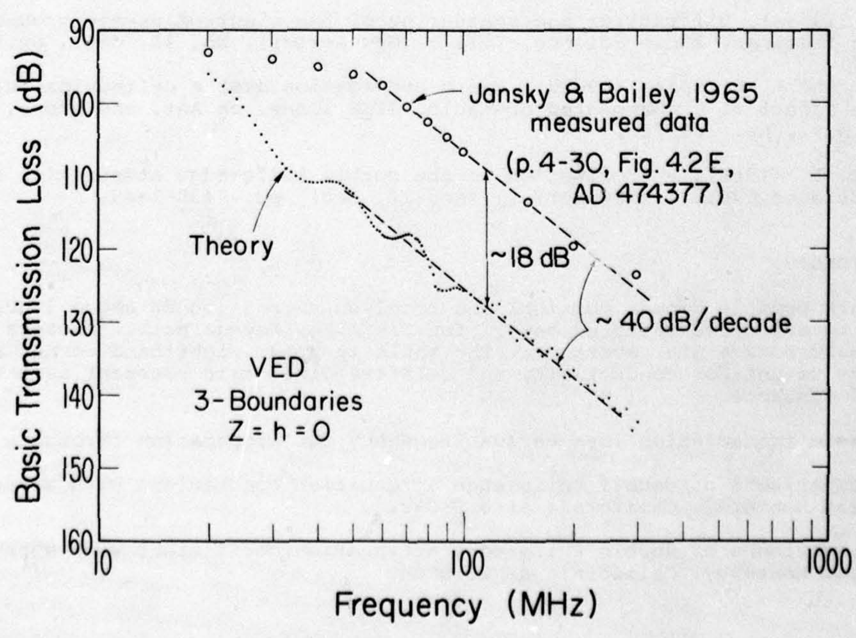

Figure 2

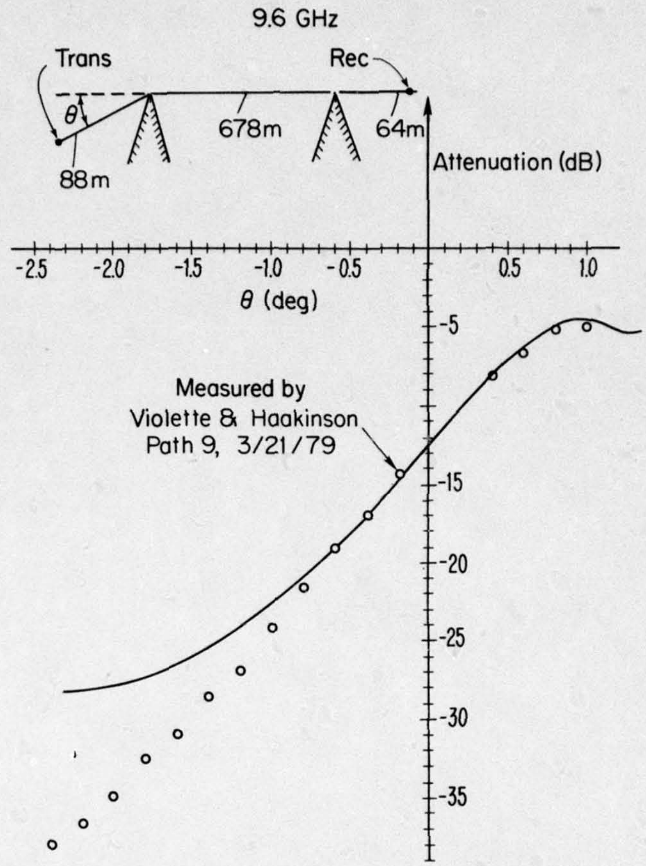

Figure 3

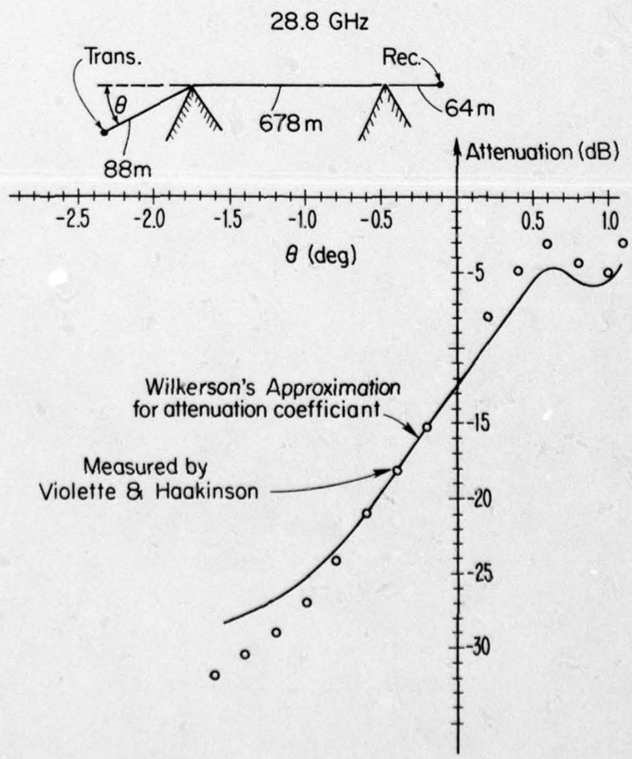

Figure 4

HIGH-FREQUENCY SIGNAL PROPAGATION AND SCATTERING IN GUIDING CHANNELS

L. B. FELSEN
Department of Electrical Engineering
Polytechnic Institute of New York
Farmingdale, New York 11735

SUMMARY

The earth's environment contains propagation channels wherein waves can be guided because of the presence of transverse boundaries or transverse refractive index gradients. By a new approach, high frequency guiding by a single concave surface or by the boundary of an inhomogeneous surface duct has recently been analyzed in terms of a judiciously chosen combination of rays and modes. In essence, the modes account for the cumulative effect of those rays that have experienced a great many reflections on the boundary. This hybrid formulation is appealing in that it requires far fewer rays and far fewer modes than if the field representation involves rays only or modes only, as has been customary. By an extension of the theory, it has now been shown that the hybrid method can also be applied to channels wherein guiding occurs between multiple transverse boundaries. Here, modes near cutoff can represent efficiently all those rays that have made many excursions between the channel walls. As an illustration, results are presented for a parallel plane waveguide excited by a line source.

1. INTRODUCTION

Terrain probing along the earth's surface or in subsurface layers may involve propagation channels that can support electromagnetic or acoustic waves guided along a single surface or between multiple surfaces. In the high-frequency range, the propagation phenomena may be described either in terms of guided modes and continuous spectra (when required), or in terms of multiply reflected ray-optical fields. The calculations may require the summation over many modes or many rays, and they become even more complicated when profile perturbations introduce scattering centers or non-uniformities along the propagation path.

In a recently developed theory, a judiciously chosen mixture of modal and ray fields has been shown to provide an effective method for calculating signal strengths and providing new insights into the physical mechanism of propagation and scattering. The ray-mode mixture involves far fewer rays and modes than when only rays or only modes are employed to characterize the field. The theory was first constructed for source and observation points on concave terrain contours where the relevant modal fields are whispering gallery modes guided along a single boundary described by a surface impedance (Ishihara, T. and L. B. Felsen, 1979). Subsequent extensions have dealt with ducts having an inhomogeneous refractive index profile that causes field trapping near a planar surface (Felsen, L. B. and T. Ishihara, 1979). In both cases, the ray fields that undergo many reflections between the source point Q and the observation point P cannot be calculated by geometrical optics because the local plane wave assumption underlying the geometric optical model cannot be satisfied for such fields. In qualitative terms, those rays lying within the duct of the most closely bound whispering gallery mode (Fig. 1) must be excluded from a ray-optical calculation and accounted for in some other way. Various schemes involving canonical integrals (the analogs of Fock integrals for shadow boundary effects on convex surfaces), guided modes and the above-noted appropriately chosen mixture of rays and modes have been explored in this context (Ishihara, T. and L. B. Felsen, 1979; Felsen, L. B. and T. Ishihara, 1979). Among these formulations, the hybrid ray-mode model is simplest and physically most appealing. For details of the analysis and for numerical comparisons of the accuracy of the various alternative formulations, which confirm the validity of the hybrid model, see(Ishihara, T. and L. B. Felsen, 1979; Felsen, L. B. and T. Ishihara, 1979).

When guiding is produced by two boundaries, there exist rays that experience many reflections between these boundaries as they progress from Q to P. While the ray-optical description of the field along these rays is legitimate, their summation poses numerical problems. Here, it is found that the cumulative effect of such rays can be accounted for in terms of an appropriately chosen numbers of waveguide modes near cutoff.

2. HYBRID FORMULATION FOR PARALLEL PLANE WAVEGUIDES

For illustration, consider a homogeneously filled parallel plane waveguide with perfectly conducting boundaries, excited by a magnetic line source on one of the boundaries. The exact Green's function can here be expressed as a modal sum involving the propagating and evanescent waveguide modes. The Green's function can also be expressed as a Fourier transform with respect to the axial coordinate z. In the resulting integral representation, there exists a resonant denominator whose zeros provide pole singularities that correspond to the waveguide modes. If the integration path is deformed around those singularities and the residue theorem is invoked, one obtains the above-mentioned modal sum, each mode being identified by the characteristic angle θ_m (Fig. 2). On the other hand, if the resonant denominator is expanded in a geometric series, thereby removing the poles, one obtains a series of integrals. When these are evaluated asymptotically by the saddle point method, each furnishes a contribution that can be identified exactly with a geometric-optical ray field characterized by the ray angle θ_n (Fig. 2).

If one does not wish to include all of the multiply reflected rays in the formulation, one may expand the resonant denominator into a partial sum up to θ_N plus a remainder term. By contour deformation in the resulting remainder integral such that the contour coincides with the steepest descent path corresponding to the last ray with θ_N, and by subsequent asymptotic (saddle point) evaluation, one may show that the remainder integral is well approximated (- 1/2) of the contribution from the last ray provided that $\theta_N \neq \theta_M$ or θ_{M-1}, where θ_M and θ_{M-1} are the characteristic angles of those waveguide modes that lie on either side of θ_N (i.e., $\theta_M > \theta_N > \theta_{M-1}$) (see Fig. 2). These steps are directly analogous to those performed in dealing with the surface guided fields (Ishihara, T. and L. B. Felsen, 1979; Felsen, L. B. and T. Ishihara, 1979).

Thus, the exact solution yields for the field G on the lower boundary of Fig. 2, (Kamel, A. and L. B. Felsen):

$$G = \sum_{m=0}^{\overline{M}} (\text{propagating waveguide modes}) + \sum_{m=\overline{M}+1}^{\infty} (\text{evanescent waveguides modes}) \tag{1}$$

Unless the lowest evanescent mode with $m=\overline{M}+1$ is very near the propagating regime, the evanescent mode sum can be neglected for large enough ranges between P and Q in Fig. 2. The hybrid ray-mode formulation yields

$$G \sim \sum_{m=M}^{\overline{M}} (\text{propagating waveguide modes}) + \sum_{m=M+1}^{\infty} (\text{evanescent waveguide modes})$$

$$+ \sum_{n=0}^{N} (\text{ray fields}) - \frac{1}{2}(\text{Nth ray field}). \tag{2}$$

A negligible remainder term, which is also found to appear (Ishihara, T. and L. B. Felsen 1979; L. B. Felsen and T. Ishihara, 1979) has been omitted in (2). The criterion for choosing M and N is schematized in Fig. 2: if θ_N is the departure angle of the last included ray (the one with the highest number of reflections), then the modes needed are those with $\theta_M > \theta_N$. It is evident that if N is kept constant but the range z between the source point and observation point is increased, the departure angle θ_N decreases and will eventually approach the characteristic angle θ_{M-1} of the first excluded mode. When z is such that $\theta_N < \theta_{M-1}$, this latter mode must be added to the mode sum. Analogous considerations prevail when z decreases, thereby leading eventually to the removal of the mode with θ_M. Alternatively, if the number of modes ($\overline{M}$-M) is kept constant, the number of included rays N must be adjusted with varying range z such that all possible rays with $\theta_N < \theta_M$ are included. When $\theta_N = \theta_M$ or θ_{M-1}, the saddle point for the last ray in the contour integral representation coincides with the pole for the nearest waveguide mode. In this transition region, the simple ray-mode model fails and must be patched up by a transition function (a Fresnel integral; see Felsen, L. B. and N. Marcuvitz (1973) that accounts for the proximity of a pole and a saddle point. Note that at least one of the propagating modes (the one closest to cutoff) must be included, whence $\theta_N < \theta_M$. The conclusions summarized above may also be confirmed by applying partial Poisson summation to the ray series in (1), thereby converting it into the hybrid formulation in (2) (Kamel, A. and L. B. Felsen). The procedure is directly analogous to that reported in Felsen, L. B. and T. Ishihara (1979).

Typical numerical results (Kamel, A. and L. B. Felsen) obtained from the exact and hybrid formulations are depicted in Fig. 3, where the magnitude of $|G|$ is plotted over a normalized range kz from 250 to 290, k being the wavenumber in the medium. The normalized waveguide height is ka = 50 and admits $\overline{M} = 16$ propagating modes. The exact field is calculated from (1); for this case, the evanescent modes can be omitted since they contribute negligibly over the specified range of observation points. Also plotted in Fig. 3 is the hybrid ray-mode solution obtained from (2) when N=2 as in Fig. 2 (i.e., the direct ray and the rays with one and two reflections at the upper boundary have been retained). From the criterion $\theta_m \geq \theta_N = \theta_2$, it is found that M = 14 for 250 < kz < 261, whereas M = 13 for 261 < kz < 290, in view of the fact that the characteristic mode angle θ_{13} for m=13 coincides with the ray departure angle θ_2 when kz = 261. The hybrid ray-mode formulation in (2) is discontinuous at $\theta_M = \theta_N$ but the jump is not very large and can be eliminated approximately by drawing a smooth curve through the average value at $\theta_M = \theta_N$. By a more rigorous procedure, one may employ the Fresnel integral transition function that provides continuous field values through the transition region surrounding kz = 261. Both the approximate and rigorous methods are seen to furnish excellent agreement between the exact and hybrid solutions. Note that whereas the exact solution requires 16 propagating modes, the hybrid solution requires 3 rays and three or four modes, respectively, for 250 < kz < 261 and 261 < kz < 290. When N=3 so that rays with three reflections at the upper boundary are included as well, one finds $\theta_3 = \theta_{14}$ at kz = 282. Consequently, two propagating modes (with m = 15, 16) are required for 250 < kz < 282 while three modes (with m = 14-16) are required for 282 < kz < 290. The numerical accuracy is comparable to that depicted in Fig. 3. Similar results are obtained for other values of N and other range intervals, (Kamel, A. and L. B. Felsen). When the first non-propagating mode is very close to cutoff, its contribution must be included in (1) and (2). Numerical comparisons again confirm the validity of the hybrid calculation in that event (Kamel, A. and L. B. Felsen).

3. A NEW CLASS OF DIFFRACTION PROBLEMS

The hybrid ray-mode formulation of propagation leads to a new class of diffraction problems when a scatter is located inside the duct. In previous studies (Batorsky, D. V. and L. B. Felsen, 1971), a ray-optical method was devised to account for the presence of obstacles or strong scattering centers within the guiding structure. The field in each of the incident modes is represented by its congruence of rays, and the scattering of these rays by the obstacle is calculated from the geometrical theory of diffraction. The diffracted rays, which experience multiple reflection at the waveguide boundaries or continuous refraction within the duct, are then converted into guided modes to establish the scattering matrix elements that describe the effect of the obstacle on reflection and transmission of the incident modes as well as coupling to other modes. It is to be emphasized that all of the rays are converted into the propagating guided modes by this scheme.

In the hybrid formulation, each of the retained incident modes and each of the incident ray species will give rise to a ray-optical scattering process as described above. The multiply reflected ray fields excited by the scattering center can be decomposed into another hybrid mixture that may be preferable for calculation at various ranges of the observation point with respect to the scatterer. The hybrid selection could be made so as to minimize the complexity of the scattering calculation. The flexibility introduced thereby is illustrated in the example of Fig. 4. The principal difference between the mode theory of diffraction

and the hybrid theory is the dependence of the ray-mode mixture on range. For the incident field, the relevant range is from the source to the obstacle whereas for the scattered field, it is from the obstacle to the observer.

4. CONCLUSIONS

The hybrid ray-mode formulation affords a new approach to source-excited high-frequency propagation in guiding regions formed by transverse refractive index inhomogeneities and (or) bounding surfaces. Conventional methods have expressed the field either in terms of rays or in terms of (discrete and continuous) modes. The hybrid ray-mode mixture improves upon these methods since it requires far fewer rays and modes than when only modes or only rays are considered. This facilitates numerical treatment of the problem. It also grants new physical insights since the formulation implies that propagation processes characterized by rays with many reflections can be treated collectively in terms of a few modes while processes characterized by many modes can be expressed succinctly in terms of a few rays. In effect, the hybrid formulation quantifies the truncation error of a mode series in terms of rays, or equivalently, the truncation error of a ray series in terms of modes. Moreover, since the number of modes in a modal expansion can now be suitably restricted, the eigenvalue problem in a complicated ducting environment may often be reduced to a simpler form for the retained cluster of modes. This feature economizes on computer time and required computer capacity. The hybrid formulation also appears to be well suited to treatment of lateral inhomogeneities along the duct provided that these occur gradually over a length interval equal to the local wavelength of the signal spectrum. Finally, the ray-mode field representation provides a new approach to scattering from strong inhomogeneities since physical insights derived from scattering of either a modal field or a ray field can be exploited to advantage.

REFERENCES

Batorsky, D. V. and Felsen, L. B. 1971 "Ray Optical Calculation of Modes Excited by Sources and Scatterers in Weakly Inhomogeneous Ducts," Radio Science 6, p. 911-923.

Felsen, L. B. and N. Marcuvitz, 1973, "Radiation and Scattering of Waves," Prentice Hall, Inc., Englewood Cliffs, New Jersey, Chapter 4.

Felsen, L. B. and T. Ishihara, 1979, "Hybrid Ray-Mode Formulation of Ducted Propagation", J. Acoust. Soc. Am. 65, p. 595-607.

Ishihara, T. and L. B. Felsen, 1979, "High Frequency Fields Excited by a line Source Located on a Concave Cylindrical Impedance Surface," IEEE Transactions on Ant. and Propag. AP-27, p. 172-179.

Kamel, A. and L. B. Felsen, "Hybrid Ray-Mode Representation of the High-Frequency Parallel Plane Waveguide Green's Function," in preparation.

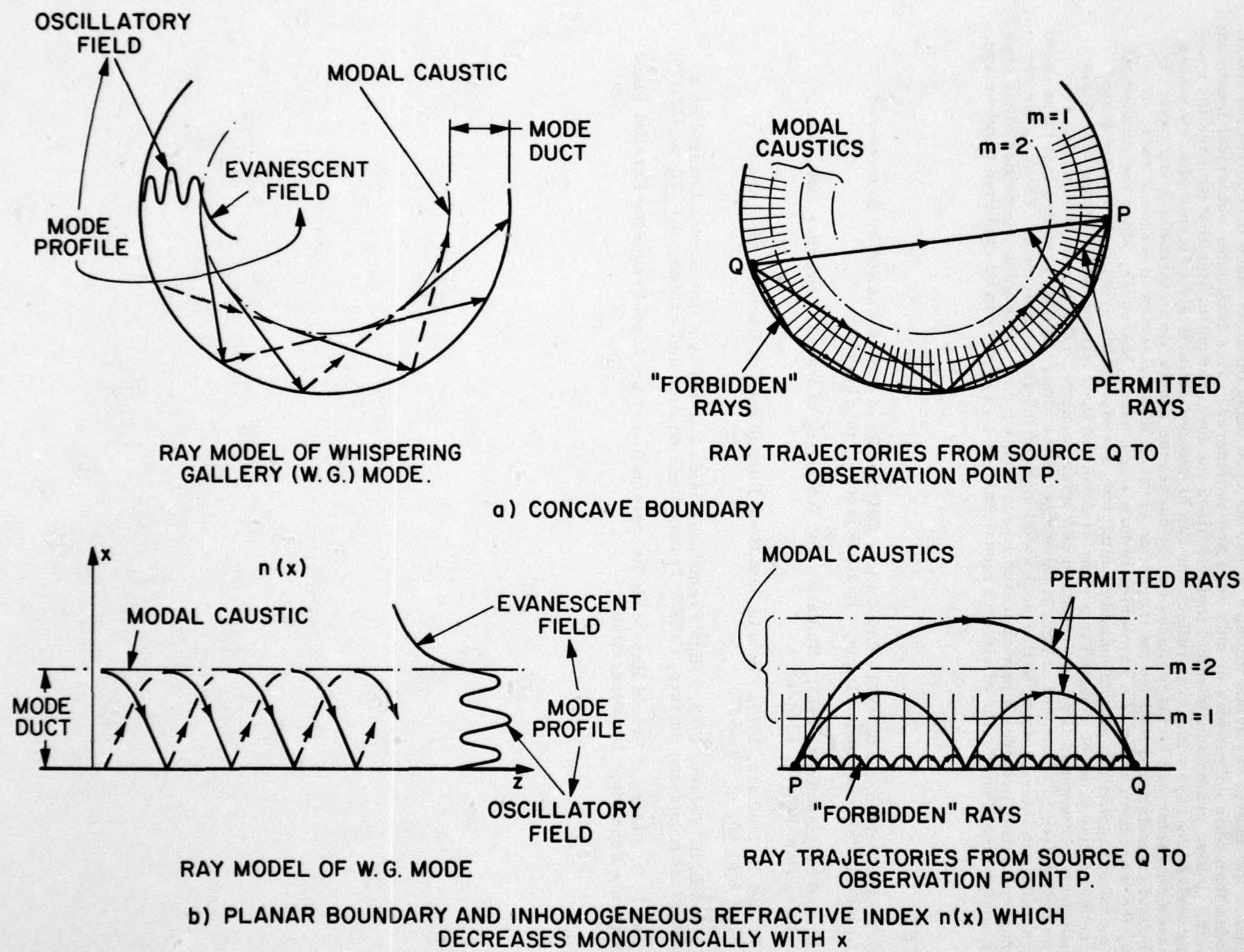

Fig. 1. Whispering gallery modes and rays. ——> - - - -> modal ray congruences. Rays proceeding entirely within the shaded region that includes the duct width of the most tightly bound (m=1) W.G. mode must be excluded from the ray-optical field representation.

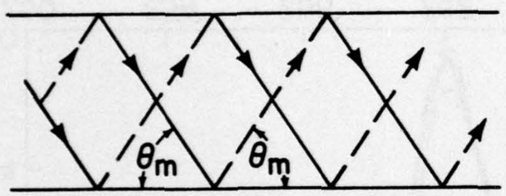

Ray model of waveguide mode. ⟶ ⟶ modal ray congruences. θ_m is the characteristic (modal) angle.

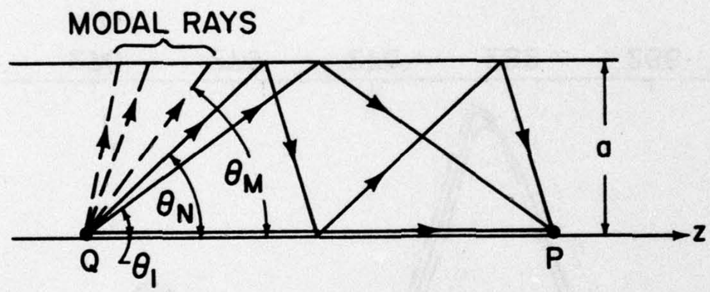

Ray trajectories from Q to P, including direct and multiply reflected rays. The last included ray is described by the angle θ_N. Rays with more reflections $(\theta_n > \theta_N)$ are accounted for by all those waveguide modes with $\theta_m \geq \theta_M$, where θ_M is the mode whose characteristic angle is closest to, but larger than, θ_N. The figure shows truncation of the ray series after the reflected ray with $\theta_N = \theta_2$.

Fig. 2. Hybrid ray - mode model for parallel plane waveguide

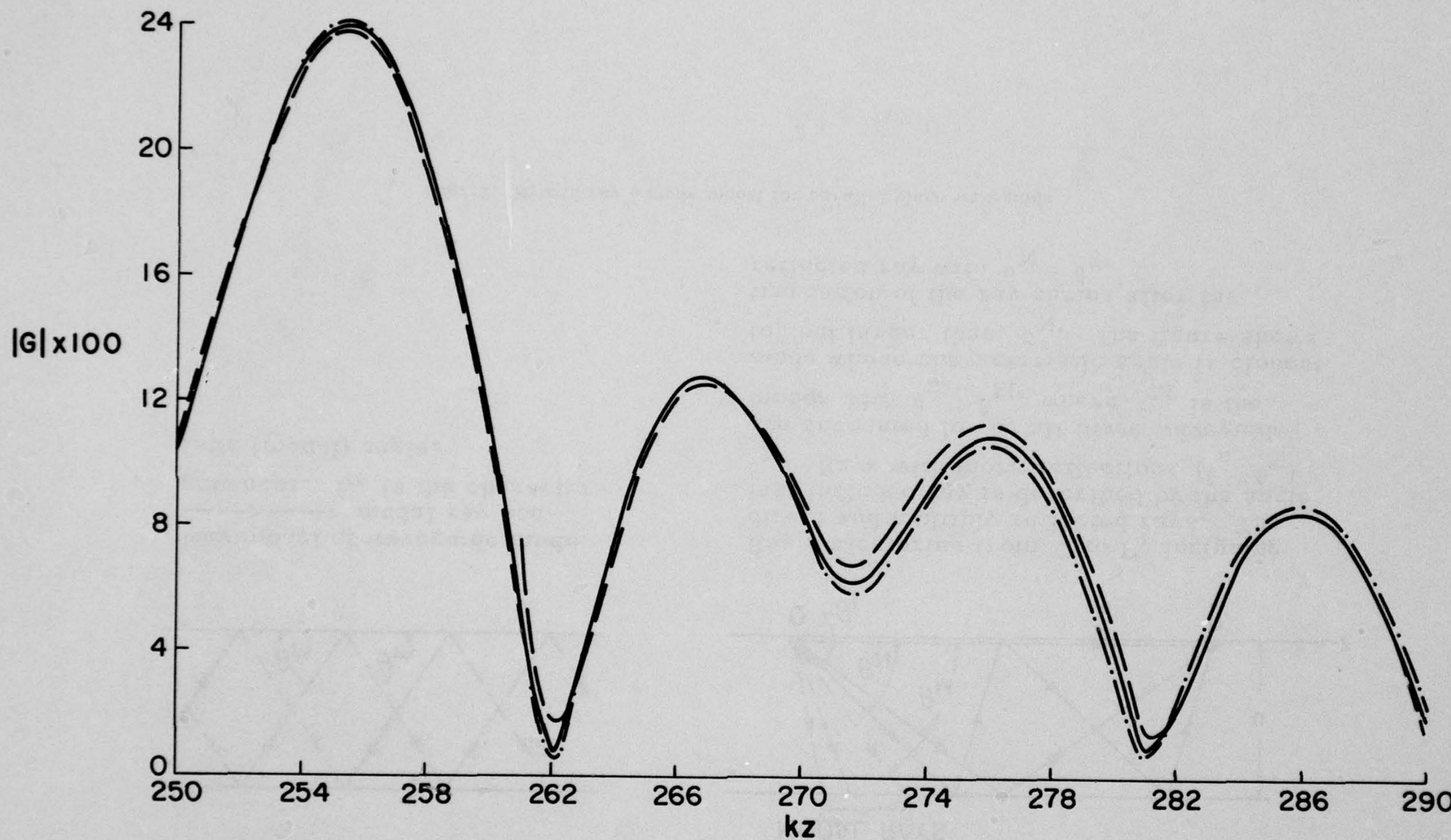

Fig. 3. Field magnitude in the range interval $250 < kz < 290$, when ka = 50. ——— Exact result calculated from (1), with $\overline{M} = 16$. — — — Hybrid ray-mode result calculated from (2), with N = 2. —·—·— Hybrid ray-mode result calculated from (2), with N = 2, when Fresnel transition function is used (when curve is not shown, it coincides with the exact result).

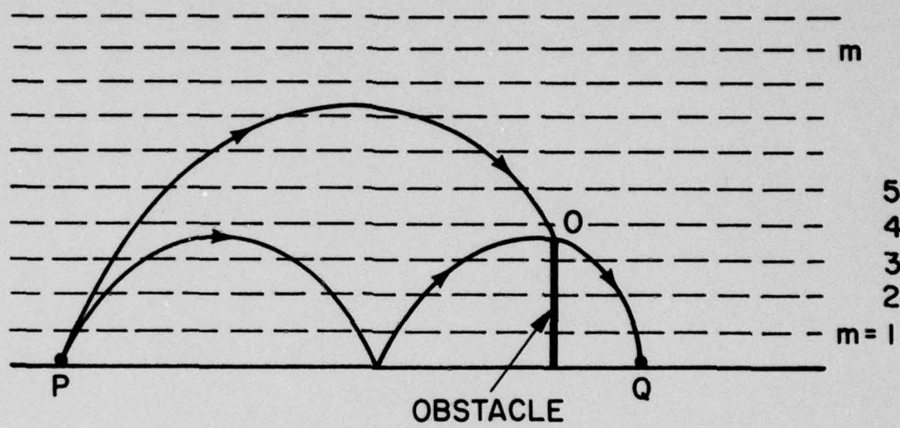

Fig. 4. Hybrid ray-mode formulation of scattering by a vertical strip obstacle in a surface duct. The modes retained (M=3) are of those whose caustics lie below the edge since the reflection of these modes is as from an infinite plane and therefore evaluated trivially. The modes whose field strength are appreciable at the edge are accounted for by the two incident rays. The scattered fields are evaluated as from an equivalent non-isotropic line source located at the edge O. Only a single ray proceeds from there to the observation point Q, and the excited modal fields (m = 1, 2, 3) are negligible

GROUND WAVE PROPAGATION OVER IRREGULAR, INHOMOGENEOUS TERRAIN: COMPARISONS OF CALCULATIONS AND MEASUREMENTS AT FREQUENCIES FROM 121 kHz to 50 MHz

R. H. OTT
U. S. Department of Commerce
National Telecommunications and Information Administration
Institute for Telecommunication Sciences
Boulder, Colorado 80303 USA

SUMMARY

A method for calculating the ground-wave field over irregular, inhomogeneous terrain was previously developed by Ott and comparisons with alternative analytical methods were made for idealized terrain profiles like concave parabolas, sea-land-sea paths, and single Gaussian ridges. The excellent agreement between methods like Fock currents for concave surfaces, the classical residue series, an integral equation developed by Hufford, Ott's alternative method based upon an elementary function (closely related to the Sommerfeld flat-earth attenuation function) for the parabolic wave equation provided encouragement for the usefulness of the method and the associated algorithm. The computer algorithm implementing integral equation (called PROGRAM WAGNER) uses linear interpolation to represent the terrain height versus distance and a surface impedance which also varies with distance. The transmitting antenna height is arbitrary and is included in the integral equation formulation whereas the height of the receiving antenna is treated approximately by modifying the surface field at the observation point by an effective height-gain function.

In this paper, comparisons of observed field strength measurements for several paths with field strength predictions based on PROGRAM WAGNER are given for frequencies ranging from 120 kHz to 50 MHz. Although most of the comparisons show encouraging agreement, the 20 MHz comparisons over an extremely rugged path in the Colorado Mountains provided a challenge for the algorithm.

1. Introduction

A large number of groups within the Department of Defense, as well as private industry, have funneled their problems concerning radio propagation over irregular, inhomgeneous terrain to the Institute for Telecommunication Sciences in Boulder, Colorado. The scope of the problems covered items like: 1) optimum location for transmitting and receiving antenna sites for the MX missile system, 2) the effects of a bluff or ridge on the launching efficiency of HF surface waves over the sea, 3) the possible shadow created by an island located somewhere in the azimuthal scan of a coastal radar, 4) the effects of hilly terrain on the location of antennas used in earth-satellite communication links and finally, 5) the effects of hilly terrain with variable ground constants on the communication reliability of mobile receivers in certain battlefield conditions from MF to VHF. This paper, hopefully, will demonstrate the usefulness, as well as possible shortcomings, of the integral equation plus associated algorithm for the above examples.

The use of the integral equation is referenced several times in the open literature; e.g., Hansen (1977) used PROGRAM WAGNER to estimate the effects of a bluff along a path from Point Loma in San Diego, California to Point Mugu near Santa Cruz island. Monteath (1973) pointed out the use of our integral equation program for solving the problem of propagation over irregular, inhomogeneous terrain. Wait (1974) discusses the use of our integral equation for cases where the geometry is not amenable to mode matching. A draft new report on propagation over irregular, inhomogeneous terrain based on PROGRAM WAGNER was recommended in the CCIR XIV Plenary Assembly in June 1978 in Kyoto, Japan as a contribution to propagation by "diffraction" and will be recommended to the Special Preparatory Meeting for GWARC-79 scheduled for October 1979 in Geneva.

The paths and frequencies selected for comparison with measured data are summarized in Table I. Since PROGRAM WAGNER is a two-dimensional model, the terrain sites selected for comparison were all "ridge-like". The spacing of points refers to the distance projected on a horizontal plane used to sample the signal strength. The computational time is for a CDC 6600 computer.

A paper (Ott et al., 1979a) describes some recent comparisons of computed field-strength values with measurements on nine paths was condensed to form this paper.

TABLE I
Predictions/Comparisons for 6 Paths

Path	Frequency	Reference	x-spacing	Time(sec)
Transmitter (WGR-TV) in Buffalo, NY-over Lake Erie toward Cleveland, Ohio	59.75 MHz (horizontal polarization)	Head,H.T.(1958)	1(1)100m;100(50)1000m 1(1)47km;47(0.25)155km	1213 (596 pts)
Transmitter (KCBS) north of San Francisco Bay, south through San Francisco, over Santa Cruz Mountains	740 kHz	CBS Radio (1971)	0.5(0.5)72km	113 (144 pts)

TABLE I (Continued)

Path	Frequency	Reference	x-spacing	Time(sec)
Transmitter (KBLU) in Yuma, AZ, beyond Tinajas Altas Mountains toward Mexico	560 kHz	Heckscher, J. (1977)	0.5(0.5)41km; 41(0.1)45km 45(0.5)61km;61(0.1) 73km 73(0.5)83km	203 (294 pts)
			0.5(0.5)46km;46(0.1) 48.5km;48.6(0.5)67km	55 (154 pts)
			0.5(0.5)46km;46(0.1) 48.5km;48.5(0.5)67km	56 (154 pts)
Santa Ritas, AZ near Greenvalley, AZ and adjacent to AZ Experimental Range	1.619 MHz	W.A.Kissick, et al., (1978)	0.1(0.1)km;1(0.5)7km 7(0.1)20km;20(0.5)30km (conductivity from geological maps) (σ change at 12.95 km)	70 (172 pts)
Dry Lake, NE, Transmitter on east slope of Highland Peak to Dry Lake Valley	2.0 MHz	W.A.Kissick, et al. (1978)	0.1(0.1)15km;15(0.5) 21km;21(0.1)23km;23 (0.5)42km;42(0.1) 44.5km;44.5(0.5)52km; 52.46 km	263 (261 pts)
Colorado Mountain Data toward Berthoud Pass Campground	20.084 MHz	M.E.Johnson, et al. (1967)	0.1(0.1)50.4km; 50.46km	599 (505 pts)

2. The Integral Equation

The derivation of the integral equation used in the algorithm PROGRAM WAGNER is given in Ott (1970, 1971). The final result is

$$f(x) = W(x,0) - \sqrt{\frac{i}{\lambda}} \int_0^x f(\xi) e^{-ik\omega(x,\xi)} \{y'(\xi) W(x,\xi) - \frac{y(x)-y(\xi)}{x-\xi}$$

$$+ (\Delta(\xi) - \Delta_r) W(x,\xi)\} \left[\frac{x}{\xi(x-\xi)}\right]^{1/2} d\xi, \qquad (1)$$

where x, ξ, y(x), and y(ξ) are defined in Figure 1 and f(x) is the field normalized to twice the free-space field. The factor ($\Delta-\Delta_r$) arises in mixed-path problems. The factor Δ_r is constant with distance and is the relative value of the normalized surface impedance. This factor is computed using the values for σ and ε_r for the first section of a mixed path. The factor Δ varies with distance in a mixed path problem. The variation of Δ with x may be continuous or contain abrupt changes. The factor ($\Delta-\Delta_r$) is zero for a single section path. The remaining factors in (1) are defined as

$$\omega(x,\xi) = \frac{[y(x)-y(\xi)]^2}{2(x-\xi)} + \frac{y^2(\xi)}{2\xi} - \frac{y^2(x)}{2x};$$

$$W(x,\xi) = 1 - i\sqrt{\pi p}\, w(-\sqrt{u});$$

$$p = -ik\,\Delta^2(x-\xi)/2 \quad ;$$

$$u = p\left\{1 - \frac{y(x)-y(\xi)}{\Delta(x-\xi)}\right\}^2, \quad \xi < x;$$

$$w(-\sqrt{u}) = e^{-u}\operatorname{erfc}(i\sqrt{u})$$

$$= \frac{1}{i\pi}\int_{-\infty}^{\infty} \frac{e^{-t^2}\,dt}{\sqrt{u+t}} \quad \text{(Abramowitz and Stegun, 1964)} \;;$$

$$\Delta = \begin{cases} \dfrac{\sqrt{\eta-1}}{\eta}, & \text{vertical polarization} \\ \sqrt{\eta-1}, & \text{horizontal polarization}\;; \end{cases}$$

$$\eta = \varepsilon_r - \frac{i\,18(10^3)\sigma}{f(\text{MHz})};$$

f = frequency, in MHz;

σ = ground conductivity (S/m);

ε_r = relative dielectric constant.

The latest version of the computer program (called PROGRAM WAGNER) implementing the method based upon the solution of a parabolic wave equation is described in Ott, et al. (1979b). The solution of the integral equation neglects the effects of side-scatter and back-scatter which, for the case of most propagation paths, are second-order effects.

The integral equation in (1) is of the form of a linear Volterra integral equation of the second kind, i.e.,

$$f(x) = g(x) - c \int_{o}^{x} f(x)k(x,s)ds \quad , \qquad (2)$$

where f(x) is the unknown attenuation function whose value is to be determined in the interval $o \leq s \leq x$. The functions g(x) and k(x,s) are known, and c is a constant. This integral equation is solved by a stepwise calculation that divides the interval x into subintervals of arbitrary width. The details of the numerical solution, as well as documentation and description of the computer program, are given in Ott (1979b).

3. Comparisons with Measurements

3.1 Two FCC Paths

In Table I, the spacings used were not necessarily optimum and were arrived at by deciding the 100 meter spacing yielded reasonable agreement for the WGR-TV path from Buffalo, New York. When the terrain was relatively flat, spacings as large as 1 km were used.

The algorithm, PROGRAM WAGNER, is best suited to propagation frequencies below VHF. Also, because of problems in maintaining numerical accuracy during the integration process, predicting attenuation for vertical polarization is usually more successful than for horizontal polarization.

In the upcoming comparisons, the ordinate scales are in the familiar dBμ/kW, which is to say the field intensity measured in dB above 1μV/m and normalized to the case of 1 kW radiated from a (vertical) half-wave dipole.

To test what might be considered an extreme case for the applicability of WAGNER, data from a study by Head (1958) on a path near Buffalo, New York, was chosen. Field strength measurements were available along a radial from WGR-TV over a path that extended out to about 155 km. The station transmitted horizontally polarized waves at a frequency of 59.75 MHz. The initial portion of the path (about 47 km) was over Lake Erie, with the remaining portion over land containing variable terrain features. A plot of the path profile is shown in the lower part of Figure 2; it should be noted that the irregularity of the terrain is greatly exaggerated because of the expanded height scale. The predicted field, represented by the solid line, is shown in the upper part of Figure 2. The abrupt change at about 47 km is caused by the passage of the wave from the smooth surface of Lake Erie (with assumed dielectric constant = 81 and conductivity = 0.01 S/m) to the land with dielectric constant = 15 and conductivity = 0.03 S/m).

Measured values are represented by X's that start near the shore of the lake and are plotted at various distances over the land portion of the path. The upper end of the vertical line through each X is the maximum field that was measured during a 100-ft. mobile run at each receiving site. The lower end is the minimum observed field, and the X's are plotted at the median values.

The calculated field appears to follow the general trend of the observed values although individual points are not predicted. One reason for this, of course, could be that local terrain effects at the measurement sites (e.g., buildings, telephone wires, etc.) greatly influence the received field. There is also some indication, especially in the first few measurements near Lake Erie, that complex interference effects not accounted for by the simple ground-wave model are operating.

A second comparison of calculations and observations was made on data from a study by CBS Radio (1971) on a path in the San Francisco region. Measurements were available on a radial from KCBS a station transmitting vertically polarized waves at a frequency of 740 kHz. Figure 3 shows the path profile, measured field strength values, and prediction curve over a path of about 73 km. As can be seen, the prediction is well in accord with the observed data except for the end of the path. Whether the disagreement in this region is because of inaccurate values of electrical ground constants or, perhaps, the wrong assumption for the effect of atmospheric refraction is not known. Table II shows the ground constants used over various portions of the path.

In the examples in figures 2 and 3, a standard 4/3-earth" atmosphere was assumed. The computer program is capable of including other values of constant atmospheric ray bending through the use of the effective earth's radius concept.

It should again be noted that the first few measurements near the transmitting end of the path indicate a more complex interference mechanism than is assumed in the present model.

TABLE II
Ground Constants for KCBS Path

Distance (km)	ε_r	σ (S/m)
to 19.19	15	0.1
21.98	81	5
22.50	15	0.03
25.05	81	5
30.41	15	0.03
37.72	81	5
72.73	15	0.008

3.2 RADC Paths: KBLU to Junction and Water

Rome Air Development Center (Heckscher, 1979) has made a number of field strength measurements in an area southeast of Yuma, Arizona, using as a source the Yuma commercial broadcast station KBLU (560 kHz). The measurement sites are along jeep roads that run in various directions throughout the area. Although no series of measurements are strictly along a radial from KBLU, some are approximately so. Two series were found in the southern-most sector, and path profiles were determined from USGS maps along two radials from KBLU. The profiles are shown in the lower portions of Figures 4, 5, and 6. Path #1 (Fig. 4) crosses a minor ridge (Vopoki Ridge) at about 45 km and, later on, a higher ridge (Tinajas Altas Mtns.) at about 65 km. Path #2 (Figs. 5 and 6) crosses Vopoki Ridge also at about 45 km, but nearer the southern end.

The measurements corresponding to these two radials are tabulated below in terms of the field intensity, E(mV/m), measured at each location times the distance, d(km), from the transmitter are given in Table III.

TABLE III

	Path #1			Path #2	
d(km)	E·d(V)	d(km)	E·d(V)	d(km)	E·d(V)
75	38	41	205	50	178
77	52	43	196	52	185
78	55	44	204	54	192
80	62	46	223	57	193
81	68	48	267	61	204
83	72	49	243	64	180

From other measurements nearer the transmitter, E·d was found to approach a value of about 250. Thus, in order to compare with the WAGNER predictions in DBU, the measurements obey the relationship

$$DBU = E_o + 20 \log a_m = 112.94 - 20 \log d(km) + 20 \log a_m, \qquad (3)$$

where E_o is the reference field used in WAGNER and $a_m = (E \cdot d)/250$ is the attenuation at each receiving site. The values of measured DBU for each path are given in Table IV.

TABLE IV

	Path #1			Path #2	
d(km)	DBU	d(km)	DBU	d(km)	DBU
75	61.6	43	78.2	52	76.0
78	61.9	44	78.3	54	76.0
80	62.8	46	78.7	57	75.6
81	63.5	48	79.9	61	75.5
83	63.7	49	78.9	64	74.0

PROGRAM WAGNER was run for Path #1 using the following electrical ground constants:

d(km)	ε_r	σ(S/m)
0-41.1	10	0.02
41.4-44.9	8	10^{-5}
44.9-61.1	10	0.02
61.1-72.5	8	10^{-5}
72.5-83.0	10	0.02.

The conductivity value of $\sigma = 0.02$ S/m represents the nearly level, sandy portions of the area and was obtained from RADC on-site measurements. The values of $\sigma = 10^{-5}$ S/m and $\varepsilon_r = 8$ represent the conductivity and dielectric constant of the rock composing the mountains and ridges of the area. The type of rock was determined from a geological map of Arizona, and σ and ε_r were obtained from tables in a paper discussing ground constants of various rock materials (Head, 1958).

Figure 4 is a plot of predicted DBU from WAGNER (the solid curve) for Path #1, together with measured DBU represented by crosses. The last six measurements, which were taken along this profile, appear to agree very well with prediction. The first six crosses are measurements taken along Path #2, but plotted here because of the near proximity and similarity of terrain for the two paths in this area. These measurements do not agree as well because of slight differences between the two profiles.

Data for Path #2 was run on WAGNER with the following values for electrical ground constants.

d(km)	ε_r	σ(S/m)
0-46.0	10	0.02
46.0-48.1	8	10^{-5}
48.1-67.0	10	0.02 .

Figure 5 shows the WAGNER prediction together with the measurements taken along this radial. The abrupt drop in predicted field at about 46 km is due to the change in ground constants at this point. Because this radial crosses Vopoki Ridge at its

southern-most end where the ridge merges into the surrounding plain, it was decided to run WAGNER again for this same profile using the values $\varepsilon = 10$ and $\sigma = 0.02$, throughout the length of the path. The result is shown in Figure 6. The better agreement between prediction and measurements would indicate that the received signal was travelling mostly over terrain characterized by a conductivity of $\sigma = 0.02$.

3.3 ITS Measurements

In the first half of 1978, signal strength measurements were made by ITS (Kissick et al., 1978) along four different paths located in the western part of the U.S. An attempt was made to locate the paths in areas where access roads provided numerous sites along the radial at which measurements could be taken. Sky-wave contamination was eliminated by making only daytime measurements. Also, the distances were relatively short. The two paths and their location designations were:

(1) Santa Rita: located near the Santa Rita Mountains of southern Arizona;

(2) Nevada: a path west of Pioche, Nevada.

In Figures 7 and 8, the measured values denote the average of about 256 samples taken over a period of about 2.5 minutes. In order to compare the measurements with the output of WAGNER in terms of field-strength in decibels above 1 μV/m (designated DBU), the following relationship is used:

$$DBU = 139.37 + 20 \log f_{MHz} - P_t + P_m , \qquad (4)$$

where P_m is the measured received power in dB above 1 mW and P_t is an unknown constant (for each frequency run). To adjust the DBU such that the first measured point (or some chosen one) equals the WAGNER DBU prediction at that distance, d, solve (20) for P_t:

$$P_t = 139.37 + 20 \log f_{MHz} + P_m(d=d_1) - DBU(\text{WAGNER at } d=d_1) = \text{const.} \qquad (5)$$

The remaining DBU are then calculated from (4).

In general, values of electromagnetic ground constants were determined from geological maps of the areas involved in conjunction with tables of conductivity and dielectric constant contained in a paper by Lytle (1974). Estimates of σ and ε for various types of rocks are given in the tables, which values were then used for the appropriate segments of the radio path as determined by the geological maps. The one exception to this procedure was in the case of San Francisco, where much of the path was over water. For this path, sea water values were used over water and FCC suggested values were used for the portion over land. We felt the FCC maps were more appropriate for portions of this path which went over swampy regions where the soil type was difficult to identify.

Santa Rita

On the Santa Rita Mountains path, measurements were taken at 16 sites along a 23 km radial. Computer runs were made for two different sets of ground constants, the only difference being in the length of the "mountain" segment of the profile. One set assumed the "mountain" constants, $\sigma = 10^{-5}$ S/m and $\varepsilon = 5$, Mo extend from 7.2 km to 16.4 km; the other set had this segment extending from 7.2 km to 12.95 km (see ground constant tables in the figures).

Figure 7 shows comparisons at 1.619 MHz for the Santa Rita path; again, the terrain profile is shown in the lower portion of the figure. In general, Lytle's values for σ and ε_r correspond to rock with all moisture absent while the observed values by Kissick were under wet conditions. Kissick may also have observed the effect of the top or surface soil.

Nevada

Figure 8 shows comparisons at 2 MHz for the Dry Lake, Nevada, path. In general, the data lie somewhat above the WAGNER predictions, but the trend of the measurements and calculations are similar. It would appear that $\sigma = 0.02$ S/m is not the correct value for the conductivity over the "plains" portions of the profile. A higher value of σ would raise the prediction curves and give much better agreement with measurements.

Colorado Mountains

A study of the Colorado mountain data report (Johnson et al., 1967) was made to find paths for measurement/prediction comparison purposes. The sites (at 5, 10, 20, 30, and 50 km from the transmitter) fall more-or-less along the same radial, and this was probably an adequate path for the study.

Figure 9 shows comparisons of predicted and observed field strength at 20.08 MHz. This particular terrain profile probably represents an extreme in terms of roughness; however, the large amount of computer time required (913 sec in the case of WAGNER) to go just 6 km accurately suggests more reserach on the problem is required, and a definite limitation in the integral equation method, as discussed in the references mentioned earlier. Obviously, if enough sample points are used, the integral equation will yield accurate predictions. The problem comes in defining a "numerically efficient algorithm", which we discuss next.

4. Accuracy, Timing Aspects for the Algorithm PROGRAM WAGNER

In the several examples previously considered, convergence was obtained using nearly three points per wavelength. A conservative estimate for the spacing of points regardless of terrain profile, even for the Colorado mountain example, might be

Observation interval spacing, $\Delta x \approx 1/3$ wavelength

At 20 MHz, this would imply one point every 5 meters.

Since an error analysis for the algorithm PROGRAM WAGNER has not been performed, the use of the term "convergence" becomes a vague issue. The best estimate as to whether convergence is reached or not is to examine the solution at observation points along the radial beyond the point where a solution is desired and determine if the predicted results start to oscillate in a manner totally uncorrelated with any terrain features. Obviously, the question of convergence comes before one can discuss accuracy requirements, and again the need for an error analysis arises. In the solution of over determined matrices a general "rule of thumb is to use 4 sample points for each unknown. In some respects, the criteria of three points per wavelength does not seem to be overly restrictive since some Moment Method solutions require ten points per wavelength.

On the question of timing, a certain amount of arbitrariness arises. We have used the criteria that 15 minutes of CDC 6600 time is unreasonable" as an upper bound on the applicability for PROGRAM WAGNER. In general, the time goes as the square of the number of observation points.

5. Concluding Remarks

Six examples of measurement/calculation comparison discussed in the previous sections partially verify the applicability of PROGRAM WAGNER for estimating ground wave propagation over irregular terrain. These examples show that the integral equation method can provide very accurate detail on the signal strength and thus the terrain should be described as accurately as possible (e.g , topographical maps with 10 foot contour interval levels). Further comparisons with other data are obviously needed before the method is completely validated. However, to the authors knowledge, no other method attempting a detailed prediction for this complex problem has been published. It is hoped that the method presented here will at least partially fulfill the need for a better prediction of propagation effects in various applications.

Extensions of the model to include off-path terrain effects (the three-dimensional ground wave problem) are planned for the future. A full wave treatment would also provide more accurate estimates of the field, especially in those regions where complex interference phenomena are encountered. Wait (1974) has pointed to the use of alternative methods for evaluating propagation over irregular terrain in cases where the terrain can be considered a single knife-edge or a combination of several knife-like discontinuities, and his approach should be considered, especially when the behaviour of the field in the vicinity of a single terrain feature is desired.

Also, an error analysis should be considered so that the question of convergence and accuracy can be properly answered.

Finally, persons interested in obtaining card decks plus computer listings for the algorithm should contact Dr. R. H. Ott at the address shown on page 6-1.

6. Acknowledgement

The Electromagnetic Compatibility Analysis Center (ECAC) partially supported the research described in this paper. Ms. Jacqueline R. Janoski, Mr. J. A. Zoellner, and Dr. R. A Whiteman of ECAC initiated the idea to provide ECAC with an up-to-date, efficient prediction algorithm for propagation over irregular, inhomogeneous terrain. Mr. Mark Weissberger of ECAC made many helpful suggestions during the course of the research. Mrs. Rita Reasoner of ITS provided invaluable computer programming assistance. Also, the work was partially supported by the Department of the Air Force, Space and Missile Systems Organization, Norton Air Force Base under the sponsorship of Captains Bob Barrett and Bob Barberg and technical direction from TRW staff and by Mr. J. Cullhane, Dr. Leo Baggerely, and Mr. Jim Wolcott.

AD-A082 015 ADVISORY GROUP FOR AEROSPACE RESEARCH AND DEVELOPMENT--ETC F/G 20/14
TERRAIN PROFILES AND CONTOURS IN ELECTROMAGNETIC WAVE PROPAGATI--ETC(U)
DEC 79 A W BIGGS

UNCLASSIFIED AGARD-CP-269 NL

2 OF 4
AD
A082015

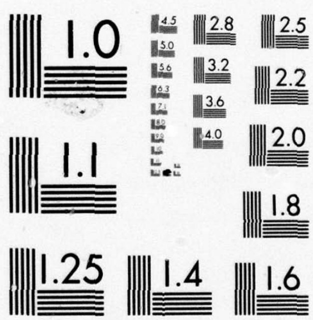

MICROCOPY RESOLUTION TEST CHART

NATIONAL BUREAU OF STANDARDS-1963-A

8. References

Abramowitz, M. and I. A. Stegun (1964), Handbook of Mathematical Functions, National Bureau of Standards, AMS 55, Ch. 7.

CBS Radio (1971), Field intensity measurements to establish performance of directional antenna station KCBS, San Francisco, California, Report E 70704-A, CBS Radio, Columbia Broadcasting System, Inc.

Hansen, P. (1977), Measurements of basic transmission loss for HF ground wave propagation over seawater, Radio Science, 12, No. 3, pp. 397-404, May-June.

Head, H. T. (1958), Field strength measurement survey for Association of Maximum Service Telecasters, Inc., Buffalo, New York; A. D. Ring and Associates, Washington, D.C.

Heckscher, J. (1979), RADC Technical Report, to be published.

Hopkins, M. (1977), ECAC-HDBK-77-07, ECAC's topographic data handbook, IITRI, Annapolis, Md., April; or ECAC's topographic data users manual, ECAC-UM-77-013.

Hufford, G. A. (1952), An integral equation approach to the problem of wave propagation over an irregular terrain, Quart. J. Appl. Math., 9, pp. 391-404.

Johnson, M. E., M. J. Miles, P. L. McQuate, and A. P. Barsis (1967), Tabulations of VHF propagation data obtained over irregular terrain at 20, 50 and 100 MHz, Part II: Colorado Mountains, ESSA Tech. Report No.: IER 38-ITSA 38-2, U. S Department of Commerce, Environmental Sciences Services Administration, Institute for Telecommunication Sciences, Boulder, CO 80303.

Kissick, W. A., E. J. Haakinson, and G. H. Stonehocker (1978), Measurements of LF and MF radio propagation over irregular, inhomogeneous terrain, NTIA Report No. 78-12, Boulder, Colorado 80303.

Lytle, R. J. (1974), Measurement of earth medium electrical characteristics: Techniques, results and applications, IEEE Trans. GeoScience and Electronics, GS12, pp. 81-101.

Monteath, G D. (1973), Applications of the Electromagnetic Reciprocity Principle, (Pergamon Press, New York), p. 116.

Ott, R. H. (1970), An alternative integral equation for propagation over irregular terrain, Radio Sci. 5, No. 5, pp. 767-771, May.

Ott, R. H. (1971a), An alternative integral equation for propagation over irregular terrain, 2, Radio Sci., 6, No. 4, pp. 429-435.

Ott, R. H. (1971b), A new method for predicting HF ground wave attenuation over inhomogeneous, irregular terrain, U. S. Department of Commerce, Res. Rept. No. OT/TRER 7, Jan. (NTIS Access No. AB721179).

Ott, R. H. (1974), Fock currents for concave surfaces, IEEE Trans. Atn. Prop., AP 22, No. 2, March, pp. 357-360.

Ott, R. H., L. E. Vogler, and G. A. Hufford (1979a), Ground-wave propagation over irregular, inhomogeneous terrain: Comparisons of calulations and measurements, IEEE Trans. on Antennas and Propagation, Vol. AP-27, No. 2, March, pp. 284-286.

Ott, R. H., L. E. Vogler, and G. A. Hufford (1979b) Ground wave propagation over irregular, inhomogeneous terrain: Comparisons of calculations and measurements, U. S. Department of Commerce, NTIA Report 79-20.

Wait, J. R (1974), Recent analytical investigations of electromagnetic ground wave propagation over inhomogeneous earth models, Proc. IEEE 62, No. 8, August, pp. 1061-1072.

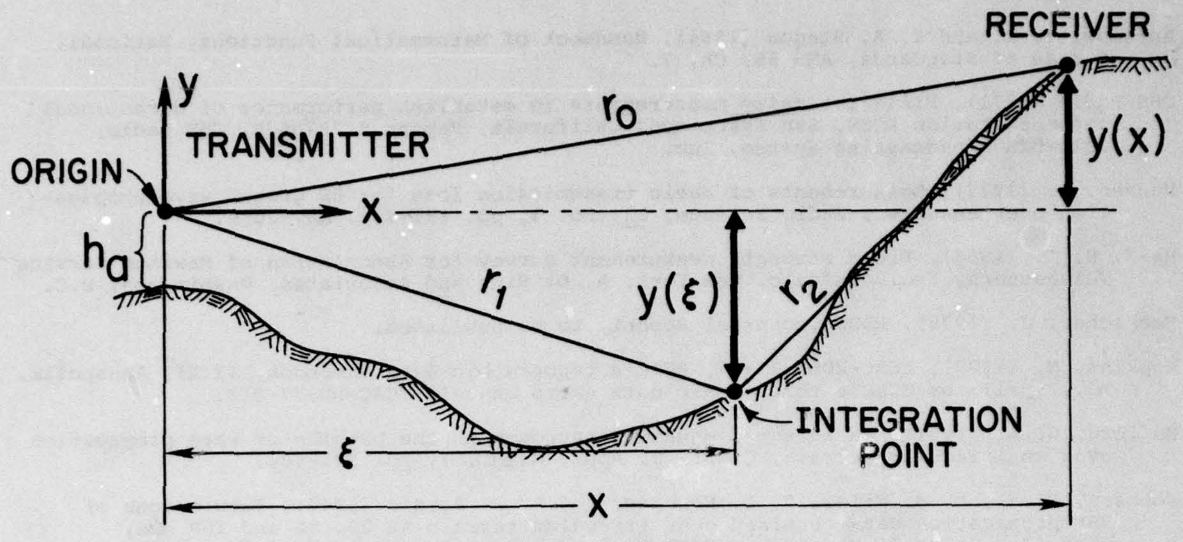

Figure 1. Great circle path geometry for integral equations.

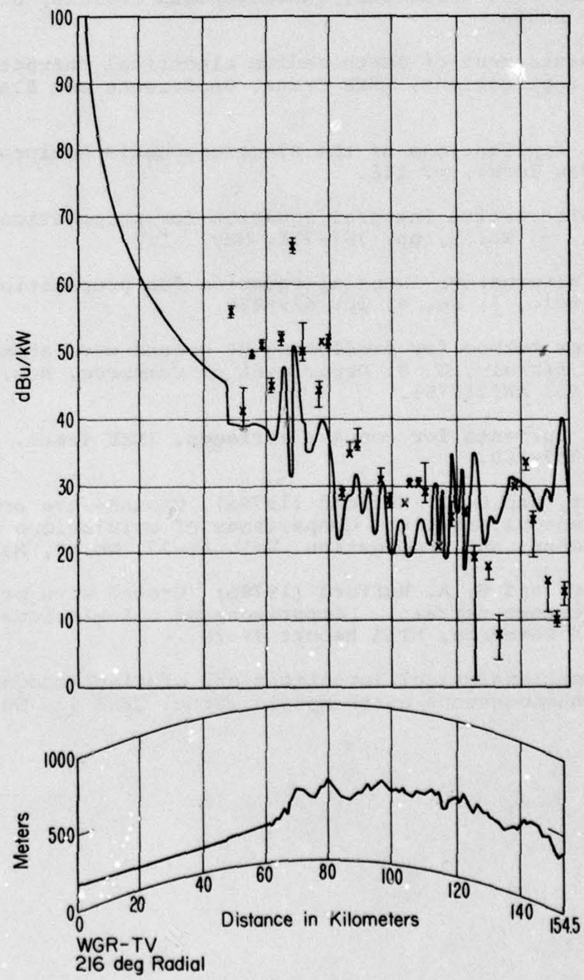

Figure 2. Path profile (lower portion) and received signal (in dB above 1 μV/m for 1 kW effective radiated power) for WGR-TV. Crosses denote measured spatial averages taken on 100 ft. mobile runs; circles denote "residue-height gain" predictions (see text). WGR antenna: 133 m above ground, 320 m above sea level.

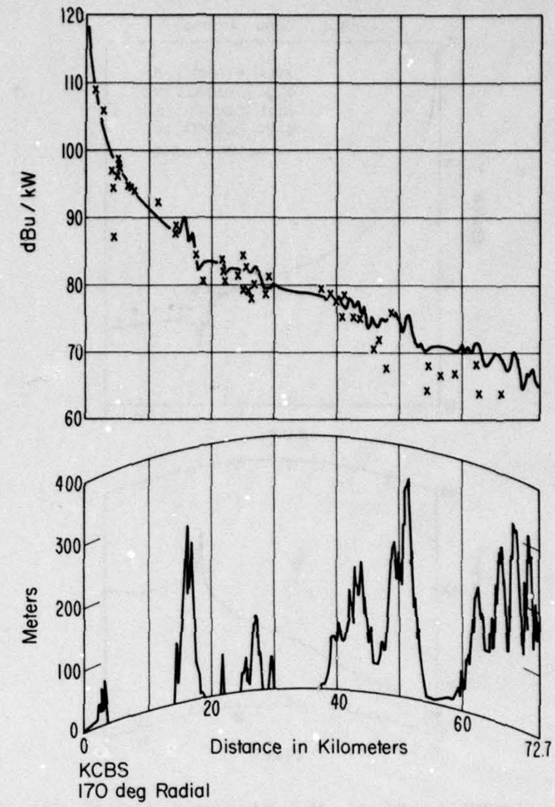

Figure 3. Path profile (lower portion) and received signal (in dB above 1 μV/m for 1 kW effective radiated power) for KCBS. Crosses denote measured medians.

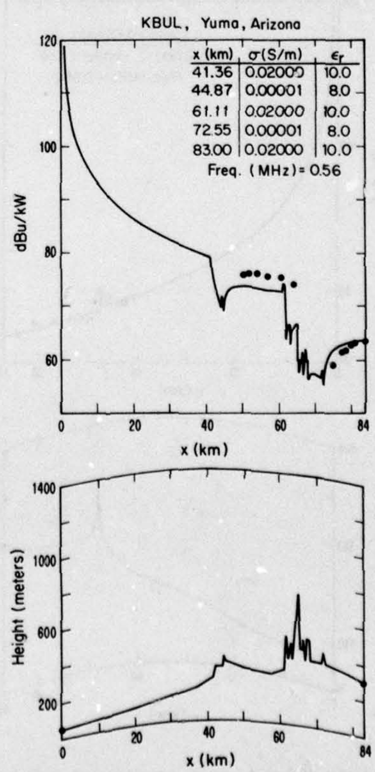

Figure 4. Path profile (lower portion) and received signal (in dB above 1 μV/m for 1 kW effective radiated power) for KBLU. Circles denote measured averages.

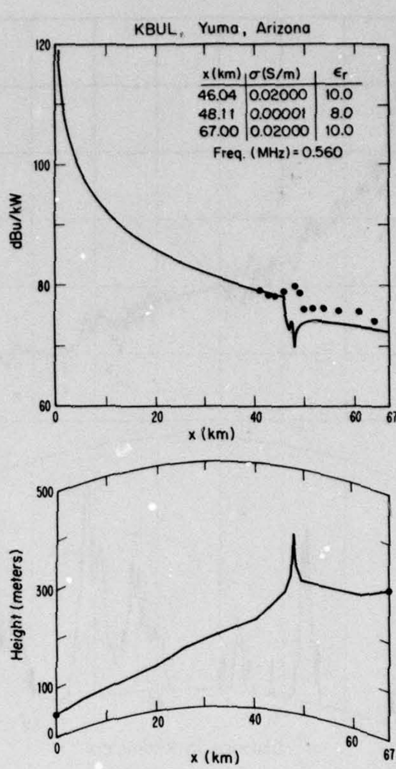

Figure 5. Path profile (lower portion) and received signal (in dB above 1 μV/m for 1 kW effective radiated power) for KBLU. Circles denote measured averages.

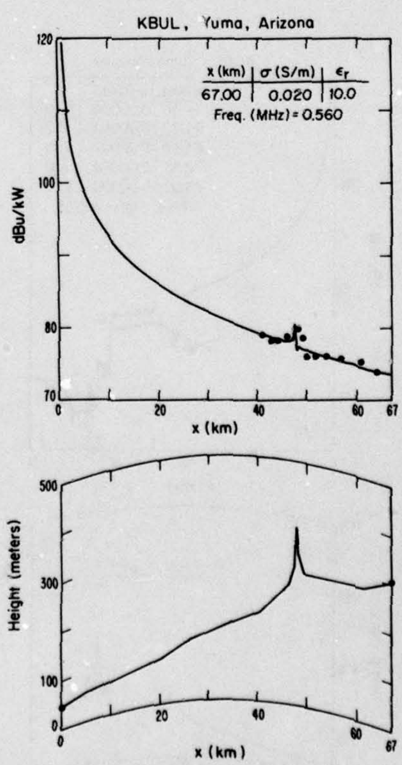

Figure 6. Path profile (lower portion) and received signal (in dB above 1 μV/m for 1 kW effective radiated power) for KBLU. Circles denote measured averages. Conductivity = 0.02/m for the entire path.

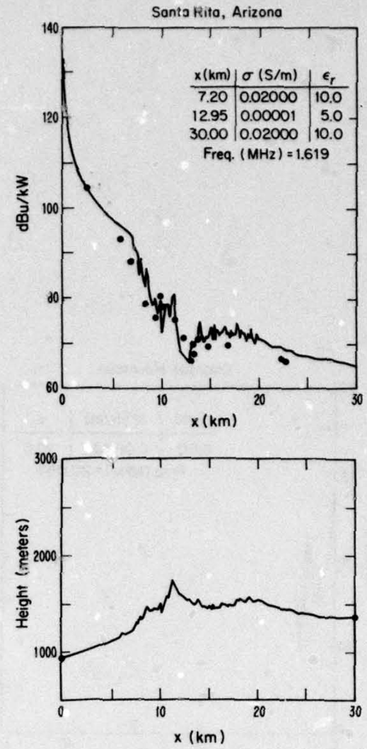

Figure 7. Path profile (lower portion) and received signal (in dB above 1 μV/m for 1 kW effective radiated power) for Santa Ritas, Arizona, path. Circles denote measured 2.5 min. averages. Frequency = 1.619. MHz.

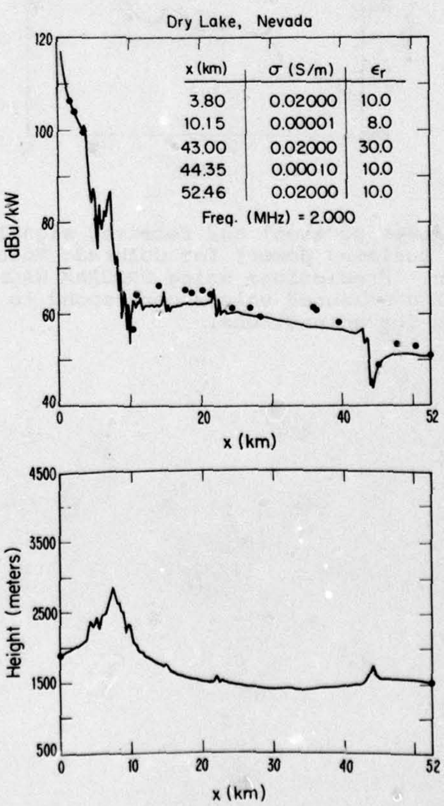

Figure 8. Path profile (lower portion) and received signal (in dB above 1 μV/m for 1 kW effective radiated power) for Dry Lake, Nevada, path. Circles denote measured 2.5 min. averages. Frequency = 2 MHz.

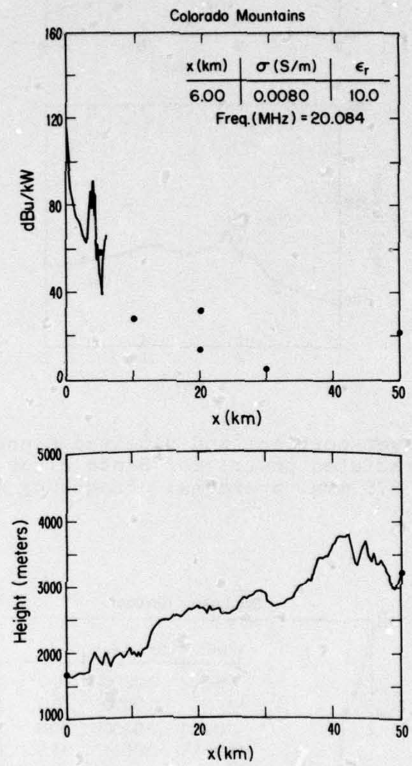

Figure 9. Path profile (lower portion) and received signal (in dB above 1 μV/m for 1 kW effective radiated power) for Colorado Mountain path. Circles denote measured median. Predictions using PROGRAM WAGNER, 100 m spacing intervals. At 20 km, the two measured values correspond to two sites close to the radial selected for comparisons.

AN EXPERIMENTAL STUDY OF SURFACE WAVE PROPAGATION ON A LOW PERMITTIVITY MEDIUM

J. Appel-Hansen, Electromagnetics Institute,
Technical University of Denmark, 2800 Lyngby, Denmark

R. J. King, Department of Electrical and Computer
Engineering, University of Wisconsin-Madison
Wisconsin 53706 USA

SUMMARY

It is experimentally shown that a surface wave having d^{-2} dependence can propagate on a medium having a dielectric constant near unity, when excited by a low-gain source near the interface. This occurs for both parallel and perpendicular polarization.

1. INTRODUCTION

It is well known that the familiar Sommerfeld attenuation function accurately describes ground-wave propagation over a medium having relative dielectric constant, ε_r, which is large in magnitude (e.g., earth). In this case the attenuation function asymptotically becomes $-1/2P$, provided $\arg P < 0$, with

$$P = \frac{-ikd\Delta^2}{2} \tag{1}$$

being the complex numerical distance [King and Wait, 1976]. The suppressed time factor is $\exp(i\omega t)$. Here, $k = 2\pi/\lambda$ where λ is the free-space wavelength, d is the distance and

$$\Delta = \frac{(\varepsilon_r - 1)^{\frac{1}{2}}}{\varepsilon_r} \tag{2}$$

is the surface impedance normalized by η_o $(=120\pi)$ for a grazing parallel (vertically) polarized plane above a homogeneous medium. When multiplied by the free-space spreading factor, the result is often referred to as the Norton surface wave; in the case of a dipole source near the surface, this spreading factor is d^{-1}, and so the Norton wave near the surface is seen to be proportional to $[k(d\Delta)^2]^{-1}$. It is dominant over the sum of the direct and surface-reflected waves at points near the surface as the latter two essentially cancel each other. Clearly, this wave behaves as d^{-2} and is enhanced by making $|\Delta|$ small. In the case of the earth, this is realized by having $|\varepsilon_r|$ large, as when the conduction current in the ground is much larger than the displacement current. Moreover, such a wave is only significant for parallel polarization.

But it has recently been shown [Wait, 1967; King and Wait, 1976] that, theoretically, exactly the same solutions apply when $\varepsilon_r \cong 1$, as this also makes $|\Delta|$ small as seen from (2). Furthermore, for perpendicular (horizontal) polarization the surface impedance in (1) can be replaced by the normalized grazing plane wave surface admittance,

$$\delta = [\varepsilon_r - 1]^{\frac{1}{2}} \tag{3}$$

and this too becomes small when $\varepsilon_r \cong 1$. In fact, if we let $\varepsilon_r = 1 + \chi$ where χ is the susceptibility, then

$$\Delta \cong \delta \cong \chi^{\frac{1}{2}} \tag{4}$$

for $|\chi| << 1$. This equivalence of Δ and δ for small $|\chi|$ leads to the conclusion that parallel and perpendicular polarized Norton waves propagate with essentially the same d^{-2} behavior, and this fact is supported in the experiments reported here.

Comment is in order regarding the limit as $\varepsilon_r \to 1$. In this case it can be shown that even though the Sommerfeld attenuation function approaches unity, its coefficient vanishes as does also the Fresnel reflected wave. Thus, the direct or free-space field is regained as expected.

In a related problem, a d^{-2} behavior has been observed for so-called lateral waves (up-over-and-down mode) propagating at HF in forested or vegitated environments [Tamir, 1967, 1977; Sachs and Wyatt, 1968; Wait, et al., 1974]. In this case the source and receiver points are <u>inside</u> the medium (forest), but when they approach the forest-air interface the lateral wave and the surface wave must become identical. There is considerable data to support the lateral wave theory, and this lends credibility to the hypothesis that a Norton surface wave can be guided by an interface having an ε_r near unity when the source is <u>outside</u> the medium. However, most of the lateral wave experimental data has been taken in large-scale, dense jungle environments. Thus, it is probably fair to say this data is more qualitative than quantitative. An exception is some data taken by Tamir [1970] who showed the existence of a lateral wave using a laboratory model at 25 GHz. Also, the coupling loss has proven to be an elusive factor [Wait, et al., 1974].

The purpose of the present experimental study is to demonstrate the existence of the Norton surface wave excited by a low-gain source situated above the air-dielectric interface, in a controlled laboratory environment.

2. EXPERIMENTAL SETUP

The experimental setup is shown in Fig. 1. The dielectric structure was built of eight polystyrene foam blocks 1 x 1 x 0.5 m^3 arranged in a two-layer row so that the maximum transmission

length was 4 m. This resulted in a dielectric structure having a height and width of 1 m each. In order to minimize extraneous reflections from surroundings, the structure was placed on dielectric floor panels in an anechoic chamber. The chamber is a 12 x 14 x 16 m^3 rectangular room lined with 2 m high pyramidal absorbers [Appel-Hansen, 1973]. Due to the size of the chamber relative to that of the dielectric structure, only part of the chamber is shown in the figure. Also, the dimensions of the absorbers are shown half-size.

Open-ended S-band waveguides were used as transmitting and receiving antennas at a test frequency of 3.00 GHz. The transmitting waveguide was placed at the end of the dielectric structure near a gate leading to a laboratory where the transmitter, receiver, positioning apparatus, and other auxiliary equipment were located. The lower edge of the transmitting waveguide rested on the upper edge of the foam dielectric structure. The polarization could be changed from vertical to horizontal simply by rotating the transmitting and receiving waveguides 90° about their longitudinal axes. A rolling cart, azimuth positioner and foam support normally used for antenna measurements, supported the receiving waveguide or probe. The cart was placed on rails in a pit so that the probe aperture could be slid longitudinally about 1 meter over the surface of the dielectric structure. Due to the probe's limited traverse and the size of the foam blocks, the field above the dielectric was first probed for a distance variation of 3 to 4 m. Then the two stacked blocks nearest to the transmitting antenna were removed, and the field was probed from 2 to 3 m, etc. The field could be probed in this manner over a propagation length which varied from 0 to 4 m in 1 m steps. For comparison, "free-space" propagation was also recorded by simply removing the eight foam blocks and using the same apparatus.

3. EXPERIMENTAL RESULTS

The measured field versus distance for both parallel and perpendicular polarizations is shown in Figs. 2 and 3, respectively. For parallel polarization the measured free-space curve was determined to have a d^{-1} variation which is very nearly equal to that of a vertical electric dipole positioned 4 cm $\pm$ 0.5 cm behind the actual waveguide aperture. This is denoted as the location of the "virtual source." Neither this location nor the effective dipole moment changed when the open-ended waveguide was placed on the foam, i.e., the field level very near the source was unchanged. Similarly, for perpendicular polarization the virtual source was found to be 3 cm $\pm$ 0.5 cm behind the actual aperture, and the effective dipole moment was unchanged with and without the foam. Thus, within measurement accuracy, the position of the virtual source is the same, about 3.5 cm, for both polarizations.

The insets show how the raw experimental data between 3 and 4 m was averaged. At these large ranges, the field is 30-40 dB down so it is comparable to extraneous reflections from edges of the foam structure and from the dielectric floor panels. These reflections are particularly noticeable in the perpendicular polarization case. This made averaging difficult, but the relative differences in level and in slope are still clearly discernable.

The relative slope of d^{-2} is also shown for comparison. The experimental data is seen to approach this slope near the maximum distance of 4 m, thereby strongly supporting the theory that a Norton wave can exist for both polarizations.

Further experimental investigations are underway, and these will be reported soon along with a full theoretical treatment. By comparing the theoretical and experimental data, it is hoped that ε_r can be determined. In fact, this could be a useful technique for measuring the dielectric constant in situ. From some previous reflectivity measurements of supports made from the same foam dielectric [Appel-Hansen and Solodukhov, 1979], it is believed that $\varepsilon_r \simeq 1.035$ for the experiments reported here.

Besides applications to propagation over vegetation and the measurement of dielectric constants, the presence of the surface wave may be important in the operation of radomes and in the interpretation of experiments using foam supports. In some cases, the theory may also apply to propagation in a layered troposphere or the ionosphere.

The able assistance of Povl Laugesen in carrying out these experiments is gratefully acknowledged. This work was sponsored by the NATO Research Grants Programme, Grant No. 1590.

4. REFERENCES

1. APPEL-HANSEN, J., 1973, "Reflectivity level of radio anechoic chambers", IEEE Trans. on Antennas and Propagation, AP-21(4), 490-498.
2. APPEL-HANSEN, J. and V. V. Solodukhov, 1979, "Echo width of foam supports used in scattering measurements", IEEE Trans. on Antennas and Propagation, AP-27(2), 191-193, March.
3. KING, R. J. and J. R. Wait, 1976, "Electromagnetic groundwave propagation - theory and experiment", Monograph in Symposia Mathematica, Vol. XVIII, Academic Press, 133-161.
4. SACHS, D. L. and P. J. Wyatt, 1968, "A conducting-slab model for electromagnetic propagation within a jungle medium", Radio Science, 3(2), 125-134.
5. TAMIR, T., 1967, "On radiowave propagation in forest environments", IEEE Trans. on Antennas and Propagation, AP-15(6), 806-817.
6. TAMIR, T., 1970, "Experimental verification of a lateral wave above a lossy interface", Electronics Letters, 6(12).
7. TAMIR, T., 1977, "Radio wave propagation along mixed paths in forest environments", IEEE Trans. on Antennas and Propagation, AP-25(4), 471-477.
8. WAIT, J. R., 1967, "Radiation from dipoles in an idealized jungle environment", Radio Science, 2(7), 747-750.

9. WAIT, J. R., R. H. Ott and T. Telfer, 1974, "Work shop on radio systems in forested and/or vegetated environments", Advanced Concepts Office, U.S. Army Communications Command, Technical Report ACC-ACO-1-74 (Available from the U.S. National Technical Information Service, Springfield, Va. AD-780712).

An abbreviated version of this paper has appeared as a correspondence in Electronics Letters, 15(4), 101-102, February 15, 1979.

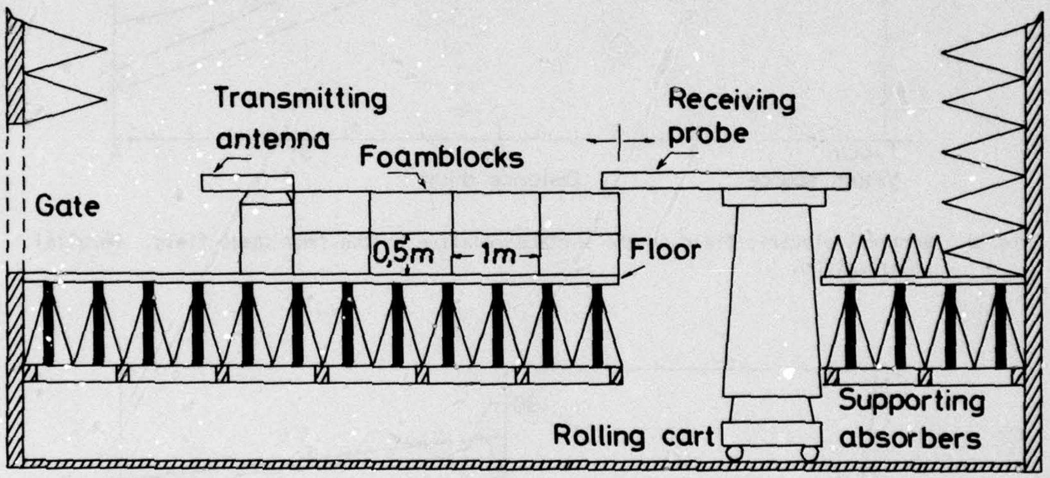

Fig. 1. Dielectric foam structure and apparatus for probing field on the surface.

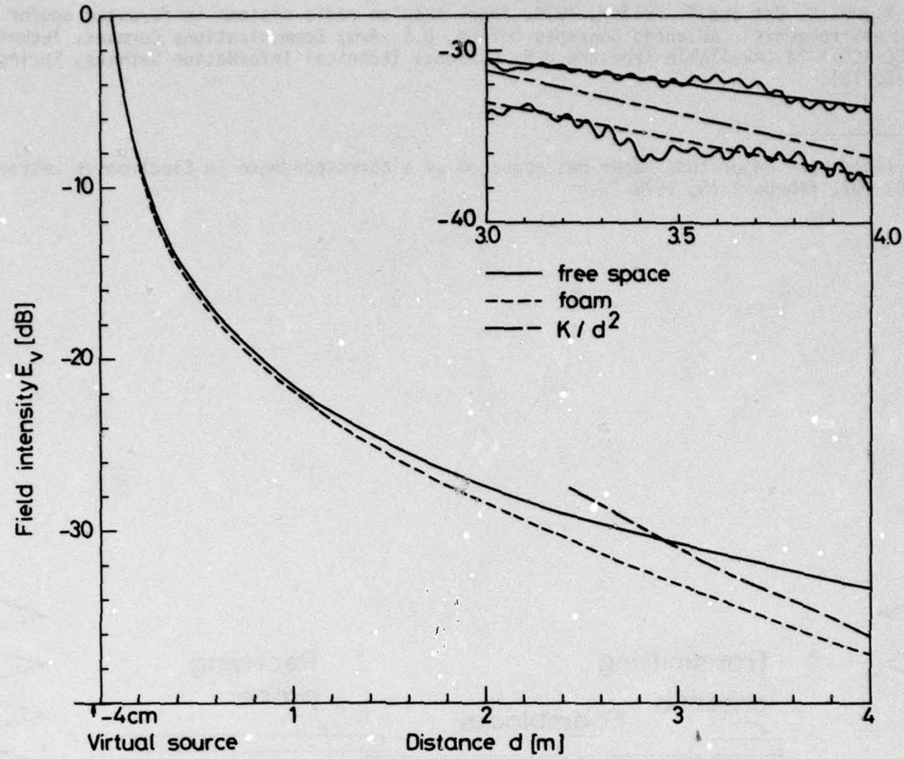

Fig. 2. Vertical electric field on the surface relative to the free-space field. Parallel polarization.

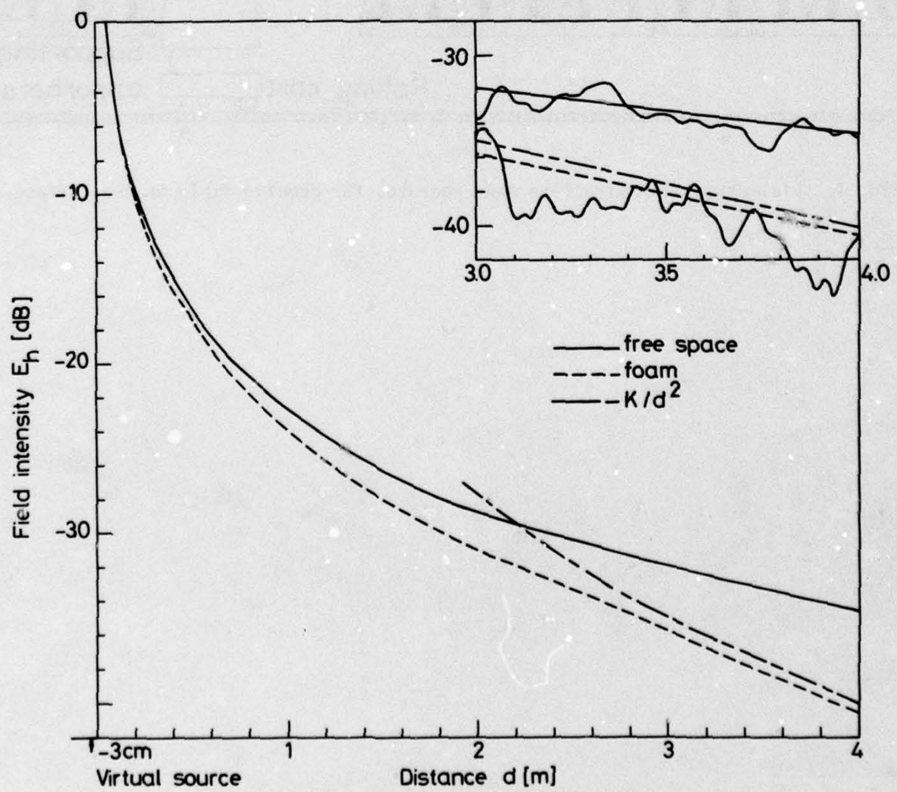

Fig. 3. Horizontal electric field on the surface relative to the free-space field. Perpendicular polarization.

MULTIPATH ANALYSIS OF ILS GLIDE PATH

T. Breien x)
Norsk Marconi AS
Ryensvingen 5
OSLO 6, Norway

SUMMARY

A major problem with Instrument Landing System (ILS) Glide Path is the dependence of the signal quality upon site conditions. Unwanted scattering from the surroundings causes error in the guidance signal. Computer performance analysis is of great interest because of the high cost of flight inspection. A new method to analyse the problem is described.

For practical use, it is very convenient to model the surroundings as a set of plane wedges. The scattering from each wedge is analysed using Uniform Theory of Diffraction (UTD), which assumes smooth, sharp and perfectly conducting wedges. Theoretical and practical work has been carried out to study the influence of finite conductivity, surface roughness and round edges on the scattered signal.
The conclusion is that for most Glide Path surroundings, UTD gives adequate accuracy.

An effective UTD computer program for analysis of Glide Path performance has been developed. Comparisons between computed and measured results show good agreement.

1. INTRODUCTION

A major problem with Instrument Landing System (ILS) Glide Path is the dependence of the signal quality upon site conditions. Reflections from the surroundings create multipath signals which cause guidance errors.

ILS Glide Path is an approach and landing aid which determines the descent angle of the aircraft. The signal transmitted from the ground station is a horizontal polarized 330 MHz carrier, amplitude modulated by 90 Hz and 150 Hz tones. The modulation index of each tone varies with the elevation angle. The difference in modulation indices (DDM) gives the elevation angle. Scattering from the terrain may result in unacceptable deviation in DDM.

Several Glide Path antenna types exist, with different influence of the surroundings on the system performance. In all cases the siting of the antenna system is critical.

Installation cost of a Glide Path antenna system is high. Flight trials of a system are very expensive, about $ 20.000. Therefore it is important to select the optimum antenna system and siting with the minimum of effort. This paper describes a new method to analyse the problem by computer.

A multipath analysis of a Glide Path system involves development of a geometrical model of the surroundings and then computing the effect of the multipath signals on the guidance accuracy. Several such computer programs are well known, but suffer from either the demand of large computer resources or unconfirmed accuracy.

2. GEOMETRICAL MODELS

To calculate the scattering from the surroundings, a geometrical model has to be developed. The scattering from curved surfaces is more complicated to calculate than from plane surfaces. Therefore, the surroundings should be modelled as a set of plane surfaces. The calculation is further simplified by bounding the surfaces by straight edges.

To establish the best manner to subdivide the surroundings in a set of plane wedges, the effect of deviation from the geometrical model must be studied. The deviations of interest are surface roughness, radius of curvature and conductivity.

The effect of roughness is a reduction of the coherent and an increase of the incoherent scattered signals. The airport terrain is usually smooth in relation to the ILS Glide Path signal wavelenght (1 metre approximately) so coherent scattering dominates. The effect of surface roughness on the coherent signal will be discussed later.

The finite conductivity of the ground results in a reduction of the scattered signal. The conductivity of different types of grounds should be included in the mathematical model used.

3. DISCUSSION OF MATHEMATICAL METHODS

There exist several mathematical methods to calculate the scattering from perfectly conducting wedges, but very few of them can easily be extended to include finite conductivity and roughness. The mathematical methods of interest are given in Table 1.

x) Formerly with ELAB, The Norwegian Institute of Technology, N - 7034 TRONDHEIM-NTH, Norway

Mathematical method	Reference
Physical Optics (PO)	Classical
Physical Theory of Diffraction (PTD)	UFIMTSEV, P.YA., 1962
Uniform Geometrical Theory of Diffraction (UTD)	KOUYOUMIJIAN, R.G., PATHAK, P.B., 1974
Uniform Asymptotic Theory of Diffraction (UAT)	LEWIS, R.M., BOERSMA, J., 1969

Table 1. Mathematical methods to calculate the scattering from a perfectly conducting wedge

PTD is an improvement of PO by introducing a correcting surface current which takes care of the deviation of the surface from an infinite plane.

UTD and UAT are refinements of Geometrical Theory of Diffraction (GTD). GTD is an extension of Geometrical Optics (GO) by introducing edge diffracted rays in addition to the reflected rays. The diffracted rays are easily calculated by a simple diffraction coefficient, $D_0(\varphi)$. The main problem with GTD is that the diffraction coefficient is not valid near the shadow and reflection boundaries due to singularities at the boundaries. UTD and UAT avoid this weakness by different methods: UTD by using another mathematical method to calculate the diffraction coefficient, while for UAT the formulation of the reflected ray is modified to include singularities which cancell the diffraction coefficient ones.

An attempt to weigh the advantages of the four methods is shown in Table 2.

Properties	PO	PTD	UTD	UAT
Applications	1	4	2	2
Simple formulation of the problem	1	3	2	2
Accuracy	2	1	1	1
Computer resources	4	4	2	2
Often used method	1	4	2	3

Key
1: Best
4: Worst

Table 2. Advantages of the mathematical methods for ILS Glide Path applications

As seen from the table, PTD is very little attractive due to the limited application, complicated mathematical formulation of the problem and the large computer resources required. PO is also deleted in the evaluation because of the larger computer resources required, a serious drawback, and its somewhat limited accuracy.

To select the most convenient method, the ability to include finite conductivity should be studied. Finite conductivity can be substituted by a surface impedance. For a scattering object with a relative permittivity equal $\hat{\varepsilon}_r$ and an angle φ' of incident of the electrical field, the surface impedance for horizontal and vertical polarized fields are

$$Z^h = \frac{Z_0}{\sqrt{\hat{\varepsilon}_r - \cos^2\varphi'}} \qquad Z^v = \frac{Z_0}{\hat{\varepsilon}_r}\sqrt{\hat{\varepsilon}_r - \cos^2\varphi'}$$

The scattering from an impedance wedge is discussed by several authors. The basic study is by MALIUZHINETS G.D., 1958. His asymptotic solution for the edge diffracted fields is non-uniform, giving singularities at the optical boundaries like GTD. Based on this work, JAMES, G.L., 1977 has derived a uniform solution which is quite easy to modify to the standard formulation of UTD, called ZUTD.

The diffraction coefficient for horizontal and vertical polarization is (Figure 1)

$$D_{h,v}(\varphi) = \frac{-e^{-j\pi/4}}{2n\sqrt{2\pi k}} \cdot \frac{1}{\Psi_{h,v}(\varphi')} \Big\{ \Psi_{h,v}(\varphi+\pi)\Big[\cot an\frac{\pi+\beta^i}{2n}\cdot G[kLa^+(\beta^i)] - \cot an\frac{\pi+\beta^r}{2n}\cdot G[kLa^+(\beta^r)]\Big]$$

$$+ \Psi_{h,v}(\varphi-\pi)\Big[\cot an\frac{\pi-\beta^i}{2n}\cdot G[kLa^-(\beta^i)] - \cot an\frac{\pi-\beta^r}{2n}\cdot G[kLa^-(\beta^r)]\Big]\Big\}$$

where

$$\Psi_{h,v}(\alpha) = M(-\alpha + \pi/2 - \theta_B^{h,v}) \cdot M(-\alpha - \pi/2 + \theta_B^{h,v}) \cdot M(-\alpha + n\pi - \pi/2 + \theta_A^{h,v}) \cdot M(-\alpha + n\pi + \pi/2 - \theta_A^{h,v})$$

$$M(\alpha) = \prod_{n'=1}^{\infty} \prod_{m=1}^{\infty} \left[1 - \left(\frac{\alpha}{n'\pi(2n'-1) + \frac{\pi}{2}(2m-1)}\right)^2\right]^{(-1)^{m+1}}$$

$$\theta^h = \arcsin(Z_0/Z^h), \qquad \theta^v = \arcsin(Z^v/Z_0)$$

$$L = \frac{r' r''}{r' + r''}, \quad a^{\pm} = 1 + \cos(2nN^{\pm}\pi - \beta), \quad \beta^i = \varphi - \varphi', \quad \beta^r = \varphi + \varphi'$$

No extension of UAT to include a surface impedance is known. Consequently, UTD including ZUTD is chosen as the most convenient mathematic method for multipath analysis of ILS Glide Path.

Applications of ZUTD have shown that the inclusion of the finite conductivity of the terrain require large computer resources compared to UTD. Therefore, it is of importance to study in which applications ZUTD can be substituted by UTD to give a satisfactory accuracy.

Figure 2 shows the electrical field around a straight wedge of different materials computed by using ZUTD. An important result is correlation between Fresnels reflection coefficient R (φ) and the diffraction coefficient D (φ), shown in Figure 3. This figure shows that for many applications adequately accurate results can be obtained by using UTD, and if necessary multiplying D_0 (φ) by R (φ).

4. THE ROLE OF THE SCATTERING OBJECT'S DEVIATION FROM THE GEOMETRICAL MODEL

The terrain should be modelled as a set of wedges with surface impedance. The effects of different types of deviation from this simple model will be discussed.
Three types of deviation from the geometrical model are of interest: Rough surface, rough edge and a round edge.

For a small roughness compared to the wavelength, it is shown (SENIOR, T.B.A., 1960) that the effect on the scattered coherent signal can be substituted by a surface impedance. Hence knowing the roughness it is possible by using ZUTD to find the effect of a small surface roughness on the scattered signal from the wedge. The corresponding $\hat{\varepsilon}$ is very high, and according to the findings of ZUTD the influence of the roughness is negligible.

For roughness of the same magnitude as the wavelength, no theoretical method is known to calculate the effect on the wedge scattered signal, nor for rough edges. Therefore, some measurements on scales down models have been carried out.

Figure 4 shows the equipment arrangement for a perfect wedge. The surface roughness was modelled by crumpling an aluminium foil which was fastened to the wedge. Figure 5 shows the recorded horizontal polarized electrical field for a surface roughness of $\Delta h \approx 0.25\lambda$. The interesting result was that the behaviour of the diffracted field was the same as if the wedge was smooth with a surface impedance. This implies that the qualitative result for small-scale roughness (SENIOR, T.B.A., 1960) can be extended to include roughness of the order of the wavelength.

The influence of a rough edge was studied separately. The remarkable result was that even for a very rough edge ($\Delta h \approx \lambda$), no effect on the scattered field could be observed.

The effect of a round edge is also of a great interest for practical applications of UTD. Several experiments were carried out, but no effect on the scattered signal could be recorded, not even for a radius of curvature equal to 7λ.

5. SUMMARY OF REQUIREMENTS ON THE SURROUNDINGS TO APPLY UTD/ZUTD

Practical experience with ILS Glide Path and computer analysis show that the surroundings within 2 km and rising terrain in the approach sector mainly affect the performance. It is sufficient to model these parts of the surroundings and if possible, apply UTD/ZUTD.

To use UTD/ZUTD, the requirements on the surroundings are:

- The dimensions of each part of the surroundings modelled as a side of a wedge must be much larger than the wavelength (λ)
- Edges in the topography can be modelled as a sharp edge if the radius of curvature is less than about 7λ and the roughness Δh less than about λ.
- The surface roughness Δh must be less than 0.25λ if the edge diffracted field is of significance, else it should satisfy (BECKMANN, P., SPIZZICHINO, A., 1963) $\Delta h \leq \lambda / 12 \sin\varphi$
- The surroundings should be homogenious down to at least the penetration depth

By studying the terrain for several ILS Glide Path sites, it is concluded that for nearly all sites, the surroundings satisfy requirements and UTD/ZUTD can be used.

6. ILS GLIDE PATH COMPUTER PROGRAMS

Experience with use of UTD computer programs has shown that considerable computer resources can be saved if the geometrical models of the surroundings can be restricted to a few different types. An obvious disadvantage is that not all sites can be analyzed by such a tailored computer program. Figure 6 shows the geometrical models used for this program (BREIEN, T., 1979).

For those sites which diverse from the common ones, a very flexible computer program has been developed. No restrictions are laid on the geometrical model of the terrain. The price is a much more complicated program structure. This program can be used on all sorts of multipath analysis, not only for ILS Glide Path (BREIEN, T., VIK, K.L., 1979).

The effect of a finite conductivity is not included in these programs. The findings of the analysis of this effect on the scattered field given in section 3 are qualitatively applied on the computed results. For most of the multipath analysis this effect is of minor importance. The reason can be either wet ground or a very grazing incident field, both resulting in a Fresnels reflection coefficient near unity for horizontal polarized field.

7. MULTIPATH ANALYSIS OF VAGAR AND MOLDE ILS GLIDE PATH

The computer program, restricted to a few typical geometrical models of the surroundings, was run for several ILS Glide Path facilities to predict performance or investigate unexpected results. To show the correspondence between computed and measured performance, the results from Vagar and Molde ILS Glide Path will be discussed.

Figure 7 shows the Glide Path antenna at a test site and the surroundings at Vagar Airport, Faroe Islands. The antenna is 13 m high and consists of 13 elements arranged in a vertical array. The low radiation towards the ground minimizes the extent of the necessary reflecting surface to establish the glide path guidance signal. It is sufficient to model only the first 200 m of the terrain.

The antenna is sited on a 25 m long plain, at the end there is an edge where the terrain slopes down to the fjord. During the flight trials the ground was very wet and covered with a thin layer of snow. Therefore the terrain can be modelled with satisfactory accuracy as perfectly conducting.

The terrain also satisfies the roughness criteria given in section 5 for modelling as a set of plane surfaces. Figure 8 shows the terrain profile together with the geometrical model. The slope of the terrain varies with the azimuth angle as indicated.

The performance of the ILS Glide Path was analyzed for level flights at 1500 feet. Figure 9 shows the computed DDM as a function of the elevation angle for three different azimuth angles (α is varied). The large deviations from the correct DDM are due to diffraction from the edge and reflections from the sloping terrain. The DDM as measured by a flight inspection aircraft is also shown. The deviations from correct DDM are of the same order as computed, and the large difference between the computed results obtained for different azimuth angles are confirmed by the measurements. The disagreement between measured and computed results for a specific azimuth angle can be explained by the high sensivity to the slope of the terrain.

The computer program has also been used at Molde Airport, Norway, with great success. Prior to test at a Glide Path with a Sideband Reference Antenna system a multipath analysis was performed to indicate the expected guidance quality.

In contrast to the 13 m array antenna the Sideband Reference Antenna system assumes the ground to be a perfect reflecting surface. The interference between the directly radiated and reflected signals gives the guidance information (DDM). Experience has shown that the reflecting surface should be plane out to at least 300 m.
Figure 10 shows the surroundings of interest. At Molde Airport the plane reflecting surface is rather short (210 m) and the terrain drops sharply into the sea. Due to the tide, the sea level varies between 0.9 m and 3.5 m under the reflecting surface. The surface and edge roughness satisfy the requirements of section 5, the geometrical model is given in the figure.

Figure 11 shows the computed results and those obtained later by a flight calibration aircraft. The correspondence is very good, mainly a result of the suitability for modelling of the surroundings.

8. CONCLUSIONS

Several mathematical methods to calculate the scattering from the surroundings of ILS Glide Path facilities have been studied. Uniform Theory of Diffraction (UTD) is used because of the small computer resources required and the possibility to extend UTD to include finite conductivity of the surroundings, ZUTD. The surroundings are modelled as a set of plane, smooth wedges.

The influence of non-perfect geometry and roughness of the wedges is studied by measurements on scaled-down models. The degree of surface roughness is rather critical for the reflected and diffracted signal. The roughness has the same effect on the diffracted signal as a surface impedance. A surprising result is that the shape of the edge (straightness and radius of curvature) has minimal influence on the diffracted signal. This result favours using UTD on real surroundings which definitely are not a set of perfect wedges.

A UTD computer program designed for ILS Glide Path has been developed. The program is approximately 30 times more efficient than those based on Physical Optics. Comparisons between computed results and flight recordings show a very good agreement for the sites studied. By using the computer program, expensive flight inspection measurements can be reduced.

REFERENCES

BECKMANN, P., SPIZZICHINO, A., 1963 — "The Scattering of Waves from Rough Surfaces", Pergamon Press.

BREIEN, T., 1979 — "Multipath Analysis of ILS Glide Path", ELAB. Report STF 44 A79100 (In Norwegian).

BREIEN, T., VIK, K.L., 1979 — "GTD Computer Analysis of Scattering of Electromagnetic Waves", ELAB Report STF 44 A79129 (In Norwegian).

JAMES, G.L., 1977 — "Uniform Diffraction Coefficient for an Impedance Wedge", Electronic Letters, pp. 403-404.

KOUYOUMJIAN, R.G., PATHAK, P.B., 1974 — "A Unifrom Geometrical Theory of Diffraction for an Edge in a Perfectly Conducting Surface", IEE Proceedings, pp. 1448-1461.

LEWIS, R.M., BOERSMA, J., 1969 — "Uniform Asymptotic Theory of Edge Diffraction", J. Math Phys, pp. 2291 - 2305.

MALIUZHINETS, G.D., 1958 — "Exitation, Reflection and Emission of Surface Waves from a Wedge with given Face Impedances", Sov. Phys. Dokl., pp. 752-755

SENIOR T.B.A., 1960 — "Impedance Boundary Conditions for Statistically Rough Surfaces", Appl. Sci. Res., Section B, pp. 437-468.

UFIMTSEV, R.YA., 1962 — "Method of Edge Waves in the Physical Theory of Diffraction", U.S. Airforce Foreign Technology Div., Wright Patterson AFB, Ohio, USA.

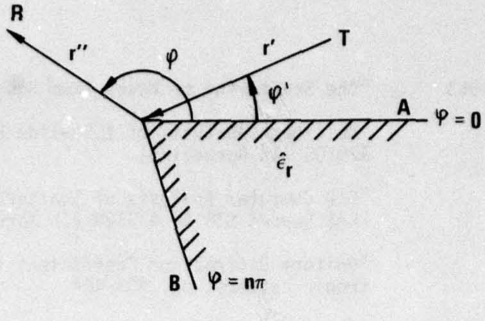

Figure 1 Wedge with a finite conductivity

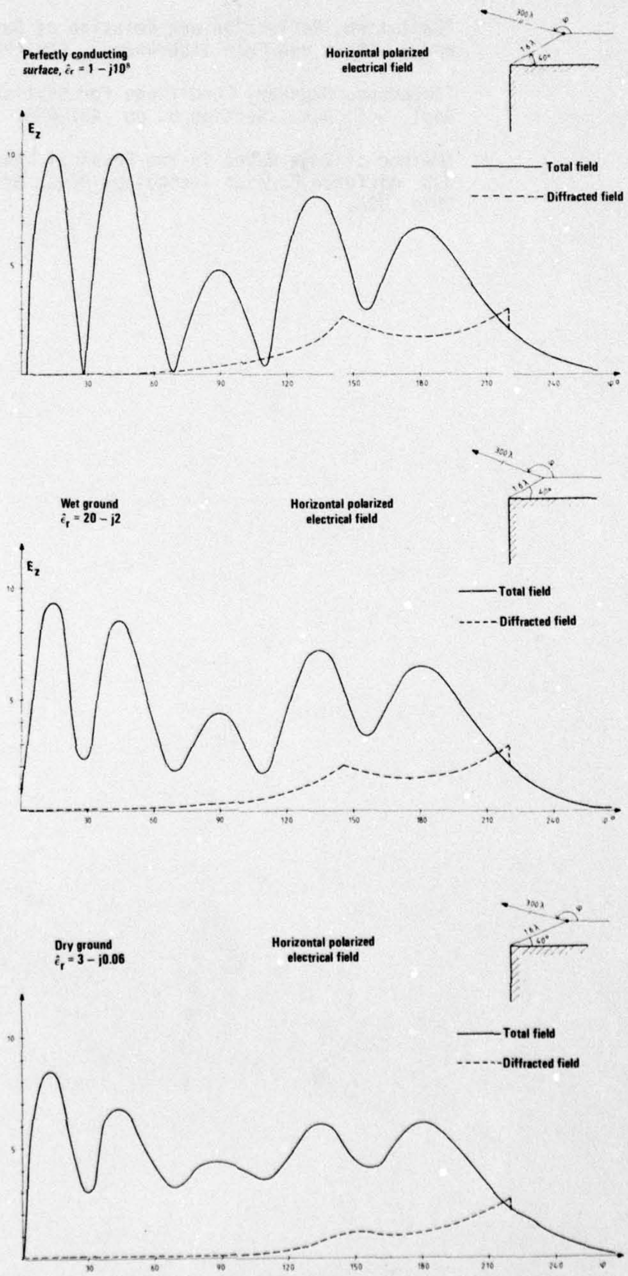

Figure 2 Horizontal polarized electrical field around a 90° wedge
a) Perfectly conducting surface
b) Wet ground
c) Dry ground

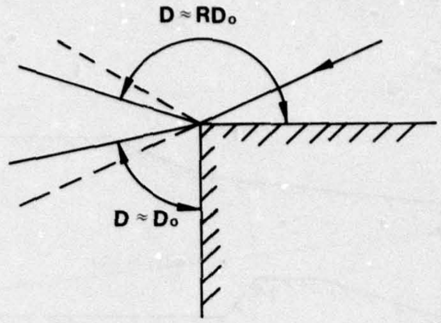

Figure 3 Correlation between Fresnels reflection coefficient R (φ) and diffraction coefficient D (φ) for horizontal polarization.

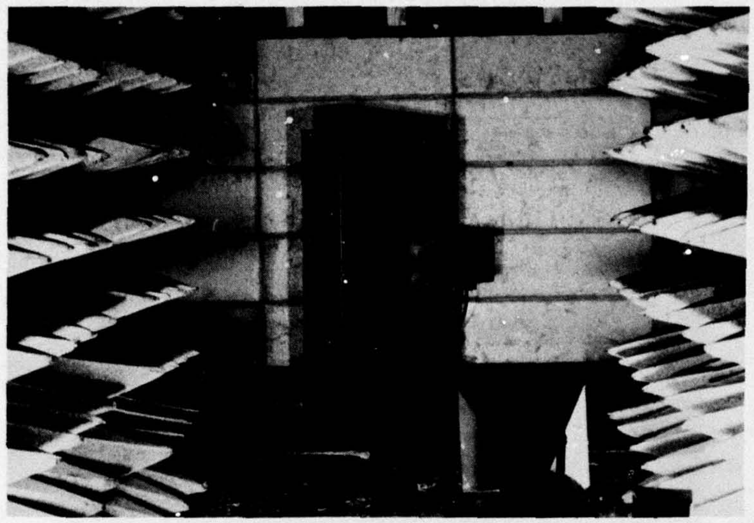

Figure 4 Equipment arrangement for measuring the effect of non-perfect wedges.

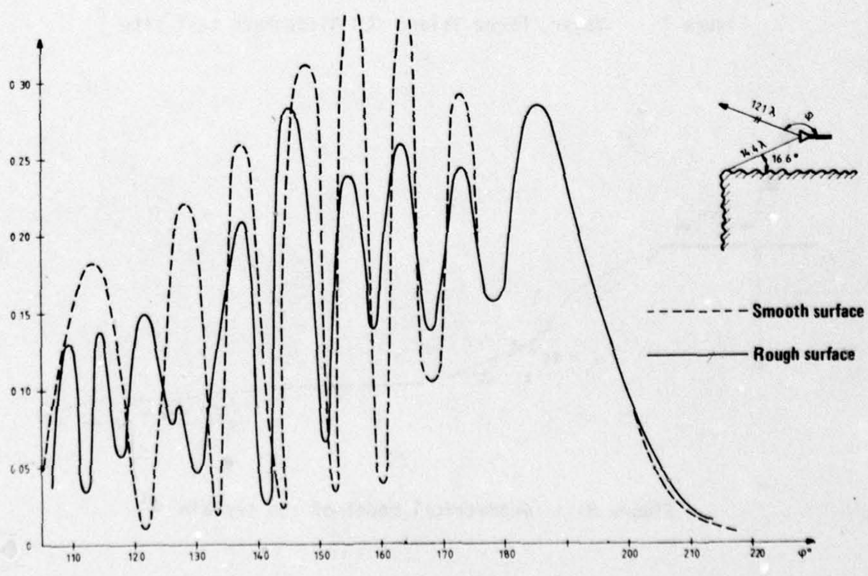

Figure 5 Measured horizontal polarized electrical field around a wedge with a surface roughness

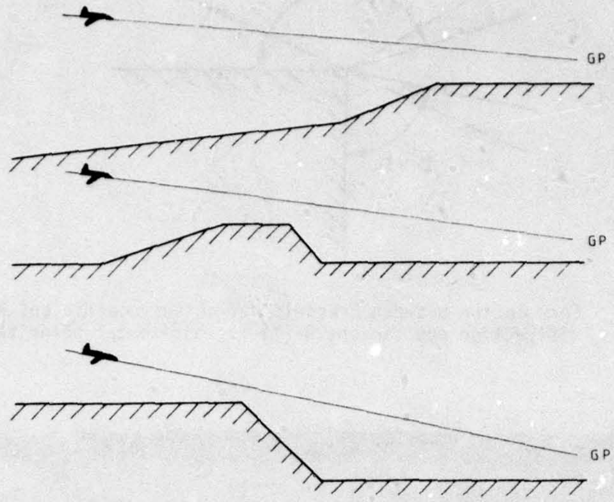

Figure 6 Geometrical models used for ILS Glide Path analysis

Figure 7 Vagar, Faroe Island ILS Glide Path test site

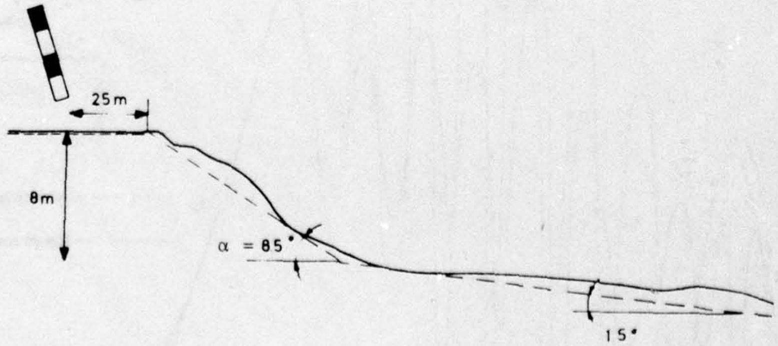

Figure 8 Geometrical model of the terrain

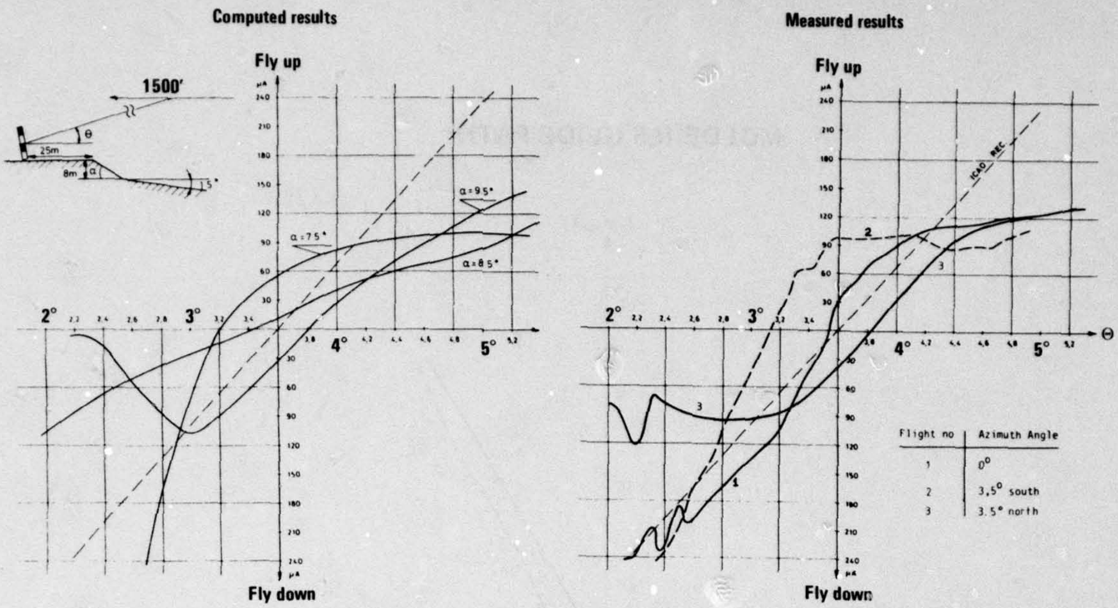

Figure 9 Computed and measured results of Vagar ILS Glide Path test site

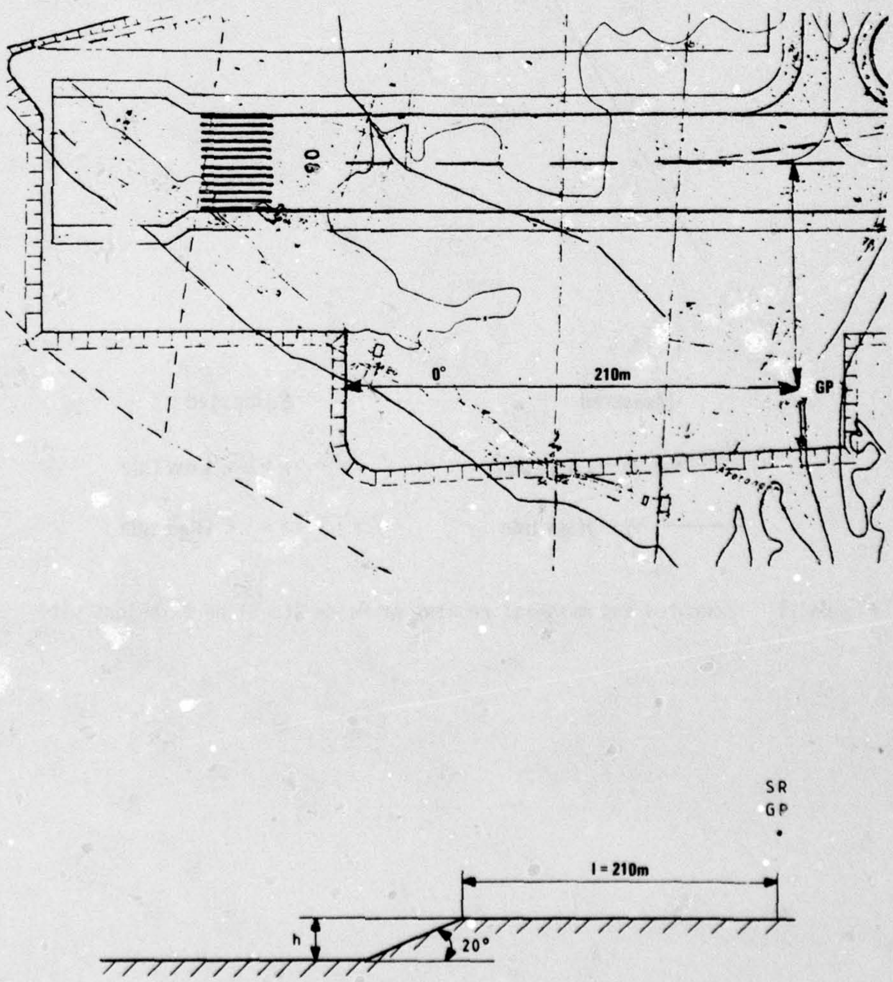

Figure 10 Molde ILS Glide Path test site and geometrical model used

MOLDE ILS GLIDE PATH

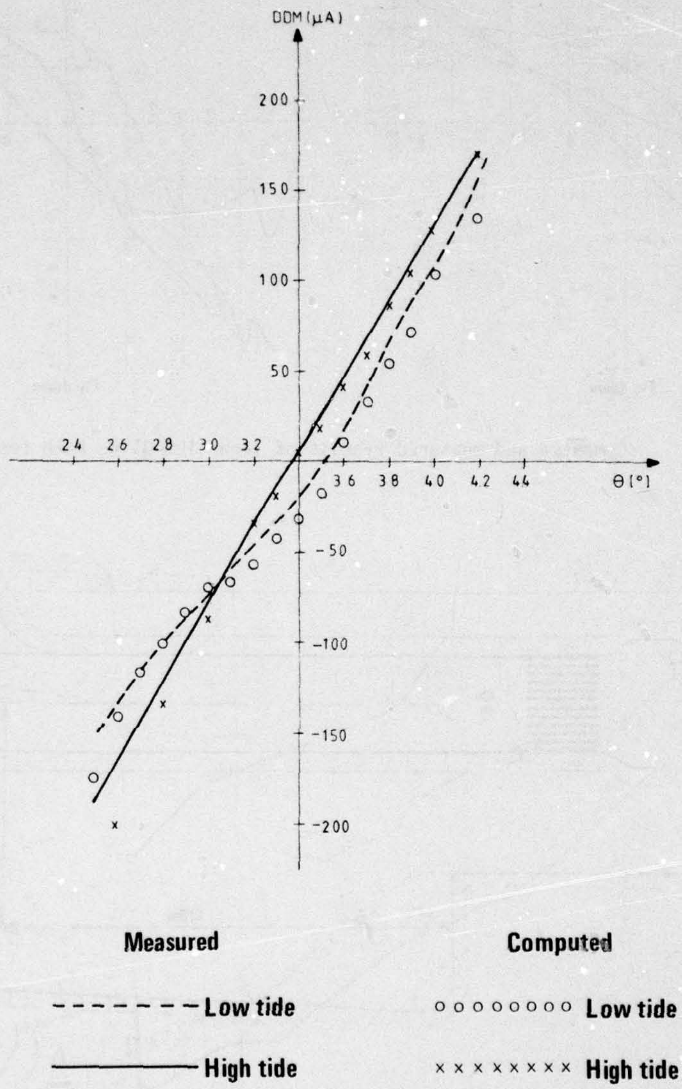

Figure 11 Computed and measured results of Molde ILS Glide Path test site

AIRBORNE MEASUREMENTS OF ELECTROMAGNETIC WAVE REFLECTIONS FROM LAND AND SEA WATER

Allen L. Johnson
U. S. Air Force Avionics Laboratory
Wright-Patterson AFB, Ohio

SUMMARY

Multipath fading caused by terrain reflections can disrupt an airborne communication or navigation system. The severity of the multipath is dependent upon the antenna illumination factor, surface reflection coefficient, and the divergence of the reflected signal. Airborne measurements have verified that severe multipath is regularly encountered over water when the aircraft is communicating with a satellite at a low elevation angle. Techniques which can reduce the multipath fading effect include the use of directive antennas, circular polarization and diversity techniques.

1. INTRODUCTION

The reflection of electromagnetic waves from the terrain can cause interference in the form of multipath fading, which can severely disrupt an airborne communication or naviagation system. The basic problem explored in this paper is the development of the theoretical and measured multipath fading characteristics of a satellite-to-aircraft communication/navigation system and suggested techniques for improving system performance.

2. MULTIPATH MODEL

The multipath model which is proposed consists of a direct component and two reflective components, a specular and a diffuse, Figure 1. The severity of the effect of multipath fading is dependent upon the antenna pattern, the reflection coefficient, and the curvature of the reflecting surface. The depth of multipath fading is given by (Franklin, S. B.., 1971):

$$\text{Fade depth in db} = 20 \log (1 - K^2 |R| D)$$

where K^2 is the antenna illumination factor (ratio of antenna gain in direction of reflection to gain in direction of direct path); R is the reflection coefficient of the reflecting surface; and D is the divergence factor for the spreading from the curved earth.

2.1 Antenna Illumination Factor

The antenna pattern, or antenna illumination factor, has a major influence on the multipath severity. Three types of antennas are illustrated in Figure 2. The first is a blade type antenna which has a horizon coverage pattern. The horizon coverage pattern tends to illuminate the reflecting surface and generally results in a large illumination factor.

The antenna illumination factor is dependent upon the azimuth direction. Any real antenna mounted on an aircraft has nulls and peaks in its pattern, and the gain toward the satellite or toward the reflecting surface varies with the aircraft heading. The average illumination factor, K^2, from a measured blade antenna pattern on an aircraft is given in Table I. A range of K^2 for the best and worst case aircraft directions is given in Table II.

The overhead antenna pattern characteristics of a cross-dipole antenna give considerable protection to the multipath reflective component when the satellite is at a high elevation angle. This discrimination results in a low antenna illumination factor, Table I.

A third antenna type is a directive antenna primarily used at the microwave frequencies. The directive antenna, again, gives good protection against the reflected signal unless the satellite is right on the horizon, Table I.

TABLE I: Antenna Illumination Factor (K^2) for Various Antennas*
(For Aircraft at 30,000 Ft.)

ELEVATION ANGLE	AVERAGE HORIZON ANTENNA	AVERAGE OMNI ANTENNA	AVERAGE OVERHEAD ANTENNA	AVERAGE DIRECTIONAL ANTENNA
90°	.18	.10	.026	.003
80°	.14	.10	.026	.003
70°	.14	.10	.032	.003
60°	.14	.10	.032	.003
50°	.14	.14	.032	.003
40°	.18	.18	.04	.01
30°	.22	.32	.05	.02
20°	.50	.56	.08	.03
10°	.71	.71	.20	.10
0°	.94	.94	.89	.16
-3°	1.00	1.00	1.00	1.00

*from Burnside, W. D. et al 1973
Clanton, S., 1974
Maroth, V., 1963

TABLE II: Antenna Illumination Factor Variances (K^2)*
(For Aircraft at 30,000 ft.)
Typical Horizon Coverage Antenna

ELEVATION ANGLE	MINIMUM K^2	AVERAGE K^2	MAXIMUM K^2
90°	.10	.18	1.00
80°	.10	.14	.79
70°	.03	.14	.56
60°	.03	.14	.31
50°	.03	.14	.56
40°	.03	.18	.56
30°	.03	.22	.79
20°	.03	.50	.79
10°	.10	.71	.89
0°	.89	.94	1.00
-3°	1.00	1.00	1.00

*from Clanton, S., 1974

2.2 Reflection Coefficient

The reflection coefficient used in the preceding equation is a combination of the basic reflection coefficient of the surface multiplied by the specular, or diffuse, reflection coefficient. The basic reflection coefficient is dependent upon the type of reflecting surface, the polarization of the reflected wave, the elevation angle of the reflection and frequency.

For a horizontally polarized incident wave, the reflection coefficient is given by (Reed and Russell, 1964):

$$R_h = \frac{\sin\psi - \sqrt{n^2 - \cos^2\psi}}{\sin\psi + \sqrt{n^2 - \cos^2\psi}}$$

where n^2 is a complex reflectivity factor $= \varepsilon_r - j\,\dfrac{18000\,\sigma}{f_c}$

ψ is the grazing angle shown in Figure 3

ε_r is the relative dielectric constant

σ is the conductivity in mhos/meter

f_c is the carrier frequency in MHz

Neither the amplitude nor phase of the horizontal reflection coefficient is very sensitive to the physical surface constants nor frequency, Figure 4. Typical values of the physical constants for various types surfaces are given in Table III.

TABLE III: Physical Properties of Various Reflecting Surfaces*

SURFACE TYPE	PERMEABILITY μ	DIELECTRIC ε_r	CONDUCTIVITY σ
Free space	$1.257 \times 10^{-6} = \mu_v$ Henry/meter	$8.855 \times 10^{-12} = \varepsilon_v$ Farad/meter	mho/meter
Distilled Water		78	1×10^{-5}
Fresh water		80	8×10^{-3}
Sea water		80	5
Ice (fresh water)		3	2×10^{-4}
Dry, sandy, flat coastal land (dry earth)		5	1×10^{-4}
Marshy, forested, flat land (wet earth)		30	1×10^{-2}
Farmland -- low hills		15	1×10^{-2}
Pastoral land, medium hills		13	5×10^{-3}
Rocky land, steep hills		10	2×10^{-3}
Mountainous		5	1×10^{-3}
City, residential area		5	2×10^{-3}
City, industrial area		3	1×10^{-1}

*from Kerr, D. E., 1951
Reed and Russell, 1964

When there is water, snow or ice over another surface such as land, the depth of penetration of the electromagnetic wave determines whether the top surface or a combination of the top and underlying surface determine the physical constants. The depth of penetration is given by (Jordan, E. C., 1955):

$$\delta = \frac{\left(\frac{\mu\varepsilon}{2}\left[\left(1 + \frac{\sigma^2}{\omega^2 \varepsilon^2}\right)^{\frac{1}{2}} - 1\right]\right)^{-\frac{1}{2}}}{\omega}$$

where: δ = depth of penetration

μ = permeability in Henry/meter

ε = dielectric constant in Farad/meter

σ = conductivity in mhos/meter

$\omega = 2\pi f_c$ in Hertz

f_c = carrier frequency in Hertz

The depth of penetration for several surfaces at 300 MHz is given in Table IV.

TABLE IV: Depth of Penetration (For 300 MHz)

Sea Water	0.015 meters
Fresh water	5.93 meters
Ice	45.93 meters
Average land	2.06 meters

For a vertically polarized incident wave, the reflection coefficient is given by (Reed and Russell, 1964):

$$R_V = \frac{n^2 \sin\psi - \sqrt{n^2 - \cos^2\psi}}{n^2 \sin\psi + \sqrt{n^2 - \cos^2\psi}}$$

The amplitude of the vertical reflection coefficient goes through a minimum at a grazing angle (called the Brewster angle) which is dependent on the physical surface constants and frequency. Two examples are shown in Figure 4. The phase goes through a 180° reversal around the point of minimum amplitude.

For a circularly polarized incident wave, the reflection coefficient is given by (Chinnick, J. H., 1977):

$$R_{cs} = \frac{\sqrt{R_h^2 + R_v^2 + 2 R_h R_v \cos(\phi_h - \phi_v)}}{2}$$

when the direct and reflected waves have the <u>same</u> sense circular polarization

and $$R_{co} = \frac{\sqrt{R_h^2 + R_v^2 - 2 R_h R_v \cos(\phi_h - \phi_v)}}{2}$$

when the direct and reflected waves have <u>opposite</u> sense circular polarization.

The amplitude of the same sense circular reflective coefficient falls between the horizontal and vertical reflection coefficients. The amplitude of the opposite sense circular reflection coefficient starts high at large grazing angles like the horizontal reflection coefficient and goes to zero as the grazing angle decreases to zero.

The surface roughness will determine the ratio of specular to diffuse reflected energy. For a smooth surface the specular component will predominate, while for a rough surface, the diffuse scattered component predominates, Figure 5 (Beckmann and Spizzichino, 1963). For a relatively smooth surface the coherent scattering is limited to the first Fresnel Zone. However, for a very rough surface such as a rough sea, the scattering may come from a considerably larger area.

Surface roughness tends to be elevation angle dependent. Even the very rough sea appears smooth when viewed from a very low elevation angle. The relationship between surface roughness and elevation angle is shown in Table V. When the grazing angle exceeds about twice the critical angle shown in Table V, the specular component becomes insignificant and the reflection coefficient depends upon the diffuse scattering factor.

TABLE V: Maximum Angles for Specular Reflection at Different Frequencies and Sea States*

Sea State Number	Description of Sea	Wave Height (m)	Rms Height, σ_h (m)	Critical Angle, γ max (deg) λ=0.7 m	λ=o.23 m	λ=0.1 m	λ=0.03 m
1	Smooth	0-0.3	0-0.065	>45	>13	>6	>1.8
2	Slight	0.3-1	0.065-0.21	12-45	4-13	1.8-6	0.5-1.8
3	Moderate	1-1.5	0.21-0.32	8-12	2.6-4	1.2-1.8	0.3-0.5
4	Rough	1.5-2.5	0.32-0.54	5-8	1.6-2.6	0.7-1.2	0.2-0.3
5	Very rough	2.5-4	0.54-0.86	3-5	1-1.6	0.4-0.7	0.12-0.2
6	High	4-6	0.86-1.3	2-3	0.7-1	0.3-0.4	0.04-0.12
7		>6	>1.3	<2	<0.7	<0.3	<0.04

*from Beckmann and Spizzichino, 1963

2.3 Divergence Factor

The divergence factor takes into consideration the convex shape of the reflecting surface.

The divergence is given by (Beckmann and Spizzichino, 1963):

$$D = \left(1 + \frac{2\, d_1 d_2}{r\,(d_1 + d_2)\ \mathrm{Sin}\ \psi}\right)^{-\frac{1}{2}} \left(1 + \frac{2 d_1 d_2}{r\,(d_1 + d_2)}\right)^{-\frac{1}{2}}$$

Refer to Figure 3 for definition of terms.

The divergence is very sensitive to the height of the receiving antenna. The divergence factors for an antenna at 100 feet, 30,000 feet, and 70,000 feet is shown in Figure 6 (Foley, et al, 1968)

2.4 Fade Rate

The multipath fade rate can be determined geometrically by calculating the rate of change of the path difference between the direct and the reflected component (Bond, F.E.,1967).

$$\text{Fade rate} = \frac{d\theta}{dt}\ \frac{d(\Delta d)}{d\theta}\ \frac{f_c}{c}$$

(See Figure 3 for definition of terms).

Where θ = *great circle angle between aircraft and satellite*

$\Delta d = d_1 + d_2 - d$

f_c = carrier frequency

c = speed of light

$d = [(r + h_1)^2 + (r + h_2)^2 - 2\,(r + h_1)\,(r + h_2)\ \mathrm{Cos}\ \theta)]^{\frac{1}{2}}$

$d_1 = [r^2 + (r + h_1)^2 - 2r\,(r + h_1)\ \mathrm{Cos}\ \beta]^{\frac{1}{2}}$

$d_2 = [r^2 + (r + h_2)^2 - 2r\,(r + h_2)\ \mathrm{Cos}\ \delta]^{\frac{1}{2}}$

$\theta = \beta + \delta$

$$\mathrm{Cos}\ \beta = \frac{r}{r + h_1}\left(w + \left[w^2 + \left(\frac{r + h_1}{r}\right)^2 - w\left(\frac{r + h_1}{r}\right)^2 - w\right]^{\frac{1}{2}}\right)$$

where

$$w = \frac{(r + h_2)^2\ \mathrm{Sin}^2\ \delta}{(r + h_2)^2 + r^2 - 2r\,(r + h_2)\ \mathrm{Cos}\ \delta}$$

These equations predict the fade rates shown in Figure 7. Measurement of the power spectral density of the signal shown in the top of Figure 7 is plotted in Figure 8 (Johnson, et al, 1979). While the diffuse power spectral density decreases at approximately f^{-2}, a very strong specular component can be seen at approximately .75 Hz. The autocorrelation function of this same signal shows a repetitive correlation with a spacing of approximately 1.3 seconds, Figure 9.

3. MEASUREMENT TECHNIQUES

3.1 Psuedo-Random Sequence

One of the measurement techniques used to separate the direct and reflected signal component is the use of psuedo-random (PRN) sequence and correlation technique. One PRN system which has been tested utilized a 127 bit direct psuedo-random sequence transmitted through the satellite (Prettie, et al, 1977). At the receiving terminal the matching 127 bit psuedo-random sequence was correlated with the receive signal and the time-delayed reflected signal, which has traveled a further distance, Figure 10. The relative amplitude

between the direct and the reflected correlation indicates the amplitude difference of the direct and reflected signals. The time difference indicates differential path delay.

The results of the PRN correlation technique with the satellite at a high elevation angle are shown in Figure 11 for an overhead type antenna (Johnson, A. L., 1978-1). The reflected signal is delayed approximately 50 microseconds and is approximately 20 db lower in amplitude than the direct signal. The results in Figure 12 are for a horizon coverage antenna at a satellite elevation angle of 24°. Here the reflected signal is only approximately 1 db below the direct signal. A rather long trail of diffuse energy is evident with delays up to 15 microseconds later than the specular component. The energy reflected from ice, Figure 13, is approximately 5 to 10 db below the direct signal. The reflections from land, even at relatively low elevation angles (Figure 14) are down significantly from the water reflected multipath.

3.2 Directive Antennas

Another technique which provides information on the reflected component is the use of a directive, bottom-mounted antenna and a separate antenna mounted on top of the aircraft (Prettie, C. W., 1977). This technique allows the measurement of the direct and reflected components for medium to high elevation angles, as shown in Figure 15. Over water the bottom antenna yielded a strong reflected signal at high elevation angles with the average reflected energy approximately 6 db less than the direct received energy (Johnson, A. L., 1979). The bottom received signal, Figure 16, appears noise-like with fade rates of 10 to 100 Hz and a peak-to-null amplitude of 10 to 15 db. Over land, at a high elevation angle, the bottom antenna yielded a less consistent reflected signal, Figure 17. The average signal energy was approximately 10 db less than the direct signal.

4. IMPROVEMENT FACTORS

4.1 Antenna Polarization

The fact that the reflection coefficient is dependent upon antenna or signal polarization leads to the obvious conclusion that different signal polarizations will experience different multipath fading depths. Experimental observations have confirmed the predicted results. Measurements of the signal received from a satellite utilizing a linear antenna polarization showed that the multipath fading depth increased sharply as the elevation angle decreased, Figure 18. Multipath fade depths of greater than 20 db were experienced at very low elevation angles (Jorden, K. L., 1969).

However, satellites which employ circular polarization provide considerable protection against low angle multipath fading. Extensive measurements are summarized in Figure 18 showing that the multipath fading tends to peak up at a moderately low elevation angle with the fade depth seldom exceeding 10 or 12 db (Johnson, A. L., 1974). As the elevation angle decreased, the fade depth decreased to approximately 5 db.

4.2 Antenna Directivity

If a directive aircraft antenna can be used to minimize the illumination of the reflecting surface, the multipath fade depth can be reduced significantly. As discussed in Section 2.1, antenna directivity is the largest multipath fade factor under the system designer's control.

4.3 Diversity Techniques

Due to the multipath geometry, the multipath fading is very frequency selective. As a result, frequency diversity techniques work extremely well to overcome the multipath fading. The results of a triple frequency diversity scheme are shown in Figure 19 (Johnson, A. L., 1968). The maximum frequency separation from Frequency 1 to Frequency 6 is 300 KHz. The elevation angle at which this multipath occurred was approximately 8°. From Figure 19 it can be seen that when Frequency 1 is in a fade, Frequency 6 is at its multipath peak. The utilization of a diversity combiner can virtually eliminate the effect of this type of multipath fading.

Another example of frequency diversity is rapid frequency hopping of a signal where the hopping rate is greater than the data rate (Johnson, A. L., 1977). Figure 20 shows the received signal level of an unhopped and a fast-hopped signal. Combining the multiple frequency hopped chips into a single data bit significantly reduces the effect of the multipath fading period.

Space, or antenna diversity, can significantly reduce the multipath fading if the antennas are spaced far enough apart to decorrelate the fading. Vertical spacing of approximately 5 to 10 wavelengths is usually sufficient to decorrelate the fading. Horizontal spacing of 50 to 100 wavelengths is needed to provide similar decorrelation.

Time diversity techniques also improve multipath fading performance. The use of error correction coding can provide the needed time diversity. Usually interleaving of data bits is required to break up the burst errors which multipath fading produce. Error correction coder/decoders can only effectively correct random error patterns.

5.0 UNEXPECTED MULTIPATH RESULTS

5.1 Coastal Multipath

An unexpected result of the bottom antenna test described in Section 3.2 was the discovery of a strong, specular reflective component as the aircraft passed over a coastal area. This effect was noted as the aircraft flew in the vicinity of the Gulf of Mexico at a high elevation angle to the satellite. An irregular, noiselike signal was experienced as the aircarft flew over Texas, Figure 21. As the aircraft approached the coast of Texas, a specular reflection was received for approximately one minute. The aircraft then flew over Mustang Island and experienced erratic land type multipath. Another specular reflection was encountered as the aircraft passed into the Gulf. The duration of the specular component represented an aircraft travel

of 10 to 15 miles. This specular component is not peculiar to the Texas coast, but has been recorded along the coast of Louisiana, Virginia, Canada, Greenland, Mexico, Central America and Hudson Bay (Johnson, et al, 1977 and 1979). The strength of the specular reflection is so great that its effect is visible on an upward-looking antenna, Figure 22. The upward antenna has a discrimination factor of approximately 30 db between the direct and reflected signal. The ringing type multipath shown in Figure 22 was recorded as the aircraft passed over the coast of Louisiana (Johnson, A. L., 1978-2). The 2 db of multipath is the result of a reflected signal which is down approximately 14 db below the direct signal.

6. CONCLUSION

Test results have confirmed that severe multipath fading can be experienced when the aircraft is communicating with a satellite at low elevation angles. Over water a deep, continuous multipath is usually experienced, while over land, a sporadic multipath is usually encountered. Techniques which can significantly reduce the multipath fading include antenna discrimination, use of circular polarization and frequency diversity.

REFERENCES

Beckmann, P. and Spizzichino, A., 1963, The Scattering of Electromagnetic Waves from Rough Surfaces, MacMillan Co., New York, 1963.

Bond, F. E., 1967, Precise Results for Differential Delay and Fading Rate For Aircraft/Satellite Link (Draft), Aerospace Corp.; Los Angeles, Calif.,; 30 Oct 67.

Burnside, W. D. and Marhefka, R. J., Yu, C. L., 1973, Roll-Plane Analysis of On-Aircraft Antennas, IEEE Transaction on Antennas and Propagation, Vol. AP-21, #6, pp. 780-786; Nov 73.

Chinnick, J. H., 1977, A Report On Low Angle Ocean Scatter Measurements, Communication Research Centre Report; Ottawa, Canada, 29 Aug 1977.

Clanton, Steve, 1974, AFSCS Antenna Patterns on B52-H, Boeing Test Report T-3-1687; Renton, Wash.; 25 April 74.

Foley, T. K., Gaumond, B. J. and Sestak, E., 1968, Experimental L-Band SST Satellite Communication/Surveillance Terminal Study, Boeing Report D6-60105-2, Vol. III; Renton, Wash.; Nov 1968.

Franklin, Sidney B., 1973, A Brief Summary of Multipath Effects That Will Tend to Limit RPV-to-Relay Range, AFAL Tech Memo; WPAFB, Ohio, 6 Nov 73.

Johnson, Allen L., 1968, Six-Month Report of Flight Test Results on Program 591, Air Force Avionics Laboratory; WPAFB, Ohio, 31 Jan 68.

Johnson, Allen L., 1974, UHF Multipath Fading, Air Force Avionics Laboratory Memo for Record, WPAFB, Ohio, 9 September 1974.

Johnson, Allen L., 1977, Test Results from June 1977 Polar Flight Test, Air Force Avionics Laboratory Tech Memo: AFAL-TM-77-57; WPAFB, Ohio; 8 Oct 1977.

Johnson, Allen L., 1978-1, Aircraft to Satellite Multipath Test, Air Force Avionics Laboratory Tech Memo: AFAL-TM-78-5, WPAFB, Ohio, 30 January 1978.

Johnson, Allen L., 1978-2, Dual Frequency SATCOM Atlantic Flight Test Report, Air Force Avionics Laboratory Tech Memo: AFAL-TM-78-34; WPAFB, Ohio, 25 Dec 78.

Johnson, Allen L., 1979, UHF Multipath Test, Air Force Avionics Laboratory Tech Memo: AFAL-TM-79-2; WPAFB, Ohio, 1 March 1979.

Johnson, Allen L., Beach, Robert C., 1977, Atlantic Flight Test, Air Force Avionics Laboratory Tech Memo: AFAL-TM-77-71; WPAFB, Ohio, 23 Dec 1977.

Johnson, A., Swanson, R. and Beach, R., 1979, 1979 SATCOM Polar Flight Test, Air Force Avionics Laboratory Tech Memo: AFAL-TM-79-1; WPAFB, Ohio 28 Feb 79.

Jordan, Edward C., 1955, Electromagnetic Waves and Radiating Systems, Prentice-Hall: New York, 1955.

Jorden, Kenneth L., Jr., 1969, Multipath Characteristics in a Satellite-Aircraft Link at 230 MHz, MIT Lincoln Laboratory Report MS2605, Lexington, Mass., September 1969.

Kerr, D. E., 1951, Propagation of Short Radio Waves, MIT Radiation Laboratory Series, Vol. 13, McGraw-Hill Book Publishers, Inc., New York, 1951.

Maroth, V., 1963, Model Radiation Pattern Study AT-1076A Antenna on the KC135 Aircraft, Engineering Report 1610.1, Dorne & Margolin; Westbury, New York; 2 April 1963.

Prettie, Clifford W., 1977, Test Plan for A Sea Multipath Spatial Diversity Experiment, ESL, Inc., Sunnyvale, Calif., August 1977.

Prettie, Dr. C., Johnson, A., Marshall, Dr. J, Grizinski, T., and Swanson, R., 1977, Project Stress Satellite Communication Test Results, AFAL-TR-77-158, Air Force Avionics Laboratory, WPAFB, Ohio, July 1977.

Reed, Henry R. and Russell, Carl M., 1964, Ultra High Frequency Propagation, Boston Technical Publishers, Inc., Lexington, Mass., 1964.

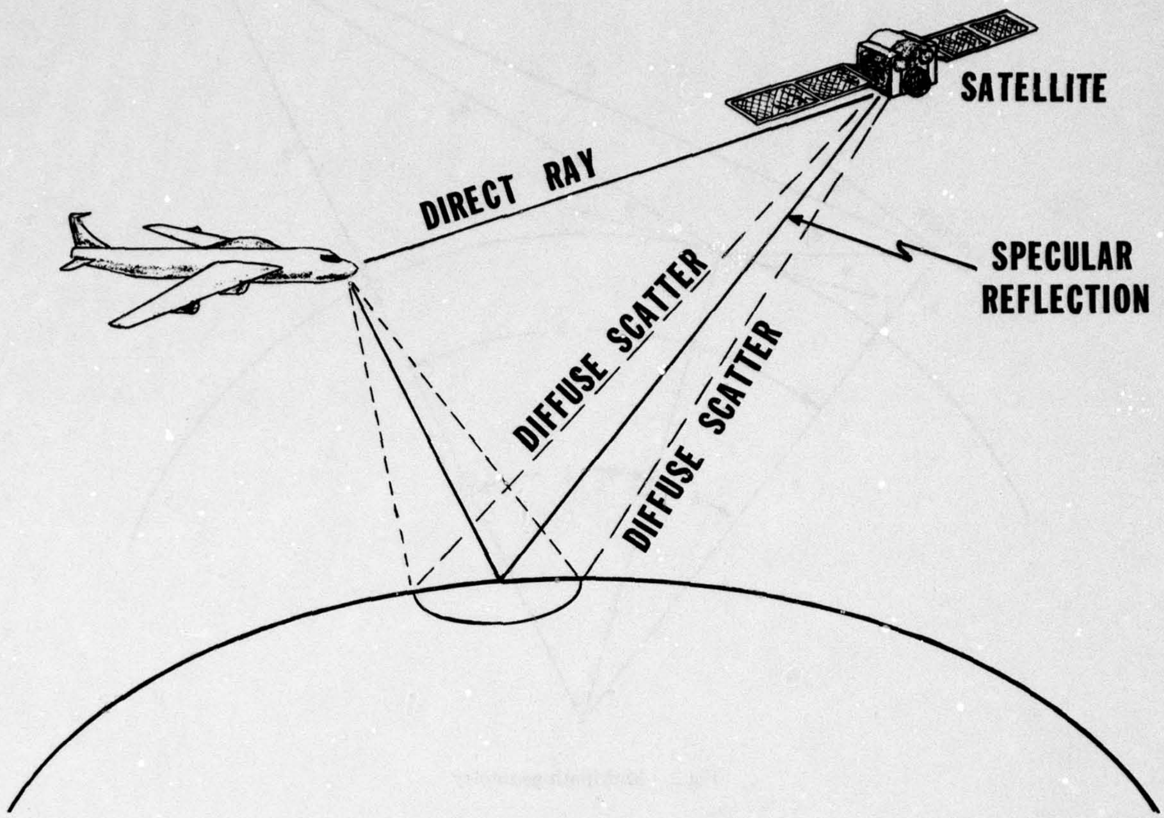

Fig.1 Multipath geometry

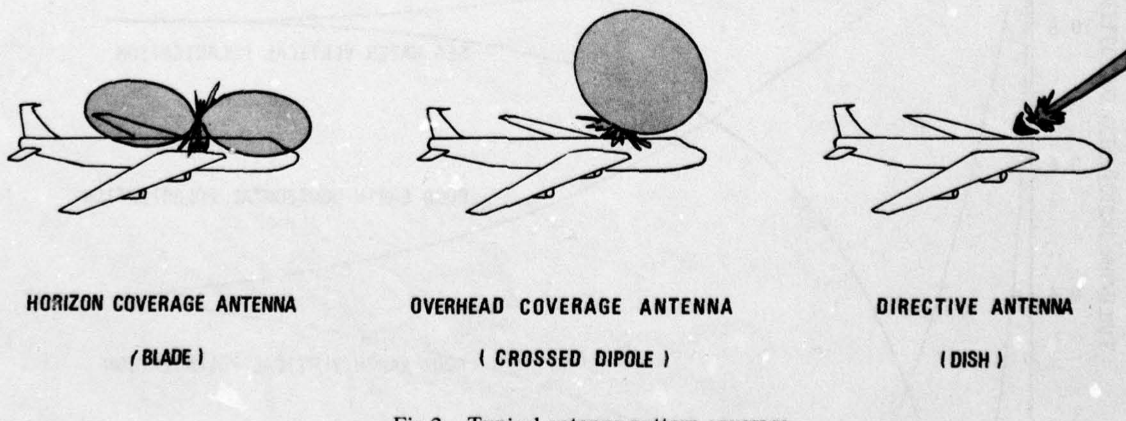

Fig.2 Typical antenna pattern coverage

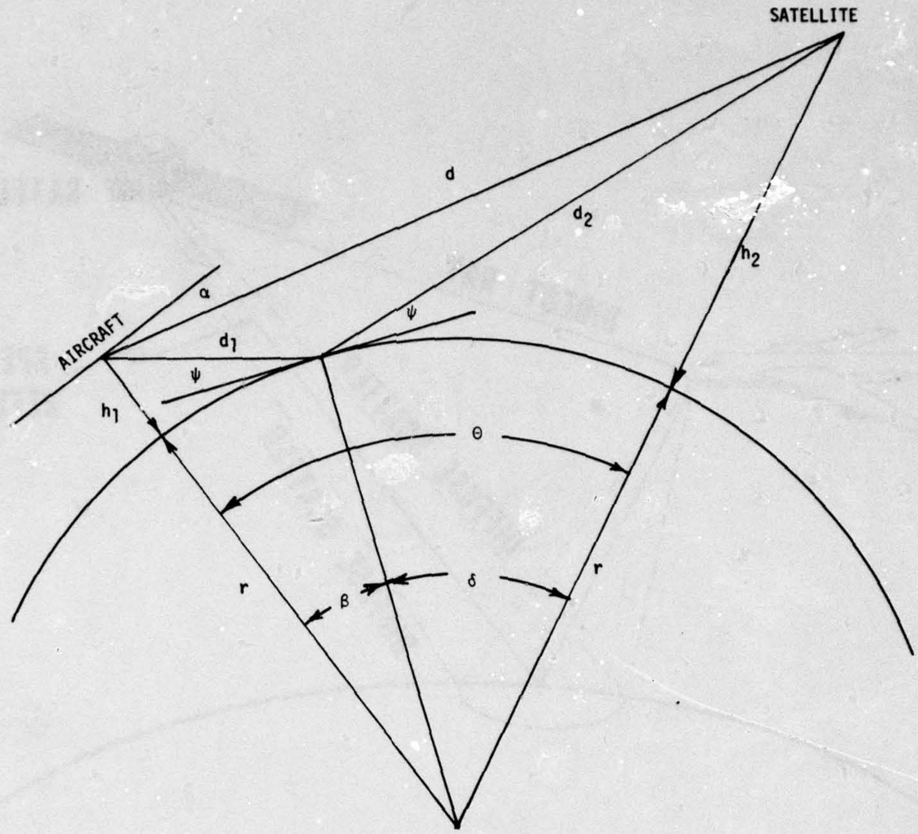

Fig.3 Multipath geometry

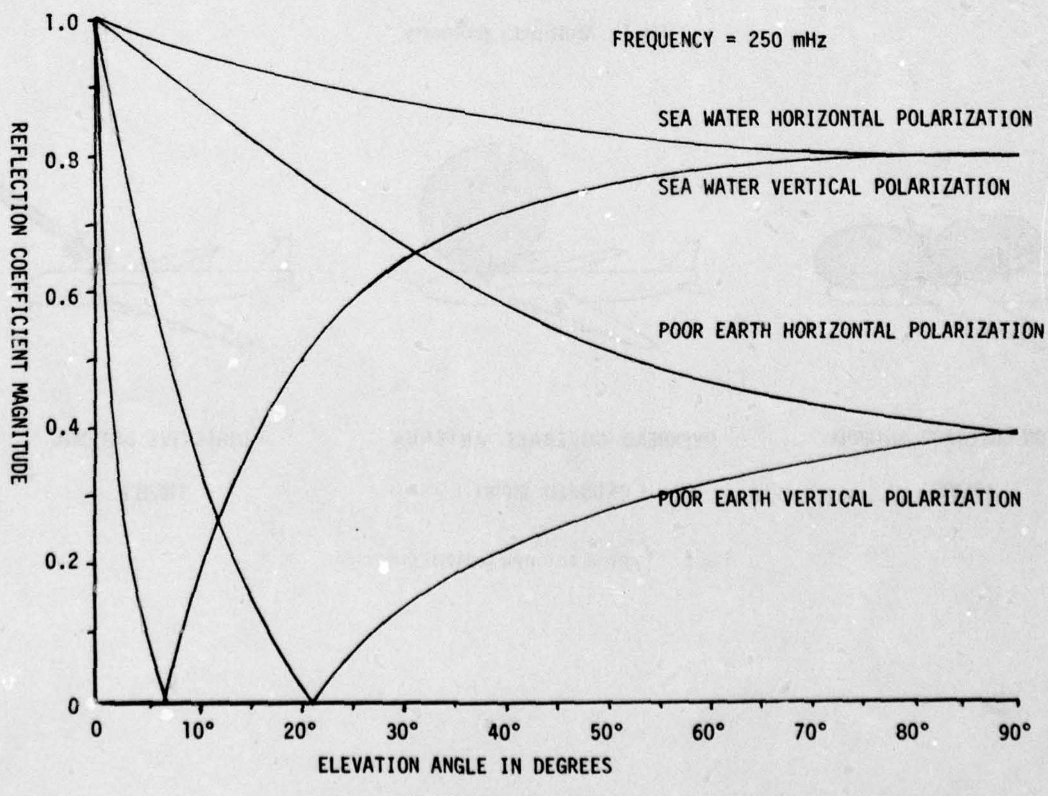

Fig.4 Variation in reflectivity with elevation angle

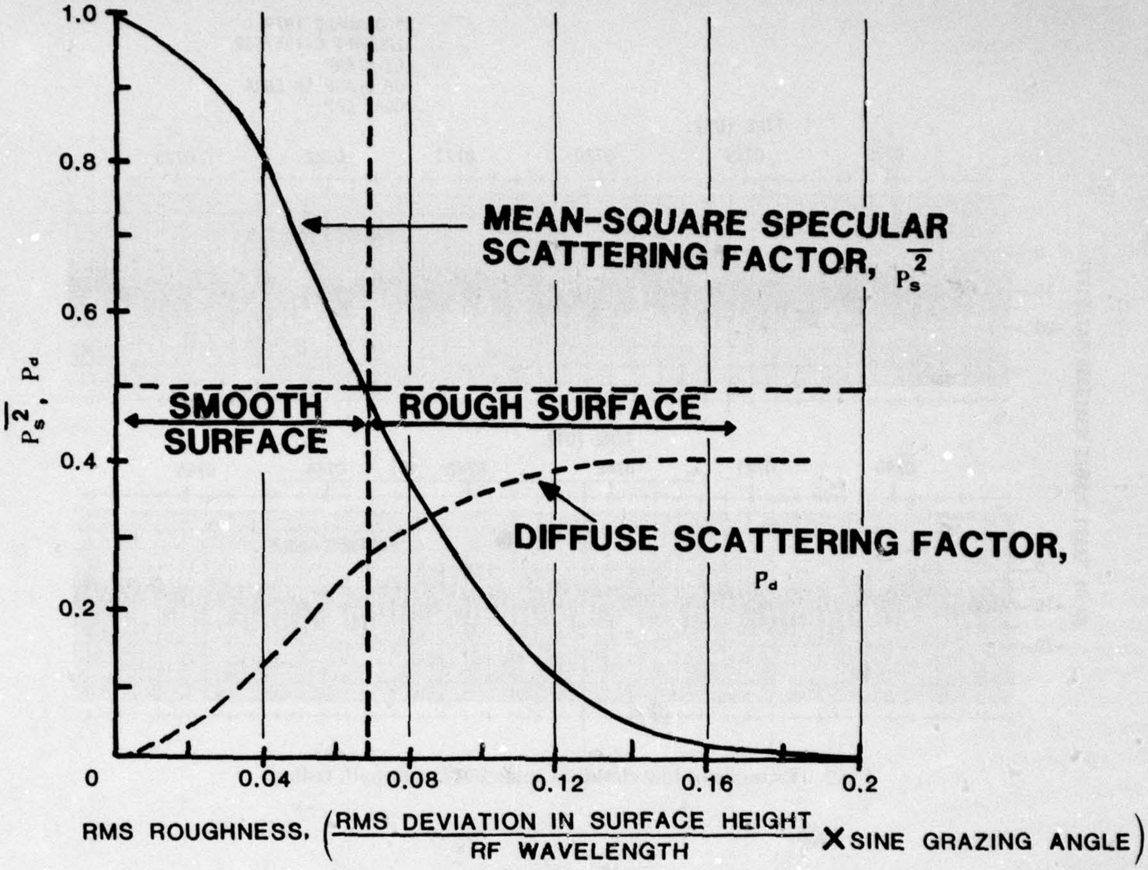

Fig.5 Scattering factors versus roughness

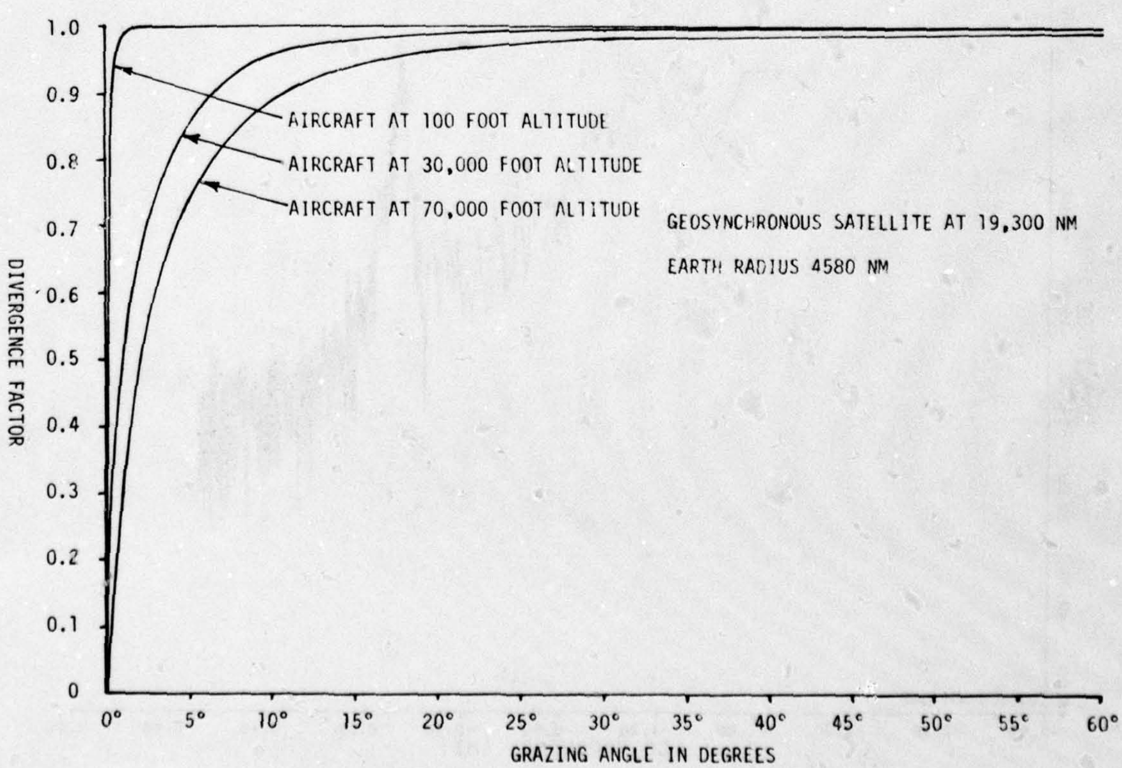

Fig.6 Divergence factor versus grazing angle

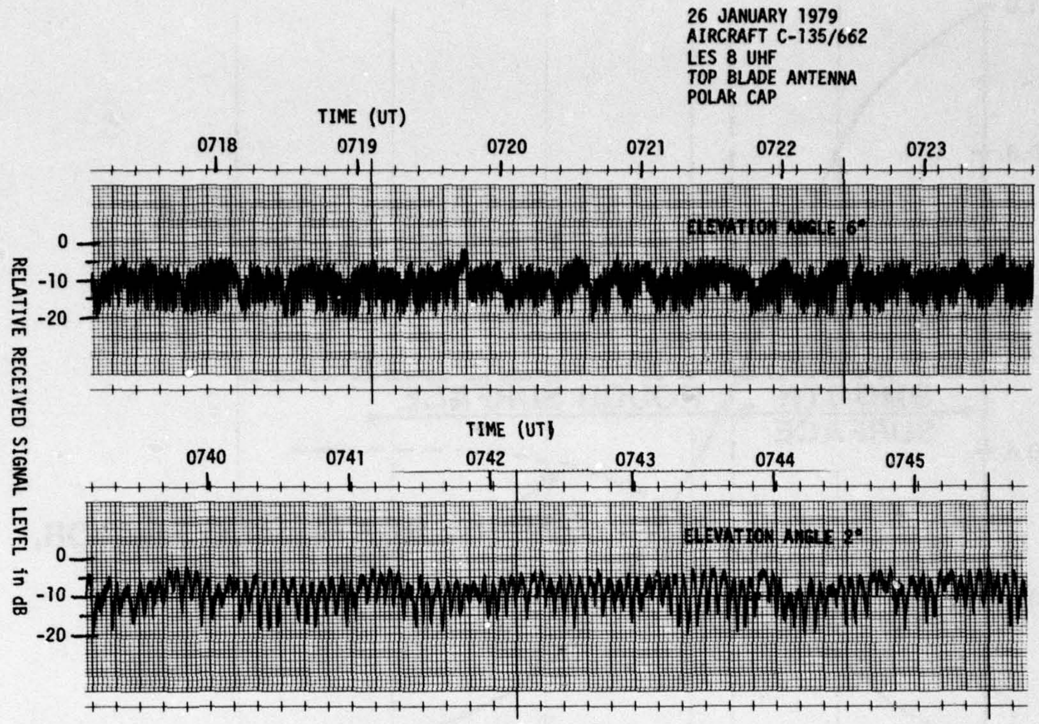

Fig.7 Example of low elevation angle UHF multipath fading

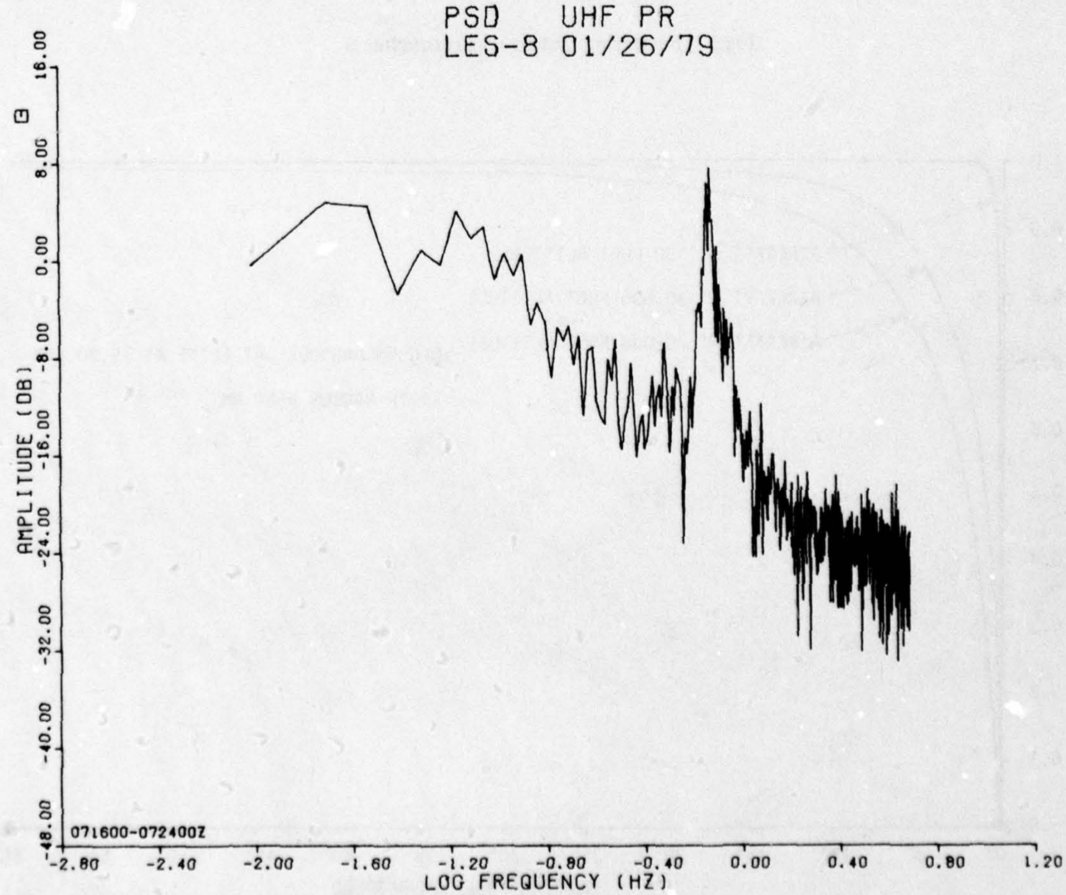

Fig.8 Power spectral density of multipath signal

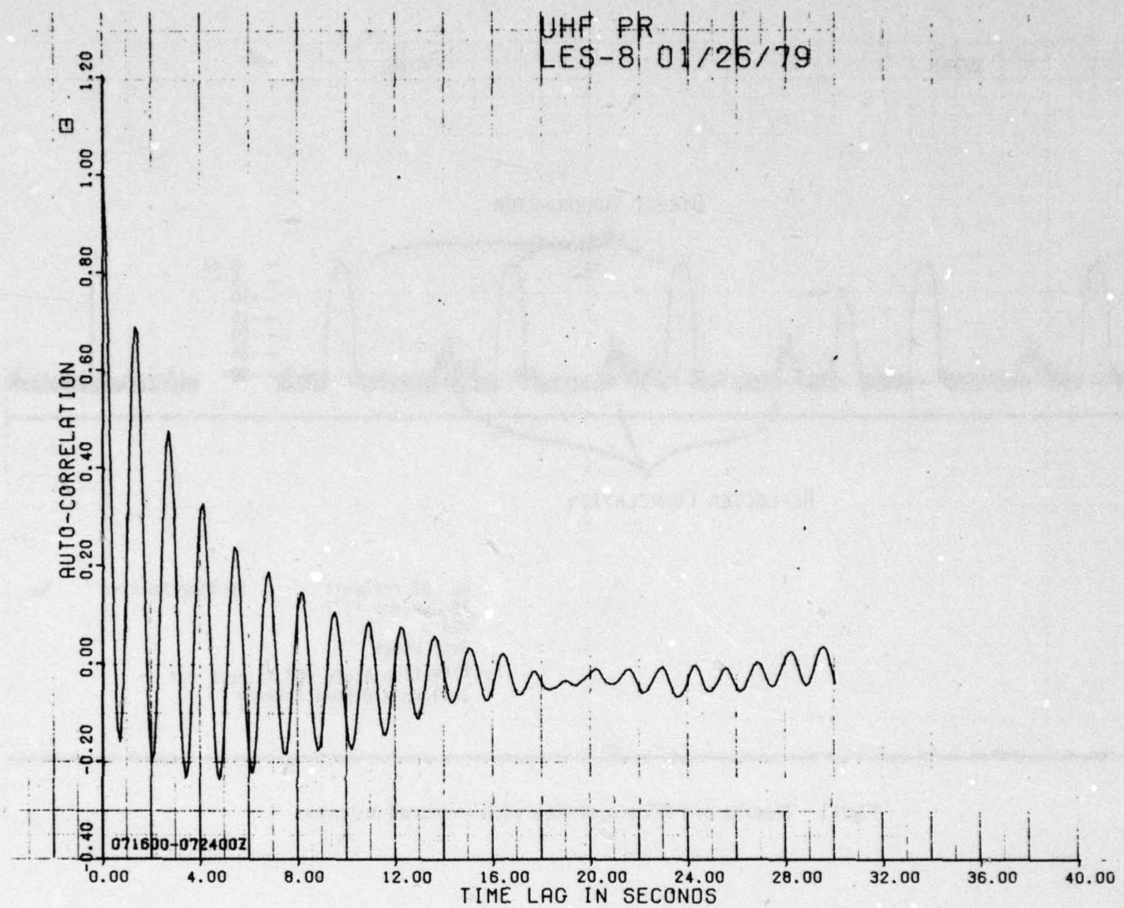

Fig.9 Autocorrelation of multipath signal

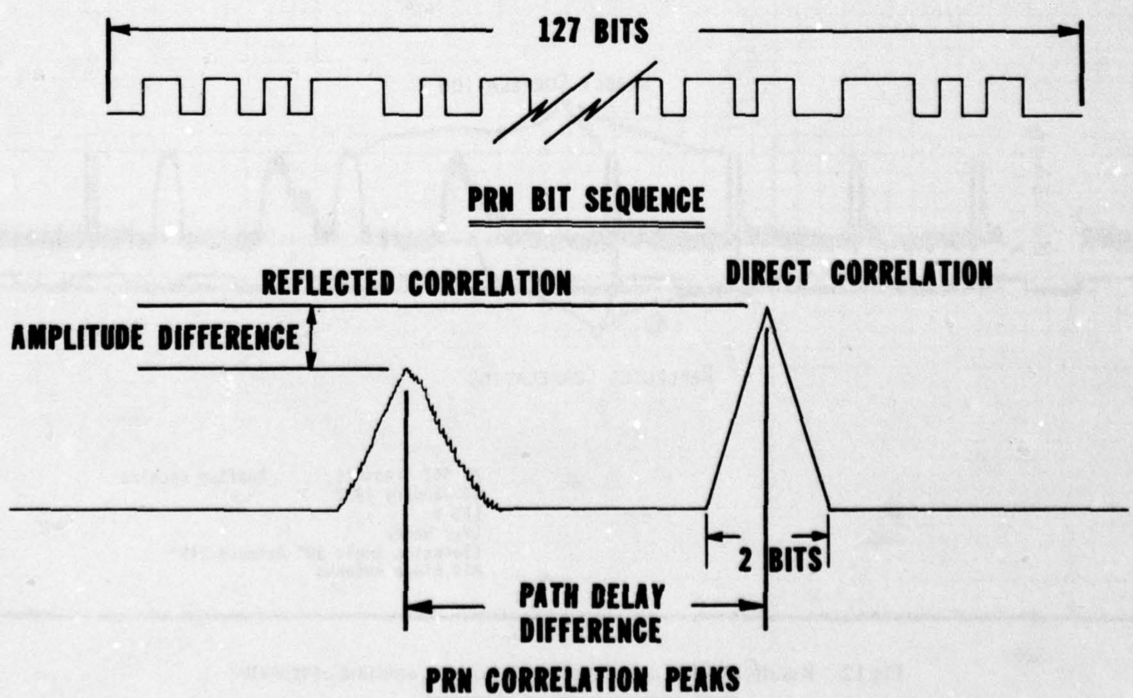

Fig.10 Psuedo-random sequence measurement technique

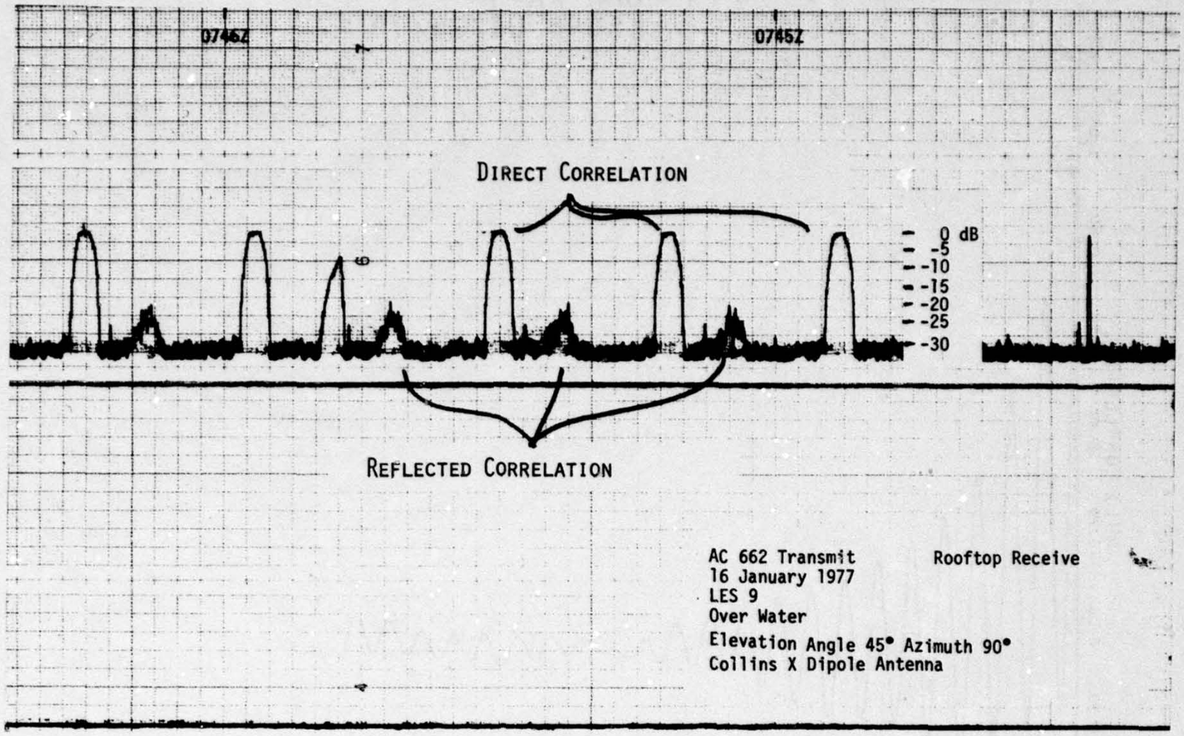

Fig.11 Results of PRN correlation with overhead antenna

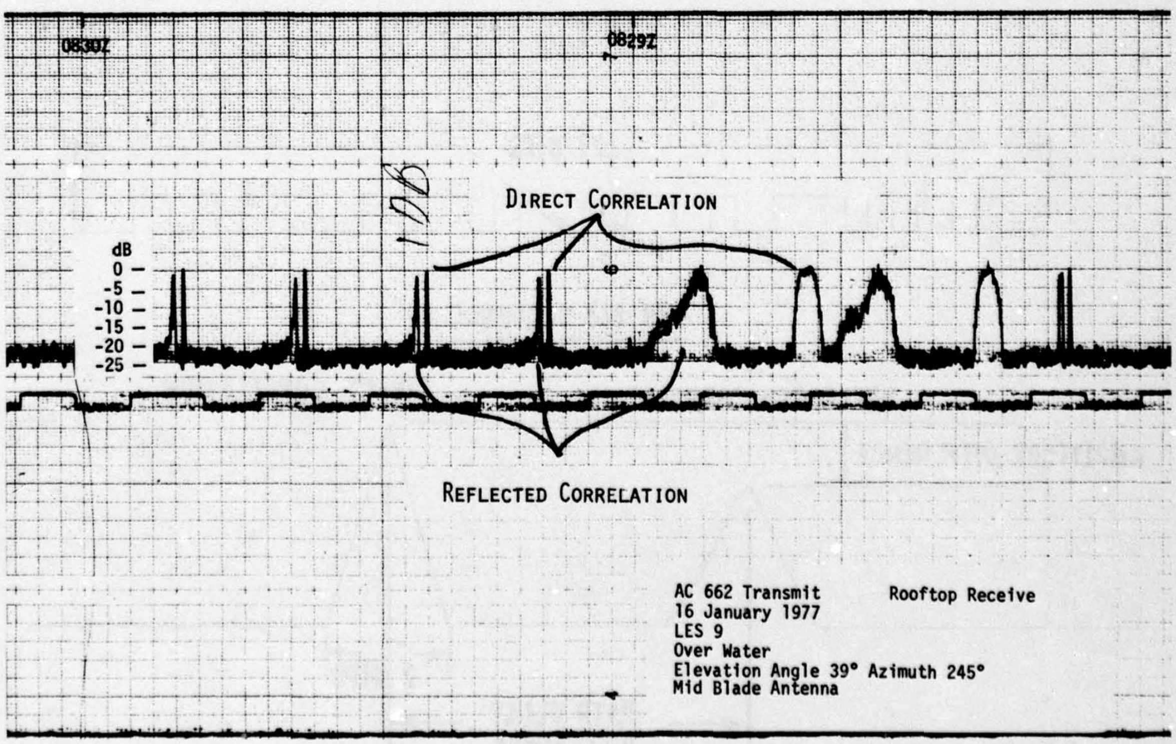

Fig.12 Results of PRN correlation with horizon antenna over water

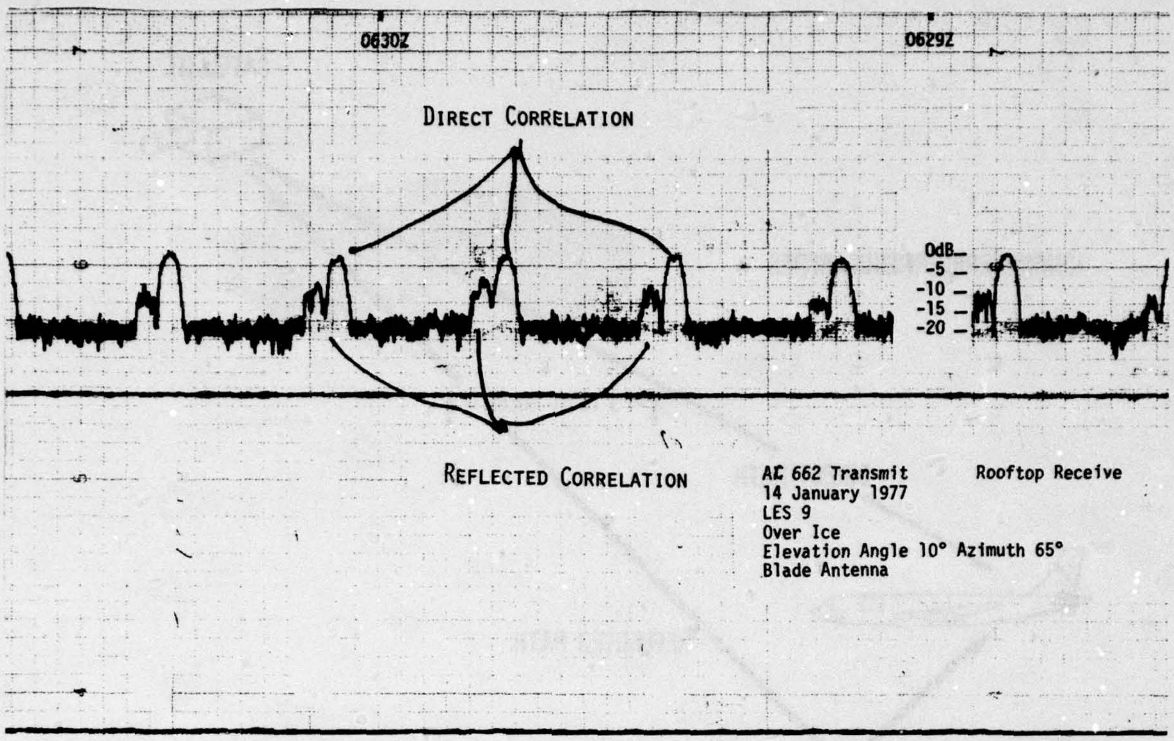

Fig.13 Results of PRN correlation with horizon antenna over ice

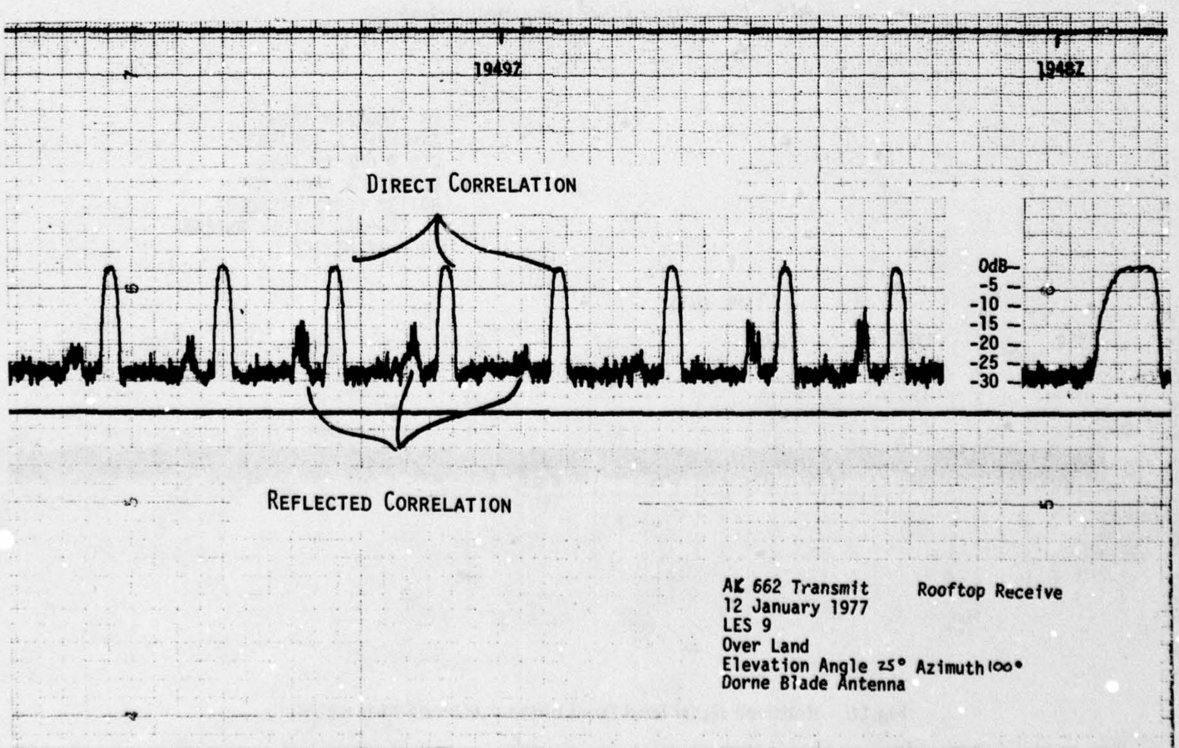

Fig.14 Results of PRN correlation with horizon antenna over land

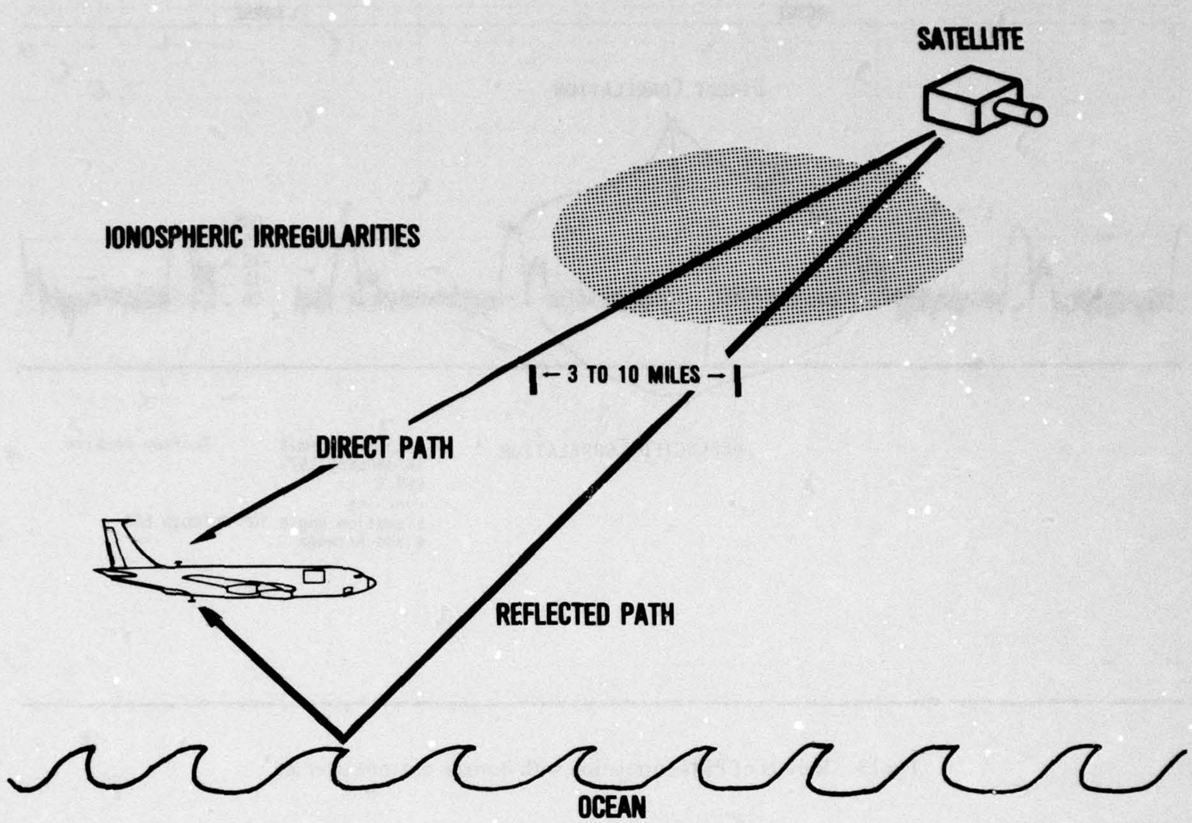

Fig.15 Geometry of fade mitigation technique

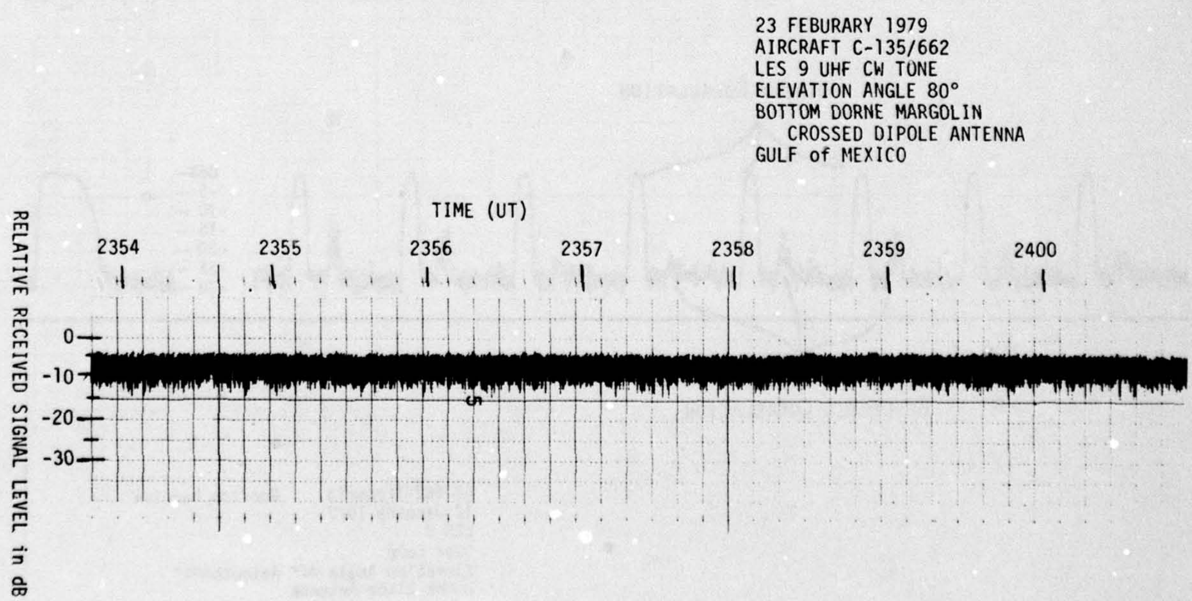

Fig.16 Received signal level from bottom antenna over water

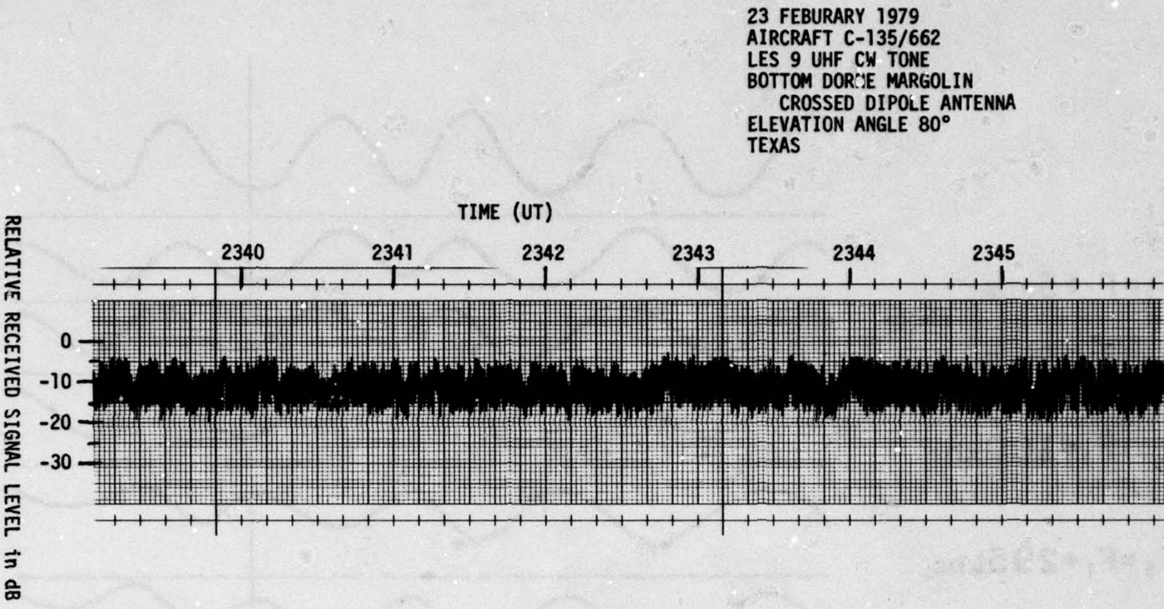

Fig.17 Received signal level from bottom antenna over land

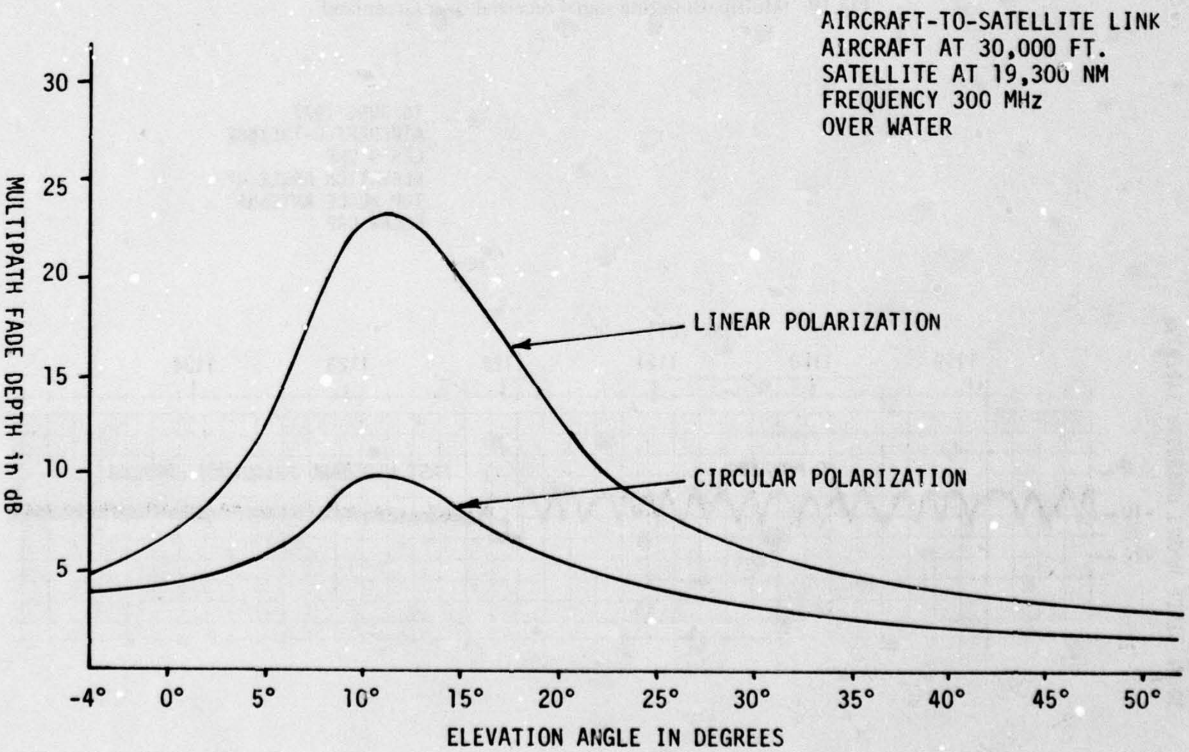

Fig.18 Typical multipath fading depth for linear and circular polarization

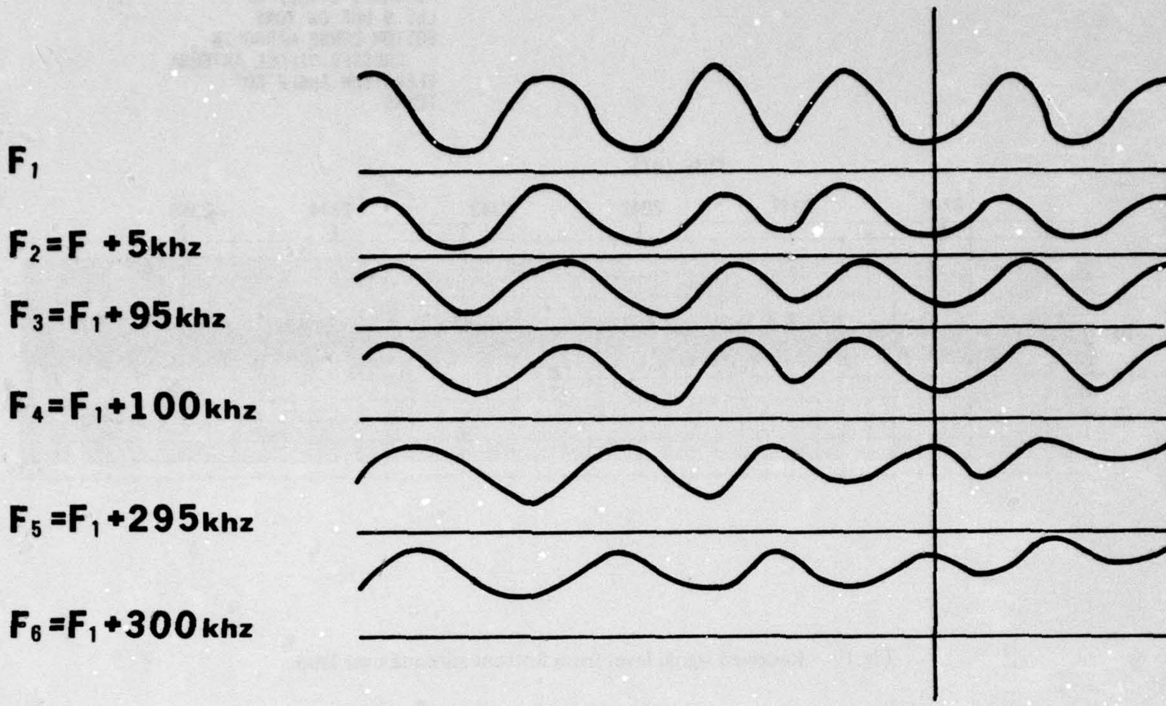

Fig.19 Multipath fading signal received over Greenland

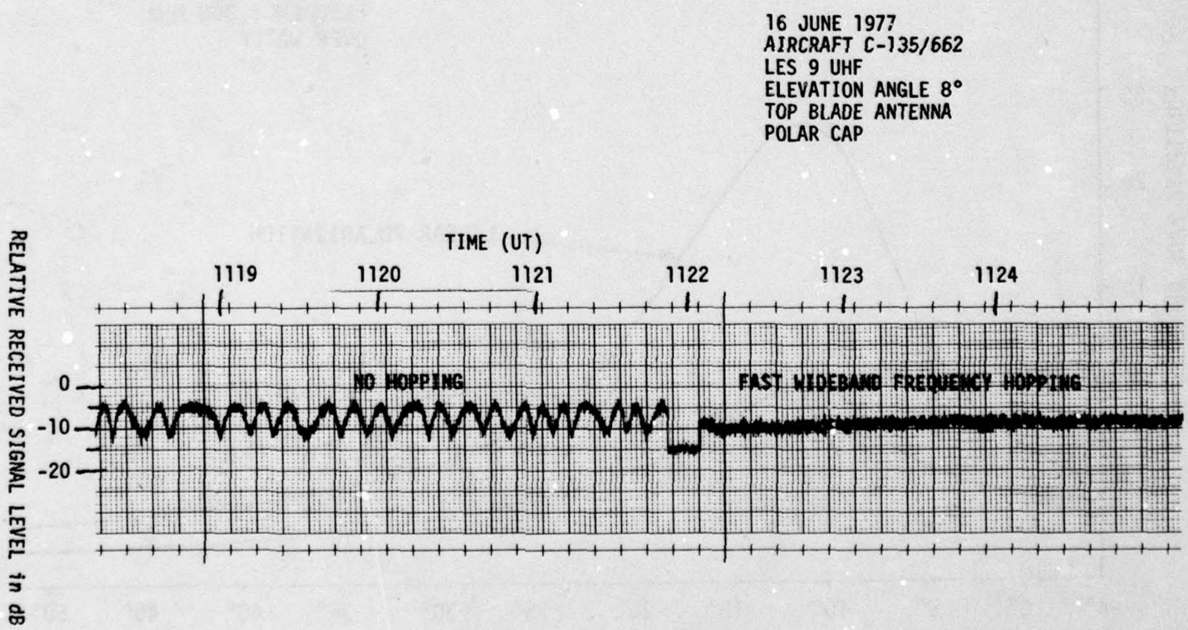

Fig.20 Multipath fading protection of fast frequency hopped signal

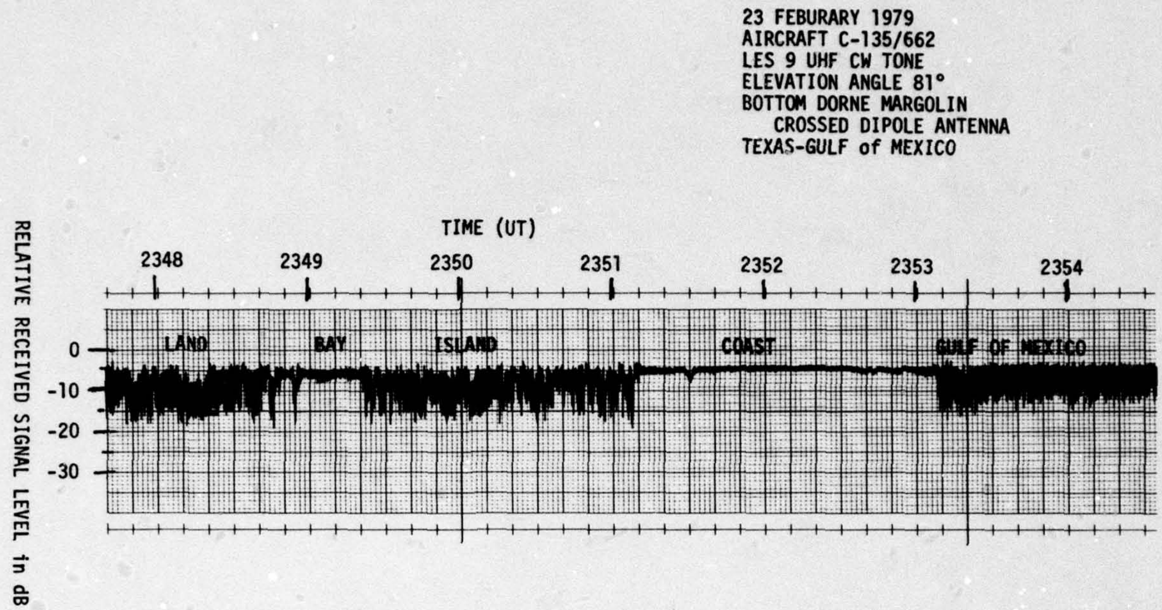

Fig.21 Coastal received signal level from bottom antenna

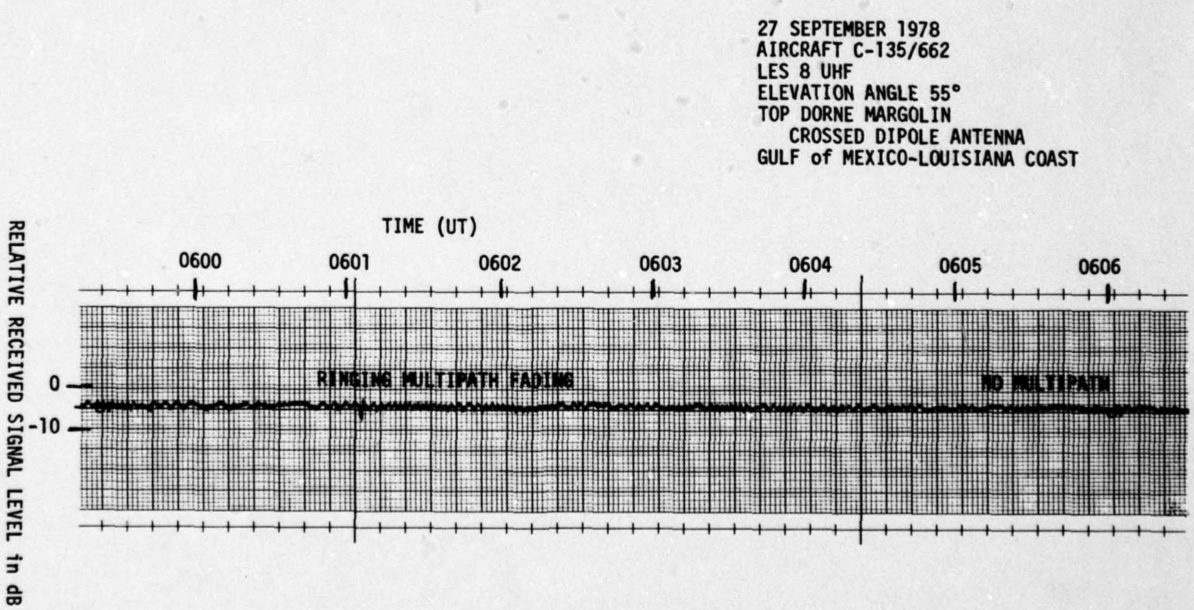

Fig.22 Coastal multipath fading received on top antenna

SCATTERED RADIATION FIELDS FROM ROUGH SURFACES

FULL WAVE SOLUTIONS

Ezekiel Bahar
Electrical Engineering Department
University of Nebraska, Lincoln, Nebraska 68588

SUMMARY

Full wave solutions are derived for the scattered radiation fields from rough surfaces with arbitrary slope and electromagnetic parameters. These solutions bridge the wide gap that exists between the perturbational solutions for rough surfaces with small slopes and the quasi optics solutions. Thus, it is shown for example, that for good conducting boundaries the backscattered fields which are dependent on the polarization of the incident and scattered fields at low frequencies, become independent of polarization at optical frequencies. These solutions are consistent with reciprocity, energy conservation and duality relations in electromagnetic theory. Since the full wave solutions account for upward and downward scattering, shadowing and multiple scatter is considered. Applications to periodic structures and random rough surfaces is also presented.

1. Introduction

The problem of electromagnetic wave scattering by rough surfaces has been studied extensively because of its broad applications in science and technology. However, because of the complexity of the problem, satisfactory solutions are available only when very stringent restrictions are made on the rough surface profile, the electromagnetic parameters of the irregular boundary or the frequency of the electromagnetic wave. Thus different solutions are derived depending on the approximate assumptions made to facilitate the analysis and there are many pertinent scattering problems for which valid solutions are not available. For example, using a perturbational approach derived for surfaces with small gradients, the backscattered fields are shown to be strongly dependent upon the polarization of the incident and scattered waves (RICE 1951, WRIGHT 1966, BARRICK and PEAKE 1968). Physical optics solutions that are restricted to high frequencies indicate that for perfectly conducting surfaces, the backscattered fields are not dependent on polarization (BECKMANN and SPIZZICHINO 1964).

A full wave approach has been developed to remove the restrictions imposed on the earlier solutions. Thus complete expansions of the fields in terms of a basis consisting of the radiation, lateral and surface wave terms were used and exact boundary conditions were imposed at the irregular boundary (BAHAR 1972a,b, 1973a,b). Using the orthogonal properties of the basis functions and employing Green's theorems to avoid differentiation of the field expansions at the irregular boundary, Maxwell's equations were converted into rigorous sets of ordinary coupled first order differential equations for the forward and backward wave amplitudes. In order to cast the full wave solutions in a form that could be readily used by the engineer and compared with earlier results, the coupled differential equations were converted into integral equations that were solved using a second order iterative approach. Using these solutions, some of the discrepancies existing in the earlier solutions were examined, such as reciprocity, energy conservation, scattering when the incident wave is near the Brewster angle and when the incident or scattered waves are near grazing angles. Furthermore, coupling between the radiation fields and the surface and lateral waves (disregarded in earlier solutions) was also examined in detail (BAHAR 1977, 1978).

However, due to the iterative approach used to obtain the simple solutions, they were restricted to moderately small slopes and the transition between the perturbational approach and the quasi optics approach was not clearly shown. To remove the restriction and to retain the relatively simple form of the final solution, in this work the rough surface is regarded as a continuum of elementary strips of varying slope and height rather than a continuum of elementary horizontal strips of varying height. It has been shown that the full wave approach is most amenable to an iterative solution when it is based on a local modal analysis that conforms most closely to the varying parameters of the irregular waveguide (BAHAR 1968, 1969; BAHAR and GOVINDARAJAN 1973, 1974). Thus starting with the full wave expression for the scattered fields by an elementary horizontal strip and performing the necessary coordinate transformations, the desired expressions are derived for scattering by a continuum of elementary strips of varying slope and height.

The small slope approximation of these full wave solutions agree with the earlier perturbational solutions while the high frequency approximation of the full wave solutions agree with the physical optics solutions for perfectly conducting boundaries. The solutions are shown to satisfy reciprocity, energy conservation and duality relations in electromagnetic theory. The full wave solutions account for both upward and downward scattering, thus multiple scattering and shadowing effects can be considered. The radiation term is shown to vanish in a continuous manner as the receiver moves across a shadow boundary, where coupling between the radiation fields and the surface and lateral waves cannot be neglected.

The full wave solutions presented here for the scattered radiation fields are not restricted by the slope or electromagnetic parameters of the boundary nor are they restricted in frequency, provided only that the receiver is in the far field. They are expressed in the relatively simple forms of the earlier solutions and can therefore be readily used by the engineer who is not familiar with the mathematical techniques used in the derivations. Application of the full wave solutions to periodic structures and random rough surfaces is also presented.

2. Formulation of the Problem

In this work we consider the scattering of vertically and horizontally polarized waves by an arbitrarily varying interface $h(x)$ between two semi-infinite media characterized by the electromagnetic parameters (see Fig. 1)

$$\varepsilon = \begin{cases} \varepsilon_0 \\ \varepsilon_1 \end{cases}, \quad \mu = \begin{cases} \mu_0 & y > 0 \\ \varepsilon_0 & y < 0 \end{cases} \tag{2.1}$$

in which the permittivity ε and permeability μ can be complex quantities with negative imaginary parts for dissipative media and an $\exp(i\omega t)$ time dependence is assumed. For simplicity the vertically and horizontally polarized waves are assumed to be excited by magnetic line sources $J_m\bar{a}_z(\frac{\text{Volts}}{m^2})$ or electric line sources $J_e\bar{a}_z(\frac{\text{Amps}}{m^2})$ respectively. It is assumed here that the complex permittivity and the permeability are not functions of x, thus scattering is only due to the rough surface h(x). Furthermore, since this problem is two dimensional, the scattered waves are not depolarized. The boundary conditions at y = h(x) can be expressed in terms of the transverse (y,z) components of the electromagnetic fields. Thus for the vertically polarized waves (BAHAR 1972a,b)

$$\left[E_y \frac{dh}{dx} + \frac{1}{i\omega\varepsilon}\frac{\partial}{\partial y} H_z\right]_{h^-}^{h^+} = 0\ ,\quad \left[H_z\right]_{h^-}^{h^+} = 0 \tag{2.2}$$

and for the horizontally polarized waves

$$\left[H_y \frac{dh}{dx} - \frac{1}{i\omega\mu}\frac{\partial}{\partial y} E_z\right]_{h^-}^{h^+} = 0\ ,\quad \left[E_z\right]_{h^-}^{h^+} = 0 \tag{2.3}$$

The complete expansions for the vertically polarized waves are

$$\begin{aligned} H_z(x,y) &= H_o^V(x,y) + H_1^V(x,y) + H_s^V(x,y) \equiv \sum_n H_n^V(x,v)\psi_n^V(v,y) \\ &\equiv \int_0^\infty H_o^V(x,v)\psi_o^V(v,y)dv_o + \int_0^\infty H_1^V(x,v)\psi_1^V(v,y)dv_1 + H_s^V(x,v)\psi_s^V(v,y) \end{aligned} \tag{2.4a}$$

where

$$H_n^V(x,v) = \int_{-\infty}^{\infty} H_z(x,y)Z^V(v,y)N_n^V(v)\psi_n^V(v,y)dy\ ,\quad n=0,1,s \tag{2.4b}$$

and

$$E_y(x,y) = \sum_n E_n^V(x,v)Z^V(v,y)\psi_n^V(v,y) \tag{2.5a}$$

where

$$E_n^V(x,v) = \int_{-\infty}^{\infty} E_y(x,y)N_n^V(v)\psi_n^V(v,y)dy\ ,\quad n=0,1,s \tag{2.5b}$$

For the horizontally polarized waves the complete expansions are

$$E_z(x,y) = \sum_n E_n^H(x,v)\psi_n^H(v,y) = E_o^H(x,y) + E_1^H(x,y) + E_s^H(x,y) \tag{2.6a}$$

where

$$E_n^H(x,v) = \int_{-\infty}^{\infty} E_z(x,y)Y^H(v,y)N_n^H(v)\psi_n^H(v,y)dy\ ,\quad n=0,1,s \tag{2.6b}$$

and

$$H_y(x,y) = \sum_n H_n^H(x,v)Y^H(v,y)\psi_n^H(v,y) \tag{2.7a}$$

where

$$H_n^H(x,v) = \int_{-\infty}^{\infty} H_y(x,y)N_n^H(v)\psi_n^H(v,y)dy\ ,\quad n=0,1,s \tag{2.7b}$$

in which ψ_o^P, ψ_1^P and ψ_s^P (P = V or H) are the basis functions for the radiation, lateral and surface wave terms respectively (BAHAR 1973a,b). The transverse wave impedance and admittance are

$$Z^V(v,y) = \frac{u}{\omega\varepsilon} = \begin{cases} \dfrac{u}{\omega\varepsilon_o} = Z_o(v),\ y > h \\ \dfrac{u}{\omega\varepsilon_1} = Z_1(v),\ y < h \end{cases} \tag{2.8}$$

and

$$Y^H(v,y) = \frac{u}{\omega\mu} = \begin{cases} \dfrac{u}{\omega\mu_o} = Y_o(v),\ y > h \\ \dfrac{u}{\omega\mu_1} = Y_1(v),\ y < h \end{cases} \tag{2.9}$$

The normalization coefficients are

$$N_n^V(v) = R_n^{Vh}(v)/2\pi\ Z_n^V(v),\quad N_n^H = R_n^{Hh}(v)/2\pi\ Y_n^H(v) \tag{2.10}$$

in which R_n^{Ph} are the reflection coefficients with respect to the reference surface y = 0

$$R_o^{Ph}(v) = R_o^P(v)\exp(i2v_oh),\quad R_1^{Ph} = R_1^P(v)\exp(-i2v_oh) \tag{2.11}$$

where $R_n^P (P = V,H)$ are the Fresnel reflection coefficients

$$R_o^V(v) = -R_1^V(v) = \frac{v_o\varepsilon_1 - v_1\varepsilon_o}{v_o\varepsilon_1 + v_1\varepsilon_o} = \frac{\eta_o \cos\theta_o - \eta_1 \cos\theta_1}{\eta_o \cos\theta_o + \eta_1 \cos\theta_1} \equiv \frac{\eta_o C_o - \eta_1 C_1}{\eta_o C_o + \eta_1 C_1} \tag{2.12}$$

and

$$R_o^H(v) = -R_1^H(v) = \frac{v_o\mu_1 - v_1\mu_o}{v_o\mu_1 + v_1\mu_o} = \frac{\eta_1 \cos\theta_o - \eta_o \cos\theta_1}{\eta_1 \cos\theta_o + \eta_o \cos\theta_1} \equiv \frac{\eta_1 C_o - \eta_o C_1}{\eta_1 C_o + \eta_o C_1} \tag{2.13}$$

in which $\eta_i = \sqrt{\mu_i/\varepsilon_i}$ is the wave impedance for medium $i(i=0,1)$, C_o and C_1 are the cosines of the angles between the wave normals and the y axis in medium 0 and 1 respectively (see Fig. 1) and

$$v_m = k_m \cos\theta_m = k_m C_m \quad , \quad m=0,1 \tag{2.14a}$$

where $k_i = \omega\sqrt{\mu_i\varepsilon_i}$ is the wave number for medium i. In view of Snell's law the propagation coefficient u is

$$u = (k_i^2 - v_m^2)^{1/2} = k_m \sin\theta_m = k_m S_m \tag{2.14b}$$

To obtain the differential equations for the field transforms H_m^P and E_m^P the complete expansions (2.4)-(2.7) are substituted into Maxwell's equations for the transverse field components and use is made of the orthogonality relationships (BAHAR 1972), Green's theorem and the exact boundary conditions (2.2) and (2.3). These field transforms are expressed in terms of the forward and backward wave amplitudes a_n^P and b_n^P respectively.

$$H_n^P = a_n^P \pm b_n^P \quad \text{and} \quad E_n^P = a_n^P \mp b_n^P \;, \quad P = V,H, \quad n=0,1,s. \tag{2.15}$$

where the upper and lower signs are used for P = V and H respectively. Thus Maxwell's equations are transformed into the following generalized telgraphist's equations

$$\frac{-d}{dx} a_n^P(x,v) - iua_n^P(x,v) = \sum_{v'} \left\{ S_{PP}^{BA}(n,n',v,v')a_{n'}^P(x,v') + S_{PP}^{BB}(n,n',v,v')b_{n'}^P(x,v') + J_n^P/2 \right. \tag{2.16a}$$

$$\frac{-d}{dx} b_n^P(x,v) + iub_n^P(x,v) = \sum_{v'} \left\{ S_{PP}^{AA}(n,n',v,v')a_{n'}^P(x,v') + S_{PP}^{AB}(n,n',v,v')b_{n'}^P(x,v') - J_n^P/2 \right. \tag{2.16b}$$

in which J_n^P are the line source transforms

$$J_n^P(x,v) = \int_{-\infty}^{\infty} J_\ell(x,y) N_n^P(v) \psi_n^P(v,y) dy, \quad \begin{cases} \ell = m \text{ for } P=V \\ \ell = e \text{ for } P=H \end{cases} \tag{2.17}$$

The transmission and reflection scattering coefficients respectively are (BAHAR 1973a,b)

$$S_{PP}^{BA}(n,n',v,v') = S_{PP}^{AB}(n,n',v,v') = \frac{1}{2}\left[\frac{N_n^P(v)}{N_{n'}^P(v')} G^P(n',n,v',v) - G^P(n,n',v,v')\right] \tag{2.18a}$$

$$S_{PP}^{AA}(n,n',v,v') = S_{PP}^{BB}(n,n',v,v') = \frac{1}{2}\left[\frac{N_n^P(v)}{N_{n'}^P(v')} G^P(n',n,v',v) + G^P(n,n',v,v')\right] \tag{2.18b}$$

in which for the vertically polarized waves

$$G^V(n,n',v,v') = \left[\frac{Z^V(v',y)N_n^V(v)}{v^2 - v'^2} \left\{ \psi_{n'}^V(v',y) \frac{\partial^2}{\partial x \partial y} \psi_n^V(v,y) - \frac{\partial}{\partial y} \psi_{n'}^V(v',y) \frac{\partial}{\partial x} \psi_n^V(v,y) \right\}\right]_{h^-}^{h^+} \tag{2.19}$$

For the horizontally polarized waves V is replaced by H and Z^V by Y^H in (2.19). To simplify the expression (2.19), use the differential equation and the boundary conditions for the basis functions $\psi_n^P(v,y)$ and note that

$$\frac{\partial}{\partial x} \psi_n^P(v,h) = \left[\frac{\partial}{\partial x} \psi_n^P(v,y) + \frac{\partial}{\partial y} \psi_n^P(v,y) \frac{dh}{dx}\right]_{y=h} \tag{2.20}$$

and

$$\frac{\partial^2}{\partial x \partial y} \psi_n^P(v,h) = \left[\frac{\partial^2}{\partial x \partial y} \psi_n^P(v,y) + \frac{\partial^2}{\partial y^2} \psi_n^P(v,y) \frac{dh}{dx}\right]_{y=h} \tag{2.21}$$

Thus it can be shown that for the radiation term (n=n'=0)

$$G^V(0,0,v,v') = \frac{R^V(v)\psi_o^V(v,h)\psi_o^V(v',h)}{2\pi(v^2 - v'^2)} \frac{u'}{u} \frac{dh}{dx} \left\{ v_o^2 + v_1^2 \frac{\varepsilon_o}{\varepsilon_1} + \left(1 - \frac{\varepsilon_o}{\varepsilon_1}\right) \frac{\varepsilon_o}{\varepsilon_1} v_1 v_1' \right\} \tag{2.22}$$

The corresponding expression for the horizontally polarized waves is obtained by interchanging ε and μ.

3. Iterative Solutions for the Scattered Radiation Fields When the Slope of the Rough Surface is Small

To obtain simple expressions for the scattered radiation fields that can be readily used by engineers, an iterative approach has been employed to solve the coupled differential equations for the wave amplitudes (2.16) (BAHAR 1978). Thus the first-order iterative solutions are obtained by ignoring the transmission and reflection scattering coefficients in (2.16). The second-order iterative solutions are obtained by substituting the first-order solution for a_n^P and b_n^P on the right hand side of (2.16). The scattered radiation fields are obtained by substituting these second-order solutions for the field transforms into the expressions $H_o^V(x,y)$ (2.4a) and $E_o^H(x,y)$ (2.6a) for the vertically and horizontally polarized waves respectively. The steepest descent method is used to evaluate the infinite integrals when the source and receiver are far from the irregular boundary (see Fig. 1).

For a magnetic line source at (x_o,y_o) of intesnsity J_m(volts),

$$\bar{J}_m = J_m\bar{a}_z = I_m\delta(x-x_o)\delta(y-y_o)\bar{a}_z \tag{3.1}$$

in which $\delta(\alpha-\alpha_o)$ is the Dirac delta function. The iterative solution for the vertically polarized scattered radiation field is,

$$H_z^r(x,y) = -\frac{I_m ik_o L}{2\pi\eta_o(\rho\rho_o)^{1/2}}\exp[-ik_o(\rho_o+\rho)]C_o^iF^V(\theta^f,\theta^i)I(C^f,C^i,h,L),\ \pi/2 < \theta_o^f,\theta_o^i < \pi/2 \tag{3.2a}$$

in which $\rho_o = (x^2+y^2)^{1/2}$ and $\rho = (x_o^2+y_o^2)^{1/2}$ are the distances of the source and the receiver from the origin and the incident wave at the origin is

$$H_o^i = \frac{-I_m\omega\varepsilon_o}{2(2\pi\ k_o\rho_o)^{1/2}}\exp[-i(k_o\rho_o - \pi/4)]\ , \tag{3.2b}$$

$$F^V(\theta^f,\theta^i) = \frac{2C_o^f[\mu_r\ C_1^fC_1^i - S_o^fS_o^i)(1-1/\varepsilon_r) + (1-\mu_r)]}{(C_o^i + C_1^i\eta_r)(C_o^f + C_1^f\eta_1)(C_o^i + C_o^f)} \tag{3.3}$$

where C_o^i and S_o^i are the cosine and sines of the angle of incidence θ_o^i and the corresponding expressions for medium 1 ($y < h$) are denoted by the subscript 1. Similarly C_m^f and S_m^f are related to the scatter angle θ_o^f. The relative quantities with the subscripts r are dimensionless.

$$\varepsilon_r = \varepsilon_1/\varepsilon_o,\quad \mu_r = \mu_r/\mu_o,\quad \eta_r = \eta_1/\eta_o \tag{3.4}$$

Furthermore

$$I(C^f,C^i,h,L) = \frac{1}{2L}\int_{-L}^{L}\exp\left\{i(C_o^f+C_o^i)k_oh + i(S_o^f-S_o^i)k_ox\right\}dx \equiv \frac{1}{2L}\int_{-L}^{L}\exp\left[i\phi(x)\right]dx \tag{3.5}$$

in which h(x) is the height of the irregular boundary with respect to the reference surface $y = 0$ and 2L is the length of the rough surface in the x direction.

For an electric line source at (x_o,y_o) of intensity J_e(Amps),

$$\bar{J}_e = J_e\bar{a}_z = I_e\delta(x-x_o)\delta(y-y_o)\ \bar{a}_z \tag{3.6}$$

The iterative solution for the horizontally polarized scattered radiation field is

$$E_z^r = -\frac{I_e ik_o L\ \eta_o}{2\pi(\rho\rho_o)^{1/2}}\exp[-ik_o(\rho_o+\rho)]C_o^iF^H(\theta^f,\theta^i)I(\theta^f,\theta^i,h,L)\ \pi/2 \le \theta_o^f,\theta_o^i \le \pi/2 \tag{3.7a}$$

in which $I(C^f,C^i,h,L)$ is given by (3.5) and the incident plane wave at the origin is

$$E_o^i = -\frac{I_e\omega\mu_o}{2(2\pi\ k_o\rho_o)^{1/2}}\exp[-i(k_o\rho_o - \pi/4)] \tag{3.7b}$$

$$F^H(\theta^f,\theta^i) = \frac{2C_o^f[(\varepsilon_r\ C_1^fC_1^i - S_o^fS_o^i)(1-1/\mu_r)+(1-\varepsilon_r)]}{(C_o^i+C_1^i/\eta_r)(C_o^f+C_1^f/\eta_r)(C_o^i+C_o^f)} \tag{3.8}$$

The above solutions for the scattered vertically and horizontally polarized radiation fields are consistent with reciprocity relations in electromagnetic theory. Thus the above expressions are invariant to the following transformations

$$\rho_o \leftrightarrow \rho\ ,\ \theta_m^i \leftrightarrow -\theta_m^f \tag{3.9}$$

The above results are also consistent with duality relations in electromagnetic theory. Thus (3.2) and (3.7) are related through the following transformations.

$$I_e \to I_m,\ I_m \to -I_e\ ,\quad \varepsilon_m \leftrightarrow \mu_m\ ,\ \eta_m \leftrightarrow 1/\eta_m\ ,\ \bar{E} \to \bar{H},\ \bar{H} \to -\bar{E} \tag{3.10}$$

The results presented here for the scattered radiation fields reduce to those derived earlier for the special case $\mu_o = \mu_1$ (BAHAR 1978, BAHAR and RAJAN 1979). They have been shown to yield the same

polarization dependence for the backscatter cross section as the results obtained using a perturbational approach (RICE, 1951; WRIGHT, 1966; BARRICK and PEAKE 1968).

Using a physical optics approach (BECKMANN and SPIZZICHINO 1964), it has been shown that the function F^P in (3.3) and (3.8) is replaced by

$$F^P(\theta^f,\theta^i) = R_o^P(C^i)F_o(\theta^f,\theta^i) \qquad P = V \text{ or } H \tag{3.11a}$$

where

$$F_o(\theta^f,\theta^i) = \frac{\cos\left[(\theta_o^f + \theta_o^i)/2\right]}{\cos\theta_o^i \cos\left[(\theta_o^f - \theta_o^i)/2\right]} \tag{3.11b}$$

Thus for perfectly conducting surface $|F^P(\theta^f,\theta^i)|$ is independent of polarization. The full wave solutions and the physical optics solutions have been compared for reciprocity, backscatter and for angles of incidence near the Brewster angle and near grazing angles.

The iterative solutions derived from the full wave analysis of the problem yield the proper polarization dependence for backscatter for $dh/dx << 1$ (WRIGHT 1966, BARRICK and PEAKE 1968). However, for $|dh/dx| > 1$ the iterative full wave solutions fail to agree with the physical optics solutions even for the perfectly conducting case. At very high frequencies the major contributions to the scattered radiation fields come only from narrow regions of the rough surface where the phase $\phi(x)$ (3.5) is stationary. Thus

$$\frac{d\phi}{dx} = (C_o^f + C_o^i)k_o h' + (S_o^f - S_o^i)k_o = 0 \tag{3.12a}$$

On substituting

$$h' = dh/dx = \tan\gamma \tag{3.12b}$$

(3.12) reduces to

$$\sin(\theta^i - \gamma_s) = \sin(\theta^f + \gamma_s) \tag{3.13a}$$

or

$$\gamma_s = (\theta^i - \theta^f)/2 \tag{3.13b}$$

where γ_s is the value of γ at points of stationary phase x_s.

Since the iterative approach is suitable only for $|h'| << 1$, it provides good results only for $\gamma_{max} << 1$. Thus the agreement between the iterative-full wave solutions and the physical optics solutions is limited to near specular scattering where $F^P(\theta^i,\theta^i) = R_o^P(\theta^i)$.

In the next section we remove the limitation on h' resulting from the iterative approach used to solve the coupled wave amplitudes (2.16). This is done while preserving the relatively simple form of the expressions for the scattered radiation fields. The results will be used to resolve the discrepancies between the physical optics solutions and the perturbational solutions. Other interesting topics such as energy conservation, reciprocity, shadowing, scattering in the downward direction ($\theta_o^f > \pi/2$) and multiple scattering are also considered.

4. Full Wave Solutions for Scattered Radiation Fields from Rough Surface with Small or Large Slopes

The generalized telegraphist's equations (2.16) obtained from the full wave analysis are rigorous. The limitations on the results presented in Section 3 are due to iterative methods used to solve (2.16). In order to remove these restrictions and to apply the results of the full wave analysis to rough surfaces with small or large slopes, several different methods have been considered to solve (2.16). The iterative method could be improved by using a better first-order iterative solution or by seeking a third-order iterative solution. Alternatively, the continuous spectrum for the radiation fields ($0 < v_o < \infty$) may be discretized for the propagating waves ($0 < v_o < k_o$) and the resulting set of first-order differential equations for the wave amplitudes can be solved numerically. In order to preserve the relatively simple form of the solutions presented in Section 3, a different procedure has been followed here.

Fields in waveguides with nonuniform cross sections or bends with varying curvatures may be represented in terms of different complete expansions (BAHAR 1966, 1968, 1969). However, it has been shown that solutions employing local modal expansions that most closely conform with the varying features of the waveguides, provide the best basis for the analysis of problems. When the chosen basis conforms very closely with the irregular boundary of the waveguide, it is necessary to consider fewer scattered modes and simple iterative solutions for the coupled wave amplitudes provide accurate results even for large variations in slope or curvature.

For instance for multimode waveguides with nonuniform cross-sections, it is preferable to represent the fields in terms of modes for radial waveguides rather than modes for rectangular waveguides (BAHAR and CRAIN 1968; BAHAR and GOVINDARAJAN 1974, 1976). Similarly for waveguide bends with nonuniform curvatures an analysis based on annular modal expansion of the fields is better than the analysis based on modal expansions for rectangular waveguides (BAHAR and GOVINDARAJAN, 1973, 1977).

Thus in this work we regard the rough surface as a continuum of elementary inclined strips of varying slope and height rather than a continuum of elementary horizontal strips of varying height. The contribution to the total scattered field from an inclined strip is obtained from the full wave analysis presented in Section 3 after making the appropriate coordinate transformations. In this way the restriction on the maximum slope of the rough surface is removed while preserving all the advantages of using the full wave approach. Furthermore, the final expressions for the solutions are practically as simple to use as the expressions presented earlier.

The contribution to total scattered field from a horizontal strip at x,y of width dx is proportional to

$$dS^P(x) = \cos\theta_o^i F^P(\theta^f,\theta^i)\exp\{i\phi(x)\}dx/2L \equiv C_o^i F^P(C^f,\theta^i)dI(x) \tag{4.1}$$

in which F^P (P = V,H) is given by (3.3) or (3.8) and $\phi(x)$ is defined in the equation for $I(C^f,C^i,h,L)$(3.5). The corresponding expression for $dS^P(x)$ for an inclined strip at (x,y) of length

$$d\ell = (dx^2 + dy^2)^{1/2} = \left[1 + (h')^2\right]^{1/2} dx = \frac{dx}{\cos\gamma} \tag{4.2}$$

and gradient

$$h' = dh/dx = \tan\gamma \tag{4.3}$$

is given by replacing x and y = h by ξ and η (see Fig. 2)

$$\xi = x\cos\gamma + y\sin\gamma \tag{4.4a}$$

$$\eta = -x\sin\gamma + y\cos\gamma \tag{4.4b}$$

Furthermore, the incident and scatter angles with respect to the reference plane y = 0, θ_o^i and θ_o^f respectively are replaced by the incident and scatter angles $\theta_o^{i\gamma}$ and $\theta_o^{f\gamma}$ with respect to inclined strip. Thus,

$$-\pi/2 < \theta_o^{i\gamma} = \theta_o^i - \gamma < \pi/2, \quad -\pi/2 < \theta_o^{if} = \theta_o^f + \gamma < \pi/2 \tag{4.5}$$

The corresponding angles $\theta_1^{i\gamma}$ and $\theta_1^{f\gamma}$ for y < h are given by Snell's law

$$k_1 \sin\theta_1^{i\gamma} = k_o \sin\theta_o^{i\gamma} \text{ and } k_1 \sin\theta_o^f = k_o \sin\theta_o^{f\gamma} \tag{4.6}$$

Substitute (4.4) and (4.5) into the expression for $\phi(x)$ (3.5) to get

$$\phi^\gamma(x) = \left[\cos(\theta^f+\gamma) + \cos(\theta^i-\gamma)\right] k_o(-x\sin\gamma + y\cos\gamma)$$

$$+ \left[\sin(\theta^f+\gamma) - \sin(\theta^i-\gamma)\right] k_o(x\cos\gamma + y\sin\gamma) \tag{4.7}$$

After some straightforward trigonometric manipulations it can be shown that $\phi(x)$ is invariant to the transformations (4.4) and (4.5),

$$\phi^\gamma(x) = \phi(x) \tag{4.8}$$

Thus $dS^P(x)$ (4.1) for an inclined plane is

$$dS^P(x) = \cos\theta_o^{i\gamma} F^P(\theta^{f\gamma},\theta^{i\gamma})\exp\{i\phi(x)\}dx/2L\cos\gamma, \quad -\pi/2 < \theta_o^{f\gamma},\theta_o^{i\gamma} < \pi/2 \tag{4.9}$$

and the total scattered radiation fields are given by

$$\left.\begin{matrix} H_z^r(x,y) \\ \\ E_z^r(x,y) \end{matrix}\right\} = \frac{-ik_o L\exp\left[-ik_o(\rho_o+\rho)\right]}{2\pi(\rho\,\rho_o)^{1/2}} \times \left\{\begin{matrix} \dfrac{I_m}{\eta_o} S^V \\ \\ I_e\eta_o S^H \end{matrix}\right. \equiv A^P S^P \tag{4.10}$$

in which

$$S^P \equiv \int_{-L}^{L} dS^P(x), \quad P = V,H \tag{4.11}$$

The specularly reflected field from a flat $\{h(x) = 0\}$ perfectly conducting boundary is given by $\pm A^P\cos\theta_o^i$.

5. Comparison of the Full Wave Solutions with the Perturbational and Physical Optics Solutions and the Reciprocity, Duality and Realizability Relationships

For h << 1 the full wave solutions (4.10) reduce to the iterative solutions (3.3) or (3.7) which are in agreement with the perturbational solutions for the backscatter cross sections (RICE 1951; WRIGHT 1966; BARRICK and PEAKE 1968). At very high quasi optical frequencies the major contributions to the total scattered field come from narrow regions about the stationary points x_s where the slope angle γ_s is given by (3.13). Thus the high frequency approximation for S^P is given by making the following substitutions

$$\gamma \to \gamma_s = (\theta_o^i - \theta_o^f)/2 \tag{5.1a}$$

$$\left.\begin{matrix} \theta_o^{f\gamma} \\ \theta_o^{i\gamma} \end{matrix}\right\} \to \theta_o^{f\gamma_s} = \theta_o^{i\gamma_s} = (\theta_o^i + \theta_o^f)/2 \equiv \theta_o^{\gamma_s} \tag{5.1b}$$

where $\theta_o^{\gamma_s}$ is the local incident or scatter angle at the stationary points. The corresponding expressions for

$$\left.\begin{matrix}\theta_1^{f\gamma}\\ \\ \theta_1^{i\gamma}\end{matrix}\right\} \rightarrow \theta_1^{f\gamma}s = \theta_1^{i\gamma}s = \theta_1^{\gamma s} \tag{5.1c}$$

are given by Snell's law. Thus it can be shown that

$$S^P \rightarrow S^P_\infty = \frac{\cos\left[(\theta_o^i + \theta_o^f)/2\right]}{\cos\left[(\theta_o^i - \theta_o^f)/2\right]} R_o^P\left[(\theta_o^i + \theta_o^f)/2\right] I(\theta^f, \theta^i, h, L) = \cos\theta_o^i F_o(\theta^f, \theta^i) R_o^P\left[(\theta_o^i + \theta_o^f)/2\right] I(\theta^f, \theta^i, h, L) \tag{5.2}$$

Thus for perfectly conducting boundaries the high frequency approximation for the full wave solution is in total agreement with the physical optics solution (3.11) (BECKMANN and SPIZZICHINO, 1963). However, for the non-perfectly conducting case, the full wave solutions (which are in agreement with the reciprocity relationship) contain the factor $R_o^P\left[(\theta_o^i + \theta_o^f)/2\right]$ instead of $R_o^P(\theta_o^i)$ in the physical optics solution (3.11). This result derived from the full wave solutions is consistent with the treatment of "Rough surface scattering based on the specular point theory" (BARRICK 1968). Note that the general full wave expression for the scattered radiation fields (4.10) as well as the small slope and high frequency approximations of the full wave solutions are invariant under the transformations (3.9) and (3.10). They therefore satisfy the reciprocity and duality relationships in electromagnetic theory. Furthermore, for a plane inclined at an angle γ and of length

$$2\ell = 2L/\cos\gamma \tag{5.3}$$

the specularly scattered radiation field $\left[\theta_o^{f\gamma} = \theta_o^{i\gamma} = (\theta_o^i + \theta_o^f)/2\right]$ is proportional to

$$2k_o\, LS^P \rightarrow 2k_o \ell \cos\theta_o^{i\gamma} R_o^P(\theta_o^{i\gamma}) \tag{5.4}$$

since $F^P(\theta^{f\gamma} = \theta^{i\gamma}) = R_o^P(\theta_o^{i\gamma})$ and $I(\theta^{f\gamma}, \theta^{i\gamma}, h, L) = 1$. Thus for the perfectly conducting case, the back scattered radiation field normal to the inclined plane ($\theta_o^{i\gamma} = 0$) is proportional to $2k_o\ell$ and the full wave solutions satisfy energy conservation for arbitrarily oriented inclined planes. The iterative solutions of Section 3 or the perturbational solutions (BARRICK and PEAKE 1968) do not possess this property.

6. Behavior of the Full Wave Solutions for θ_o^i Near the Brewster Angle θ_o^B, Grazing Incident and Scatter Angles, Specular ($\theta_o^f = \theta_o^i$) and Backscatter ($\theta_o^f = -\theta_o^i$) Angles

The full wave solutions (4.10) do not vanish even if θ_o^i and/or θ_o^f are equal to the Brewster angle $\left[R_o^P(\theta_o^B) = 0\right]$. The high frequency approximation of (4.10, (5.2), vanishes when

$$(\theta_o^i + \theta_o^f)/2 = \theta_o^B \tag{6.1}$$

and not necessarily when $\theta_o^i = \theta_o^B$ as derived from the physical optics solutions (3.11).

For the iterative, perturbational and physical optics solutions

$$-\pi/2 < \theta_o^i < \pi/2 \quad \text{and} \quad -\pi/2 < \theta_o^f < \pi/2 \tag{6.2}$$

However, for the full wave solutions

$$-\pi/2 < \theta^{i\gamma} = \theta_o^i - \gamma < \pi/2 \text{ and } -\pi/2 < \theta_o^{f\gamma} = \theta_o^f + \gamma < \pi/2 \tag{6.3}$$

The differential scattered radiation field $A^P dS^P$ vanishes when the incident or scatter angles are grazing with respect to the local tangent plane

$$\theta_o^{i\gamma} \rightarrow \pm\pi/2,\ \theta_o^{f\gamma} \rightarrow \pm\pi/2 \tag{6.4}$$

However the total scattered radiation field does not necessarily vanish for θ_o^i and/or θ_o^f equal to $\pm\pi/2$. For very good conducting boundaries $|\varepsilon_r| \rightarrow \infty$, with $\mu_r = 1$

$$dS^P(x) = dI(x)\begin{cases} 2(1 - S_o^{f\gamma}S_o^{i\gamma})/(C_o^{i\gamma} + C_o^{f\gamma})\cos\gamma & P = V \quad (6.5a)\\ -2\, C_o^{f\gamma}C_o^{i\gamma}/(C_o^{i\gamma} + C_o^{f\gamma})\cos\gamma & P = H \quad (6.5b)\end{cases}$$

For locally grazing angles, (6.4), $dS^P(x)$ (4.9) vanishes for both P = V and P = H, thus (6.5a) cannot be used for good conductors near grazing angles. For very good conducting boundaries the high frequency approximations for $|dS^P(x)|$ is independent of polarization and

$$dS^P(x) = \pm\frac{\cos\left[(\theta_o^i + \theta_o^f)/2\right]}{\cos\left[(\theta_o^i - \theta_o^f)/2\right]} dI(x), \begin{cases} + \text{ for } P = V\\ - \text{ for } P = H\end{cases} \tag{6.6}$$

For the specular case $\theta_o^i = \theta_o^f$ (6.5) reduces to

$$dS^P(x) = \exp\left[i2k_o C_o^i h\right]dx\begin{cases}\cos\theta_o^i + \tan^2\gamma(1+\cos^2\theta_o^i)/\cos\theta_o^i \\ -\cos\theta_o^i + \tan^2\gamma(1-\cos^2\theta_o^i)/\cos\theta_o^i\end{cases} \tag{6.7}$$

and (6.6) the high frequency approximation reduces to

$$dS^P(x) = \pm\exp\left[i2k_o\, C_o^i h\right]dx\,\cos\theta_o^i \tag{6.8}$$

For the specular case, the slope vanishes at the stationary points and $\gamma_c = 0$.

The backscattered radiation fields are obtained by substituting $\theta_o^f = -\theta_o^i$, thus $\theta_o^{f\gamma} = -\theta_o^{i\gamma}$ and (6.5) reduces to

$$dS^P(x) = \pm\exp\left[i2k_o(C_o^i h - S_o^i x)\right]dx\begin{cases}(1+\sin^2\theta_o^{i\gamma})/\cos\theta_o^{i\gamma}\cos\gamma \\ \cos\theta^{i\gamma}/\cos\gamma\end{cases} \tag{6.9}$$

The corresponding high frequency approximation is obtained by noting that $\theta_o^{i\gamma_s} \to 0$ and $\gamma_s \to \theta_o^i$, thus

$$dS^P(x) = \pm\exp\left[i2k_o(C_o^i h - S_o^i x)\right]dx/\cos\theta_o^i \tag{6.10}$$

Thus the high frequency approximation for $|dS^P|$ is independent of polarization.

It is interesting to note that the full wave solutions (4.10) can be used even when $\gamma \to \pi/2$ and $\cos\gamma \to 0$ since

$$dx/\cos\gamma = d\ell \tag{6.11}$$

the differential distance along the rough surface (4.2) is integrable even for $\cos\gamma \to 0$.

7. Downward Scattering, Shadowing by Rough Surfaces, Periodic Structures and Random Rough Surfaces

The differential scattered radiation fields are given by $A^P dS^P(x)$, (4.10) for

$$\gamma - \pi/2 < \theta_o^i < \gamma + \pi/2 \tag{7.1a}$$

and

$$-\gamma - \pi/2 < \theta_o^f < -\gamma + \pi/2 \tag{7.1b}$$

If the boundary $h(x)$ is single valued, $-\pi/2 < \gamma < \pi/2$. Thus in general $|\theta_o^f| \gtrless \frac{\pi}{2}$ and the full wave solutions also account for downward scattering. The expressions for $dS^P(x)$ vanish for $\theta_o^{i\gamma} = \theta_o^i - \gamma \to \pm\pi/2$ or $\theta_o^{f\gamma} = \theta_o^f + \gamma \to \pm\pi/2$ for both polarizations (P = V, H). For $\theta_o^i > 0$ the shadow region begins at x_1^i (see Fig. 3) where

$$\gamma(x_1) = \theta_o^i - \pi/2 \tag{7.2a}$$

and for $\theta_o^i < 0$ the shadow region begins at x_o^i

$$\gamma(x_1^i) = \theta_o^i + \pi/2 \tag{7.2b}$$

Thus

$$\tan\gamma(x_1^i) = h'(x_1^i) = -\cot\theta_o^i \tag{7.2c}$$

The shadow region ends at x_2^i where

$$\tan\theta_o^i = (x_2^i - x_1^i)/\left[h(x_1^i) - h(x_2^i)\right] \tag{7.3a}$$

thus

$$x_2^i - x_1^i = \left[h(x_2^i) - h(x_1^i)\right]/\tan\gamma(x_1^i) \tag{7.3b}$$

The entire illuminated region will not necessarily contribute to the scattered radiation fields at the receiver in view of (7.1b). The portion of the rough surface lying between x_1^f and x_2^f which is not visible to the receiver will not contribute to the scattered radiation field at the receiver, even if it is illuminated by the source. Similar to x_1^i and x_2^i it can be shown that x_1^f and x_2^f are given by

$$\tan\gamma(x_1^f) = h'(x_1^f) = \cot\theta_o^f \tag{7.4a}$$

and

$$x_2^f - x_1^f = \left[h(x_2^f) - h(x_1^f)\right]/\tan\gamma(x_1^f) \tag{7.4b}$$

Thus, the full wave solutions for the scattered radiation fields $A^P S^P$ vanish in a continuous manner as the receiver moves across a shadow boundary. To determine the fields near the shadow boundary and inside the shadow region, it is necessary to account for the coupling between the incident radiation fields and the lateral and surface wave terms of the full wave expansions (BAHAR 1972, 1977).

Since the full wave analysis accounts for both upward and downward scattering, it can be used to determine the radiation fields due to multiple scattering. Thus if regions of the rough surface that contribute to multiple scattering are sufficiently distant (such that the steepest descent method is applicable), the radiation field initially scattered in the direction θ_o^f (4.10) is regarded as a plane

wave incident at an angle $\theta_o^i = \pi - \theta_o^f$ for the purpose of evaluating the multiple scattered wave.

To apply the full wave approach to periodic structures, it is necessary to multiply the expression for the scattered radiation field from the element of length 2L, by the N element array factor (BAHAR 1978).

$$F_A(\theta^f,\theta^i) = \sin\left[Nk_oL(S_o^f - S_o^i)\right]/\sin\left[k_oL(S_o^f - S_o^i)\right] \tag{7.5a}$$

Thus $F_A \to N$ at the grating angles θ_{om}^f, where

$$\sin\theta_{om}^f = \sin\theta_o^i + m\lambda/2L \tag{7.5b}$$

For random rough surfaces, both the height and the slope $h' = \tan\gamma$ in the expression for the scattered radiation field (4.10) are random variables. Thus in general in order to obtain the average value for S^P (4.10) and its variance, $< S^P >$ and $D\{S^P\}$ respectively, it is necessary to know the statistics of both random variables. However, for surfaces with small slopes, γ can be set equal to zero in (4.9). In this case we obtain the second order iterative solutions.

$$< S^P > = \cos\theta_o^i\, F^P(\theta_o^f,\theta_o^i)\chi(v_y)\,\mathrm{sinc}\, v_xL \tag{7.6a}$$

in which $\chi(v_y)$ is the one dimensional characteristic function

$$\chi(v_y) = \int_{-\infty}^{\infty} w(h)\exp(iv_yh)dh \tag{7.6b}$$

where w(h) is distribution function for the random variable h and

$$v_x = k_o(S_o^i - S_o^f),\; v_y = -k_o(C_o^i + C_o^f) \tag{7.6c}$$

If the two random variables h and h' can be assumed to be totally uncorrelated

$$< S^P > = < \cos\theta_o^{i\gamma}\, F^P(\theta^{f\gamma},\theta^i)> \chi\,(v_y)\,\mathrm{sinc}\, v_xL \tag{7.7}$$

It is not necessary to know the statistics of the slope h' when the high frequency approximation of the full wave solutions are used even for the non-perfectly conducting case. Thus using (5.2)

$$< S^P > = \frac{\cos[(\theta_o^i + \theta_o^f)/2]}{\cos[(\theta_o^i - \theta_o^f)/2]}\, R_o^P[(\theta_o^i + \theta_o^f)/2]\chi(v_y)\,\mathrm{sinc}\, v_xL \tag{7.8}$$

Thus unlike the physical optics solutions, (7.8) is consistent with reciprocity for all values of $R_o^P[(\theta_o^i + \theta_o^f)]$. For the specular case ($\theta_o^f = \theta_o^i$) (7.8) reduces to (7.6). *However in general, the magnitude of* $< S^P >$ is polarization dependent even for perfectly conducting rough surfaces except for the high frequency limit.

Similarly when either the small slope or the high frequency approximations are used, the expressions for the variance of S^P can be considerably simplified. For the small slope approximation

$$D\{S^P\} = \left|\cos\theta_o^i\, F^P(\theta_o^f,\theta_o^i)\right|^2 D\{I\} \tag{7.9a}$$

where

$$D\{I\} = \frac{1}{2L}\int_{-L}^{L}\exp(iv_x\tau)\left[\chi_2(v_y,-v_y) - \chi(v_y)\chi^*(v_y)\right]d\tau \tag{7.9b}$$

in which χ_2 is the two dimensional characteristic function

$$\chi_2(v_y,-v_y) = \int_{-\infty}^{\infty}\int_{-\infty}^{\infty} W(h_1,h_2)\exp\left[iv_y(h_1-h_2)\right]dh_1\, dh_2 \tag{7.9c}$$

and $W(h_1,h_2)$ is the joint distribution function of h. The symbol * denotes complex conjugate.

Using the high frequency approximation (5.2) one gets

$$D\{S^P\} = \left|\frac{\cos[(\theta_o^i + \theta_o^f)/2]}{\cos[(\theta_o^i - \theta_o^f)/2]}\, R_o^P[(\theta_o^i + \theta_o^f)/2]\right|^2 D\{I\} \tag{7.10}$$

Thus $D\{S^P\}$ is independent of polarization for perfectly conducting surfaces only in the high frequency limit.

8. Concluding Remarks

The full wave solutions derived in this paper for the vertically and horizontally polarized scattered radiation fields are valid for irregular boundaries with arbitrary slope $h'(x) = \tan[\gamma(x)]$, where $-\frac{\pi}{2} \le \gamma(x) \le \pi/2$. They are shown to agree with the results obtained using a perturbational approach (RICE 1951, WRIGHT 1966, BARRICK and PEAKE 1968) when the slope must be assumed to be very small and γ is *set equal to zero in the full wave analysis. Furthermore, for very high frequencies the full wave* solutions are shown to agree with the physical optics solutions when the irregular boundary is perfectly conducting. Thus the full wave solutions demonstrate how the backscatter cross-section is in general dependent on the polarization of the incident and scattered waves except in the high frequency limit for perfectly conducting boundaries. In the optical limit only narrow regions about the stationary points of

the irregular boundary contribute significantly to the scattered radiation field. As the frequency is lowered, the region that contributes most to the scattered field grows. This transition from optical to very low frequencies is covered in a continuous manner by the full wave solutions. The expressions for the full wave solutions are given in the same form as the earlier solutions for ease of comparison and they can be evaluated numerically with essentially the same algorithm.

The full wave solutions are shown to satisfy energy conservation, reciprocity and duality relationships in electromagnetic theory. Special consideration has also been given to examining the behavior of the scattered radiation fields when the rough surface is excited by a plane wave incident at the Brewster angle and for grazing incident and scatter angles. Specular scattering and backscatter are also considered in detail.

Since the full wave solutions account for both upward and downward scattering, $\left(-\pi < \theta_o^f < \pi\right)$ shadowing and multiple scattering can also be taken into consideration. The full wave solutions for the scattered radiation fields vanish in a continuous manner as the receiver moves across a shadow boundary. Near the shadow boundary and in the shadow region it is necessary to account for the coupling between the radiation fields and the lateral and surface wave contributions to the full wave solutions (BAHAR 1977).

Applications of the full wave solutions to periodic structures and to random rough surfaces is also presented. Unlike the physical optics solutions, the high frequency approximation of the full wave analysis is independent of the slope h' and satisfies reciprocity even for the finite conducting case.

Since the full wave solutions are based on a rigorous analysis of the problem of rough surface scattering and are not limited to small slopes or to high frequencies, and since the same expression for the radiation fields can be used throughout, they also provide a more convenient and accurate basis for the analysis of problems of inverse scattering and remote sensing over a wide frequency range.

The full wave approach can also be applied to problems in which the permittivity ε and the permeability μ are functions of x. Thus problems of scattering due to medium inhomogeneities as well as boundary irregularities can be analyzed. Furthermore, the full wave approach can be used when the unit vector normal to the rough surface is not in the plane of incidence and the scattered waves are depolarized (BAHAR 1973a,b).

9. References

BAHAR, E., 1966, "Propagation of VLF Radio Waves in a Model Earth Ionosphere Waveguide of Arbitrary Height and Finite Surface Impedance Boundary: Theory and Experiment," Radio Science, Vol. 1, No. 8, pp. 925-938.

BAHAR, E., 1968, "Wave Propagation in Nonuniform Waveguides with Large Flare Angles and Near Cutoff," IEEE Transactions on Microwave Theory and Techniques, Vol. MTT-16, No. 8, pp. 503-510.

BAHAR, E., 1969, "Fields in Waveguide Bends Expressed in Terms of Coupled Local Annular Waveguide Modes," IEEE Transactions on Microwave Theory and Techniques, Vol. MTT-17, No. 4, pp. 210-217.

BAHAR, E., 1972a, "Generalized Fourier Transform for Stratified Media," Canadian Journal of Physics, Vol. 50, No. 24, pp. 3123-3131.

BAHAR, E., 1972b, "Radio Wave Propagation in Stratified Media with Nonuniform Boundaries and Varying Electromagnetic Parameters--Full Wave Analysis," Canadian Journal of Physics, Vol. 50, No. 24, pp. 3132-3142.

BAHAR, E., 1973a, "Depolarization of Electromagnetic Waves Excited by Distribution of Electric and Magnetic Sources in Inhomogeneous Multilayered Structures of Arbitrary Thickness--Generalized Field Transforms," Journal of Mathematical Physics, Vol. 14, No. 11, pp. 1502-1509.

BAHAR, E., 1973b, "Depolarization of Electromagnetic Waves Excited by Distributions of Electric and Magnetic Sources in Inhomogeneous Multilayered Structures of Arbitrarily Varying Thickness--Full Wave Solutions," Journal of Mathematical Physics, Vol. 14, No. 11, pp. 1510-1515.

BAHAR, E., 1977, "Coupling Between Guided Surface Waves, Lateral Waves and the Radiation Fields by Rough Surfaces--Full Wave Solutions," IEEE Transactions on Microwave Theory and Techniques, Vol. MTT-25, No. 11, pp. 923-931.

BAHAR, E., 1978, "Full Wave and Physical Optics Solutions for Scattered Radiation Fields by Rough Surfaces--Energy and Reciprocity Relationships," IEEE Transactions on Antennas and Propagation, Vol. AP-26, pp. 603-614.

BAHAR, E. and G. CRAIN, 1968, "Synthesis of Multimode Waveguide Transition Sections," Proceedings of IEE, Vol. 115, No. 10, pp. 1395-1397.

BAHAR, E. and G. GOVINDARAJAN, 1973, "Rectangular and Annular Modal Analyses of Multimode Waveguide Bends," IEEE Transactions on Microwave Theory and Techniques, Vol. MTT-21, No. 12, pp. 819-824.

BAHAR, E. and G. GOVINDARAJAN, 1974, "H-Plane Multimode Waveguide Transition Sections with Large Flare Angles--Radial and Rectangular Modal Analysis," Proceedings of IEE, Vol. 21, No. 6, pp. 443-449.

BAHAR, E. and G. G. RAJAN, 1979, "Depolarization and Scattering of Electromagnetic Waves by Irregular Boundaries for Arbitrary Incident and Scatter Angles--Full Wave Solutions," IEEE Transactions on Antennas and Propagation, Vol. AP-27, No. 2, pp. 214-225.

BECKMANN, P. and A. SPIZZICHINO, 1963, The Scattering of Electromagnetic Waves from Rough Surfaces, New York, MacMillan.

BARRICK, D. E., 1968, "Rough Surface Scattering Based on the Specular Point Theory," IEEE Transactions on Antennas and Propagation, Vol. AP-16, No. 4, pp. 449-454.

BARRICK, D. E. and W. H. PEAKE, 1968, "A Review of Scattering from Surfaces with Different Roughness Scales," Radio Science, Vol. 8, pp. 865-868.

RICE, A. O., 1951, "Reflection of Electromagnetic Waves From Slightly Rough Surfaces," Communications of Pure and Applied Math., Vol. 4, pp. 351-378.

WRIGHT, J. W., 1966, "Backscatter From Capillary Waves With Applications to Sea Clutter," IEEE Transactions on Antennas and Propagation, Vol. AP-14, pp. 749-754.

10. Illustrations

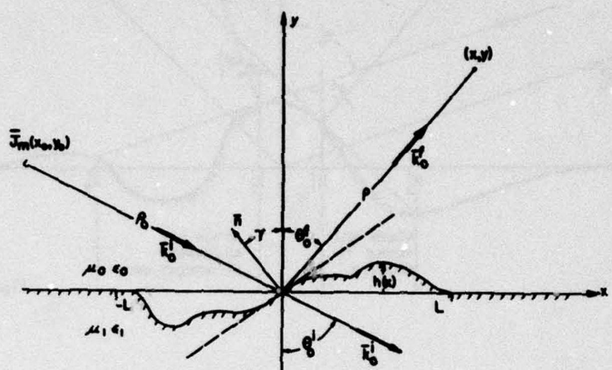

Figure 1

Fig. 1. The scattered radiation fields from irregular boundaries.

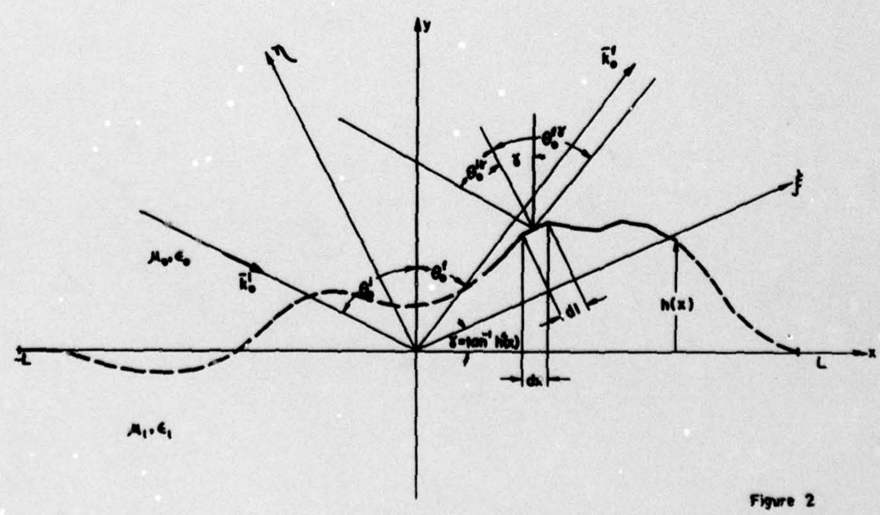

Figure 2

Fig. 2. The irregular boundary regarded as a continuum of elementary inclined strips.

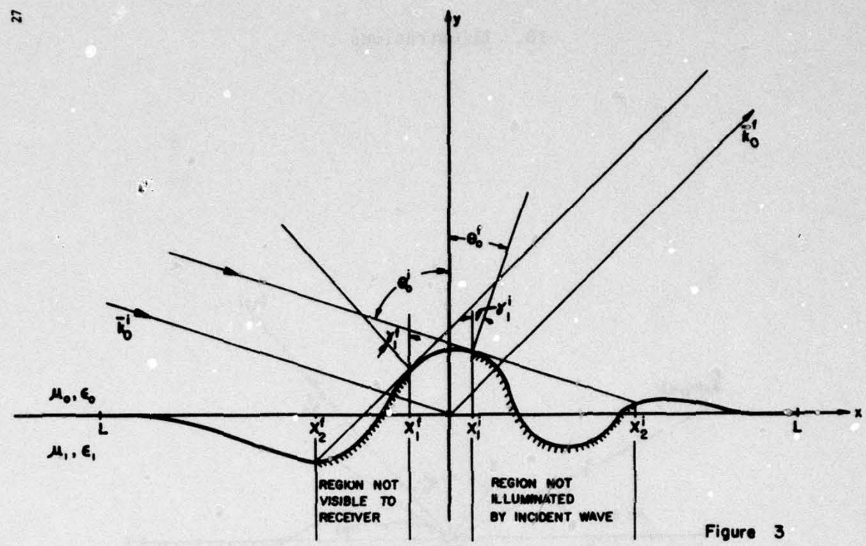

Fig. 3. Illuminated and shadow regions for rough surface scattering.

THEORETICAL ASPECTS OF TRANSIENT RADIATION AND SCATTERING IN LOSSLESS TWO MEDIUM HALF SPACES

M. Döbrich/K.J. Langenberg

Theoretische Elektrotechnik
Universität des Saarlandes
D-6600 Saarbrücken, FRG

SUMMARY

A vertical transient multipole is situated at the hight ξ above a plane boundary separating two dielectric loss-less halfspaces. The potential of the primary and reflected field is evaluated by means of Fourier- and Laplace transforms; their inversion is performed on the base of Cagniard's method. The relation between the Fourier integral representation and the generalized Sommerfeld integrals for multipoles is shown.

1. INTRODUCTION

Pulsed signals of nano-second durations are strongly time dispersive due to the radiating and receiving system, the scattering by objects and to reflection and diffraction by boundaries separating media of different constitutive parameters. A lot of theoretical and experimental investigations have been performed to solve or at least to shed some light on the various aspects of this complicated problem. The present contribution deals with the theoretical evaluation of transient multipole fields in loss-less two-medium half spaces. Because the combination of the modal fields of all spherical multipole sources is capable of representing arbitrary electromagnetic fields resulting from radiation and scattering this problem could be referred to as a canonical one.

The geometry under concern is an arbitrary rotationally symmetric transient multipole source perpendicular to a plane boundary separating two dielectric half spaces of different permittivity. The resulting electromagnetic fields can be derived by differentiation of the pertinent vector potential components. Laplace transforming these components with respect to time and using appropriate initial and transition conditions yields a representation of the primary and secondary potentials in terms of two-dimensional Fourier integrals, thus allowing the application of the modified Cagniard method (DE HOOP, A.T., 1959; FELSEN, L.B., 1965) to perform the inverse Laplace transform. The two-dimensional Fourier integrals of the primary potential can be derived also from the pertinent generalized Sommerfeld integrals of Fourier-Bessel type, which have been just recently published (CHANG, S.K., 1978). The application of the modified Cagniard method to perform the inverse Laplace transform is straightforward except for the case of subsurface situation of the observationpoint, then the implementation of numerical means is necessary. In any case the results in the time domain are very practicable convolution integrals for the transient near- and far-fields of abitrarily pulsed multipoles in the presence of a plane boundary separating two media, which can be easily evaluated using fast Fourier transform methods.

2. HERTZIAN VECTOR OF TRANSIENT 2^n-POLES

2.1 Fourier-Laplace transform for a transient Hertzian dipole

Let a transient dipole be on the z-axis with the moment $Q_1 \cdot F(t)$, where

$$(1) \quad \begin{cases} Q_1 = Q_0 \cdot d & (Q_0 = \text{charge, } d = \text{distance of the charges}) \\ F(t) = 0 & \text{for } t \leq 0 \end{cases}$$

(Fig. 1)

The $\vec{E}$- and $\vec{H}$-field is given by

$$(2) \quad \vec{H} = \nabla \times \dot{\vec{\Pi}}_1 \quad \text{and} \quad \varepsilon \vec{E} = \Delta \vec{\Pi}_1 - \frac{1}{v^2} \ddot{\vec{\Pi}}_1$$

where the Hertzian vector

$$(3) \quad \vec{\Pi}_1 = \begin{pmatrix} 0 \\ 0 \\ \Pi_1 \end{pmatrix}, \quad \Pi_1(R,t) = \frac{Q_1 \cdot F(t)}{4\pi R}$$

with

$$(4) \quad \begin{aligned} t' &= t - R/v && \text{retarded time} \\ R &= \overline{QP} = \sqrt{x^2+y^2+z^2} && \text{distance source point-observation point} \\ v &= \text{velocity of light} = \frac{1}{\sqrt{\varepsilon\mu}} \end{aligned}$$

is found as solution of the wave equation

$$(5) \quad \Delta \vec{\Pi}_1 - \frac{1}{v^2} \ddot{\vec{\Pi}}_1 = -Q_1 \delta(\vec{R}) \cdot F(t)$$

δ denotes Dirac's functional.

In the more general case of transient multipoles we may find the solution of (5) by per-

forming a Laplace transform and a two-dimensional Fourier transform. Hence, we write for the dipole

(6) $\Pi_1(x,y,z;t) \circ\!\!-\!\!\bullet\; \pi_1(x,y,z;s)\ ;\quad F(t) \circ\!\!-\!\!\bullet\; f(s)$

Inserted into (5) we get

(7) $\left(\Delta - \frac{s^2}{v^2}\right)\pi_1(x,y,z;s) = -Q_1\,\delta(\vec{R})\cdot f(s)$

The Laplace transform (6) is now subjected to a two-dimensional Fourier transform with respect to x,y

(8) $\pi_1(x,y,z;s) = \frac{s^2}{4\pi^2}\iint_{-\infty}^{\infty} d\alpha\, d\beta\; \tilde{\pi}_1(\alpha,\beta,z;s)\cdot \exp(is\alpha x + is\beta y)$

(DE HOOP, A.T.., 1959; FELSEN, L.B.., 1965). Thus (7) becomes an ordinary differential-equation

(9) $\left[\frac{d^2}{dz^2} - s^2\gamma^2\right]\tilde{\pi}_1(\alpha,\beta,z;s) = -Q_1\,\delta(z)\,f(s)$

with

(10) $\gamma^2 = \alpha^2+\beta^2+\frac{1}{v^2}\ ,\qquad \operatorname{Re}\gamma > 0\ .$

The solution being finite for $|z| \to \infty$, is

(11) $\tilde{\pi}_1(\alpha,\beta,z;s) = \frac{Q_1}{2s\gamma}\exp(-s\gamma|z|)$

2.2 Fourier-Laplace transform for a transient 2^n-pole

Two dipoles $\pm\, Q_1F(t)$ of opposite sign and distance d (Fig. 2) are situated on the z-axis. The time-function F(t) with F(t) = 0 for $t \le 0$ is the same for both dipoles. The wave-equation for this 2^n-pole with n = 2 (quadrupole) writes

(12) $\Delta\Pi_2 - \frac{1}{v^2}\ddot{\Pi}_2 = -Q_1\cdot F(t)\cdot\left\{\delta(x,y,z-\tfrac{d}{2}) - \delta(x,y,z+\tfrac{d}{2})\right\}$

As $d \to 0$ and $Q_1 \to \infty$ in a manner, that $Q_2 = d\cdot Q_1$ remains finite, (12) transforms into

(13) $\Delta\Pi_2 - \frac{1}{v^2}\ddot{\Pi}_2 = Q_2\cdot F(t)\cdot\frac{\partial}{\partial z}\,\delta(x,y,z)$

Applying the operator $-d\frac{\partial}{\partial z}$ n-times we get the wave equation for the potential Π_n of the z-directed 2^n-pole

(14) $\Delta\Pi_n - \frac{1}{v^2}\ddot{\Pi}_n = (-1)^n Q_n\cdot F(t)\,\frac{\partial^{n-1}}{\partial z^{n-1}}\,\delta(x,y,z)$

where

(15) $Q_n = Q_0\cdot d^n$

is the moment of the 2^n-pole.
The Fourier-Laplace transform of Π_n yields the equation

(16) $\left[\frac{d^2}{dz^2} - s^2\gamma^2\right]\tilde{\pi}_n(\alpha,\beta,z;s) = (-1)^n Q_n\cdot f(s)\,\frac{\partial^{n-1}}{\partial z^{n-1}}\,\delta(z)$

We may thus find $\tilde{\pi}_n(\alpha,\beta,z;s)$ by applying the operator $(-d\frac{\partial}{\partial z})^{n-1}$ on $\tilde{\pi}_1(\alpha,\beta,z;s)$ according to (11):

(17) $\tilde{\pi}_n(\alpha,\beta,z;s) = \operatorname{sign}^{n-1}(z)\cdot\frac{Q_n\cdot f(s)}{2}(s\gamma)^{n-2}\exp(-s\gamma|z|)$

with

(18) $\gamma = \sqrt{\alpha^2+\beta^2+\frac{1}{v^2}}\ ,\qquad \operatorname{Re}\gamma > 0$

3. RELATION TO EIGENFUNCTIONS AND GENERALIZED SOMMERFELD INTEGRALS

The time harmonic Hertzian dipole has the potential

(19) $\Pi_1(R,\Theta) = \frac{ikQ_1}{4\pi}\,h_0 P_0$ $\qquad (i = \sqrt{-1}\ ,\quad k = \text{wave number})$

where R,Θ are spherical coordinates of the observation point
$h_n = h_n^{(1)}(kR)$ spherical Hankel functions of the first kind,
$P_n = P_n(\cos\Theta)$ Legendre polynomials.

Application of the operator $-d\frac{\partial}{\partial z}$ and using the formula (CHANG, S.K.., 1978)

(20) $\frac{\partial}{\partial kz}h_n P_n = \frac{n}{2n+1}\,h_{n-1}P_{n-1} - \frac{n+1}{2n+1}\,h_{n+1}P_{n+1}$

we get successively

$$\pi_1 = \frac{ik\ Q_1}{4\pi}\ h_0P_0$$

$$\pi_2 = \frac{ik^2Q_2}{4\pi}\ h_1P_1$$

$$\pi_3 = \frac{ik^3Q_3}{4\pi}\ \{\frac{2}{3}\ h_2P_2 - \frac{1}{3}\ h_0P_0\}$$

$$\pi_4 = \frac{ik^4Q_4}{4\pi}\ \{\frac{2}{5}\ h_3P_3 - \frac{3}{5}\ h_1P_1\}$$

$$(21)\quad \pi_5 = \frac{ik^5Q_5}{4\pi}\ \{\frac{8}{35}\ h_4P_4 - \frac{4}{7}\ h_2P_2 + \frac{1}{5}\ h_0P_0\}$$

$$\pi_6 = \frac{ik^6Q_6}{4\pi}\ \{\frac{8}{63}\ h_5P_5 - \frac{4}{9}\ h_3P_3 + \frac{3}{7}\ h_1P_1\}$$

$$\vdots$$

$$\pi_n = \frac{ik^nQ_n}{4\pi}\ \sum_{l=0}^{n-1} a_l^{(n)}\ h_l\ P_l$$

It should be pointed out that these results are different from those presented by Heilmann (HEILMANN, A.., 1970). For the eigenfunctions $h_nP_n^m$ we have the generalized Sommerfeld integral representation (CHANG, S.K.., 1978)

$$(22)\quad h_n^{(1)}(kR)\cdot P_n^m(\cos\Theta) = \int_0^\infty f_{m,n}(\lambda)\ J_m(\lambda r)\ \exp(-\mu|z|)\ d\lambda$$

with

$$(23)\quad \mu = \sqrt{\lambda^2-k^2}\quad ;\quad R^2 = r^2+z^2$$

The function $f_{m,n}(\lambda)$ can be found by the recurrence relation

$$(24)\quad \begin{cases} f_{m,m}(\lambda) = i\left(\frac{\lambda}{k}\right)^{m+1}\cdot\frac{1}{\mu}\ P_m^m(0)\ ; \qquad f_{m,m-1}(\lambda) = 0 \\ \text{and} \\ f_{m,n+1}(\lambda) = \frac{2n+1}{n-m+1}\frac{\mu}{k}\ f_{m,n}(\lambda) + \frac{n+m}{n-m+1}\ f_{m,n-1}(\lambda) \end{cases}$$

The Bessel integral representation

$$(25)\quad h_n\cdot P_n^m\cdot\exp(\pm im\varphi) = \exp(\pm im\varphi)\int_0^\infty f_{m,n}(\lambda)\cdot J_m(\lambda)\cdot\exp(-\mu|z|)\,d\lambda$$

may be transformed into a Fourier integral representation

$$(26)\quad h_n\cdot P_n^m\cdot\exp(\pm im\varphi) = \frac{1}{4\pi^2}\iint_{-\infty}^{\infty}\tilde{f}_{m,n}(\alpha,\beta,z)\ \exp(i\alpha x+i\beta y)\,d\alpha\,d\beta$$

by introducing the Hansen formula into (25)

$$(27)\quad J_m(\lambda r) = \frac{(-i)^m}{2\pi}\int_{-\pi}^{\pi}\exp(i\lambda r\cos\psi \pm im\psi)\,d\psi$$

and using Cartesian coordinates

$$(28)\quad \begin{cases} x = r\sin\varphi\quad ; & \alpha = \lambda\cos\phi \\ y = r\cos\varphi\quad ; & \beta = \lambda\sin\phi \end{cases}$$

The resulting spectrum is

$$(29)\quad \tilde{f}_{m,n}(\alpha,\beta,z) = 2\pi(-i)^m\left[\frac{\alpha+i\beta}{\alpha-i\beta}\right]^{\pm\frac{m}{2}}\cdot\frac{f_{m,n}(\lambda)}{\lambda}\exp(-\mu|z|).$$

If we insert this result into (26) we have by means of (21)

$$(30)\quad \begin{aligned} \tilde{\Pi}_1(\alpha,\beta,z) &= \frac{Q_1\exp(-\mu|z|)}{2\mu} \\ \tilde{\Pi}_2(\alpha,\beta,z) &= \operatorname{sign}(z)\,\frac{Q_2}{2}\exp(-\mu|z|) \\ \tilde{\Pi}_3(\alpha,\beta,z) &= \frac{Q_3}{2}\cdot\mu\cdot\exp(-\mu|z|) \end{aligned}$$

etc. with $\mu = \sqrt{\alpha^2+\beta^2-k^2}$; $Re\,\mu>0$.

These harmonic Fourier transforms (30) change into the transient Fourier-Laplace transforms (17) by replacing

$$(31)\quad k = i\frac{s}{v}$$

and multiplying with f(s). This is necessary because the solutions of the equations

$$(32)\quad \begin{aligned} (\Delta+k^2)\,\Pi_n &= (-1)^n\,Q_n\,\frac{\partial^{n-1}}{\partial z^{n-1}}\,\delta(x,y,z) \\ (\Delta-\frac{s^2}{v^2})\,\pi_n &= (-1)^n\,Q_n\cdot f(s)\cdot\frac{\partial^{n-1}}{\partial z^{n-1}}\,\delta(x,y,z) \end{aligned}$$

must correspond to one another.

4. MULTIPOLES ABOVE A PLANE BOUNDARY

4.1 Mathematical formulation

Two loss-less half spaces are separated by the plane $z = 0$ (Fig. 3). The permittivity is

$$(33) \quad \varepsilon(z) = \begin{cases} \varepsilon_1 & \text{for } z \geq 0 \\ \varepsilon_2 & \text{for } z < 0 \end{cases}$$

A transient 2^n-pole in z-direction is located at $Q(0,0,\xi)$. The observation point is $P(x,y,z)$. We look for the pertinent potential

$$(34) \quad \vec{\Pi}_n = \begin{pmatrix} 0 \\ 0 \\ \Pi_n \end{pmatrix}, \qquad \Pi_n = \Pi_n(x,y,z,t)$$

which allows to find the field versus

$$(35) \quad \vec{H} = \nabla \times \vec{\Pi}_n, \qquad \varepsilon\vec{E} = \Delta\vec{\Pi}_n - \frac{1}{v_i^2}\ddot{\vec{\Pi}}_n \qquad (i=1,2)$$

4.2 Evaluation of the potential π_n

The potential π_n can be represented as follows

$$(36) \quad \Pi_n(x,y,z,t) = \begin{cases} \Pi_n^p(x,y,z,t) + \Pi_n^r(x,y,z,t) & \text{for } z \geq 0 \\ \Pi_n^d(x,y,z,t) & \text{for } z \leq 0 \end{cases}$$

(p = primary, r = reflected, d = diffracted)

The potential π_n^p must satisfy the wave equation

$$(37) \quad \left[\Delta - \frac{1}{v_1^2}\frac{\partial^2}{\partial t^2}\right]\Pi_n^p = (-1)^n Q_n F(t) \frac{\partial^{n-1}}{\partial z^{n-1}} \delta(\vec{R})$$

and the source-free potentials $\pi_n^{r,d}$ must satisfy

$$(38) \quad \left[\Delta - \frac{1}{v_i^2}\frac{\partial^2}{\partial t^2}\right]\Pi_n^{r,d} = 0$$

As before (8) we represent $\pi_n^{r,d}$ by a Fourier-Laplace integral

$$(39) \quad \pi_n^{r,d}(x,y,z;s) = \frac{s^2}{4\pi^2}\iint_{-\infty}^{\infty} d\alpha\, d\beta\, \tilde{\pi}_n^{r,d}(\alpha,\beta,z;s)\exp(is\alpha x + is\beta y)$$

Insertion into (38) yields the general solution

$$(40) \quad \tilde{\pi}_n^{r,d}(\alpha,\beta,z;s) = A_n^{r,d}\exp(s\gamma_{1,2}z) + B_n^{r,d}\exp(-s\gamma_{1,2}z)$$

where

$$(41) \quad \gamma_{1,2} = \sqrt{\alpha^2+\beta^2+\frac{1}{v_{1,2}^2}}\ ; \qquad \operatorname{Re}\gamma_{1,2} > 0$$

Since the spectra must be finite for $|z| \to \infty$ we have

$$(42) \quad \tilde{\pi}_n^r(\alpha,\beta,z;s) = B_n^r\exp(-s\gamma_1 z)\ ; \quad z \geq 0$$

and

$$(43) \quad \tilde{\pi}_n^d(\alpha,\beta,z;s) = A_n^d\exp(s\gamma_2 z)\ ; \quad z < 0$$

We invert (42), (43) and the primary spectrum (44) and use (36).

Since H_x and E_x must be continuous at $z = 0$, the following system of equations for $A_n^d(\alpha,\beta,s)$ and $B_n^r(\alpha,\beta,s)$ results:

$$(45) \quad \begin{aligned} A_n^d - B_n^r &= (-1)^{n-1}\frac{Q_n f(s)}{2}(s\gamma_1)^{n-2}\exp(-s\gamma_1\xi) \\ \varepsilon_1\gamma_2 A_n^d + \varepsilon_2\gamma_1 B_n^r &= \varepsilon_2\gamma_1(-1)^{n-1}\frac{Q_n f(s)}{2}(s\gamma_1)^{n-2}\exp(-s\gamma_1\xi) \end{aligned}$$

The solution is:

$$(46) \quad \begin{aligned} A_n^d &= (-1)^{n-1}\frac{Q_n f(s)}{2}(s\gamma_1)^{n-2}\frac{2\varepsilon_2\gamma_1}{\varepsilon_1\gamma_2+\varepsilon_2\gamma_1}\exp(-s\gamma_1\xi) \\ B_n^r &= (-1)^{n-1}\frac{Q_n f(s)}{2}(s\gamma_1)^{n-2}\frac{\varepsilon_2\gamma_1-\varepsilon_1\gamma_2}{\varepsilon_1\gamma_2+\varepsilon_2\gamma_1}\exp(-s\gamma_1\xi) \end{aligned}$$

The Laplace transforms of the potentials of the primary, reflected and diffracted fields are

(47)
$$\left\{\begin{aligned} \pi_n^p &= \frac{\mathrm{sign}^{n-1}(z-\xi)\cdot s^n\cdot f(s)\cdot Q_n}{8\pi^2}\iint_{-\infty}^{\infty} d\alpha\, d\beta\, \gamma_1^{n-2}\exp(-s\gamma_1|z-\xi|+is\alpha x+is\beta y) \\ \pi_n^r &= \frac{(-1)^{n-1}s^n f(s) Q_n}{8\pi^2}\iint_{-\infty}^{\infty} d\alpha\, d\beta\, \frac{\varepsilon_2\gamma_1-\varepsilon_1\gamma_2}{\varepsilon_1\gamma_2+\varepsilon_2\gamma_1}\gamma_1^{n-2}\exp[-s\gamma_1(z+\xi)+is\alpha x+is\beta y] \end{aligned}\right\} z \geq 0$$
$$\pi_n^d = \frac{(-1)^{n-1}s^n f(s) Q_n}{8\pi^2}\iint_{-\infty}^{\infty} d\alpha\, d\beta\, \frac{2\varepsilon_2\gamma_1}{\varepsilon_1\gamma_2+\varepsilon_2\gamma_1}\gamma_1^{n-2}\exp[s(\gamma_2 z-\gamma_1\xi)] \qquad z<0$$

5. THE PRIMARY POTENTIAL

The Laplace transform of the potential of a Hertzian dipole in Q (0/0/ξ) on the z-axis is

(48)
$$\pi_1^p(x,y,z;s) = \frac{s f(s) Q_1}{8\pi^2}\iint_{-\infty}^{\infty} d\alpha\, d\beta\, \frac{\exp(-s\gamma_1|z-\xi|+is\alpha x+is\beta y)}{\gamma_1}$$

The coordinates x,y of the observation point P (Fig. 3) are expressed in terms of cylindrical coordinates

(49)
$$\left\{\begin{aligned} x &= r\cos\varphi \\ y &= r\sin\varphi \end{aligned}\right. \quad ; \quad r = \sqrt{x^2+y^2}$$

The plane of integration is rotated by this angle φ

(50)
$$\left\{\begin{aligned} \alpha &= p\cos\varphi - q\sin\varphi \\ \beta &= p\sin\varphi + q\cos\varphi \end{aligned}\right.$$

with $\gamma_1 = \sqrt{p^2+q^2+\frac{1}{v_1^2}}$ (48) transforms into

(51)
$$\pi_1^p(r,z;s) = \frac{s Q_1 f(s)}{8\pi^2}\iint_{-\infty}^{\infty} dp\, dq\, \frac{\exp(-s\gamma_1|z-\xi|+isrp)}{\gamma_1}$$

q being real, we shift the integrationpath from the real axis of the p-plane fullfilling the condition (DE HOOP, A.T.., 1959); FELSEN, L.B.., 1965)

(52)
$$\tau = \gamma_1|z-\xi| - irp \in \mathbb{R}^+$$

The integration path is then a hyperbola (Fig. 4) given by

(53)
$$p_{-,+} = i\frac{r}{R^2}\tau \pm \frac{|z-\xi|}{R^2}\sqrt{\tau^2-R^2(q^2+\frac{1}{v_1^2})}$$

with $\tau \in [R\cdot\sqrt{q^2+1/v_1^2}, \infty[$. Now (51) can be written

(54)
$$\pi_1^p(R;s) = \frac{s f(s) Q_1}{4\pi^2}\int_{-\infty}^{\infty} dq \int_{R\sqrt{q^2+\frac{1}{v_1^2}}}^{\infty} \frac{\exp(-s\tau)}{\sqrt{\tau^2-R^2(q^2+\frac{1}{v_1^2})}}\, d\tau$$

We interchange the order of integration

(55)
$$\pi_1^p(R;s) = \frac{s f(s) Q_1}{4\pi^2}\int_{R/v_1}^{\infty} d\tau \int_{-q_0}^{q_0} dq\, \frac{\exp(-s\tau)}{\sqrt{\tau^2-R^2(q^2+1/v_1^2)}}$$

with
$$q_0 = \sqrt{\frac{\tau^2}{R^2}-\frac{1}{v_1^2}}$$

The last integral is an elementary one: $\frac{\pi}{R}\exp(-s\tau)$
Thus we have

(56)
$$\pi_1^p(R;s) = \frac{s f(s) Q_1}{4\pi R}\int_{R/v_1}^{\infty} d\tau \exp(-s\tau) = \frac{f(s)\cdot Q_1}{4\pi R}\exp(-s\frac{R}{v_1})$$

The shifting theorem leads to the final result

(57)
$$\Pi_1^p(R;t) = \frac{Q_1\cdot F(t-R/v_1)}{4\pi R}$$

In the same way we may find the primary potential of the quadrupole and octupole

(58)
$$\left\{\begin{aligned} \Pi_2^p(R,\Theta;t) &= \frac{Q_2\cos\Theta}{4\pi}\left\{\frac{F(t')}{R^2}+\frac{\dot F(t')}{v_1 R}\right\} \\ \Pi_3^p(R,\Theta;t) &= \frac{Q_3}{4\pi}\left\{(3\cos^2\Theta-1)\left[\frac{F(t')}{R^3}+\frac{\dot F(t')}{v_1R^2}\right]+\cos^2\Theta\,\frac{\ddot F(t')}{v^2 R}\right\} \end{aligned}\right.$$

etc., with $t' = t - R/v_1$ being the retarded time.

6. POTENTIAL OF THE REFLECTED FIELD

6.1 First case: $\varepsilon_1 < \varepsilon_2 \iff v_1 > v_2$

The Laplace transform of π_n^r is

$$(59)\quad \pi_n^r(x,y,z;s) = \frac{(-1)^{n-1}s^n f(s) Q_n}{8\pi^2} \iint_{-\infty}^{\infty} d\alpha\, d\beta\, \frac{\varepsilon_2\gamma_1 - \varepsilon_1\gamma_2}{\varepsilon_1\gamma_2 + \varepsilon_2\gamma_1}\, \gamma_1^{n-2} \exp[-s\gamma_1(z+\xi) + is\alpha x + i\beta y]$$

We put the origin of the coordinate system into the image source Q' (Fig. 3).

$$(60)\quad \begin{aligned} x &= R_1 \sin\Theta_1 \cos\varphi \\ y &= R_1 \sin\Theta_1 \sin\varphi \quad \text{with } R_1 = \overline{Q'P} = \sqrt{x^2 + y^2 + (z+\xi)^2} \\ z+\xi &= R_1 \cos\Theta_1 \end{aligned}$$

Now we rotate the plane of integration by this angle φ

$$(61)\quad \begin{aligned} \alpha &= p \cdot \cos\varphi - q \sin\varphi \\ \beta &= p \cdot \sin\varphi + q \cos\varphi \end{aligned}$$

Thus (59) transforms into

$$(62)\quad \pi_n^r(R_1,\Theta_1;s) = \frac{(-1)^{n-1}s^n f(s) Q_n}{8\pi^2} \iint_{-\infty}^{\infty} dp\, dq\, \frac{\varepsilon_2\gamma_1 - \varepsilon_1\gamma_2}{\varepsilon_1\gamma_2 + \varepsilon_2\gamma_1}\, \gamma_1^{n-2} \exp[-s\gamma_1 R_1 \cos\Theta_1 + isp R_1 \sin\Theta_1]$$

with

$$(63)\quad \gamma_{1,2} = \sqrt{p^2 + q^2 + \frac{1}{v_{1,2}^2}}$$

In order to transform (64) back into the time domain we substitute

$$(64)\quad \tau = \gamma_1 R_1 \cos\Theta_1 - ipR_1 \sin\Theta_1$$

As before (DE HOOP, A.T.., 1959; FELSEN, L.B.., 1965) the integrationpath is a hyperbola (Fig. 5a)

$$(65)\quad p_{+,-} = i\frac{\tau}{R_1}\sin\Theta_1 \pm |\cos\Theta_1| \cdot \sqrt{\frac{\tau^2}{R_1^2} - \left(q^2 + \frac{1}{v_1^2}\right)}$$

This hyperbola intersects the imaginary axis in $p_0 = i\sqrt{q^2 + \frac{1}{v_1^2}}\,\sin\Theta_1$ and does not intersect the branchcuts, which occur because of $\gamma_{1,2}$ at

$$(66)\quad p_1 = \pm i\sqrt{q^2 + \frac{1}{v_1^2}} \quad ; \quad p_2 = \pm i\sqrt{q^2 + \frac{1}{v_2^2}}$$

The same calculus as in chapter 5 of this paper yields the result

$$(67)\quad \pi_n^r(R_1,\Theta_1;s) = \frac{(-1)^{n-1}s^n f(s) Q_n}{4\pi^2 R_1} \int_{R_1/v_1}^{\infty} d\tau \exp(-s\tau) \int_{-q_0}^{q_0} dq\, \mathrm{Re}\, \frac{\varepsilon_2\gamma_1 - \varepsilon_1\gamma_2}{\varepsilon_1\gamma_2 + \varepsilon_2\gamma_1}\, \frac{\gamma_1^{n-1}}{\sqrt{\frac{\tau^2}{R_1^2} - \left(q^2 + \frac{1}{v_1^2}\right)}}$$

with $q_0 = \sqrt{\frac{\tau^2}{R_1^2} - \frac{1}{v_1^2}}$. We make the substitution

$$(68)\quad q(\psi) = q_0 \cdot \sin\psi$$

The final form of (67) results:

$$(69)\quad \pi_n^r(R_1,\Theta_1;s) = \frac{(-1)^{n-1}s^n f(s) Q_n}{4\pi^2 R_1} \int_{R_1/v_1}^{\infty} d\tau \exp(-s\tau) \int_{-\pi/2}^{\pi/2} \mathrm{Re}\, \frac{\varepsilon_2\gamma_1 - \varepsilon_1\gamma_2}{\varepsilon_1\gamma_2 + \varepsilon_2\gamma_1}\, \gamma_1^{n-1}\, d\psi$$

with

$$(70)\quad \begin{cases} \gamma_1(\tau,\psi) = \frac{\tau}{R_1}\cos\Theta_1 + i\sqrt{\frac{\tau^2}{R_1^2} - \frac{1}{v_1^2}}\,\sin\Theta_1 \cos\psi \\ \gamma_2^2(\tau,\psi) = \gamma_1^2 - \frac{1}{v_1^2} + \frac{1}{v_2^2} \end{cases}$$

In the time domain the potential is given by the convolution integral

$$(71)\quad \Pi_n^r(R_1,\Theta_1,t) = \begin{cases} 0 \ ; & t \le R_1/v_1 \\ \frac{(-1)^{n-1}Q_n}{4\pi^2 R_1} \int_{R_1/v_1}^{t} d\tau\, F^{(n)}(t-\tau) \int_{-\pi/2}^{\pi/2} d\psi\, \mathrm{Re}\, \frac{\varepsilon_2\gamma_1 - \varepsilon_1\gamma_2}{\varepsilon_1\gamma_2 + \varepsilon_2\gamma_1}\, \gamma_1^{n-1} \ ; & t > R_1/v_1 \end{cases}$$

We state that $t = R_1/v_1$ is the travel time of the reflected beam from the sourcepoint Q to the observation point P. For simplicity the derivatives of F(t) at $t = 0_+$ in (71) are assumed to be

$$(72)\quad F(0_+) = F'(0_+) = \dots F^{(n-1)}(0_+) = 0$$

6.2 Second case: $\varepsilon_1 > \varepsilon_2 \iff v_1 < v_2$

6.2.1 $0 \le \Theta_1 \le \Theta_0$ (Θ_0 = angle of total reflection)

The branchpoints

$$(73)\quad p_1 = i\sqrt{q^2 + \frac{1}{v_1^2}} \quad ; \quad p_2 = i\sqrt{q^2 + \frac{1}{v_2^2}}$$

are now reversed on the imaginary axis of the p-plane. The integrationpath however does not intersect the branchcut if $\Theta_1 < \Theta_0$ (Fig. 5b). The integrationpath intersects the imaginary axis at

(74) $$p_0 = i\sqrt{q^2 + \frac{1}{v_1^2}}\,\sin\Theta_1$$

and for all $q \in \mathbb{R}$ the relation

(75) $$\sqrt{q^2 + \frac{1}{v_1^2}}\cdot\sin\Theta_1 < \sqrt{q^2 + \frac{1}{v_2^2}}$$

is fullfilled, if

(76) $$\sqrt{q^2 + \frac{1}{v_1^2}}\,\sin\Theta_1 < \sqrt{q^2 + \frac{1}{v_2^2}}$$

Hence, the potential is given by (71).

6.2.2 $\Theta_0 < \Theta_1 < 90°$

Besides the integral along the hyperbola, which again is given by (71) we must consider the contribution along the branchcut (Fig. 5c) (LANGENBERG, K.J..., 1974):

(77) $$v(R_1,\Theta_1;s) = \frac{(-1)^{n-1}s^n f(s) Q_n}{8\pi^2}\int_{-\infty}^{\infty} dq \left\{ \int_{p_0}^{p_2}{}_{l} + \int_{p_2}^{p_0}{}_{r} \right\} dp\, \frac{\varepsilon_2\gamma_1 - \varepsilon_1\gamma_2}{\varepsilon_1\gamma_2 + \varepsilon_2\gamma_1}\,\gamma_1^{\,n-2} \exp[-s\gamma_1 R_1\cos\Theta_1 + ispR_1\sin\Theta_1]$$

(l = left side, r = right side of the branchcut).

As

(78) $\gamma_{1,l} = \overline{\gamma}_{1,r}$ and $\gamma_{2,l} = \overline{\gamma}_{2,r}$, where the bar denotes the complex conjugate, we may rewrite (77) by using the substitution

(79) $p = i\,u$

(80) $$v(R_1,\Theta_1;s) = \frac{(-1)^n s^n f(s) Q_n}{2\pi^2}\int_0^{\infty} dq \int_{u_2}^{u_0} du\, \mathrm{Im}\, \frac{\varepsilon_2\gamma_1 - \varepsilon_1\gamma_2}{\varepsilon_1\gamma_2 + \varepsilon_2\gamma_1}\,\gamma_1^{\,n-2} \exp[-s(\gamma_1 R_1\cos\Theta_1 + uR_1\sin\Theta_1)]$$

where the integration limits are

(81) $$u_2(q) = \sqrt{q^2 + \frac{1}{v_2^2}}\ , \quad u_0(q) = \sqrt{q^2 + \frac{1}{v_1^2}}\,\sin\Theta_1$$

We now consider the lower and upper integration limit (81) as a function of q (Fig. 6). We have just one intersection at

(82) $$q_s = \frac{1}{|\cos\Theta_1|}\sqrt{\frac{1}{v_1^2}\sin^2\Theta_1 - \frac{1}{v_2^2}}$$

Hence, the integration (80) must only be performed for $q \in [0,q_s]$ because for $q > q_s$ the hyperbola in the p-plane does no longer intersect the branchcut. Again we apply Cagniard's method (DE HOOP, A.T.., 1959; FELSEN, L.B.., 1965) substituting the exponent

(83) $$\tau_q(u) = \gamma_1 R_1 |\cos\Theta_1| + u R_1 \sin\Theta_1$$

We find

(84) $$v(R_1,\Theta_1;s) = \frac{(-1)^n s^n f(s) Q_n}{2\pi^2 R_1}\int_0^{q_s} dq \int_{\tau_2}^{\tau_0} d\tau\, \mathrm{Im}\, \frac{\varepsilon_2\gamma_1 - \varepsilon_1\gamma_2}{\varepsilon_1\gamma_2 + \varepsilon_2\gamma_1}\,\gamma_1^{\,n-2}\, \frac{\exp(-s\tau)}{\sqrt{q^2 + \frac{1}{v_1^2} - \frac{\tau^2}{R_1^2}}}$$

with

(85)
$$\tau_2(q) = \sqrt{\frac{1}{v_1^2} - \frac{1}{v_2^2}}\,R_1|\cos\Theta_1| + \sqrt{q^2 + \frac{1}{v_2^2}}\,R_1\sin\Theta_1$$
$$\tau_0(q) = \sqrt{q^2 + \frac{1}{v_1^2}}\cdot R_1$$
$$\gamma_1 = \frac{|\cos\Theta_1|}{R_1}\tau - \sin\Theta_1\sqrt{q^2 + \frac{1}{v_1^2} - \frac{\tau^2}{R_1^2}}$$

We look at the integration domain in the q,τ-plane (Fig. 7). Interchanging the order of integration we must discriminate integration domain I and II

(86)
$$\mathrm{I}:\ \tau_2(0) \le \tau \le \tau_0(0) \Rightarrow 0 \le q \le q_2(\tau)$$
$$\mathrm{II}:\ \tau_0(0) \le \tau \le \tau(q_s) \Rightarrow q_0(\tau) \le q \le q_2(\tau)$$

where $q_0(\tau)$ and $q_2(\tau)$ are the inverse functions of $\tau_0(q)$ and $\tau_2(q)$, respectively

(87)
$$q_2(\tau) = \left[\frac{1}{\sin^2\Theta_1}\left(\frac{\tau}{R_1} - \sqrt{\frac{1}{v_1^2} - \frac{1}{v_2^2}}\,|\cos\Theta_1|\right)^2 - \frac{1}{v_2^2}\right]^{1/2}$$
$$q_0(\tau) = \left(\frac{\tau^2}{R_1^2} - \frac{1}{v_1^2}\right)^{1/2}$$

Finally we introduce a normalization of the integration interval

(88)
$$q(\psi) = q_2(\tau)\cdot\sin\psi \qquad \text{(domain I)}$$
$$q(\psi) = \sqrt{q_0^2(\tau) + [q_2^2(\tau) - q_0^2(\tau)]\sin^2\psi} \qquad \text{(domain II)}$$

The integral (84) then becomes

(89) $$v(R_1,\Theta_1;s) = \frac{(-1)^n s^n f(s) Q_n}{2\pi^2 R_1}\left\{\int_{\tau_2(0)}^{\tau_0(0)} d\tau \exp(-s\tau)\, H(\tau) + \int_{\tau_0(0)}^{\tau(q_s)} d\tau \exp(-s\tau)\, G(\tau)\right.$$

With

(90) $$H(\tau) = q_2(\tau)\int_0^{\pi/2} \mathrm{Im}\, \frac{\varepsilon_2\gamma_1-\varepsilon_1\gamma_2}{\varepsilon_1\gamma_2+\varepsilon_2\gamma_1}\cdot\frac{\gamma_1^{n-1}\cos\psi}{\sqrt{q_2^2(\tau)\sin^2\psi - q_0^2(\tau)}}\,d\psi$$

and

(91) $$\gamma_1(\tau,\psi) = \frac{|\cos\Theta_1|}{R_1}\tau - \sin\Theta_1\sqrt{q_2^2(\tau)\sin^2\psi - q_0^2(\tau)}$$

furthermore

(92) $$G(\tau) = \sqrt{q_2^2(\tau)-q_0^2(\tau)}\int_0^{\pi/2}\mathrm{Im}\,\frac{\varepsilon_2\gamma_1-\varepsilon_1\gamma_2}{\varepsilon_1\gamma_2+\varepsilon_2\gamma_1}\cdot\frac{\gamma_1^{n-1}\cos\psi}{\sqrt{q_0^2(\tau)+[q_2^2(\tau)-q_0^2(\tau)]\sin^2\psi}}\,d\psi$$

and

(93) $$\gamma_1(\tau,\psi) = \frac{|\cos\Theta_1|}{R_1}\tau - \sin\Theta_1\sqrt{q_2^2(\tau)-q_0^2(\tau)}\,\sin\psi$$

In the time-domain the following convolution integrals result

(94) $$V(R_1,\Theta_1;t) = \frac{(-1)^n Q_n}{2\pi^2 R_1}\begin{cases} 0\ ; & 0\le t\le \tau_2(0)\\ \int_{\tau_2(0)}^{t} d\tau\, F^{(n)}(t-\tau)\, H(\tau)\ ; & \tau_2(0)\le t\le \tau_0(0)\\ \int_{\tau_2(0)}^{\tau_0(0)} d\tau\, F^{(n)}(t-\tau) H(\tau) + \int_{\tau_0(0)}^{t} d\tau\, F^{(n)}(t-\tau)\, G(\tau)\ ; & \tau_0(0)\le t\le \tau(q_s)\\ \int_{\tau_2(0)}^{\tau_0(0)} d\tau\, F^{(n)}(t-\tau) H(\tau) + \int_{\tau_0(0)}^{\tau(q_s)} d\tau\, F^{(n)}(t-\tau) G(\tau)\ ; & t>\tau(q_s)\end{cases}$$

with

(95) $$\tau_2(0) = R_1|\cos\Theta_1|\sqrt{\frac{1}{v_1^2}-\frac{1}{v_2^2}} + \frac{R_1}{v_2}\sin\Theta_1$$
$$\tau_0(0) = R_1/v_1$$
$$\tau(q_s) = \frac{R_1}{|\cos\Theta_1|}\sqrt{\frac{1}{v_1^2}-\frac{1}{v_2^2}}$$

The earliest time

(96) $$\tau_2(0) = R_1|\cos\Theta_1|\sqrt{\frac{1}{v_1^2}-\frac{1}{v_2^2}} + \frac{R_1}{v_2}\sin\Theta_1$$

at which the radiation arrives from the source Q at the observation point P can be interpreted as follows (FELSEN, L.B., 1973): We consider the time that a wave needs if it enters medium 2 under the angle Θ_0 of total reflection, travels in medium 2 the length L_2 and leaves medium 2 under Θ_0 and finally arrives at the observation point (Fig. 8).

We have

(97) $$\begin{aligned}(L_1 + L_3)\cos\Theta_0 &= R_1\cos\Theta_1\\ R_1\sin\Theta_1 &= (L_1+L_3)\sin\Theta_0 + L_2\end{aligned}$$

The considered time is

(98) $$\tau = \frac{L_1+L_3}{v_1} + \frac{L_2}{v_2} = \frac{R_1\cos\Theta_1}{\cos\Theta_0}\cdot\frac{1}{v_1} + \left\{R_1\sin\Theta_1 - \frac{R_1\cos\Theta_1}{\cos\Theta_0}\sin\Theta_0\right\}\frac{1}{v_2}$$

with $\sin\Theta_0 = v_1/v_2$ we have

(99) $$\tau = \tau_2(0)\,.$$

7. CONCLUDING REMARKS

We derived explicit analytical expressions for the transient fields of axial multipoles above a plane lossless half-space; these expressions are exact for any situation of the observation point, their numerical evaluation is straightforward except for the case that the observation point is situated below the plane; a computer code solving this problem is presently developed.

8. REFERENCES

CHANG, S.K.; MEI, K.K., 1978, "On the generalization of Sommerfeld integrals for multipoles", Int. Symp. on Antennas and Propagation, Sendai/Japan, pp. 363

FELSEN, L.B..; MARKUWITZ, N., 1973, "Radiation and Scattering of Waves", Prentice Hall, pp. 513

FELSEN, L.B.., 1965, "Transient solution for a class of diffraction problems", Quart. Appl. Math. 23, pp. 151

HEILMANN, A.., 1970, "Antennen", Bibliographisches Institut

DE HOOP, A.T.., 1959, "A modification of Cagniard's method for solving seismic pulse problems", Appl. Scient. Res. B8, pp. 349

LANGENBERG, K.J.., 1974, "The transient response of a dielectric layer", Appl. Phys. 3, pp. 179

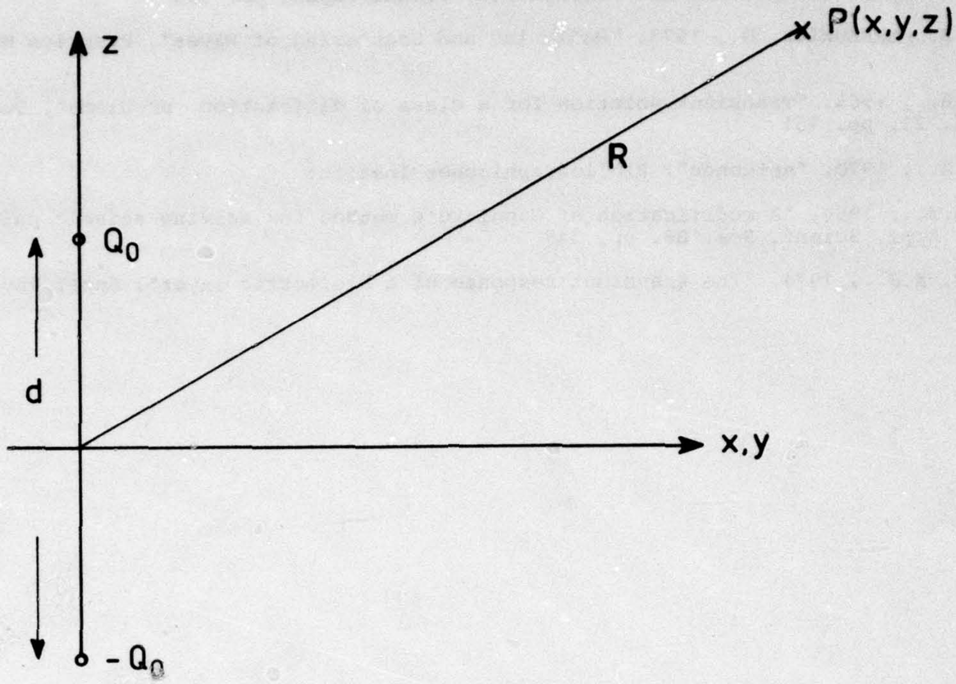

Fig. 1 Hertzian dipole

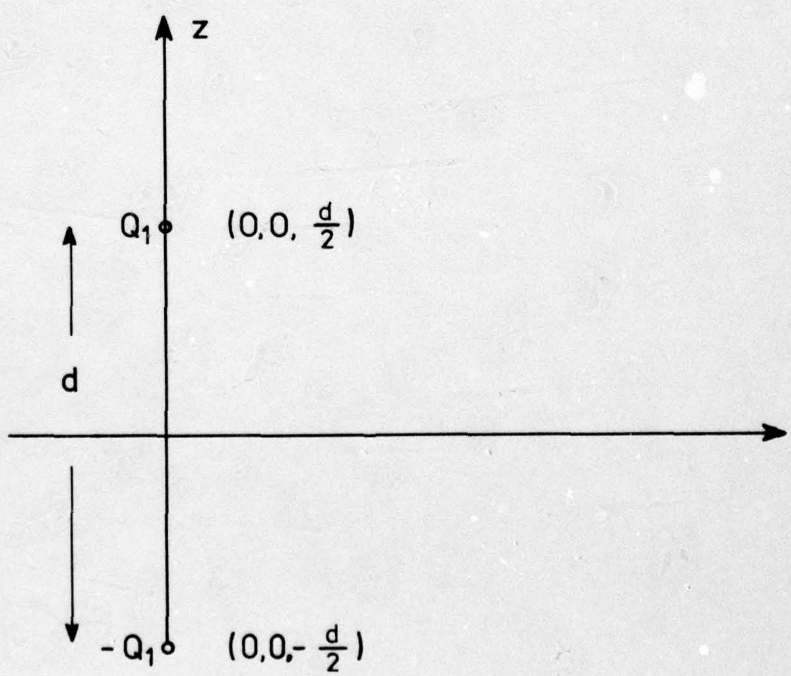

Fig. 2 Quadrupole composed by two Hertzian dipoles

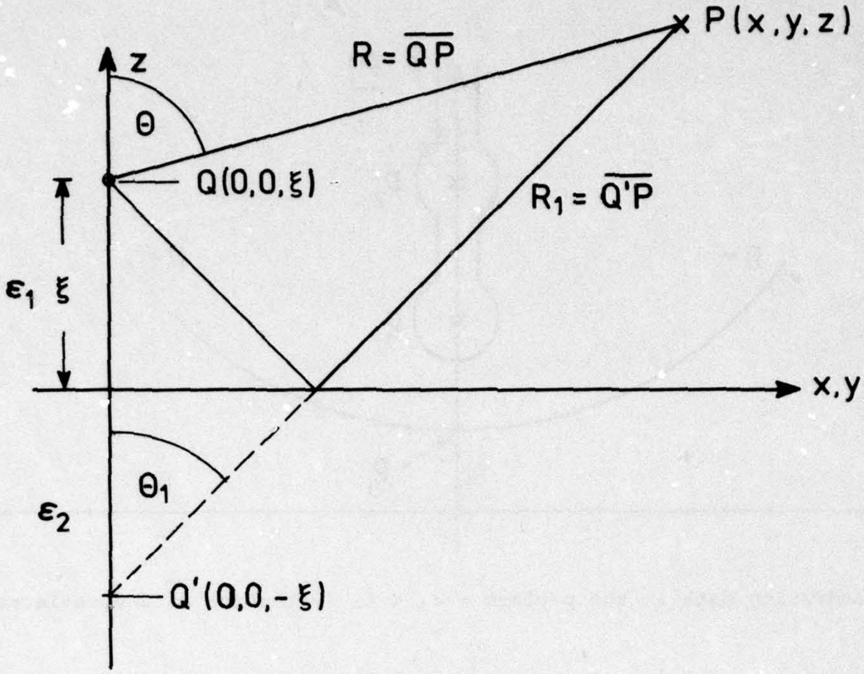

Fig. 3 Geometry of the problem

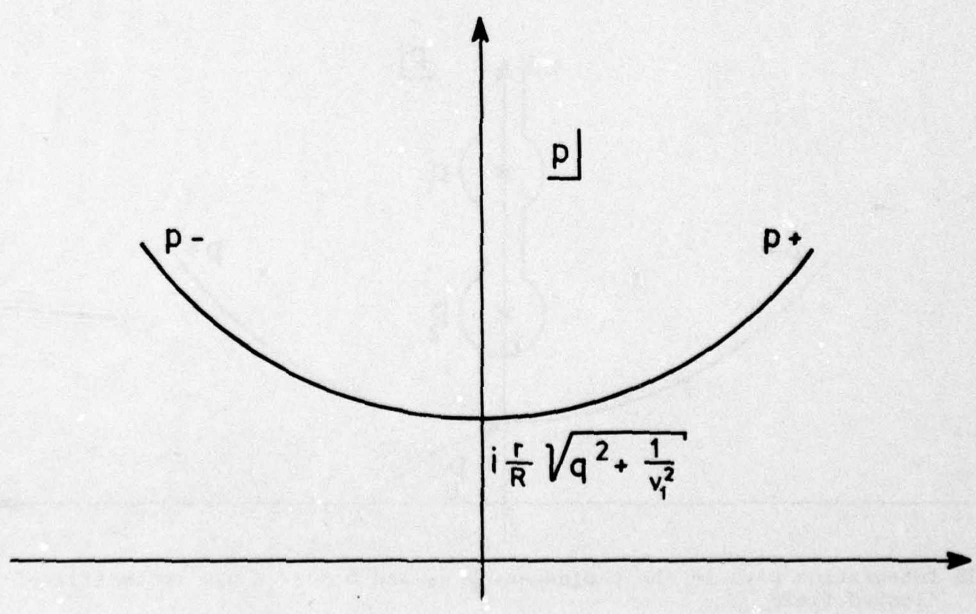

Fig. 4 Integration path in the p-plane (primary potential)

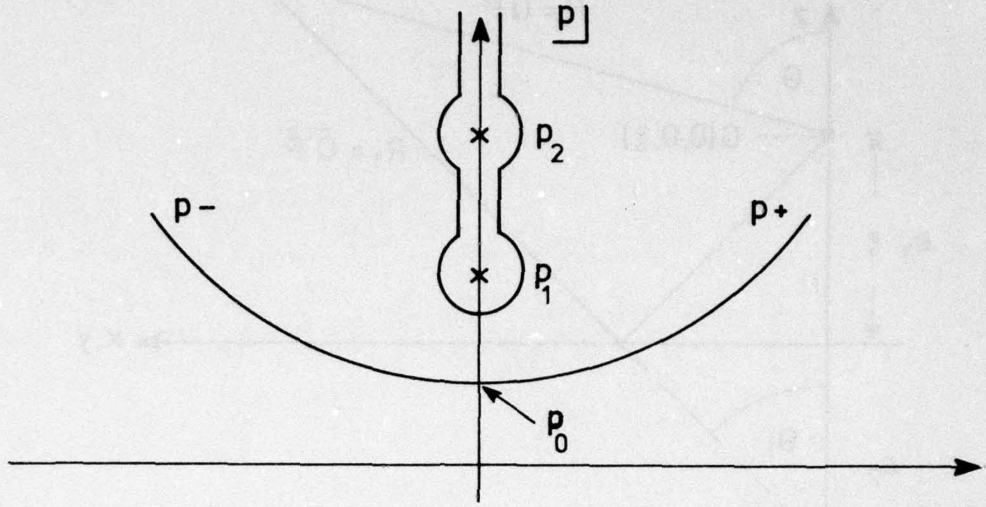

Fig. 5a Integration path in the p-plane - $\varepsilon_1 < \varepsilon_2$ (potential of the reflected field)

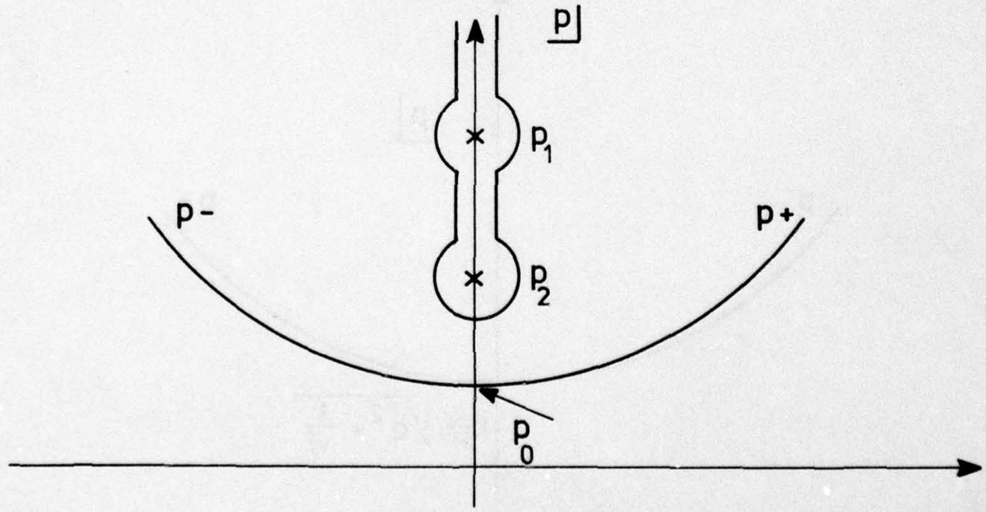

Fig. 5b Integration path in the p-plane-$\varepsilon_1 > \varepsilon_2$ and $0 \leq \theta_1 \leq \theta_0$ (potential of the reflected field

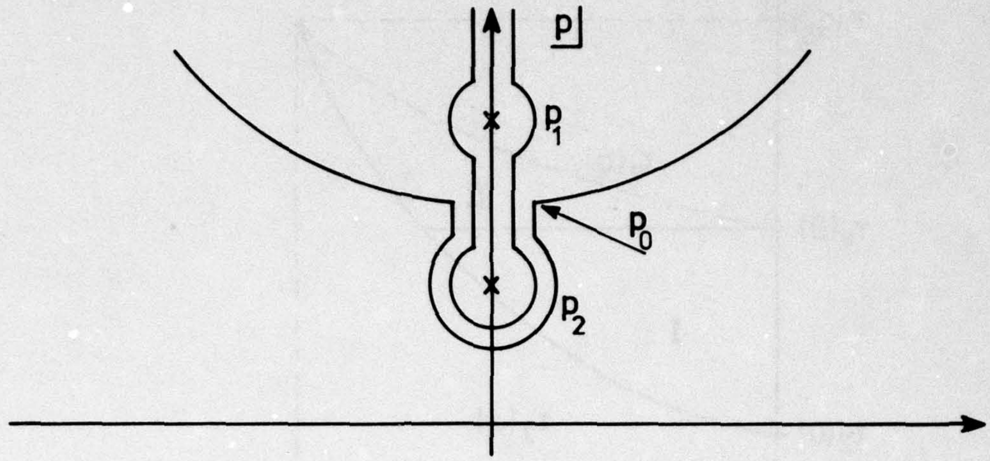

Fig. 5c Integration path in the p-plane - $\varepsilon_1 > \varepsilon_2$ and $\Theta_0 \le \Theta_1 \le 90°$ (potential of the reflected field)

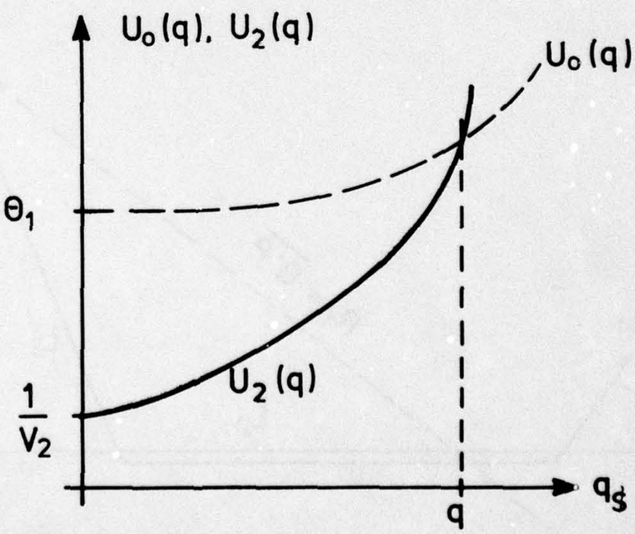

Fig. 6 Upper and lower integration limit as functions of q

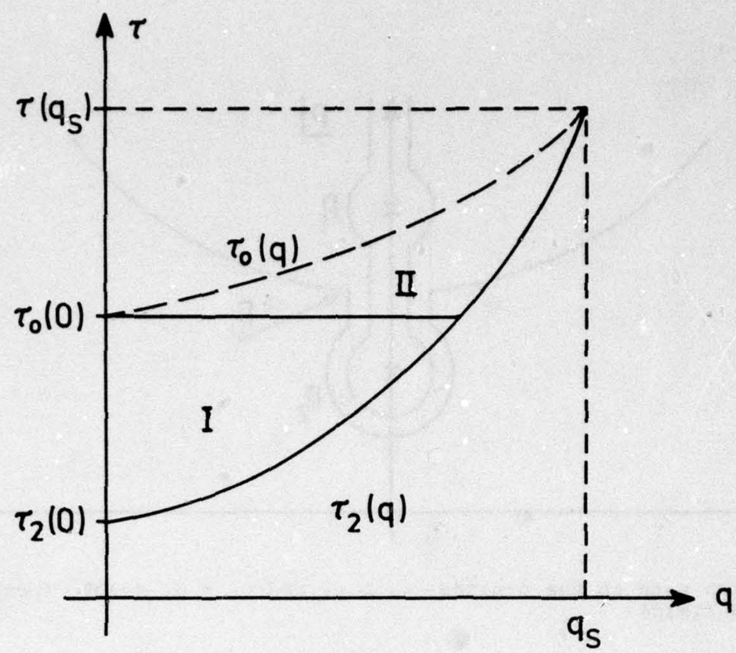

Fig. 7 Integration domain in the τ,q-plane

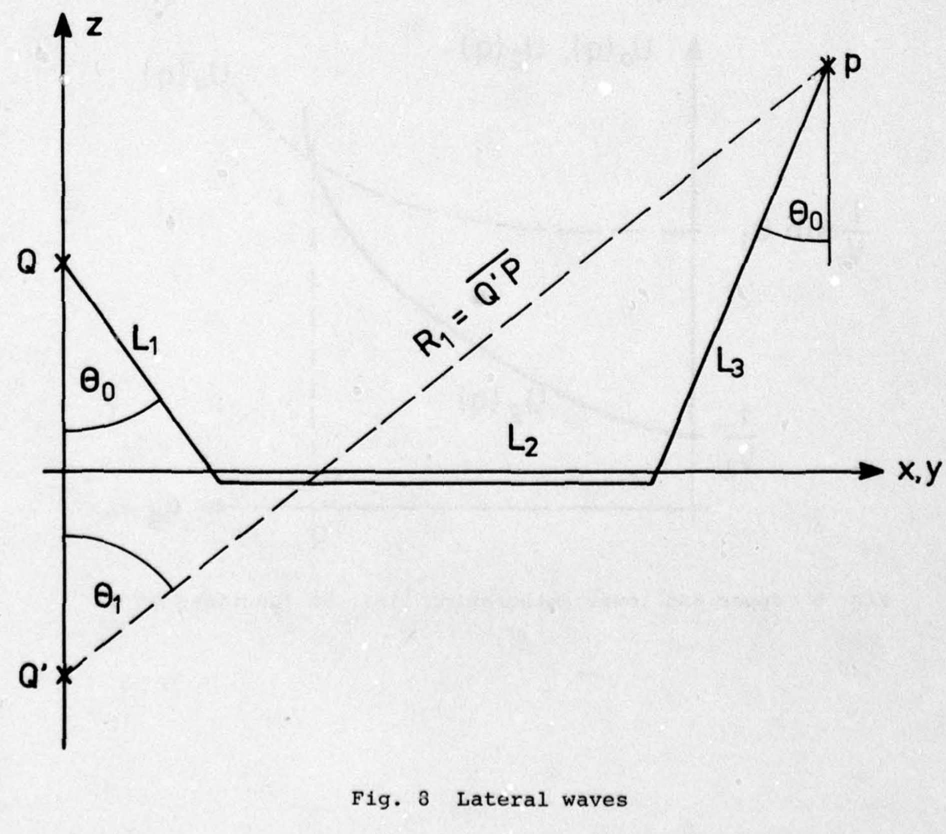

Fig. 8 Lateral waves

THEORETICAL DISTRIBUTION FUNCTIONS OF MULTIPATH PROPAGATION AND THEIR PARAMETERS FOR MOBILE RADIO COMMUNICATION IN QUASI-SMOOTH TERRAIN

by

R. W. Lorenz

Research Institute of the Deutsche Bundespost
Darmstadt, Federal Republic of Germany

SUMMARY

Due to the superposition of many partial waves arriving from different directions, the field strength received by a mobile antenna is an intensely fluctuating function of space. The well known propagation prediction methods are concentrated on the median values. For the planning of radio service areas, the statistical distribution of the amplitudes should be known to improve frequency efficiency. In the relevant literature, different theoretical distributions are proposed. But there are no reliable statements on which distribution best describes the measurements in certain types of terrain and what distribution of the distribution parameters has to be taken into account. This report considers the Weibull distribution, the Nakagami-m-distribution and the mixture of Rayleigh and log-normal distributions. The Rayleigh distribution is a special case of all three of them. Formulas are given for the determination of the distribution parameters from measurements. For the choice of the best distribution, three different methods are discussed. Results from measurements in quasi-smooth terrain in the 450-MHz-range are presented.

1. Introduction

In the Federal Republic of Germany there exists a public radio telephone service which so far has represented Europe's largest network. As early as 1951, the Deutsche Bundespost started the construction and in 1958 the network was extended almost over the whole country. Since 1978 the public mobile telephone has been fully integrated into the subscriber trunk dialling telephone system. It operates in the 150-MHz frequency band. There are about 150 base stations distributed over the country for connecting the mobile radio to the wireline network. But due to the lack of channels only about 12,000 subscribers can be admitted. Thus, the costs per subscriber for investments and maintenance are high and the probability of traffic losses is high, too. Therefore, the Deutsche Bundespost is planning a new public radio telephone network to be installed in the middle of the 80's. It will be operating in the 450-MHz frequency band. More channels will be allocated to this new network, but a reasonable increase in subscribers also should be obtained by a more efficient use of the radio frequency spectrum. This shall be achieved by

- the reduction of the geometrical co-channel distances with an optimum choice of the base station sites, taking advantage of terrain shielding,
- the application of smaller radio zones e.g. MC. DONALD, 1979, ITO, 1977, or YOSHIKAWA, 1976 and/or
- the supply of more than one radio zone from one base station, using fixed antennas with radiation patterns having special shapes, using different frequencies as suggested by LORENZ, 1978, or the same frequencies to increase the ratio of wanted to unwanted signals as suggested by STERN, 1977.

For this purpose, improved planning procedures are to be created.

Several different propagation prediction methods are well known. They can be classified in

- more theoretical models (e.g. BULLINGTON, 1947, Japanese Ministry of Postal Services, 1957, LONGLEY and RICE, 1968, HACKING, 1970, or ITO, 1971) and
- more empirical models (e.g. EGLI, 1957, OKUMURA, 1968, ALLSEBROOK and PARSONS, 1977, KESSLER and WIGGINS, 1977, LEE, 1977, LUSTGARTEN, 1977, or PALMER, 1978).

The choice depends on the way of description of the radio path by

- more or less exact interpretation of ordnance survey maps without or with consideration of vegetation and man-made obstacles,
- the use of a topographical data bank containing a certain quantization not only of the geographical height of area elements, but also a certain kind of description of obstacles or
- statistical information on the terrain, e.g. medians and deviations of terrain undulations.

A general drawback of the prediction methods known to the author is their concentration on the evaluation of median values, i.e. the field strength exceeded in 50% of locations.

Deviations can only roughly be estimated. But because of the low antenna heights of the mobiles, the fluctuations of the field strengths are very high, often more than 30 dB. For most efficient frequency spectrum usage, one needs, besides of medians, also information about the maxima and minima of the field strength. For frequency re-use in adjacent geographical regions, the field strengths in 10% or 5% of locations are to be known to get the proper statistical information about the ratios of wanted to unwanted signals. The knowledge of the field strength in 90% or 95% of locations is necessary for the calculation of the signal-to-noise ratios, bit error rates etc. The field strengths at a certain percentage of locations are called "quantiles". The prediction method should be used to calculate not only the median values, but also the other quantiles.

2. Measurements

In June 1979, LORENZ reported on results obtained in the prediction of field strength quantiles in quasi-smooth terrain, using the topographical data bank of West Germany. These results are based on measurements made in the upper Rhine valley. In medium size cities, small size cities, forests and open areas we measured a total range of 300 km. The distance chosen between two recorded measurement values was 0.1 m. The sections to be measured were selected according to the following rules:

- manifold statistical mixtures of all existing types of terrain such as width of the streets, height of the buildings, density of the forests, character of rural areas etc.
- no change in the type of terrain with respect to the characteristic classifications to be drawn from the topographical data bank within one section.
- differences in theoretical field strengths at the ends of the measured sections calculated by a simple propagation formula not larger than 2 dB.

Until now we have measured 300 sections with an average length of 1 km, i.e. 10,000 points measured in each section to calculate median field strength and the other quantiles. This is a total of 3,000,000 recorded values. The empirical cumulative distribution functions in a certain terrain which can be well defined by the topographical data bank were compared with theoretical distribution functions. Three different functions were considered:

- the Weibull distribution,
- the Nakagami-m-distribution and
- the mixture of Rayleigh and log-normal distributions, for abbreviation called by us "Suzuki distribution".

All these theoretical distributions can be described by only two parameters each. The goal of the analysis of the measurements is to find out

- which theoretical distribution best describes the measured distributions in each type of terrain and
- what is the distribution of the parameters of the theoretical distributions matched to the measured distributions.

With these questions answered, a computer prediction method can be elaborated for the field strength quantiles with the aid of the topographical data bank. The results obtained until now for quasi-smooth terrain are reported in LORENZ, June 1979. In this contribution, the properties of the theoretical distributions mentioned above are described. Formulas for the calculation of their parameters are summarized and, a method is explained for deciding which distribution best describes the measurements on the average.

3. Properties of the theoretical distribution functions

As the fluctuations of the field strength are very high, the distribution functions should be formulated for the field strength level F measured in dB (μ V/m) as random variable. Formulas known from literature for the field strength E measured in μ V/m should be transformed by

$$p(F) = p(E) \cdot \frac{dE}{dF} \qquad (1)$$

with p(x) being the probability density. The reference field strength level should be defined identically for all distribution functions. We chose the r.m.s. value of the field strength $\overline{E^2}$. Thus the transformation is

$$F - F_0 = 10 \cdot \lg\left(E^2/\overline{E^2}\right) \qquad (2)$$

3.1 Weibull distribution

It is well known that the distribution of the field strength of radio paths without free line-of-sight in short sections - say 30 m - is Rayleigh distributed due to the superposition of several partial waves with similar amplitudes and uniformly distributed phases described e.g. in NORTON, 1955.

In longer sections the mean values of the short-section distributions vary because of the different sizes of reflecting and diffracting obstacles. SHEPHERD, 1977, suggests the Weibull distribution for the description of larger sections. There are no theoretical foundations for this hypothesis except the fact that the Weibull distribution contains the Rayleigh distribution as a special case and its evaluation is rather simple. The cumulative distribution of the field strength level is

$$Q_W(F) = \int_F^{\infty} p_w(F)\,dF = \exp\left\{-g(w)\cdot\exp\left[\frac{w}{M}\left(F - F_{OW}\right)\right]\right\} \quad (3)$$

with
$$g(w) = \left[\Gamma\left(1+\frac{2}{w}\right)\right]^{w/2} \quad (4)$$

$\Gamma(x)$ = gamma function,
w = Weibull parameter and
M = 20 lg e $\approx$ 8.686 (5)

With w = 2 the Weibull distribution becomes the Rayleigh distribution

$$Q_R(F) = \exp\left\{-\exp\left[\frac{2}{M}\left(F - F_{OR}\right)\right]\right\} \quad (6)$$

which after transformation (2) is equivalent to the well known formula for the Rayleigh distribution of the field strength E,

$$Q_R(E) = \exp\left\{-E^2/\overline{E^2}\right\} \quad (7)$$

In Fig. 1 the Weibull distributions of the field strength level F are plotted versus probability on Rayleigh paper. All of them are straight lines. The quantiles of the Weibull distribution can be easily calculated from the inversion of Eq. (3).

$$F_{WQ} - F_{OW} = \frac{M}{w}\cdot\ln\left[-\frac{\ln Q}{g(w)}\right] \quad (8)$$

In Fig. 4 the quantiles for 1%, 10%, 50%, 90% and 99% related to the r.m.s. value of the Weibull distribution F_{OW} are plotted against the Weibull parameter w.

3.2 Nakagami-m-distribution

If there is line-of-sight between base station and mobile, the amplitude of the direct wave is larger than the amplitudes of the partial waves originating from reflections by obstacles in the vicinity of the mobile. In this case, a Rice distribution, RICE, 1948, can be expected. The Nakagami-m-distribution, NAKAGAMI, 1960, contains, in part, the Rice distribution, but it is also defined for parameters yielding a distribution with a larger variance than the Rayleigh distribution. The latter is also a special case of the Nakagami-m-distribution. Therefore, it seems worthwhile to investigate whether the Nakagami-m-distribution in general may be a good approximation for the description of the fluctuations of mobile radio path losses also in cases without free line-of-sight. The cumulative distribution function of the Nakagami-m-distribution is

$$Q_N(F) = \frac{m^m}{\Gamma(m)}\int_{\frac{2}{M}(F-F_{ON})}^{\infty}\exp\left\{m\left[x - \exp(x)\right]\right\}dx \quad (9)$$

with m = Nakagami parameter and
F_{ON} = level of the r.m.s. value of E.

For m = 1 Eq. (9) describes a Rayleigh distribution. With m > 1 it is a good approximation to the Rice distribution. Apart from the case m = 1, Eq. (9) can only be solved by numerical integration. The result is plotted in Fig. 2 on Rayleigh paper. Compared with the Weibull distribution, the curves for m>1 are bent upwards, for m < 1 they are bent downwards. According to NAKAGAMI, m = 0,5 is a theoretical limit for fading processes. In Fig. 5 the quantiles of the Nakagami-m-distribution are plotted against the parameter m.

3.3 Suzuki distribution

Many authors suppose that the fluctuation of the Rayleigh mean values can be well described by a log-normal distribution of the field strength mean values $\overline{E}$ or a normal distribution of the field strength level mean values $\overline{F}$. We call this mixed distribution "Suzuki distribution", since SUZUKI, 1977, was, to our knowledge, the first who described it by a mathematical formula. This cumulative distribution is

$$Q_S(F) = \frac{1}{\sqrt{2\pi}\cdot S}\int_{-\infty}^{+\infty}\exp\left\{-\exp\left[\frac{2}{M}\left(F - F_{OR}\right)\right]\right\}\cdot\exp\left\{-\frac{\left[F_{OR} - F_{OS} + \frac{S^2}{M}\right]^2}{2\cdot S^2}\right\}dF_{OR} \quad (10)$$

with s = Suzuki parameter

F_{OR} = r.m.s. value of the Rayleigh distribution, being the integration variable and

F_{OS} = r.m.s. value of the Suzuki distribution.

The integration of Eq. (10) has to be performed numerically, using the Gaussian integration formula, published e.g. in ABRAMOWITZ, 1968, chapter 25. This can be done, however, with little effort. In Fig. 3 the cumulative distribution is plotted on Rayleigh paper. The Rayleigh distribution is the special case for s = 0. There are no distributions with smaller variances than the Rayleigh distribution. Compared with the Nakagami-m-distribution for $m < 1$, the curves of the Suzuki distribution are bent in the opposite direction. In Fig. 6 the quantiles related to the r.m.s. value F_{OS} and in Fig. 7 those related to the median value F_{S50} are plotted versus the Suzuki parameter s.

4. Determination of the distribution parameters

All three distribution functions are described unambiguously by two parameters:

- the Weibull distribution by w and F_{OW},
- the Nakagami-m-distribution by m and F_{ON} and
- the Suzuki distribution by s and F_{OS}.

The second parameter F_O also can be converted into another characteristic field strength level, e.g. the mean $\bar{F}$ or the median value F_{50}. Formulas of these relations are given in detail by LORENZ, March 1979.

The two parameters of each distribution can be calculated from the mean (first moment) of the measured values

$$\hat{\bar{F}} = \frac{1}{n} \sum_{i=1}^{n} x_F \qquad (11)$$

and the second central moment of the measured values

$$\hat{\mu}_2 = \widehat{\overline{(F - \bar{F})^2}} = \frac{1}{n} \sum_{i=1}^{n} \left(x_F - \hat{\bar{F}} \right)^2 \qquad (12)$$

Here n is the number of measured events,

x_F is one single event, i.e. one measured field strength level and

^ denotes an empirical value, i.e. resulting from measurements.

In the following, the formulas for the parameters of each distribution are summarized:

4.1 Weibull distribution

$$\hat{w} = 11{,}14 / \sqrt{\hat{\mu}_2} \qquad (13) \qquad\qquad \hat{F}_{OW} = \hat{\bar{F}} + 4{,}343 \cdot \ln \left[\Gamma \left(1 + \frac{2}{\hat{w}} \right) \right] \qquad (14)$$

4.2 Nakagami-m-distribution

A formula of the parameter m cannot be calculated exactly, since there has to be found an analytical expression of the inversion of the trigamma function $\psi'(m)$, tabled by ABRAMOWITZ, 1968, chapter 6. However, for $0{,}5 \leq m \leq 10$, we found the following expression

$$\hat{m} = \frac{4{,}4}{\sqrt{\hat{\mu}_2}} + \frac{17{,}4}{\hat{\mu}_2^{1{,}29}} \qquad (15)$$

to be a good approximation.

The second parameter of the Nakagami-m-distribution is

$$F_{ON} = \hat{\bar{F}} - 4{,}343 \cdot \left\{ \psi(\hat{m}) - \ln(\hat{m}) \right\} \qquad (16)$$

with $\psi(x)$ being the digamma function, also tabled by ABRAMOWITZ.

4.3 Suzuki distribution

$$\hat{S} = \sqrt{\hat{\mu}_2 - 31{,}025} \qquad (17) \qquad\qquad \hat{F}_{OS} = \hat{\bar{F}}_S + 2{,}51 - 0{,}115\, \hat{S}^2 \qquad (18)$$

5. Choice of the distribution fitting best on the average

Due to the large number of different obstacles in mobile environment, rather different situations occur. Thus, the cumulative distributions can differ very much even in the same area measured. If e.g. in a city a road is directed towards the base station with free line-of-sight, the field strength is high and the variance small. In a perpendicular road the field strength is low, but at crossings with free line-of-sight the field strength rises by more than 14 dB. Other fluctuations, unpredictable by a topographical data bank, occur in public squares, on embankments or in grooves, lanes in forests, on big bridges and so on. Thus, large differences between theoretical and measured distribution functions should be expected.

5.1 Cramér-von-Mises Test

SUZUKI, 1977, used the Cramér-von-Mises test to select the proper distribution. This method requires integration over the square of the differences between experimental and theoretical distribution functions. The one with the minimum result is the best one. As, according to Eq. (10), the Suzuki distribution has to be integrated numerically, it is necessary to perform a double numerical integration. Considering the great variety of different experimental distributions mentioned above, it is understandable that Suzuki was not able to analyse enough measurements with this troublesome method to obtain statistically significant evidence for his theory that the mixed distribution is the best in describing the fluctuations of field strength level at a mobile. He even restricted his conclusions to Rayleigh, log-normal, Rice and Nakagami-m-distributions, excluding the mixed distribution. No one of these distributions provided a satisfactory description of his measurements in certain types of terrain.

5.2 Method of moments

Considering the problems Suzuki dealt with, we tried the method of moments to find out the theoretical distribution best describing our measurements in quasi-smooth terrain. Using the moment generating function, the central moments of all considered distributions can be calculated analytically. The two parameters of the distributions are computed each by means of the first moment and the second central moment according to Eqs. (13-18). By comparison of the higher order central moments of the theoretical and empirical distributions that with the smallest differences can be chosen. The result of this method was unsatisfying, however, when we compared the plots of empirical and theoretical distributions favoured or disfavoured by this method. This is due to the fact that the central moments describe a distribution function in the same manner as a Taylor series describes analytical functions. The point of development is the mean value of the cumulative distribution function. Thus, the moments describe the adjacent points near the mean value of the distribution functions quite well, but not their tails. These are, however, more important in practice and the description of their statistical behaviour is the goal of our analysis. In addition, the values of the higher order empirical moments vary very much due to the unimportant small irregularities of a measured distribution. Moreover, it is a troublesome analytical work to derive the formulas of central moments of orders higher than 4 for the Nakagami-m- and Suzuki distributions.

5.3 Analysis of quantiles

As we are interested in quantiles between, say, 1% and 20% and between 80% and 99%, the theoretical distribution should be chosen which best describes these quantiles. In Fig. 8 the theoretical quantiles F_{99}-F_{50} are plotted for the three distributions versus the parameters s, w and m. The parameters are arranged on the abscissa in such a way that the second central moments μ_2 are identical according to Eqs. (13), (15), and (17). In Fig. 8 all measured quantiles in small size cities are included as an example. In any case, the large fluctuations are not encouraging. By plotting a similar figure for the quantile F_{90} we get smaller deviations from the curve of the theoretical Suzuki quantiles. There is, however, a way to show more conclusively that the Suzuki distribution on the average really describes the measurements best in small size cities. In Fig. 8 the crosses are related to individual measured sections. For analysing a large number of measurements statistical methods should be used. Thus, we classify the distribution parameters $\hat{s}$, $\hat{w}$ and $\hat{m}$. The results for small size cities in quasi-smooth terrain are plotted in Figs. 9, 10 and 11, respectively. Each value of w, m or s is related to a certain quantile and as we know the probability of the parameters, we can calculate the value of the quantile having the same probability. In Fig. 12 the distribution functions of the quantiles F_{50}-F_{99} of the three considered theoretical distribution functions are plotted, using the distributions of the parameters as shown in Figs. 9, 10 and 11, respectively. The same analysis is made for the quantiles F_1-F_{50} and plotted in Fig. 13. The measured quantiles $\hat{F}_{50}$ -$\hat{F}_{99}$ and $\hat{F}_1$-$\hat{F}_{50}$ were classified, too, and the results are marked by crosses in Figs. 12 and 13. The good agreement allows the convincing conclusion to be drawn that the Suzuki distribution best describes the fluctuations of the field strength in a mobile environment in small size cities. In addition, it is evident from Fig. 9 that the parameter $\hat{s}$ is distributed normally, which renders the computation rather simple.

5.4 Results in quasi-smooth terrain

So far, we have measured medium size cities, small size cities, forests and open areas in quasi-smooth terrain of the upper Rhine valley (see LORENZ, June 1979). Apart from open areas, the Suzuki distribution describes the measurements best in all cases and the Suzuki parameters are normally distributed in each case.
The results are summarized in the following table:

Type of quasi-smooth terrain	$\overline{s}$	σ_s
Medium size cities	3,3 dB	1,5 dB
Forests	3,7 dB	1,7 dB
Small size cities	3,9 dB	1,9 dB

There are two reasons why the fluctuations in small size cities are largest:

- transitions to open areas occur more often than in medium size cities and

. in the upper Rhine valley narrow roads are typical in small size cities. Thus, the attenuation due to diffraction is high.

In quasi-smooth open areas line-of-sight mostly occurs. Therefore, the Nakagami-m-distribution should be expected. It is evident from Figs. 4 and 5, however, that the differences between the quantiles of the Nakagami-m and Weibull distributions are small. Hence, the latter should be included into the analysis because of its easier computability. The Suzuki distribution is not applicable in open areas, because its variance cannot become smaller than that of the Rayleigh distribution. In Figs. 14 and 15 the cumulative distributions of the parameters $\hat{m}$ and $\hat{w}$ calculated from measurements in quasi-smooth open areas which are identified by the topographical data bank, are plotted on Gaussian probability paper. In about 80% of the measurements the value of the Rayleigh distribution ($m = 1$ respectively $w = 2$) is exceeded, i.e. the variance is smaller than that of the Rayleigh distribution. The rest of 20% results from insufficiencies or errors contained in the data bank. This terrain is not really open, but there are large single buildings surrounded by orchards or parks, new building sites or avenue trees causing large reflections and diffractions. Apart from these 20%, the Weibull parameter is normally distributed. The distribution of the Nakagami parameters m also can be approximated by a normal distribution. In Figs. 16 and 17 the distributions of the quantiles F_{50}-F_{99} and F_1-F_{50} are plotted. The curves were computed by means of the distributions of the parameters m or w , respectively, according to Figs. 14 and 15. The crosses result from the classification of the measured quantiles. The highest values of F_{50}-F_{99} are overestimated by both distributions. But as the median attenuation in open areas is much smaller than in cities and forests, this quantile is unimportant in practice. In open areas the ratio of wanted to unwanted signals of co-channel transmitters is the crucial limit of a frequency efficient mobile communication system. Here the upper quantiles are important.

In Fig. 17 the measured values $\hat{F}_1$-$\hat{F}_{50}$ seem to be better described by the Weibull distribution, especially the high values. But these values were measured in areas, where the information of the data bank is wrong, since the area is not really open. In this case, higher median attenuations arise and the quantile F_1 related to a calculated median value for open areas is not as high as indicated in Fig. 17. This has been the only case, so far, that a correlation between median attenuation and quantiles has been observed in our measurements.

6. Conclusion

In cities and forests the median attenuation is high. Thus, the signal-to-noise ratio is the crucial limit of a mobile communication link. This can be described by the lower quantile, e.g. F_{50}-F_{99}, as plotted in Fig. 12 for the example of quasi-smooth small size cities. The measured quantiles are well described by the Suzuki distribution on the average. The Suzuki parameter is distributed normally. This conclusion holds also for medium size cities and forests. The parameters of the distribution of the Suzuki distribution parameters are listed in section 5.4.

In open areas the median attenuation is low. Thus, the ratio of wanted to unwanted signals of co-channel transmitters is the crucial limit of the mobile communication link. This can be described by the upper quantile, e.g. F_1-F_{50}, as plotted in Fig. 17. Due to errors in the data bank, there are areas, which are not really open and where high values of median attenuation are measured together with high values of the upper quantiles. Quantiles related to median values calculated by means of the formulas of open areas are smaller. Therefore, the Nakagami-m-distribution describes the upper quantiles in open areas better than the Weibull distribution. The parameters m are distributed normally with the mean $\bar{m} = 1.8$ and $\sigma_m = 1.1$. The differences between the quantiles of the Nakagami-m-distribution and the Weibull distribution are small, however, especially, if smaller differences of quantiles are to be computed, e.g. F_5-F_{50}. As the Weibull distribution is much easier to handle, it may be applied to open areas. This approximation is somewhat inferior, but since the quantiles of the Weibull distribution are higher than those of the Nakagami-m-distribution, the margin of the ratio of wanted to unwanted signals is larger for planning purposes. The Weibull parameter is normally distributed with the mean $\bar{w} = 2.9$ and the standard deviation $\sigma_w = 1.0$.

References

ABRAMOWITZ, M., STEGUN, I.A., 1968, "Handbook of Mathematical Functions", Dover Publications, 5th Edition.

ALLSEBROOK, K., PARSONS, J.D., 1977, "Mobile Radio Propagation in British Cities at Frequencies in the VHF and UHF Bands", IEEE Trans. VT-26, pp. 313-323

BULLINGTON, K., 1947, "Radio Propagation at Frequencies above 30 MHz", Proc. IRE 35, pp. 1122-1136

MC DONALD, V.H., 1979, "Advanced mobile phone service: The Cellular Concept", BSTJ 58, pp. 15-42

EGLI, J.J., 1957, "Radio Propagation Above 40 MC Over Irregular Terrain", Proc. IRE 45, pp. 1383-1391

HACKING, K., 1970, "UHF propagation over rounded hills", Proc. IEE 117, pp. 499-511

ITO, Sadao, MATSUZAKA, Y., 1977, "800 MHz Band Land Mobile Telephone System - Overall View," Review of the Electrical Communication Laboratories 25, pp. 1147-1156

ITO, Shiro et al., 1971, "Computer drawing of field strength map", NHK Lab. Note No. 140

KESSLER, W.J., WIGGINS, M.J., 1977, "Simplified Method for Calculating UHF Base-to-Mobile Statistical Coverage Contours over Irregular Terrain", Conf. Record 27th annual Conference IEEE Vehicular Technology Group, Orlando, Florida, pp. 227-236

LEE, B.K., 1977, "VHF Propagation Prediction With Path Profile Methods", AGARD Conf. Proceedings 244-17, Aspects of Electromagnetic Wave Scattering in Radio Communications, Cambridge, Mass.

LONGLEY, A.G., RICE, P.L., 1968, "Prediction of Tropospheric Radio Transmission Loss Over Irregular Terrain, A Computer Method-1968", ESSA Technical Report ERL 79-ITS 67

LORENZ, R.W., 1978, "Small cell structures for mobile radio", Nachrichtentechn. Z. 31, pp. 192-196, (in German)

LORENZ, R.W., 1979, "Theoretical Distribution Functions of Multipath Fading Processes in the Mobile Radio and Determination of their Parameters by Measurements", Techn. Ber. 455 TBr 66, Forschungsinstitut der Deutschen Bundespost, (in German) (March)

LORENZ, R.W., 1979, "Spatial Distribution of Electromagnetic Field Strength for Mobile Radio", NATO Workshop on EW Impact on Communication Systems. Brussels, (June)

LUSTGARTEN, M.N., MADISON, J.A., 1977, "An Empirical Propagation Model (EMP-73)", IEEE Trans EMC-19, pp. 301-309

NAKAGAMI, M., 1960, "The m-distribution - A General Formula of Intensity Distribution of Rapid Fading", in W.C. Hofman: Statistical Methods in Radio Wave Propagation. Pergamon Press, pp. 3-36

NORTON, K.A. et. al., 1955, "The Probability Distribution of the Amplitude of a Constant Vector Plus a Rayleigh-distributed Vector", Proc. IRE 43, pp. 1354-1361

OKUMURA, Y. et.al., 1968, "Field strength and its variability in VHF and UHF land-mobile radio service", Review of the Electrical Comm. Lab. 16, pp. 825-873

PALMER, F.H., 1978, "The CRC VHF/UHF Propagation Prediction Program: Description and Comparison with Field Measurements", AGARD Conf. Proc. 238, Canada, pp. 49-1-49-15

The Radio Research Laboratory, 1957, "Atlas of Radio Wave Propagation Curves for Frequencies between 30 and 10,000 Mc/s", Ministry of Postal Services, Tokyo, Japan

RICE, S.O., 1948, "Statistical Properties of a Sine Wave Plus Random Noise", BSTJ 27, pp. 109-157

SHEPHERD, N.H., 1977, "Radio Wave Loss Deviation and Shadow Loss at 900 MHz", IEEE Trans VT-26, pp. 309-313

STERN, M., GRAZIANO, V., 1977, "A New Portable and Mobile Radiotelephone System Goes to Washington (and Baltimore)", Telephony, pp. 26-35

SUZUKI, H., 1977, "A Statistical Model for Urban Radio Propagation", IEEE Trans. COM-25, pp. 673-680

YOSHIKAWA, N., NOMURA, T., 1976, "On the Design of a Small Zone Land Mobile Radio System in UHF Band", IEEE Trans. VT-25, pp. 57-67

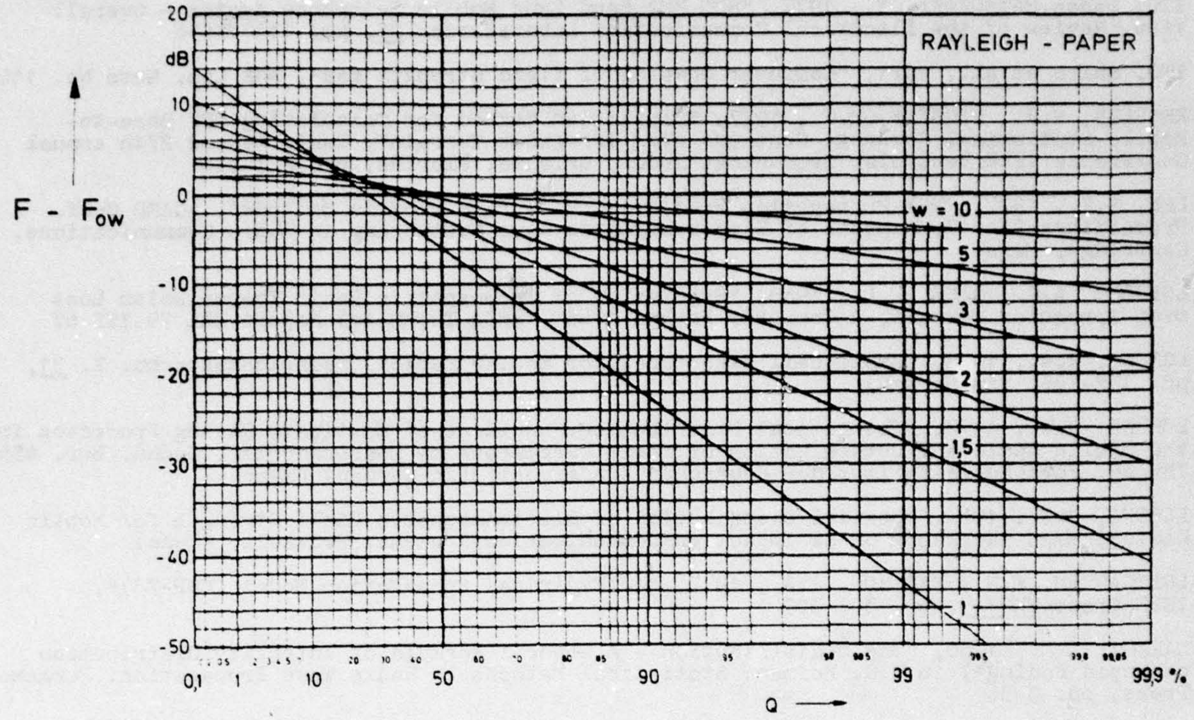

Fig.1 Weibull distribution

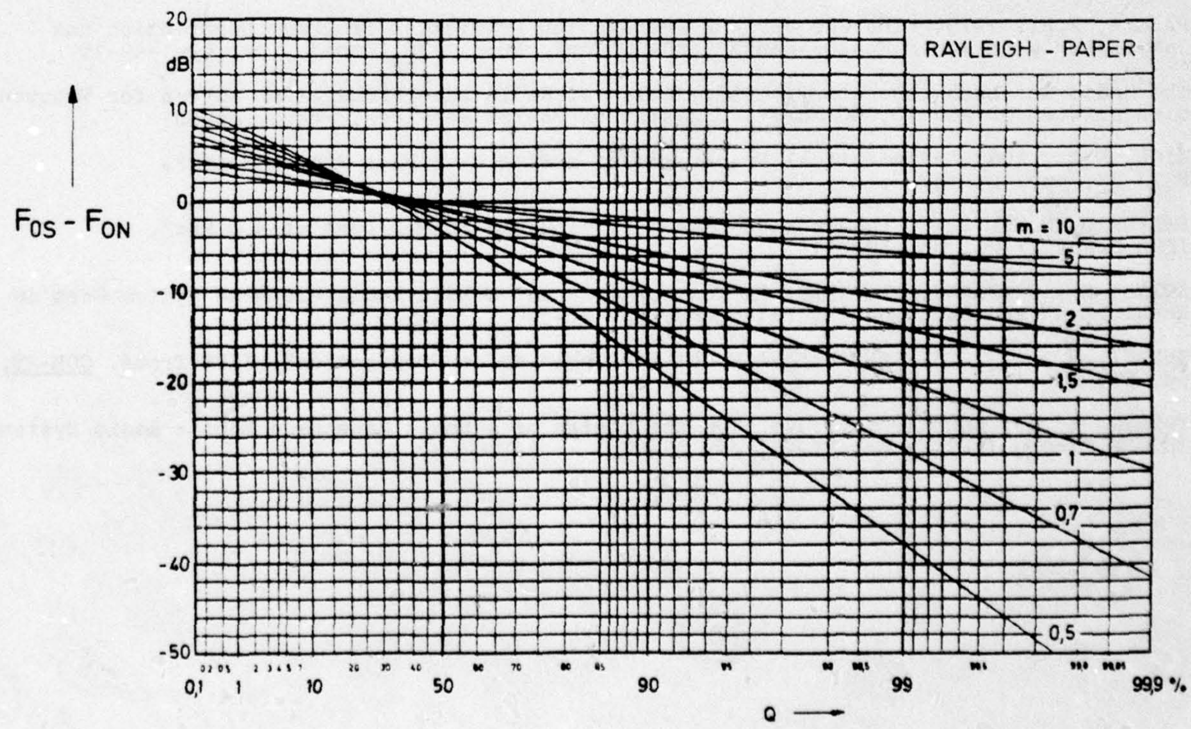

Fig.2 Nakagami-m-distribution

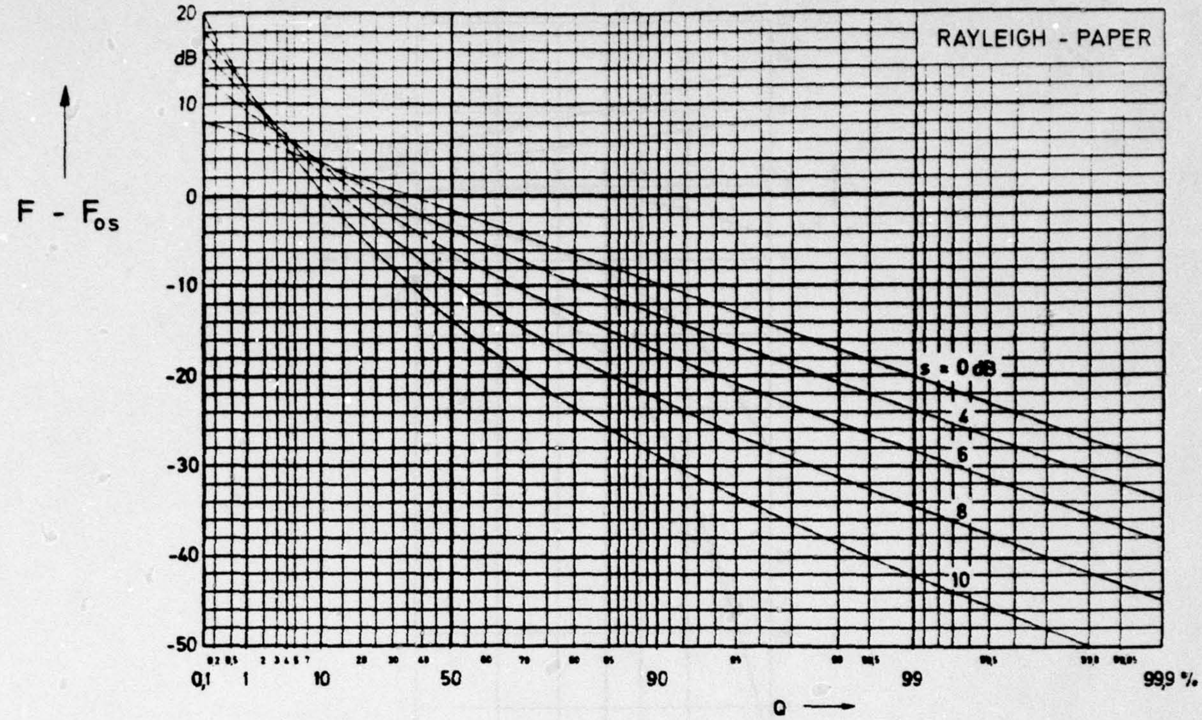

Fig.3 Mixture of Rayleigh and log-normal distributions, called "Suzuki distribution"

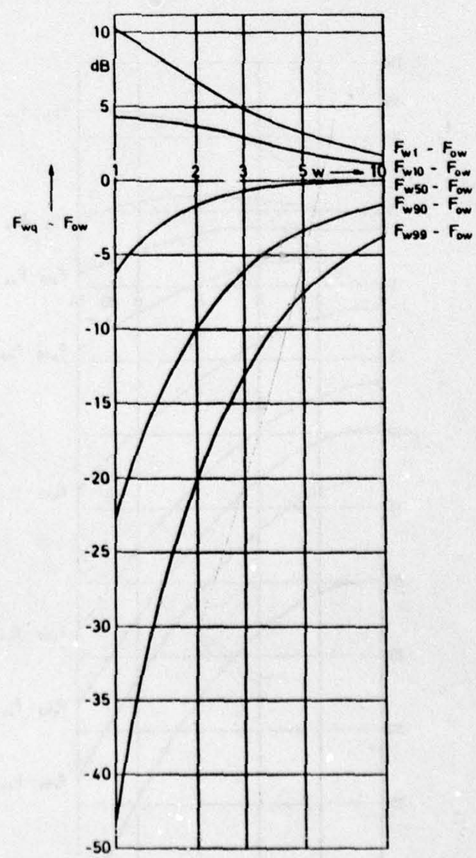

Fig.4 Quantiles of the Weibull distribution (1%, 10%, 50% = median value, 90% and 99%) related to the level F_0 of the r.m.s. field strength E^2

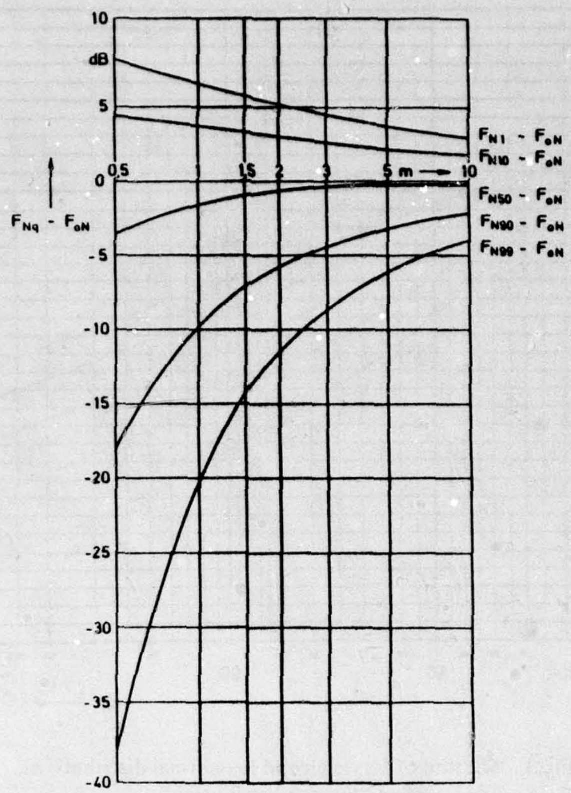

Fig.5 Quantiles of the Nakagami-m-distribution

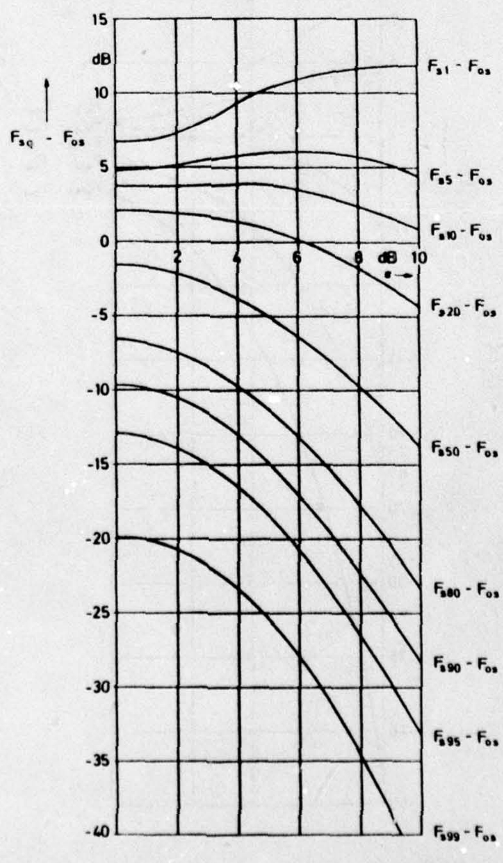

Fig.6 Quantiles of the Suzuki distribution

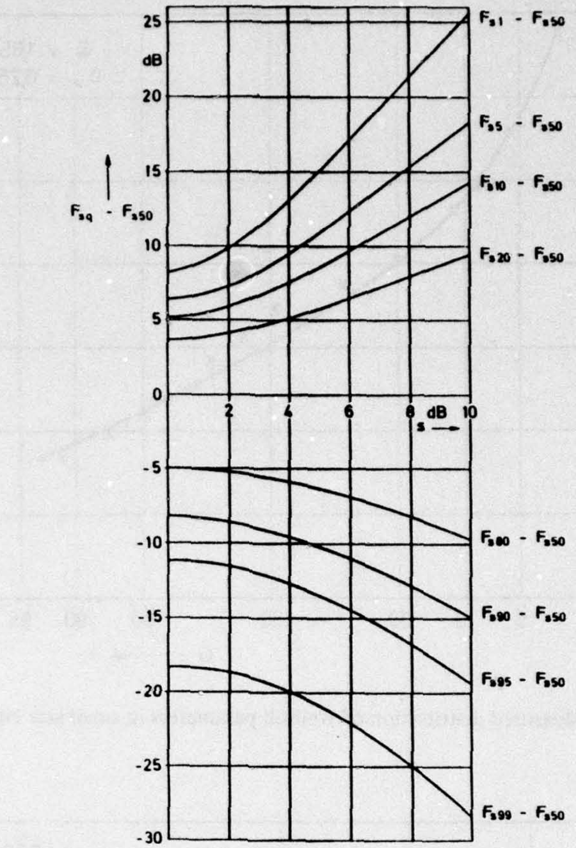

Fig.7 Quantiles of the Suzuki distribution related to the median value of the field strength level F_{50}

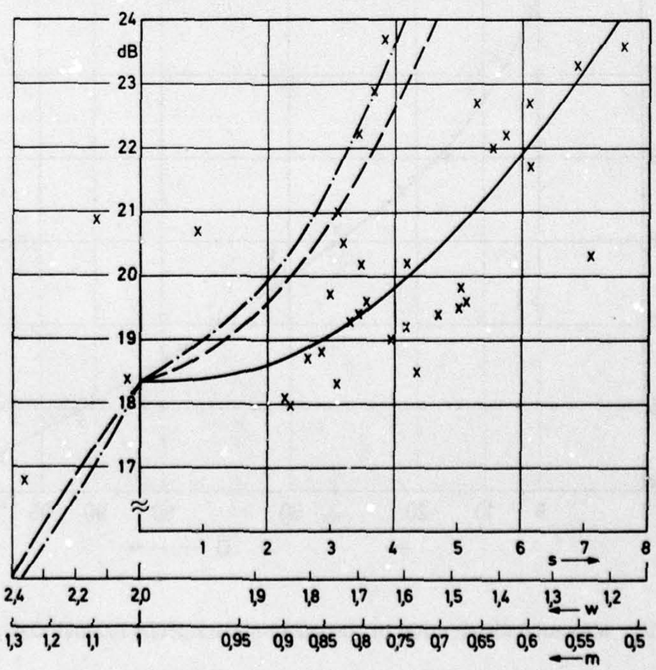

Fig.8 Quantiles $F_{50} - F_{99}$ versus the distribution parameters for equivalent standard deviations

——— Suzuki distribution

– – – – Weibull distribution

– · – · – · Nakagami-m-distribution

x Measured values in small size cities

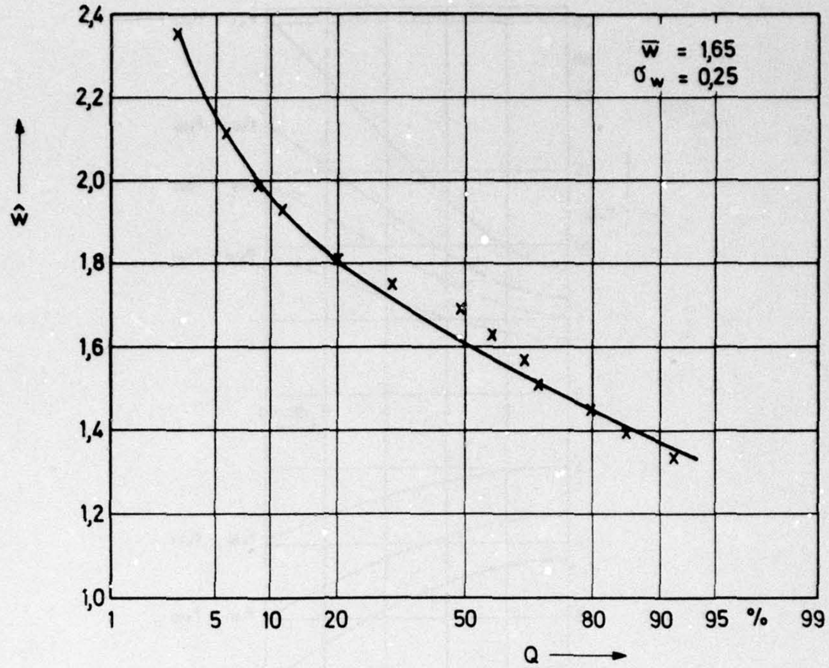

Fig.9 Measured distribution of Weibull parameters in small size cities

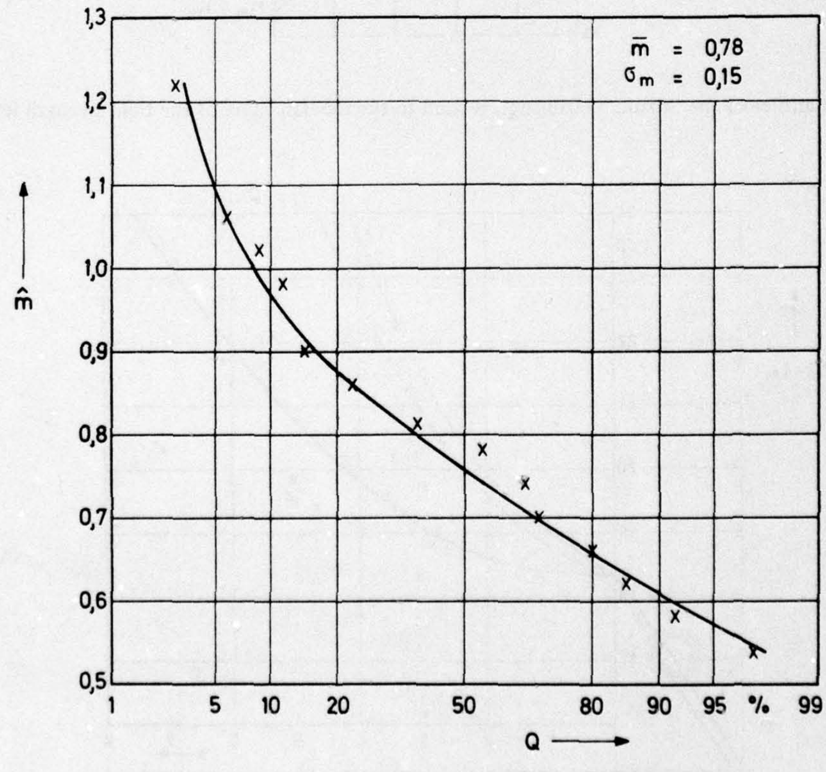

Fig.10 Measured distribution of Nakagami-m-parameters in small size cities

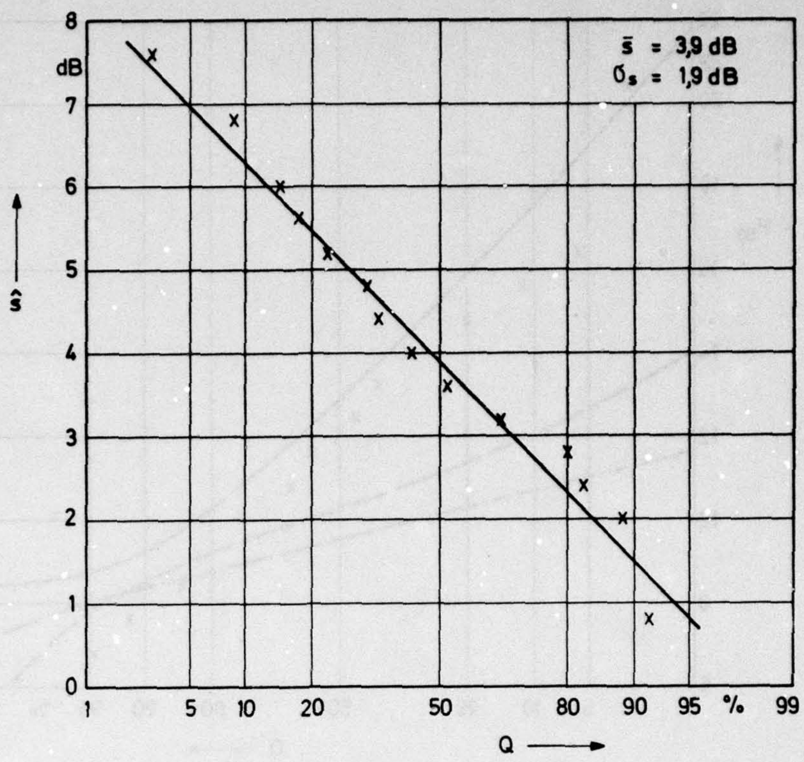

Fig.11 Measured distribution of Suzuki parameters in small size cities

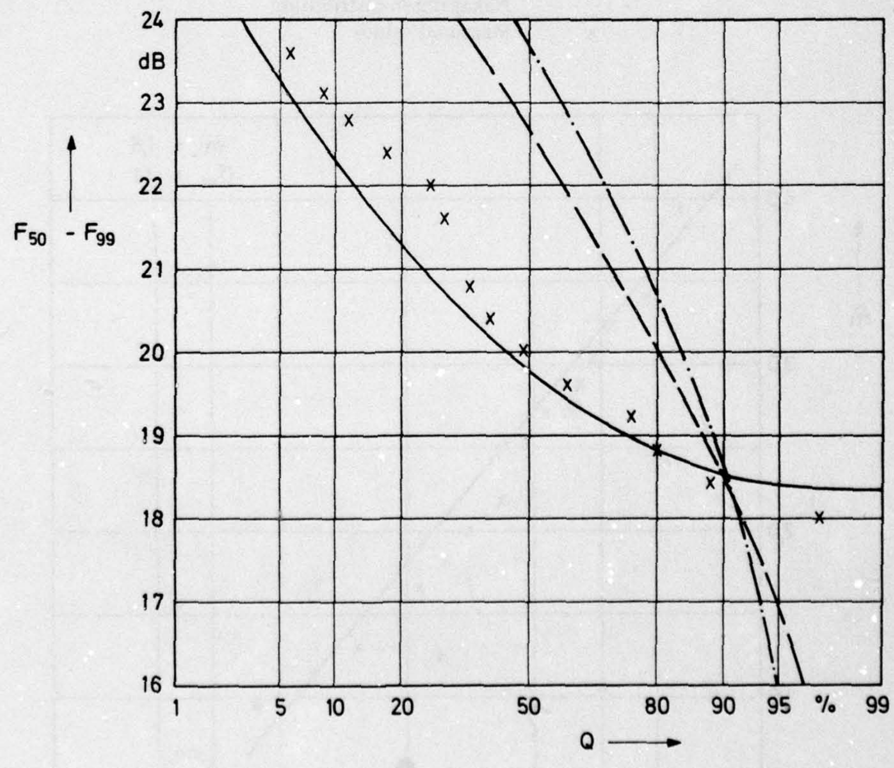

Fig.12 Distribution of the quantiles $F_{50} - F_{99}$ in small size cities

———— Suzuki distribtuion
— — — — Weibull distribution
— · — · — · Nakagami-m-distribution
x Measured values

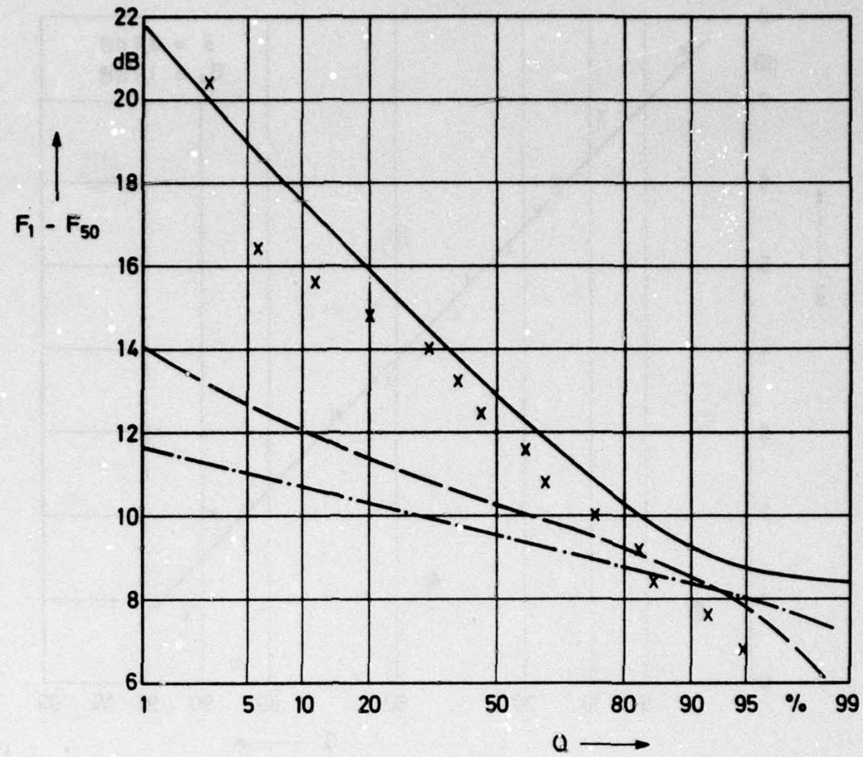

Fig.13 Distribution of the quantiles $F_1 - F_{50}$ in small size cities

————	Suzuki distribution
– – – –	Weibull distribution
– · – · – ·	Nakagami-m-distribution
x	Measured values

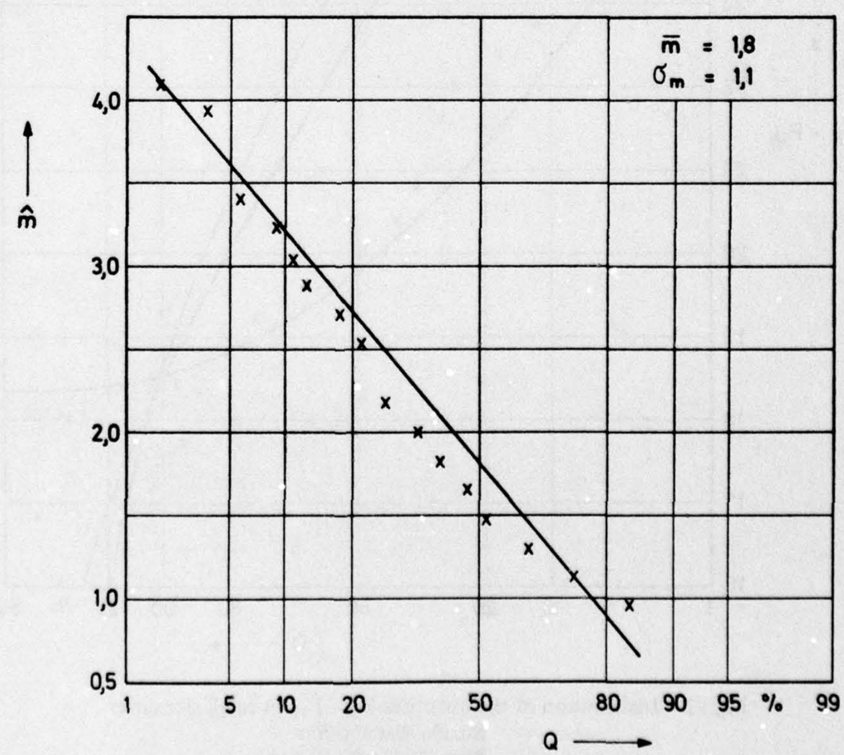

Fig.14 Measured distribution of Nakagami-m-parameters in open areas

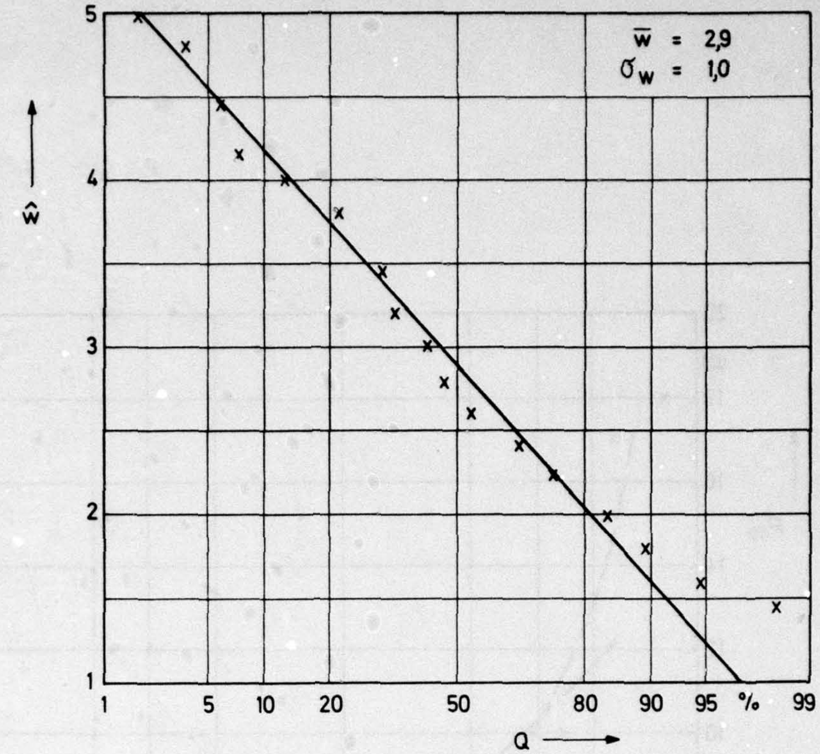

Fig.15 Measured distribution of Weibull parameters in open areas

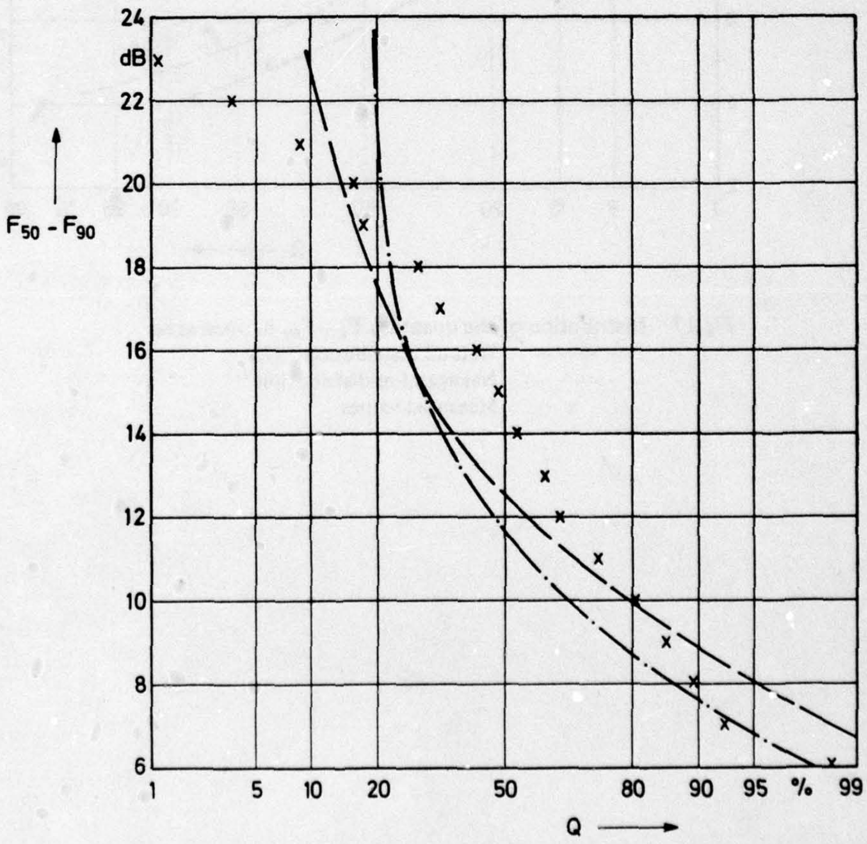

Fig.16 Distribution of the quantiles $F_{50} - F_{99}$ in open areas

– – – – Weibull distribution

– · – · – · Nakagami-m-distribution

x Measured values

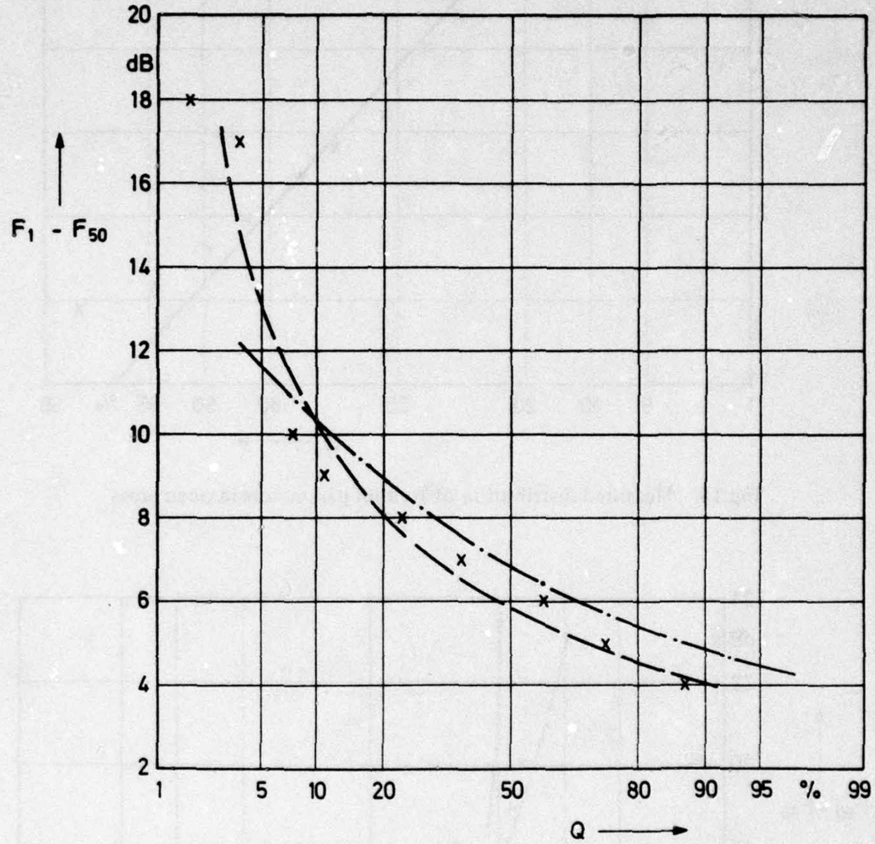

Fig.17 Distribution of the quantiles $F_1 - F_{50}$ in open areas
– – – – Weibull distribution
– · – · – · Nakagami-m-distribution
x Measured values

ON THE INFLUENCE OF SURFACE STATISTICS, GROUND MOISTURE CONTENT AND WAVE POLARISATION ON THE SCATTERING OF IRREGULAR TERRAIN AND ON SIGNAL POWER SPECTRA

K.J. Hortenbach

Deutsche Welle, Köln
Fed. Rep. of Germany

SUMMARY

The scattering properties of statistically rough terrain with large roughness scale have been shown by the specular point theory to depend fundamentally on the probability distribution of the surface slopes. In theoretical studies Gaussian surface statistics have widely been used for ease of computation regardless of the actual terrain features. To meet the actual requirements, slope probability distributions of terrain profiles are determined from contour maps of really existing hilly terrain and are found to differ reasonably from Gaussian distributions. With the results obtained the scattering properties of different types of terrain are investigated making visible the shape and fine structure of the effective scattering area by plotting contours of constant average scattered power density on the main scattering plane. Computations and comparisons are carried out for Gaussian and actual roughness statistics, different polarisations and moisture content of the ground. It is shown that the effective scattering area exhibits a detailed fine structure which is most complex when the angle of the incident radiation is near the pseudo-Brewster angle. This structure modifies the radiation patterns of antennas operating above irregular terrain as well as the signal characteristics. The power density spectrum of a signal transmitted or received by an aircraft flying over irregular terrain generally becomes spread due to the scattering process. The shape of the resulting spectrum depends on the orientation of the velocity vector of the aircraft relative to the scattering area and on its structure. This is demonstrated by calculating the scattering power density spectra of an incident monochromatic wave for different statistical and electrical properties of the terrain and different polarisations. The calculation is performed by integrating over the scattered power density as given by the structure of the effective scattering area along a path of constant Doppler shift. It is shown that the shape of the resulting spectrum also has a fine structure and can be highly asymmetrical relative to the frequency of the directly incident wave which is verified experimentally.

1. INTRODUCTION

Radio links between mobile terminals operating above irregular terrain as e.g. aircraft-to-aircraft or aircraft-to-satellite links can be detrimentally affected by electromagnetic wave scattering from the rough surface. Therefore, the variations of scattering properties and signal characteristics due to surface statistics, wave polarisation and ground parameters must be taken into account for the development of adequate modulation techniques, the design of appropriate antennas as well as the correct interpretation of experimental data.

For the prediction of rough surface scattering a suitable model for the surface roughness must be selected. The most realistic and generally applicable models describe the roughness heights above a reference plane by a stationary random process. The scattering properties of such models are given by the average scattering cross section per unit area as a function of the probability density and the autocorrelation function of the random process.

Theories on rough surface scattering are based on quite different approaches depending on the roughness scale w.r.t. the electromagnetic wave length (PEAKE, W.H., BARRICK, D.E., 1976). In the following we shall restrict ourselves to large scale roughness, i.e. we assume the standard deviation of the roughness heights being large compared with the wave length. This is justified for gently sloping terrain at frequencies in the VHF-/UHF-range.

2. THE SCATTERING CROSS SECTION

From the well-known Stratton-Chu integral equation the physical optics or Kirchhoff integral is derived which is solved by the application of the stationary phase principle yielding the average scattering cross section per unit area (BARRICK, D.E., 1970)

$$\sigma^{o}_{p,q} = \pi \sec^4 \beta \; p(\zeta_x, \zeta_y) \, |R_{p,q}(\eta)|^2 \tag{1}$$

where

$p(\zeta_x,\zeta_y)$ = probability density of surface slopes, evaluated at the stationary or specularly reflecting points,

$|R\,p,q\,(\eta)|$ = Fresnel reflection coefficient for an infinite plane tangent to the surface at the specular points for scattered (first subscript) and incident (second subscript) polarisation states. (The subscripts stand for horizontal and vertical polarisation.)

η = local angle of incidence at the specular point.

Introducing the coordinate system of Fig. 1 η is expressed by

$$\cos \eta = \left[\frac{1}{2} (1 + \cos \Theta_o \cos \Theta - \sin \Theta_o \sin \Theta \cos \phi) \right]^{1/2} \tag{2}$$

where Θ and ϕ are the scattering angles in the vertical and horizontal plane and Θ_o is the angle of incidence.

β = angle between local surface normal and z-axis, given by

$$\tan^2 \beta = \zeta_x^2 + \zeta_y^2 = \frac{\sin^2\Theta_o + \sin^2\Theta - 2 \sin \Theta_o \sin \Theta \cos\phi}{(\cos \Theta_o + \cos \Theta)^2} \tag{3}$$

The average scattering cross section per unit area as given by (1) is valid under the following restrictions:

1) The standard deviation of the roughness height is large compared to the wave length.

2) The correlation radius of the random process describing the roughness is large compared to the standard deviation of the heights. Restrictions 1) and 2) involve that the radii of curvature are large compared to the wavelength everywhere justifying the application of the tangent plane (physical optics-, Kirchhoff-) approximation. This approximation involves writing the scattered field at the surface as the product of the incident field and the proper reflection coefficient.

3) The illuminated area is large compared to the square of the correlation radius.

4) Multiple scattering and shadowing is neglected. Shadowing may be taken into account subsequently by multiplying (1) by a "shadowing function" which has been derived for Gaussian surfaces by different authors, e.g. (WAGNER, R.D., 1967; SMITH, B.G., 1967; SANCER, M.I., 1969; BROCKELMAN, R.A. and HAGFORS,T., 1966).
The field described by (1) originates from the incoherent superposition of individual fields reflected by a number of discrete, independent specular reflection points (KODIS, R.D., 1966; BARRICK, D.E., 1968).

2. ROUGH SURFACE STATISTICS

According to (1) the slope probability density function of the surface roughness must be specified to calculate the scattering cross section. The slope probability density function can be derived from the probability density of the surface heights and the surface autocorrelation function.

In the literature Gaussian surface height distributions have been used almost exclusively. This is not so much for physical evidence but for mathematical convenience as well as for the lack of information about the statistics of natural terrain. The assumption of Gaussian height statistics may be justified physically for a slightly rough sea or gently rolling terrain but certainly not for rough sea or mountainous regions. In these cases broad valleys and narrow ridges occur giving rise to strongly skewed distributions. However, for slight roughness scales as well as for grazing incidence the scattering properties do not depend very strongly on the height distribution as is the case for large roughness scales and other directions of incidence. Likewise, the autocorrelation function has usually been assumed to be Gaussian-shaped or exponential. However, the shape of the autocorrelation function of very rough surfaces is not of great importance except near the origin.

From the literature only few efforts to introduce non-Gaussian statistics into the analysis have become known (BECKMANN, P., 1973). On the other hand, only few attempts have been made to investigate the statistics of natural terrain (HAYRE, H.S. and MOORE, R.K., 1961).

2.1. Gaussian statistics

The two-dimensionally rough terrain shall be described by a stationary random process $z = \zeta(x, y)$ where z is the surface height at the point (x, y). The random heights shall be Gaussian distributed with zero mean $\langle \zeta \rangle = o$ and the standard deviation h_o. The probability density of the surface heights is then

$$p_\zeta(z) = \frac{1}{\sqrt{2\pi}\, h_o} \exp\left(- \frac{z^2}{2\, h_o^2} \right) \tag{4}$$

For the autocorrelation function of the random process a bell-shaped function is assumed which is quadratic near the origin:

$$B(r) = h_o^2 \exp(- r^2/L^2), \quad r = \sqrt{x^2 + y^2} \tag{5}$$

where L is the correlation radius and r the distance of a point on the xy-plane from the origin.

From (4) and (5) the probability density function of the surface slopes ζ_x and ζ_y can be derived (BECKMANN,P., 1967).

$$p_{\zeta_x,\zeta_y}(z_x, z_y) = \frac{1}{\pi \cdot \tan^2 \beta_o} \exp\left[- \frac{z_x^2 + z_y^2}{\tan^2 \beta_o} \right] \tag{6}$$

where

$$\tan \beta_o = 2\, h_o/L \tag{7}$$

is proportional to the r.m.s.-value and $z_x^2 + z_y^2 = \tan^2 \beta$ gives the angle β between the local surface normal and the z-axis. In terms of the angles of incidence and scattering $\tan \beta$ is given by (3).

By a transformation of the random variables the p.d.f. of the slope angles is obtained from (7)

$$p_\beta(\beta) = p_{\tan\beta}(\beta) \left| \frac{d(\tan\beta)}{d\beta} \right|$$

$$= \frac{2(1+\tan^2\beta)\tan\beta}{\tan^2\beta_o} \exp(-\tan^2\beta/\tan^2\beta_o) \tag{8}$$

By integration of (6) over all values of one of the two variables, e.g. ζ_y, the p.d.f. of the corresponding one-dimensionally rough profile is obtained. The corresponding p.d.f. of the angles then yields

$$p_\gamma(\gamma) = \frac{1+\tan^2\gamma}{\sqrt{\pi}\tan\gamma_o} \exp[-(\tan\gamma/\tan\gamma_o)^2] \tag{9}$$

where $\tan\gamma = \zeta_x$, $\tan\gamma_o = 2h_0/L(x)$.
Fig. 2 shows a plot of (9) for different values of γ_o.

2.2. Natural terrain statistics

In order to investigate the surface statistics of actual natural terrain one-dimensional profiles of hilly terrain taken from contour maps have been analyzed. A χ^2-test for normality confirmed that the surface heights were generally not normally distributed with reasonable significance. The autocorrelation functions were found to be quadratic near the origin and decreasing to half the initial value within 0.6 to 2 kilometres. The standard deviation of the heights ranged between 40 and 90 metres.

An average p.d.f. of the slope angles is shown in Fig. 2 for comparison with the curves computed from (9). At small angles the measured values agree fairly well with a Gaussian distribution with small γ_o, at large angles with a Gaussian distribution with large γ_o. Therefore, the p.d.f. of the actual profile is approximated by the superposition of two Gaussian p.d.f.'s:

$$p_\gamma(\gamma) = \frac{1+\tan^2\gamma}{\sqrt{\pi}} \left[\frac{c_1}{\tan\gamma_{o1}} \exp -[(\tan\gamma/\tan\gamma_{o1})^2] + \right.$$

$$\left. + \frac{c_2}{\tan\gamma_{o2}} \exp[-(\tan\gamma/\tan\gamma_{o2})^2] \right] \tag{10}$$

The constants were fitted to

$c_1 = 0.6, \quad \gamma_{01} = 2.5^0$

$c_2 = 0.4, \quad \gamma_{02} = 15^0$

Equ. (10) is also shown in Fig. 2.

The p.d.f. of the surface slopes corresponding to (10) is

$$p_{\zeta_x}(z_x) = \frac{c_1}{\sqrt{\pi}\tan\gamma_{o1}} \exp\left[-\frac{z_x^2}{\tan^2\gamma_{o1}}\right] + \frac{c_2}{\sqrt{\pi}\tan\gamma_{o2}} \exp\left[-\frac{z_x^2}{\tan^2\gamma_{o2}}\right] \quad (11)$$

The linear and quadratic means of ζ_x are, respectively

$$\langle\zeta_x\rangle = \int_{-\infty}^{\infty} p_{\zeta_x}(z_x)\, z_x\, dz_x = 0$$

$$\langle\zeta_x^2\rangle = \int_{-\infty}^{\infty} p_{\zeta_x}(z_x)\, z_x^2\, dz_x = \frac{c_1}{2}\tan^2\gamma_{o1} + \frac{c_2}{2}\tan^2\gamma_{o2}$$

and the standard deviation

$$\tan\gamma_o = (c_1/2\tan^2\gamma_{o1} + c_2/2\tan^2\gamma_{o2})^{1/2}$$

With the constants listed above, this yields

$$\tan\gamma_o = 0.12 \quad \text{and} \quad \gamma_o = 6.8^0.$$

Extending (11) to the case of two-dimensional roughness one finally obtains

$$p_{\zeta x,\zeta y}(z_x,z_y) = \frac{1}{\pi}\left(\frac{c_1}{\tan^2\beta_{o1}} \exp\left[-\frac{z_x^2+z_y^2}{\tan^2\beta_{o1}}\right] + \frac{c_2}{\tan^2\beta_{o2}} \exp\left[-\frac{z_x^2+z_y^2}{\tan^2\beta_{o2}}\right]\right) \quad (12)$$

It must be noted that the summation of two Gaussian p.d.f.'s with different parameters was made just to fit a measured curve. It does not mean that the measured profile is to be understood as a superposition of two Gaussian processes with different variances. If this were the case the random variables themselves would have to be summed rather than their p.d.f.'s.

3. WAVE POLARISATION

In equ. (1) the proper reflection coefficient $R_{p,q}(\eta)$ for an infinite plane tangent to the surface at the specular points has to be inserted which depends on the polarisation states of the incident and scattered waves. As the Fresnel reflection coefficients are valid for horizontal and vertical polarisation the electric vector of an arbitrarily polarized incident wave must be decomposed into its horizontal and vertical components. The corresponding reflected fields are calculated separately and then recombined to a resultant field.

The complex reflection coefficients for an arbitrarily oriented surface are given by (MITZNER, K.M., 1966)

$$\underline{R}_{HH} = \underline{R}^-(\eta)\cos\beta_1\cos\beta_2 + \underline{R}^+(\eta)\sin\beta_1\sin\beta_2 = |R_{HH}|e^{j\vartheta_{HH}}$$

$$\underline{R}_{VV} = \underline{R}^-(\eta)\sin\beta_1\sin\beta_2 + \underline{R}^+(\eta)\cos\beta_1\cos\beta_2 = |R_{VV}|e^{j\vartheta_{VV}}$$

$$\underline{R}_{HV} = -\underline{R}^-(\eta)\sin\beta_1\cos\beta_2 + \underline{R}^+(\eta)\cos\beta_1\sin\beta_2 = |R_{HV}|e^{j\vartheta_{HV}}$$

$$\underline{R}_{VH} = -\underline{R}^-(\eta)\cos\beta_1\sin\beta_2 + \underline{R}^+(\eta)\sin\beta_1\cos\beta_2 = |R_{VH}|e^{j\vartheta_{VH}}$$

where (13)

$$\sin\beta_1 = \sin\Theta\sin\phi/\sin 2\eta$$

$$\cos\beta_1 = (\sin\Theta_o\cos\Theta + \cos\Theta_o\sin\Theta\cos\phi)/\sin 2\eta$$

$$\sin\beta_2 = \sin\Theta_o\sin\phi/\sin 2\eta$$

$$\cos\beta_2 = (\cos\Theta_o\sin\Theta + \sin\Theta_o\cos\Theta\cos\phi)/\sin 2\eta$$

The quantities $\underline{R}^+(\eta)$ and $\underline{R}^-(\eta)$ are the Fresnel coefficients

$$\underline{R}^+(\eta) = \frac{\underline{n}^2\cos\eta - \sqrt{\underline{n}^2 - \sin^2\eta}}{\underline{n}^2\cos\eta + \sqrt{\underline{n}^2 - \sin^2\eta}} = |\underline{R}^+|\,e^{j\vartheta^+} \tag{14}$$

for vertical polarisation and

$$\underline{R}^-(\eta) = \frac{\cos\eta - \sqrt{\underline{n}^2 - \sin^2\eta}}{\cos\eta + \sqrt{\underline{n}^2 - \sin^2\eta}} = |R^-|\,e^{j\vartheta^-} \tag{15}$$

for horizontal polarisation.

In the above equations the indices "+" and "-" refer to a local coordinate system at the specular point, the indices "H" (horizontal) and "V" (vertical) refer to the mean surface plane, the left index for the scattered, the right one for the incident field. The complex refractive index $\underline{n}$ will be considered in Ch. 4.

When the normal of the reflecting facet is not within the plane of incidence, the reflected wave is deflected laterally and becomes depolarized. Therefore, the field reflected by an arbitrarily oriented facet consists of a component with the same polarisation as the incident wave described by $\underline{R}_{HH}$ or $\underline{R}_{VV}$ and a cross polarized component given by $\underline{R}_{VH}$ or $\underline{R}_{HV}$, respectively. When the reflecting surface normal is within the plane of incidence the cross polarisation coefficients vanish and $\underline{R}_{HH}$ and $\underline{R}_{VV}$ simplify to $\underline{R}^-$ and $\underline{R}^+$ respectively.

A circularly polarized incident wave can be decomposed into a vertically and a horizontally polarized component which are phase shifted by $\pi/2$. The scattered horizontal and vertical fields are then given by

$$R_{H,Z} = \left[|R_{HH}|^2 + |R_{HV}|^2 + 2|R_{HH}||R_{HV}| \sin(\vartheta_{HH} - \vartheta_{HV}) \right]^{1/2}$$
$$R_{V,Z} = \left[|R_{VV}|^2 + |R_{VH}|^2 - 2|R_{VV}||R_{VH}| \sin(\vartheta_{VV} - \vartheta_{VH}) \right]^{1/2} \tag{16}$$

The resultant scattered field is rotating again. As the components are reflected differently it is generally elliptically polarized.

4. GROUND MOISTURE CONTENT

In (14) and (15) the complex refractive index is given by

$$\underline{n}^2 = \varepsilon_r - j \frac{Z_o}{2\pi} \varkappa \lambda \tag{17}$$

where $Z_o = \sqrt{\mu_o / \varepsilon_o} = 120\,\pi$ ohms is the free space impedance, ε_r the relative dielectric constant, $\varkappa$ the ground conductivity and λ the wave length.

Both ε_r and $\varkappa$ depend on the water content and the temperature of the ground (ALBRECHT, H.J., 1965)

$$\varkappa = 7.7 \cdot 10^{-5} \, (0.73\, W^2 + 1)(1 + 0.03\, t) \tag{18}$$

$$\varepsilon_r = 180\, k \sqrt{\varkappa} \, \exp(-0.01\, t) \tag{19}$$

where W is the water content in percent and t the ground temperature in degrees Centigrade. The value of k depends upon the type of ground, equalling 0.5 for sandlike ground and 1.0 for average soil with a maximum of 1.5 for clay and electrically similar materials.

5. THE STRUCTURE OF THE SCATTERING AREA

After the surface statistics, the polarisation states of incident and scattered waves and the moisture dependent electrical ground constants have been specified, the scattering properties of different types of terrain can now be investigated. This is done by plotting contours of constant average scattered power density as given by the scattering cross section (1) on the mean surface plane.

The average power scattered by a surface element dA and received by an antenna at a distance r_s from the surface element is given by

$$\frac{d\langle P_s \rangle}{dA} = P_d \, g(\theta,\phi) \, \frac{\sigma^\circ}{4\pi r_s^2} \tag{20}$$

where $g(\theta,\phi)$ is the antenna characteristic and P_d is the directly incident power which is assumed to be emitted by a far distant source illuminating homogeneously the entire scattering surface. When the mean surface is flat, r_s can be expressed by the antenna height above the mean surface $h = r_s \cos\theta$ and (20) can be written in normalized form

$$S(\Theta,\phi) = \frac{4\pi h^2}{P_d}\,\frac{d\langle P_s\rangle}{dA} = \cos^2\Theta\cdot g(\Theta,\phi)\cdot\sigma^{\circ}(\Theta,\phi) \qquad (21)$$

Inserting (1) yields

$$S(\Theta,\phi) = \pi \sec^4\beta\,\cos^2\Theta\;\; g(\Theta,\phi)\; p(\zeta_{x,sp},\zeta_{y,sp})\;|R_{p,q}(\eta)|^2 \qquad (22)$$

Equ. (22) is evaluated by inserting the slope probability density functions (6) for Gaussian surfaces and (12) for the measured actual profile. The influence of wave polarisation is studied by substituting the Fresnel coefficient (16) for circularly polarized incident waves and vertically as well as horizontally polarized receiving antennas. The variations of the electrical ground parameters are taken into account considering very dry and very wet soil. In the examples shown the receiving antenna diagram is approximated by

$$g(\Theta,\phi) = \cos^4\psi(\Theta,\phi) = (\cos\phi\;\sin\Theta)^4 \qquad (23)$$

where ψ is the radiation angle measured against the lobe axis. The right hand equality is valid for an antenna pointing into the direction of the x-axis.

Figs. 3 to 6 show the results obtained. The receiving antenna is located at a height h above the origin, the transmitting source at infinite distance above the x-axis. The angle of incidence is assumed to be $\theta_0 = 70^0$ in the plane y/h = o. As the curves obtained are symmetrical w.r.t. the x-axis, only one half of the xy-plane is shown. On the other half the curves for equal roughness statistics but different electrical ground constants are shown for comparison. The curves of Figs. 3 and 4 relate to Gaussian surfaces with $\beta_0 = 10^0$, Figs. 5 and 6 to the measured actual profile, one each for horizontally and vertically polarized receiving antennas. For greater clearness the scale of the y/h-axis is extended by a factor 2 against the x/h-axis. The parameters represent the scattered power per unit area as received by the specified antenna. The power density values are in dB relative to the normalizing factor in (21). The hyperbolas also drawn in the figures will be explained in the next chapter.

The curves of constant power density are extremely narrow, far extended ovals with a complicated fine structure. The power density decreases rapidly in the direction perpendicular to the plane of incidence. Therefore, significant contributions to the received scattered field will arise from regions near the plane of incidence only, especially when the antenna height is low. Consequently, a one dimensional treatment of the surface roughness may be justified for this case.

The "geometrical" reflection point, - i.e. the reflection point which would exist on a flat xy-plane at $x = h \tan\theta_0$, $y = 0$ is marked by "sp". It is noted that the regions of maximum scattered power density are not located around this point but between the sub-antenna point and the geometrical reflection point.

With a vertically polarized receiving antenna the curves exhibit a more complicated structure than for horizontal polarisation. This is caused by the pseudo-Brewster angle. At this angle which corresponds closely to the angle of incidence with the ground constants considered, the Fresnel reflection coefficient is minimum. Accordingly, the scattered power densities are distinctly less than those for horizontal polarisation.

With wet ground a maximum exists between the sub-antenna point and the geometrical reflection point, too. With increasing distance from the antenna, side-lobes are formed while the main lobe in x-direction is suppressed, This is caused by the laterally scattered depolarized field components exceeding the non-depolarized ones. In case of dry ground the power density maximum has exceeded the geometrical reflection point, whereas a minimum has been established between this and the sub-antenna point.

In Figs. 5 and 6 the corresponding curves for the actual terrain are shown. With horizontal polarisation no large variations due to the different ground constants are observed. In both cases the power maximum is close to the geometrical reflection point, caused by the emphasis on horizontal and weakly tilted surface plates as given by the slope p.d.f. (12).

Near the maximum the scattered power decreases more rapidly, at greater distances more slowly than with the Gaussian surface. This behaviour becomes evident from the shape of the slope p.d.f., considering that the tilt angle of the surface must increase with increasing distance from the geometrical reflection point in order to satisfy the condition of specular reflection.

With vertical polarisation the maxima are close to the geometrical reflection point, too. With dry ground a minimum is located between the sub-antenna point and the geometrical reflection point as is the case with the Gaussian surface. When the ground is wet, a small flat maximum appears near the antenna apart from the sharp main peak.

6. THE POWER DENSITY SPECTRUM

The field scattered by a very rough surface consists of components originating from independent discrete specularly reflecting points distributed randomly over the effective scattering area. The frequency of each individual component is subject to a different Doppler shift, if the geometrical relations between transmitter, receiver and scattering surface are varied. In this manner, the spectrum of a signal received e.g. by an aircraft flying over irregular terrain becomes spread due to the reception of the scattered fields.

Utilizing the effective scattering structures derived in Ch. 5, the power density spectrum of a monochromatic incident wave can be calculated using a procedure mentioned by TYLER, G.L. and INGALLS, D.H. (1971).

The Doppler shift is given by

$$f = f_m \cos \psi \qquad f_m = v/\lambda \tag{24}$$

where v is the velocity, λ the wavelength and ψ the angle between the velocity vector and a specular reflection point. As a constant angle ψ defines a cone, the intersection of this cone and the scattering surface is the locus of constant Doppler shift. The scattered power received between two Doppler shifted frequencies f and $f + \delta f$ is proportional to the scattering cross section included between the Doppler loci corresponding to the cones $\psi(f)$ and $\psi(f + \delta f)$. With $dA = r\,dr\,d\phi$ this yields

$$\langle P_s(f, f+\delta f)\rangle = \frac{P_d}{4\pi} \int_{\phi_1}^{\phi_2} \int_{r(\phi;\psi)}^{r(\phi;\psi+\delta\psi)} g(\Theta,\phi) \frac{\sigma^{\circ}_{p,q}}{r_s^2}\, r\, dr\, d\phi \tag{25}$$

The limits of integration depend on the intersection between the Doppler cones and the rough surface, i.e. on the direction of the velocity vector with respect to the xy-plane. When δf is made infinitesimally small, the power density spectrum is obtained which is the derivative of the power spectrum with respect to frequency

$$S(f) = \frac{d\langle P_s(f)\rangle}{df} = \frac{P_d}{4\pi} \frac{d\psi}{df} \frac{d\langle P_s(\psi)\rangle}{d\psi} \tag{26}$$

With (24) the first differential quotient is

$$\frac{d\psi}{df} = - \frac{1}{f_m \sin \psi} \tag{27}$$

The second one is obtained using Leibnitz' rule of differentiation with respect to a parameter in the limit of integration

$$\frac{d\langle P_s(\psi)\rangle}{d\psi} = g(\psi)\int_{\phi_1}^{\phi_2} \sigma^{\circ}_{p,q}\,\frac{r}{r_s^2}\,\frac{dr}{d\psi}\,(\phi,\psi)\,d\phi$$

Substituting $r = h \tan\theta$ and $r_s = h/\cos\theta$ this yields

$$\frac{d\langle P_s(\psi)\rangle}{d\psi} = g(\psi)\int_{\phi_1}^{\phi_2} \sigma^{\circ}_{p,q}\,\tan\theta\,\frac{d\Theta}{d\psi}\,(\phi,\psi)\,d\phi \tag{28}$$

Thus, the surface integral is reduced to a line integral. The integration path $\phi(\theta,\psi)$ is a line of constant Doppler shift given by the intersection between the xy-plane and the Doppler cone. To evaluate (28) further the equation of the conic section must be specified. The general conic section can be expressed by

$$\cos\psi = \cos\varepsilon\,\sin\Theta\,\cos(\chi-\phi) - \cos\Theta\,\sin\varepsilon \tag{29}$$

where ε is the elevation angle of the velocity vector with respect to the xy-plane and χ an azimutal angle w.r.t. the x-axis. The type of the conic section depends on the angles ε and ψ. It is a hyperbola for $\varepsilon < \psi$, an ellipse for $\varepsilon > \psi$, a parabola for $\varepsilon = \psi$ and a circle for $\varepsilon = 90^0$.

In the following examples the velocity vector is assumed to be within the plane of incidence and parallel to the mean scattering plane, i.e. $v = v_x$, $\varepsilon = \chi = 0$. For this case (29) simplifies to

$$\cos\psi = \sin\Theta\,\cos\phi \tag{30}$$

or, in Cartesian coordinates

$$\frac{(x/h)^2}{\cot^2\psi} - (y/h)^2 = 1 \tag{31}$$

with

$$\cot^2\psi = \frac{(f/f_m)^2}{1-(f/f_m)^2}$$

Equ. (30) describes hyperbolas centered at the origin with the parameter f/f_m. The hyperbolas are plotted in Figs. 3 and 4 together with the contours of constant scattered power density. By integrating the scattered power density along these hyperbolas of constant Doppler shift, we obtain the power density at the corresponding frequency. Evidently, the shape of the spectrum depends on the fine structure of the effective scattering area as well as on the type and orientation of the conic section.
Differentiating (30) we find

$$\frac{d\Theta}{d\psi} = -\frac{\sin\psi}{\cos\Theta\,\cos\phi}$$

and by substitution into (28)

$$\frac{d\langle P_s(\psi)\rangle}{d\psi} = -g(\psi)\sin\psi\cos\psi\int_0^{2\pi}\frac{\sigma^\circ_{p,q}[\phi,\theta(\phi,\psi)]}{\cos^2\phi - \cos^2\psi}\,d\phi \tag{32}$$

The integrand has a pole at $\phi = \psi$ or $\theta = \pi/2$, respectively, as the path of integration extends to infinity due to the assumption of a flat earth. If the mean surface were a spherical earth, the range of θ would be limited by the horizon. To prevent the integrand from becoming infinite, an "artificial horizon" is introduced by limiting θ to a maximum value given by the antenna height and the earth's radius.

$$\sin\Theta_{max} = a_e/(a_e + h) \tag{33}$$

with a_e = 6370 km.

Inserting (32) and (27) into (26) we finally obtain

$$S(f) = \frac{P_d}{4\pi}\,\frac{f/f_m}{f_m}\,g(\arccos f/f_m)\;2\int_0^{\arccos[f/(f_m\sin\Theta_{max})]}\frac{\sigma^\circ_{p,q}(\phi,\,f/f_m)}{\cos^2\phi - (f/f_m)^2}\,d\phi \tag{34}$$

where

$$\sigma^{o}_{p,q}(\phi,f/f_m) = \sigma^{o}_{p,q}(\phi,\Theta)\Big|_{\Theta=\arcsin(f/f_m\cdot\cos\phi)}$$

The integral is solved numerically.

The shape of the power density spectrum depends strongly on the angle of incidence. Setting $|R_{p,q}|$ = const. and $g(\theta,\phi) = 1$, (34) is solved for a Gaussian surface with $B_0 = 10^0$. The resulting spectra normalized to $S_0 = P_d/4\pi$ are shown in Fig. 7. The spectral lines of the directly incident waves placed at $f/f_m = \sin\theta_0$ are plotted within the same diagram. The spectrum is symmetrical only for normal incidence. With growing angle of incidence it becomes more and more asymmetrical w.r.t. its maximum as well as to the spectral line of the directly incident wave. Moreover, the maximum increases with the angle of incidence. This can be explained by the increase in surface area included between lines of constant Doppler shift towards higher angles of incidence and higher frequency. Reversing the direction of velocity the spectra appear mirror-inverted to the ordinate.

If the angle between the velocity vector and the plane of incidence is increased the asymmetry diminishes. When the velocity is perpendicular to the plane of incidence, the spectra become symmetrical w.r.t. the frequency of the directly incident wave which then is no longer subject to a Doppler shift.

Introducing now the appropriate reflection coefficients representing the ground constants, polarisation states and surface statistics already used to calculate the effective scattering area, we obtain the spectra shown in Figs. 8 to 10 which are normalized to the total average scattered power

$$\langle P_s\rangle = \int_{-fm}^{+fm} S(f)\,df$$

The spectra exhibit a fine structure corresponding to that of the scattering area. The asymmetry of the spectra obtained for the Gaussian surfaces is less pronounced with small roughness scales (Fig. 9) than with the larger ones (Fig. 8). Likewise, the spectra obtained for the natural terrain (Fig. 10) are relatively symmetrical near the frequency which corresponds to the direction of geometrical reflection. This is due to the fact that

the maximum of the power density is closer to the geometrical reflection point and the power decreases more uniformly into all directions than with larger roughness (Figs. 3 to 6). As the decrease is less rapid at larger distances the spectral power density rises again towards the upper frequency limit. It becomes evident that the shape depends more strongly on the geometrical than the electrical properties of the scattering surface.

The theoretical spectra had to be compared with experimental data obtained with a satellite-to-aircraft link during a low level flight experiment (HORTENBACH, K.J., 1977). This flight had been performed just over that terrain, the statistics of which had been used to calculate the effective scattering surface structure and the corresponding theoretical spectra. The spectra of the received signal could be evaluated after enveloppe detection only. Therefore, the theoretical spectra modified by a linear rectifier were calculated for comparison. Neglecting convolution terms of higher order, the spectrum of the demodulated signal, after low pass filtering and separation of the dc-component, is given by (DAVENPORT, W.B. and ROOT, W.L., 1958)

$$S_{dem}(f) \sim 2 \int_{f_o-f_m+f}^{f_o+f_m} S(f')\, S(f-f')\, df' + 2\, P_d \left[S(f-f_T) + S(f+f_T) \right] \qquad (35)$$

$$0 \leq f \leq 2f_m$$

where S (f) is the original spectrum and $f_T = f_o + f_m \sin \theta_o$ is the Doppler shifted frequency of the directly received signal.

The first term of (35) represents the self-convolution of the input spectrum, the second term describes a shift of the spectrum along the frequency axis, the spectral line of the directly received signal being placed at the origin, thereby reversing the lower part of the spectrum w.r.t. this line and superposing it to the upper part.

Fig. 11 shows a measured signal spectrum with different theoretical spectra for comparison. Good agreement is obtained for the Gaussian surface with $\beta_o = 10^o$ and dry ground as well as for the actual terrain. The close agreement between these two theoretical spectra based on different surface statistics confirm the earlier statement that the scattering characteristics of a rough surface do not depend very strongly on the surface statistics when the angle of incidence tends towards grazing.

The discontinuity at $f/f_m = 1 - \sin \theta_o$ is due to the asymmetrical shape of the spectra and originates from the demodulation process.

7. CONCLUSION

The intention of this contribution is to demonstrate the influence of surface statistics, wave polarisation and electrical ground parameters on the scattering properties of irregular terrain, the fine structure of the effective scattering area and the shape of the signal spectrum. The structure of the scattering area was found to be most complex when the receiving antenna is vertically polarized and the angle of incidence is near the Brewster angle.

8. REFERENCES

ALBRECHT, H.J., 1965, "On the Relationship between Electrical Ground Parameters", Proc. IEEE, Vol. 53, No.5, p. 544

BARRICK, D.E., 1968, "Rough Surface Scattering based on the Specular Point Theory", IEEE Trans. Ant. Prop., Vol. AP - 16, No. 4, pp. 449-454

BARRICK, D.E., 1970, "Radar Cross Section Handbook", Vol. 2, Ch. 9, Plenum Press, New York

BECKMANN, P., 1967, "Probability in Communication Engineering", Harcourt, New York, pp. 219-227

BECKMANN, P., 1973, "Scattering by Non-Gaussian Surfaces", IEEE Trans. Ant. Prop., Vol. AP-21, No.2, pp. 169-175

BROCKELMAN, R.A., HAGFORS, T., 1966, "Note on the Effect of Shadowing on the Scattering of Waves from a Random Rough Surface", IEEE Trans. Ant. Prop., Vol. AP-14, No. 5, pp. 621-629

DAVENPORT, W.B., ROOT, W.L., 1958, "An Introduction to the Theory of Random Signals and Noise", McGraw Hill, New York, Ch. 12

HAYRE, H.S., MOORE, R.K., 1961, "Theoretical Scattering Coefficient for Near Vertical Incidence from Contour Maps", J. Res. NBS-D (Radio Prop.), Vol. 65-D, No.5, pp. 427-432

HORTENBACH, K.J., 1977, "Die statistischen Eigenschaften der Feldstärkeschwankungen auf Satelliten-Flugzeug-Funkstrecken in verschiedenen Höhen über unregelmäßigem Gelände (The statistical properties of fieldstrength variations on satellite-aircraft radio links at different altitudes above irregular terrain)", Dissertation, Technische Hochschule Aachen

KODIS, R.D., 1966, "A Note on the Theory of Scattering from an Irregular Surface", IEEE Trans. Ant. Prop., Vol. AP-14, No. 1, pp. 77-82

MITZNER, K.M., 1966, "Change in Polarisation on Reflection from a Tilted Plane", Radio Science, Vol. 1 (New Series), No. 1, pp. 27-29

PEAKE, W.H., BARRICK, D.E., 1967, "Scattering from Surfaces with different Roughness Scales ; Analysis and Interpretation", Ohio State University, Techn. Rep. 1388-26

SANCER, M.I., 1969, "Shadow-Corrected Electromagnetic Scattering from a Randomly Rough Surface", IEEE Trans. Ant. Prop., Vol. AP-17, No. 5, pp. 577-585

SMITH, B.G., 1967, "Geometrical Shadowing of a Random Rough Surface", IEEE Trans. Ant. Prop., Vol. AP-15, No. 5, pp. 668-671

TYLER, G.L., INGALLS, D.H.H., 1971, "Functional Dependences of Bistatic Radar Frequency Spectra and Cross Sections on Surface Scattering Laws", J. Geophysical Res., Vol. 76, No. 20, pp. 4775-4785

WAGNER, R.D., 1967, "Shadowing of Random Rough Surfaces", J. Acoust. Soc. Am., Vol. 41, No. 1, pp. 138-147

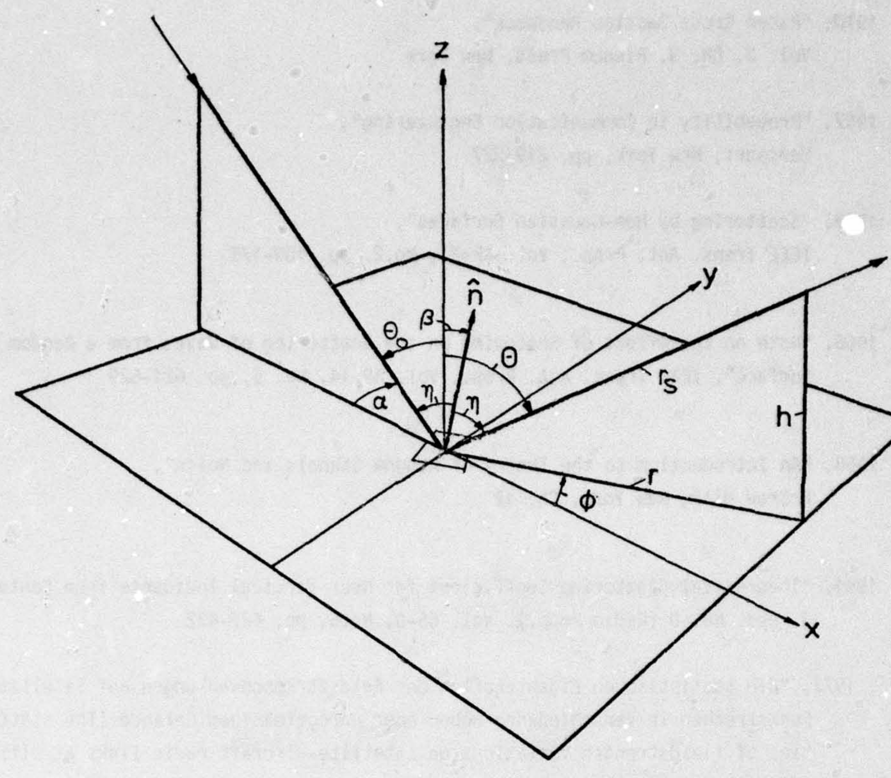

Fig. 1 Coordinate Sytem

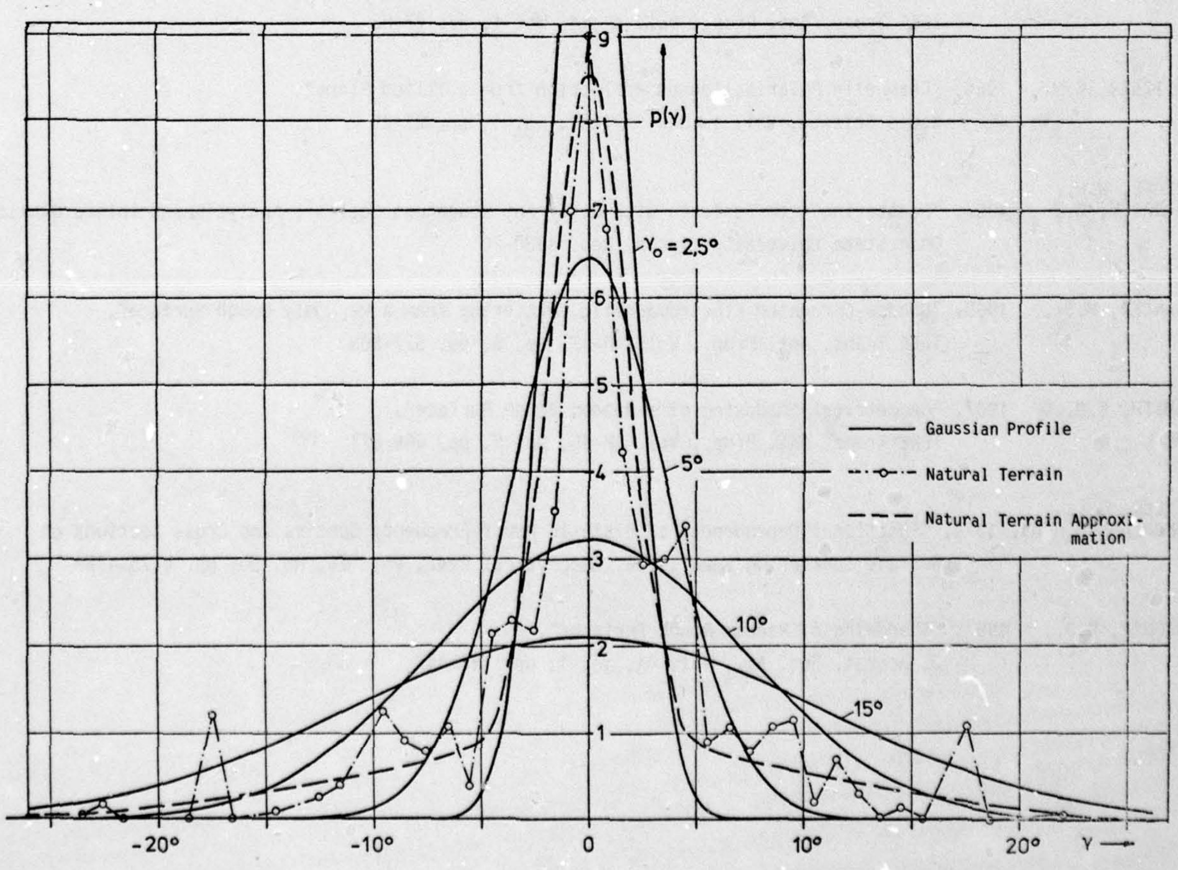

Fig. 2 Probability density functions of slope angles for Gaussian surfaces and natural terrain.

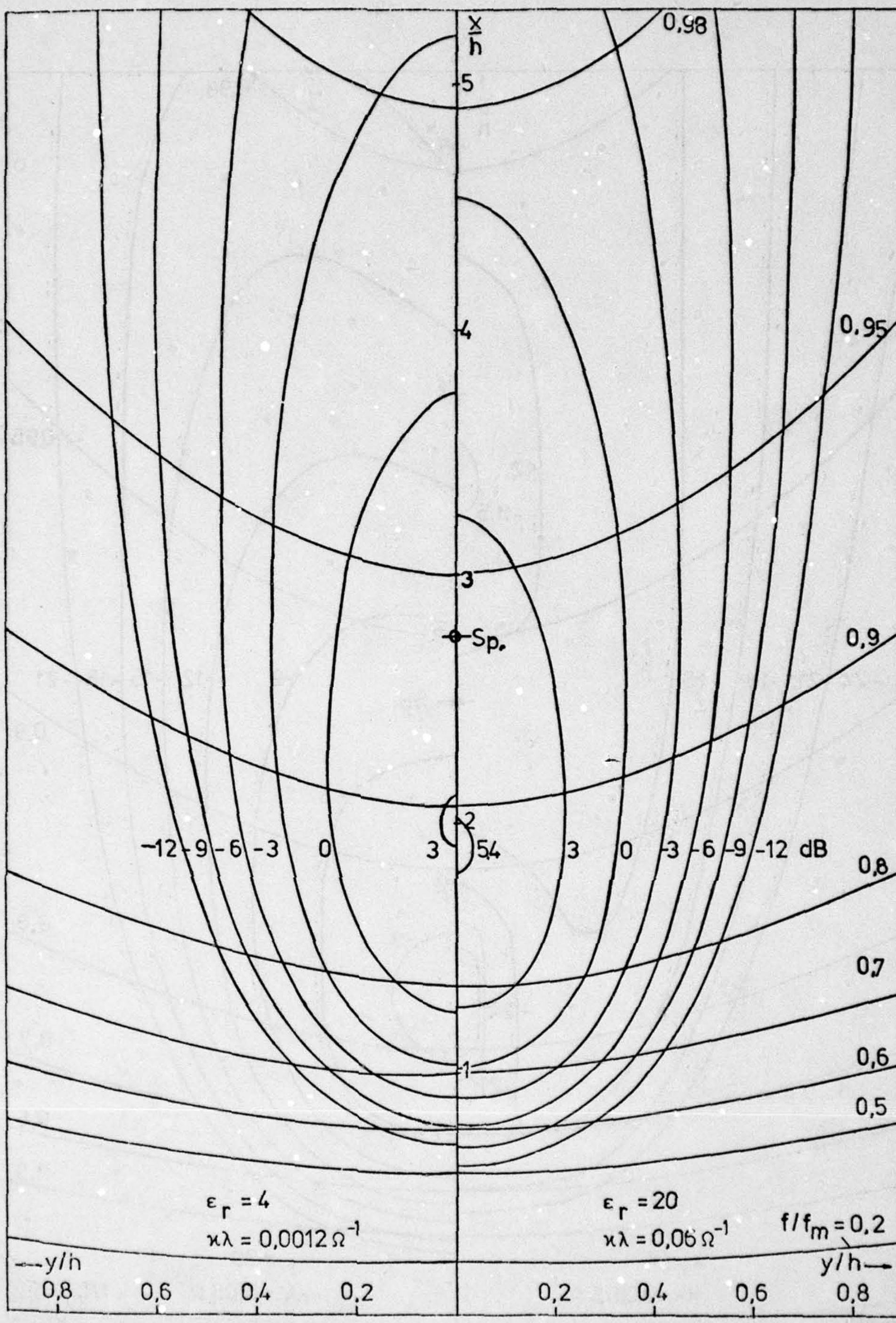

Fig. 3 Contours of constant scattered power density for Gaussian surface ($\beta_0 = 10^0$) and horizontally polarized receiving antenna. Incident wave circularly polarized, $\theta_0 = 70^0$.

Left: dry soil ($\varepsilon_r = 4$, $\varkappa\lambda = 0.0012$ S)

Right: wet soil ($\varepsilon_r = 20$, $\varkappa\lambda = 0.06$ S)

The hyperbolas are lines of constant Doppler shift for $v = v_x$.

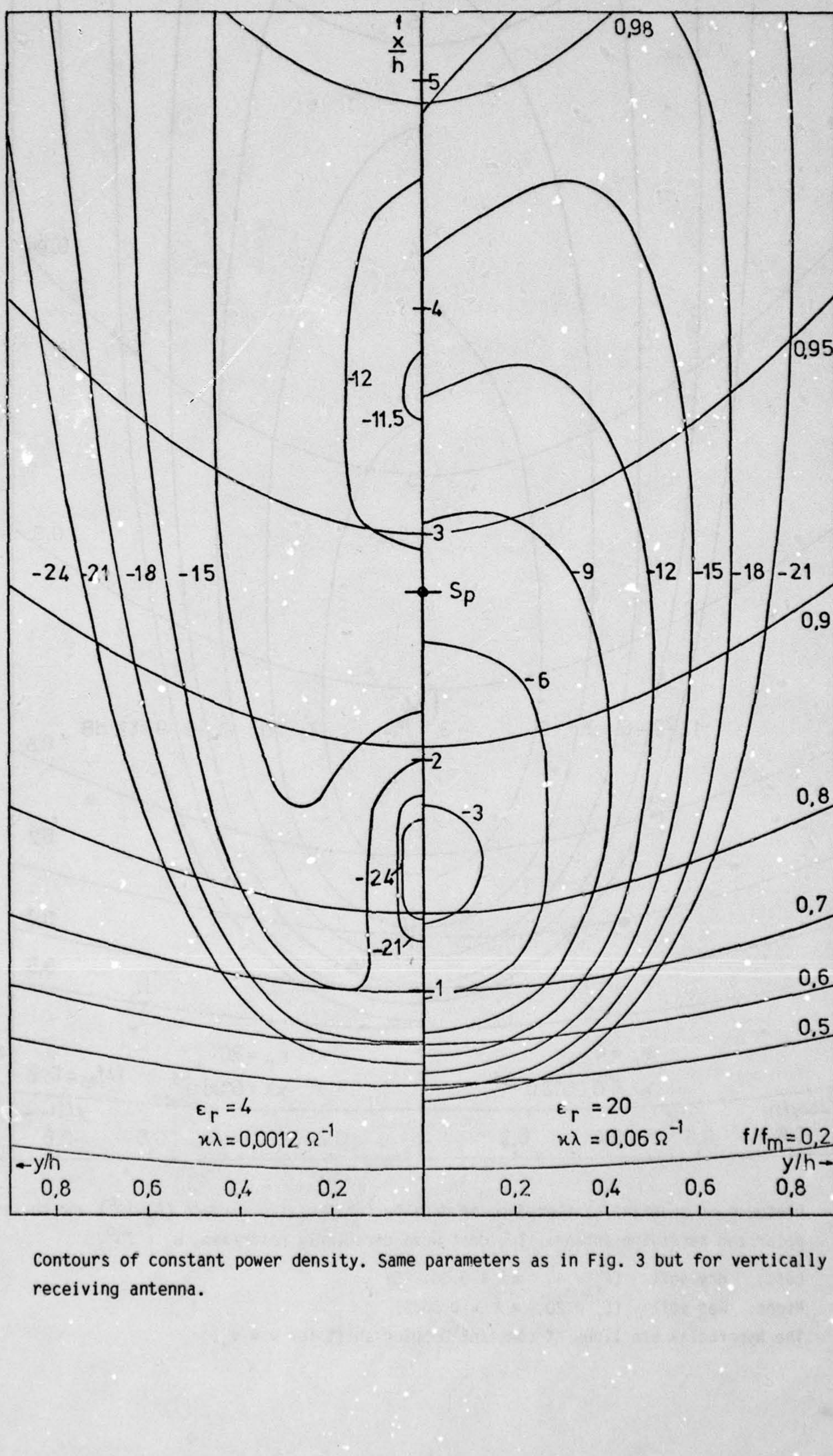

Fig. 4 Contours of constant power density. Same parameters as in Fig. 3 but for vertically polarized receiving antenna.

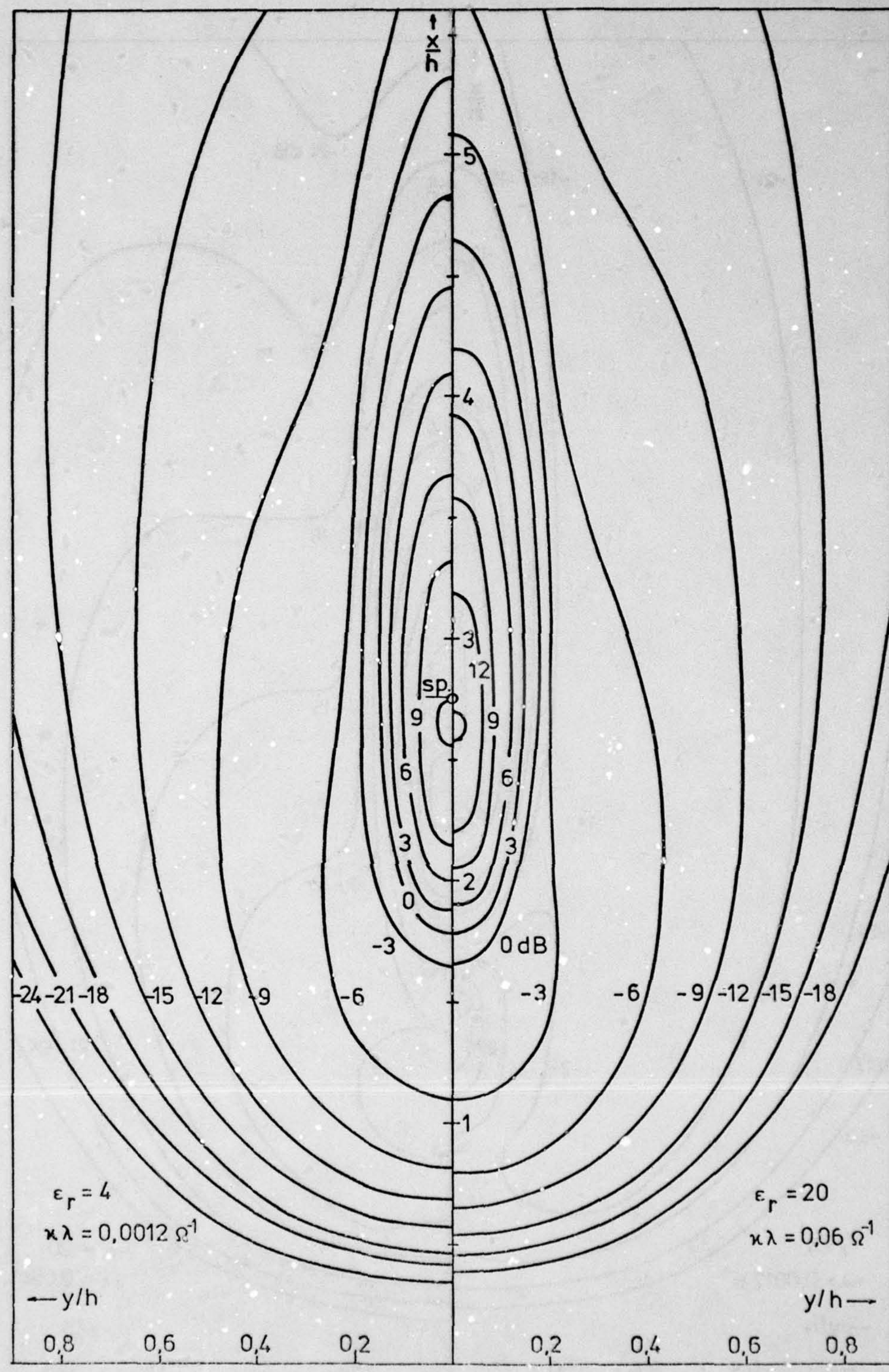

Fig. 5 Contours of constant power density for natural terrain and horizontally polarized receiving antenna. Incident wave circularly polarized, $\theta_0 = 70^0$.

Left: dry soil ($\varepsilon_r = 4$, $\varkappa\lambda = 0.0012$ S)

Right: wet soil ($\varepsilon_r = 20$, $\varkappa\lambda = 0.06$ S)

AD-A082 015 ADVISORY GROUP FOR AEROSPACE RESEARCH AND DEVELOPMENT--ETC F/G 20/14
TERRAIN PROFILES AND CONTOURS IN ELECTROMAGNETIC WAVE PROPAGATI--ETC(U)
DEC 79 A W BIGGS
UNCLASSIFIED AGARD-CP-269 NL

3 OF 4
AD A082015

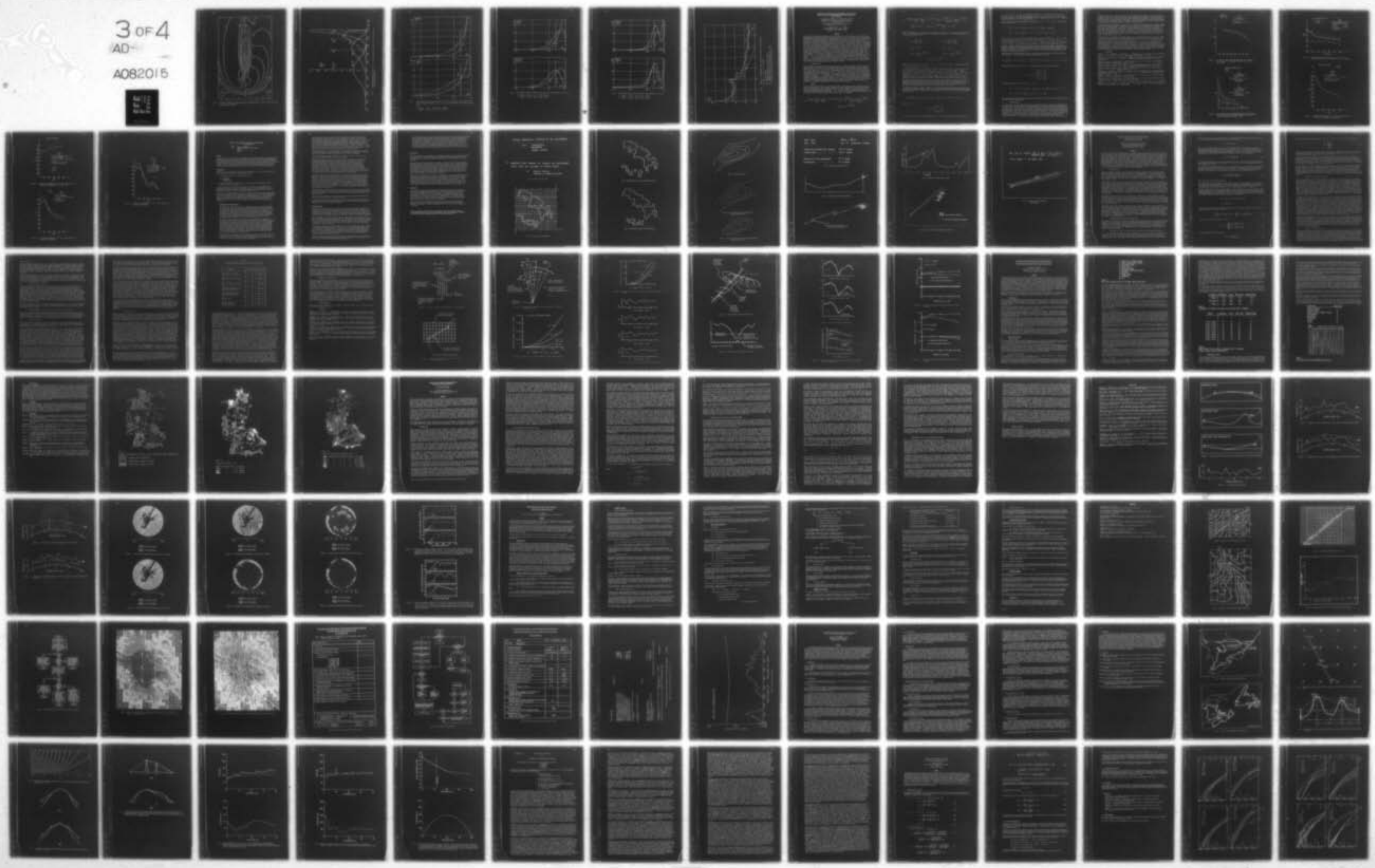

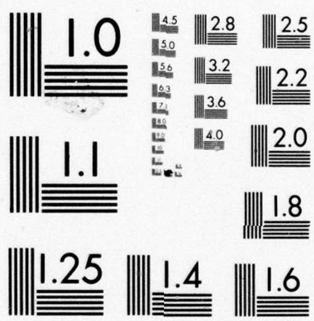

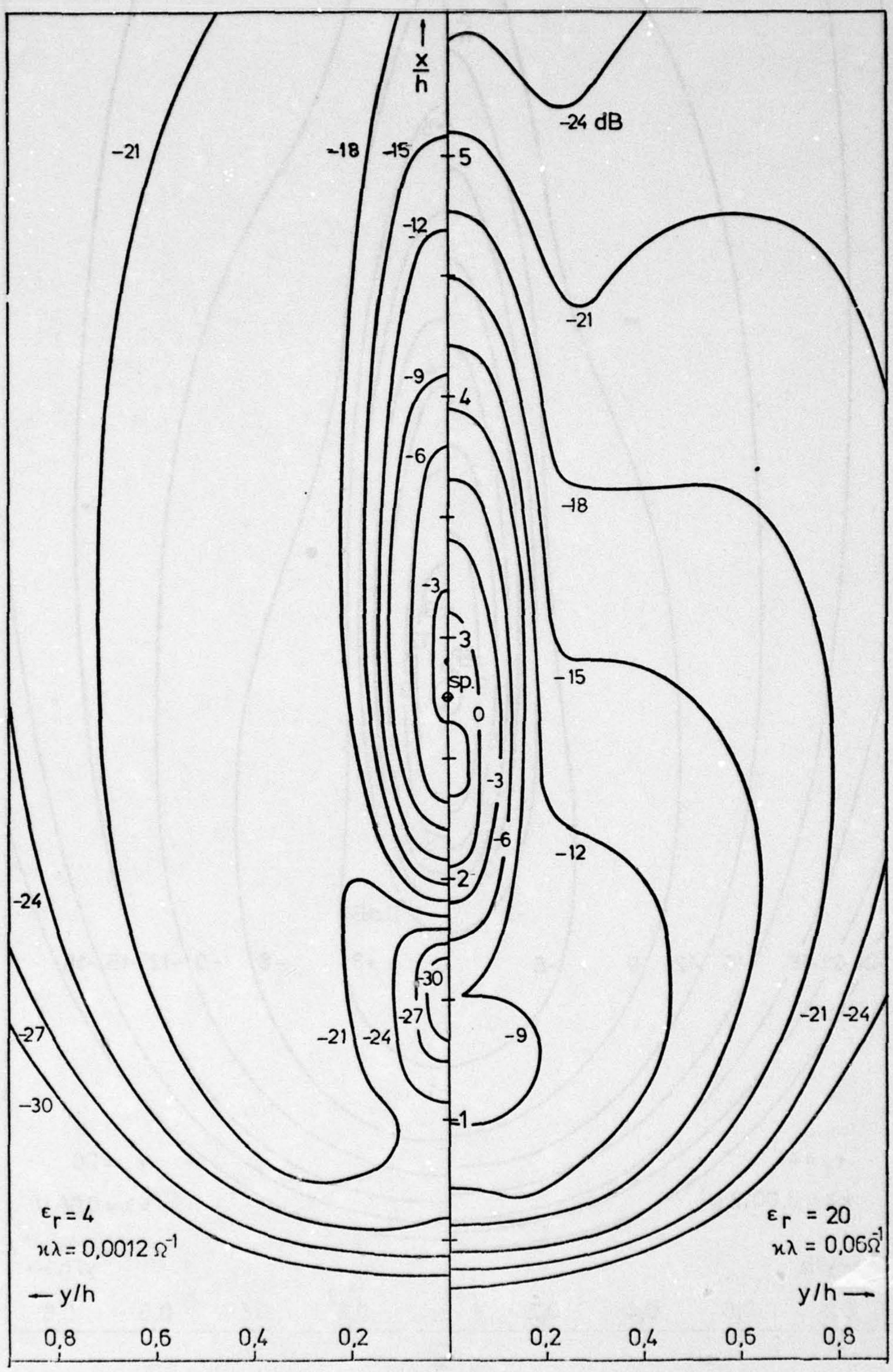

Fig. 6 Contours of constant scattered power density. Same parameters as in Fig. 5, but for vertically polarized receiving antenna.

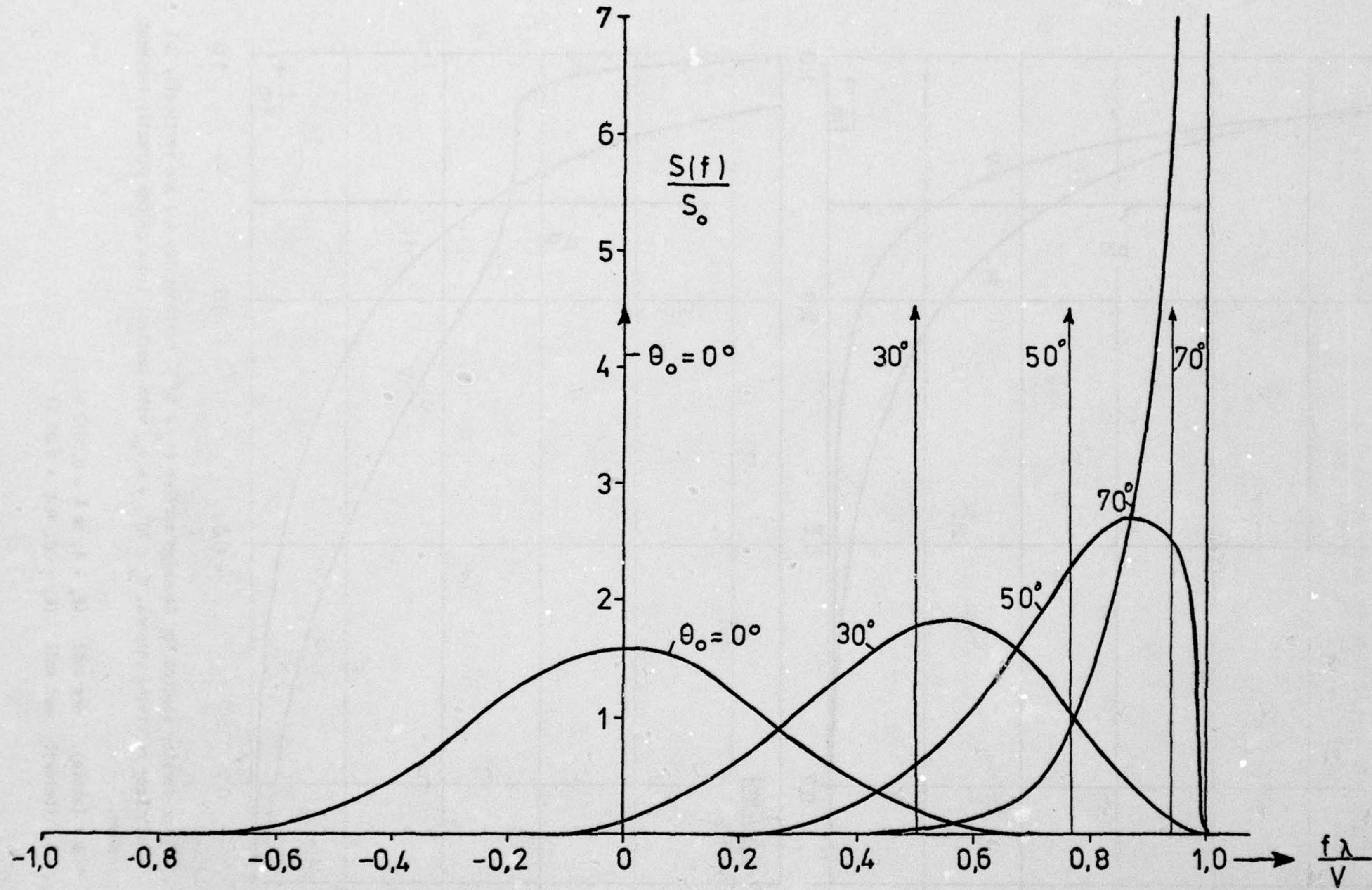

Fig. 7 Simplified power density spectra for $v = v_x$ and Gaussian surface ($\beta_0 = 10^0$) with spectral lines of directly incident waves.

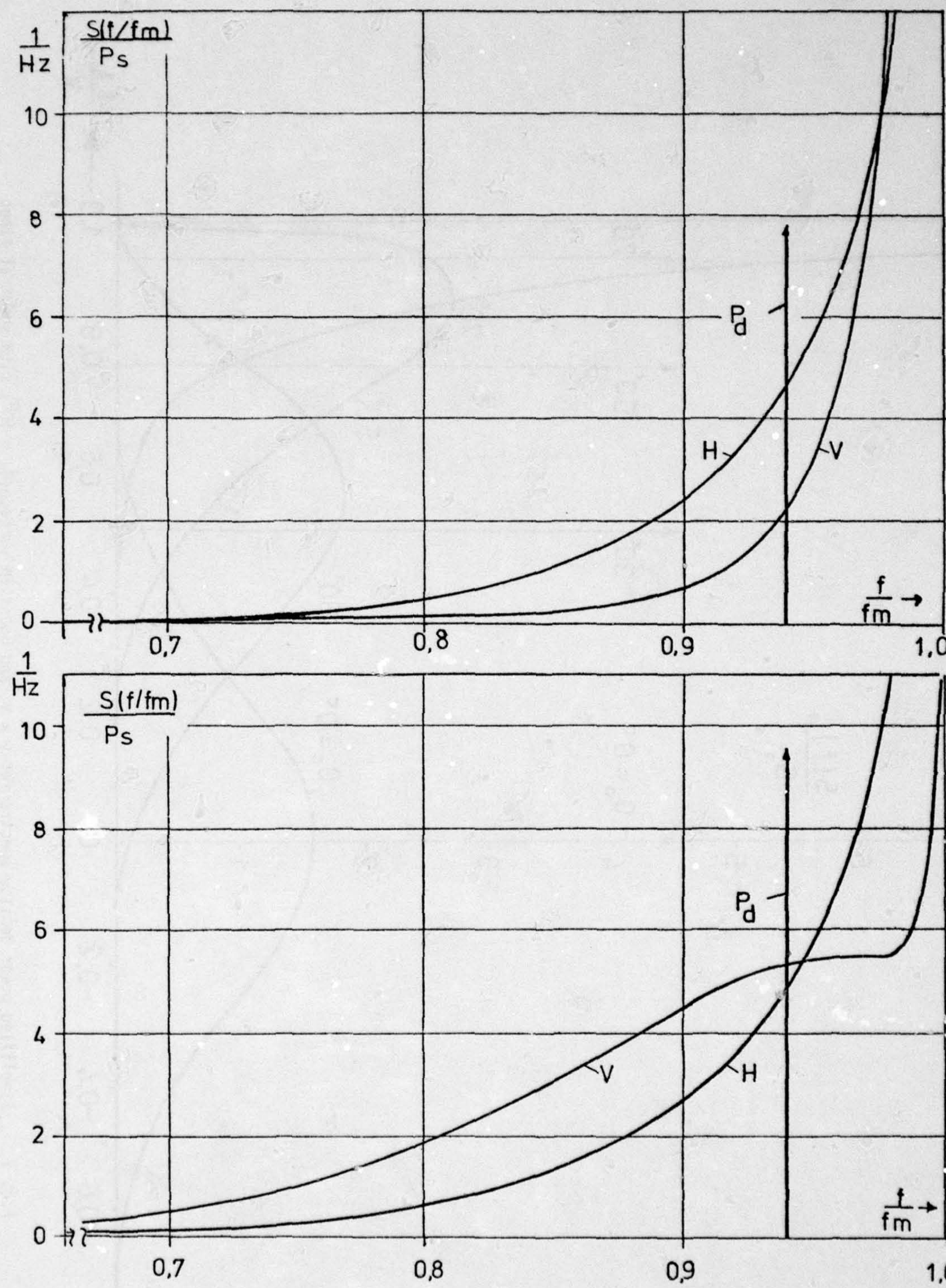

Fig. 8 Power density spectra for Gaussian surface ($\beta_0 = 10^{\circ}$), horizontally (H) and vertically (V) polarized receiving antenna, $\theta_0 = 70^{\circ}$, $v = v_x$, with spectral lines of the directly incident wave.

a (above): dry soil ($\varepsilon_r = 4$, $\varkappa\lambda = 0.0012$ S)

b (below): wet soil ($\varepsilon_r = 20$, $\varkappa\lambda = 0.06$ S)

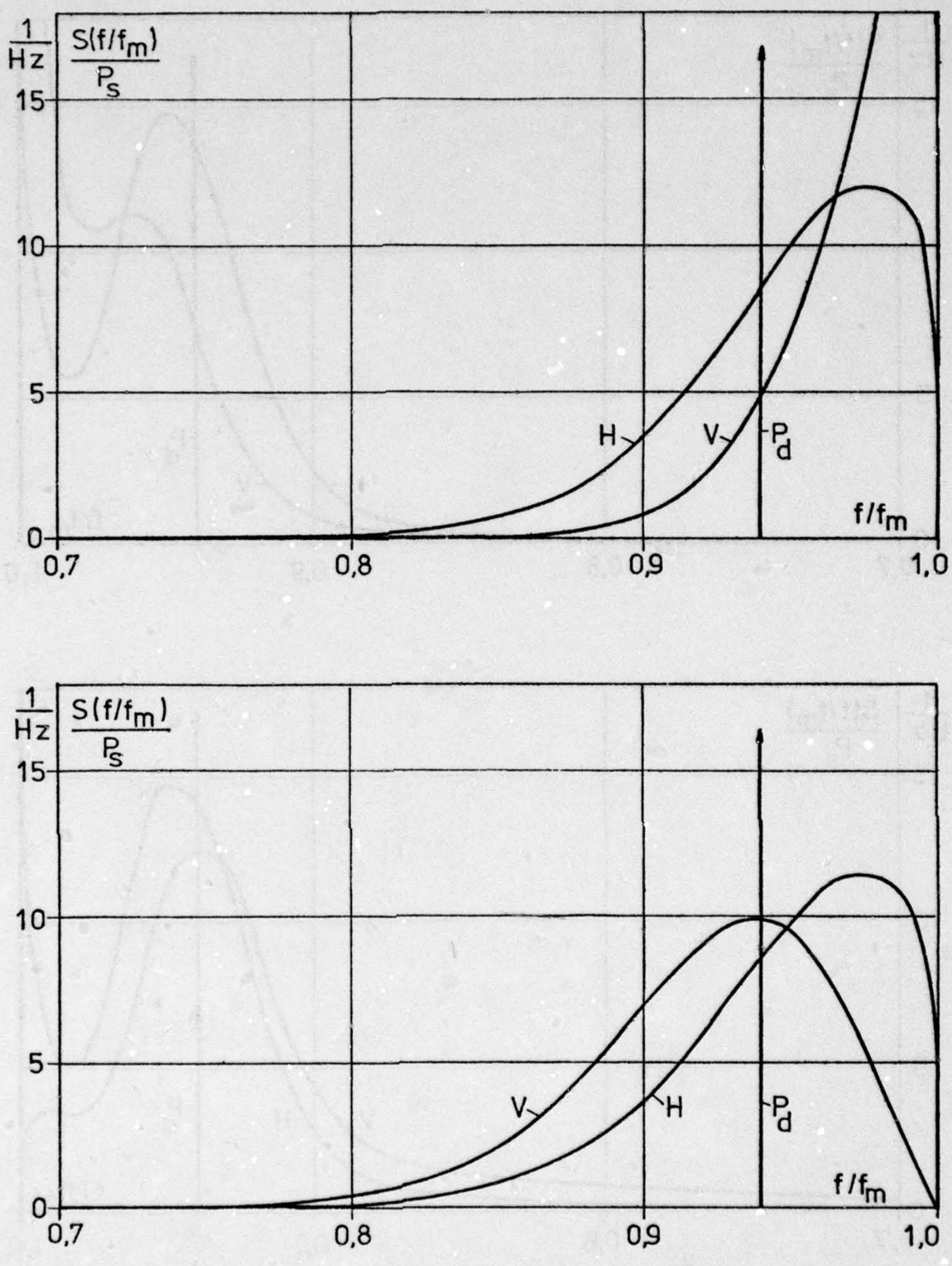

Fig. 9 Power density spectra for Gaussian surface ($\beta_o = 5^o$). Same parameters as in Fig. 8.

a (above): dry soil ($\varepsilon_r = 4$, $\varkappa\lambda = 0.0012$ S)

b (below): wet soil ($\varepsilon_r = 20$, $\varkappa\lambda = 0.06$ S)

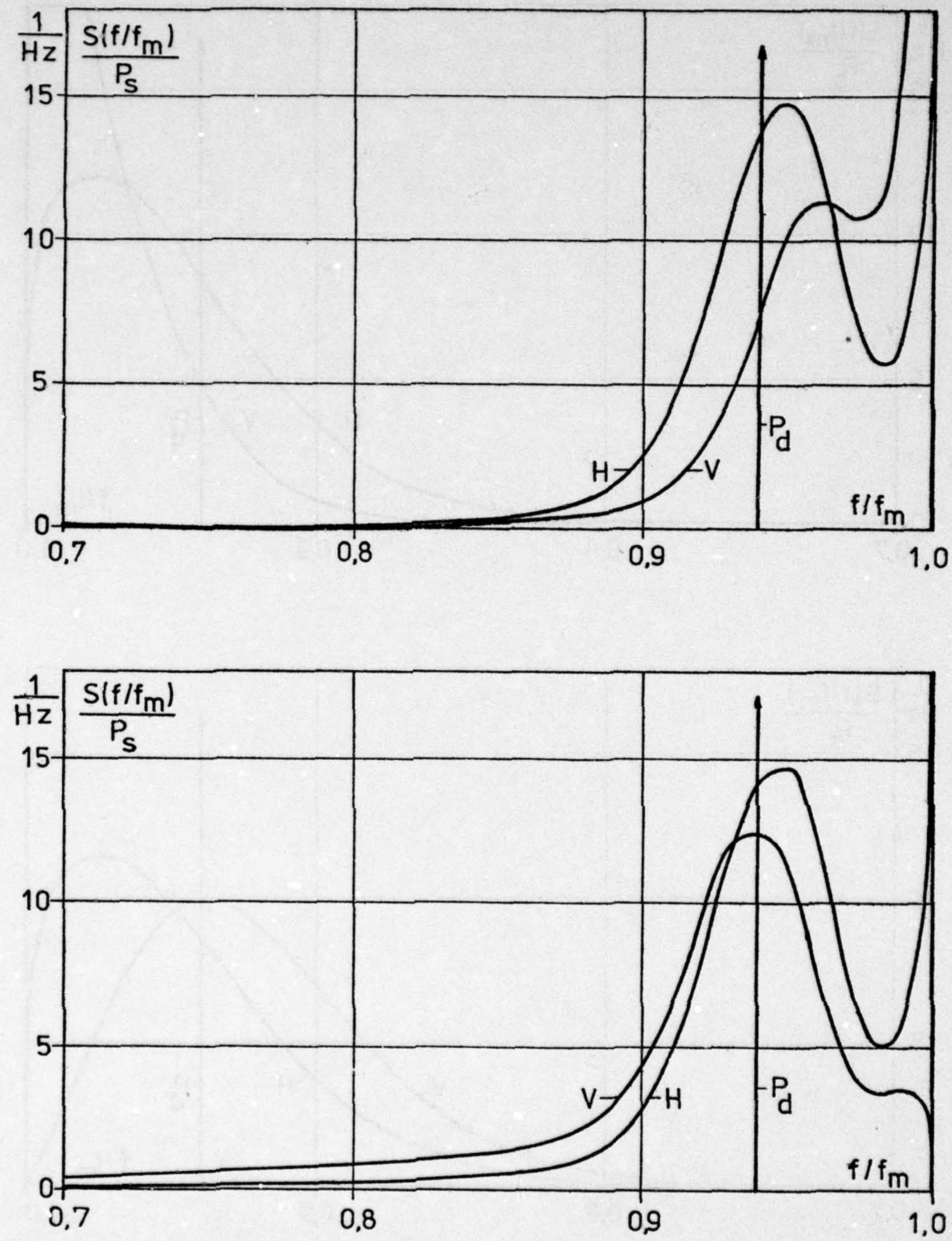

Fig. 10 Power density spectra for natural terrain. Same parameters as in Fig. 8.

a (above): dry soil ($\varepsilon_r = 4$, $\varkappa\lambda = 0.0012$ S)

b (below): wet soil ($\varepsilon_r = 20$, $\varkappa\lambda = 0.06$ S)

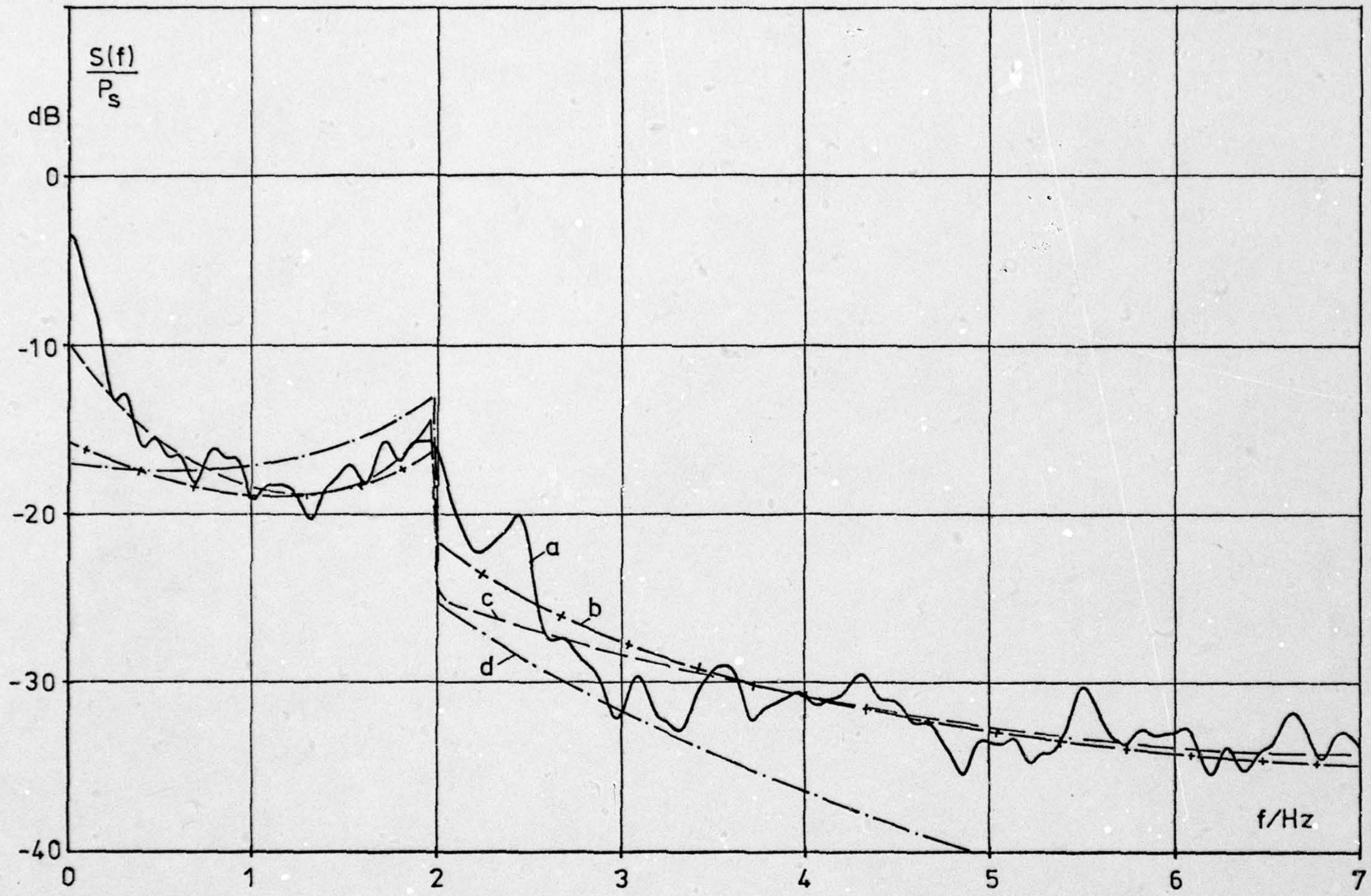

Fig. 11 Spectra of the demodulated signal received with vertically polarized antenna

$\theta_o = 70^o$, $v = v_x$, $\varepsilon_r = 4$, $\varkappa\lambda = 0.0012$ S

a) measured spectrum

b) theoretical spectrum for the natural terrain

c) theoretical spectrum for the Gaussian surface ($\beta_o = 10^o$)

d) theoretical spectrum for the Gaussian surface ($\beta_o = 5^o$)

THEORETICAL MODELLING AND EXPERIMENTAL DATA MATCHING FOR ACTIVE AND PASSIVE MICROWAVE REMOTE SENSING OF EARTH TERRAIN

J. A. Kong, L. Tsang, M. Zuniga, and R. Shin
Department of Electrical Engineering and
Computer Science and Research Laboratory
of Electronics
Massachusetts Institute of Technology
Cambridge, MA 02139, USA

J. C. Shiue and A. T. C. Chang
NASA Goddard Space Flight Center
Greenbelt, MD 20771, USA

SUMMARY

In both active and passive microwave remote sensing of earth terrain, it has been long recognized that volume scattering plays a decisive role in the determination of the radar backscattering cross-sections and the radiometric brightness temperatures. Two theoretical models have been developed to characterize terrain media: (1) a random medium with a variance, a horizontal correlation length, and a vertical correlation length; (2) a homogeneous dielectric containing discrete scatterers. The earth terrain is then modelled as layers of such scattering media bounded by air above and half-space below. The development of the theoretical approaches is guided by the motivation that data sets obtained in a field and plotted as functions of frequency, angle, and polarization must be matched with the same set of parameters characterizing the same field. In matching the theoretical results with experimental data collected from vegetation and snow-ice fields, we summarize the following findings: (1) for observation angles near nadir, rough surface effects are important; (2) for snow-ice field the horizontal correlation length is greater than the vertical correlation length whereas for vegetation field their relative sizes depend on the types of vegetation; (3) the vertically polarized backscattering cross-section σ_{vv} is always larger than the horizontally polarized backscattering cross-section σ_{hh} for half-space scattering media and may become smaller for a two-layer model; (4) for snow field displaying diurnal change, a three-layer model including a thin top layer caused by sun-light illumination must be used, (5) for a random medium with equal horizontal and vertical correlation lengths, the measured data can also be matched with a corresponding discrete scatterer model.

1. INTRODUCTION

In developing theoretical models for both active and passive microwave remote sensing of earth terrain, we account for the volume scattering effects by modelling the terrain material such as ice, snow, or vegetation with either a random medium (Tsang and Kong, 1976, 1978; Zuniga et al., 1979) or a homogeneous medium containing discrete scatterers (Tsang and Kong, 1976; Chang et al., 1976; Tsang et al., 1977; Kong et al., 1979). The random medium has an average permittivity ε_1 and its random part is characterized by a correlation function with variance δ, horizontal correlation length ℓ_ρ and vertical correlation length ℓ. In the discrete-scatterer model, we characterize the scatterers as spheres of radius a, permittivity ε_s and effective fractional volume f imbedded inside a homogeneous medium with permittivity ε_1. With the earth terrain modelled as layers of such scattering media bounded by air above and half-space earth below, we then calculate the radar backscattering cross-sections for active remote sensing and the radiometric brightness temperatures for passive remote sensing.

2. THEORY

For the random medium model, radar backscattering cross-sections are calculated with an iterative procedure to the integral equations for the scattered intensities which gives rise to a Born series that converges quickly for small albedo. The first order terms yield the backscattering cross-section σ_{vv} for the vertically polarized return and σ_{hh} for the horizontally polarized return. For a layer of random medium with thickness d_1, the results are relatively simple and they are given as follows:

$$\sigma_{hh} = \frac{\delta k_1'^4 \ell \ell_\rho^2}{4} \frac{|X_{10i}|^4}{|D_{2i}|^4} \left|\frac{k_{ozi}}{k_{1zi}}\right|^4 e^{-k_o^2 \ell_\rho^2 \sin^2\theta_{oi}} \left\{ \frac{(1 - e^{-4k''_{1zi}d_1})(1 + |R_{12i}|^4 e^{-4k''_{1zi}d_1})}{2k''_{1zi}(1 + 4k'^2_{1zi}\ell^2)} + 8d_1 |R_{12i}|^2 e^{-4k''_{1zi}d_1} \right\}$$

$$\sigma_{vv} = \frac{\delta k_1'^4 \ell \ell_\rho^2}{4} \frac{|Y_{10i}|^4}{|F_{2i}|^4} \left|\frac{k_{ozi}}{k_{1zi}}\right|^4 e^{-k_o^2 \ell_\rho^2 \sin^2\theta_{oi}} \left\{ \frac{(1 - e^{-4k''_{1zi}d_1})(1 + |S_{12i}|^4 e^{-4k''_{1zi}d_1})}{2k''_{1zi}(1 + 4k'^2_{1zi}\ell^2)} \right.$$

$$\left. \cdot \left|\frac{k^2_{1zi}}{k_o^2} + \sin^2\theta_{oi}\right|^2 + 8d_1 |S_{12i}|^2 e^{-4k''_{1zi}d_1} \left|\frac{k^2_{1zi}}{k_o^2} - \sin^2\theta_{oi}\right|^2 \right\}$$

where the subscript i indicates the incident direction and the correlation function is taken to be gaussian horizontally and exponential vertically. The other symbols in (1)-(2) are defined as follows

$$R_{\ell m} = \frac{k_{\ell z} - k_{mz}}{k_{\ell z} + k_{mz}} \qquad S_{\ell m} = \frac{\varepsilon_m k_{\ell z} - \varepsilon_\ell k_{mz}}{\varepsilon_m k_{\ell z} + \varepsilon_\ell k_{mz}}$$

$$X_{\ell m} = 1 + R_{\ell m} \qquad Y_{\ell m} = 1 + S_{\ell m}$$

$$D_2 = 1 + R_{01}R_{12}\, e^{i2k_{1z}d_1} \qquad F_2 = 1 + S_{01}S_{12}\, e^{i2k_{1z}d_1}$$

$$k_{\ell z} = (k_\ell^2 - k_\perp^2)^{1/2}$$

where $k_o^2 = \omega^2\mu_o\varepsilon_o$, $k_1^2 = \omega^2\mu_o\langle\varepsilon_1\rangle$, $k_2^2 = \omega^2\mu_o\varepsilon_2$, $k''_{1z} = \mathrm{Im}(k_{1z})$, and the subscripts ℓ and m denote 0, 1, and 2.

As the layer thickness d_1 becomes very large, the terms involving $\exp[-4k''_{1zi}d_1]$ can be omitted and we see that the bracket terms in (1) and (2) become simply $[2k''_{1zi}(1 + 4k'_{1zi}\ell^2)]^{-1/2}$. The scattering cross-sections decay as $\exp[-k_o^2\ell_\rho^2\sin^2\theta_{oi}]$ and they are proportional to $|X_{10i}|^4$ for σ_{hh} and $|Y_{10i}|^4$ for σ_{vv}, which implies that σ_{vv} is always larger than σ_{hh} for a half-space random medium. The presence of the bottom boundary is thus very important in order to account for experimental data with $\sigma_{hh} > \sigma_{vv}$.

The second order terms which give rise to depolarization effects, and the results for backscattering by multilayer random media are too complicated to be given here. The wave approach to random media has also been extensively studied with a modified radiative transfer (MRT) theory that accounts for strong coherent interactions between top and bottom boundaries and applies to data sets collected from ice fields.

In the case of passive remote sensing, we can calculate brightness temperatures by using the radiative transfer theory. The radiative transfer equation inside a scattering medium which can be either a random medium or a homogeneous medium containing discrete scatterers takes the form

$$\cos\theta \frac{d}{dz} \bar{I}(\theta, z) = \kappa_a C_1 T_1 - \kappa_e \bar{I}(\theta, z) + \int_0^\pi d\theta' \sin\theta' \,\bar{\bar{P}}(\theta, \theta') \cdot \bar{I}(\theta', z)$$

where for $0 < \theta < \pi$

$$\bar{I}(\theta, z) = \begin{bmatrix} I_v(\theta, z) \\ I_h(\theta, z) \end{bmatrix},$$

I_v is the vertically polarized intensity, I_h is the horizontally polarized intensity,

$\kappa_e = \kappa_a + \kappa_s$ with κ_a denoting absorption loss and κ_s the scattering loss, $C_1 = K\epsilon_1'/\epsilon_0\lambda^2$ with K denoting the Boltzmann constant, and $\bar{\bar{P}}(\theta, \theta')$ is the scattering function matrix for the scattering medium. For the random medium model, κ_e in general takes the form of a 2×2 diagonal matrix.

For a layer of scattering medium with boundaries at $z = 0$ and $z = -d_1$, the boundary conditions are, for $0 < \theta < \pi/2$,

$$\bar{I}(\pi - \theta, z = 0) = \bar{\bar{C}}_{11_0}(\theta) \cdot \bar{I}(\theta, z = 0) + \bar{\bar{C}}_{01}(\theta_o) \cdot \bar{I}_{sky}(\theta_o)$$

$$\bar{I}(\theta, z = -d_1) = \bar{\bar{C}}_{11_2}(\theta) \cdot \bar{I}(\pi - \theta, z = -d_1) + \bar{\bar{C}}_{21}(\theta_2) \cdot \bar{I}_2(\theta_2)$$

where $\bar{I}_{sky}(\theta_o)$ is the intensity corresponding to the sky temperature, $\bar{I}_2(\theta_2)$ is the intensity corresponding to the temperature in the medium $z < -d_1$, $\bar{\bar{C}}_{11_0}(\theta)$ is the coupling matrix at the boundary $z = 0$, $\bar{\bar{C}}_{11_2}(\theta)$ is the coupling matrix at the boundary $z = -d_1$, $\bar{\bar{C}}_{01}(\theta_o)$ is the coupling matrix from air region to the random medium, and $\bar{\bar{C}}_{21}(\theta_2)$ is the coupling matrix from bottom layer to the random medium. The radiative transfer equations can be solved by replacing the integral with Gaussian quadratures and obtaining a system of ordinary differential equations with constant coefficients. The system of equation can then be solved by finding the eigenvalues and eigenvectors and matching the boundary conditions.

The radiative transfer approach can also be applied to the solution of backscattering cross-sections. The radiative transfer equations take the form

$$\cos\theta \frac{d}{dz} \bar{I}(\theta, \phi, z) = -\kappa_e \bar{I}(\theta, \phi, z) + \int_0^{2\pi} d\phi' \int_0^{\pi} d\theta' \sin\theta' \, \bar{\bar{P}}(\theta, \phi; \theta', \phi') \cdot \bar{I}(\theta', \phi', z)$$

where the intensity matrix $\bar{I}(\theta, \phi, z)$ contains all four Stoke's parameters,

$$\bar{I}(\theta, \phi, z) = \begin{bmatrix} I_v(\theta, \phi, z) \\ I_h(\theta, \phi, z) \\ U(\theta, \phi, z) \\ V(\theta, \phi, z) \end{bmatrix}$$

The boundary conditions are, for $0 < \theta < \pi/2$,

$$\bar{I}(\pi - \theta, \phi, z = 0) = \bar{\bar{C}}_{01}(\theta_o) \cdot \bar{I}_{oi}(\pi - \theta_o, \phi_o) + \bar{\bar{C}}_{11_0}(\theta) \cdot \bar{I}(\theta, \phi, z = 0)$$

$$\bar{I}(\theta, \phi, z = -d_1) = \bar{\bar{C}}_{11_2}(\theta) \cdot \bar{I}(\pi - \theta, \phi, z = -d_1).$$

The radiative transfer equations can again be solved with an iterative procedure as well as with numerical approaches.

3. DATA MATCHING

In the exercise of data matching with the theoretical results, the basic requirement is to come up with one single set of parameters that matches all experimental data plotted as functions of angle, frequency and polarization and collected from the same field at the same time. In Figure 1 we illustrate the angular match of active remote sensing data obtained from a snow field for vertically like-polarized backscattering cross-sections. The thickness of the snow is obtained from ground truth data. In matching active remote sensing data as shown in Figure 2 for alfalfa at 13 GHz, for two different heights, we find that it is necessary to place a rough surface at the vegetation-soil boundary. We simply superimpose, incoherently, the very rough surface result proportional to $\exp[-\tan^2\theta/s^2]/s^2$ to the volume scattering results by properly taking into account the

attenuation due to vegetation absorption. The rough surface effect is evident especially at angles near nadir. We must note that the parameters are chosen such that data at frequencies 9 GHz and 16.6 GHz from the same field are also matched. Since the rough surface effects are superimposed incoherently it is also possible to place a rough surface on the top of a vegetation field. In Figure 3 we show the match of a corn field for both like-polarization and depolarization returns simultaneously.

In the passive remote sensing of snow field, we encounter the phenomenon of diurnal change where the brightness temperature decreases as a function of frequency in the morning and increases in the afternoon. In order to explain this phenomenon, we have to resort to a three layer model where we assume that in the afternoon due to sun light illumination, a thin layer with higher loss tangent is created so that it provides more emission and masks the scattering effects at higher frequencies. In Figure 4 we show a spectral plot of T_B in the morning and in Figure 5 we show the spectral dependence T_B in the afternoon. Notice that in the thick snow layer, all parameters remain the same so that sun light only affects the top 7 cm.

In Figures 6 and 7 we show the correspondence of the random medium model and the discrete scatterer model by matching brightness temperature measurements from a snow field. Since the data can be matched with a random medium having $\ell_\rho = \ell_z = 0.2$ cm, we show that a homogeneous medium of the same background dielectric of $\varepsilon_1 = (1.5 + i0.00375)\varepsilon_o$ containing spherical scatterers also matches the data. It is noted that the effective fractional volume f is by no means equivalent to the actual volume occupied by the discrete scatterers. It is well known that the physical volume of ice particles constituting snow leads to over estimation of scattering effect and a rigorous theory which includes the homogeneous dielectric medium as a special case can only be obtained from a multiple scattering theory for closely packed scatterers (Tsang and Kong, 1979).

REFERENCES

CHANG, T. C., P. GLOERSEN, T. SCHMUGGE, T. T. WILHEIT, and H. J. ZWALLY, 1976, "Microwave Emission from Snow and Glacier Ice", Journal of Glaciology, 23-39, 1976.

KONG, J. A., R. SHIN, J. C. SHIUE, and L. TSANG, 1979, "Theory and Experiment for Passive Microwave Remote Sensing of Snowpacks", Journal of Geophysical Research, accepted for publication.

TSANG, L., and J. A. KONG, 1976, "Microwave Remote Sensing of Snowpacks", IEEE Transactions of Antennas and Propagation, AP-24, 283-287.

TSANG, L., and J. A. KONG, 1977, "Theory for Thermal Microwave Emission from a Bounded Medium Containing Spherical Scatterers", Journal of Applied Physics, 48, 3593-3599.

TSANG, L., and J. A. KONG, 1978, "Radiative Transfer Theory for Active Remote Sensing of Half Space Random Media", Radio Science, 13, 763-774.

TSANG, L., J. A. KONG, E. NJOKU, D. H. STAELIN, and J. W. WATERS, 1977, "Theory of Microwave Thermal Emission from a Layer of Cloud or Rain", IEEE Transactions on Antennas and Propagation, AP-25, 650-657.

TSANG, L., and J. A. KONG, 1979, "Multiple Scattering of Acoustic Waves by Random Distributions of Discrete Scatterers", to be published.

TSANG, L., and J. A. KONG, 1979, "Multiple Scattering of Electromagnetic Waves by Random Distributions of Discrete Scatterers", to be published.

ZUNIGA, M., and J. A. KONG, 1979, "Active Remote Sensing of Random Media", to be published.

ZUNIGA, M., J. A. KONG, and L. TSANG, 1979, "Depolarization Effects in the Active Remote Sensing of Random Media", to be published.

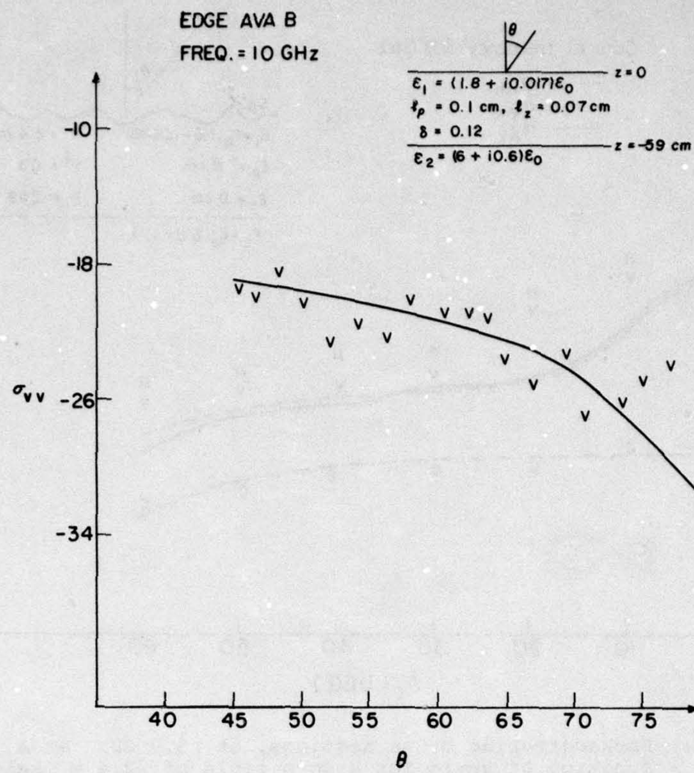

Figure 1. Vertically polarized backscattering cross section at 10 GHz as a function of angle for a 59 cm snow layer.

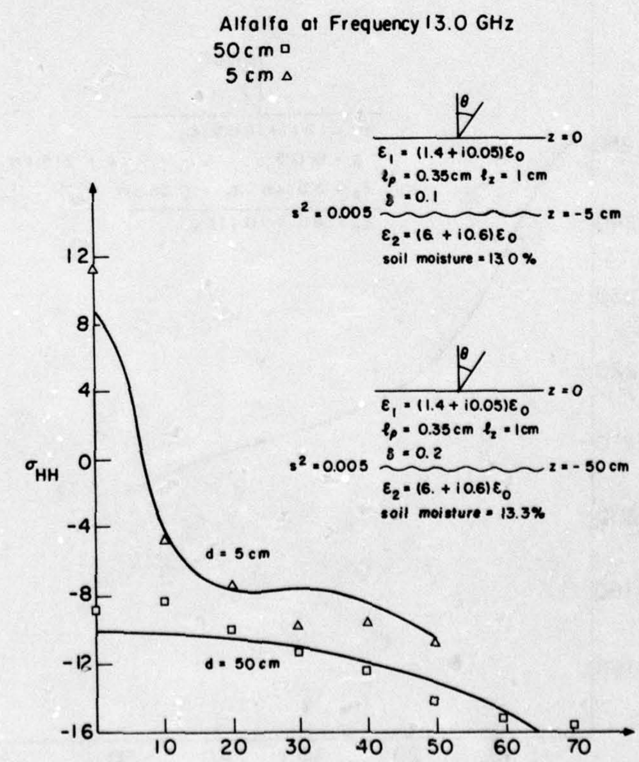

Figure 2. Horizontally polarized backscattering cross sections at 13.0 GHz as a function of angle for alfalfa fields of heights 50 and 5 cms.

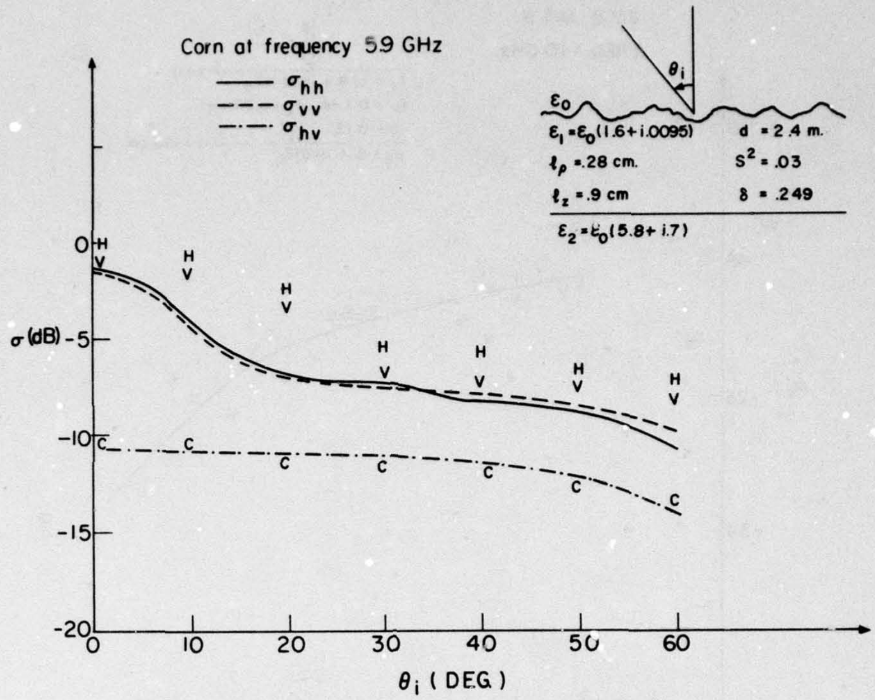

Figure 3. Backscattering cross sections, at 5.9 GHz as a function of angle for a corn field of 2.4 m height.

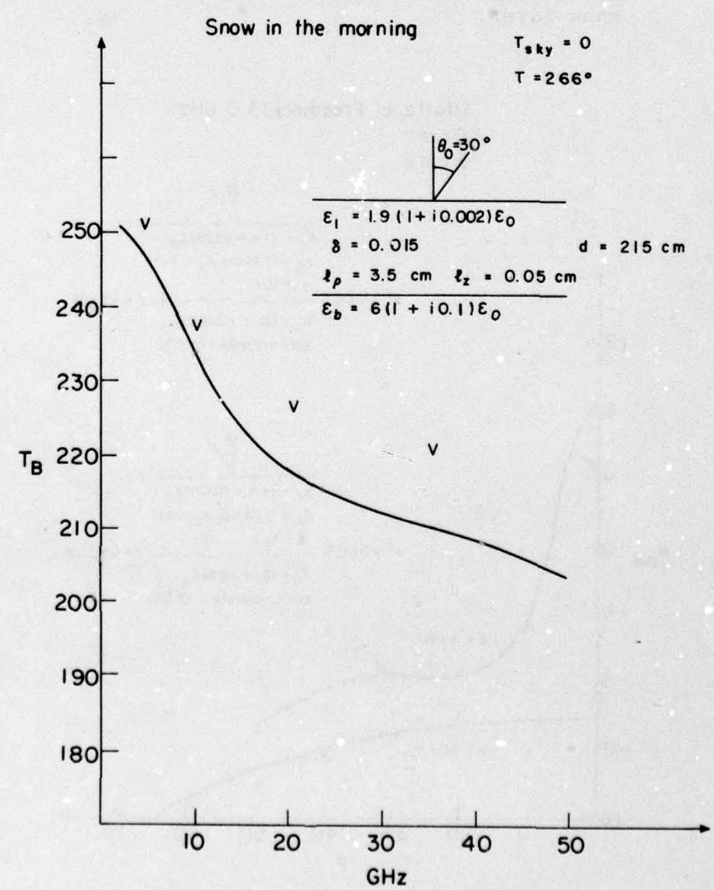

Figure 4. Brightness temperature of 215 cm snow layer as a function of frequency in the morning.

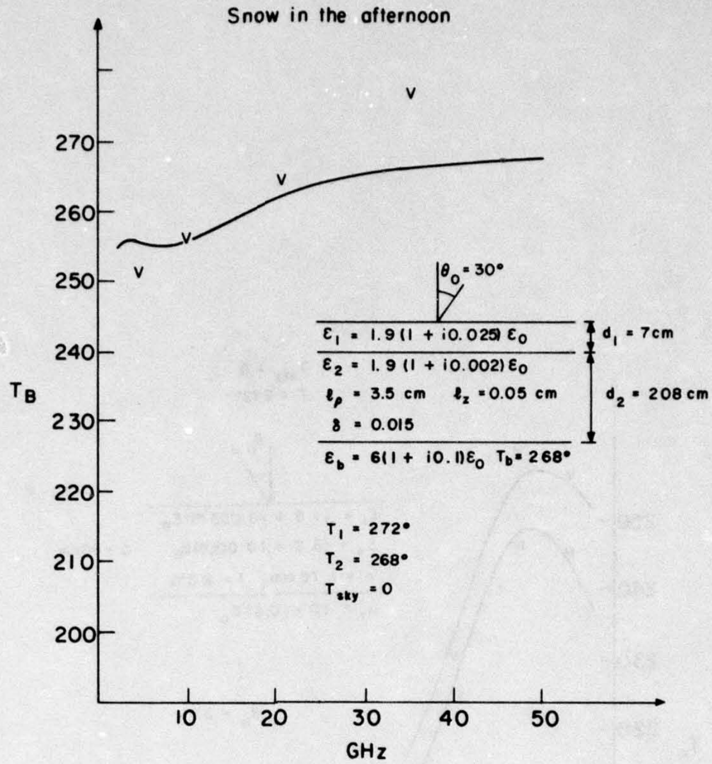

Figure 5. Brightness temperature of 215 cm snow layer as a function of frequency in the afternoon.

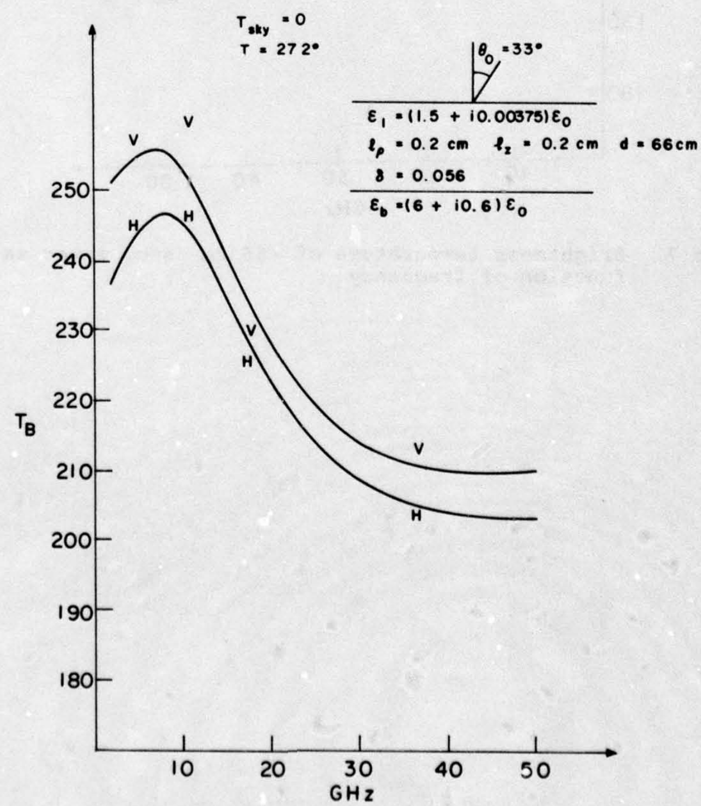

Figure 6. Brightness temperature of 66 cm snow layer as a function of frequency.

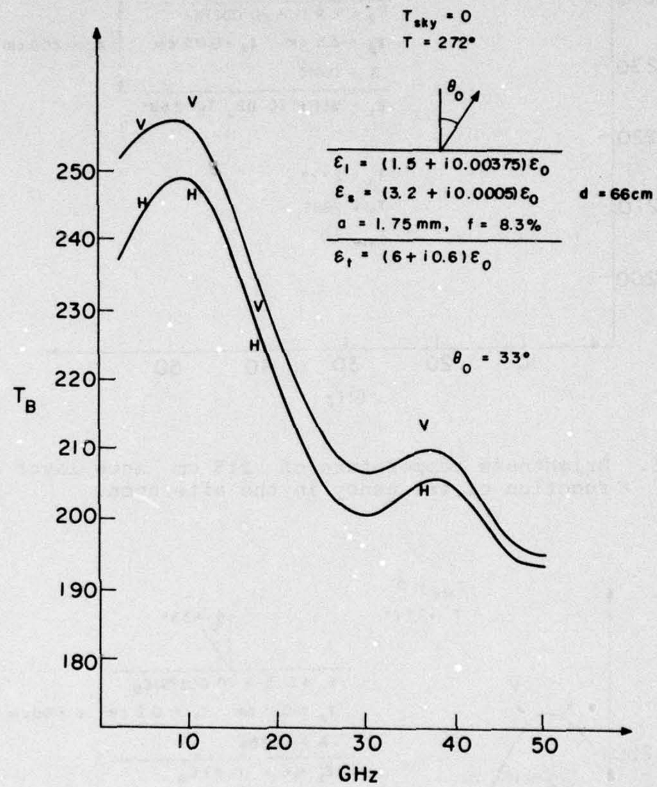

Figure 7. Brightness temperature of 66 cm snow layer as a function of frequency.

SOME OF THE PROBLEMS IN DIGITAL TERRAIN MODEL CONSTRUCTION

AUTHOR: MRS. G.B. THERSBY,
BRITISH AEROSPACE DYNAMICS GROUP,
FILTON,
BRISTOL,
UK.

SUMMARY

The aim of this paper is to identify those aspects of terrain which may effect electromagnetic wave propagation and to consider some of the arguments for and against accurate terrain modelling, both from the point of view of the user and the software designer. Two possible approaches to digital terrain modelling will be outlined as examples and the problems associated with each will be discussed. The paper will also consider the problems associated with producing a data base which is both efficient in terms of computer storage and access times, and which comprehensively models the terrain and associated data necessary for advanced propagation prediction modelling techniques.

INTRODUCTION

Given the task of constructing a propagation prediction model for use in a specified region, the user has two basic requirements, shown in Figure 1, namely:

1. To define the factors to be considered by the model

   e.g. diffraction
   reflection
   ground clutter

2. To define how much must be known about the terrain and the environment before these defined factors can be modelled.

If there is not to be a chicken and egg situation, the terrain and the environment must be modelled perfectly in all details. Fortunately, since this is impracticable, the art of propagation prediction modelling is usually constrained by cost considerations and hence the requirement for a perfect terrain and environment model is reduced.

However, the propagation prediction techniques have advanced over the years and the requirement for detailed terrain modelling has increased. Two possible approaches to terrain modelling will be described as examples and their limitations and advantages discussed. Some of the ways in which the terrain models and the propagation prediction techniques limit each other will be considered, together with the problems associated with designing a terrain model which is efficient in terms of computer storage and access, as well as modelling the terrain very accurately.

2. DEVELOPMENT OF TERRAIN MODELLING

Over the last ten years or so, the bias in propagation prediction modelling techniques has changed from a so-called 'statistical' approach to one based on a terrain profile. The 'statistical' approach specified the amount of degradation which could be expected over limits of certain lengths, over various types of terrain. The terrain was categorised over fairly large areas, greater than 100 sq.km. often, and the averaging effect of considering areas of terrain to have similar propagation attributes without determining its shape gradually lead to increased interest in the ideas of determining the terrain profile over which the link was to operate, and to the development of propagation prediction methods which used a path profile as a basis.

This interest in path profiles in turn lead to a requirement for the organisation of much larger volumes of data than that previously used. This was true whether the profiles themselves would be extracted, say from maps, then stored for future use, or whether a terrain model was designed, from which profiles could be extracted. At the beginning, the path profiles were considered almost solely as ground heights and it soon became apparent that even just extracting ground heights from a map for many profiles would be time consuming and it would probably be easier to have a computer do some of the work. The early digital terrain models used a rectangular mesh and stored the ground heights at the intersections of the mesh. The mesh size was not necessarily constant, often it varied according to the terrain variation so that flat, undulating or hilly terrain could be modelled with similar accuracy.

For most profiles constructed from a mesh data base, the original height data at the mesh intersections will be degraded by some type of interpolation. It is, however, more convenient as well as less costly to accept the degradation produced by the interpolation method than to extract many individual profiles from a map.

Although for some types of terrain and certain frequencies the ground height alone will enable reasonable predictions of path loss to be made, in most cases it is necessary to know something about the type of the ground surface and what is on top of it. It is at this stage that the mesh data bases show their limitations. Unless the mesh is exceptionally fine, the surface culture cannot be represented accurately. Figure 2 shows two areas of trees with the rectangular mesh which had been used for ground height data storage. The tree areas may be represented by defining a culture factor at each mesh intersection, as in Figure 3, or by assigning a culture factor to the contents of a mesh, as in Figure 4. Neither case produces an exact outline of the tree area, although each gave an approximation to the shape of the tree area which can be easily utilised by a computer program.

Although the combination of aerial photography and local surveys can produce very accurate (±1m) ground heights for the chosen mesh size, its potential for representation of surface culture data is much more limited, particularly for the outline of buildings.

A more recent approach to digital modelling was to store the outline of contours, ridge lines and other height points by a string of co-ordinates.

This approach can also be utilised for the surface culture and theoretically can produce a terrain model which is superior to the mesh data base. Unfortunately, to produce a high quality terrain model, a very large amount of data is required. To define a contour line accurately, for instance, the sampling interval for co-ordinates along the contour must be small. Figure 5 (a) shows a typical contour line and Figures 5 (b) and 5 (c) the difference in accuracy achieved by halving the sampling interval. The storage of the outline of an area, be it a contour line or the plan of a building, does enable surface culture to be modelled in something approaching the same degree of detail as the ground heights. However, as well as actually storing the data it is necessary to retrieve and use it; often the very large volumes of data are used only in part because of computer cost/time considerations making extensive use impracticable.

When constructing this type of terrain model, it is necessary to consider how the data be organised to ensure not only efficient access to the most often used portions of the data, but also to allow updates, particularly to the surface culture data where change is almost continuous. Since to keep the information up to date aerial photography will probably be required, producing the updates will be expensive, so the cost of including the new data should be as low as possible. If the height and surface culture data are stored separately this can ease the task of updating slightly. Often, arrangement of the surface culture data in levels, with, say, the ground type as level 1, crops as level 2, trees and buildings as level 3, can aid the user's visualisation of the types of updates which may be required, or the capability for, say, crop rotation, to be included in the design of the software which will use the terrain model.

The terrain models which use co-ordinate strings as a basis have more potential for accurate representation than the mesh-based models. The potential greater accuracy is achieved, however, only with the penalties of much larger volumes of data to be handled, and more complicated software to access it.

Figure 6 shows the comparison in storage between a terrain model using mesh storage and one using co-ordinate strings, each covering the same area.

A prospective user must, therefore, determine whether his available computer installation is more suited to one type of terrain model than another before deciding how much detail can be included, and how the terrain should be modelled.

3. REQUIRED ACCURACY

The degree of accuracy required for a terrain model will be at least partly a function of its proposed use. For ground to ground links it is the relative accuracy which is important, a consistent small error in ground heights will have little effect in the results obtained from a propagation prediction model. For very low level ground to air links or vice versa, the absolute accuracy can become more critical. Equally, this is where a knowledge of the position and height of trees, for instance, becomes more important as Figures 7 (a) and 7(b) demonstrate.

However, although a very accurate terrain model has advantages over an inaccurate one, it can easily be degraded in effective use because the user cannot define ground locations accurately - this is even more true when one terminal is on, say, a helicopter! Often, with care the ground location can be defined to within 50m; equally there are occasions when an exact spot cannot be identified. These errors in location are not always important but in very hilly regions can become so, as shown in Figure 8.

Unfortunately, the degree of accuracy necessary on a digital terrain model will tend to remain as a qualitative assessment because of a difficulty of, as it were, removing buildings from a link to measure the propagation loss with and without the buildings to know, rather than assess its effects. Similarly, there are difficulties in assessing one digital model against another - one data base may produce better correlation against one set of measurements than another, with the same prediction model being used in each case but the widely available sets of measurements for a given area are few.

Without large numbers of measurements, over a wide band of frequencies it will be hard to truly assess one digital model against another but these measurements are also necessary to prove the accuracy of a digital terrain modelling technique at all.

For surface culture, the accuracy requirement can be more critical than the accuracy requirement for ground heights, because this must be considered as three dimensional whereas it is easy to leave the ground height as a two dimensional effect. Figure 9 demonstrates the requirement for an accurate model of culture data as far as the position on the ground of the obstruction is concerned. Again, this accuracy requirement becomes negated if the location of the terminal is not known to the same sort of definition as the position of the area of buildings, as demonstrated by Figure 10. For surface culture, it is also necessary to know the height of the obstruction as well as the area which it covers, but the accuracy requirement will be a function of the use for which the data is mainly required.

4. VERIFICATION

Since the function of a terrain model is for propagation prediction, it is necessary that users or potential users should have confidence in the model and also understand its limitations. The limitations of a terrain model often become more apparent at high frequencies or over long links.

Although terrain models may be said to be accurate to x metres for height data and y metres for location data, it is much harder to determine the values of x and y to be achieved since these are functions of both the type of terrain and the intended use of the model. This type of quantitative assessment of the accuracy of a terrain model can give the user either great faith in the model, or a sense of distrust; it does little to allay any doubts as to the limitations of the model when used in propagation predictions. The user is more likely to gain confidence in a terrain model by usage, finding that predictions made using the model have reasonable agreement with measured data. This confidence can be achieved only if sufficient measurements over that terrain are available.

Comparison of terrain models need some care. Although sets of predictions made using different terrain models may indicate that one model is significantly better than another when the predictions are compared with measured data, it is necessary to check that the information contained in each model and the set of path loss measurements are contemporary. If the terrain models were constructed at different times it is possible that, for instance, the landscape shown by one terrain model has changed since the measurements were made. When a large set of measured data is available, changes to the terrain in one locality are often less significant than when only a small set of measurements may be used for comparison.

5. CONCLUSIONS

It is possible to produce terrain models which accurately represent many of the factors affecting electromagnetic wave propagation over land. Good accuracy is usually achieved only by the extraction and storage of large volumes of information and necessitates fairly complex software to utilize the information in propagation prediction. This is true whether the terrain model is based on a very fine mesh or on co-ordinate strings to accurately define an outline. The use of co-ordinate strings to represent outlines makes it easier to store the characteristics constants of the terrain than with a mesh system and also to add information into the terrain model.

The verification of a terrain model so that the model may be used with confidence is important. Measurements of propagation path loss made over the area of the terrain model must be available to achieve user confidence, as well as to assess the limitations of the model.

British Aerospace is pleased to acknowledge that the work described in this paper was carried out under contract to MOD with technical guidance given by the Army EMC Agency, School of Signals, Blandford.

1. DEFINE PROPAGATION FACTORS TO BE CONSIDERED

E.G. DIFFRACTION
REFLECTION
GROUND CLUTTER

2. DETERMINE WHICH ASPECTS OF TERRAIN AND ENVIRONMENT WHICH MUST BE INCLUDED IN TERRAIN MODEL

E.G. GROUND HEIGHTS
POSITION OF TREES, BUILDINGS

Fig.1 Contents of a terrain model

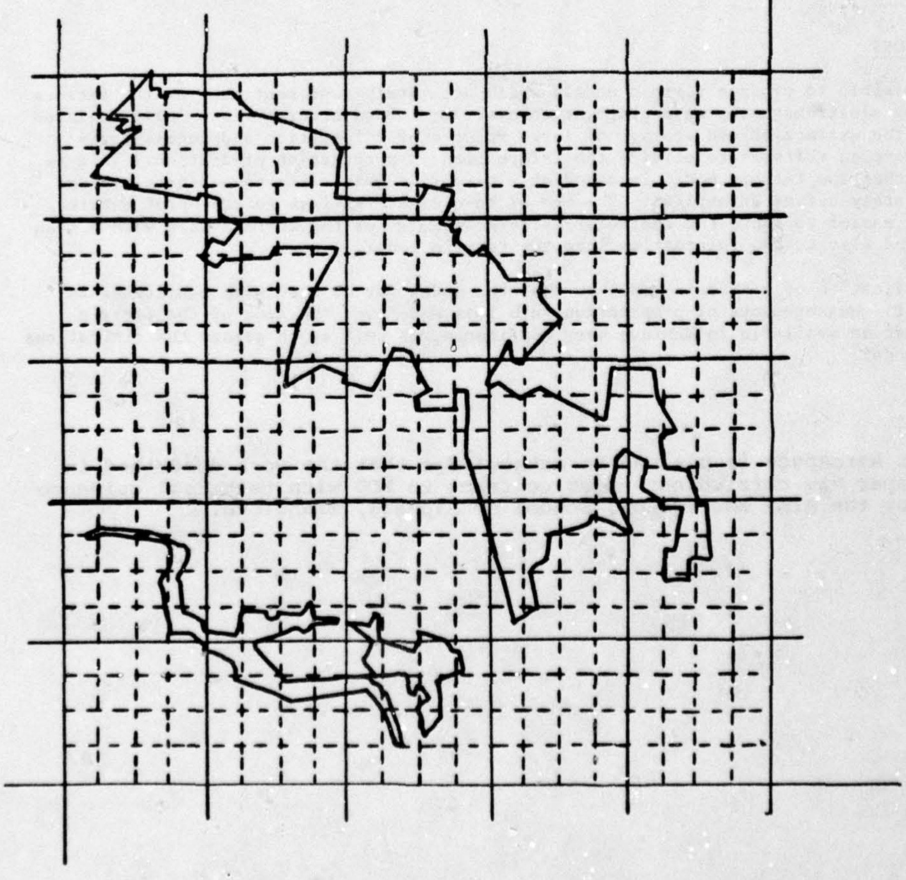

Fig.2 Area of trees on a rectangular grid

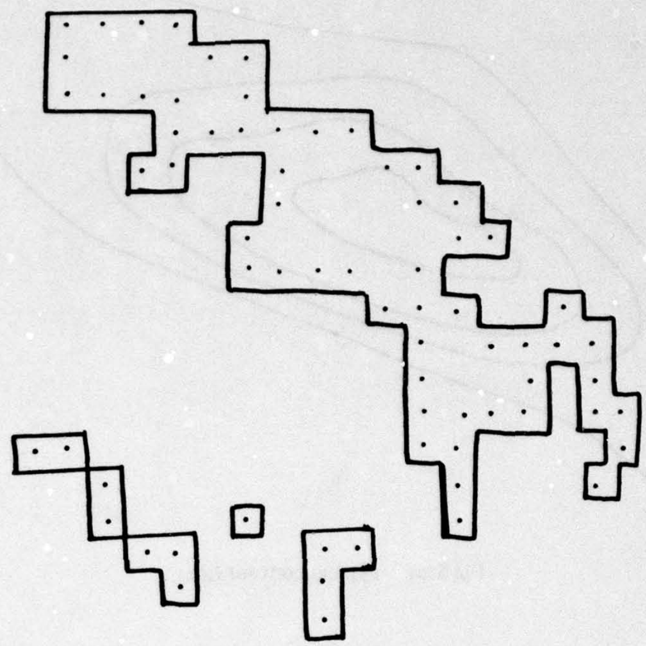

Fig.3 Representation of areas of trees using grid intersections

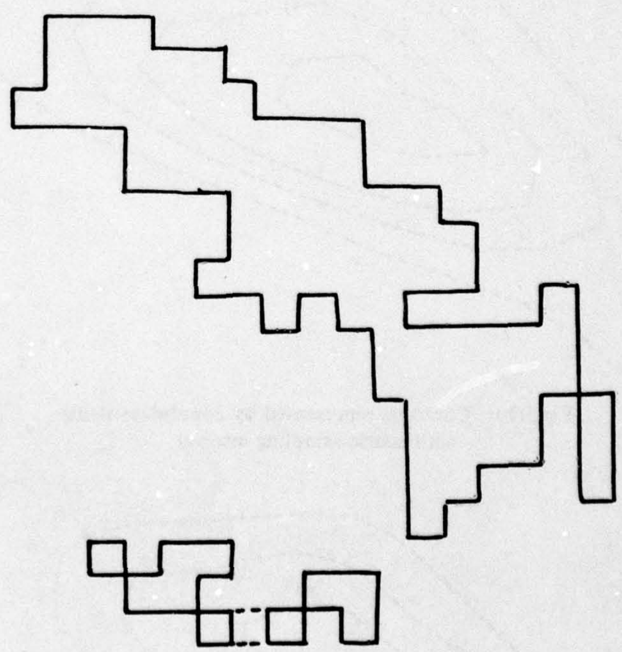

Fig.4 Representation of areas of trees using mesh areas

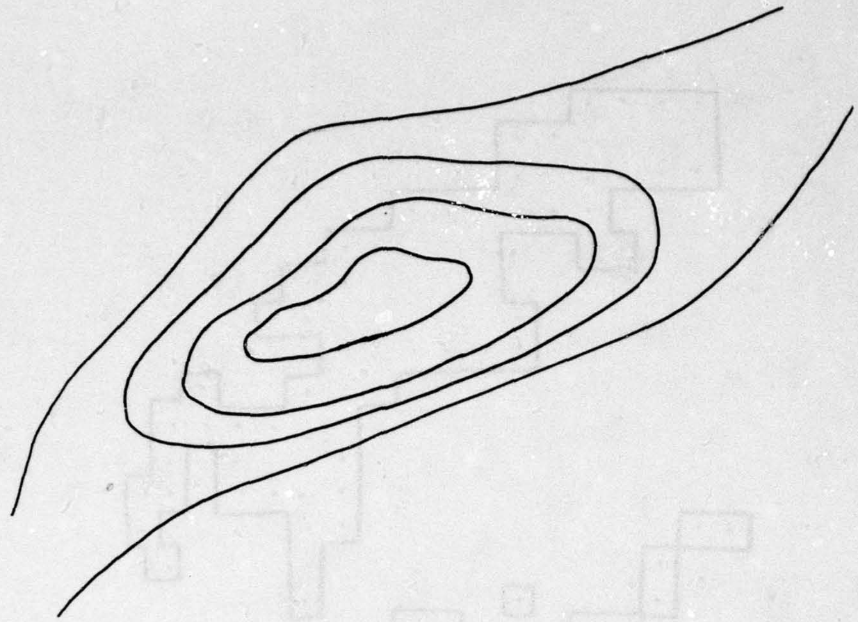

Fig.5(a) Typical contour lines

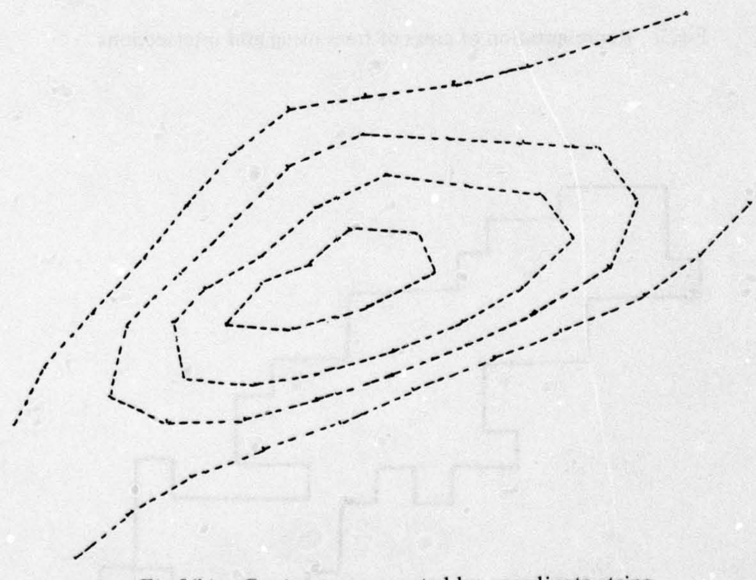

Fig.5(b) Contours represented by coordinate string with coarse sampling interval

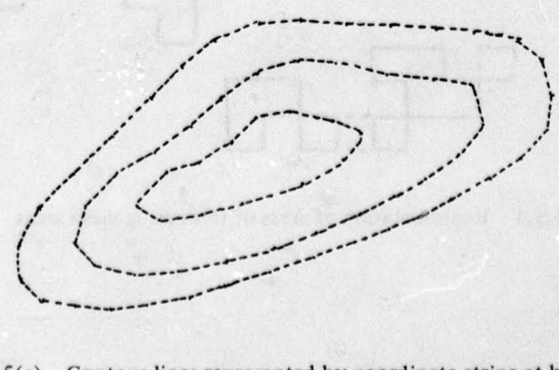

Fig.5(c) Contour lines represented by coordinate string at half the sampling interval of 5(b)

AREA SIZE:	20 KM x 20 KM
AREA TYPE:	FLAT TO UNDULATING + VILLAGES
TERRAIN DATA, COORDINATE STRINGS:	93 K WORDS
CULTURE DATA, ...:	46 K WORDS
TERRAIN DATA, GRID INTERSECTIONS:	18 K WORDS
CULTURE DATA, ...:	18 K WORDS

Fig.6 Comparison of storage requirements

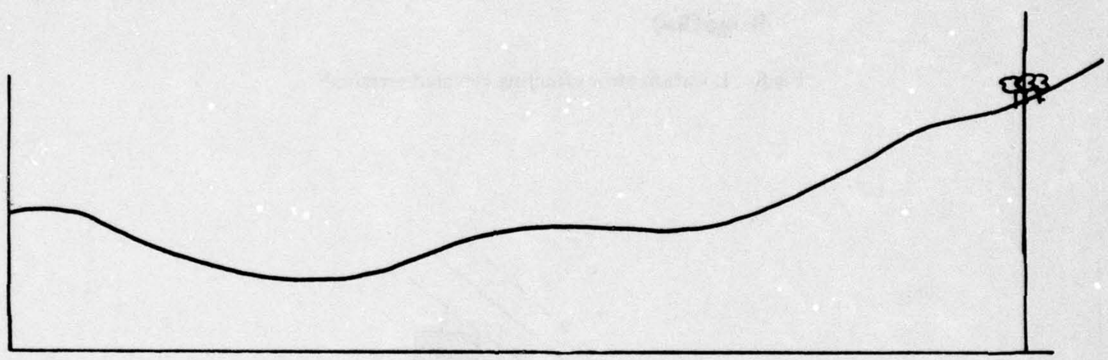

Fig.7(a) Actual link: both terminals unobstructed

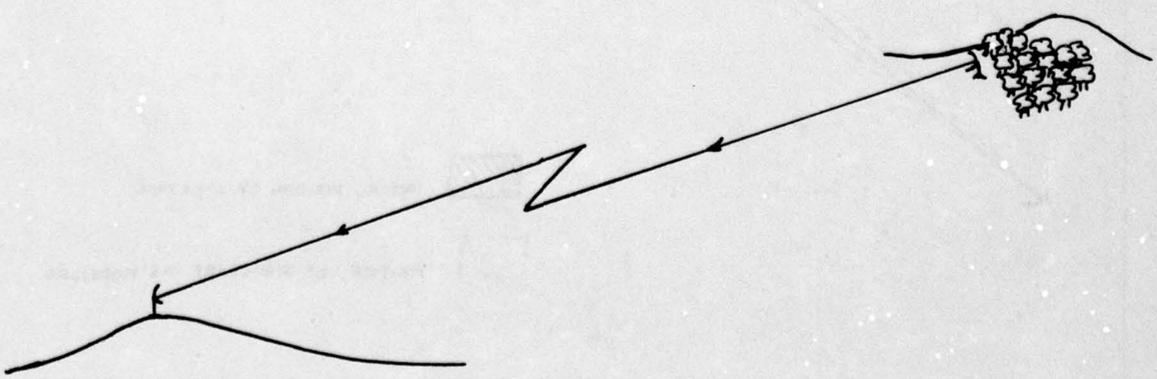

Fig.7(b) Path profile for link in 7(a), as interpreted by a terrain model

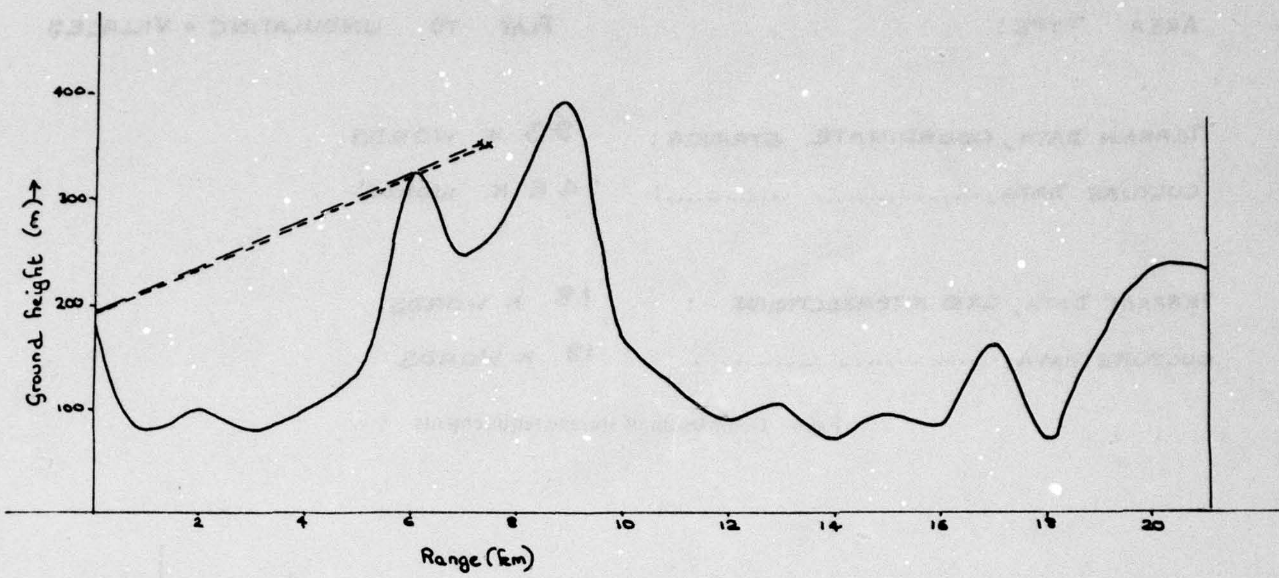

Fig.8 Location error effecting elevated terminal

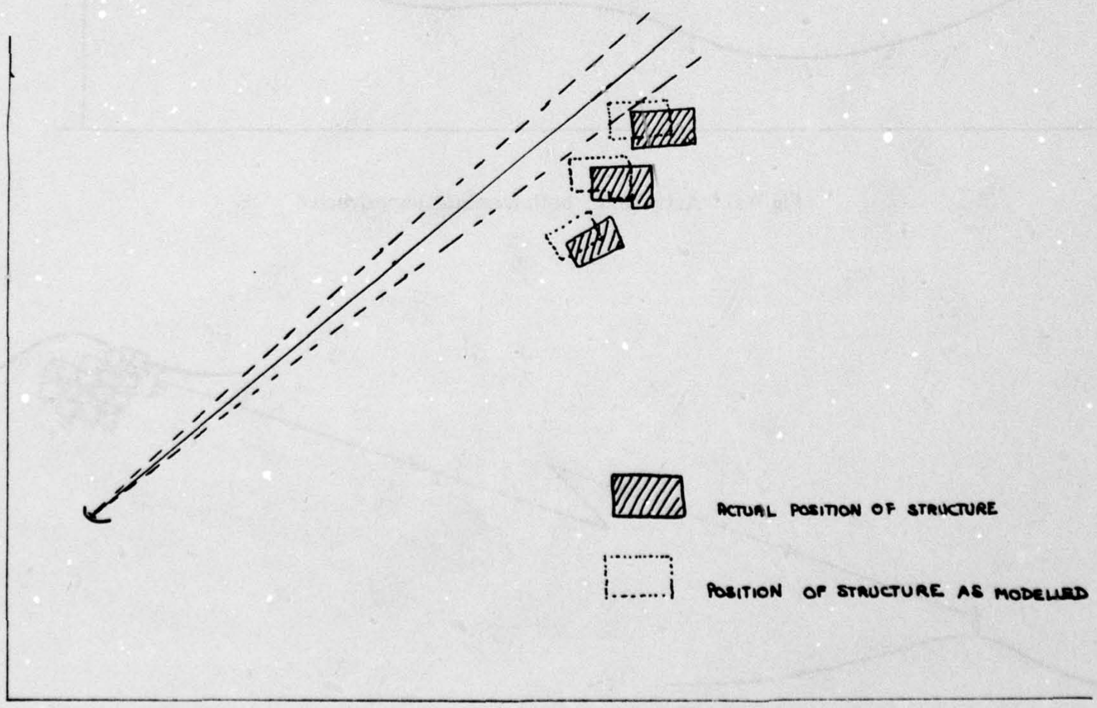

Fig.9 Effect of error in location of buildings in terrain model

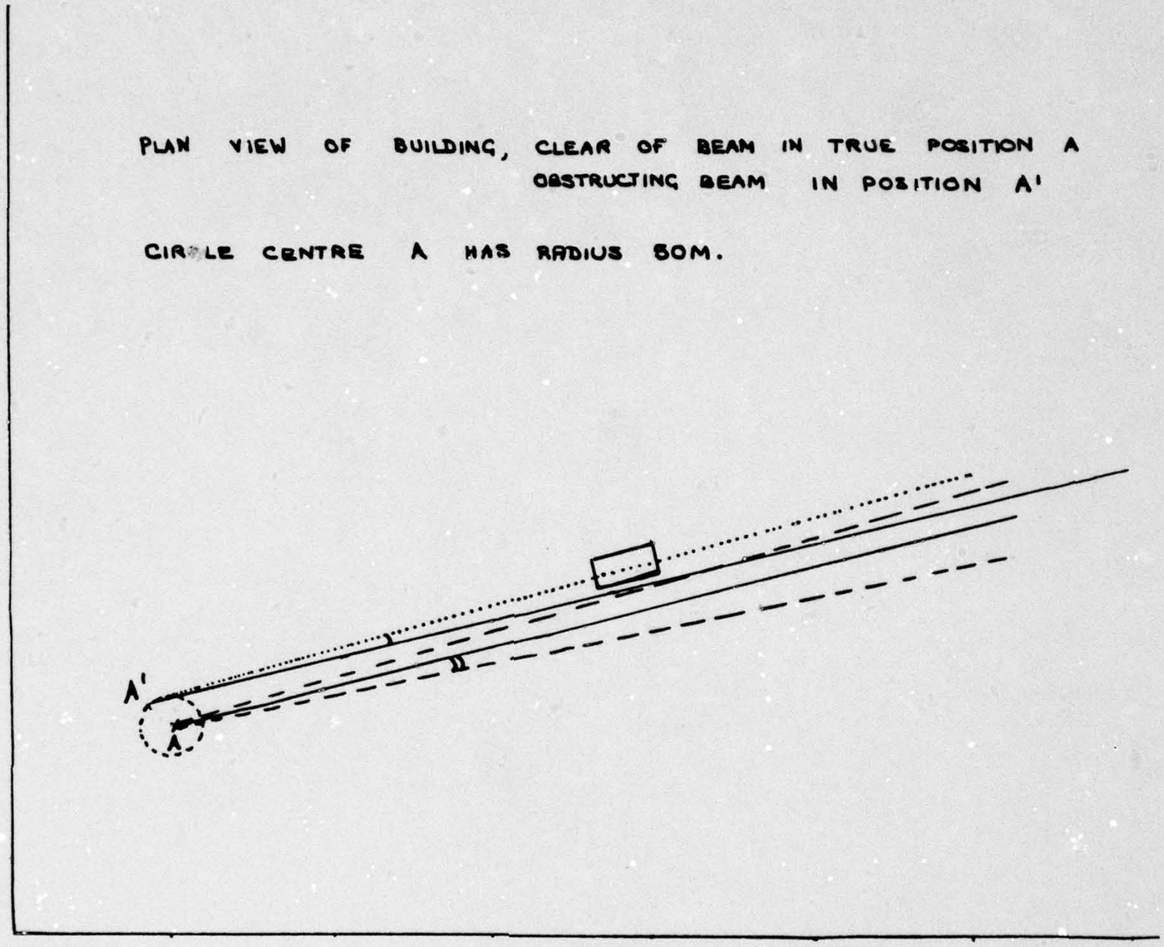

Fig.10 Terminal location error producing obstructed beam

AZIMUTH BEAMWIDTH EFFECT ON RADAR SENSED TERRAIN HORIZON PROFILES

Gordon E. Carlson and Paul W. Sapp
Electrical Engineering Department
University of Missouri-Rolla
Rolla, Missouri, USA 65401

SUMMARY

Terrain horizon profiles obtained by an azimuth-scanning monopulse radar differ from the horizon profile being sensed due to the smoothing introduced by the azimuth beamwidth. It is desirable to be able to generate such smoothed horizons from digitized terrain data for utilization by and simulation analysis of various airborne systems. A method is presented for smoothed horizon generation The mathematical model used computes elevation angle measurements for a phase-monopulse radar by considering a number of individual scattering points within the antenna beamwidth at the horizon range. Simplification of the mathematical model permits rapid generation and thus reasonable computer costs. Example smoothed horizons are shown and errors due to mathematical model simplification are analyzed. The smoothed horizon generation method is applied to the simulation analysis of a horizon checkpointing system. Results indicate that good position identification can be achieved with relatively wide azimuth beamwidths.

1. INTRODUCTION

Terrain aviodance systems for low-altitude aircraft incorporate an azimuth-scanning, forward-looking, monopulse radar to sense the horizon profile resulting from terrain features within the radar range (CHANZIT, L. and GREENSPAN, M., 1976). Such profiles can be termed range-limited horizons. They can also provide navigation checkpoints if they are digitized and correlated with reference horizons generated prior to the flight from digitized terrain data and stored on-board the aircraft (CARLSON, G. E., BENOIT, C. M., etal., 1977).

A range-limited horizon is the maximum elevation angle to terrain within the designed range limit as a function of azimuth angle. Portions of the terrain profile at the range limit which are not obscured by closer terrain will appear as part of the range-limited horizon even though they are not part of the true horizon. A range-limited horizon is approximately the terrain profile at the range limit for higher aircraft altitudes since the elevation angle to terrain at the range limit is greater than that to closer terrain at almost all azimuth angles. It is approximately the true horizon for very low aircraft altitudes since terrain at the range limit is obscured by closer terrain at almost all azimuth angles. For simplicity, range-limited horizons will be referred to as horizons in this paper.

An important consideration in the utilization or analysis of systems which use radar sensed horizons is how well these horizons portray the horizon being sensed. One practical radar characteristic which affects the horizon data obtained is the non-zero antenna azimuth beamwidth. Horizon points determined by the radar actually are obtained from the sum of antenna gain weighted returns from scatterers within the antenna beam at the range of the horizon. This results in a smoothed version of the horizon with greater smoothing for wider beamwidths.

Simulated radar sensed horizons generated from digitized terrain are of interest for reference purposes in mission briefing and for reference data in systems such as an horizon correlation navigation checkpointing system. Also, simulation performance of systems such as terrain avoidance and horizon checkpointing systems should include the effect of radar beamwidth smoothing. Thus, rapid generation of beamwidth smoothed radar sensed horizons from digitized terrain data is required. A generation method is developed in this paper. An application of the method for generating beamwidth smoothed horizons to the analysis of beamwidth smoothing effects on the performance of the horizon checkpointing system is also presented.

2. BEAMWIDTH SMOOTHED HORIZON GENERATION

The method for generating beamwidth smoothed radar sensed horizons from digitized terrain data follows in two steps. First, a simplified mathematical model is developed for computing a single beamwidth smoothed terrain profile measurement from terrain profile samples at a fixed range. Intervening terrain is ignored. This is followed by a description of a method for searching the terrain data to find horizon contributors and using the model to compute the smoothed horizon. Example horizons are then shown and model errors are analyzed.

2.1. Mathematical Model for Smoothed Fixed-Range Elevation Angle Measurement

It is assumed that the radar uses phase monopulse to measure the elevation angle to the terrain. It is further assumed that the radar antennas have a wide fan beam in the elevation direction. Thus, the antenna gain is essentially constant as a function of elevation angle over the range of elevation angles encompassed by the terrain profile.

For a point target, the phase difference, $\Delta\phi$, between the backscattered signal received at the two elevation phase monopulse receiving antennas is

$$\Delta\phi = \frac{2\pi d}{\lambda} \sin \Delta\beta \tag{1}$$

where d is the antenna separation, λ is the wavelength of the radiated energy and $\Delta\beta$ is the elevation angle of the point target with respect to a plane passing between the antennas and perpendicular to a line between them. That is, $\Delta\beta$ is the elevation angle with respect to the antenna elevation boresight. A phase detector measures the phase difference for each radar pulse and the elevation angle is then computed by

$$\Delta\beta = \sin^{-1} \left[\frac{\lambda}{2\pi d} \Delta\phi\right] \tag{2}$$

If the elevation angle to the antenna boresight is β_{BS}, then the elevation angle of the point target with respect to the radar is $\beta = \beta_{BS} + \Delta\beta$. It will be assumed that $\beta_{BS} = 0$ for simplicity, so $\Delta\beta = \beta$.

The actual received signal from terrain at a fixed range, R_L, and antenna azimuth angle, θ_A, consists of the sum of terrain returns weighted in amplitude by the gain of the antenna in the direction of individual scatterers. It is assumed that the antenna is uniformly illuminated so the two-way gain as a function of azimuth angle θ is

$$G(\theta) = \left[\frac{\sin[2.78(\theta - \theta_A)/\theta_B]}{2.78(\theta - \theta_A)/\theta_B}\right]^2 \tag{3}$$

where θ_B is the half-power beamwidth.

For simplicity, the reflectivity of all terrain points is considered to be the same. Also, only those terrain points within the half-power azimuth beamwidth are assumed to contributed to the received signal. This is a reasonable assumption since 91% of the received power comes from these points when uniform reflectivity is assumed.

Digital computation of the returned signal at the azimuth angle θ_A is performed by assuming that there are M point scatterers separated in azimuth by $\Delta\theta = \theta_B/(M-1)$ within the azimuth beamwidth. One receiving antenna is used as reference and the constant terrain backscatter amplitude is normalized to unity. The amplitude and phase of the returns at the second receiving antenna from the k^{th} point scatterer are

$$|R| = G[\theta_A + (k - [M+1]/2)\Delta\theta] \equiv W_k \tag{4}$$

$$\phi_k = \frac{2\pi d}{\lambda} \sin \beta_k \tag{5}$$

where $1 \leq k \leq M$ and β_k is the elevation angle to the k^{th} point scatterer. The total received signal at the second antenna is

$$\overline{R} = \sum_{k=1}^{M} W_k \cos\left[\frac{2\pi d}{\lambda} \sin \beta_k\right] + j\sum_{k=1}^{M} W_k \sin\left[\frac{2\pi d}{\lambda} \sin \beta_k\right] \tag{6}$$

The output of the phase detector is thus

$$\phi_A = \tan^{-1} \frac{\sum_{k=1}^{M} W_k \sin\left[\frac{2\pi d}{\lambda} \sin \beta_k\right]}{\sum_{k=1}^{M} W_k \cos\left[\frac{2\pi d}{\lambda} \sin \beta_k\right]} \tag{7}$$

and the measured elevation angle is

$$\Delta\beta = \sin^{-1} \left[\frac{\lambda}{2\pi d} \phi_A\right] \tag{8}$$

Using the small angle approximations ($\tan^{-1}\alpha = \alpha$. $\sin\alpha = \alpha$, $\cos\alpha = 1$) to simplify gives

$$\Delta\beta = \frac{\sum_{k=1}^{M} W_k \beta_k}{\sum_{k=1}^{M} W_k} \tag{9}$$

Now β_k is not necessarily a small angle. However, the combination of direct and inverse trigonometric functions in equation 8 lead to equation 9 being valid for $\beta \leq 26°$ for a typical phase monopulse radar with $\lambda = 1.8$ cm. and $d = 1$ cm.

In a practical radar system, angle measurements obtained from a number of pulses are averaged to obtain an adequate signal-to-noise ratio. Typically averaging could be performed while the azimuth angle at which the measurement is being made, θ_A, is within the antenna beam as it scans. This is a non-coherent averaging and is modeled by averaging the results obtained by equation 9 for successive antenna azimuth locations at $\Delta\theta$ spacings for which θ_A is included in the antenna beamwidth.

For the model, the data processing required to obtain a single beamwidth smoothed terrain profile point at a fixed range thus requires the averaging of the results of M computations of equation 9 to be compatible with the above averaging concept. This is illustrated in Fig. 1 for $M = 5$. Actually, $M = 9$ was chosen for most horizons generated since sample cases showed that they had essentially the same appearance and statistics as horizons generated with more samples per beamwidth. Note that terrain profile points for two beamwidths, that is 2M-1 points, are required to compute each smoothed terrain profile point.

2.2. Generation of Smoothed Horizons

It is assumed that digitized terrain data is supplied as terrain heights for a regular grid of terrain locations. Terrain heights are required for points along N radial lines emanating from the radar location where $N = (\theta_S/\Delta\theta) + 1$, θ_S is the azimuth width, and $\Delta\theta$ is the azimuth angle separation of required horizon points. For computation simplicity, terrain height is computed for points where the radial lines cross either vertical or horizontal grid lines by linear interpolation between the terrain heights at the nearest grid points along these lines. The choice between vertical or horizontal grid lines is made to minimize the spacing between points computed. This is illustrated in Fig. 2 where it is shown that terrain heights are computed to one grid crossing beyond the range limit. Elevation angles to the terrain points determined are computed from the ground range and specified aircraft altitude. Subsequent computations require elevation angles to terrain points along the radial lines but between those computed above. Linear interpolation is used to approximate these values.

To obtain the smoothed horizon, a horizon is first generated for zero beamwidth by finding the maximum elevation angle to the terrain within the range limit and the range to this maximum elevation angle along each radial line. It serves to identify the true horizon points and the range to them. As indicated in the previous section, two beamwidths and thus 2M-1 points are required to compute the smoothed horizon data points at each azimuth angle desired. If all of this set of points on the true horizon are at the range limit, then the true horizon data points are used to compute the smoothed horizon data point. If points in this set on the true horizon occur at ranges other than the range limit, then elevation angles are computed along the radial lines in question at 20 meter intervals (20 meters chosen to represent typical radar range resolution) starting at the maximum range to any point in the set and decreasing until the total range encompassed by the set is spanned. A smoothed fixed-range profile elevation angle is then computed at each of the ranges identified and the maximum elevation angle computed is taken as the smoothed horizon data point at the azimuth angle considered. This procedure is illustrated in Fig. 3 and provides an efficient search for smoothed horizon data points.

Typically, smoothed horizon data points were obtained at 1 degree azimuth intervals since earlier work (CARLSON, G. E., etal., 1976) had shown that this was sufficient to characterize horizon profiles. To further reduce computation time when larger beamwidths are involved, horizon data points were generated with a spacing of 2 degrees. In analyzing the horizon correlation checkpointing system, it was desirable to maintain a data spacing of 1 degree. Linear interpolation was used to supply the additional points. Little error was incurred since the smoothed horizons for wider beamwidths are smoother than those for narrower beamwidths.

2.3. *Analysis of Model Errors*

The error incurred by using the simplified mathematical model of Equation 9 rather than the more complete model of Equation 8 for computing individual smoothed terrain elevation measurements is considered first. The difference between the elevation angles computed by Equations 8 and 9 is the error. Its statistics were evaluated in a Monte Carlo fashion by using uncorrelated, normally distributed, pseudo-random numbers for each elevation angle β_k and evaluating the statistics of the error for 100 realizations of the error. This was done for β_k with means, μ_H, from 0° to -16° and standard deviations σ_H, from 0.125° to 2° which span the range of values for horizon segments in one beamwidth obtained from typical terrain. The resulting mean and standard deviation of the error are plotted

in Figs. 4 and 5.

Unsmoothed horizon segments of up to 8° in length were generated from digitized terrain data with standard deviations of up to 300 m to determine the elevation angle variations in typical horizon segments within an azimuth beamwidth. The largest variations occur for the roughest terrain and longest segment and the average standard deviation of this largest variation was computed to be 0.68°. For this magnitude of horizon variation, Figs. 4 and 5 show that mean and variance of the error incurred by using the simplified mathematical model is negligible even for horizon data which is 16° from the antenna boresight.

A Monte Carlo simulation was used to evaluate the effect of reducing computation time by using linear interpolation to obtain smoothed horizon data points at 1° spacings. The standard deviation of the errors incurred is less than 2.5% of the standard deviation of the horizon being measured for a 4° beamwidth and less than 1% for an 8° beamwidth. In the case of the performance evaluation of the horizon correlation checkpoint system, these errors are small enough to be neglected.

2.4. Smoothed Horizon Examples

A horizon generated from digitized terrain data for an area near the Klamath River in northern California is shown in Fig. 6 along with smoothed horizons generated for 2°, 4°, and 8° beamwidths. Note that the elevation angle is exaggerated by a factor of approximately three. The terrain data was obtained from the United States Geological Survey (USGS) and was originally generated by the Defense Mapping Agency (DMA) by reading contour lines on 1:250000 scale USGS maps and interpolating to give a grid of data points with 63.5 m separation. Every third data point (190.5 m separation) was used to reduce computation time. Previous analysis (CARLSON, G. E., etal., 1976) indicated that this spacing is sufficient to characterize the horizons. The area used can be classified as rough terrain with a terrain height standard deviation of $\sigma_T = 226$ m and an average terrain height autocorrelation length of 2300 m. The horizons were generated for an aircraft altitude of 500 m above the maximum terrain height beneath a 6 Km flight path centered on the horizon viewing location.

The horizons shown in Fig. 6 illustrate the beamwidth smoothing. It can be seen that the basic horizon shape remains even with an azimuth beamwidth of 8° in this case. Examples of horizons from both rougher and smoother terrain have been computed with similar results (SAPP, P. W., 1978).

3. AZIMUTH BEAMWIDTH EFFECT ON HORIZON CORRELATION CHECKPOINTING

The method for generating beamwidth smoothed horizons described above has been used to analyze the effect of azimuth beamwidth smoothing on a navigation checkpointing system which uses horizon correlation. A brief description of this system and the analysis results obtained is included here to illustrate an application of the beamwidth smoothed horizons and to show the effect of beamwidth smoothing on significant horizon shape.

3.1. System Description

The flight path for a particular mission is planned by using topographic data for the mission area. The topography along the flight path is considered in identifying checkpoints which are close enough together so the desired flight path can be maintained and which have horizons with significant data content.

A set of reference horizons which would be seen from the airborne vehicle is generated for possible vehicle locations with spacing ΔR along a line array which crosses the flight path at each checkpoint location as shown in Fig. 7. For sketching convenience, the profiles are indicated as coming from a fixed range even though this would not be true in an actual case. The length of the line array required is established by the expected vehicle cross-track position error when it arrives at the checkpoint. This depends on vehicle dynamics, inertial navigator accuracy, guidance philosophy, and checkpoint separations. The reference horizons are generated from digitized terrain data and correspond to the planned vehicle altitude and heading. The horizons consist of digital data and give elevation angle to the horizon as a function of azimuth angle with respect to flight path heading. The horizon sampling interval is determined by the sampling rate required to adequately describe the horizon and must also be compatible with onboard sensor capabilities. The reference horizons for a particular mission are stored on magnetic tape in the vehicle for inflight digital correlation with sensed horizons.

During flight, an on-board radar sensor is used to obtain sensed horizons as often as possible along the flight path. This is also shown in Fig. 7 where the spacing between locations where sensed horizons are obtained is ΔS. As the sensed horizons are obtained, they are correlated with all the reference horizons in the upcoming line array until identification is achieved with one of the reference horizons in that array. The identification specifies the time at which the array is crossed (along-track position) and the location along the array at which it is crossed (cross-track position) as shown in Fig. 7. Actually, it may be desirable to make comparisons with several upcoming line arrays to avoid the possibility of mission abort due to a single erroneous line array mismatch.

A sensed horizon is generated with a narrower azimuth angular extend, θ_S, than the angular extent of the reference horizons, θ_R, as shown in Fig. 7. It is compared with overlapping horizon segments along the extent of the reference horizon to find the segment which it

best matches. Thus horizon identification for position determination is achieved even if the airborne vehicle heading is incorrectly known, provided the sensed horizon is within the limits of the reference horizon angular extent. The angular offset along the reference horizon at which the identification occurs determines the vehicle heading.

The horizon correlations indicated above are to be performed by the computer on-board the aircraft and must produce output values which are measures of how well sensed horizons and segments of reference horizons match. The correlation technique must be as simple as possible, consistent with good horizon selectivity so that the horizon comparisons can be made quickly. Various correlation techniques have been studied (CARLSON, G. E., etal., 1975). Based on simplicity and performance, it was determined that comparison of a sensed horizon and a reference horizon segment is best performed by computing the integral absolute difference (IAD) between the sensed horizon with its mean value removed and the reference horizon segment with its mean value removed. Mean values are removed to eliminate sensitivity to sensed horizon mean value errors.

The minimum IAD value (I_m) obtained for one sensed horizon when computed for each segment of all reference horizons in one array of reference horizons is used to determine if the sensed horizon was obtained from the neighborhood of the line array. Figure 8 shows an example variation of I_m for sensed horizons taken from points along the flight path on both sides of the reference array. The value of I_m as a function of the along-track distance from the line array of reference horizons at a checkpoint location is referred to as the horizon comparison function. As indicated, a detection threshold is set and a sensed horizon is determined to be from the neighborhood of the line array when I_m is less than this threshold. The minimum value of I_m which is also less than the detection threshold identifies the sensed horizon which was obtained closest to the reference line array and thus identifies the aircraft crossing time for the line array; that is, the along-track aircraft position. The particular reference horizon in the array and the azimuth heading angle along it at which the minimum I_m occurs identifies the aircraft cross-track position and heading at the array crossing.

The detection threshold indicated in Fig. 8 must be established for any particular horizon comparison so it can be determined if the sensed horizon was obtained from the neighborhood of the reference horizon array. The threshold must be high enough to permit checkpoint identification even if there are system errors, but low enough so false identifications do not occur. The value of this threshold depends on the particular system parameters used, on the terrain roughness and on the magnitude of horizon system errors expected. Thus, threshold values must be determined for each line array used as a checkpoint.

3.2. Performance Results

Analysis of system performance was done by simulation of the horizon correlation operation for checkpoint line arrays at three different geographical locations. Terrain data used is that described in the earlier section. In addition to the northern California location previously indicated (Case 2), an area of very rough terrain ($\sigma_T = 328$ m) in the Salmon mountains in northern California (Case 3) and an area of moderately rough terrain ($\sigma_T = 95$ m) in the Appalachian mountains in West Virginia (Case 1) were used.

A horizontal, 6 Km, straight flight path at an altitude of H_A above the maximum terrain height beneath the flight path and centered on the checkpoint line array center was used for each location considered in the simulation. The Monte Carlo technique was used with a uniform distribution of the flight path center over an area of ΔR by ΔS with respect to the line array center to obtain statistics for system characteristics. This is approximately equivalent to considering a uniform distribution of flight path location over the checkpoint array area due to the array natures of both the sensed and reference horizon viewing locations. The system characteristics include: (1) the horizon comparison functions, I_m, (2) the position determination error, and (3) the heading determination error. Random errors were added to the reference and sensed horizons to assess their impact on system performance and thus to determine their maximum allowable value. In addition, simulations were performed for systems where the reference horizons are generated without smoothing as well as for systems where reference horizons are generated with beamwidth smoothing corresponding to the sensed horizons. Results are shown for both cases and indicate whether the complexity of beamwidth smoothing is required for reference horizons. Further details of the analysis techniques used are presented in a reference (CARLSON, G. E., BENOIT, C. M., etal., 1977).

Analyses were performed with antenna azimuth beamwidths from 0° to 8° and results are presented as a function of beamwidth. System parameter tradeoffs have been previously performed (CARLSON, G. E., etal., 1976 and CARLSON, G. E., BAIR, G. L., etal., 1977) and the system parameters chosen for the analysis results to be presented are shown in Table I.

The performance parameters selected to characterize system performance are: (1) the circular error probable (CEP = radius of circle in which 50% of errors lie) of the position determination error, (2) the standard deviation of the heading determination error, and (3) the maximum allowable random horizon error. For the most part, results are presented for only the Klamath River area in northern California (Case 2 with $\sigma_T = 226$ m) due to space limitations. The sensed horizon at the checkpoint location for this case is the horizon which was previously shown in Fig. 6.

TABLE I

SYSTEM PARAMETER VALUES CHOSEN FOR SYSTEM ANALYSIS

Parameter	Symbol	Value	Units
Sensed Horizon Length	θ_S	90	degrees
Reference Horizon Length	θ_R	130	degrees
Horizon Sampling Interval	$\Delta\theta$	1	degree
Reference Horizon Viewing Location Separation	ΔR	200	meters
Sensed Horizon Viewing Location Separation	ΔS	100	meters
Range Limit	R_L	5000	meters
Flight Path Height Above Terrain	H_A	500	meters

The horizon comparison functions for non-smoothed horizons and horizons smoothed with an 8° beamwidth are shown in Fig. 9. Plotted are the mean values and the mean values plus and minus one standard deviation. There is a slight decrease in the average function value away from the line array location when both reference and sensed horizons are beamwidth smoothed. This is as expected since horizons are smoother and the IAD is smaller for smoother horizons. When beamwidth smoothing is only present on the sensed horizon, then there is an increase in the average function value at the line array crossing. This is also as expected since reference and sensed horizons which are generated with different beamwidths are inherently dissimilar and yield a poorer horizon match at the array crossing. Standard deviations of the three horizon comparison functions shown are essentially the same. The change in the horizon comparison function with beamwidth smoothing is small enough so no great effect on system performance is expected.

The maximum allowable random horizon error was determined in two steps. For this computation, the value of I_m at any flight path location was reasonably assumed to be Gaussian. This assumption was checked by computing several histograms (CARLSON, G. E., etal., 1975). First, the required detection threshold was determined to give a probability of false alarm (incorrect horizon match identification) of less than 0.001 for all individual flight path positions outside the neighborhood of the checkpoint line array (1 Km on each side of the array) when no random errors were added to the horizon. Random errors with increasing standard deviation were then added to the reference and sensed horizons. The maximum error standard deviation which would still produce a probability of detection of 0.99 was taken as the maximum allowable random horizon error. The results are plotted in Fig. 10 as a function of antenna azimuth beamwidth for all three analysis cases and both smoothed and non-smoothed reference horizons. In all cases, the maximum allowable random horizon error decreases with wider beamwidth. Greater effect is noted when both sensed and reference horizons are smoothed. This is basically because of the reduction of the IAD value away from the line array in this case with the attendent reduction in threshold. This reduction is greater than the increase in threshold required to maintain a probability of detection of 0.99 when non-smoothed reference horizons are used.

Along-track and cross-track position determination errors were obtained by computing the difference between the sensed and reference horizon locations which gave the minimum value of I_m. Statistics computed for these errors indicated that the mean value was zero. The variances were used to compute the circular error probable (CEP). This was done for a range of random horizon errors. The results are shown for Case 2 in Fig. 11 as a function of beamwidth for zero random horizon error and for the maximum allowable random horizon error determined above. Results for the other two cases analyzed are similar (SAPP, P. W., 1978). Results for both smoothed and non-smoothed reference horizons are shown. The heading determination error was obtained by computing the difference

between the heading of the center of the sensed horizon and the center of the segment of the reference horizon for which minimum I_m or match was attained. Again, the mean value of this error was zero. The standard deviation of this error is plotted for Case 2 in Fig. 12 as a function of beamwidth for zero random horizon error and for the maximum allowable random horizon error determined above. Results for both smoothed and non-smoothed reference horizons are shown.

Actually, better position and heading determination accuracy can be achieved with interpolation between I_m values obtained (CARLSON, G. E., BAIR, G. L., etal., 1977). However, the above results show the effect of azimuth beamwidth on system performance. It can be seen that position and heading determination accuracy do not depend significantly on the azimuth beamwidth for the range of beamwidths considered. Also, the accuracy is essentially the same for both smoothed and non-smoothed reference horizons.

4. SUMMARY AND CONCLUSIONS

A method was developed for generation of range-limited horizons which incorporate the azimuth beamwidth smoothing which would occur if they were obtained by sensing with a monopulse radar. An approximate mathematical model was first developed to combine the individual fixed-range scatterer data as weighted by the antenna gain pattern to obtain a measured elevation angle at one azimuth. This approximate model was shown to be sufficiently accurate for horizon simulation purposes. A digitized terrain data searching technique was defined to be used in conjunction with the mathematical model to generate the desired beamwidth smoothed horizons.

The method developed was employed to analyze the effect of antenna beamwidth smoothing on the performance of a horizon correlation navigation checkpointing system. It was found that beamwidths up to 8° did not significantly affect the position and heading determination accuracy of such a system. The maximum allowable random horizon error is reduced for larger beamwidths. However, beamwidths of up to 4° do not give very large reductions. It was determined that there is no great advantage to including the anticipated beamwidth smoothing in the reference horizons. This is true since significant horizon functions are preserved even with the larger beamwidths.

5. ACKNOWLEDGEMENT

This research was supported by the Geography Programs Branch, Office of Naval Research, Arlington, Virginia, USA 22217.

6. REFERENCES

CARLSON, G. E., BAIR, G. L., and BENOIT, C. M., 1975, "Geographic Orientation for Low-Altitude Aircraft Using Horizon Matching", University of Missouri-Rolla Electrical Engr. Communications Sciences Report, CSR-75-3.

CARLSON, G. E., BAIR, G. L., and BENOIT, C. M., 1976, "Forward-Sensed Terrain Profile Comparison for Aircraft Geographic Orientation", University of Missouri Electrical Engr. Communications Sciences Report, CSR-76-3.

CARLSON, G. E., BENOIT, C. M., and SAPP, P. W., 1977, "Range-Limited Horizon Correlation for Navigation Checkpointing", University of Missouri-Rolla Electrical Engr. Communications Sciences Report, CSR-77-1.

CARLSON, G. E., BAIR, G. L., SAPP, P. W., and SIMMONS, D. M., "Evaluation of Range-Limited Horizon Correlation by Using Pseudo-Terrain", 1977, University of Missouri-Rolla, Electrical Engr. Communications Report, CSR-77-2.

CHANZIT, L., and GREENSPAN, M., 1976, "AN/APQ-148 Multimode Radar for the A-6E All Weather Attack Aircraft", 1976, Proc. of the 1976 IEEE National Aerospace Electronics Conference, Dayton, Ohio.

SAPP, P. W., 1978, "The Effect of Finite Sensor Beamwidth on the Performance of a Horizon Correlation Guidance System", 1978, M.S. Thesis, University of Missouri-Rolla, Rolla, Missouri.

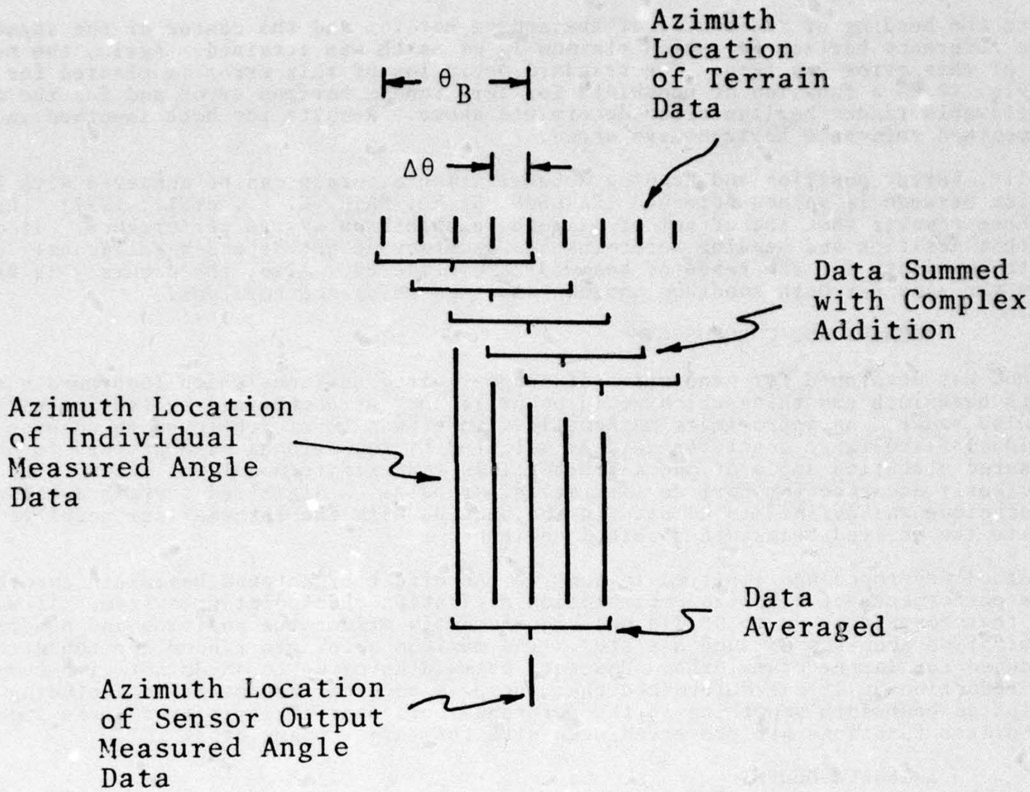

Figure 1. Terrain Return Data Processing for a Single Range.

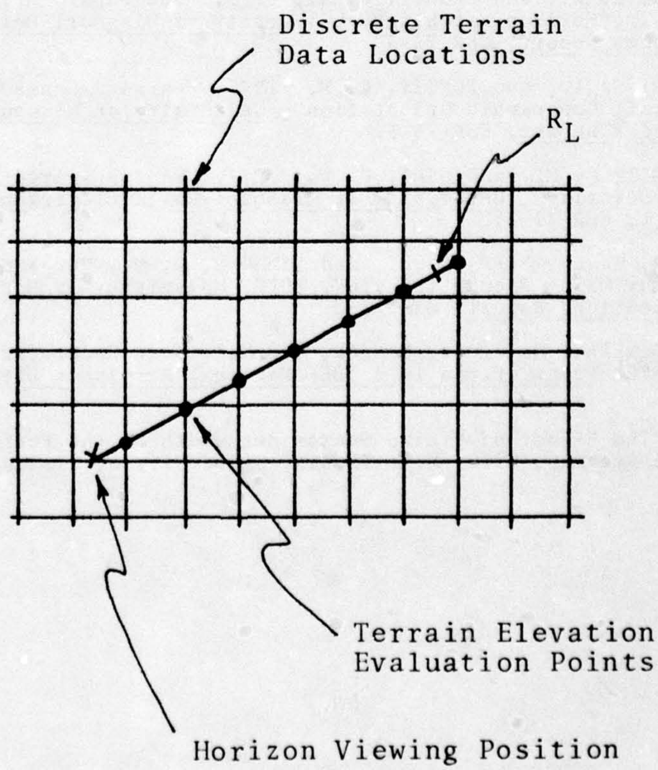

Figure 2. Terrain Points Used to Evaluate One Horizon Elevation Data Point.

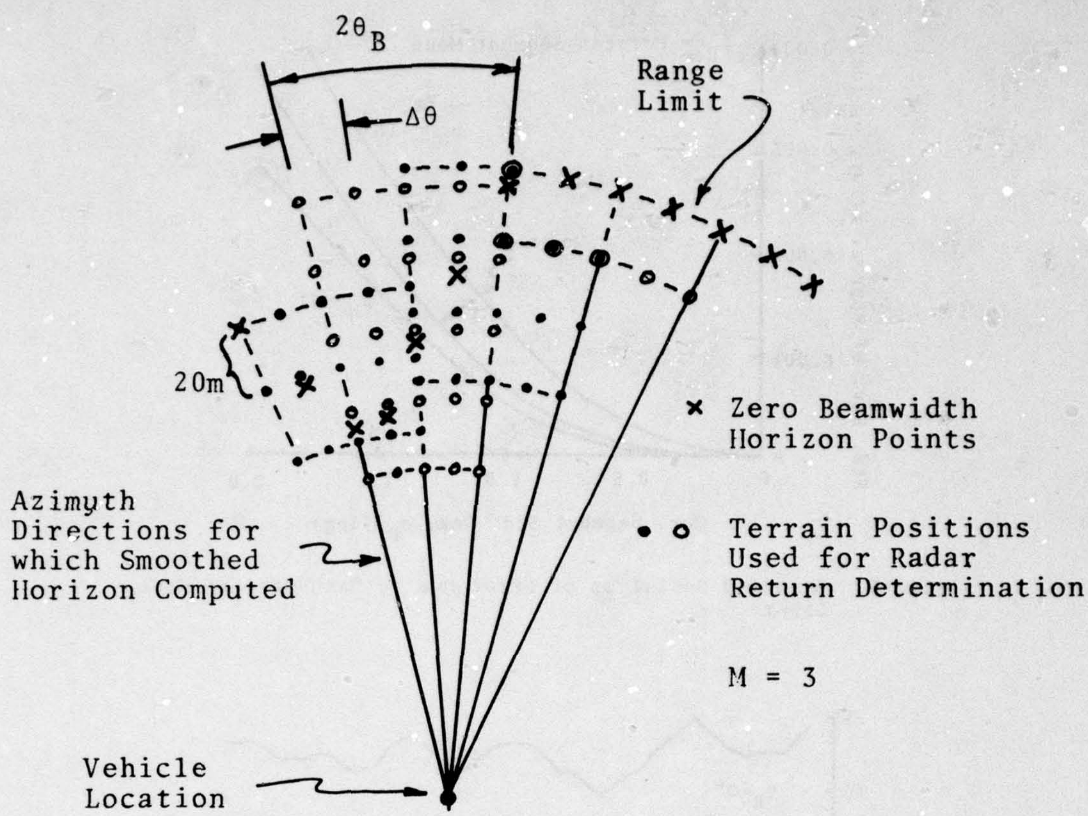

Figure 3. Geometry for Radar Return Determination for Finding Smoothed Horizon.

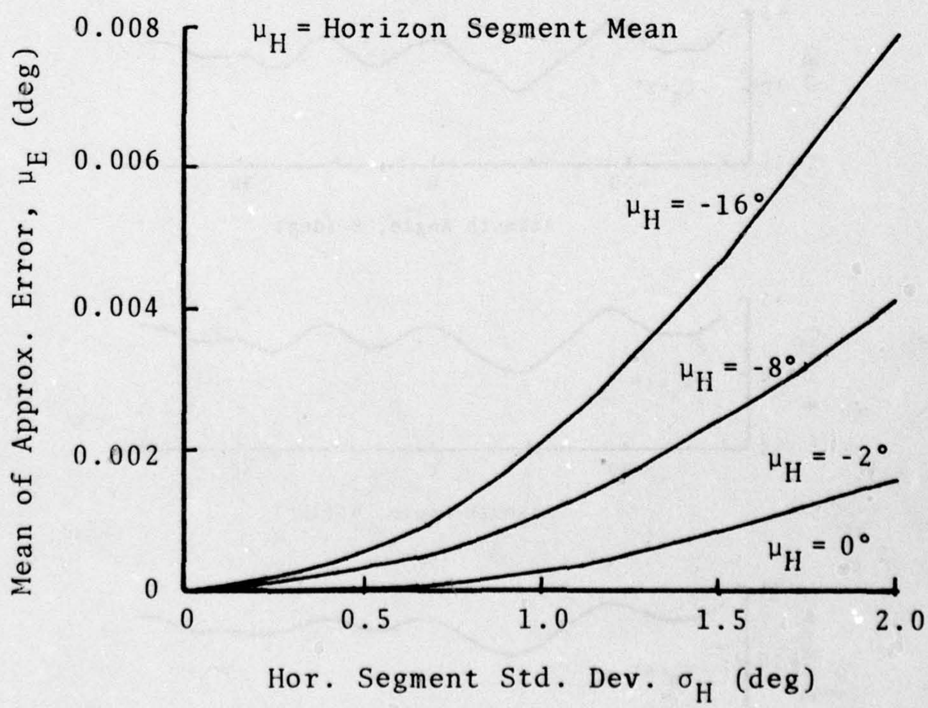

Figure 4. Mean of Error Due to Mathematical Model Approximation.

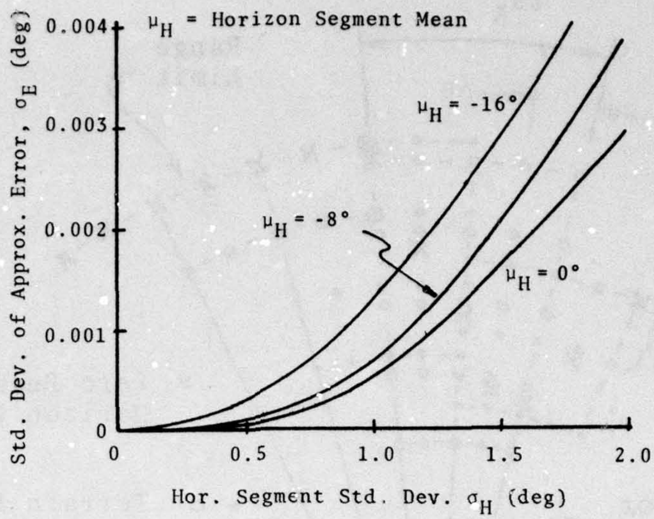

Figure 5. Standard Deviation of Error Due to Mathematical Mode Error.

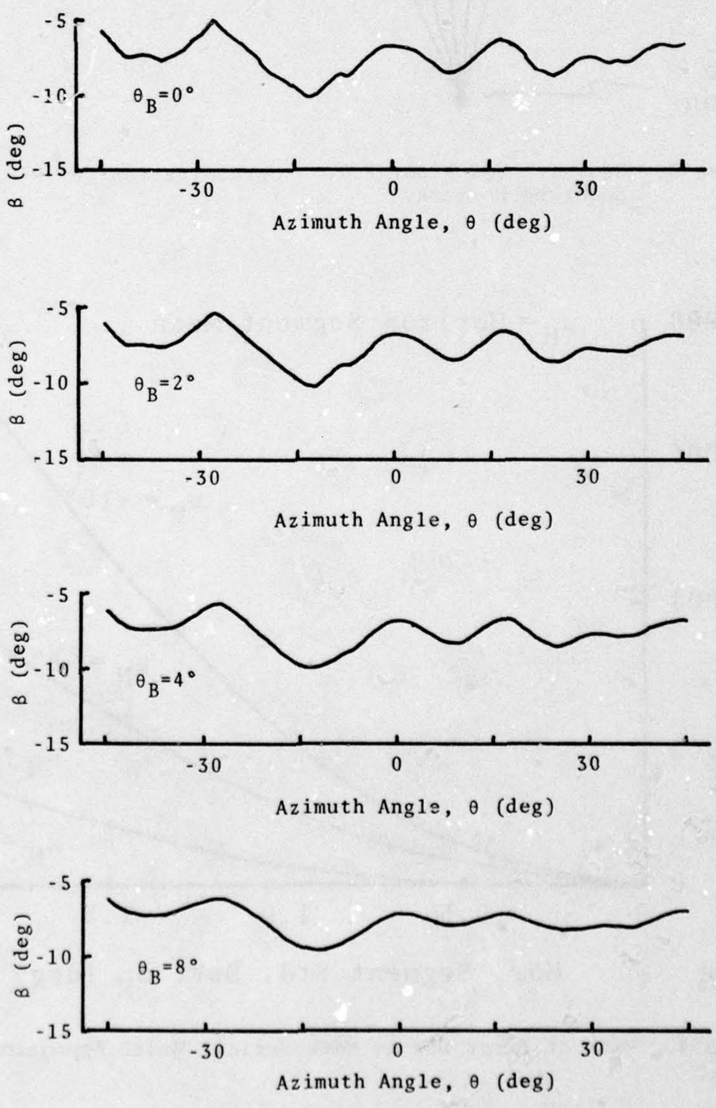

Figure 6. Sensed Horizon for Various Sensor Beamwidths.

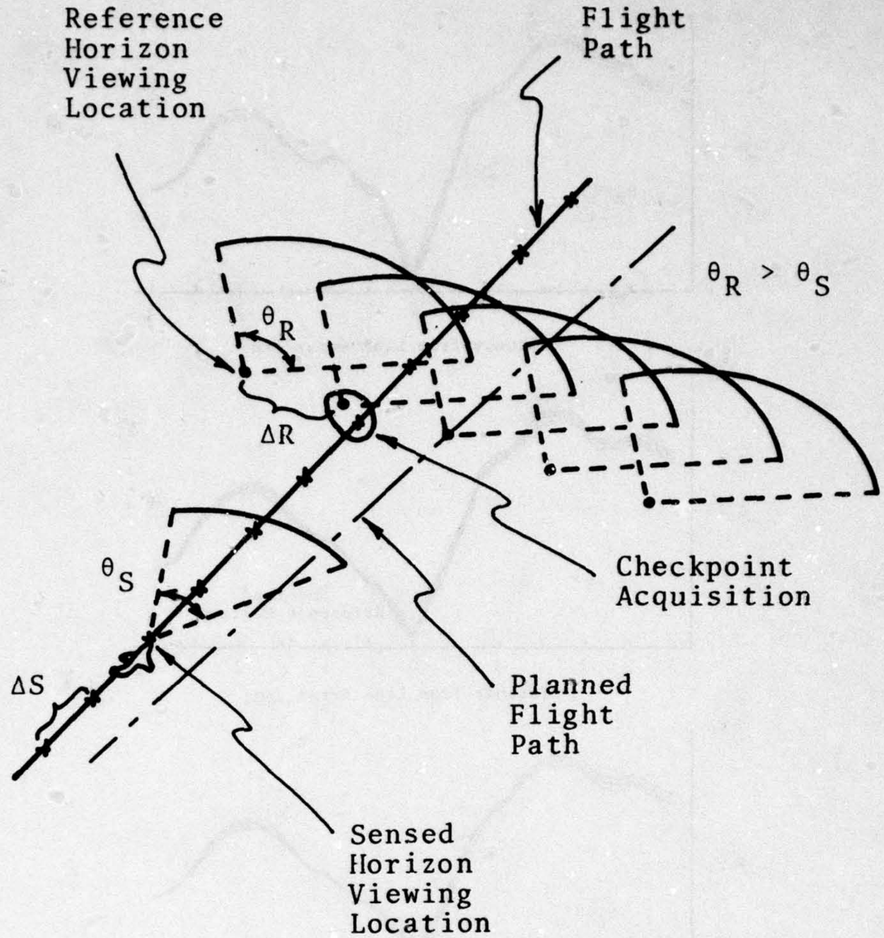

Figure 7. Horizon Comparison System Concept.

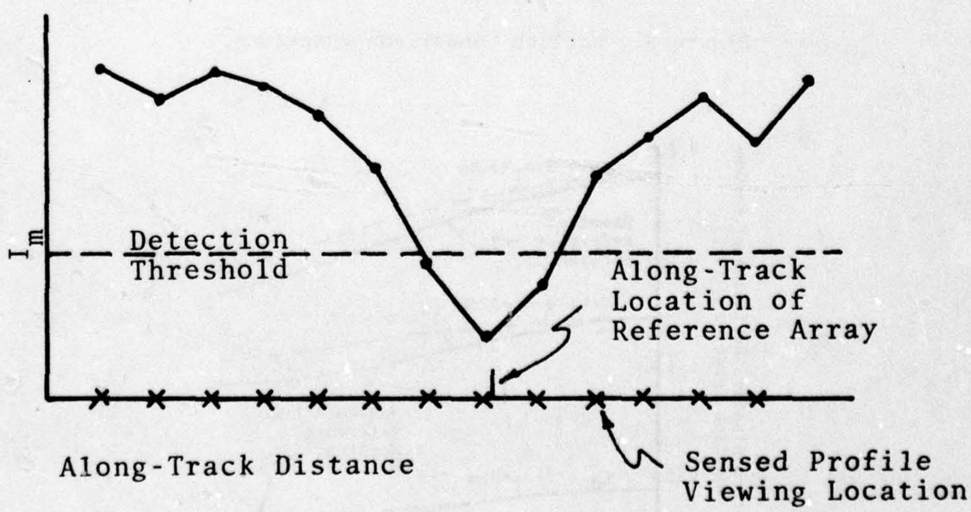

Figure 8. Along-Track Position Identification.

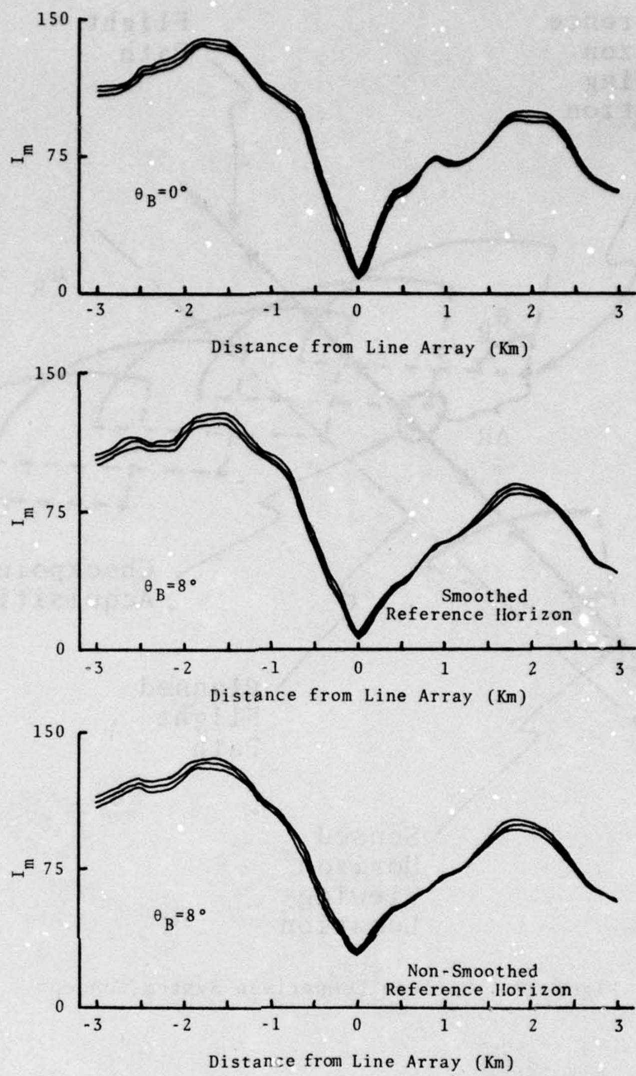

Figure 9. Horizon Comparison Functions.

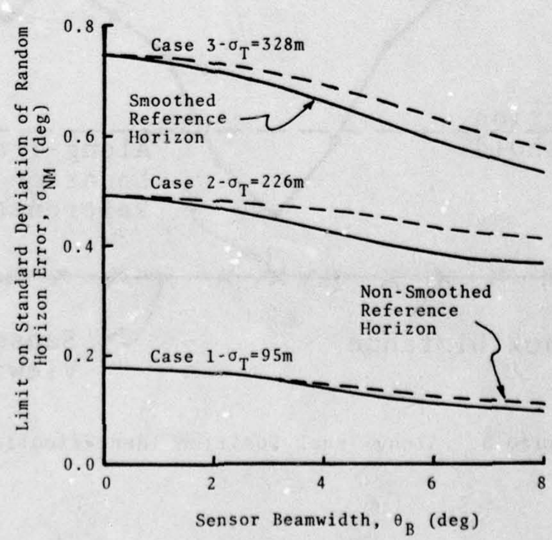

Figure 10. Maximum Allowable Random Horizon Error as a Function of Sensor Beamwidth.

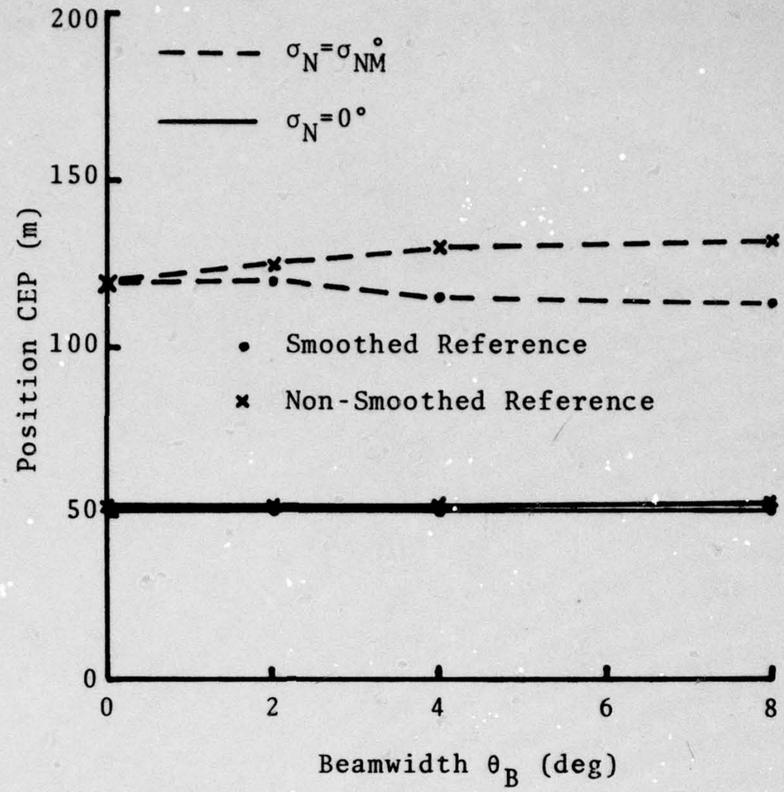

Figure 11. Limits of Position Determination Accuracy (Case 2 - σ_T=226m).

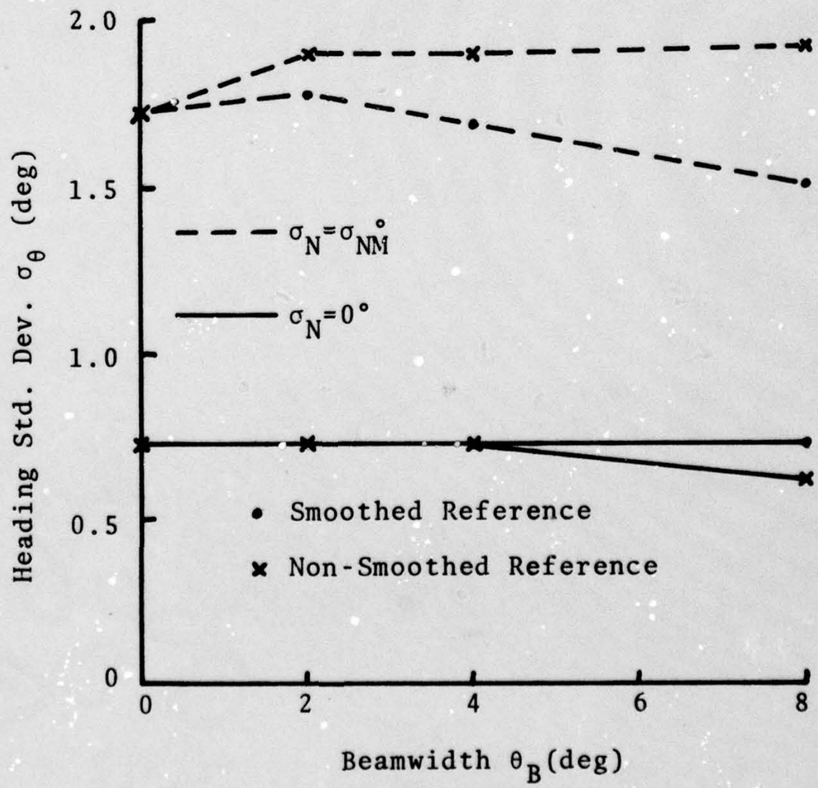

Figure 12. Limits of Heading Determination Accuracy (Case 2 - σ_T=226m).

BIOLOGICAL AND GEOPHYSICAL FACTORS OF ELECTROMAGNETIC WAVE PROPAGATION AND THEIR USE IN DIGITAL DATA BANKS

Ekkehard R. Küsters
German Military Geophysical Office
5580 Traben-Trarbach, Germany

SUMMARY

A radar clutter data bank is being built up by the German Forces. The basis for this data bank is a topographic data bank that covers the whole Federal Republic of Germany, using a grid of 5 seconds of arc, and contains data about the elevation and the soil cover. In the radar clutter data bank the different categories of soil cover are to be correlated with their specific effects on the propagation of electromagnetic waves. Greatest problems in this respect arise with the categories "deciduous forest" and "farmland" because of the phenological changes that take place almost all over the year. The lack of processed data about the phenology of plants, which are of importance, made it necessary to evaluate old statistics in order to gain mean values, and to establish a phenological observation net to get actual data. As it is impossible and unnecessary to ascertain data for each grid field, however, a coarser subdivision of the Federal Republic of Germany was made into regions that are homogeneous with respect to the phenological events.

Because of the influence of hydrometeors on electromagnetic wave propagation, the data bank contains data about the most important cloud types, too: their altitude and vertical extension, the frequency of their occurrence depending on season and region, and their drop spectra.

1. INTRODUCTION

During the last one hundred years great progresses have been made in the improvement of communication techniques using electromagnetic waves beyond the visible range. Though this made factors like e.g. fog, clouds, and rainfall that had disturbed the primitive optical systems lose much of their importance, even the modern systems are susceptible to disturbances, not only of technical but also of natural kind.

During the bird migration periods in spring and autumn it often happens, that the flocks of birds are that large and dense, that they are visible in radar. In extreme cases a complete shading of flying targets can be caused by the echoes of migrating birds.

But not only birds are natural obstacles in the propagation of electromagnetic waves. Variations of the terrain profile are the reason for refraction -, diffraction -, and reflection phenomena. Furthermore reflections can be caused by inversion layers, hydrometeors influence the electromagnetic waves by absorption and diffraction, the image given by airborne radar is a function of the soil type and/or soil cover.

New telecommunication lines for example should be planned in a way that negative influences of the environment on the quality of the signals do not exceed an unavoidable minimum. To make sure that terrain influences can be regarded in the first stage of planning already -without the time-consuming interpretation of maps- the German Telecommunications Central Office established a data bank. In this data bank the Federal Republic of Germany is subdivided into about 17 million grid fields, the size of which is approximately 150 m in north - south direction and 95 m in east - west direction (5 seconds of arc). For each one of these grid fields the informations "maximum elevation above sea level" and "soil cover" are stored.

When the German Forces planned to build up a radar clutter data bank, they thought the topographic data bank to be a good basis for their purposes, and therefore they acquired it. But though the informations stored there are very detailed already, a hard job was still lying ahead, and that was to superimpose those data of the structure of the surface with such geological, biological, and meteorological characteristics that are relevant for electromagnetic wave propagation.

2. DATA OF SOIL COVER

2.1. Classification

One of the data collectives of the topographic data bank is the one concerning the soil cover. As it is not possible to give detailed informations about any grid field ("4 houses, 7 trees" etc.), the different types of soil cover are classed under ten categories (table 1).

In any of these classes the soil cover is to be correlated with its specific radar backscatter factors. This is relatively easiest with the classes 1, 2, 9, and 10, for here the backscatter is either constant all over the year (in N° 1 and 2), or changes are caused by certain meteorological effects only. The latter is the case with fresh- and seawater, where the wind has a direct influence on the radar image, because the occurrence and the height of waves is correlated with the direction and the velocity of the wind and the time it works on the water.

2.2. Influence of vegetation

In the classes 3 to 8 the soil has a vegetation cover , so here the backscatter is influenced by biological factors that are subject to certain changes.

The influence of vegetation on electromagnetic wave propagation has been of interest since this phenomenon was noticed, and therefore experimental and theoretical investigations on this topic started in the 1950s already (GRANT, C.R. & B.S. YAPLEE, 1957). Because of the great number of environmental factors that are responsible for changes in the backscatter of vegetation, research

1. Large city, Industrial area
2. Small housing area, Village
3. Coniferous forest
4. Mixed forest
5. Deciduous forest
6. Heathland, Dwarf-pine region
7. Farmland
8. Swamp, Marsh
9. Freshwater
10. Sea

Table 1
Soil cover classification in the radar clutter data bank

has been continued through the 60s and 70s (e.g. TAMIR, T.,1967, KING, H.E. et al.,1970, DE LOOR, G.P. & A.A. JURRIENS, 1971) until now (KONG, J.A. et al., 1979). But there is no comprehensive work, yet; all of these investigations are restricted to a few plant species or one special vegetation type. That makes it necessary to evaluate all existing papers for correlations between the soil cover classes 3 to 8 and backscatter values in the radar clutter data bank.

As the trees and shrubs growing in coniferous forests (soil cover class 3) and on heathland (N° 8) don't have such a distinct change of foliage as deciduous trees have, here the seasonal variations are less important for differences in backscatter than the influence of the wind is. Strong winds may bend the trees and thus alter their angle towards the transmitter. But the way trees are bent is not always the same, it depends on their height and strength. So in the radar clutter data bank additional data about coniferous forests are required concerning the average growth height of the trees under different climatic conditions.

The soil cover 8 (marshland) shows similar conditions like those mentioned above: also here changes caused by wind effects have greater influence on the backscatter than phenological ones.

Still greater than with the classes mentioned up to now are the problems that arise with the soil cover "mixed forest","deciduous forest", and especially with "farmland". Here the biological effects of the growing and decaying of the plants and their leaves, that means phenological events, become predominant.

2.2.1. Deciduous Forest

Winter is the only season when the correlation between the status of the deciduous forest and its influence on radar is not too problematic. The reason for that is the winter rest in plants' life. As long as the trees are bare of leaves, just the trunks and the soil are responsible for the radar image. In spring, however, when the forests become green again, a phase of rapid changes takes place in the backscatter, because the backscatter is a matter of the plants' water contents. As the unfolding and spreading of leaves is caused by pumping water into those cells of the plants' tissues that had been resting in the buds during wintertime, and making them swell this way, the phase of increasing backscatter lasts until the vegetation canopy has closed, that means until the water contents above the ground is constant again.

New leaves unfold almost all through the summer, too, but their number is small compared with that of the events in spring, and therefore this fact is negligible in a prediction program for clutter changes.

The date of the beginning of the unfolding of leaves depends on meteorological parameters, mainly on the temperature. That means that there are differences between different years and moreover between different regions and elevation levels.

In order to get at least a well-founded knowledge of the regional differences, a 25 years observation period of about 3000 stations was evaluated. The mean values found out this way are the basis for the clutter data bank. In a rough approach one can say, that the unfolding of the leaves takes place first in the valleys of the great rivers, then in moderate altitudes of the mountain regions and very late in coastal regions and on the mountain ridges (Fig. 1).

These data, however, do not give informations about the exact date of the event in actual cases (though for many questions that are to be answered by means of the data bank this is not necessary, either). In order to get these informations annually, a military observation net, consisting of about 120 stations located at places of special interest, has been built up, that report the observations of relevant phenological events by telex to the German Military Geophysical Office. Basing on the earliest report, calculations can be made, at what time the event is going to take place in the other regions.

In autumn changes start with the degradation of the photosynthetic pigments in the leaves and the diminution of their water contents. This event takes place slowly; it is induced by temperature effects, too, (SCHNELLE, F., in press). After all the leaves have turned, there may be sudden changes in backscatter because trees may be defoliated completely during one stormy day. Turning of the leaves and defoliation take place first on the mountain ridges, in coastal areas, and in the Upper Rhine Valley. The low mountain range is the region where the trees keep their leaves longest.

2.2.2. Farmland

The situation that is found with farmland is still more complicated than that of forest regions, because of the large amount of different crops with different radar signatures, and their rapid phenological changes (DE LOOR, G.P.,1976).

Though the grid of the data bank is delicate enough to distinguish fields of the average size, simplifications had to be made. The reason for that is, that it is too difficult to find out, which crop is standing on a certain field at this very moment, because in many regions the agricultural landuse is based on the principle of crop rotation, that means each field bears another crop almost every year. So the annual updating of the exact use of any field would be impossible. But there is one thing that is constant, and that is the ratio of the different types of agricultural landuse. As in different parts of Germany these ratios differ in a characteristic way (e.g. in coastal areas and on the mountains "grassland" is the most frequent landuse, in moderate elevation levels "grain" is predominant), the Federal Republic of Germany was subdivided into three geographic regions (north, central, south), using 52°24' and 49°12' as border lines. Because of differences in landuse that depend on the elevation, the regions themselves have been subdivided, too. In the northern part of Germany, where there are only a few spots that rise higher than 100 m, two elevation levels were distinguished: below and above 50 m above sea level. In the central and southern part of the Federal Republic of Germany three levels were chosen: below 200 m, between 200 and 500 m, and above 500 m in the central part, respectively below 300 m, between 300 and 700 m, and above 700 m in South Germany (ANONYMOUS, 1977).

Apart from their constant and characteristic ratio of landuse the regions and their elevation levels were chosen this way, because they show a relatively homogeneous phenological development of the plants.

The next simplification for the data bank was, that the different crops were classed under just four categories: grassland, grain, root crop, and special crops, such as corn, rape, tobacco, etc.

For any level of the three regions the data bank contains the percentage of each one of these four crop types, and, in ten-days-intervals, their growing characteristics. Examples of these data are shown in table 2 and 3, and in figure 2 and 3.

Elevation	Grassland	Grain	Root Crop	Special Crops
< 200 m	31.3	50.4	14.4	3.9
200 - 500 m	32.8	52.5	10.8	3.9
> 500 m	52.6	38.5	8.1	0.8

Table 2
Percentage of different crop types in the central part of Germany

Decade	Grassland	Grain	Root Crop	Special Crops
.	.	.	.	.
.	.	.	.	.
21.04. - 30.04.	15	20	0	0
01.05. - 10.05.	15	20	5	5
11.05. - 20.05.	20	25	10	10
21.05. - 31.05.	25	30	15	10
01.06. - 10.06.	35	40	20	20
11.06. - 20.06.	45	55	20	30
21.06. - 30.06.	50	70	25	45
01.07. - 10.07.	10	75	25	60
.	.	.	.	.
.	.	.	.	.

Table 3
Growth height (cm) of crops in the central part of Germany.
Elevation level: Between 200 and 500 m.

3. METEOROLOGICAL DATA

The influence of condensation products of water vapour suspended in the atmosphere (hydrometeors) on electromagnetic waves depends apart from the wavelength on the number of the hydrometeors per unit of volume and on their size. The latter one is the most important factor, because the influence of the drops rises with the sixth power of their diameter. The problem in regarding this effect is, that the drop diameters differ greatly, even in one single cloud there are always spectra

of the drop size. These drop spectra show great differences, depending e.g. on temperature and type of the cloud, but each cloud type has its own characteristic spectrum (CZERWINSKI, N.,1974).

A first step towards respecting the influence of hydrometeors in the radar clutter data bank has been made (ANONYMOUS, 1976).

To simplify matters, meteorological events in Germany were classified under four general weather situations: westerly flow, northerly flow, easterly flow, and high pressure over Central Europe.

For each one of these general weather situations the percentage of the occurrence was ascertained, taking 1973 as a reference year, because it showed a quite "typical" course of the weather with respect to temperature and precipitation.

As the four situations mentioned above reveal certain differences between the northern and the southern part of Germany, concerning the frequency of their appearance and their symptoms, the 50^{th} degree of latitude was taken as a border line. Because furthermore the atmospheric parameters of the general weather situations vary between winter and summer, the year was subdivided into the time from 01. April till 30. September (summer) and from 01. October till 31. March (winter).

By means of these subdivision 16 categories of weather events were gained: westerly flow, North Germany, summer; westerly flow, North Germany, winter;....; high pressure over Central Europe, South Germany, winter. For each one of them the data of a typical vertical profile of pressure, temperature, and moisture from the ground until 12 km above ground and the diurnal changes of these factors in six hours' intervals are stored in 100 m - steps (until 2 km above ground), resp. 1 km - steps.

These profiles are the basis for data about the probability of the occurrence of clouds, their type, and their vertical extension, dependent on season, general weather situation, region, and time of the day.

The different types of clouds were correlated with eight significant drop spectra (table 4). These data make it possible to calculate the theoretical influence of hydrometeors on electromagnetic waves for any place and any time.

But nevertheless this data collective is a quite rough one, that does not respect small scale effects of the orography on e.g. the occurrence and altitude of clouds or on the frequency and severity of thunderstorms. To remedy this lack of the data bank, for some regions of Germany more detailed informations about meteorological peculiarities are being gathered and stored at the moment.

Cloud type	Spectrum N°
Cumulus congestus	1
Cumulus humilis	2
Stratus fractus, Cumulus fractus	3
Stratocumulus	4
Altocumulus	5
Altostratus	6
Stratus	7
Cirrus	8

DROP DIAMETER (μ)	NUMBER of DROPS in the SPECTRA 1 - 8 (per cm^3)							
	1	2	3	4	5	6	7	8
1				20				
2		20		20				
3	40	30		20				
4	40	80		40				
5	30	300		40				
6	30	50	0.2	40	10	2	3	
7	30	1	0.2	10	10	2	3	
8	20	0.1	0.06	10	20	5	4	
9	10	0.1	0.06	3	20	5	4	
10	10	0.01	0.09	3	8	3	9	
20	3		0.06	0.1	0.2	0.7	7	
30	2		0.08			0.2	0.4	
40	1		0.03			0.02	0.02	0.5
50	1		0.02					

Table 4
Cloud types and the corresponding drop spectra.

4. SOIL EFFECTS

Inversion layers preferably occur at places where the exchange of air masses in the lower atmosphere is blocked by orographic structures. Such structures are e.g. narrow valleys or mountain chains in a right angle to the main wind direction. These critical areas can be found out easily by means of the existing data. But whether here inversions are really more frequent than in other places or not, depends on other factors, too. For example the temperature of the air layer near the ground is influenced by the soil relative humidity (ZDUNKOWSKI, W.G. et al.,1975). Over dry soil the periodic day/night fluctuation of the temperature is greater than over moist soil, due to the fact that especially nocturnal cooling is reduced by the moisture. But as the storage capacity of the soil as well for water as for temperature depends on the soil type, variations of the soil type are of still greater importance for the temperature distribution near the ground than mere humidity (ZDUNKOWSKI, W.G. & D.C. TRASK, 1971). That makes it desirable to have data stored about the soil, too. But this is one of the future aspects of the data bank.

5. CONCLUSION

Though the data bank contains a lot of informations about factors that may influence the propagation of electromagnetic waves, already, the efforts that have been made up to now were not much more than a few steps towards a comprehensive data bank. The military use of digital data is increasing rapidly, and consequently the demand for more and more detailed informations will rise, too. That makes it necessary to update the informations permanently, to check whether simplifications can be replaced by more accurate data, or whether other simplifications are possible and useful, and to compile new data if there are new military demands.

6. REFERENCES

ANONYMOUS, 1976, "Vertikalprofile, Tropfenspektren und daraus abgeleitete Größen für die Atmosphäre in Mitteleuropa." Studie Amt für Wehrgeophysik (German Military Geophysical Office) No 76 148. Traben-Trarbach.

ANONYMOUS, 1977, "ZTL/Integriertes Bewertungsmodell für Aufklärungssysteme -Bewuchshöhenszenarium für die Radarclutter-Datenbank." Studie Amt für Wehrgeophysik (GMGO) No 77 201. Traben-Trarbach.

CZERWINSKI, N., 1974, "Anwendung von Tropfenspektren." Promet 4 (3), p.14-15.

GRANT, C.R. & B.S. YAPLEE, 1957, "Backscattering from Water and Land at Centimeter and Millimeter Wavelengths." IRE Proc. 45, p. 976-982.

KING, H.E., C.J. ZAMITES, Jr., D.E. SNOW & R.I. COLLITON, 1970, "Terrain Backscatter Measurements at 40 to 90 GHz." IEEE Trans. Ant. Prop., AP-18 (6), p. 780-784.

KONG, J.A., L. TSANG, M. ZUNIGA, R. SHIN, J.C. SHIUE & A.T.C. CHANG, 1979, "Theoretical Modelling and Experimental Data Matching for Active and Passive Microwave Remote Sensing of Earth Terrain." AGARD-CPP 269, p. 19-1 - 19-8.

DeLOOR, G.P., 1976, "Radar Methods" in: "Remote Sensing for Environmental Sciences". E.SCHANDA (Ed.) Ecol. Studies 18, p. 147-186.

DeLOOR, G.P. & A.A. JURRIENS, 1971, "The Radar Backscatter of Vegetation." AGARD Conf.Proc. 90, p. 12-1 - 12-7.

SCHNELLE, F. (in press), "Phänologische Spezialkarten der Laubentfaltung und Laubverfärbung von Roßkastanie, Weißbirke, Rotbuche und Stieleiche auf dem Gebiet der Bundesrepublik Deutschland."

TAMIR, T., 1967, "On Radio-Wave Propagation in Forest Environments." IEEE Trans. Ant. Prop. AP-15 (6), p. 806-817.

ZDUNKOWSKI, W.G. & D.C. TRASK, 1971, "Application of a Radiative-Conductive Model to the Simulation of Nocturnal Temperature Changes over Different Soil Types." J.Appl.Meteor. 10, p.937-948.

ZDUNKOWSKI, W.G., J. PAEGLE & J.P. REILLY, 1975, "The Effect of Soil Moisture upon Atmospheric and Soil Temperature near the Air-Soil Interface." Arch.Met.Geoph.Biokl., Ser.A, 24, p.245-268.

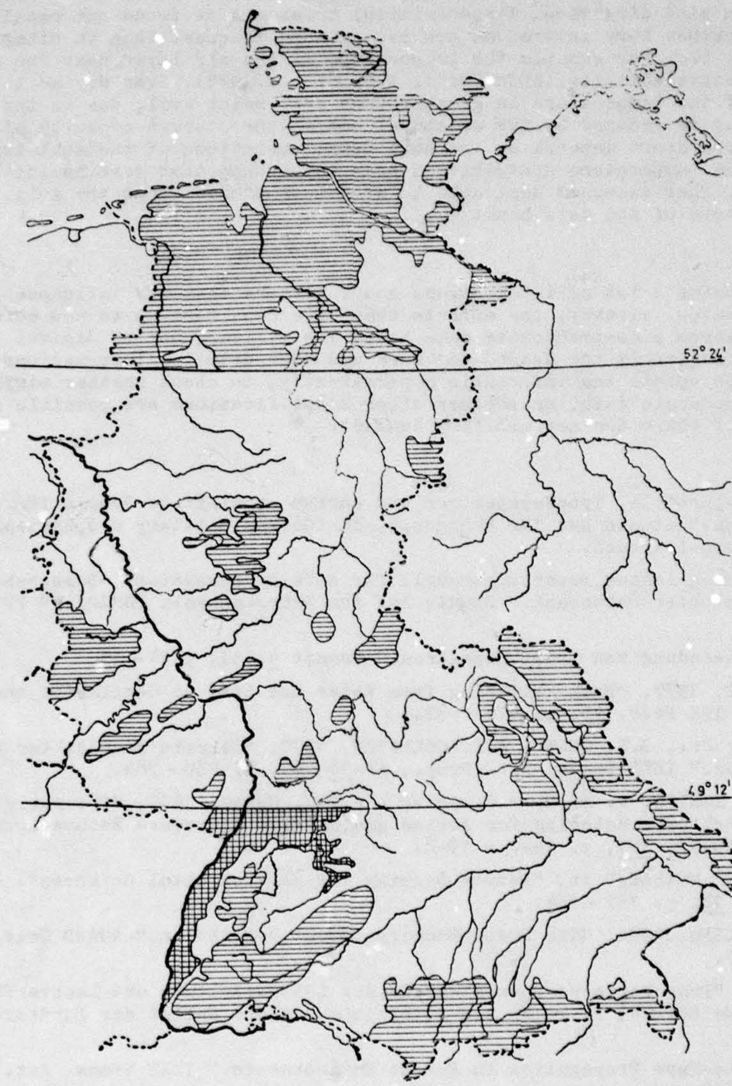

Fig. 1

Status of deciduous forest, first decade of May (schematic)

Leaves just unfolding

Vegetation canopy closing

Vegetation canopy closed

Fig. 2
Sowing of oats, 1977

= Beginning at		1. March	
=	"	"	11. March
=	"	"	21. March
=	"	"	31. March

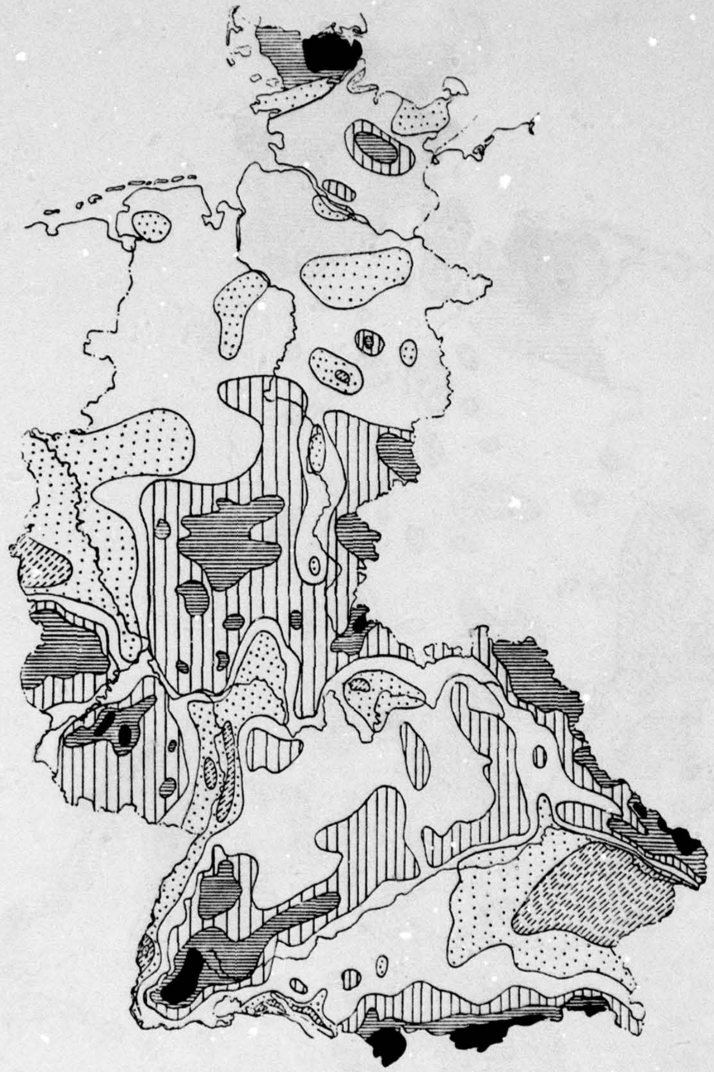

Fig. 3

Harvest of winter barley, 1977

= Beginning of the harvest 4. July
= " " " " 11. July
= " " " " 18. July
= " " " " 25. July
= " " " " 1. August
= " " " " 8. August

PREDICTION OF RADAR COVERAGE AGAINST VERY LOW ALTITUDE AIRCRAFT*

John R. Delaney
M. Littleton Meeks

Lincoln Laboratory
Massachusetts Institute of Technology
Lexington, Massachusetts

SUMMARY

MIT Lincoln Laboratory has been investigating the prediction of radar coverage against very low-altitude, terrain-following aircraft since the Spring of 1978. The goal of these investigations is the accurate prediction of radar coverage utilizing a digitized terrain data base. Radar coverage is often approximated as the area where line of sight would exist between the radar and a target of appropriate altitude. Refraction of radar transmissions in the atmosphere, diffraction over terrain features and reflection from terrain (multipath) can all cause that approximation to be poor.

A model has been developed for the effects of propagation on radar coverage, accounting for refraction, diffraction and reflection. The model was applied to digitized terrain data for three sites, one with relatively hilly terrain, one with relatively smooth terrain and one with mixed terrain. Results show that approximating the radar coverage by the potential target locations within line of sight can be quite misleading. Results also show that the coverage of lower frequency radars can be better than that of higher frequency radars in terrain where diffraction is the dominant phenomena. Moreover, the coverage of lower frequency radars in reflection-dominated terrain can be quite satisfactory if sufficient power is transmitted.

Field experiments have been undertaken to test the validity of the model. The results of one simple experiment confirm that the model correctly combines the effects of diffraction and reflection. The results of additional experiments will be available by September.

1. INTRODUCTION

Flying very low-altitude, terrain-following paths is a tactic used by aircraft trying to avoid detection by ground-based radar systems. Tactical fighter-bombers, strategic bombers, and cruise missiles, both tactical and strategic, are expected to use this tactic. While ground-based radar coverage is greatly reduced by this tactic, it is not completely eliminated. A mission planner must estimate the areas around an enemy radar where an aircraft on such a flight path could be detected and choose a route for the aircraft avoiding such areas to the greatest extent possible. How well very low-altitude, terrain-following flight works as a tactic thus depends on how reliably a mission planner can predict radar coverage against aircraft on such flight paths. In particular, if planners generally underestimate the coverage, high attrition may occur.

Mission planners and radar engineers may assume that when the line-of-sight from a conventional radar to an aircraft is blocked by a hill, ridge or the like, the aircraft cannot be detected. Many people also assume that reflection effects (multipath) produce a radar propagation 'null' close to the ground, allowing an aircraft at very low altitude to fly by a ground radar undetected although within the radar line-of-sight. Both of these assumptions are naive and may lead to seriously inaccurate estimates of radar coverage.

Three propagation phenomena significantly impact radar coverage: refraction, diffraction and reflection. The sketches in Fig. 1 are intended to illustrate how those phenomena affect radar coverage. Refraction normally causes radar coverage to extend slightly beyond the true horizon. Extreme refraction, sometimes called superrefraction or 'ducting', leads to much greater extensions in coverage. Superrefraction can be of major significance over water or in parts of the tropics where it occurs much of the time. But inland and in the temperate zone, it is a rare occurrence.

When calculating those areas to which a radar has line-of-sight, nominal refractive effects are often incorporated by using four-thirds the normal value for earth radius when compensating for the effect of earth curvature on the line-of-sight. But daily and seasonal variations in refractive effects are not accounted for by this approach.

Diffraction has effects which should worry mission planners. A hill could block the line-of-sight from a radar to an aircraft as in the figure, but enough radar signal energy could be diffracted over the hill to the aircraft, reflected from the aircraft and diffracted back over the hill to allow detection. Interfering clutter returns could prevent detection, but the effects of clutter on detection are beyond the scope of this paper. In speaking of detection hereinafter, clutter effects will be ignored, although the overall program of work at Lincoln Laboratory is very much concerned with the effects of clutter.

*This work was sponsored by the Defense Advanced Research Projects Agency.

Reflection effects present the possibility that a radar could have a line-of-sight to an aircraft and yet the strength of the radar return from that target could be too weak to detect due to destructive interference between signals following direct and indirect paths to and from the aircraft. Of course, constructive interference can also occur depending on the relative path lengths. Above a perfectly reflecting surface, the consequence is the classic multipath 'lobing' pattern. Aircraft at very low altitudes above such a surface usually fall in the 'null' below the lowest 'lobe', so when multipath occurs the potential for destructive interference is of most interest.

Our goal is to predict, with reasonable accuracy and confidence, the coverage of ground based radars against aircraft flying low-altitude, terrain-following paths. In this work, we use digitized terrain representations and computer algorithms which calculate the effects of refraction, diffraction, and reflection. An iterative three-step methodology has been adopted. The first step is to develop a propagation model incorporating the three phenomena of interest based on the current propagation literature. The second step is simultaneously to predict radar coverage for several sites and to test the validity of the model by carrying out appropriate field experiments. Making predictions at this early stage helps focus the field experiments on aspects of the propagation model which have a significant impact on the coverage predictions. Sensitivities discovered in the model can be tested in the field. Early predictions can provide a best current estimate of how the three propagation phenomena influence radar coverage. The third step of the method is to modify the propagation model as necessary based upon the experimental results. The second and third steps are repeated as often as appears both necessary and possible to improve predictive capabilities of the propagation model.

The first step of the above mentioned method has been completed. The model developed is described in Part 2, and some of the reasoning which went into that development is presented there. The initial pass through the second step is largely complete as well. Radar coverage predictions have already been made using the first generation propagation model. Part 3 describes the results and points out what we believe to be some significant implications about the effects of propagation as currently modeled. Part 4 describes the results of one experiment conducted recently and the plans for additional experiments to be conducted before September of 1979. Completion of those experiments will mark the completion of the second step. A few summary comments appear in Part 5.

2. FIRST GENERATION PROPAGATION MODEL

The purpose of the model is to predict point-to-point, one-way propagation loss, nominally from a ground based radar to an aircraft at very low altitude. A profile of the terrain between the two points is used in the calculations; Fig. 2 illustrates such a profile. Profiles can be obtained from a number of sources. The currently implemented version of this model obtains its profiles from portions of the Digital Land Mass Simulation (DLMS) data base. This data base, produced and maintained by the Defense Mapping Agency of the Department of Defense, contains sample terrain elevations organized geographically. Interpolation of elevations is necessary to calculate a profile. By limiting the terrain used in the calculations to a profile, the problem of propagation loss prediction is simplified; it becomes a two-dimensional problem. One can conceive of situations for which this simplification leads to inaccurate loss predictions, but these situations are apt to be rare. The first Fresnel reflection-zones are generally quite narrow for the situations in which we are interested.

Refraction of radar transmissions by the atmosphere is a much studied phenomena. Fairly sophisticated models of refractive effects have been developed (Schelleng, Burrows and Ferrell, 1933; Bauer, Mason and Wilson, 1958; Bean and Dutton, 1966; Blake, 1968), some of these use detailed descriptions of the temperature and humidity as a function of altitude and location. Such models are necessary for applications involving long paths through non-homogeneous parts of the atmosphere. But, our concern is with paths no more than 50 to 60 km long and between points no more than 100 to 120 m off the ground. For such cases, it seems reasonable to assume in our first iteration that the atmosphere propagated through is homogeneous and that the vertical lapse rates of temperature and humidity are linear. Then the effects of refraction can be taken into account by using a fictitious value for the radius of the earth when calculating diffractive and reflective effects. Figure 3 illustrates how this is done for the terrain profile in Fig. 2. The proper fictitious value is a function of the aforementioned lapse rates. For a specific site, it can be estimated from climatic and geographic information. An average value for inland areas in the temperate zone would be the usual four-thirds of the true value.

Diffraction of radar transmissions over terrain obstacles has not received as much attention as refraction in the atmosphere. But the more general problems of electromagnetic wave diffraction over ideal obstacles and through ideal apertures have been favorites of electromagnetic physicists since Kirchhoff. Analytic solutions exist, at least in series form, for a variety of ideal obstacles such as infinite half-planes (knife edges),

cylinders, spheres, etc. (Sommerfeld, 1951; Fock, 1965; Rice, 1954) and these solutions have been used to estimate propagation losses over residual terrain obstacles (Schelleng, Barrows and Ferrell, 1933; Neugebauer and Bachynski, 1958; Millington, Hewitt, and Immirzi, 1962; Deygout, 1966). But some ideal obstacle problems remain unsolved, e.g., the propagation loss over a series of parallel half-planes, and debate continues over the proper way to estimate losses over analogous terrain obstacles, i.e., two ridges.

As in much of the previous work on diffraction, our model assumes that only the most prominent obstacles between the radar and aircraft have significant impacts. Location of these obstacles is equivalent to finding the shortest path from transmitter to target not passing through the terrain. Such a path consists of one or more straight line segments meeting at an angle or joined by short curved segments (continuous with the terrain profile). Each meeting, or joint, marks a particular obstacle blocking the line-of-sight to the target. Figure 4 illustrates this path with the same profile as in Figure 3. If the path consists of but a single line segment (i.e., if there is an unblocked line-of-sight) no diffraction is presumed to occur. Otherwise, diffraction is presumed to occur at every obstacle. If two line segments meet at an angle over a particular obstacle, the obstacle is presumed to diffract like an infinite half-plane. Otherwise, the obstacle is modeled by a cylinder fitted to the curved line segment. Figure 5 indicates how the profile in Figs. 3 and 4 is translated into idealized diffracting obstacles.

Reflection of radar transmissions from terrain has received much the same sort of attention as diffraction. Analytic solutions exist for reflection from various sorts of ideal surfaces (Kerr, 1951; Bechmann and Spizzichino, 1963; Smith, 1967; Wagner, 1967) and the solutions have been used to estimate propagation loss on non-ideal terrain. A fair degree of success in estimating propagation loss has been achieved by researchers working on microwave landing systems for aircraft (Evans et al, 1976; Evans et al, 1979), but the geometries and terrains considered by those researchers are different from those we must consider. They are concerned with aircraft at very low altitudes only when relatively close to the radar and their 'terrain' consists of runways, artificially smoothed approach-areas and airport structures. It is not at all clear that the reflection models used by the microwave-landing-system community are appropriate for estimating very low altitude radar-coverage in an air defense scenario.

Lacking field data which would indicate the applicability to our problem of a particular model for reflection losses, a plausible model was constructed from the available literature. The model had to be simple; otherwise, the computational burden of using the model would be prohibitive. Despite the simplicity, the model does demonstrate what we believe are fundamentally correct dependences on terrain roughness as measured by both height and slope irregularities.

Terrain reflection between the radar and aircraft is presumed to be possible if no diffracting obstacle separates them. Otherwise, reflection may occur between the radar and the first diffracting obstacle, the last diffracting obstacle and the aircraft, and between any two sequential diffracting obstacles (if more than one exists). The precise location of the reflection point is calculated by fitting a line to the central eighty percent of the terrain in a reflection interval (radar to aircraft, radar to obstacle, obstacle to obstacle, etc.) and calculating the reflection point on that line. Figure 6 illustrates such fitted lines and reflection points for the example.

The deviation of the terrain from the fitted line in the central eighty percent of a reflection interval is used in calculating the reflection coefficient. Sample standard deviations in both height and slope are computed for the purpose. In other models of reflection (Kerr, 1951; Bechmann and Spizzichino, 1963), only terrain statistics for the first Fresnel zone are used to calculate the reflection coefficient. Why do we calculate statistics over a presumably broader interval?

The reason is simplicity. One could use iterative methods to calculate the actual position of the first Fresnel zone in a particular interval, but that would be time consuming. For the grazing angles encountered in our low-altitude radar-coverage calculation, the first Fresnel zone typically includes more than fifty percent of the terrain in a reflection interval anyway. Therefore, the sample standard deviations in question are fair estimates of the actual first Freznel zone values.

The reflection coefficient, ρ, calculated for a particular interval can be written as

$$\rho = -\rho_A \rho_B \rho_S e^{j2\pi\Delta R/\lambda}$$

where

$$\rho_B = e^{\frac{-(4\pi\,\sigma_h \sin\psi/\lambda)^2}{2}}$$

$$\rho_S = \frac{1 + \mathrm{erf}\,(\alpha)}{1 + \mathrm{erf}\,(\alpha) + e^{-\alpha^2}/\sqrt{\pi}\alpha}$$

$$\alpha = \sin\psi/\sqrt{2}\,\sigma_s$$

ΔR is the difference in length between the direct and indirect paths, λ is the wavelength, σ_h is the height sample standard deviation, σ_s is the slope sample standard deviation, ψ is the grazing angle, and ρ_A is an absorption coefficient.

The absorption coefficient, ρ_A, is used to account for the effects of absorption by any vegetative cover in the first Fresnel zone and can be varied from one to zero as seems appropriate. The coefficient, ρ_B, is the RMS specular reflection coefficient for a Gaussian surface (Bechman & Spizzichino, 1963) and the coefficient, ρ_S, is a correction to ρ_B to account for shadowing in the first Fresnel zone (Smith, 1967). Note the minus sign; a phase change of π radians is presumed to occur on reflection. No attempt is made to calculate a more precise value of phase change or an additional reflection loss resulting from air-ground dielectric mismatch as in some other models. For the grazing angles encountered, the computational effort seems unwarranted.

Figure 6 also helps in understanding how the effects of reflection and diffraction are combined. Four diffraction 'paths' exist over each obstacle, D_j and D_{j+1}, D_j and I_{j+1}, I_j and D_{j+1}, and I_j and I_{j+1}. The diffraction loss and change in phase is separately calculated for each 'path'. The four diffraction losses for each obstacle (if any) and the reflection losses for each reflection interval are used to calculate the propagation along every possible combination of direct and indirect paths between the radar and the aircraft. No attempt is made to account for interactions between sequential diffracting obstacles. The individual losses are added coherently to get an overall loss.

3. COVERAGE IMPLICATIONS OF PROPAGATION MODEL

To determine the effects of propagation, as modeled in Part 2, on the detectability of very low-altitude, terrain-following aircraft, the model was exercised on three sets of digitized terrain elevation data. Hypothetical radar sites were chosen for each set; one on Fort Devens, Massachusetts in relatively hilly terrain, one near Vera Cruz, Indiana in very flat terrain, and one near Oshkosh, Nebraska, overlooking a wide river valley with rolling plains on either side, definitely mixed terrain.

In carrying out the calculations, a set of nominal parameters was assumed. The hypothetical radar antenna was assumed 30 m off the ground. The aircraft was assumed to fly exactly 60 m above the ground. Such perfect terrain following is not possible but this approximation greatly simplifies the calculations. Refractive effects were included by using four thirds the actual earth radius as the fictitious radius. No vegetative absorption was considered, i.e. $\rho_A = 1$. It was assumed that the radar could detect the aircraft at a maximum range of 100 km in free space, in the absence of propagation effects. In practice, such a free-space detection range is determined by a number of factors such as radar transmitted power, antenna size, detection algorithm, and the aircraft radar signature, aspect angle, etc. For simplicity, all those parameters are combined in the free-space detection range.

The effect of excursions from the nominal antenna height, aircraft altitude, etc. on radar coverage also were tested by repeating the calculations with one parameter value changed each time. An antenna height of 10 m was tested. Aircraft altitudes of 30 m and 90 m were tested, as were fictitious earth radii equal to one and three-halves times the actual value, absorption factors of 0, .3, .7, .8, and .9, and free-space detection ranges of 35 km and 250 km.

Three different frequencies were postulated for the radar, 10 GHz (X-band), 1 GHz (L-Band) and 150 MHz (VHF), spanning the likely range of frequencies for surveillance radars. Coverage calculations were performed at each frequency for the nominal case and all the excursions.

To aid in the calculation of propagation loss, the terrain-elevation data for each site was translated from the standard DLMS format to a polar grid, with 500 m between each elevation in range and 5° in azimuth. Propagation loss was calculated from the radar to the aircraft for each point on the grid and the loss compared with the free-space loss at the free-space detection range. Where the former loss exceeds the latter, the aircraft is deemed undetectable; otherwise, it is deemed detectable.

Figure 7 shows the calculated coverage of the nominal case, X-band radar at the Fort Devens site and contrasts it with the areas where the aircraft would be within line-of-sight of the radar. Note that the line-of-sight calculation is done using a fictitious earth radius four-thirds the actual value; this is the usual 'radar line-of-sight' calculation. Also note the area where line-of-sight to the aircraft is blocked and yet it is detectable. A hill or ridge blocks line-of-sight in those locations, but diffraction over that obstacle allows a radar return with enough energy for detection purposes. Of course, clutter returns, ignored in this paper, could still block detection.

A larger such area can be found in Figure 8 where only the radar frequency has been changed. At VHF, one expects diffraction to produce a more pronounced effect and it does. To the southeast of the site, a prominent ridge blocks line-of-sight and X-band coverage, but the VHF radar coverage extends up to 10 km beyond that ridge. This diffractive effect on coverage is even larger if the free-space detection range is larger as in Fig. 9.

If a mission planner routed an aircraft below the line-of-sight of the radar in Fig. 9, believing it would be undetectable behind the aforementioned ridge, the coverage calculations indicate he would be disappointed with the results. Where the line-of-sight is blocked, diffraction can lead to significant amounts of coverage for lower frequency radars, especially with large free-space detection ranges.

Lower frequencies appear advantageous in relatively hilly terrain when diffraction is the dominant propagation phenomena. But what is the situation in relatively flat terrain where one would expect reflection to be dominant? The conventional wisdom is that in flat terrain, reflection will limit radar coverage only slightly for higher frequencies like X-band but strongly at lower frequencies.

Figures 10 and 11 seem to show that the conventional wisdom is both right and wrong for the relatively flat, Vera Cruz site. In the former figure which represents the nominal X-band case, there is a noticeable, but not large, area where a line-of-sight is calculated to exist between radar and aircraft but where the aircraft is calculated to be undetectable. In the latter figure, where the nominal case, VHF radar is assumed, the overall radar coverage is somewhat smaller. But the coverage is not nearly as limited as might have been expected. Strong multipath lobing has not occurred. Figure 12 is similar to Fig. 11 but the coverage has been calculated with a free-space detection range of 250 km, not the nominal 100 km. The patchy areas where the aircraft was calculated to be undetectable, given the nominal free-space detection-range, have vanished in Fig. 12. Furthermore, the aircraft is calculated to be detectable in a noticeable area where it is also calculated to be beyond the radar line-of-sight. Diffraction seems to influence coverage more than reflection for this radar.

The reasons why the conventional wisdom is not upheld by the coverage calculations for the VHF radars appear to lie in the method of calculating the reflection coefficient and the values that coefficient must assume to prevent detection due to reflective effects. Very low grazing angles result from having the aircraft at very low altitude some thirty to fifty kilometers from the radar. The conventional wisdom is based on the expectation that for such grazing angles, relatively flat terrain will be 'rough' at higher frequencies like X-band, producing little specular (coherent) reflection, but 'smooth' at lower frequencies like VHF, producing strong specular reflection. And a strong specular reflection is necessary to produce significant cancellation between direct and indirect path transmissions.

Strong specular reflection is characterized by reflection coefficients with magnitudes near one. Consider the various factors of the reflection coefficient described in Part 2. The only ones explicitly dependent on the grazing angle are ρ_B, the Bechmann-Spizzichino factor, and ρ_S, the Smith factor. For strong specular reflection to occur, both factors must have magnitudes close to one. Defining 'close' for the moment to be greater than 0.9, the following constraints on the grazing angle are implied:

$$\psi \leq .037\ \lambda/\sigma_h$$

and

$$\psi \geq 1.4\ \sigma_s$$

Typical values of σ_h and σ_s are difficult to state. But recall that the size of the first Fresnel zone is often quite large, possibly 10 km or more long. Under such circumstances, it is difficult to find real terrain for which σ_h is less than 10 m and σ_s is less than 10 mrad. And even those values would not allow both inequalities to be satisfied simultaneously for wavelengths less than about 3.75 m. Since the largest wavelength used in exercising the model was 2 m, strong specular reflection was very rare.

Also, the greater the ratio of the free-space detection range to the aircraft range, the closer the magnitude of reflection coefficient must be to one in order to produce sufficiently strong specular reflection to prevent detection. For example, with the nominal free-space detection of 100 km and an aircraft at 25 km range, the reflection coefficient must be greater than .75 in magnitude to prevent detection. With a 250 km free space detection range, that magnitude must exceed 0.9.

In light of the above observations concerning the reflection coefficient, it is not surprising that calculated radar coverage was essentially insensitive to the tested variations in the absorption factor ρ_A, with one exception. The exception was the Vera Cruz site with a VHF radar. Reducing the value of ρ_A from 1 to 0.9 to 0.8 to 0.7 gradually eliminated all effects of reflection on coverage; the patchy areas of undetectability in Fig. 11 shrank and disappeared as the absorption factor shrank. This observation is a bit ironic. Absorption is expected to be greater at higher frequencies, like X-band; but it is calculated to have an impact on coverage only at lower frequencies.

By contrast, the calculated coverage for each site and frequency was found to be very sensitive to excursions in free-space detection range. A comparison of Fig. 8 to Fig. 9 and Fig. 11 to Fig. 12 illustrates the point. For both sites one can see the large change in predicted coverage that accompanies an increase in free-space detection range from 100 to 250 km. The reason for the sensitivity was alluded to above. The amount of excess loss in electromagnetic field-strength relative to the free-space loss tolerable at a given range is proportional to the free-space detection ranges, regardless of whether the losses are caused by diffraction or reflection. The effect, as noted before, is to increase coverage beyond the radar line-of-sight through diffraction and to compensate for reflection within the radar line-of-sight.

Reducing the radar antenna height naturally enough reduces the calculated radar coverage for each site and frequency, but with distinctly larger changes for the Vera Cruz site than for the other two. This is not an unexpected result. Compared to the overall visibility of the terrain, the 20-m change in antenna height tested is much more significant for the relatively flat terrain surrounding the Vera Cruz site.

An unexpected result was that the fictious earth-radius excursions produced negligible changes in calculated coverage for the Ft. Devens and Oshkosh sites but notable changes for the Vera Cruz site, implying that refraction significantly impacts coverage only at the last site. The reason seems to be that refraction impacts coverage only at longer ranges, 40 km or more, and only at the Vera Cruz site is there a large area of coverage far from the site in the nominal case.

The effects of the changes in aircraft altitude were much as expected. Reducing the altitude reduced overall coverage, increasing the altitude increased overall coverage, but not by the same degree. Again, though, the Vera Cruz site produced a somewhat unusual result at the lowest frequency, VHF. The patchy areas where an aircraft is undetectable although within radar line-of-sight are closer to the radar and less extensive in total area when the aircraft altitude is 30 m than when the altitude is 60 m. By the same token, when the altitude is increased to 90 m, the patches move further out and become larger. This peculiar sensitivity can again be traced to the calculation of the reflection coefficient and the interaction between the magnitude of the coefficient, and the aircraft range as they determine detectability.

The interesting consequence of the excursions should not distract one from the most significant observations about the coverage calculations. These calculations show that excellent coverage is achieved by a radar with a low frequency and a large free-space detection range at each site, either because of diffraction or in spite of reflection.

4. EXPERIMENTAL TEST OF THE PROPAGATION MODEL

As an initial test of the propagation model, a simple experiment involving the combined effects of reflection and diffraction was undertaken. The objective was to measure the propagation at low angles over a segment of flat terrain with a hill mask lying along the path. These measurements, made in February 1979 at a single L-band frequency (1090 MHz), used an existing system at Lincoln Laboratory: a system designed to make angle-of-arrival measurements of the signals transmitted from transponder beacons aboard aircraft as a part of a study of microwave landing-systems (funded by the Federal Aviation Agency). For the measurements reported here the transponder was carried in a helicopter in order to probe the propagated field-strength as the helicopter descended vertically behind the hill. In this way, height-gain profiles were obtained for direct comparison with predictions from the propagation model.

Propagation was measured along a 3.5-km path over a hill (height 41 m above local ground) lying 900 m from the ground terminal of the system. The terrain between the ground terminal and the hill was the flat western part of Hanscom Field (Bedford, Mass.). This reflective foreground produced a well defined lobe-pattern which could be observed when the helicopter was above the mask. On the far side of the hill, the ground was generally flat but with vegetative cover that made appreciable ground reflection unlikely.

The ground terminal of the system included eleven vertically polarized dipole-antennas mounted at various heights on an 8-m tower. The signal received on each dipole was recorded separately in digital format so that the data could be processed by computer immediately following the experiment.

The propagation model described above was used to calculate the pattern propagation factor $\underline{F}$ as a function of helicopter height for the following cases: (a) ground reflections on the tower side of the mask, (b) ground reflections on the helicopter side of the mask, and (c) ground reflections of both sides. The model computations were designed for ranges longer than the 3.5-km range in this experiment and, therefore, for much smaller grazing angles. In the course of analyzing these measurements, the model was modified so that it calculated

the reflection coefficient at the specular point with the Fresnel reflection formula, assuming vertical polarization, a relative dielectric constant of 15, and a conductivity of 0.005 mho/m, values appropriate for dry ground. Figure 13 shows computer-generated plots of $\underline{F}$ vs. height of the helicopter above ground for each of these situations, respectively. In Fig. 13(a) lobing appears above the mask, and the signal drops off around the mask as in the case of simple knife-edge diffraction. In Fig. 13(b), however, there is no lobing, but below the mask there is a rapidly changing relative phase between the direct and reflected wave which produces rapid variations in $\underline{F}$ that can be seen in Fig. 13 (b). Both effects appear combined in Fig. 13(c). For our initial experiment the assumptions leading to Fig. 13(a) are the appropriate ones.

Three examples of the measured pattern-propagation-factor are shown in Fig. 14. The plotted points represent measurements, and the curves show the corresponding values computed as described in the preceding paragraph. The agreement is generally good. Where there are deviations, the measured values are in almost every case lower than the computed values. Below the mask these discrepancies are probably the result of secondary masking or attenuation by trees on the helicopter side of the mask. Generally, the discrepancies seem correlated on the three antennas. Above the mask the discrepancies can be ascribed, we believe, to small changes in helicopter heading which reduced the gain of the transponder antenna.

In May 1979, using the same equipment, a second experiment was performed to measure propagation along more realistic paths. The antenna tower and recording system were placed at the top of Hartwell's Hill, 1 km north of Hanscom Field. This location provides a representative site for emplacement of a search radar. The helicopter made vertical descents at ranges of 11 and 14 km such that two hill masks interrupted the line of sight to the helicopter at heights some 50 m above the lowest point in the helicopter descent. In this way direct measurements of reflection and diffraction effects were obtained for comparison with model computations. The experimental data will be reduced before September, 1979. In the months ahead additional measurements will be made at longer ranges and lower frequencies to guide further development of the computational model.

5. SUMMARY COMMENTS

The observations presented in Part 3 of this paper concerning the effects of refraction, diffraction, and reflections on radar coverage against very low-altitude, terrain-following aircraft are only as valid as the propagation model used to calculate coverage, the model described in Part 2. Experimental results presented in Part 4 demonstrate that the model is generally valid in the way it combines diffractive and reflective effects, but that it might be well to include the effects of air-ground dielectric mismatch in future versions of the model. Far more experimentation is needed to validate the model thoroughly.

References

Bauer, J. R., Mason, W. C., and Wilson, F. A., 1958, Radio Refraction in a Cool Exponential Atmosphere, MIT Lincoln Laboratory Report 186, Lexington, Mass.

Bean, B.R., and Dutton, E. J., 1966, Radar Meteorology, National Bureau of Standards Monograph 92, Washington, D.C.

Beckmann, P. and Spizzichino, A., 1963, The Scattering of Electromagnetic Waves from Rough Surfaces, The Macmillan Company, N.Y.

Blake, L.V., 1968, "Ray Height Computation for a Continuous Non-linear Atmospheric Refractive Index Profile," Radio Science, Vol. 3 (new series) pp. 85-92.

Deygout, J., 1966 "Multiple Knife-Edge Diffraction of Microwaves," IEEE Transactions on Antennas and Propagation, vol. AP-14, issue 4, pp. 480-489.

Evans, J.F., et al, 1976, MLS Multipath Studies, Volume I: Mathematical Models and Validation, Project Report ATC-63, MIT Lincoln Laboratory, Lexington, Mass.

Evans, J.F., et al, 1979, MLS Phase III Final Report, Volume I: Overview and Propagation Model Refinements, Project Report ATC-88, MIT Lincoln Laboratory, Lexington, Mass.

Fock, V.A., 1965, Electromagnetic Diffraction and Propagation Problems, Pergamon Press, New York, New York.

Kerr, D. E. (ed), 1951, Propagation of Short Radio Waves, MIT Radiation Laboratory Series, vol. 13, McGraw-Hill Book Company, New York, New York.

Millington, G., Hewitt, R. and Immirzi, F. S., 1962, "Double Knife-Edge Diffraction in Field Strength Predictions," Proceedings of the IEE, vol. 109, part C, No. 16, pp. 419-429.

Neugebauer, H.E.J., and Bachynski, M.P. 1958, "Diffraction by Smooth Cylindrical Mountains," Proceedings of the IRE, vol. 46, pp. 1619-1627.

Rice, S.O., 1954, "Diffraction of Plane Radio Waves by a Parabolic Cylinder," Bell System Technical Journal vol. 33, pp. 417-429.

Schelleng, J.C., Burrows, C. R., and Ferrell, E. B., 1933, "Ultra-Short-Wave Propagation," Proceedings of the IRE, vol. 21, pp. 427-463.

Smith, B. G., 1967, "Geometric Shadowing of a Random Rough Surface," IEEE Transactions on Antennas and Propagation, vol. AP-15, No. 5.

Sommerfield, A., 1951, Optics, Academic Press, New York, New York.

Wagner, R. J., 1967, "Shadowing of Randomly Rough Surfaces," Journal of the Acoustical Society of America, vol. 41, pp. 138-47.

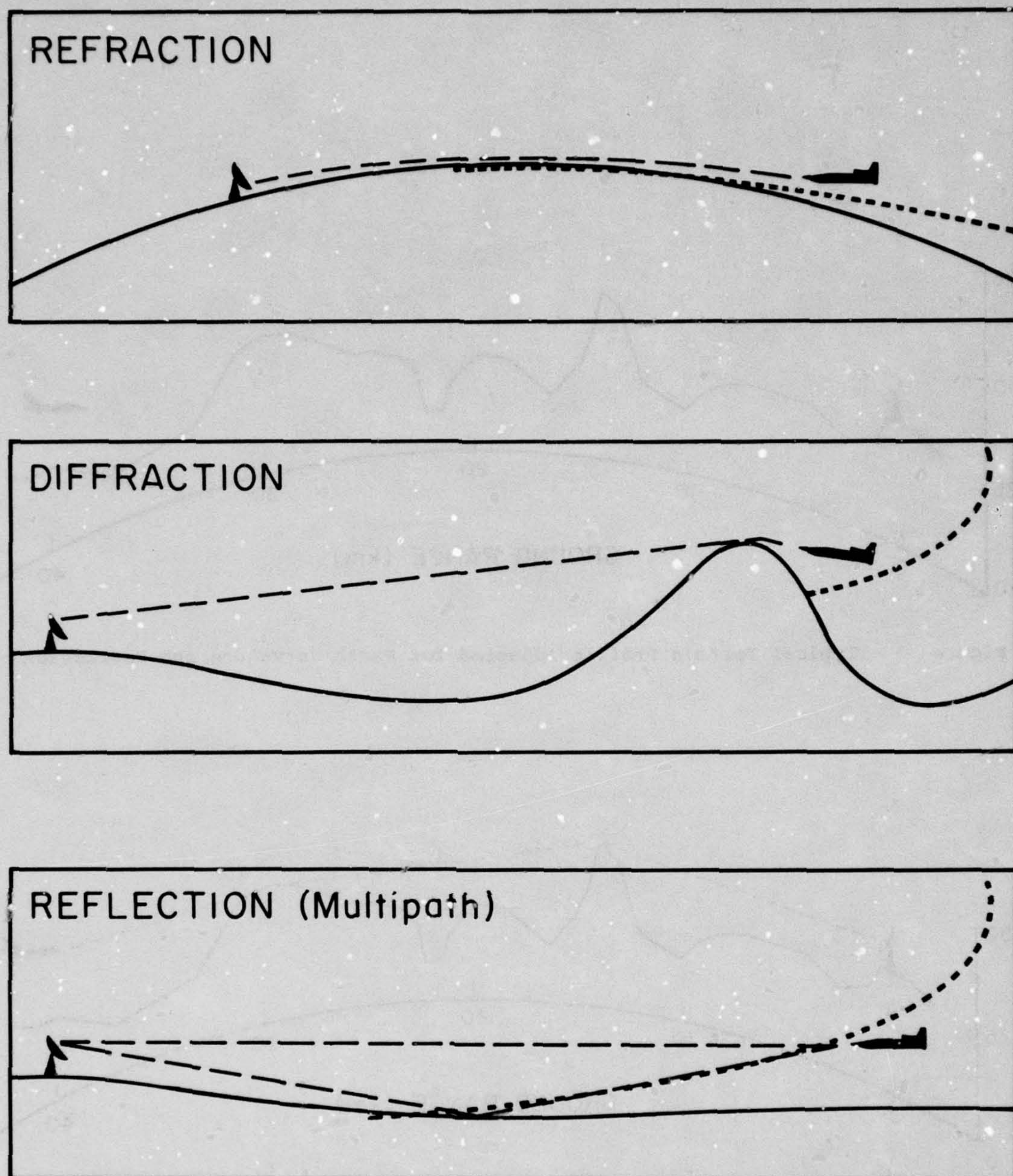

Figure 1 - Dotted Lines Show Coverage Limits Determined by Propagation Phenomena

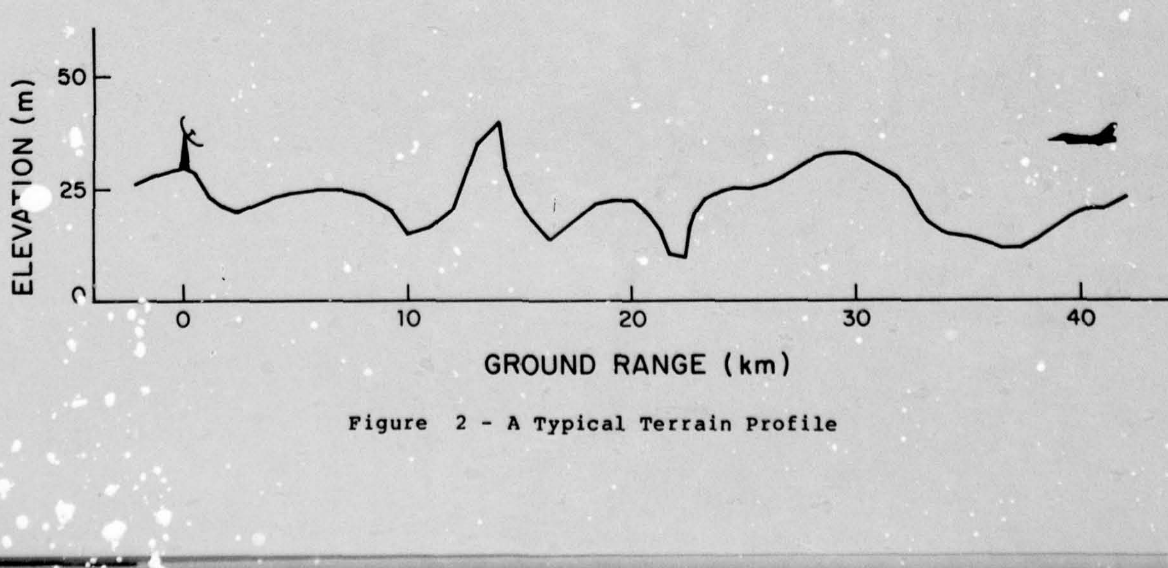

Figure 2 - A Typical Terrain Profile

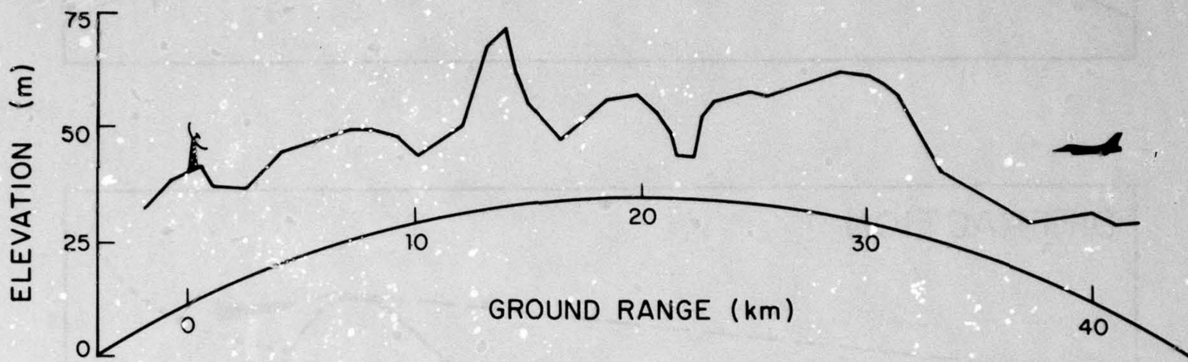

Figure 3 - Typical Terrain Profile Adjusted for Earth Curvature and Refraction

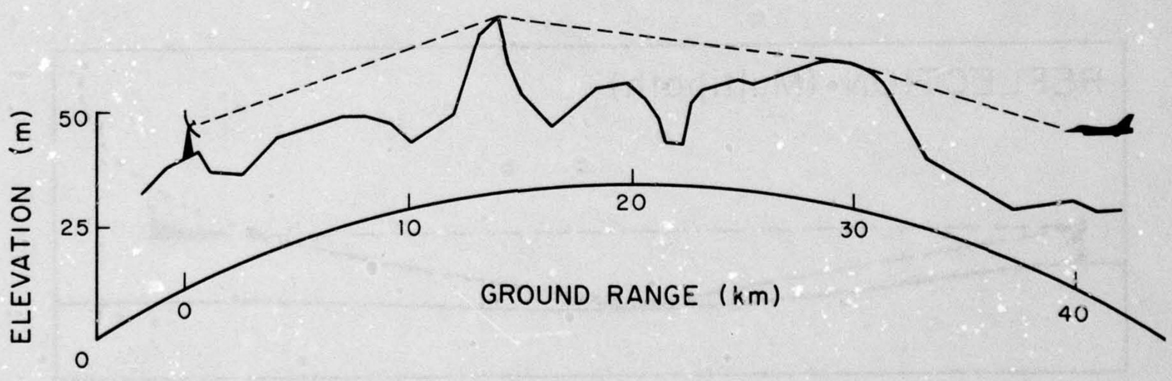

Figure 4 - Typical Terrain Profile, with Adjustments, Showing Diffracting Features

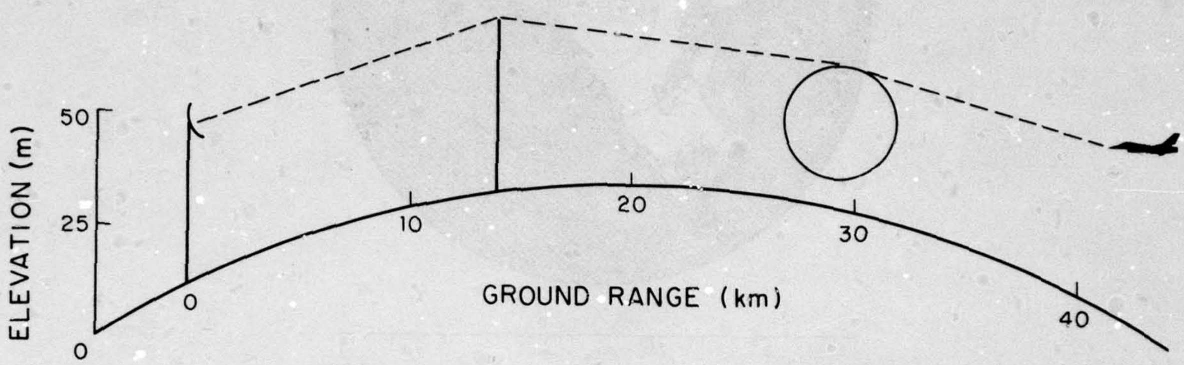

Figure 5 - Idealization of Adjusted Typical Terrain Profile

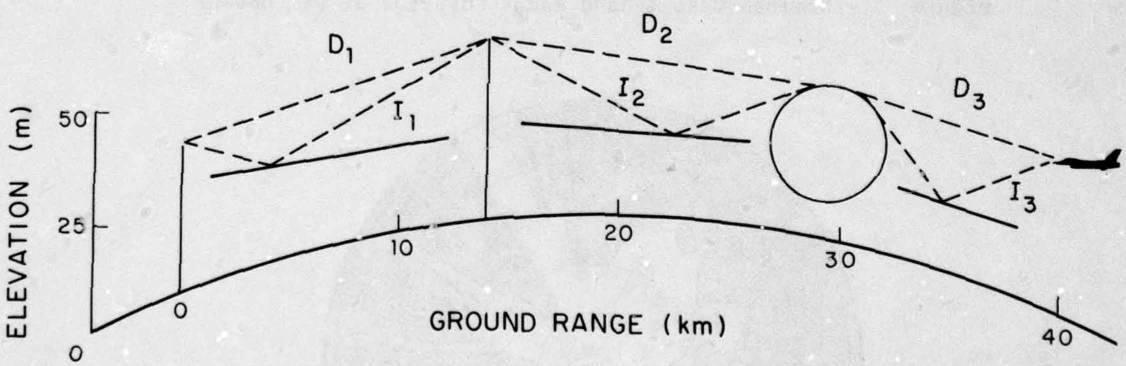

Figure 6 - Idealization of Adjusted Typical Terrain Profile with Effective Reflecting Surfaces

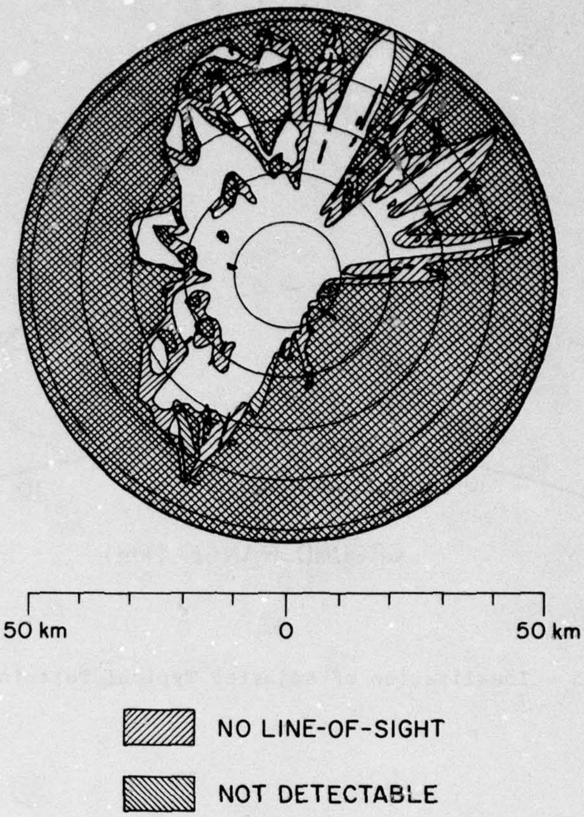

Figure 7 - Nominal Case X-Band Radar Coverage at Ft. Devens

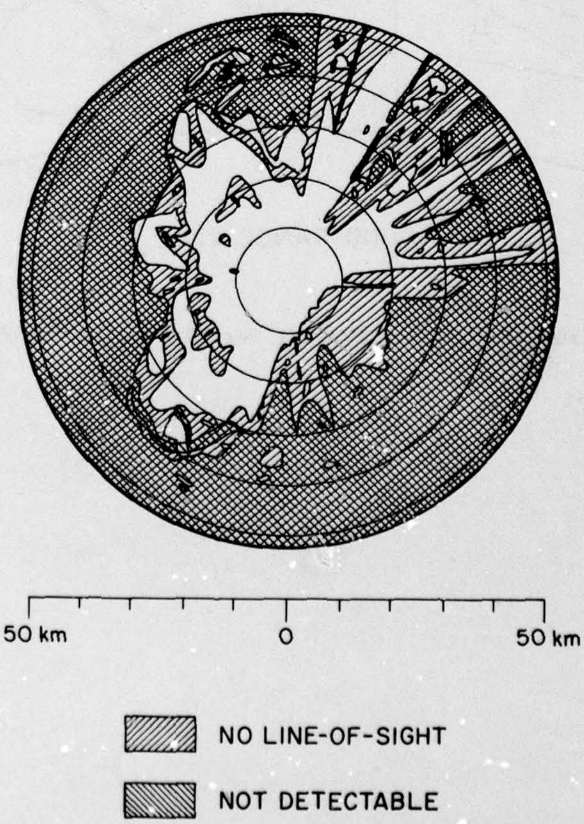

Figure 8 - Nominal Case VHF Radar Coverage at Ft. Devens

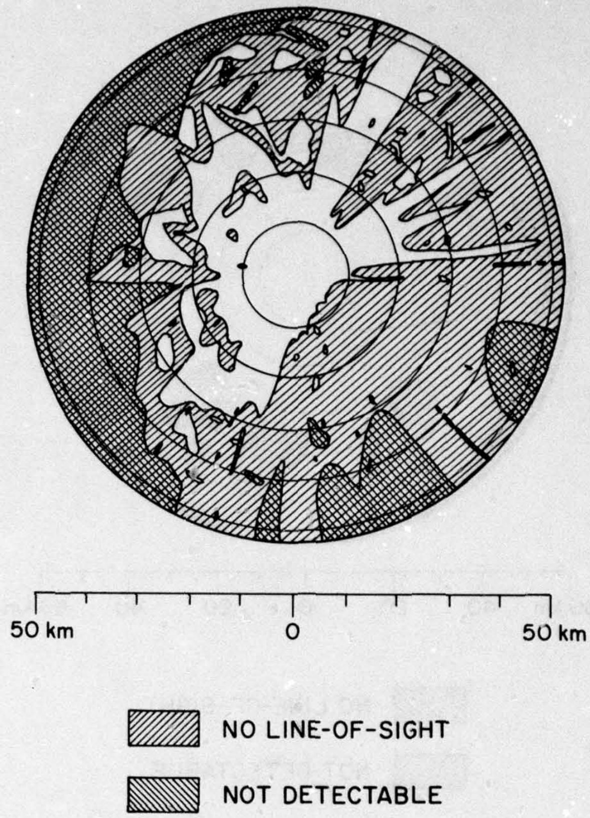

Figure 9 - Extended Range VHF Radar Coverage at Ft. Devens

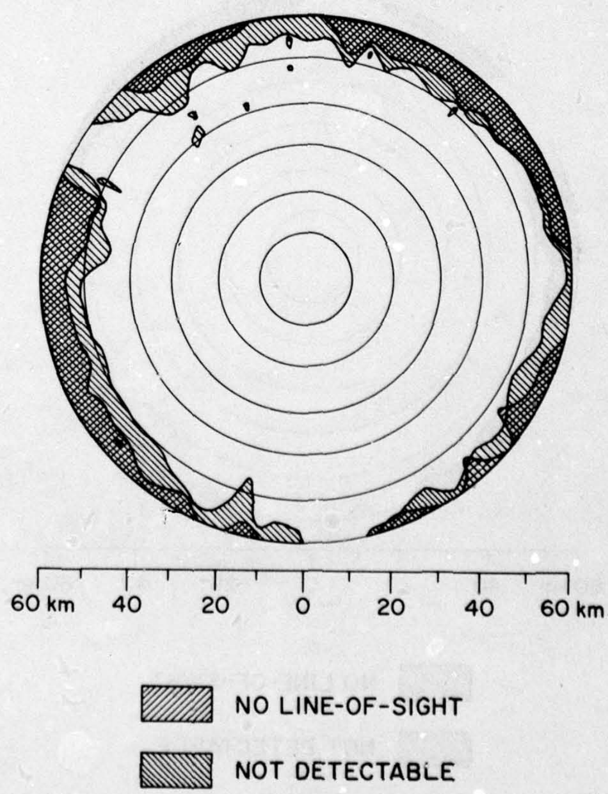

Figure 10 - Nominal Case X-Band Radar Coverage at Vera Cruz

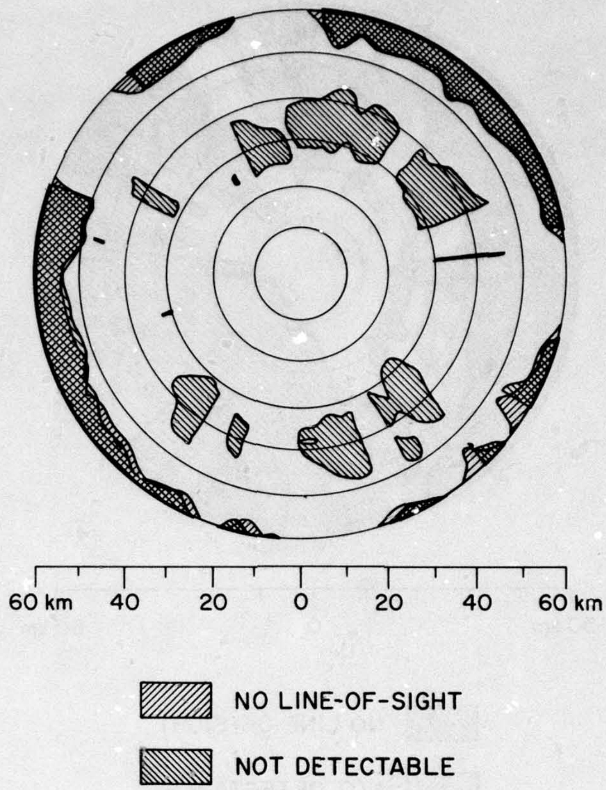

Figure 11 - Nominal Case VHF Radar Coverage at Vera Cruz

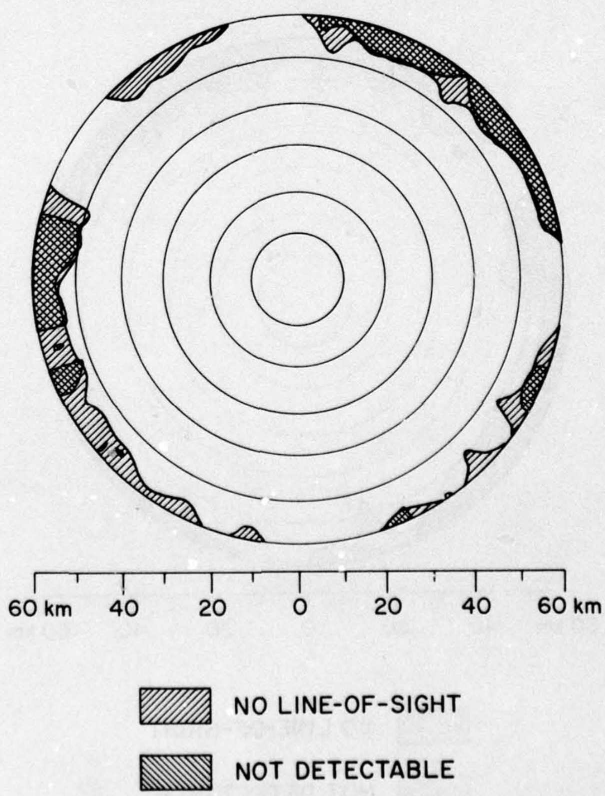

Figure 12 - Extended Range VHF Radar Coverage at Vera Cruz

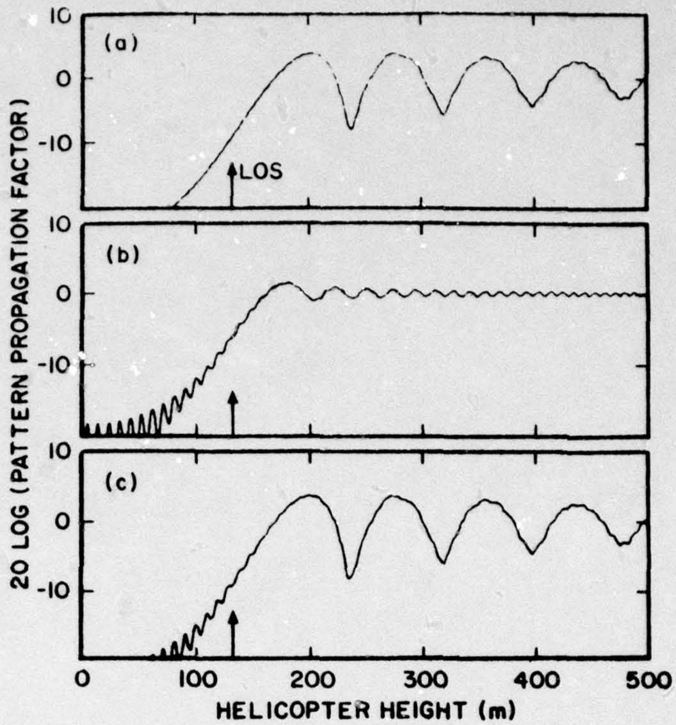

Figure 13 - The Pattern Propagation Factor as a Function of Helicopter Height Computed for a Dipole Antenna 6.26 m Above Ground. In (a) ground reflection occurs only between the tower and the mask, in (b) ground reflection occurs only between helicopter and mask, and in (c) reflections occur on both sides of the mask. The position of the line of sight over the hill top is labeled LOS.

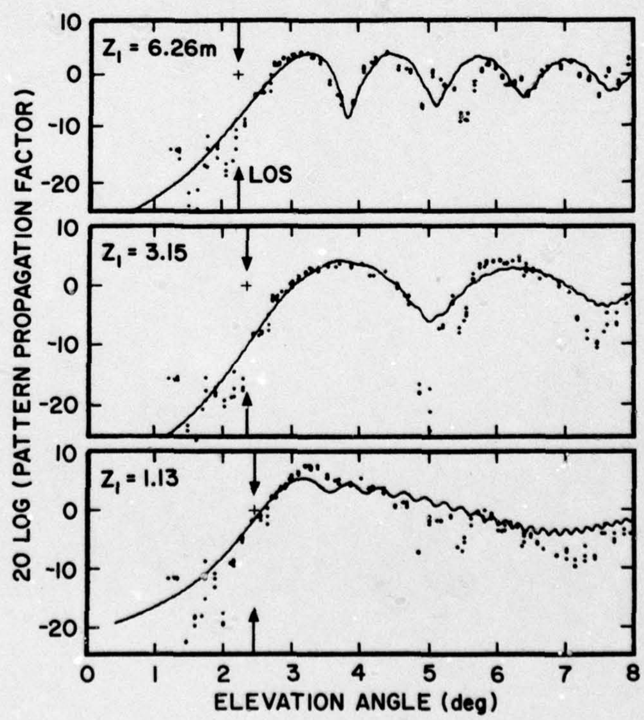

Figure 14 - Pattern Propagation Factor as a Function of Helicopter Elevation Angle. The smooth curves are computed for the dipole antenna heights Z_1 as indicated in (a), (b), and (c). The points represent measurements. The positions of the lowest line of sight are indicated for each dipole. Elevation angle is measured from ground level.

RADIO NETWORK AND RADIO LINK SURVEYS DERIVED BY COMPUTER FROM A TERRAIN DATA BASE

C E Dadson
The Joint Radio Committee of the Nationalised Power Industries,
London, UK

SUMMARY

The paper describes a method of deriving calculations for the coverage area of mobile radio networks using a computer and a topographical data base. This method is widely used in the UK, and since its inception in 1971, some 1800 surveys have been carried out.

The topographical data base was manually produced from Ordnance Survey maps of scale 1:25,000, providing 800,000 height reference points at 0.5 kilometre intervals for England, Wales and Scotland (except the Highlands and Islands). Path profiles are produced by the computer and calculations are provided for each 0.5 km point over the survey area, which can be up to a maximum of 90 km square. The computer requires the user to input details of the base station transmitter location, antenna height, radiated power and type of antenna.

A similar program produces calculations and a path profile for point-to-point radio links.

The paper describes the method used to derive the data base, and discusses its application to radio path calculations.

1. INTRODUCTION

The radio communication services of the energy producing industries of the United Kingdom are co-ordinated through the Joint Radio Committee of the Nationalised Power Industries (JRC) and together they form one of the largest user groups of mobile radio and radio links in the country. At the present time the industries are operating 32,000 mobiles, using 1500 base stations and 900 radio links. The mobile radio services are operating in the VHF band and the radio links use the bands 450/470 MHz, 1500 MHz and 7000 MHz. In addition, the electricity and gas industries have radio telemetering networks in operation in the 450/470 MHz band, controlling some hundreds of outstations.

The planning and design of these radio services require that detailed information is available concerning the terrain in the areas where radio coverage is required, and the availability of possible base stations sites. In the UK, planning restrictions control the development of potentially suitable base station sites, so that it is not always possible to select the optimum location, and the final choice frequently becomes a compromise between what is best and what is available. The need for a quick method of providing information on the expected radio coverage from given sites led the JRC in 1967 to set up a study project with the University of Manchester Institute of Science and Technology to assess the feasibility of using the computer to calculate radio network area coverage. The work was completed in two years, and it was evident that the technique could be applied to mobile radio networks (Edwards and Durkin, 1969).

Computer-aided design of mobile radio networks, radio telemetering networks and radio links in now an accepted practice in the JRC member industries, and to date some 1800 surveys have been carried out, using computer programs which have been developed from the initial work at Manchester. Government departments, manufacturers and other users regularly make use of this facility, which is now made generally available by the JRC, and work has also been carried out for other countries.

2. ESSENTIAL ELEMENTS OF THE COMPUTER DERIVED SURVEY

The computer programs used in this discussion have four basic operations:

(a) There is a terrain data base, providing detailed information for the UK, from which is selected data for the area to be surveyed.

(b) Input data for the survey to be carried out provides details of the base station location, the height above ground of the base station transmitter and mobile receiver antennas, effective radiated power and types of antenna used.

(c) The calculations are carried out on IBM 370/168 computer, using programs MAPS, SERV and RADIO.

(d) The output is provided in the form of a listing of field strengths and received power at half-kilometre intervals over the area surveyed, and a transparency plot is also produced for overlay on maps of selected scales, giving a pictorial presentation of the signal levels.

Each of these processes is described in detail below.

3. TERRAIN DATA BASE

3.1. Storage of Geographical Data

The data-storage requirement, computation time, resolution and accuracy of the results all depend upon the density and form of the geographical data. For this reason, considerable attention was given to these aspects of the data preparation.

Extensive trials showed that ground-height data recorded at 0.5 km intervals gave an acceptable compromise between the volume of data stored (and hence the computation time) and the accuracy of reconstruction of ground profiles from the stored data. The use of a coarser quantisation grid resulted in a loss of essential features along the radial. Furthermore, estimation of the field strengths at 0.5 km intervals is normally adequate for mobile radio-network studies.

With this scheme therefore, each data recording represents the terrain height within a 0.5 km square. A selection of procedures for the allocation of a height to each of these squares was compared from the viewpoint of preservation of the essential features of the ground profile in the reconstruction process. The following method was found to be the most satisfactory.

The UK data base was prepared using maps published by the Ordnance Survey Department, of scale 1:25,000. Each map represents an area 10 km square, and is referenced according to the national grid referencing system based upon a 100 km matrix. The data base contains height data for 2,200 of these 10 km square maps, each of which is identified by a two-letter, two-digit reference marking its precise position in the national grid referencing system.

Each of these maps is divided into 0.5 km squares, and each square is represented by either

(a) the actual height of a peak, basin, plateau or valley found in the square, or

(b) the arithmetic mean of the maximum and minimum heights found in the square, if it does not contain any of the topographical features listed under (a).

The data extracted from a single map is therefore a 20 x 20 submatrix of terrain heights, stored conventionally in rows. Each group of 400 data values is preceded by its reference marker, so that the relevant submatrices can be subsequently drawn together to form the matrix of heights of the area under consideration.

3.2. Coding Methods Used

The Ordnance Survey (OS) maps have height contours at intervals of 25 feet, and each terrain height reference is represented by four digits. The data was derived by operator examination of the OS maps, and this is still considered to be the only satisfactory method. The basic rules for coding were:

(a) a closed contour, with no other contours within it, contained in a single half-kilometre square, is defined as a peak, and that height is encoded;

(b) when such a contour covers more than one square, it is defined as a plateau, and the height is encoded in the squares traversed;

(c) where a valley traverses a square, the lowest point of the valley is encoded;

(d) if no feature lies within a square, the value of the arithmetic mean of the maximum and minimum heights is taken.

Examples of these basic features are given in figure 1.

There are, of course, exceptions to these four rules, and each exception has to be treated specially. For instance, where a peak and a valley occur in the same square, examination of the surrounding squares determines which of the features is identified. Figure 2, gives an example of this, where square A3 shows the valley and the peak. In this case the peak was encoded and the valley was recorded in the squares to the left and below.

In the same figure, looking at square B3, the coding is 600, although the square contains a valley of less than 575 feet. This has been done to preserve the ridge between the main and subsidiary valleys.

3.3. Path Profile Reconstruction

In the process of calculating received signal level from a given base station transmitter, the computer reconstructs the ground path profile between the two points. This is a process which is repeated for each calculation, of which there can be as many as 32,400 in the largest surveys.

It will be seen by reference to figure 3, that the line AB, which represents a section of the radial path between the transmitter and receiver, traverses the 0.5 km squares shown. The profile is reconstructed by the use of three interpolation routines which evaluate the heights on the radial by reference to the adjoining vertical, horizontal and diagonal squares of the matrix as shown, giving calculated heights numbered 1-8 for the vertical interpolation, 9-13 for the horizontal and 14-27 for the diagonal. 28 and 29 are taken at data reference heights.

The average number of height interpolations is five per kilometre, the worst being two per kilometre when the radial co-incides with a vertical or horizontal row of the matrix.

It is possible to give finer definitions of the reconstructed ground profile by additional processing, but it was found that the yield in terms of accuracy was not commensurate with the increased computation time required to carry out the additional calculations.

Figure 4 illustrates a profile derived and plotted by computer, with the heights taken from the Ordnance Survey map superimposed. It will be seen that the predominant features of the radial path are reproduced by the computer.

3.4. Data Bases for Other Countries

The ERC computer programs MAPS, SERV and RADIO have been used to produce calculations for radio projects in France, Germany, Italy and Iran, for which the topographical heights were represented in metres and all calculations were in metric units. A metric version of the programs is also available in the UK.

4. RADIO PATH CALCULATIONS

4.1. Path Losses

The three main elements of a mobile radio network are

(a) the transmitter base station, including the antenna,

(b) the radio path,

(c) the mobile station.

Of these, the only non-variable element for a given radio path is the radio path itself, since the transmitter power and aerial characteristics can be changed, and the mobile receiving antenna and receiver sensitivity can also be varied.

In using program SERV, therefore, items (a) and (c) above are input by the user and item (b) is calculated by the computer. It is then possible to determine the received signal level and field strength at the mobile location for a given base station aerial height and effective radiated power. This operation is carried out by program SERV for each half-kilometre square over the area to be surveyed, radio path attenuation being calculated for the radial from the base station to each half-kilometre square. The path attenuation calculation takes into account the following factors:

(a) line-of-sight loss,

(b) defraction loss caused by intervening topographical obstacles,

(c) loss due to inadequate Fresnel-zone clearance,

(d) earth curvature refraction.

The procedure is described below and is illustrated in the flow diagram, figure 5.

4.2. Line of Sight Path

The computer constructs a line joining transmitter and receiver aerials and tests to see that at no point is there a ground height above sea level which exceeds the height of the reconstructed line. If it is established that line of sight exists, the program tests whether Fresnel-zone clearance is obtained over the path, using well-known methods (Bullington 1947, Millington, Hewitt and Immizi 1962, Epstein and Peterson, 1953).

Either free-space or plane-earth losses are predominant if both the above tests are satisfied, but if the tests show that an obstruction exists or that Fresnel-zone clearance is not obtained, calculations proceed to determine the resultant losses.

4.3. Free-space and plane-earth losses

The losses due to free-space and plane-earth propagation are calculated and the larger loss is selected.

For free-space propagation between half-wave dipole antennas, the effective power of the receiving antenna is given by the equation

$$P_{dB} = 32.2 + 20 \log_{10} f + 20 \log_{10} d - 10 \log_{10} P$$

Where P_{dB} is in decibels below 1 watt

d = total transmission path in miles

P = effective radiated power in watts

f = transmitter frequency in MHz

(Rock 1961 and Hamsher 1967)

For plan-earth propagation between half-wave dipole antennas, the effective power at the receiving antenna is given by the equation

$$P_{dB} = 144.6 - 20 \log_{10} (x) + 40 \log_{10} d - 10 \log_{10} P$$

Where P_{dB} is in decibels below 1 watt

d = total transmission path in miles

P = effective radiated power in watts

f = transmitter frequency in MHz

x = is a function of the difference in ground height between the transmitter and receiver, obtained as follows:

Let the ground height in feet, at the transmitter = HGT
and the ground height in feet at the receiver = HGR

Let the height in feet above ground of transmitter dipole = H_t
and the height in feet above ground of receiver dipole = H_r

H' is a function of the difference between HGT and HGR, and is an effective height above a ground plane which is at HGR when HGT > HGR, and at HGT when HGR > HGT. It is derived by the process

is HGT - HGR $\geqslant$ 0?

YES

$$x = [(HGT - HGR) + H_t]\, H_r = H' H_r$$

NO

$$x = [(HGR - HGT) + H_r]\, H_t = H' H_t$$

This means that for constant H_t, H_r and d, the plane-earth loss will approach a maximum as $|HGT - HGR| \Rightarrow 0$ and will accordingly decrease as $|HGT - HGR|$ increases.

In a mobile radio network, the plane-earth loss predominates in most cases because of the relatively low siting of the receiving antenna.

4.4. Obstructed Path

The program evaluates the loss caused by obstructed path profiles, grading the obstruction into single or multiple diffraction edges. Calculations are made for up to three diffraction edges, and any greater number of obstructions is converted into a three-diffraction-edge condition, using a method of Bullington (Bullington 1947, and Epstein and Peterson 1953).

4.5. Earth Curvature

The effect of earth curvature is taken as four-thirds of true value to allow for atmospheric refraction of the transmitted radio wave. (Epstein and Peterson 1953). However, it is found that for the relatively short transmission paths of mobile radio networks, earth curvature has little effect on the total transmission path.

4.6. Directional Antennas

Normally, the program assumes an omnidirectional antenna, but options have been included which enable calculations to be made using various types of Yagi antenna. In addition, it is possible for a look-up table to be inserted for any special type of antenna not included in the available list.

5. PRESENTATION OF OUTPUT

The output is presented in two parts, both of which are produced for every job.

Firstly a listing is produced for every half-kilometre of the survey area, giving the signal strengths in dB below one watt and the corresponding field strengths in micro-volts per metre.

Secondly, a plot is produced on transparent film which can be placed over the Ordnance Survey map, enabling the user more easily to relate the calculations to the terrain.

Figures 6 and 7 depict an overlay produced from the following input data:

Map reference of transmitter station (Transmitter location, Millbank, Westminster, London)	TQ 302787
Transmitter frequency	165.000 MHz
Transmitter antenna type	Omnidirectional
Transmitter antenna height above ground	150.0 feet
Effective radiated power	7.0 feet
Receiver antenna height above ground	3.0 feet

The input data also contained a list of the map squares forming the survey area, which in this case covered an area of 50 km x 60 km, comprising 30 map squares each 10 km square. The map reference points are the same as those used in the UK Ordnance Survey grid.

The plain area in the centre of the plot illustrates the area where the field strength is in excess of 10 micro-volts per metre. The half-kilometre squares marked with a + show where the signal level is less than 10 micro-volts per metre but more than two, and the areas marked with a ⊠ indicate areas where the signal level is 2 micro-volts per metre or less. It should be noted that large areas which have signal levels of less than 2 micro-volts per metre are marked by the one symbol. The base station is located by the 2 micro-volt symbol in square TQ 37.

Where it is required to test the effect of aerial height variation, or to study the results of possible changes in effective radiated power, it is a very simple matter to produce overlays for each requirement and to compare the results before deciding on the dimensions to be used.

Figure 8 shows a data form which provides input information and choice of options for the running of program SERV.

7. LIMITATIONS

In order to maintain a reasonable balance between accuracy and computation time, some constraints are necessary, and the output must be interpreted in the knowledge of these limitations.

7.1. *Topographical Data*

Basically, this cannot be any more accurate than the maps from which it is prepared. In the case of the UK data base, the information was prepared from maps of scale 1:25,000, which proved to be the most practical method of assembling the large amount of data required. It is believed that the greatest data height inaccuracies are no more than 25 feet, and over most of the country accuracy is estimated to be within 2.5 feet.

It should be noted that the reference height given for each half-kilometre represents either a mean height for the half-kilometre square or the height of a significant topographical feature.

A finer data base using a $\frac{1}{4}$ km matrix instead of the $\frac{1}{2}$ km matrix would not materially improve the accuracy of the output, but would increase data base storage by a factor of four, and would considerably increase computing time and cost to quite unacceptable levels for most applications.

7.2. Output Calculations

Output signal levels and field strengths are representative of the signal within a half-kilometre square. Actual measurement in the square may produce readings which vary from the computer derived figure, but the latter has been shown to be well within acceptable limits.

7.3. Area of Survey

The present program used in the UK limits the area of survey to a maximum of 90 km square. This could be extended, but experience shows that it is adequate for most mobile radio network requirements. Any area within this limitation can be surveyed, and it is not necessary for the base station to form part of the actual area, as long as it and the network area fall within the overall boundaries of the 90 km square.

7.4. Output Plots

Output plotting scales are limited to those for which maps are currently available in the UK or on the Continent, but other map scales can be introduced with only minor modification to the program.

The listing of signal levels and field strengths is produced by computer print-out, and consideration is now being given to producing this on magnetic tape so that it can be used in association with other programs.

7.5. Man-Made Obstructions

A criticism of the system described above is its inability to take into account the effect of buildings, forests and other man-made obstructions. This is a problem which has been studied with little success so far, and emphasises the fact that the programs must be applied as an aid to network planning rather than as a final solution to a requirement.

In a country like UK, where urban, agricultural and forestry features all occur within quite limited areas, it would be necessary to give each type of obstruction a weighted obstruction factor in decibels.

8. POINT-TO-POINT RADIO LINKS

Program RADIO has been developed from the work carried out on SERV, to construct radio path profiles and calculations using the topographical data bank.

Options are built into the program to allow the user:

(a) Either, given the transmitter power, calculate the received power, or, calculate the transmitter power to give a specified field strength at the receiver.

(b) Either, to plot the transmission path between two specified aerial heights, or to plot the free space transmission path with equal minimum aerial heights.

The calculations may be repeated for a number of combinations of transmitter and receiver heights.

The distance over which a radio path calculation and plot can be produced, using the existing programs, is about 400 km.

In order to improve the accuracy of the calculations, the antenna height above sea level at each terminal of the radio link is given as an input, and this figure is substituted in the computer calculations for the data base reference heights at the two terminals.

Figure 9 is the diagram of the logic of the program, which comprises the main program and a number of function sub-programs which calculate transmission, obstruction and free space losses, and assemble the height data.

The following figures represent the input and complete set of output data as plot for a typical link path.

Figure 10 - Completed input data form.

Figure 11 - Output of calculated results for radio path in one direction. (A similar output is produced for the return path).

Figure 12 - Computer plotted path.

It will be noted that a flat earth is assumed and that the radio path has been curved towards the earth at 4/3 of earth radius. However, this is an additional option which allows the radius of earth curvature to be adjusted to 1 or $\frac{2}{3}$ of earth radius.

Other options allow the scale of the plot to be varied.

9. FUTURE DEVELOPMENT

Several useful developments of this work are under consideration for application to mobile radio and radio path link problems.

A derivation of the program SERV is used by the UK Home Office Directorate of Radio Technology for the planning of mobile radio frequency allocations (Dadson, Durkin and Martin 1975) and the topographical data base is associated with other programs for radio propagation surveys for broadcasting surveys (British Broadcasting Corporation, 1970).

The programs have been used by the JRC in the investigation of radio interference problems between stations on the same frequencies, and the possible production of maps showing the interference patterns of networks using multiple base stations is now being studied.

Considerable interest has been shown in this work by other users in the UK, many of whom are using the service provided by the Joint Radio Committee, and a number of enquiries have been received from other Countries.

It is probable that many other problems associated with radio path calculations can also be resolved quickly and accurately by the use of computer techniques, with a suitable topographical data base.

10. APPRECIATION

The author expresses his thanks to the Electricity Council and to the Joint Radio Committee of the Nationalised Power Industries for permission to present this paper. The assistance given by his colleagues in the preparation of the material is also appreciated. Thanks are also due to PMA Consultants Ltd, Horley, Surrey, for the provision of information on the topographical data bank.

June 1979

REFERENCES

BULLINGTON, K, October 1947,
"Radio Propagation at Frequencies above 30 MHz", Proc IRE, Vol 48

BRITISH BROADCASTING CORPORATION REPORT No 1970/26
"An Investigation Into the Prediction of Field Strength: the Guildford Experiment"
(Lee, Causebrook and Sandell)

DADSON, DURKIN and MARTIN, 1975,
"Computer Prediction of Field Strength in the Planning of Radio Systems", IEEE Transactions on Vehicular Technology, USA

EDWARDS, R, and DURKIN, J, 1969,
"Computer Prediction of Service Areas for VHF Mobile Radio Networks", Proc IEE, Vol 116

EPSTEIN, J, and PETERSON, D W, 1953,
"An Experimental Study of Wave Propagation at 850 MHz", Proc IRE, Vol 41

HAMSHER, D H, 1967,
"Communication System Engineering Handbook", McGraw-Hill

MILLINGTON, G, HEWITT, R, and IMMIZI, F S, 1962,
"Double Knife Edge Diffraction in Field Strength Prediction", Proc IEE, Monograph No 507E

ROCK, F E, 1961,
"Radio Interference and Spectrum Utilisation of VHF fm Net Equipment in a Mobile Environment", IRE Trans

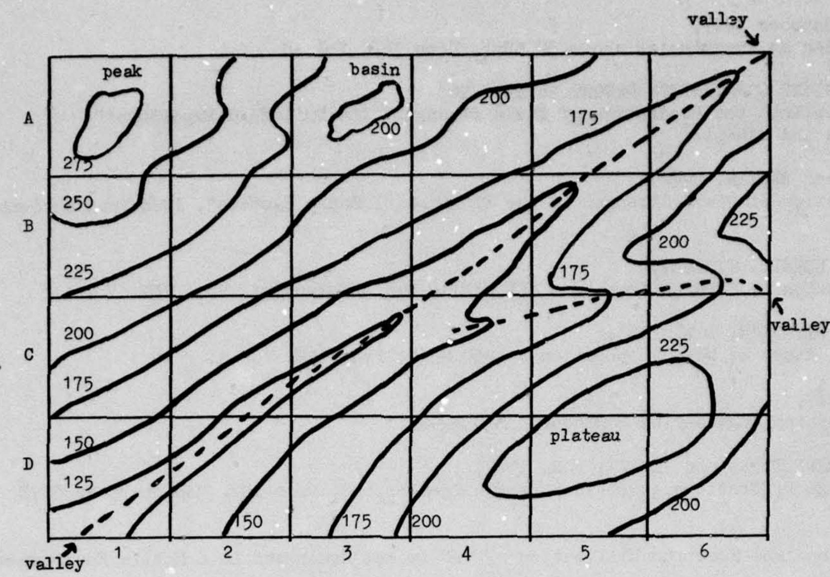

Figure 1 Examples of Basic Geographical Features

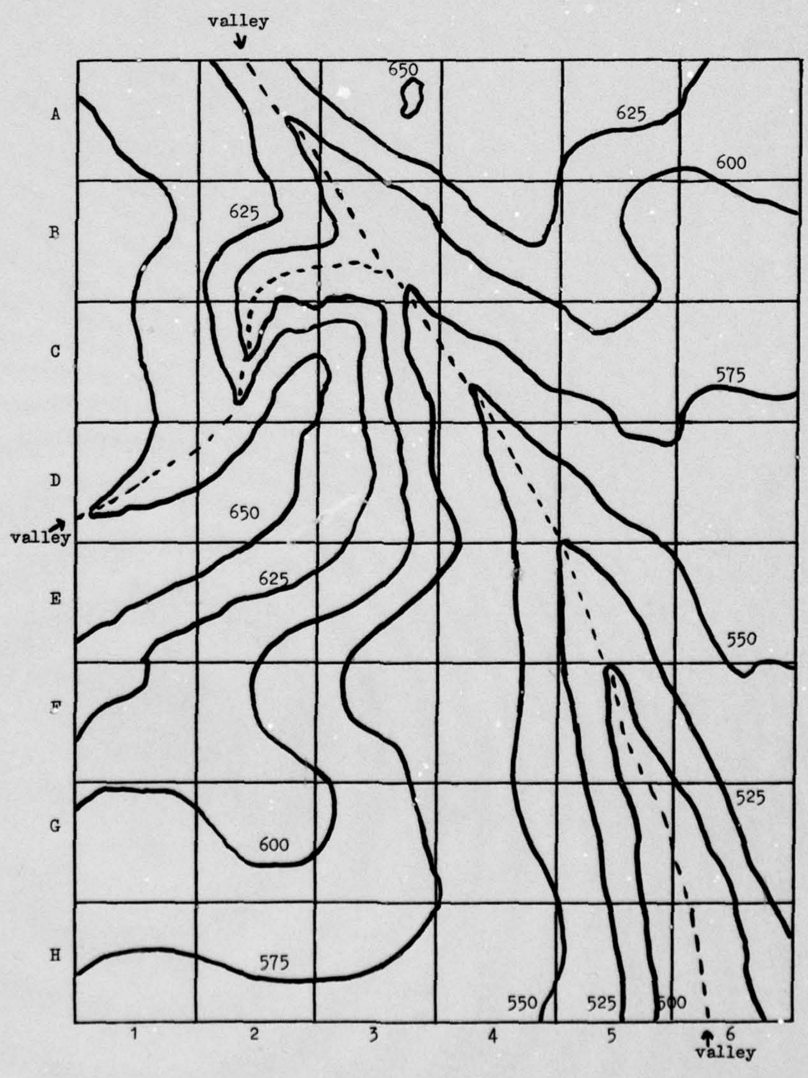

Figure 2 Examples of Two Cases Requiring Special Treatment

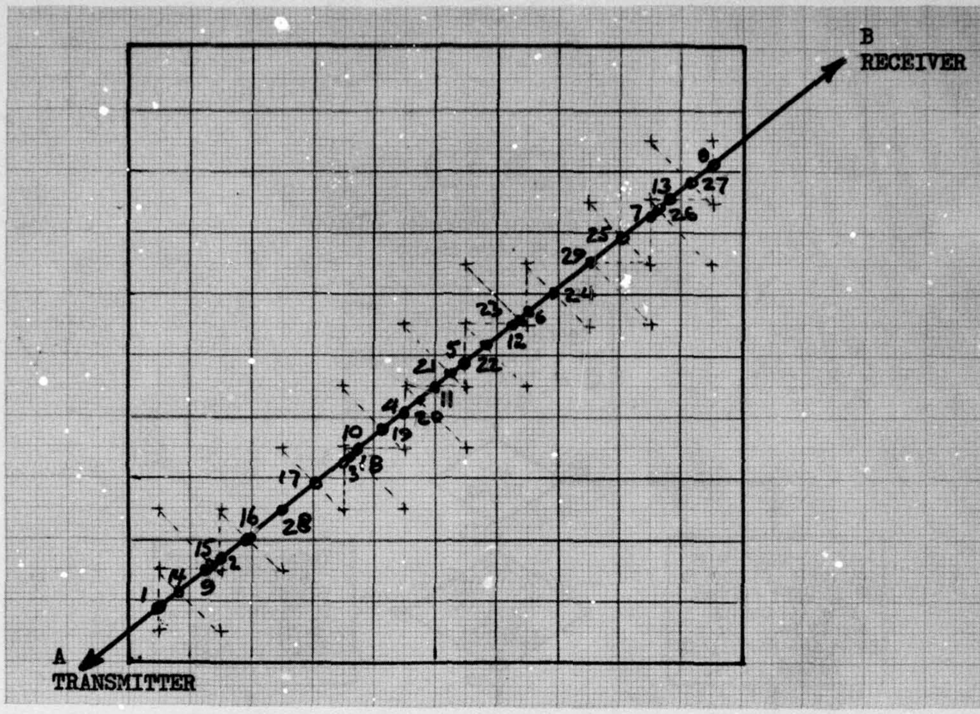

Figure 3 Interpolated Heights for Radio Path A-B

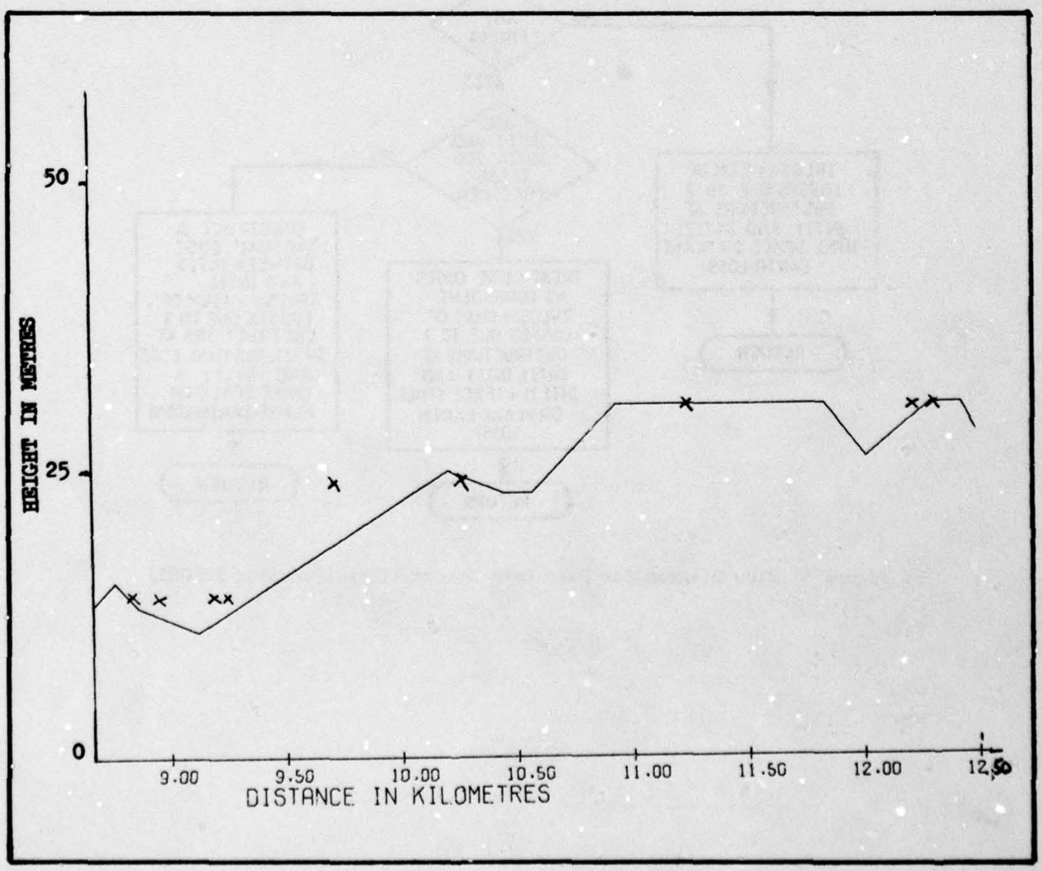

Figure 4 Computer Derived Profile, with Actual Map Heights Super-imposed

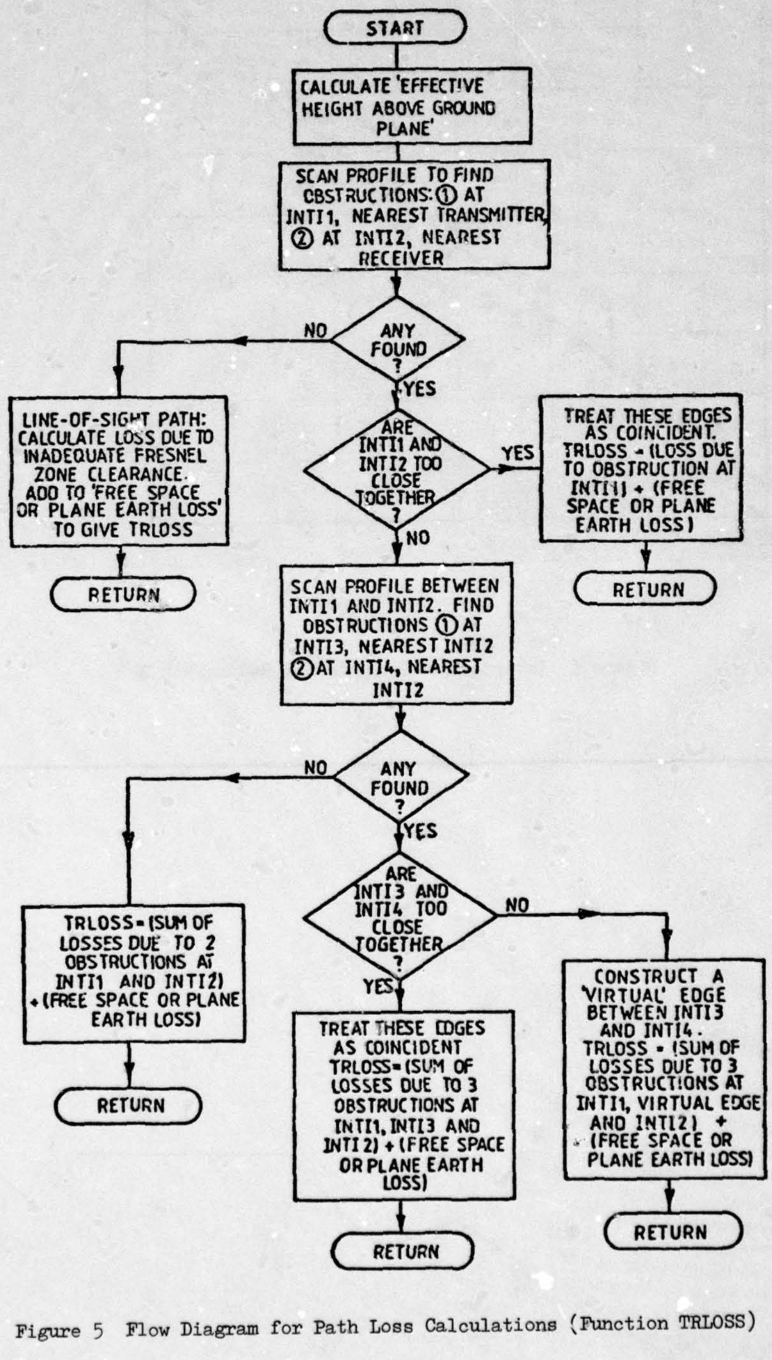

Figure 5 Flow Diagram for Path Loss Calculations (Function TRLOSS)

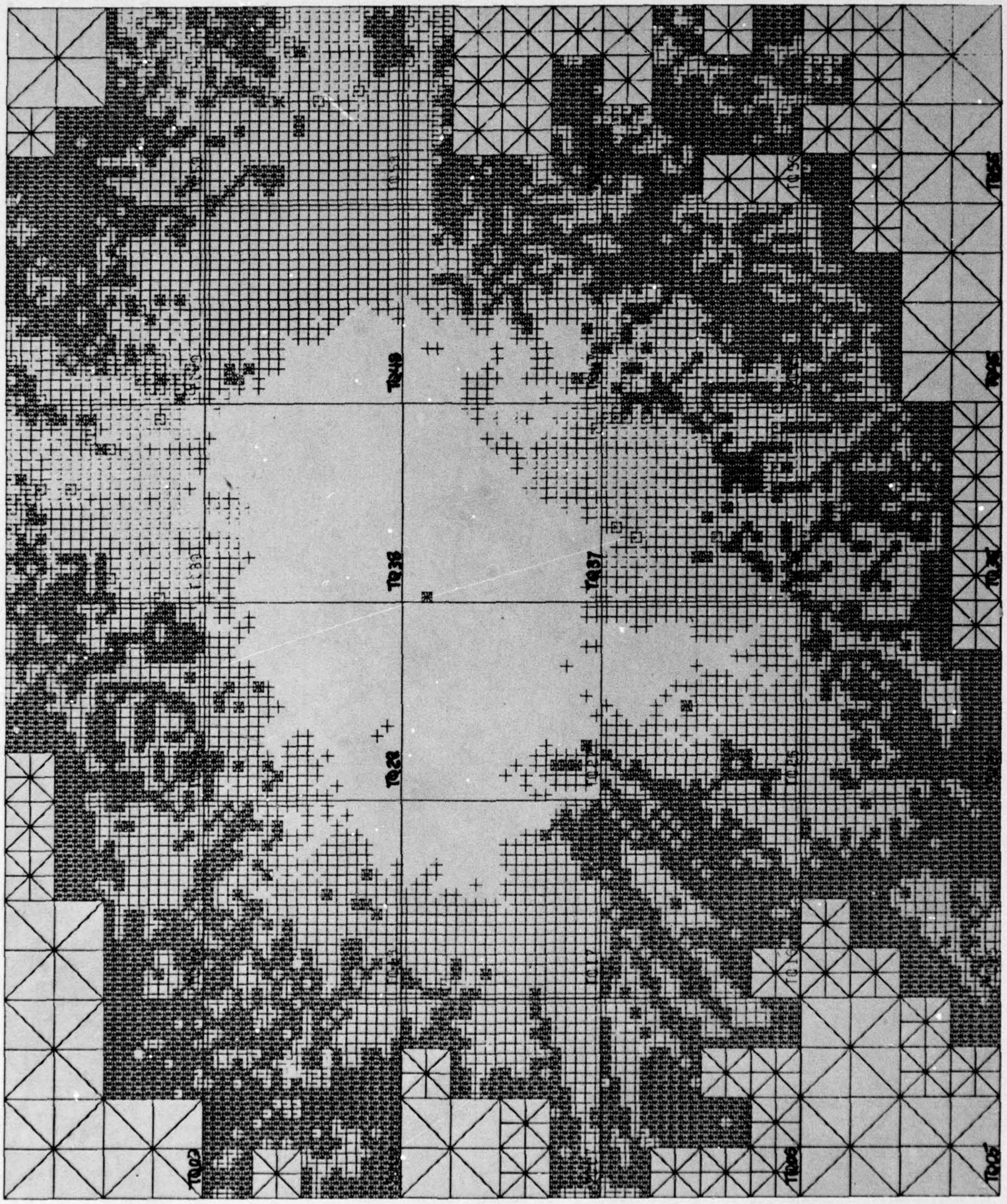

Figure 6 Example of Computer Derived Area Coverage Plot for a Base Station in Square TQ 37, Produced on Transparent Film

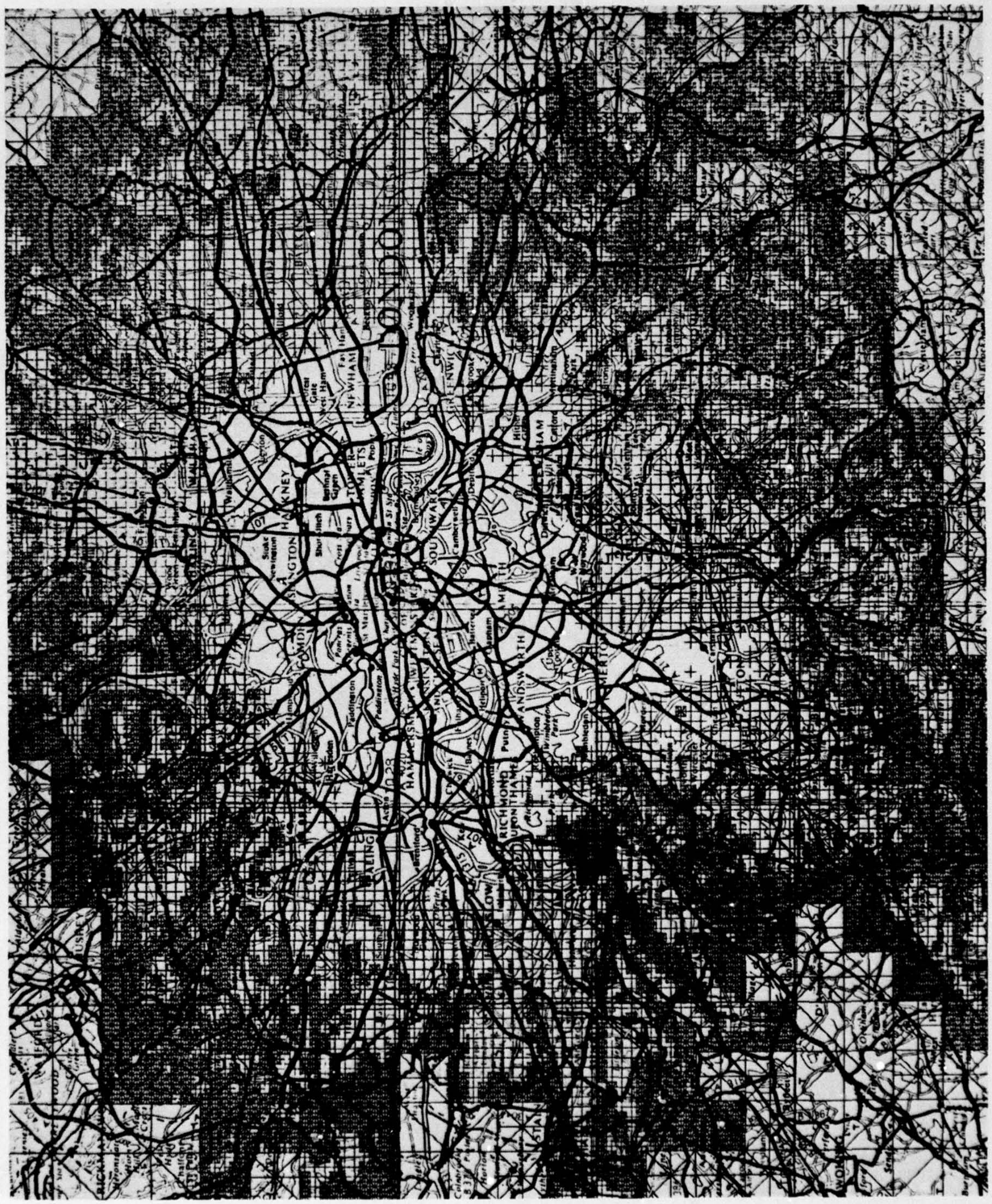

Figure 7 The Transparent Plot Overlaid on the Ordnance Survey Map for the Area of Survey

THE JOINT RADIO COMMITTEE OF THE NATIONALISED POWER INDUSTRIES

COMPUTER DERIVED RADIO NETWORK SURVEY

DATA PREPARATION

Note: Where 1:50,000 or 1:200,000 plot is requested, item 5 and 6 must be stated in metres.

User Organisation:	Date:
1 Job title	
2 Transmitter frequency in MHz	
3a Type of aerial: State whether 1 Omnidirectional or 2 Directional: 2 element Yagi 3 element Yagi 4 element Yagi 6 element Yagi 8 element Yagi Other type	
3b If directional, state $^{\circ}$E of N of main lobe	
3c If 'other type', information must be provided in accordance with JRC Memorandum 13/77, item 2.2.3	
4 Power gain ratio in dB of mobile receiving aerial	
5 Height above ground in feet/metres of base station transmitting aerial	
6 Height above ground in feet/metres of mobile receiving aerial	
7 Maximum effective radiated power in watts of base station transmitting aerial	
8 Total number of map references following	
9 Map reference of base transmitting station	
10 Map reference of areas to be surveyed	
11 Scale of Calcomp Plot (delete those not required) a 1:25,000 (OS 2½" to 1 mile approx) b 1:250,000 (OS ¼" to 1 mile) c 1:63,360 (OS 1" to 1 mile) d 1:50,000 (OS metric series) e 1:200,000 (Continental only)	
12 Signal levels required on Calcomp Plot (Specify) NB: Normally a = 10μv/metre b = 2μv/metre	Level a μv/m Level b μv/m

Figure 8 Radio Network Survey Data Preparation Form

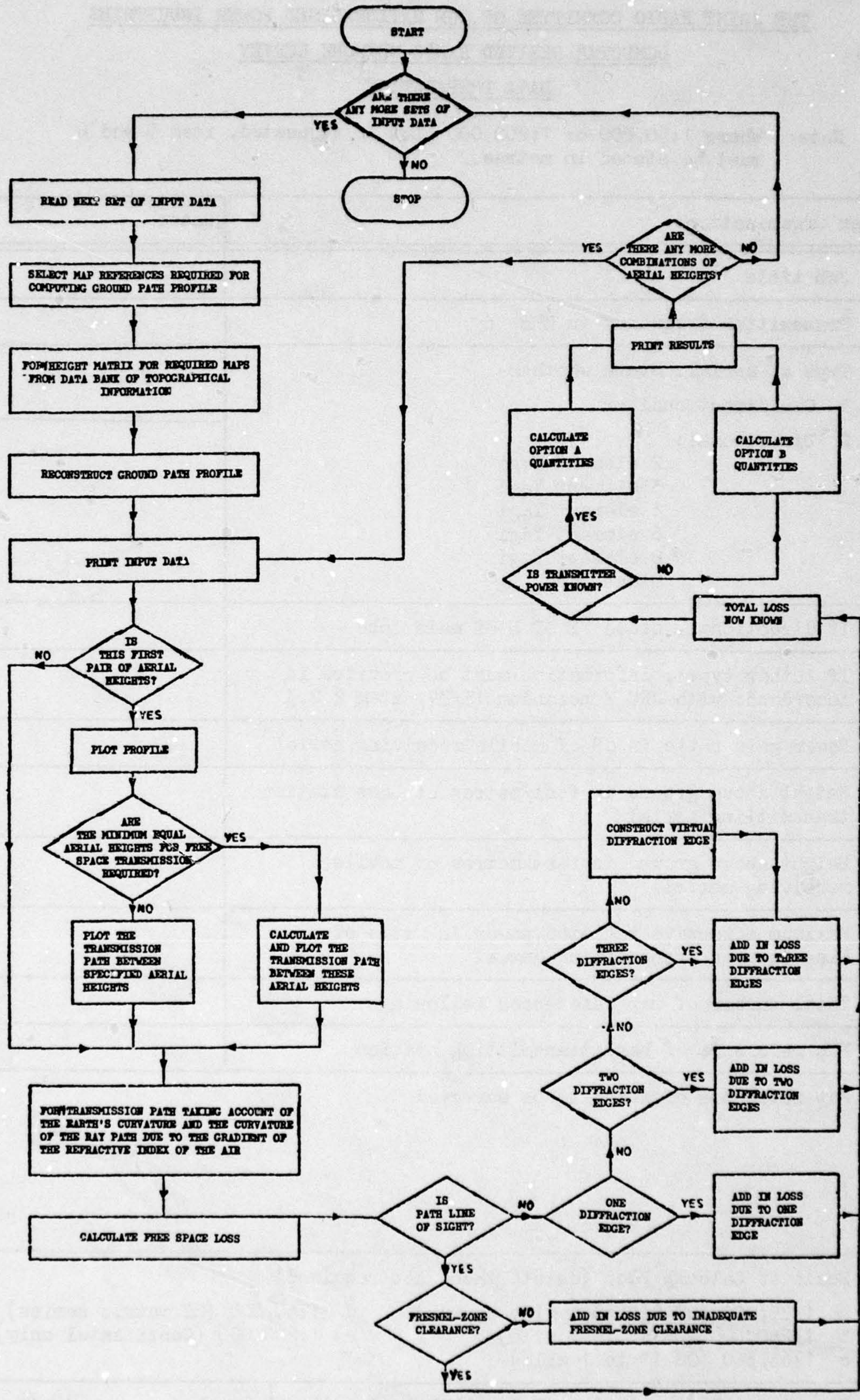

Figure 9 Flow Diagram of Program RADIO

The Joint Radio Committee of the Nationalised Power Industries

Computer Calculations and Plot of Point-to-Point Radio Links

Data Preparation

User: JRC	Date: 10 June 1979	
Job Title: AGARD		
1 General Information	Station 1	Station 2
1.1 Name of station	Station 1	Station 2
1.2 National Grid Reference	SZ 504943	SU 394114
1.3 Height of ground above sea level in ~~feet~~/metres	3	6
1.4 Height of aerial above ground in ~~feet~~/metres	18	1
1.5 Number of incremental steps for variation of aerial height		
1.6 Incremental step value of height in feet/metres		
1.7 Transmitter frequency in MHz	456	461
1.8 Transmitter feeder loss in dB	3.5	0.0
1.9 Gain of transmitter aerial in dB	0.0	-3.0
1.10 Gain of receiver aerial in dB	0.0	-3.0
1.11 Receiver feeder loss in dB	3.5	2.0
2 For Option A Transmitter power in watts	2.0	0.5
3 For Option B Receiver field strength in dB relative to 1 μV per metre (normally 45 dB for 450/470 MHz band)		
4 For Option C or D Specify aerial heights in feet/metres above ground for path profile plot (Option C)	0	
or Enter 0 (Option D)		
5 For Option C or D Specify required earth curvature radius	4/3	
6 For Option C or D Specify plot option required (See sec 5.6 of memo)	A4	

Figure 10 Point-to-Point Radio Link Data Preparation Form

POINT TO POINT LINK

```
                                   INPUT DATA

GROUND HEIGHT AT TRANSMITTER AT STATION 1                            3 METRES
GROUND HEIGHT AT RECEIVER AT STATION 2                               6 METRES
HEIGHT OF TRANSMITTER AERIAL AT STATION 1                           18 METRES
HEIGHT OF RECEIVER AERIAL AT STATION 2                               1 METRES
FREQUENCY OF TRANSMITTER AT STATION 1                              456 MHZ
GAIN OF TRANSMITTER AERIAL AT STATION 1
   IN THE DIRECTION OF STATION 2                                   0.0      DB
GAIN OF RECEIVER AERIAL AT STATION 2
   IN THE DIRECTION OF STATION 1                                  -3.00000 DB
TRANSMITTER FEEDER LOSS,STATION 1                                  3.50000 DB
RECEIVER FEEDER LOSS,STATION 2                                     0.0     DB
TRANSMITTER POWER AT STATION 1                                     2.00000 WATTS

MAP REFERENCE OF TRANSMITTER AT STATION 1
SZ   504943

MAP REFERENCE OF RECEIVER AT STATION 2
SU   394114

                                    RESULTS

RECEIVER POWER AT STATION 2                                     -132.27361 DBW
OVERALL LOSS BETWEEN STATION 1
   AND STATION 2                                                 135.28391 DB
EFFECTIVE RADIATED POWER FROM STATION 1                            0.89337 WATTS
FIELD STRENGTH AT STATION 2
   DUE TO STATION 1                       29.01083 DB RELATIVE TO ONE MICRO VOLT PER METRE

PATH PROFILE HAS BEEN PLOTTED WITH AERIAL HEIGHTS OF    65   AND    65 METRES
   AT STATION 1                                 AND STATION 2             RESPECTIVELY

THESE ARE THE MINIMUM HEIGHTS AT WHICH THE PROPAGATION PATH BECOMES FREE SPACE

          EXTRA HEIGHT REQUIRED ON BOTH AERIALS FOR 1ST FRESNEL ZONE CLEARANCE    26 METRES
```

Figure 11 Output of Results for Radio Path in One Direction

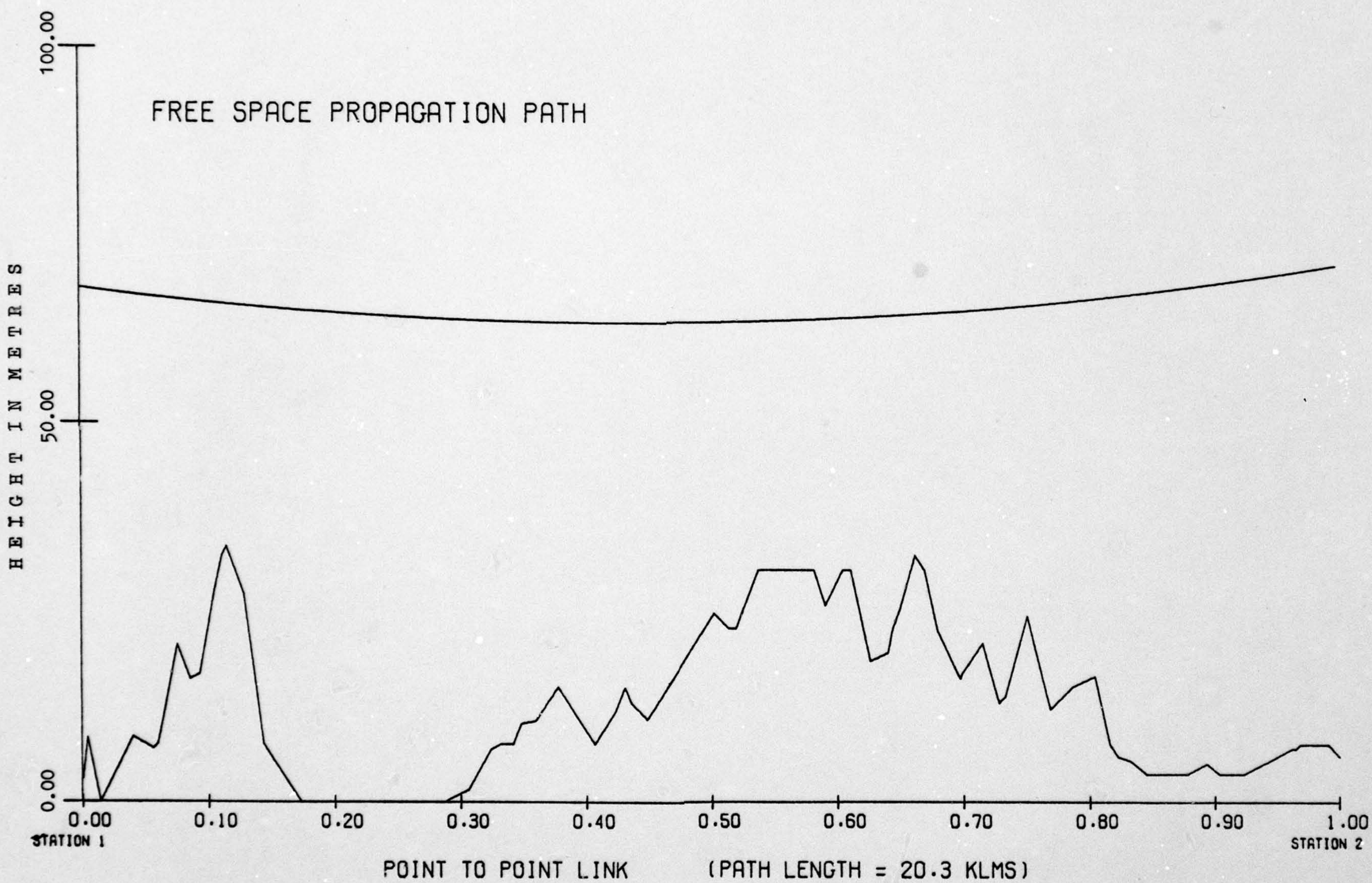

Figure 12 Computer Plot of Radio Path

VHF/UHF PATH-LOSS CALCULATIONS USING TERRAIN PROFILES DEDUCED FROM A DIGITAL TOPOGRAPHIC DATA BASE

F.H. Palmer
Communications Research Centre
Department of Communications
Ottawa, Canada K2H 8S2

SUMMARY

A digital topographic data-base comprising some 150,000 sq. km of southern Ontario had been completed. A further 400,000 sq. km of Ontario and the Maritime provinces are presently being scaled. These data-bases, which have a horizontal resolution of 500 metres, allow terrain profiles to be constructed automatically. The profiles, together with a variety of terrain surface cover information also derived from the data-base, are used in the calculation of path-loss, signal-strength, and signal-to-noise ratios for various types of VHF/UHF systems. These calculations are based on the method of Deygout, but incorporate a number of additional factors necessary to achieve good agreement between predicted and measured path-losses. Such factors include treatment of the effects of various types of terrain surface cover and of multiple, non-isolated obstacles. Comparisons of predictions and measurements made over a wide variety of terrain types indicate that rms prediction errors of 4-5 dB can be achieved in the VHF/UHF bands.

1. Introduction

A computer based VHF/UHF propagation prediction program which utilizes a digital terrain data-base and which features an interactive data input facility has been developed at the Communications Research Centre, Ottawa. This program is specifically adapted to Canadian requirements and has been designed to give the best fit to experimental data gathered in Canada. An overview of this program was given by Palmer (1978).

In this report, a rather more detailed description is given of the topographic data base and of the path-profile information which is derived from it. This is followed by a description of the techniques used to calculate path loss, and its variability, using digital path profiles.

2. The Data Bases

Both manual and automatic digitizing table techniques have been used to scale the topographic map data necessary for construction of the data base.

2.1 Manual Scaling

While the prediction model was being developed, a relatively small (112 x 120 km) topographic data base comprising the city of Ottawa and surrounding suburban and rural areas was constructed (Fig. 1). Both 1:25 000 and 1:50 000 topographic maps of the area were manually scaled using the superimposed 1 km square Universal Transverse Mercator (UTM) grid.

Initially, for each north-south UTM grid line within the data-base area the grid reference point, or 'northing', was recorded for every point at which a terrain elevation contour line intersected the north-south grid line. For each such intersection in the data-base area the following set of information was recorded: north-south grid-line number, northing of contour line intersection, contour line elevation, and a numerical code representing the type of terrain cover at that point. Since the spacing of the north-south grid lines was 1 km, the terrain elevations and terrain cover codes were then averaged over 1 km intervals in order to make the data-base resolution equal in the north-south and east-west directions. The averaged sets of data thus formed a square grid with 1 km spacing. Each of the 13,440 data sets consisted of the north-south grid line number, the northing of the centre of the 1 km interval over which the averaging was carried out, the average elevation over the 1 km interval, the maximum and minimum elevations in the 1 km interval, and the average terrain cover code.

This method is suited to situations where numbers of relatively unskilled personnel are available for scaling and where automatic digitizing tables are unavailable. The resolution of the data-base may be increased by scaling new north-south grid lines interleaved between the originals. The new sets of 'raw' data can then be merged with the old, without the need to rescale the original data. The enlarged raw data can then be averaged over north-south intervals equal to the new east-west grid line spacing. The chief drawback of the method is that topographic information is treated differently in the north-south and east-west directions, leading to some misrepresentation of contours. In practice, however, this drawback is not usually significant.

2.2 Automatic Scaling

A number of 1:50 000 topographic maps have been scaled using a GTCO Corporation "Micro Datatizer". Map contour information is automatically digitized and recorded on magnetic tape as a curser is moved along each contour line on the map. Appropriate computer programs are then used to convert the contour information into a square grid with whatever resolution is desired. In the present case, a grid of 500 metre squares was constructed, each square containing the same information as in the case of the manually derived data base. This method does not require a high degree of skill on behalf of the digitizer operator. Also, all of the contour information on the original topographic maps may be used in the derivation of the data base. Somewhat surprisingly however, the time required to digitize a map in this way is comparable to that required by the manual technique discussed earlier. In addition, each scaler requires an expensive digitizing table which limits the number of maps which may be scaled simultaneously.

2.3 Current Practice

In the past year or two we have been able to obtain a considerable amount of manual scaling effort at no direct cost to ourselves. Since available funds did not permit the purchase of more than one digitizing table it was decided to proceed with the construction of larger, operational data bases using manual scaling techniques. These data bases have horizontal resolutions of 500 metres. Currently, about 150,000 square kilometres of southern Ontario have been completed (Figure 1), and a further 100,000 square kilometres is being scaled. About 300,000 square kilometres of the Maritime Provinces are being scaled as indicated in Figure 2. It is hoped that this program can continue so that a digital data base will ultimately exist for all of southern Canada.

3. Path Profiles

Path profiles were derived from the original Ottawa-area data base using interpolation techniques similar to those described by Edwards and Durkin (1969). As illustrated in Figure 3, this involves determination of distance and terrain height for each point at which the propagation path intersects the boundary of a data-base cell. In the larger data bases it has proved more convenient to interpolate terrain heights, from the nearest data base points, at constant 500 metre intervals along the great circle path between transmitter and receiver. If the propagation path lies outside the data base, the user has the option of typing in the path profile manually. In this case the program interpolates between points separated by more than 0.5 km so that the profile used for the loss calculations has points separated by no more than 0.5 km. The user is also asked to specify the average type of ground surface cover along the path.

The path profile and ground cover data are used to provide considerably more than simply a listing of terrain height as a function of distance. The latitude and longitude of the path midpoint is used to determine climate type which, when combined with empirical models based on data from experimental programs carried out within the data-base areas, is used to predict the diurnal and seasonal variability of path-loss for specified percentages of time. The percentage of water along the propagation path is determined from the ground cover codes and is also used in the determination of diurnal and seasonal variability. The ground cover codes are used to associate a conductivity and permittivity with each point along the path. These parameters are used in the determination of the magnitude and phase of signals reflected from smooth areas of terrain, as well as in the calculation of minimum effective antenna heights. The cover codes are used to determine by how much the elevation of each profile point should be increased to account for the presence of trees or buildings along the path, and the amount by which the effective radius of curvature of the ground surface should be modified when such terrain cover is present. When signal-to-noise calculations are desired, the cover codes are used to determine the levels of man-made noise.

4. Determination of Path Loss and Field Strength

At any specified point, the initial goal is to determine the path-loss which is exceeded at 50% of receiving locations in an area comparable in size to the data base resolution and which is exceeded for 50% of the time. This loss will be termed L(50,50) where the first 50 refers to location and the second 50 to time. Following this, correction factors are determined which relate L(50,50) to $L(P_1,P_2)$ which is the is the path-loss exceeded at P_1 percent of receiving locations and for P_2 percent of the time. Signal strength in microvolts at the receiver input, field-intensity in microvolts per metre at the receiving antenna, and signal-to-noise ratio are inversely proportional to $L(100-P_1, 100-P_2)$.

4.1 Calculation of L(50,50)

Ideally, solutions could be found which would simultaneously account for surface waves, reflected waves, and waves diffracted by various obstacles along the propagation path. in practice of course, this cannot be done for any but the simplest cases. Approximations are made in which the various propagation effects are treated separately and the corresponding losses are simply summed.

4.1.1 Surface Waves

Surface wave intensities are not computed since they are, in most cases, negligible. For very low antenna heights this lack is partially rectified by using effective antenna heights, rather than actual antenna heights, in the diffraction loss calculations.

4.1.2 Reflections

The user may elect to include the effects of ground reflections. In this case, the program will search for sections of terrain which are horizontal and which satisfy the geometrical criteria for reflections. The terrain surface cover information is used in the calculation of the amplitude and phase of the reflected wave. Reflections may be found from areas between successive obstacles. If more than one such area is found the interferences losses or gains of the individual areas are arithmetically summed.

4.1.3 Diffraction Losses

The diffraction loss model forms the heart of the prediction program. First, the radius of curvature of each point along the profile is determined using parabolic fits to successive sets of three profile points. Points represented by downward opening parabolas are assigned positive radii of curvature while those opening upward are assigned negative radii. The locations of obstacles are determined by a 'stretched string' technique whereby a string is imagined to be tightly stretched over the terrain between transmitter and receiver. Obstacle parameters are determined using the method of Deygout (1966). The procedure for two obstacles is shown in Figure 4. For each obstacle, the height of the obstacle relative to the line-of-sight, H; the radius of curvature of the obstacle crest, r; and the Fresnel zone radius at the location of the obstacle, R; are determined. The Fresnel zone radius is determined, in the case of two obstacles, by using the distances $d_t^{(1)}$ and $d_r^{(1)}$ for obstacle 1, and by using the distance $d_t^{(1)}$ and $d_r^{(1)}$ for obstacle 2.

Points below, but within 0.6 of a Fresnel zone of the 'string', are also deemed to be obstacles. An extension of this procedure is used in the present program for up to 15 obstacles along the path. Two basic parameters are derived for each obstacle: $\alpha = \lambda^{2/3}\, r^{1/3}/R$ and $\beta = H/R$. The diffraction loss due to each obstacle is computed as a function of α and β using an extension of the nomograms originally presented by Dougherty and Maloney (1964) and by d'Assis (1971). The nomogram used as a basis for the loss calculations in the present program is shown in Figure 5. It appears that a single nomogram may not be adequate for all cases and further work is presently under way to clarify the situation. It should be noted that exactly the same procedures are used, regardless of the nature of the terrain profile: from smooth earth to mountainous terrain.

It is important that obstacles be defined correctly. Any parts of a profile bounded by points assigned negative radii of curvature are taken to define individual obstacles. Inspection of Figure 6 reveals that while this procedure is adequate for smoothly varying (analog) profiles it can break down for digital profiles where the 'stretched string' technique may take a number of consecutive points, on what is clearly a single obstacle, to be obstacles in their own right. In the present model, the point having the largest value of β is taken to be representative of the entire obstacle.

Further problems arise in connection with multiple, non-isolated, obstacles. Figure 7a shows two well separated sharp-crested obstacles. The total diffraction loss in this case is the sum of the losses due to each obstacle. Figure 7b shows a case in which obstacles exist at the same locations, and have the same values of β, as in Figure 7a. The experimentally determined path loss over such a profile is less than the sum of the two individually calculated losses. Several criteria have been derived in the past to determine the degree of isolation of obstacles (see, for example, Rice et al. (1965), Causebrook (1974)). In the present program, α is taken as a measure of isolation. The loss due to any pair of obstacles is taken to be the sum of the individual losses, reduced by a factor $f(\alpha_m)$ where α_m is the smaller of the values of α associated with each obstacle. The function $f(\alpha_m)$ is empirically determined so as to achieve the best agreement with experiment.

4.1.4 Terrain Cover

The terrain cover codes derived from the data base, or input manually by the user, are used to add appropriate height increments to the basic terrain heights along the profile except for 1 km regions immediately adjacent to the transmitting and receiving sites where the antennas are assumed to be sited upon the ground surface. If trees or buildings are present within 1 km of the transmitter or receiver, the user may input their characteristics directly. Within these areas, signal losses through or around the trees or buildings are computed, as well as diffraction loss over the obstacles.

5. Time Variability: $L(50,P_2)$

$L(50,P_2)$, the median path-loss over a given area which is exceeded for P_2 percent of the time, is assumed to be given by the expression $L(50,P_2) = L(50,50) + \Delta L(P_2)$, $\Delta L(P_2)$ is determined in two different ways, depending upon circumstances. If the propagation path is in the Ontario data-base, empirical expressions based on long-term measurement programs carried out by CRC are used to determine $\Delta L(P_2)$. Similar measurement programs are planned for the Maritimes, and this data will be used to construct similar empirical expressions to be used for paths in the Maritime data-base. If the propagation path is not in the data-base, $\Delta L(P_2)$ is determined using the curves presented by Rice (1965) for continental temperate or maritime temperate climates.

6. Location Variability: $L(P_1,50)$

$L(P_1,50)$, the path loss exceeded for P_1 percent of receiving sites within a radius of a few hundred metres at a given time, is assumed to be given by expression $L(P_1,50) = L(50,50) + \Delta L(P_1)$. In this case, the expected standard deviation, σ, of path loss over an area a few hundred metres in extent is first computed. The distribution of path-loss is then assumed to be log-normal, and values of path-loss exceeded for any desired percentage of locations are then easily derived. For paths within the data-base a value for terrain roughness is derived for the area immediately in front of the receiver. This value is then used to compute a standard deviation σ_1 due to the terrain itself. Next, the terrain cover codes are used to determine the type of surface cover and a standard deviation σ_2, based on experiment is derived. σ^2 is then assumed equal to $\sigma_1^2 + \sigma_2^2$. For paths not in the data base a modified form of the expressions presented by Longley (1976) are used to compute σ.

7. Calculation of $L(P_1,P_2)$

$L(P_1,P_2)$ is assumed to be given by the expression $L(P_1,P_2) = L(50,50) + \Delta L(P_1) + \Delta L(P_2)$.

8. Prediction Accuracy

A number of plots showing predicted and measured path-losses over known profiles were presented by Palmer (1978). Further examples, showing predictions made using the Ontario data-base are shown in Figures 8-9. A rather different example is shown in Figure 10. This represents an idealized 200 km path over a smooth earth. The dots represent values derived from the CCIR Atlas (1955). The agreement is good up to about 120 km. Beyond that distance the signal-levels predicted by our program are higher than those predicted by CCIR because of the inclusion of tropo-scatter terms in the CRC model. The various approximations to diffraction and tropo-scatter losses are indicated by the small discontinuities in predicted signal-strength at 58 km and at 130 km.

The standard deviation of the differences between measured and predicted path-losses is about 5 dB for comparisons carried out thus far.

9. Conclusions

The terrain data base and methods of determining path-loss that are used in the CRC VHF/UHF prediction program have been described. A number of points stand out. A digital terrain data-base can provide much more information about a propagation path than just a tabulation of terrain height as a function of distance. It provides, for example, estimates of surface permittivity and conductivity, climate type, radio of land to water along the path, obstacle radii of curvature, terrain cover height, path-loss variability due to both terrain and terrain cover, and man-made noise levels. All of this information is necessary for the accurate calculation of path loss and its variability. Some of the problems associated with identification of single obstacles, and due to the discrete nature of path-profile, have been discussed. Overall, it has been found that Deygouts' method of obstacle determination is accurate and well suited to machine calculation provided that care is taken to adequately define and account for large, non-isolated obstacles. There are many aspects of the program which still require refinement. These include refinement of some subtle features of obstacle identification, calculation and verification of the spatial and temporal variability of path loss, and the data output displays.

10. References

CAUSEBROOK, J.H., 1974; "Computer Prediction of U.H.F. Broadcast Service Areas", BBC Engineering Research Report BBC RD 1974/4.

CCIR, 1955; "Atlas of Ground-Wave Propagation Curves for Frequencies Between 30 Mc/s and 300 Mc/s", ITU, Geneva.

D'ASSIS, M.S., 1971; "A Simplified Solution to the Problem of Multiple Diffraction over Rounded Obstacles", IEEE Trans. Ant. and Prop., AP-19, 292-295.

DEYGOUT, J., 1966; "Multiple Knife-Edge Diffraction of Microwaves", IEEE Trans. Ant. and Prop., AP-4, 480-489.

DOUGHERTY, H.T. and L.J. MALONEY, 1964; "Application of Diffractions by Convex Surfaces to Irregular Terrain Situations", Radio Science, 68D, 239-250.

EDWARDS, R. and J. DURKIN, 1969; "Computer Prediction of Service Areas for V.H.F. Mobile Radio Networks", Proc. IEE, 116, 1493-1500.

LONGLEY, A.G., 1976; "Location Variability of Transmission Loss-Land Mobile and Broadcast Systems", U.S. Office of Telecommunications Report 76-87.

PALMER, F.H., 1978; "The CRC VHF/UHF Propagation Prediction Program: Description and Comparison with Field-Measurements", AGARD Conference Proceedings No. 238, 'Operational Modelling of the Aerospace Propagation Environment', pp. 49-1 to 49-14.

RICE, P.L., et al., 1966; "Transmission Loss Predictions for Tropospheric Communication Circuits", Vols. I and II, National Bureau of Standards Technical Note 101.

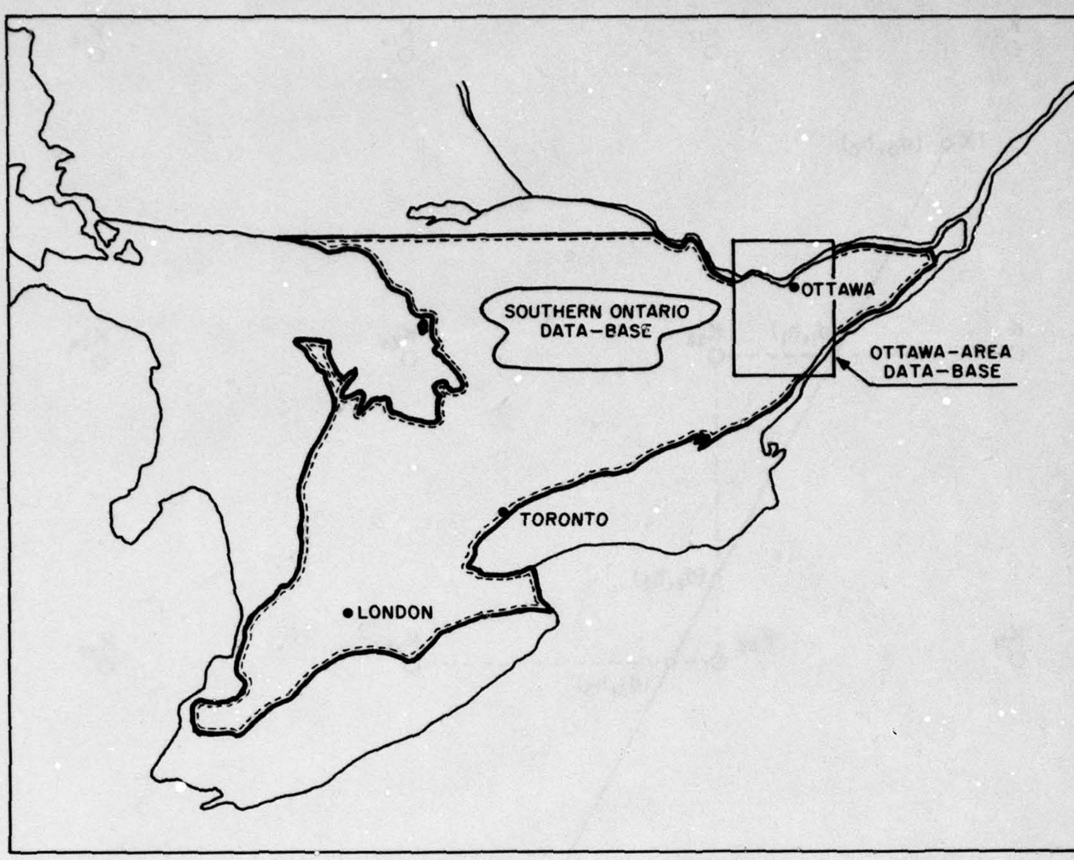

Fig. 1 Extent of the southern Ontario data base.

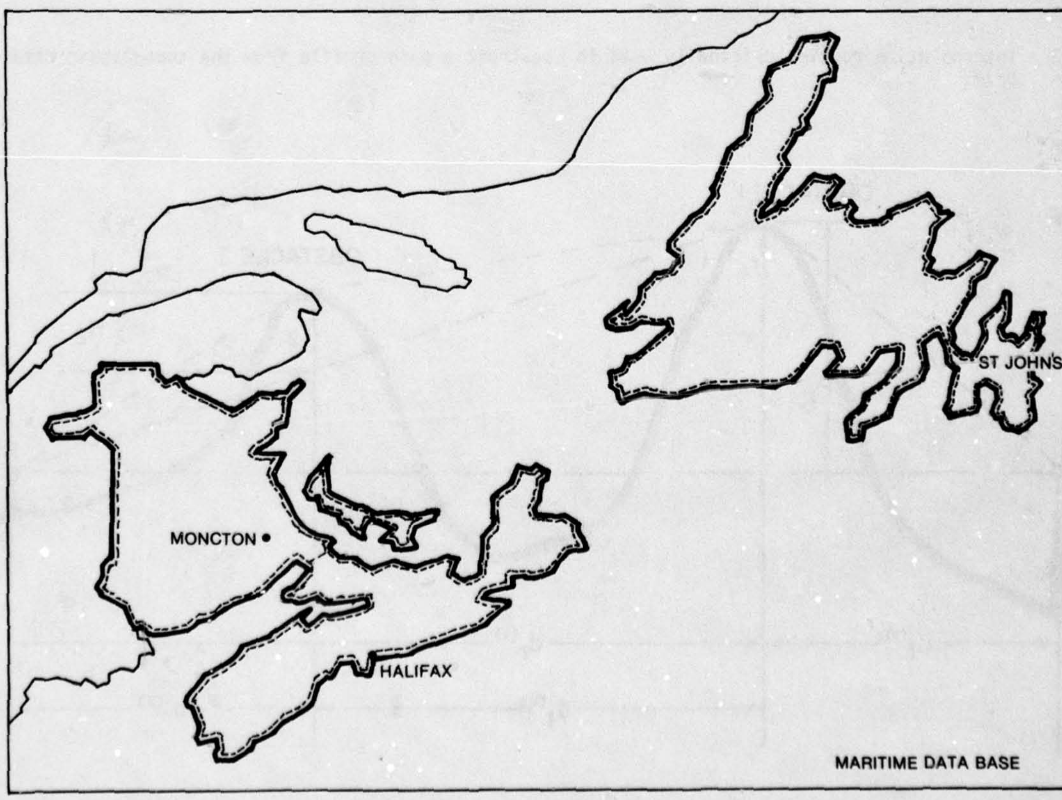

Fig. 2 Extent of the Maritime Provinces data base.

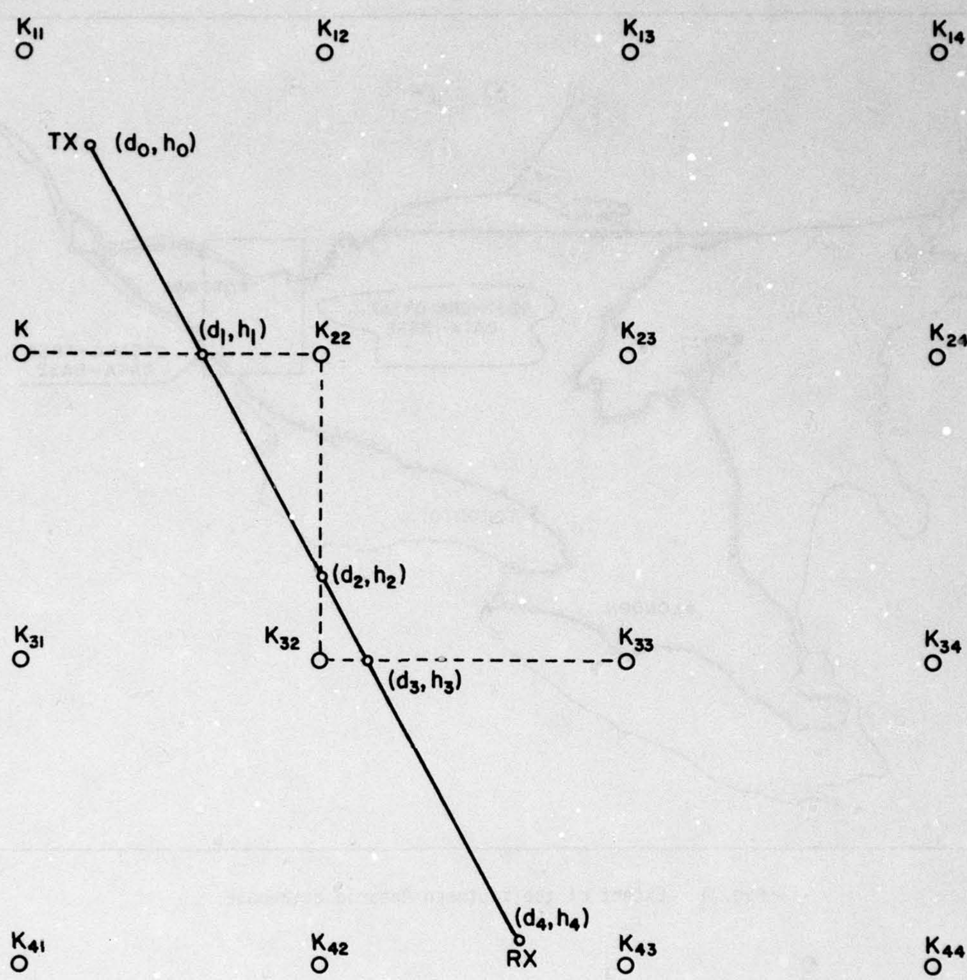

Fig. 3 Interpolation routine originally used to construct a path profile from the topographic data base grid.

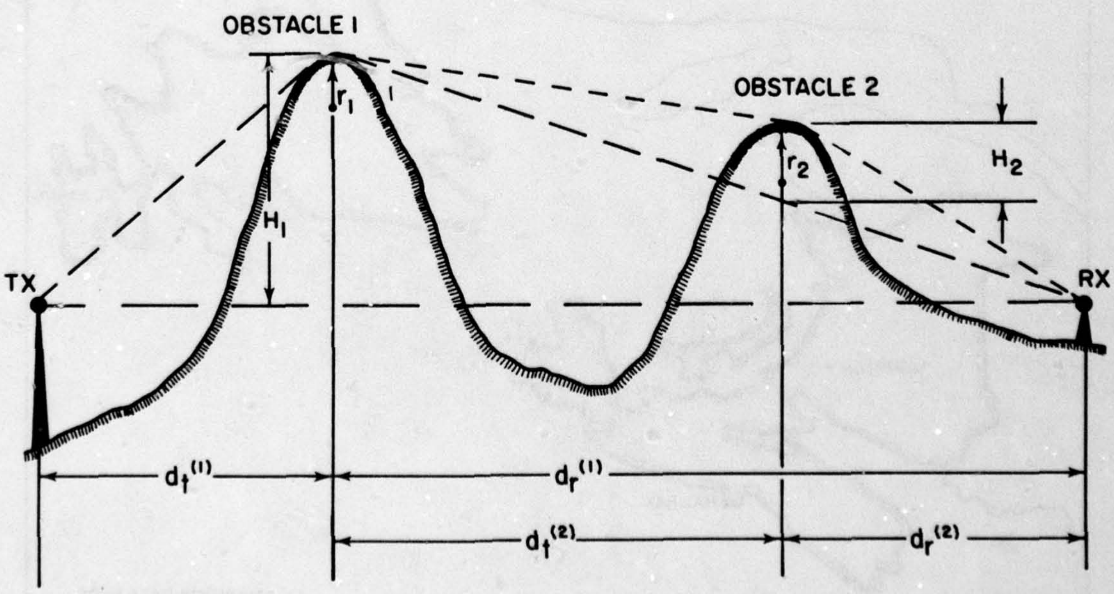

Fig. 4 Geometry used to determine obstacle parameters in the determination of total diffraction loss over a path.

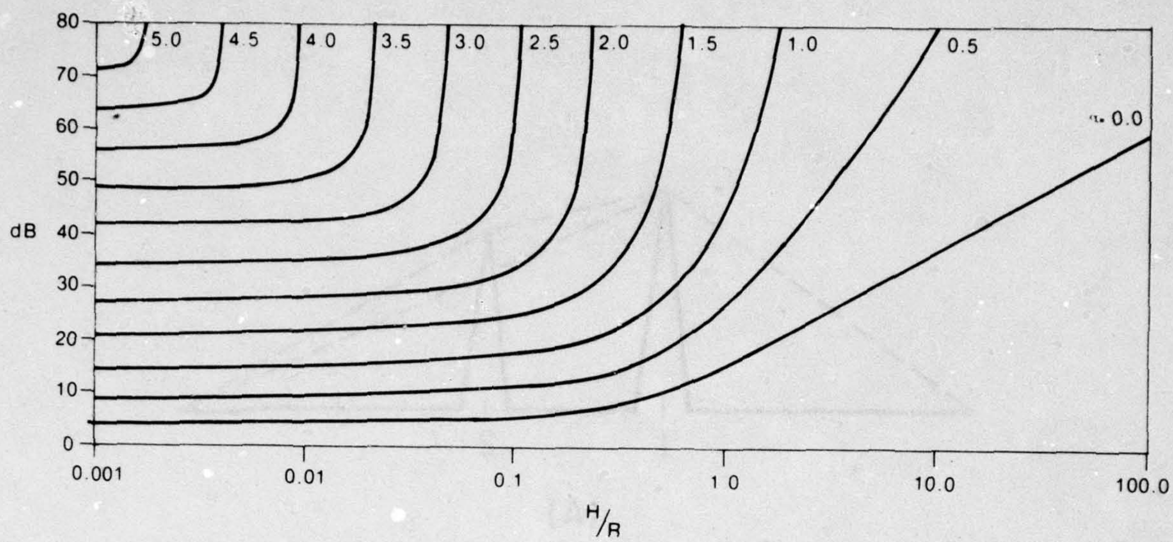

Fig. 5 Nomogram used to determine diffraction loss, for non-line-of-sight paths, in terms of the parameters α and β = H/R.

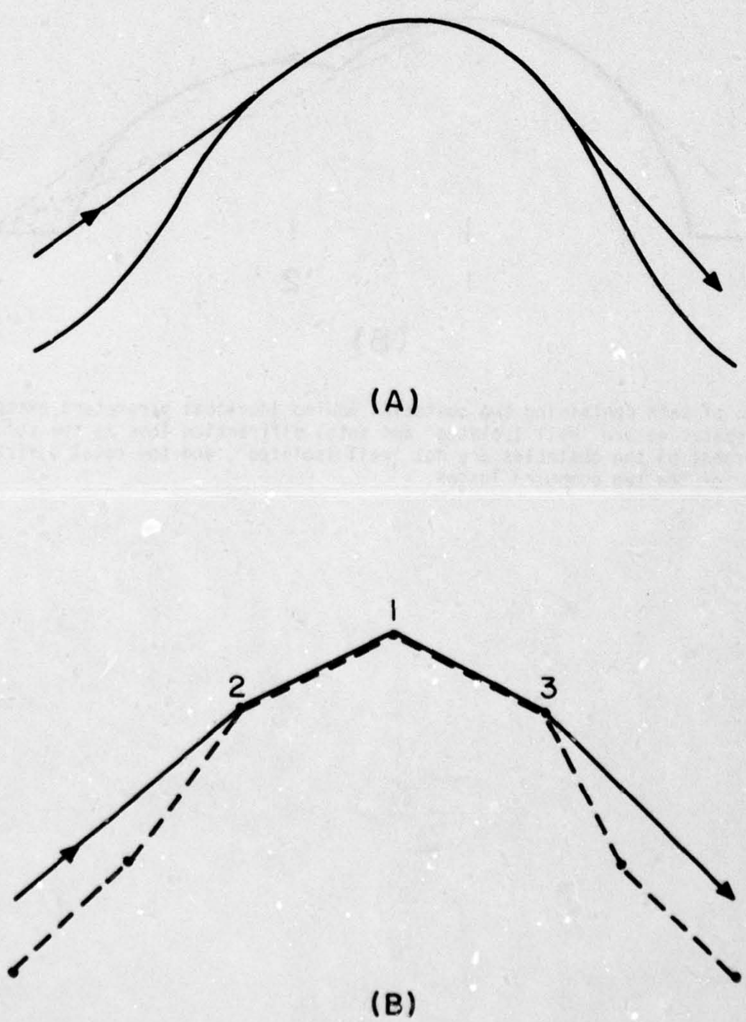

Fig. 6 Illustration of the differences between analog and digital representation of obstacles.
a) analog b) digital

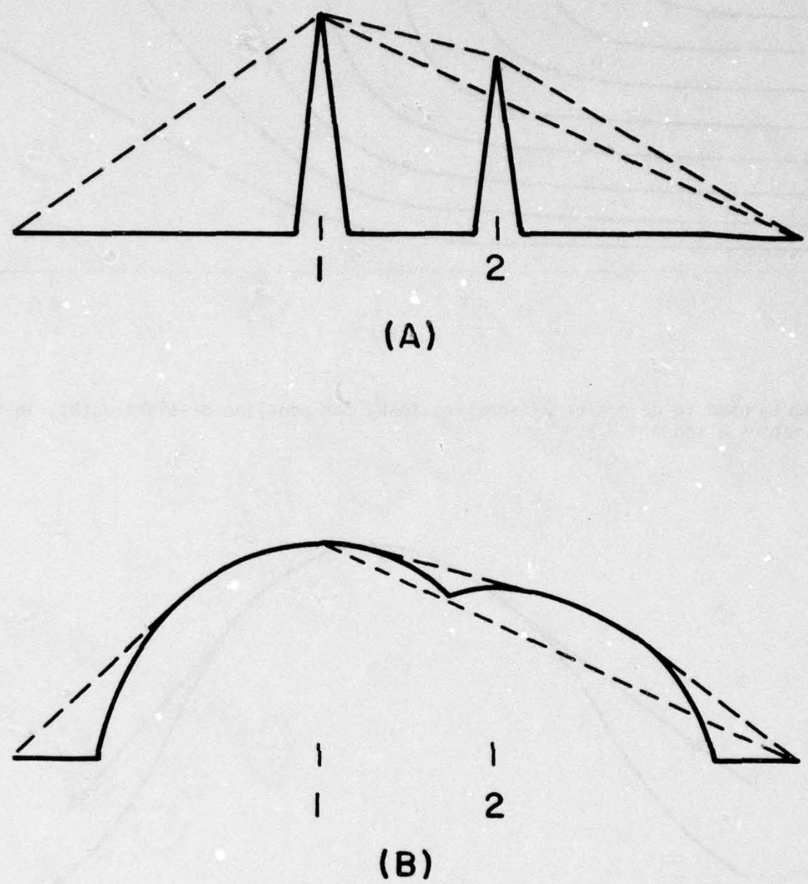

Fig. 7 Illustration of path containing two obstacles having identical parameters except for values of α. a) the two obstacles are 'well isolated' and total diffraction loss is the sum of the two computed losses; b) the obstacles are not 'well isolated', and the total diffraction loss is less than the sum of the two computed losses.

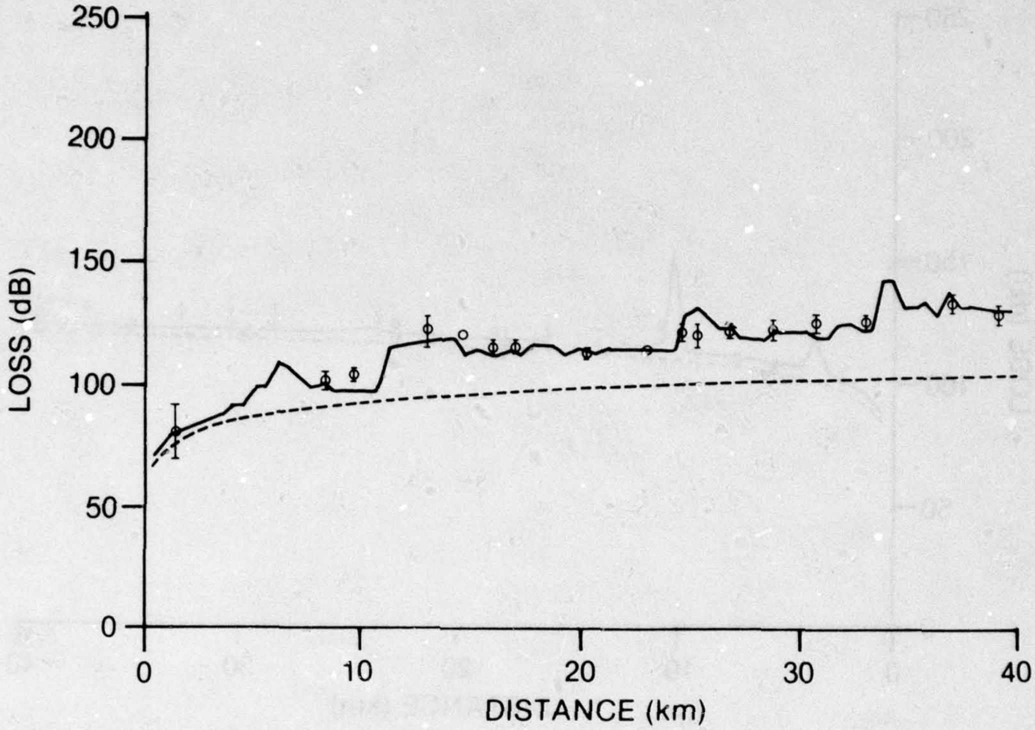

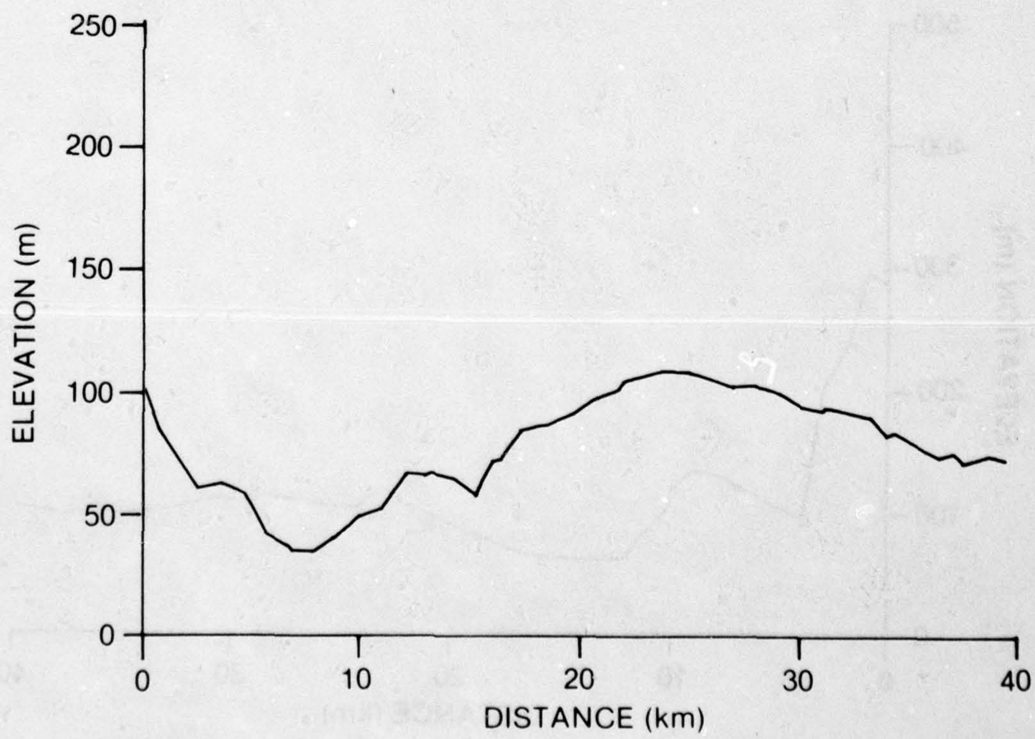

Fig. 8 *Terrain and path-loss profiles as a function of distance from a fixed transmitter.* Frequency: 88 MHz; HTX: 45 m; HRX: 7 m. Circles represent measured median values of path-loss; bars represent the standard deviation about the median for a series of measurements within a 100 metre distance increment.

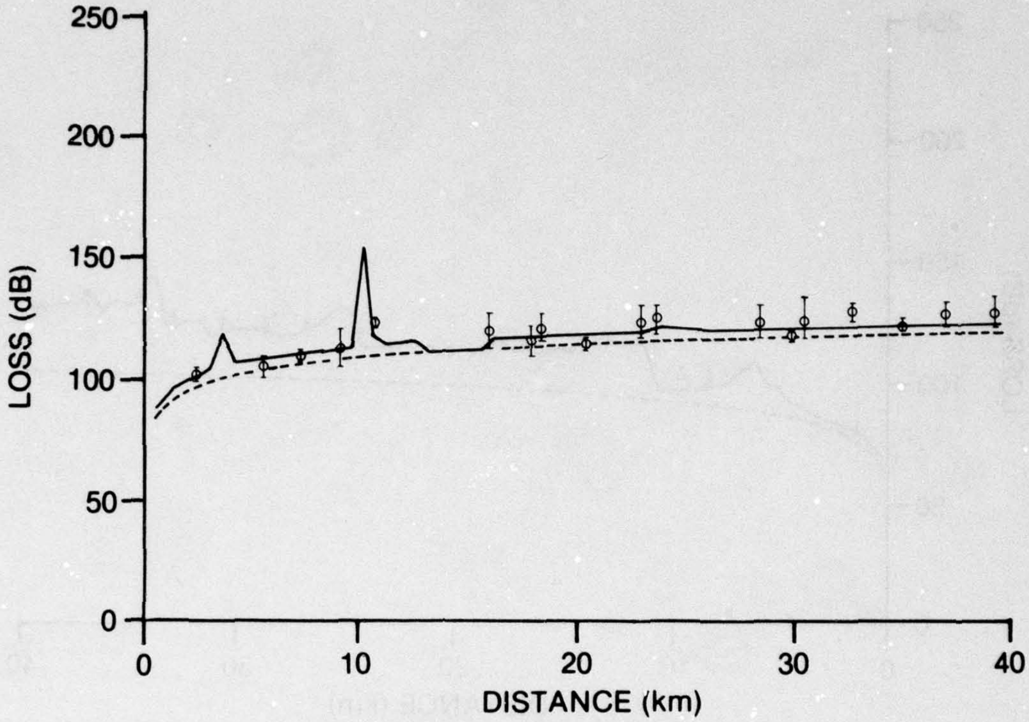

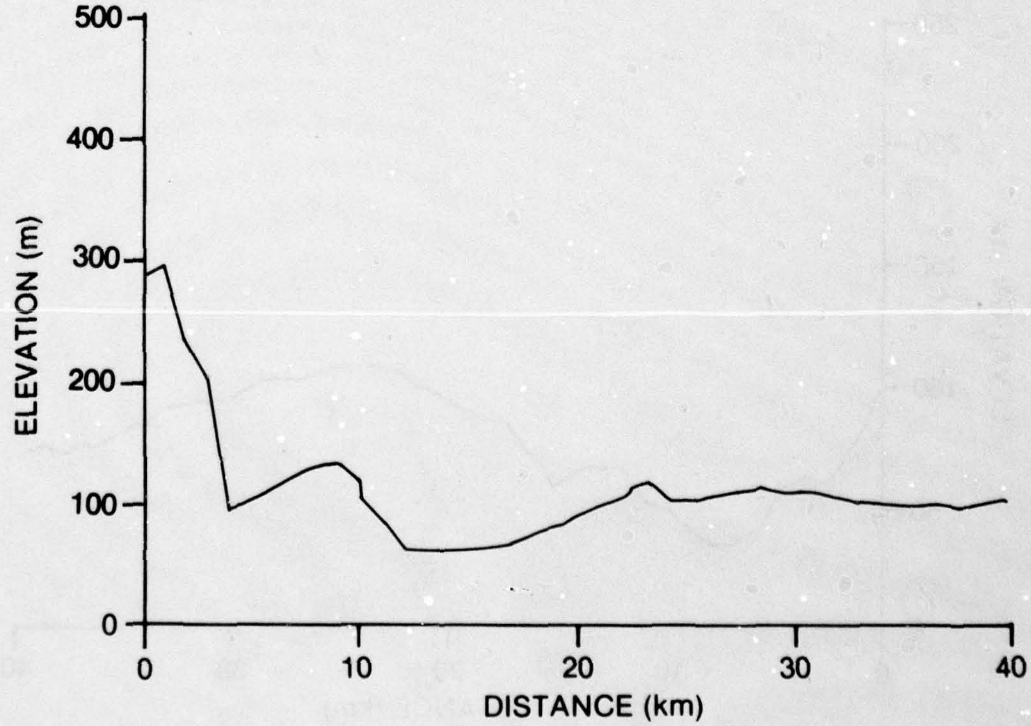

Fig. 9 Terrain and path-loss profiles as a function of distance from a fixed transmitter. Frequency: 572 MHz; HTX: 142 m; HRX: 7 m. Circles and bars have same meaning as in Figure 8.

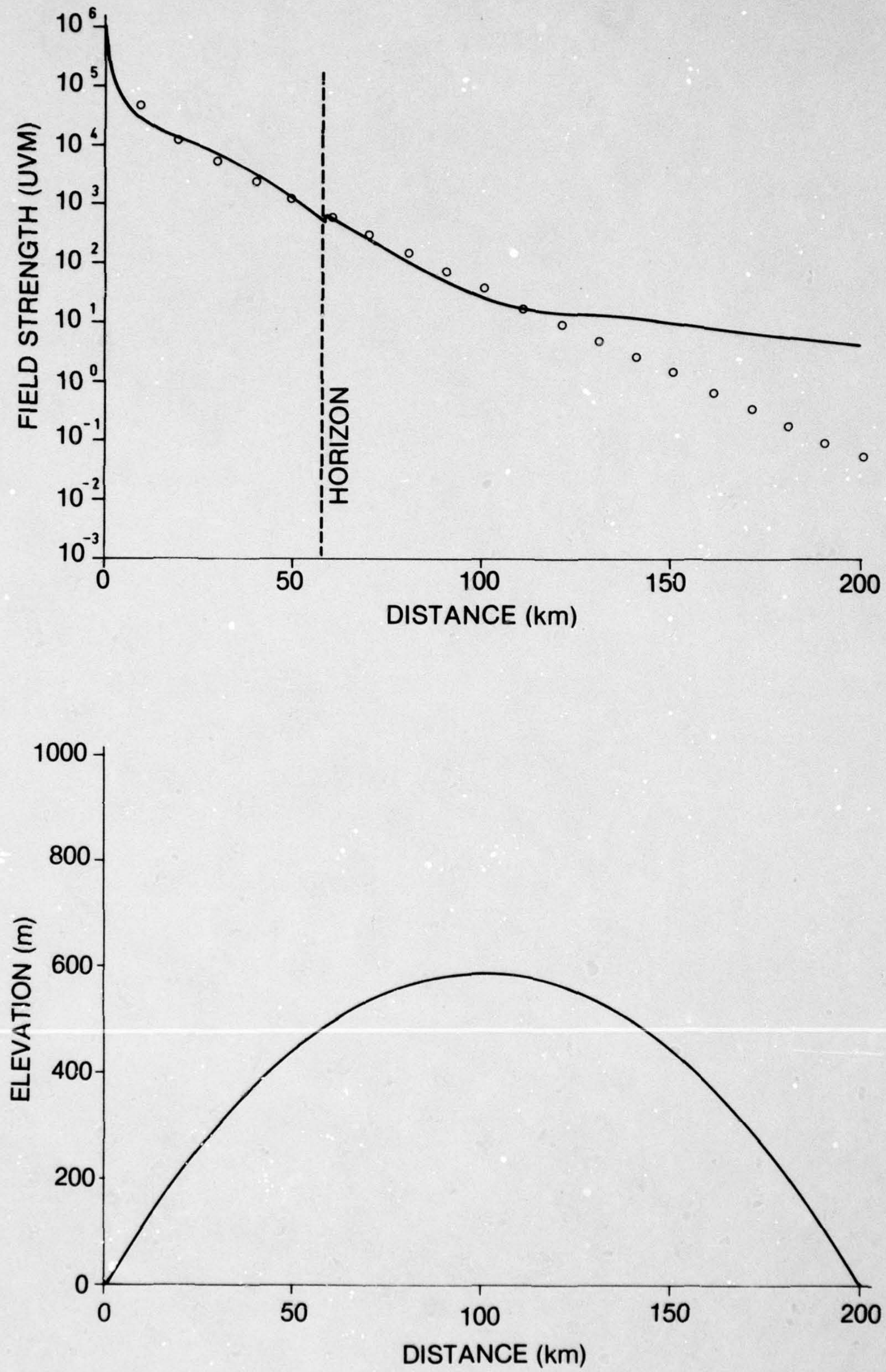

Fig. 10 Terrain and field-strength profiles as a function of distance from a transmitter situated above an idealized smooth earth. Frequency: 200 MHz; P_T: 2500 W; HTX: 50 m; HRX: 50 m. The solid line represents signal strength computed using the present model while circles represent values derived from the CCIR Atlas (1955). The two estimates of signal strength diverge beyond 100 km because of the lack of a tropo-scatter term in the CCIR model.

SESSION IV ROUND-TABLE DISCUSSION

ON

METHODS OF DIGITAL TERRAIN MAPPING

Participants at Round Table: H.J.Albrecht (Chairman)
J.S.Belrose
L.B.Felsen
L. Hoivik
F.H.Palmer

By way of introduction, H.J.Albrecht presented the following list of topics suggested as general guideline for the discussion:

1. State of the art
   1.1 Data Selection
   1.2 Methods of data collection

2. Further advancement and trend
   2.1 Additional data
   2.2 New methods of data collection

3. Application in electromagnetic wave propagation
   3.1 General theoretical aspects
   3.2 Path-loss predictions
   3.3 Terminal surroundings
   3.4 Other areas

He illustrated the significance of sufficient knowledge on terrain characteristics with regard to the relevant propagation mechanism. Particular reference was made to terrestrial line-of-sight paths and those depending on diffraction. Ground reflections may have to be considered with ionospheric propagation paths. Detrimental reflections and scattering from terminal surroundings were mentioned for all possible paths, including those using scattering in various regions of the atmosphere, as well as satellite links. Some specific difficulty of predicting terrain effects is indicated if undesired paths are considered. Continuing, H.J.Albrecht commented on meteorological variations and those caused by vegetation on the ground which lead to the question, whether and to what extent such information could be fed into a digital terrain map. Under certain geographical and seasonal conditions, meteorological effects, such as inversion layers, may occur so regularly that they may be taken into account accordingly. This would point towards a possible area of future improvement.

Returning to the state of the art, L. Hoivik referred to the quality of map material available today. Most maps have been produced from stereo-photographs or from older conventional maps; they do not always meet the standard desired. The present situation of selection and collection of data is illustrated by various methods and the availability of modern machines has to be considered. They are designed to generate maps in an automatic or semi-automatic fashion. Most of these machines use a line-following device on a conventional map and digitize the information automatically, with all the errors contained in the original map. Another method is represented by the manual extraction of data. There is a plan to approach the problem more directly, either by using stereo-photographs and digitize them directly, at the same time processing and compensating for errors as far as possible, or, even better, by utilizing directly appropriate radar information gathered by a plane flying over the terrain.

Referring to the situation in Canada, F.H.Palmer confirmed that the manual extraction of data is, presently, the main method, perhaps doing it twice to check on the data so obtained. He added that the plans already mentioned are promising although they could only be carried out by rather expensive methods, as compared to the manual methods employed so far. But automatic systems seem to represent the future approach of preparing digital terrain maps for large areas. J.R.Delaney reported on experience gained from using data produced by automatic and semi-automatic machines, such as line-followers and those using stereometry. Although errors may not be caused by operators, they do exist and may be produced, for example, by methods employed to extract data from contours or by the inevitable data interpolation.

Returning to the general question of reliability, H.J.Albrecht mentioned vegetation effects on long-term reliability as an example, and the difficulty of taking into account the planned use of farm land, as had been indicated in one of the papers presented during the session. Thus it is very difficult to predict such changes to a digital terrain map. The existence of this serious problem was confirmed by F.H.Palmer. He and L.Hoivik commented on the detrimental effect of a variable snow cover, perhaps not so pronounced on VHF-frequencies but more on higher frequencies. Referring to the actual use of the data map, F.H.Palmer added that conditions may not be as critical where position and characteristics of single elements, such as trees and buildings, do not have to be known exactly, for example for mobile and broadcasting communication systems if compared to the situation existing with point-to-point links. Thus the question of updating a data base should be connected to the application envisaged. H.J.Albrecht suggested to possibly assess categories of reliability with respect to various services which could be used as a reference for this purpose, e.g. one-to-one or many-to-many communication links.

Continuing on the subject of requirements for digital data maps, L.Boithias commented that, in general, such studies are made to determine the coverage of broadcasting transmissions as well as that of the central transmitter in a mobile network. The problem may be simpler in the latter case if the field-strength should be known only with respect to a threshold value. On the other hand, it is important to distinguish between conditions in built-up and in country areas. L.Boithias then drew attention to a method used in France, which perhaps could not be employed generally, but may be of interest: a relief map of the area concerned is illuminated by a small lamp simulating the position of the transmitter location and a photograph of the entire image then indicates the transmission coverage.

Addressing the question of optimum resolution, L.Boithias asked whether the 500m-steps frequently referred to represent an agreed or even a standardized method. He suggested that the optimum value ought to be discussed. L.Hoivik commented on higher accuracies being desirable for radar applications, as compared to communication requirements. Referring to this subject and to experience gained in the Ottawa area, F.H.Palmer reported that the 500m-resolution gave results similar to the one using 1 km-steps, yet there were areas which did not model sufficiently well with the 1 km-resolution. He then suggested that data bases perhaps may best be constructed with a variable resolution depending upon the type of terrain and application, varying from perhaps 5 kms to 100 m, if necessary.

Commenting on applications generally, H.J.Albrecht added that data bases are not only produced for purposes connected with the field of electromagnetic wave propagation, they may also be used for entirely different applications, such as road engineering etc.. The maps would then have to be considered a compromise tool.He referred to possible further progress in the whole area, mentioning that the more real-time the maps would be, the better for the applications, thereby commencing the discussion on the second category of topics.

With regard to the problem of real-time updating, J.R.Delaney pointed out that, at least for agricultural information, vegetation, snow cover, etc., the known automated methods do not appear to be adequate, thus leaving the manual ones as the only possibility, even for years to come. An additional problem may then be the fact that the number of appropriately skilled people is limited. It would probably be difficult to update digital maps on a real-time basis, even for a small part of the globe.

Referring to radar applications, G.E.Carlson drew the attention to the additional importance of scattering characteristics of terrain. Although a large quantity of data has been collected, the information is not standardized, nor is it comparable. He emphasized that further studies ought to be directed at these aspects. This was supported by F.H.Palmer who again addressed the probable usefulness of a data base with variable resolution but he felt that more work would have to be done with regard to the optimum resolution to be applied, depending upon the actual use. L.Hoivik pointed out that, as in the case of the Norwegian data base, a limiting factor may be the man-power available to extract data, another one may be the computer capability of handling the data. He expressed the opinion that advances will be directed at automatic devices if data are stored in the form of images with much higher data density.

Summarizing sections 1 and 2 of the round-table discussion, H.J.Albrecht mentioned that the value of digital data maps appears to be well-established in general planning and similar use, yet questionable in quite a number of applications. This fact then represented a suitable introduction to the third category of topics, the general aspects and details of applications in the field of electromagnetic wave propagation.

With respect to some of the theoretical questions, L.B.Felsen remarked that this topic may best be commented upon in three parts, first addressing theoretical questions like a theoretician, secondly trying to comment on some of the implications of the theory on the computer, and finally, to see how one translates the results of the theory for the real world; the latter area may cause some problems but this is where this meeting hopefully could contribute something. Dealing first with theoretical questions, some reference may be made to a round-table discussion on surface characteristics some three years ago (AGARD-EPP meeting on EM propagation characteristics of surface materials and interface aspects, Istanbul, 1976, AGARD-CP-208, round-table participants: J.S.Belrose, A.W.Biggs, L.B.Felsen, E.Raschke, and H.J.Albrecht) and looking at the purely theoretical aspect, not much has changed. At that time, the validity or otherwise of the impedance condition was debated, and it is still being debated, and the same caution is still called for when addressing it.Yet, this question may change to a purely academic one if interpreted in terms of the third part of this comment, the implications for the real world.

L.B.Felsen continued that, in general, if one does use a model, it should be reasonably well justified. In terms of theoretical models, a number of different contributions were presented during the meeting, there was the integral-equation type of model based on the compensation theorem, as well as the model based on the local modal expansions with asymptotic evaluations, and also one using a GTD model (geometric theory of diffraction. All of these models seem to work under various circumstances and some of them would be complementary to one another. All of them may have their relative advantages and disadvantages. Regarding their implementation, an important step forward can be reported since the meeting three years ago, namely with respect to workable computer programmes. This is illustrated by the three model categories mentioned. It now appears to be important to see which computer programme is more efficient than another one.

With regard to perhaps one of the most difficult problems the theoretician has to deal with, L.B.Felsen mentioned the question of optimum application of the results yielded by a good theory and a good workable computer programme. As an example, if it is required to predict path loss over a certain terrain, the question would be what data would have to be fed into the programme. Any chain of calculations, any kind of system approach is only as good as the poorest data fed into the programme. Thus there appears to be little point in having a highly sophisticated theoretical model and a very good computer programme if the data available is very poor. With regard to computer programmes, it should be emphasized that it is not only necessary to have a programme per se but one should also know how good it is. An error estimate is necessary, going along with the programme. Often computer outputs are used as references and thus knowledge on their errors is all important. Returning to the digital data bases of the type discussed at this meeting, L.B.Felsen then addressed the problem of coupling such data into the computer programme, and again emphasized the question of the accuracy to be expected and also, how good the theory should be to be compatible with that data. He stressed the need of some sort of standardization, involving all contributors to such programmes, those collecting terrain data, those responsible for theoretical models, as well as the people producing the computer programmes. The objective should then be to come up with a sequence of realistic test problems which could then be tried by the various techniques.

Enlarging upon the subject of application-oriented types of digital terrain maps, J.S.Belrose pointed out that, in principle, different types are needed for the field-strength prediction of the far field, for purposes of television or FM-coverage or radar coverage, and, on the other hand, for near-field characteristics, such as the effects of high-rise buildings, power lines and other structures on the directional pattern of medium-frequency antennas or on TV-ghosting or on the effects of the local terrain on instrument landing systems used in aircraft. For the latter category, an actual map is not required, in other words, the basic concept is not that of producing a map with a grid or contours or some other standard mapping procedure. In the case of near-field problems, an exact knowledge is necessary on the position of structures, and the exact dimensions. Thus the data are also digital but it is not digital terrain mapping. Such considerations are directly connected to the application in mind. J.S.Belrose then continued with comments extending the analysis concerning the medium-frequency re-radiation problem. Using the example of calculations done on a power line and on the effects of that power line on the pattern of antennas, he pointed out that the basic programme is actually a wire-grid modelling programme. Buildings can be analysed by that approach. Such a type of analysis can be extended to include losses to better represent the conditions in the real world. It is a question whether or not discontinuities in conductivity can be included, an example being a monopole on a radial ground screen sitting on top of a lossy earth which is contoured. This example may seem to be somewhat of a horrendous problem but it is typical of pattern distortion due to objects sitting on a finitely conducting earth.

Commenting on the warning of using computers to solve the problems, L.Hoivik added that an additional difficulty may arise from differences between maps on the basis of projections which cannot always be joined one to the other since there may be distortions; it is important to keep such limitations in mind when using computers for data evaluation. R.W.Lorenz referred to differences in digital terrain mapping procedures, for example the method used in Germany and other approaches, with geographical coordinates being employed to define elements in five arc-sec steps, as compared to 500 m-steps of other methods, with the advantage of easier calculations for path predictions. Adding to this aspect of coordinates, L.Hoivik emphasized that the situation in Norway requires all data to be in geographical coordinates due to the geographical expansion of the country.

L.Boithias added that it may be advantageous to establish a table which lists the service in mind, the frequency band, the accuracy required, the extension of the area under consideration, etc. It appears that frequencies of one-meter wavelength or shorter are usually considered when discussing digital maps, although other frequency bands are of course possible. The maps are also applicable for radar coverage but here the problem is different; perhaps it could not be dealt with by digital maps. He also emphasized the problem of coordination in communication, between terrestrial and other stations in the same frequency band, with particular regard to the possible interference between them. This enormous task should be studied by means of computers. Digital maps may be especially useful but maps of 1000 km radius may be needed and frequencies up to several GHz would have to be considered. In addition to the requirement of assessing the parameters and the required accuracies as a function of service, frequency and other relevant characteristics H.J.Albrecht mentioned as another major objective that such questions ought to be clarified first, rather than producing the maps first and then try to use them for various applications. It should also be avoided to seriously use a few comparative measurements which are not significant statistically but may demonstrate an extremely good agreement with a one-to-one or point-to-point link, yet may show disagreeing results when employing the same link and the same data map after some time has elapsed, with perhaps some snow cover or other changes having occurred in the meantime.

Returning to his earlier comments, L.B.Felsen recalled that the overall evaluation is only as good as the weakest link but that this does not mean that each link in the chain should not be developed as well as it is possible. Referring to the actual situation, it seems that certain theoretical models have now been pushed to a point of implementation enabling one to make numerical calculations with computer programmes that are reasonably efficient. Thus what is now needed is better data to feed in and, without it, not

much progress is anticipated. Confirming the opinion that the data ought to be carefully assessed, categorizing important and less important data, L.B.Felsen added that this could also optimize the data collection process. The theoreticians are now in a position to make reasonably good predictions if they are given reasonably good data, and further improvement is indicated. For best results, however, the data collection process and the data feeding process have to be clearly coordinated with the theoretical requirements. He proposed a joint approach to set up a number of test cases to see where the concentration has to be such that the overall process is optimized.

Jin au Kong commented on the view expressed on electromagnetic wave propagation models and classified the problems into categories as a function of altitudes: the communication links using line-of-sight paths and mobile communications are of low altitudes with ground-wave, surface-wave, and diffraction effects being important. On the other hand, with high altitudes and remote sensing problems, ground effects are not as crucial to the theoretical and experimental results. Thirdly, there are the intermediate communication and remote sensing problems. In other words, the communication applications refer to transmission problems and remote sensing with the use of radiometers and radar may be described by back-scattering problems. He pointed out that, for high altitude remote sensing applications, a digital map should contain topographical information, the slopes and the heights with a resolution corresponding to that of the sensors. With remote sensing, finer grids would be required for sensors featuring higher resolution than for radiometers or radar where the resolution could be much poorer and yet provide useful information. From that point of view, the purpose of a digital map would be to predict the features, e.g. the vegetation cover or the change of the vegetation cover. The updating of the digital map perhaps could be accomplished by a single or a few surveying flights over the area. It could be imagined that a digital map of such kind, in addition to the topographical information which is not normally a variable, could be used for predictions. Some variation may of course occur, for example, due to the development of an urban area. Features could also be predicted from a theoretical point of view if a good topographical map can be made with an additional set of parameters such as a theoretical model which describes some statistical properties pertaining to the area, like the correlation length, a possible correlation function characterizing the media involved at any given time. Then, the variation of that area could be predicted. Also, if the results check with a model verified from both, the theory and the experimental point of view, the resulting information can be used to extract features from unknown areas for a flight just by providing the topographical information. Summarizing, a digital map which correlates to the theoretical modelling in a remote sensing area could be used to provide information on unknown areas, thus assessing a vegetation cover or a snow cover.

R.F.Checcacci referred to some of the papers presented during the meeting and pointed out that the objective may be to compute the energy which is transferred from the transmitter to the receiver but of importance is also the scattered energy from obstacles, particularly in the future. Enlarging upon this point, he added that with an increasing number of transmitting links in an area, the possibility of interference has to be taken into account, in other words, the scattered energy from one link to the other. C.E.Dadson expressed the opinion that some users of a data base and the computer programmes mainly want an output in plotted form and that they may not be interested in very accurate data on signal levels or field-strength. They are only interested in whether their signals are going to be good or bad or whether a particular area requires special attention. In other words, one has to make sure that things are not going to become too sophisticated for the actual use of the work. Responding to this comment, L.B.Felsen agreed that this attitude may be applicable in some cases. If, however, radio waves are to be used for navigational purposes, for ranging and similar applications, perhaps more precise information is required. It always depends on the user that uses the medium. Again it is important to specify what the needs are and to try to match the tools to the needs, and this seems to be the key to further progress.

Commenting that all areas mentioned in the suggested guidelines had been discussed at reasonable length, H.J.Albrecht invited the participants at the round table to sum up their opinions. In his concluding remark, L.Hoivik emphasized that, regardless of the opinions expressed on the usefulness of digital terrain maps and on the limitations to their applications, such maps will be produced and will be available, and that it is then necessary to use these maps to the fullest extent. Addressing the theoreticians, L.B.Felsen added that, at this stage, it seems most important to ascertain what is the minimum type of data that is needed in order to get out certain - what is regarded as critical - information and this may perhaps influence the manner in which the data should be collected. Of course, it is possible to collect data uniformly across the board, however, this may not serve the needs as well as if one knew where to concentrate. F.H.Palmer also referred to the fact that these data bases will be constructed and commented that they should be used to the best but the requirements of the various uses ought to be kept in mind. He added that degraded data bases, e.g. as far as resolution is concerned, may be far more economical than trying to use the complete versions that will exist. J.S.Belrose commented on the importance of re-radiation with particular regard to the near-field environment. In his final remarks, and in an attempt to "summarize the summarizing conclusions", H.J.Albrecht expressed the opinion that the applicability of digital terrain maps is possible and has been proved in many areas if tied to the appropriate application, yet there are also areas where they have to be employed with considerable caution, "cum grano salis".

ELECTRIC FIELD COMPONENTS IN PRESENCE OF A SEA-SEA BOTTOM INTERFACE AT ELF

Giorgio Tacconi
Italian National Research Council-CNR
and
University of Genova

SUMMARY

Electromagnetic waves at the Extremely Low Frequencies range, ELF, show a high penetration power in to dissipative media, like sea water or geological layers. Those signals clearly obey the Maxwell equations and, because of the order of magnitude of their wave lengths, namely the relative skin depth, can be used for practical applications in structures like sea water and any other geological scenario. The inherent possibility of transferring informations from one layer to another can be used either for communications or for evaluate the presence and the sizes of the geological structures namely interfaces between two media, i.e. sea - bottom. The paper, after a conceptual theoretical recall, shows a collection of computed curves of the electric field ρ component E_ρ, ϕ component E_ϕ and relative phase versus distance, for a selection of bottom depths and frequencies, in the sea. Such theoretical exercise is validate by some experimental results also presented in this paper.

1. Some theoretical recalls

The electric field component of an infinitesimal horizontal dipole in a conducting half space has been studied by several authors. Referring to the scenario in Fig. 1 three cases are herewith recalled for the calculation of the electric field components.

i) $\delta \ll \rho \ll \lambda_0$ and $z + h \ll \rho$ (Banos and Wesley, 1953)

$$E_\rho = \frac{Idl}{2\pi\sigma} \cdot \frac{e^{-\gamma_1 (z+h)}}{\rho^3} \cos\varphi \tag{1}$$

$$E_\varphi = \frac{Idl}{2\pi\sigma} \frac{e^{-\gamma_-(z+h)}}{\rho^3} 2 \sin\varphi \tag{2}$$

$$E_z \cong 0 \tag{3}$$

ii) $z = h = 0$ and $\rho \ll \lambda_0$ (J.R. Wait, 1961)

$$E_\rho = \frac{Idl}{2\pi\sigma} \frac{1 + (1+\gamma\rho)e^{-\gamma_1 \rho}}{\rho^3} \cos\varphi \tag{4}$$

$$E_\varphi = \frac{Idl}{2\pi\sigma} \frac{2 - (1+\gamma\rho)e^{-\gamma_1 \rho}}{\rho^3} \sin\varphi \tag{5}$$

$$E_z \cong 0 \tag{6}$$

iii) for the remaining area

$z \neq h \neq 0$ and $\rho \simeq \lambda_0$ (von Aulock, 1952)

$$E_\rho = \frac{Idl}{4\pi\sigma} \left\{ \left[\frac{\partial^2}{\partial_\rho^2} - \gamma^2 \right] \left[\frac{e^{-\gamma\sqrt{\rho^2+(z-h)^2}}}{\sqrt{\rho^2+(z-h)^2}} + \frac{e^{-\gamma\sqrt{\rho^2+(z+h)^2}}}{\sqrt{\rho^2+(z+h)^2}} \right] - \right. \tag{7}$$

$$\left. - \frac{2}{\rho}\frac{\partial}{\partial_\rho} \left[\mathcal{J}(\rho\ (z+h) - \frac{e^{-\gamma\sqrt{\rho^2+(z+h)^2}}}{\sqrt{\rho^2+(z+h)^2}} \right] \right\} \cos\varphi$$

$$E_\varphi = -\frac{Idl}{4\pi\sigma} \left\{ \left[\frac{1}{\rho}\frac{\partial}{\partial_\rho} - \gamma^2 \right] \left[\frac{e^{-\gamma\sqrt{\rho^2+(z-h)^2}}}{\sqrt{\rho^2+(z-h)^2}} + \frac{e^{-\gamma\sqrt{\rho^2+(z+h)^2}}}{\sqrt{\rho^2+(z+h)^2}} \right] - \right. \tag{8}$$

$$\left. - \frac{2\partial^2}{\partial_\rho^2} \left[\mathcal{J}(\rho\ (z+h) - \frac{e^{-\gamma\sqrt{\rho^2+(z+h)^2}}}{\sqrt{\rho^4+(z+h)^2}} \right] \right\} \sin\varphi$$

$$E_z = \frac{I dl}{4\pi\sigma} \left\{ \frac{\partial^2}{\partial z \partial \rho} \left[\frac{e^{-\gamma \sqrt{\rho^2 + (z-h)^2}}}{\sqrt{\rho^2 + (z-h)^2}} + \frac{e^{-\gamma \sqrt{\rho^2 + (z+h)^2}}}{\sqrt{\rho^2 (z+h)^2}} \right] \right\} \cos\varphi \tag{9}$$

$$\mathcal{S}[\rho, (z+h)] = \frac{\gamma}{2} \left\{ I_0 \left[\frac{\gamma}{2} \left(\sqrt{\rho^2 + (z+h)^2} - (z+h) \right) \right] K_1 \left[\frac{\gamma}{2} \left(\sqrt{\rho^2 (z+h)^2} + (z+h) \right) \right] \cdot \right. \tag{10}$$

$$\cdot \left[\frac{z+h}{\sqrt{\rho^2 + (z+h)^2}} + 1 \right] - \left[I_1 \ \frac{\gamma_1}{2} \left(\sqrt{\rho^2 + (z+h)^2} - (z+h) \right) \right] K_0 \cdot$$

$$\left. \cdot \left[\frac{\gamma}{2} \left(\sqrt{\rho^2 + (z+h)^2} + (z+h) \right) \right] \left[\frac{z+h}{\sqrt{\rho^2 + (z+h)^2}} - 1 \right] \right\}$$

I_0 and I_1 are the modified Bessel Functions of the first kind, and K_0 and K_1 are the modified Bessel Functions of the second kind.

The computation of the E components must take into account also the boundary charges which are induced at the end of the dipole in the boundary provided the quasi-static conditions are established. Those charges are:

$$\pm \left(Q_0 = \frac{\varepsilon_0}{\sigma} I \right) \tag{11}$$

consequently the charge moment:

$$Q_0 \, dl = \frac{\varepsilon_0}{\sigma} I \, dl \tag{12}$$

and the quasi-static field in the dielectric medium for $(\rho^2 + z^2)^{\frac{1}{2}}$ due to this moment is

$$E_{\rho 0} = \frac{I dl}{2\pi\sigma} \frac{2\rho^2 - z^2}{\sqrt{\rho^2 + z^2}^5} \cos\varphi \tag{13}$$

$$E_{\varphi 0} = \frac{I dl}{2\pi\sigma} \frac{1}{\sqrt{\rho^2 + z^2}^3} \sin\varphi \tag{14}$$

$$E_{z 0} = \frac{I dl}{2\pi\sigma} \frac{3\rho z}{\sqrt{\rho^2 + z^2}^5} \cos\varphi \tag{15}$$

the quasi-static field in the conducting medium in such conditions is due to the current moment Idl and is similar to the above relations (13) (14) (15).

2. Calculation Methodology

The formula of Von Aulock for a propagation phenomenon in a semi-infinite medium has been used for the calculation. Such formulation suggest a simple physical interpretation of the various contributions to the field strength at a point. Those contributions are: 1. the direct wave; 2. the reflected wave; 3. the boundary charges.

Practically this formulation represents a method of describing shallow water propagation considering the presence of two boundaries by means of the "images" approach and the contribution from charges induced at the air-sea interface, generated by the incident field. This method has been published by J.T. Weaver and will not be described here. (WEAVER J.T. 1967).

As outlined before, cylindrical coordinates are used and the curves of Figs. 1,2,3,4,5,6,7 refer to the magnitude of the radial (ρ)-component $|E|_{\rho tot}|$ (direct + reflected + surface charge) wave.

the radial (ρ)-component $|E_\rho|$ (direct + reflected) wave

the perpendicular (ϕ)component $|E_{\phi tot}|$ (direct + reflected + surface charge)

the perpendicular (ϕ)component $|E_\phi|$ (direct + reflected)

the phase (ψ) for the above components.

The source is assumed to be at the surface with a unity strength.
The receiver is assumed to be placed on the bottom which is assumed to have infinite impedence.

The bottom depth is assumed to be 20, 40, 60 m and the interested frequencies 2, 6, 14 Hz.

In Fig. 8, only frequencies of 2 and 14 Hz have been considered. The heavy-dotted curves (upper) refer to a propagation in a layer of sea water between surface and the bottom with the receiver on the bottom. The continuous-line curves (lower) refer to a propagation similar to the previous one but without the bottom, or better with an infinite deep bottom. The receiver is now still at the depth of the bottom (as before) but in a semi-infinite sea.

The two pairs of curve comparisons show clearly the improvement in level at the receiver due to the presence of the bottom (in this case 20 m) with respect to a deep water propagation.

3. Experimental validation

Measurements were made in a shallow water zone with a transmitting dipole close to the sea surface and the receiving dipole placed on the bottom, ($\sim$16 m). (TACCONI G. 1977). Experimental results are shown in the same Fig. 8 (light-dotted curves) for 2 and 14 Hz. It is clear how experimental curves lie between the theoretical most favourable situation and the less favourable one.

Fig. 7b shows a comparison between the $E_{\rho tot}$ theoretical and experimental, versus range.

4. Conclusions

The collection of data, presented in this paper, was initially produced to study the propagation of electromagnetic waves at ELF in shallow waters. On subsequent reflection the problem was reconsidered from an other point of view, namely to use propagation data for the investigation of the structure of the interfaces and their sizes.

5. References

- AULOCK von W. Low frequency electromagnetic dipole fields in a semi-infinite conductor, Navy Dept.Techn.Rept N° 104 (1952).
- BANOS A. and J.P. WESLEY. The horizontal electric dipole in a conducting half space. Univ. of Cal. Scripps Inst. Oceanography (1953).
- WAIT J.R. The electromagnetic fields of a horizontal dipole in the presence of a conducting half-space. *Can.Journ.* of Physics (1961).
- TACCONI G. Fundamentals of ELF communication and detection, AGARD lecture Series N° 88 (Oct. 1977)
- WEAVER, J.T. The quasi-static field of an electric dipole embedded in two-layer conducting half-space, Canadian Journ. of Physics (1967).

6. Acknowledgments

Part of the scientific material shown in this paper has been developed under the contract N° 77.01224.07 of the Italian National Research Council (CNR).

The author is grateful to the MARIPERMAN of the Italian Navy for its support.

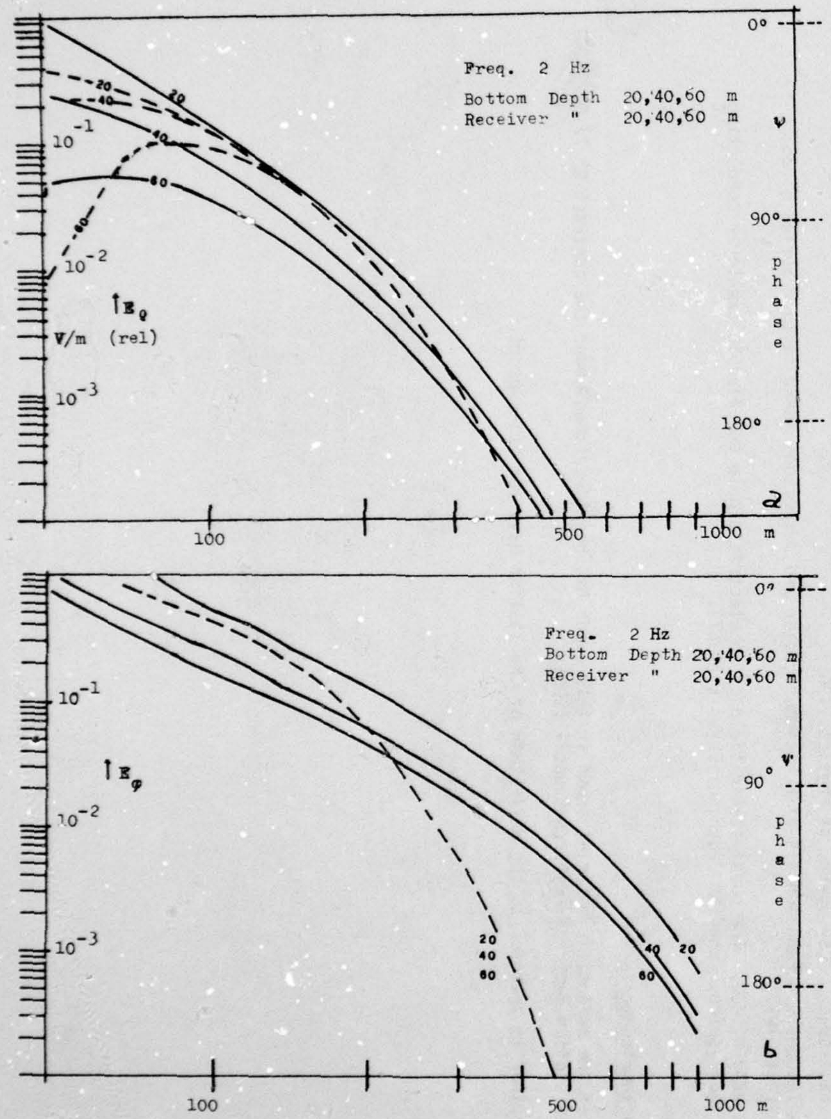
Freq. 2 Hz
Bottom Depth 20,40,60 m
Receiver " 20,40,60 m
E_ϱ
V/m (rel)
10^{-1}
10^{-2}
10^{-3}
0°
90°
180°
phase
ψ
a
b
100
500
1000 m
Freq. 2 Hz
Bottom Depth 20,40,60 m
Receiver " 20,40,60 m
E_φ
20
40
60

FIG 1

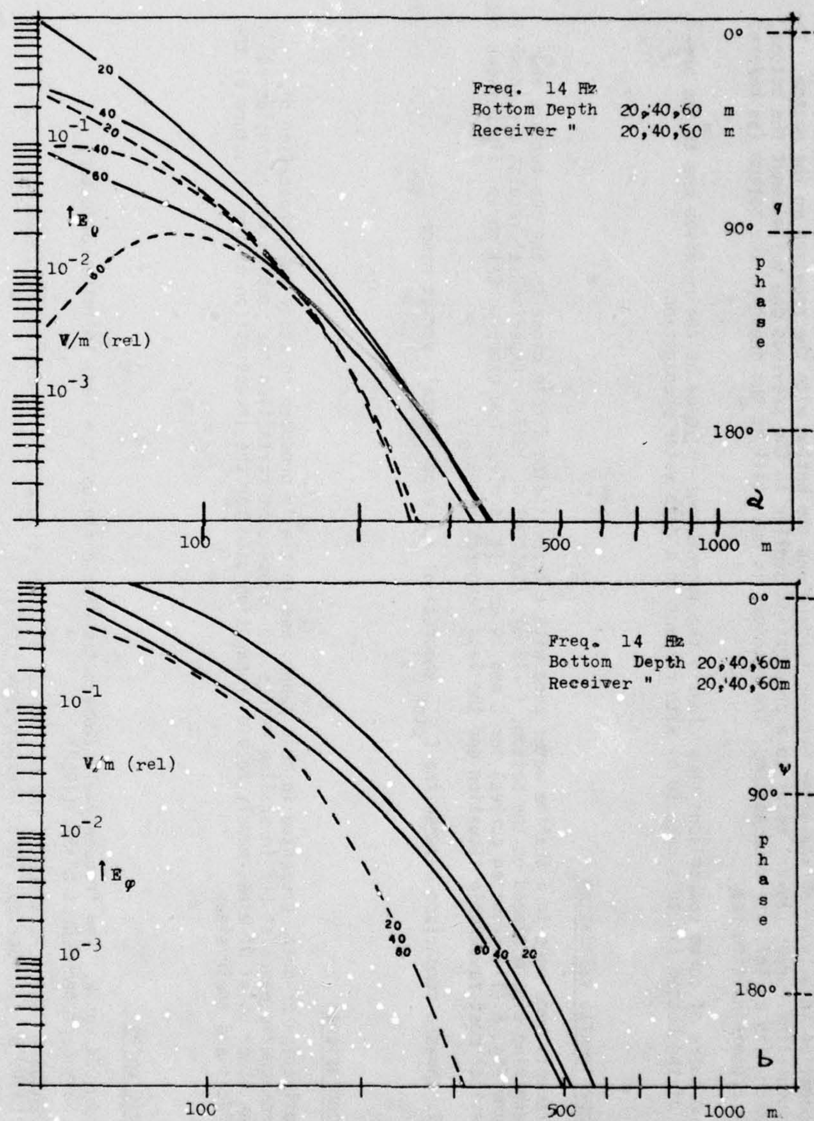
Freq. 14 Hz
Bottom Depth 20,40,60 m
Receiver " 20,40,60 m
E_ϱ
V/m (rel)
10^{-1}
10^{-2}
10^{-3}
0°
90°
180°
phase
ψ
a
b
100
500
1000 m
Freq. 14 Hz
Bottom Depth 20,40,60m
Receiver " 20,40,60m
E_φ
20
40
60

FIG. 2

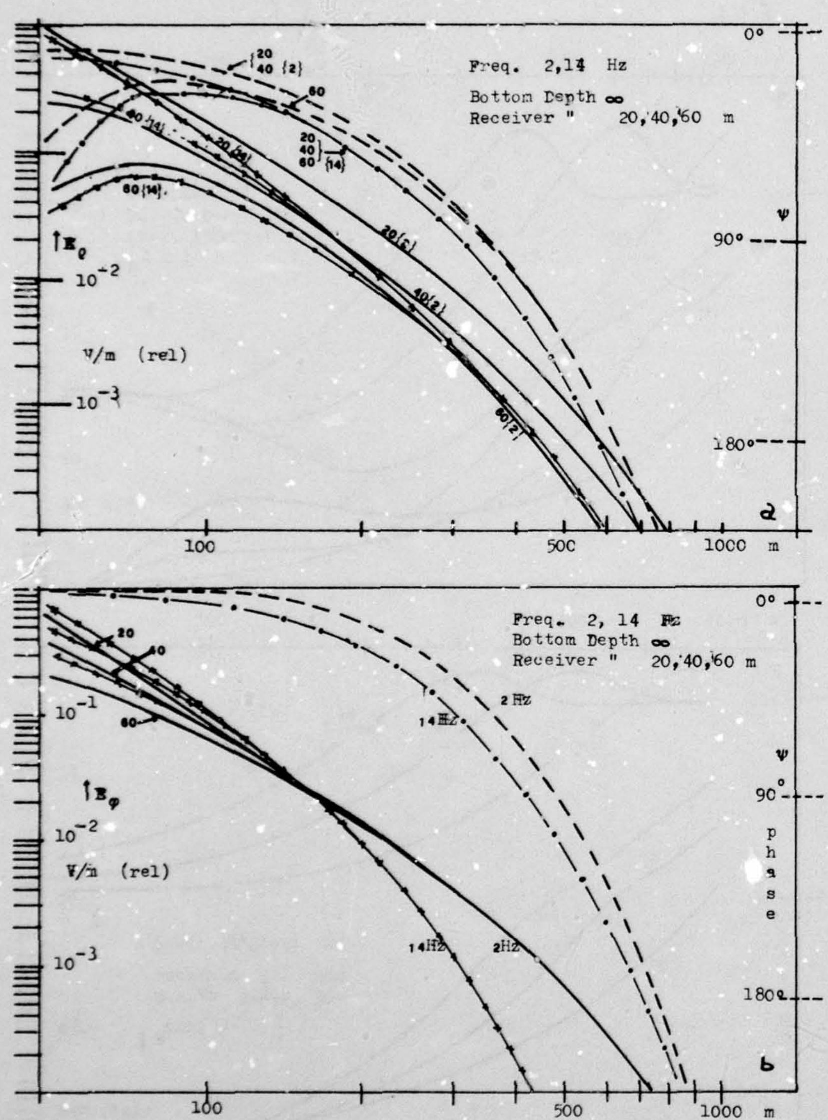
Freq. 2,14 Hz
Bottom Depth ∞
Receiver " 20,40,60 m
0°
90°
180°
ψ
E_φ
10^{-2}
V/m (rel)
10^{-3}
100
500
1000 m
a
Freq. 2, 14 Hz
Bottom Depth ∞
Receiver " 20,40,60 m
2 Hz
14 Hz
10^{-1}
10^{-2}
V/m (rel)
10^{-3}
phase
b

FIG 3

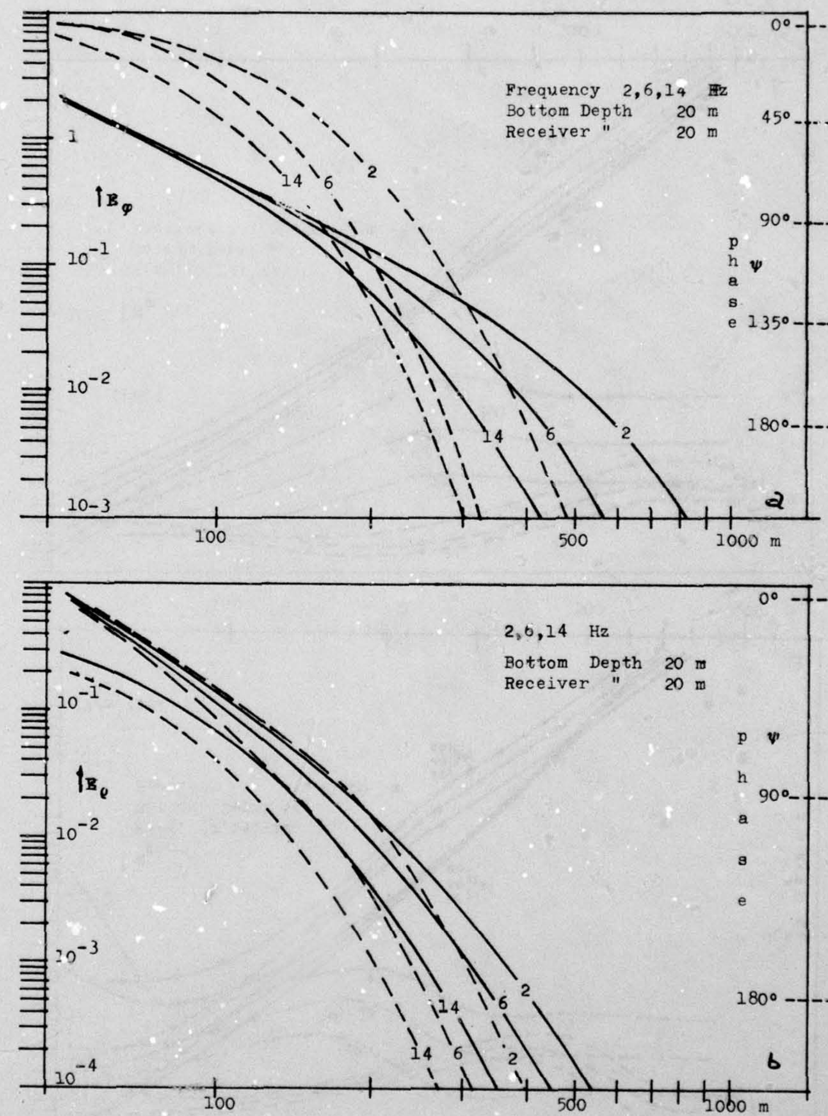
Frequency 2,6,14 Hz
Bottom Depth 20 m
Receiver " 20 m
0°
45°
90°
135°
180°
phase
ψ
E_φ
1
10^{-1}
10^{-2}
10^{-3}
100
500
1000 m
a
2,6,14 Hz
Bottom Depth 20 m
Receiver " 20 m
10^{-4}
b

FIG 4

AD-A082 015 ADVISORY GROUP FOR AEROSPACE RESEARCH AND DEVELOPMENT--ETC F/G 20/14
TERRAIN PROFILES AND CONTOURS IN ELECTROMAGNETIC WAVE PROPAGATI--ETC(U)
DEC 79 A W BIGGS
UNCLASSIFIED AGARD-CP-269 NL

4 OF 4
AD
A082015

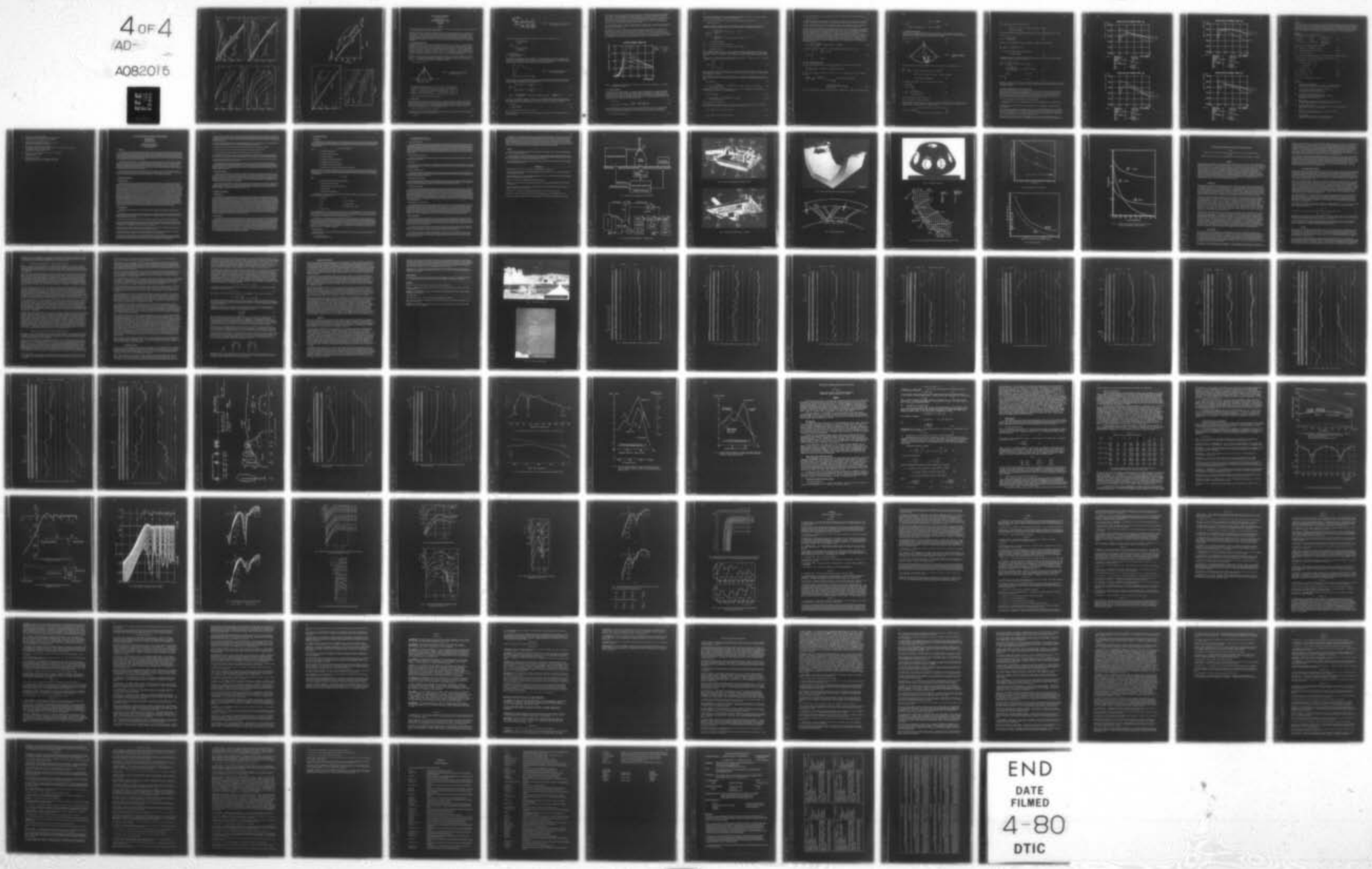

END
DATE
FILMED
4-80
DTIC

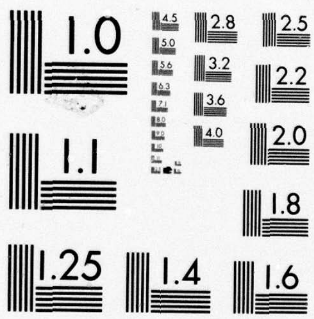

MICROCOPY RESOLUTION TEST CHART
NATIONAL BUREAU OF STANDARDS-1963-A

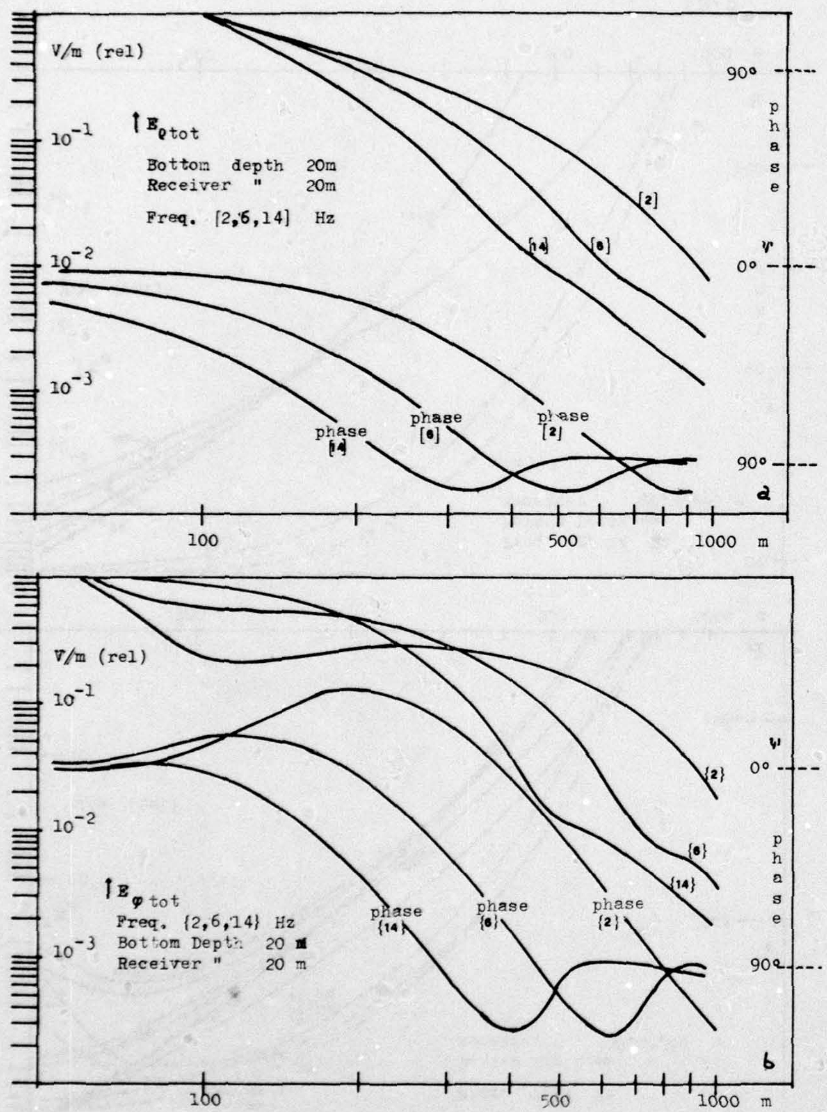
V/m (rel)
$E_{\varrho tot}$
Bottom depth 20m
Receiver " 20m
Freq. [2,6,14] Hz
phase [14]
phase [6]
phase [2]
90°
0°
phase
a
E_{φ} tot
Freq. {2,6,14} Hz
Bottom Depth 20 m
Receiver " 20 m
b
100
500
1000 m

FIG. 5

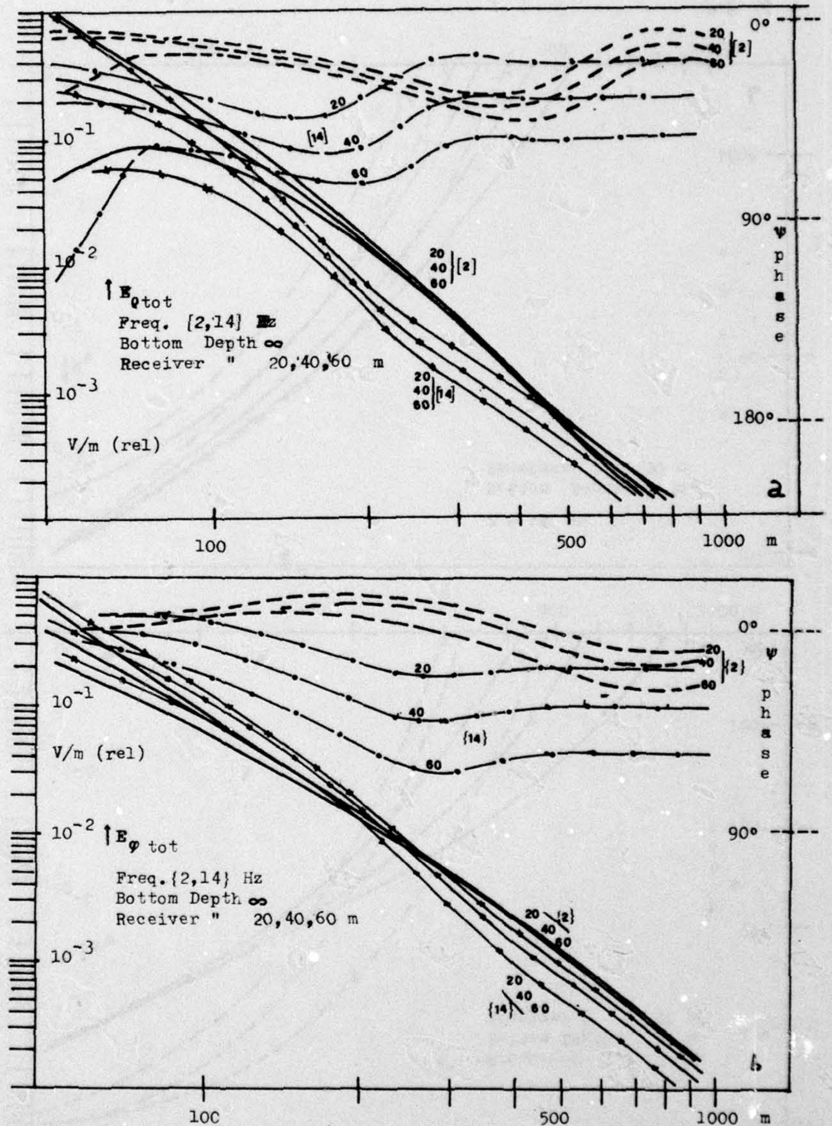
$E_{\varrho tot}$
Freq. [2,14] Hz
Bottom Depth ∞
Receiver " 20,40,60 m
V/m (rel)
0°
90°
180°
phase
a
E_{φ} tot
Freq. {2,14} Hz
Bottom Depth ∞
Receiver " 20,40,60 m
b
100
500
1000 m

FIG. 6

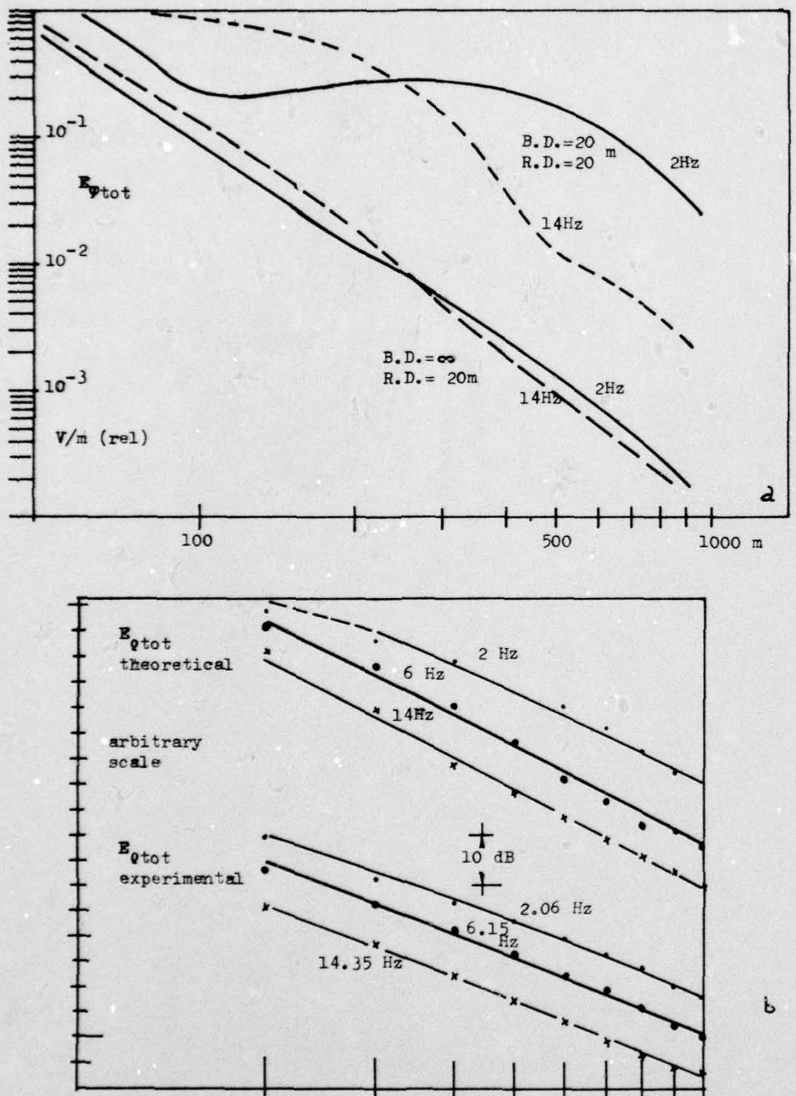

10^{-1}
$E_{\varphi tot}$
10^{-2}
10^{-3}
V/m (rel)
B.D.=20 m
R.D.=20
2Hz
14Hz
B.D.=∞
R.D.= 20m
14Hz
2Hz
100
500
1000 m
a
$E_{\varrho tot}$ theoretical
2 Hz
6 Hz
14Hz
arbitrary scale
10 dB
$E_{\varrho tot}$ experimental
2.06 Hz
6.15 Hz
14.35 Hz
m
100
500
800
b

FIG.7

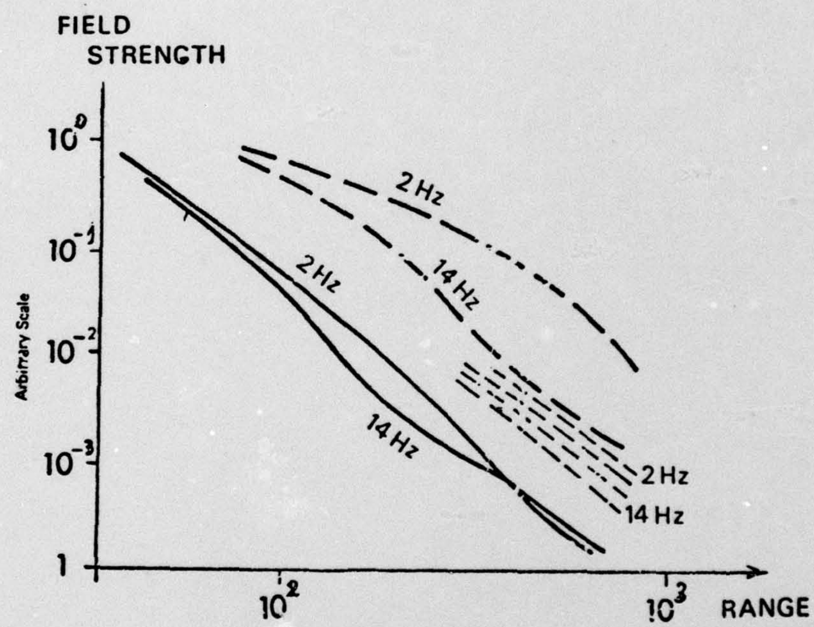

FIELD STRENGTH
Arbitrary Scale
10^0
10^{-1}
10^{-2}
10^{-3}
1
2 Hz
14 Hz
2 Hz
14 Hz
2 Hz
14 Hz
10^2
10^3
RANGE

FIG.8

RADAR ALTIMETER MEASUREMENTS

Flemming Thomsen
Electromagnetics Institute
Technical University of Denmark
2800 Lyngby
Denmark

ABSTRACT

A theoretical method for calculating the output signal of a satellite radar altimeter as a function of time has been developed for ice and snow covered areas.

The method is based on non-coherent scattering from a layered semi-permeable dielectric as described by Tsang and Kong. By this method it is possible to measure the surface roughness and the backscatter coefficient as function of incidence angle as described by McGoogan, Miller, Brown and Hayne. By considering the last part of the echoes and the cross and like-polarized signals it is possible to discriminate between the surface-echo and the bulk-echo, and thus describe the properties of the layering. The method has been applied to results of the S-193 radar altimeter experiment and will be used on data from GEOS 3.

1. The measuring situation

Satellite altimeters have been applied by the Skylab S-193 [1] and [2], the GEOS 3 [3] and the SEASAT experiments. The main purpose of these experiments is to map the geoid, but the measurements give an additional possibility of determining the characteristics of the surface of the earth. The measuring situation is shown in figure 1. We are considering pulse limited altimeters with pulse lengths between 10 and 100 nanoseconds. The transmitted pulse is assumed to be rectangular. When the skin depth of the radiation is great, compared to the spatial width of the transmitted pulse, the subsurface material will give considerable contributions to the total echo. Considering altimeter measurements of snow and fresh water ice surfaces, we find skin depths ranging from 10 to several hundred meters.

The result of this is first of all an error in the determination of the surface altitude, but it gives access to a determination of the subsurface parameters. Some relevant data of the altimeters are shown in table 1. The antenna radiation pattern is assumed to Gaussian as described by (1). This approximation is valid, because the angles under consideration are small.

$$G(\theta) \simeq G\cdot\exp(-2/\gamma\cdot\sin^2\theta) \qquad (1)$$

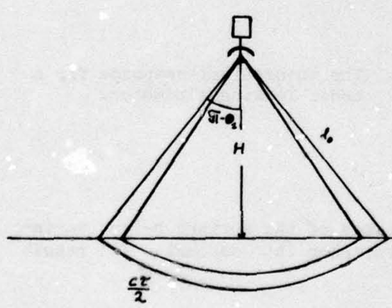

Figure 1. The geometry of the altimeter measuring situation.

experiment	frequency	pulse width	height	antenna gain
S-193	13.9 GHz	10,100 nsec	435,5 km	41 dB
GEOS 3	13.9 GHz	12,5	843 km	37 dB

Table I: Some relevant data of S-193 and GEOS 3.

2. Surface echo

The illumination of the surface as function of time is schematically shown in figure 2. The active region is limited by the pulse and consists, for later times, of a ring with a constant area. The surface scattering is described by the surface-backscatter coefficient σ^0, which has been calculated by Barrick [11]. Noting the fact that we are only considering small angles of incidence, we can use the rough surface approximation (2) in the calculation of σ^0.

$$\sigma^0(\theta) = |R(\theta)|^2 \sec^4\theta\cdot\frac{1}{s^2}\cdot\exp(-\frac{1}{s^2}\,tg^2\theta) \qquad (2)$$

The parameter s is given by the RMS of the surface height variation σ_s and the autocorrelation length TL in horizontal plane of these, by equation (3)

$$s = 2\,\sigma_s/TL \qquad (3)$$

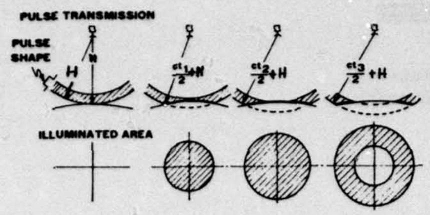

Figure 2. The development of the illuminated areas as function of time.

By neglecting the height variations of the surface, the echo can be calculated by eq. (4).

$$P_r(t)/P_t \begin{cases} \dfrac{G^2(0)\cdot\sigma_s(0)\cdot\lambda^2\cdot c\cdot t}{4(4\pi)^2H^3} & 0 \leqslant t \leqslant \tau \\ \dfrac{G^2(\theta)\cdot\sigma_s(\theta)\cdot\lambda^2\cdot c\cdot\tau}{4(4\pi)^2\cdot H^3} & t \geqslant \tau \end{cases} \tag{4}$$

τ = pulse width
$G(\theta)$ = antenna gain given by (1)
H = satellite height

This function is schematically shown in figure 3. The leading edge is linear and the trailing edge is decaying at a rate depending on the antenna gain and the angular dependence of the backscatter coefficient. The height variation tends to decrease the slope of the leading edge, as a result of earlier arriving echoes from higher surface elements and later from lower elements.

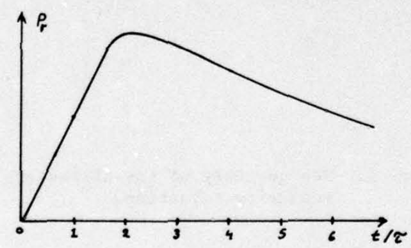

Figure 3. The theoretical response for a nadir looking altimeter.

In reference [4] G.S. Brown performs calculations in which the influence of the surface height variations and a small tilting angle ξ of the antenna axis from nadir, are taken into account. The result of this calculation is shown in equations (5) and (6).

$$\frac{P_r(t)}{\hat{P}_t} \simeq \begin{cases} P_{FS}(\theta)\cdot\sqrt{2\pi}\;\sigma_P\;|1 + \mathrm{erf}(\dfrac{t}{\sqrt{2}\,\sigma_c})|/2 & t \leqslant 0 \\ P_{FS}(t)\cdot\sqrt{2\pi}\;\sigma_P\;|1 + \mathrm{erf}(\dfrac{t}{\sqrt{2}\,\sigma_c})|/2 & t \geqslant 0 \end{cases} \tag{5}$$

$$P_{FS}(t) \simeq \frac{G^2(0)\cdot\lambda^2\cdot c\;\sigma^0(0)}{4\cdot(4\pi)^2\cdot H^3}\cdot\exp(-\frac{4}{\gamma}\sin^2\xi - \frac{ct}{H}(\frac{4}{\gamma}\cos 2\xi + \frac{1}{s^2}))\quad I_o(\frac{4}{\gamma}\sqrt{\frac{ct}{H}}\sin 2\xi) \tag{6}$$

$P_{FS}(t)$ is the "flat surface response". The time t = 0 is defined as the time where the center of the pulse gives echoes from the average level of the surface. The theory is based on delta pulses, and the finite length of the pulse is accounted for, by the constants σ_P and σ_c given by (7) and (8).

$$\sigma_P = 0.425\cdot\tau \tag{7}$$

$$\sigma_c = \sqrt{\sigma_P{}^2 + (2\sigma_s/c)^2} \tag{8}$$

I_o is the modified Bessel function of zero order.

The surface response as function of time has been displayed in figure 4 with the tilting angle ξ from nadir as parameter.

The altitude of the surface is determined by the time where the response has reached half its maximum value, which is nearly independent of the surface roughness. The surface parameter σ_c is measured by the slope of the leading edge, and the RMS of height variations σ_s can be calculated by (8). The tilting angle ξ, results in an error in the determination of the slope (σ_s), an error in determination of the value of σ^o, and a change of the slope of the trailing edge. By scanning the antenna, it is possible to determine the surface parameters from the variations of the slope of the trailing edge, and the errors in determination of σ_s and σ^o can be reduced.

Note that the slope of $P_r(t)/(2\ P_r(0))$ as function of t/τ is always below 1. When the surface is smooth, the slope will tend toward 1. Under the S-193 experiment, slopes greater than 1 have been measured, which indicate a subsurface echo.

The depolarization of the received echo has not been measured by these experiments. Theories of the depolarization of radar echoes from rough surfaces have been developed [6],[7], but generally the depolarized echoes are much smaller than those actually measured. Scatterometer measurements of the depolarized field of first year sea ice, [8],[9],[10], where the volume echo is assumed to be negligible show depolarized echoes 10-20 dB below similarly polarized echoes. The measurement is, however, performed as CW-measurement, thus giving an increased depolarization because of multiple scattering.

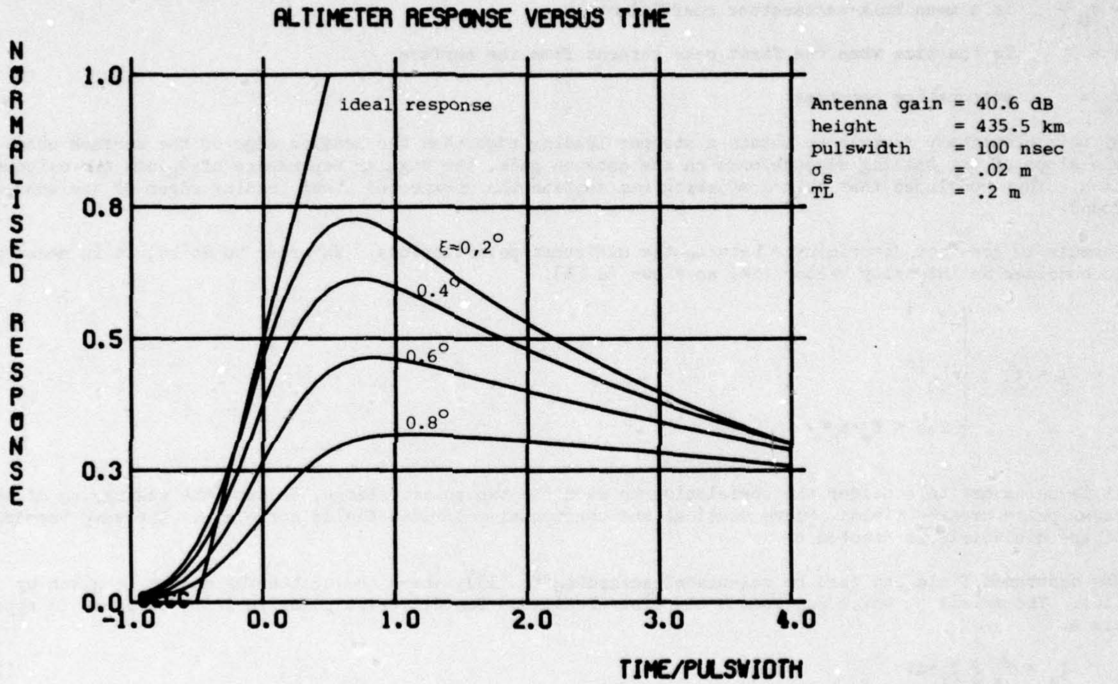

Figure 4. Normalized altimeter response as function of time with the tilting angle ξ of the antenna from nadir as parameter.

3. The Bulk response

The scattering of an incidence field in a dielectric where the permittivity is varying stochastically, was described by Tsang and Kong [12],[5]. The relative permittivity is considered to consist of mean permittivity ε_{rm} and a stochastically varying part ε_{rf}. The dielectric is supposed to model a sheet of ice or snow with some layering. This is achieved by expressing the autocorrelation of the permittivity by (9). Normally, the autocorrelation length ℓ_p in the horizontal plane is greater than the autocorrelation length ℓ in the vertical direction.

$$\varepsilon_r = \varepsilon_{rm} + \varepsilon_{rf} \tag{9}$$

$$< \varepsilon_{rf}(\underline{r}_1)\ \varepsilon^*_{rf}(\underline{r}_2) > = \delta \cdot \varepsilon_{rm}^{\ 2} \cdot \exp\left(-\frac{|Z_1-Z_2|}{\ell} - \frac{(x_1-x_2)^2 + (y_1-y_2)^2}{\ell_p^2}\right) \tag{10}$$

The scattered field from a volume element dV can be calculated using eq. (10). E_s is the scattered field in the far field of dV, and E_i is the incidence field. P_1 is a function of the direction θ', ϕ' of the incident field, the direction θ, ϕ of the scattered field and the polarizations.

$$|E_s(r,\theta,\phi)|^2 = \frac{1}{r^2}\ P_1\ |E_i|^2\ dV \tag{11}$$

The different contributions to the scattered field are non-coherent, thus the total scattered energy can be found by integrating (11) over the scattering volume.

Equation (11) leads to definition of a volume scattering coefficient σ_B defined by (12)

$$\sigma_B(\theta,\phi,\theta',\phi') = 4\pi\cdot P_1 \tag{12}$$

In order to understand the signal form of the bulk echo, a simplified calculation is performed. By considering the active volumes on figure 1 the bulk response can be calculated according to (13)

$$\frac{P_r(t)}{\hat{P}_t} = \begin{cases} \dfrac{\lambda^2 G^2(\theta) < \sigma_B >}{8(4\pi)^2\cdot H^3}(ct)^2\cdot\exp(-\kappa_a ct) & 0 \leq t \leq \tau \\[2ex] \dfrac{\lambda^2 G^2(\theta)_m < \sigma_B >}{8(4\pi)^2\cdot H^3}c^2\tau(2t-\tau)\cdot\exp(-\kappa_a(ct-H(|\sec\theta_m| -1))) & t \geq \tau \end{cases} \tag{13}$$

θ_m is a suitable mean angle

$< \sigma_B >$ is a mean bulk-backscatter coefficient

$t = 0$ is the time when the first echo returns from the surface

$\kappa_a =$ attenuation constant

By this elementary formula we obtain a steeper leading edge than the leading edge of the surface echo. The slope of the tailing edge depends on the antenna gain, the angular dependence of σ_B and the attenuation. This concludes that bulk-scattering can explain the unexpected steep leading edges of the echoes found.

Formula 10 does not discriminate between the different polarizations. In order to do so, it is necessary to consider an intensity vector (14) as shown in [5].

$$\underline{I} = \frac{1}{2\eta}\begin{pmatrix} |E_v|^2 \\ |E_h|^2 \\ 2\mathrm{Re} < E_v\cdot E_h^* > \end{pmatrix} \tag{14}$$

It is necessary to consider the correlation between the two polarizations, because the scattering of the radar pulse creates fields, where vertical and horizontal polarized fields correlate. The wave impedance of the dielectric is denoted η.

The scattered field can then be calculated according to (15), where the scattering matrix is given by (16). The matrix $\underline{\underline{p}}$, which represents the distribution on the different polarizations, is given in appendix A.

$$\underline{I}_s = \frac{1}{r^2}\underline{\underline{P}}\,\underline{I}_i\cdot dV \tag{15}$$

$$\underline{\underline{P}} = \frac{k^4\delta\cdot\ell\cdot\ell_P^2}{8\cdot\pi(1+k^2\cdot\ell^2(\cos\theta-\cos\theta')^2)}\cdot\exp\left(-\frac{k^2\ell_P^2}{4}(\sin^2\theta' + \sin^2\theta - 2\sin\theta\cdot\sin\theta'\cos(\phi-\phi'))\right)\cdot\underline{\underline{p}} \tag{16}$$

Note that $\underline{\underline{P}}$ only depends on the three variables, θ, θ', and $\phi-\phi'$. When symmetry can be utilized, the calculations can be simplified by integrating $\underline{\underline{P}}$ over ϕ.

$$\underline{\underline{Q}} = \int_0^{2\pi}\underline{\underline{P}}\,d\phi = Q_o\cdot\underline{\underline{q}} \tag{17}$$

$$Q_o = \frac{k^2\,\delta\,\ell_P^2}{4(1+k^2\ell^2(\cos\theta-\cos\theta')^2)}\exp\left(-\frac{k^2\ell_P^2}{4}(\sin^2\theta' + \sin^2\theta)\right) \tag{18}$$

The matrix $\underline{\underline{q}}$ is given in appendix A.

It is only necessary to consider $\underline{\underline{Q}}$ as a 2 x 2 matrix, because the other terms vanish. The scattering coefficients are calculated by integrating the power loss in equation (15).

$$\kappa_{sv}(\theta) = \int_0^{\pi}(Q_{11}(\theta',\theta) + Q_{21}(\theta',\theta))\sin\theta'\,d\theta' \tag{19}$$

$$\kappa_{sh}(\theta) = \int_0^{\pi}(Q_{12}(\theta',\theta) + Q_{22}(\theta',\theta))\sin\theta'\,d\theta' \tag{20}$$

The total loss coefficient κ_e can be expressed as a sum of scattering loss κ_s and absorption loss κ_a.

$$\kappa_e(\theta) = \kappa_s(\theta) + \kappa_a \tag{21}$$

The scattered energy can be regarded as a sum of multiple scattered fields. The phases of these do not correlate, and the total scattered power can be calculated by adding the different power contributions.

The power scattering equation (15) can be utilized to derive a set of energy transportation equations as shown in [5]. This is, however, not suitable when we are dealing with a short pulse radar.

The bulk echo will be calculated by integrating the scattering of first and second order. This simplification is justified by the fact that Q_0 is normally small. Note that all the multiple scattered rays arriving at the altimeter at a certain time have covered paths of nearly equal lengths (only differing by $c\tau$). Consequently, a heavy attenuation in the dielectric does not justify the omittance of higher order scattering. The polarization of a nadir looking altimeter is meaningless, but as a matter of convenience, horizontal polarization is chosen. The effect of the surface on the radar pulse is a refraction and a depolarization and scattering caused by the rough surface. The first effect has been accounted for in this work, while the second effect has been neglected. The refraction can be taken into account by using a virtual antenna at a higher level with a narrower antenna beam. In the following, we will restrict us to a non-refracting surface. The incidence field in the dielectric can be described by (21).

$$I(\Omega_i) = \begin{pmatrix} 0 \\ 1 \\ 0 \end{pmatrix} \frac{P_t(t)\cdot G(\Omega_i)}{4\pi\cdot r^2} \cdot \exp\left[-\kappa_e\left(\frac{ct}{2} + H(1 - |\sec\theta_i|)\right)\right] \tag{22}$$

The incident solid angle is denoted by Ω_i. The transmitted pulse is given by eq. (22a).

$$P_t(t) = \begin{cases} \hat{P}_t & -\frac{2H}{c} \leq t \leq \tau - \frac{2H}{c} \\ 0 & \text{otherwise} \end{cases} \tag{22a}$$

3a. First order bulk-scattering

The first order scattering can be calculated by integrating (15) using (22) resulting in (23)

$$\frac{P_r}{\hat{P}_t} = \frac{\lambda^2}{(4\pi)^2} \cdot \iiint \frac{1}{r^4} \cdot G^2(\Omega)\cdot \underline{\underline{p}}\,(\Omega, -\Omega) \begin{pmatrix} 0 \\ 1 \\ 0 \end{pmatrix} \cdot r^2 dr \sin\theta\, d\theta\cdot d\phi \tag{23}$$

By the insertion of $\underline{\underline{p}}$ the cross-polarized field vanishes. By using (16) and (1), (23) is reduced to (24).

$$\frac{P_{rlike}}{\hat{P}_t} = \frac{\lambda}{8\pi\cdot H^2} \; \frac{k^3\,\delta\,\ell\,\ell_P^2}{4}\,\frac{c\tau}{2} \cdot \int_{\pi-\arccos\frac{H}{H+\frac{ct}{2}}}^{\pi} G^2(\theta)\cdot\exp(-\kappa_e(ct+2H(1-|\sec\theta|)))$$

$$\frac{\exp(-(k^2\ell_P^2 + \frac{4}{\lambda})\sin^2\theta)}{1+k^2\ell^2\cdot 4\cdot\cos^2\theta}\,\psi(\theta)\sin\theta d\theta \tag{24}$$

$\psi(\theta)$ is the relative width of the active volume. This is normally one, but smaller for boundary regions.

$$\psi(\theta) = \begin{cases} 1 & |\sec\theta| \geq 1 + \frac{c(t-\tau)}{2H} \\ \left(\frac{ct}{2} + H(1 - |\sec\theta|)\right) \frac{2}{c\cdot\tau} & |\sec\theta| \leq 1 + \frac{c(t-\tau)}{2H} \end{cases} \tag{25}$$

3b. Second order scattering

The geometry of the second order scattering is shown in figure 5. By noting that the sum of the covered paths is bounded by (25a) it can be seen, that the active volume for secondary scattering from a point s is the space between two ellipsoids with s as center.

$$2\ell_o - c\tau \leq r_1 + r_2 + r \leq 2\,\ell_o \tag{25a}$$

$$\ell_o = H + \frac{ct}{2} \tag{25b}$$

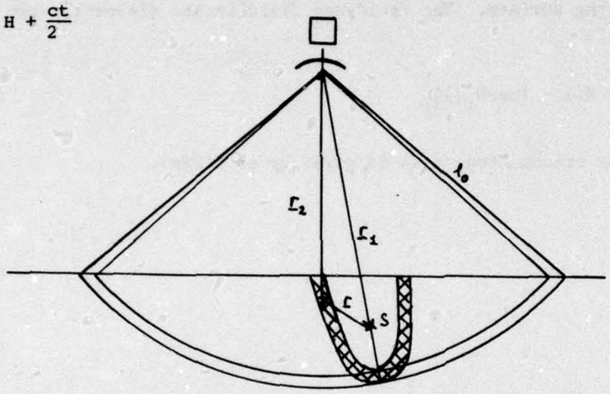

Figure 5. The active volume for secondary scattering from s.

By denoting the width of the active volumen Δr, the second order echo can be expressed by (26)

$$\frac{P_r(t)}{P_t} = \frac{\lambda^2}{(4\pi)^2} \int \frac{1}{r_2^2} G(\theta_2)\cdot G(\theta_1)\ \underline{\underline{P}}(\theta_2,\theta,\phi_2-\phi)\underline{\underline{P}}(\theta,\theta_1,\theta-\theta_1) \begin{pmatrix} 0 \\ 1 \\ 1 \end{pmatrix}$$

$$\exp(-(\kappa_e(\theta)r + \kappa_e(\theta_2)(r_2 - H|\sec\theta_2|) + \kappa_e(\theta_1)(r_1 - H|\sec\theta_1|))$$

$$\Delta r \quad \sin\theta\cdot\sin\theta_1 \quad d\theta d\phi d\theta_1 d\phi_1 dr_1 \tag{26}$$

By elementary calculations r and Δr are expressed by (27) and (28)

$$r = \frac{\ell_o\ (\ell_o - \frac{r_1}{2})}{\ell_o - \frac{r_1}{2}\ (1-\cos\theta_e)} \tag{27}$$

$$\Delta r \simeq \frac{c\tau}{2}\ \left(1 + \frac{(\frac{r_1}{2})^2\cdot\sin^2\theta_e}{(\ell_o + \frac{r_1}{2}(\cos\theta_e - 1))^2}\right) \tag{28}$$

The angle θ_e between $\underline{r}_1$ and $\underline{r}$ is given by (29)

$$\cos\theta_e = \cos\theta\cdot\cos\theta_1 + \sin\theta\cdot\sin\theta_1\cdot\cos(\phi-\phi_1) \tag{29}$$

As a consequence of the fact, that $\theta_1 \simeq \pi$ and $\theta_e \simeq \pi-\theta$, we notice that Δr and r can be regarded as independent of $(\phi-\phi_1)$. By this approximation (26) can be reduced to a volumeintegral by using (16). By using the vector $\underline{f}$ given by (30), (26) is reduced to (31).

$$\underline{f}(\theta_2,\theta,\theta_1) = \underline{\underline{Q}}\cdot\underline{\underline{Q}}\cdot \begin{pmatrix} 0 \\ 1 \\ 0 \end{pmatrix} = \begin{pmatrix} Q_{11}(\theta_2,\theta)\cdot Q_{12}(\theta,\theta_1) + Q_{12}(\theta_2,\theta)\cdot Q_{22}(\theta,\theta_1) \\ Q_{21}(\theta_2,\theta)\ Q_{12}(\theta,\theta_1) + Q_{22}(\theta_2,\theta)Q_{22}(\theta,\theta_1) \end{pmatrix} \tag{30}$$

$$\frac{P_r}{\hat{P}_t} = \frac{\lambda^2}{(4\pi)^2} \int \frac{1}{r_2^2} G(\theta_1)\cdot G(\theta_2)\cdot \underline{f}(\theta_2,\vartheta,\theta_1)\cdot \Delta r(\theta).$$

$$\exp(-(\kappa_e(\theta)\cdot r + \kappa_e(\theta_2)(r_2 - H|\sec\theta_2|) + \kappa_e(\theta_1)(r_1 - |H \sec\theta_1|))$$

$$\sin\theta\sin\theta_2 \quad d\theta\cdot d\theta_1\cdot dr_1 \tag{31}$$

The integral contains r_2 and θ_2, which are functions of θ, θ_1 and r_1 as expressed by (32) and (33)

$$r_2 = 2\ell_o - r_1 - r \tag{32}$$

$$\cos\theta_2 = -\frac{r_1\cos\theta_2 + r\cos\theta}{2\ell_o - r_1 - r} \tag{33}$$

Equation (31) can be simplified, when the attenuation is superior to the scattering.

$$\frac{P_t}{\hat{P}_t} = \frac{\lambda^2}{(4\pi)^2}\cdot e^{-\kappa_a ct} \iiint \frac{1}{r_2^2} G(\theta_1)\cdot G(\theta_2)\cdot$$

$$\exp(-\kappa_a\cdot H\ (2-|\sec\theta_1|-|\sec\theta_2|))\cdot \underline{f}(\theta_2,\theta,\theta_1)\Delta r(\theta)$$

$$\sin\theta\cdot\sin\theta_1 \quad d\theta d\theta_1 dr_1 \tag{34}$$

The general behaviour of the second order bulk scattering can be seen from a rough simplification of (34) utilizing the fact, that $\theta_1 \simeq \pi$ and $\theta_2 \simeq 0$.

$$\frac{P_r(t)}{\hat{P}_t} = \begin{pmatrix}1\\1\end{pmatrix} \frac{(\frac{ct}{2})^2 \frac{c\tau}{2}}{16\cdot H^3} \left(\frac{k^3\delta\ell\ \ell_p^2}{4}\right)\cdot G(0)^2 \exp(-\kappa_a ct)$$

$$\int_0^\pi \frac{\exp(-\frac{k\ell_p^2}{2}\sin^2\theta)}{(1+k^2\ell^2(1+\cos\theta)^2)^2}\cdot(1+\cot^2\frac{\theta}{2})\ \psi(\theta)\ \sin\theta d\theta \tag{35}$$

$$\psi(\theta) = \begin{cases} tg^2\,\frac{\theta}{2} & 0 \leq \theta \leq \frac{\pi}{2} \\ 1 & \frac{\pi}{2} \leq \theta \leq \pi \end{cases} \tag{36}$$

Equation (35) shows, that the second order response is proportional to the time squared, and thus the volume behind the wavefront. This indicate, that higher order scattering could be significant for later parts of the response.

4. Method for separation of bulk and surface echo

Figures 6-9 show some examples of theoretical responses for the S-193 altimeter. The surface and bulk parameters are believed to be representatives of a snow surface. The curves show the surface echo and the like, and cross polarized component of the bulk-echo. Here, the surface echo vanishes for the later parts of the echo because the scattering area disappears from the antenna beam. The cross polarized surface echo is expected to be proportional to the similarly polarized surface echoes. Thus, we find the following two criteria for a significant bulk echo:

a) The leading edge of the pulse response is abnormally steep

b) The cross polarized echo is increasing relatively to the like polarized for the later parts of the echo.

When these criteria are fulfilled the crossed polarized echo is simulated by a proper choice of bulk parameters.

This process is not ambiguous and requires a certain a priori knowledge about range of the parameters. When the bulk parameters have been determined, the surface echo is found by subtraction of the bulk echo. This is justified by the fact that the bulk echo consists of scattered fields of random phase, but these scattered fields do not correlate with the phase of the incident field. The surface parameters can be determined by the method described in section 2.

The simulations have been used for S-193 altimeter data, but the lack of cross-polarized and sufficiently late measurements have made it impossible to discriminate between the bulk and surface echo.

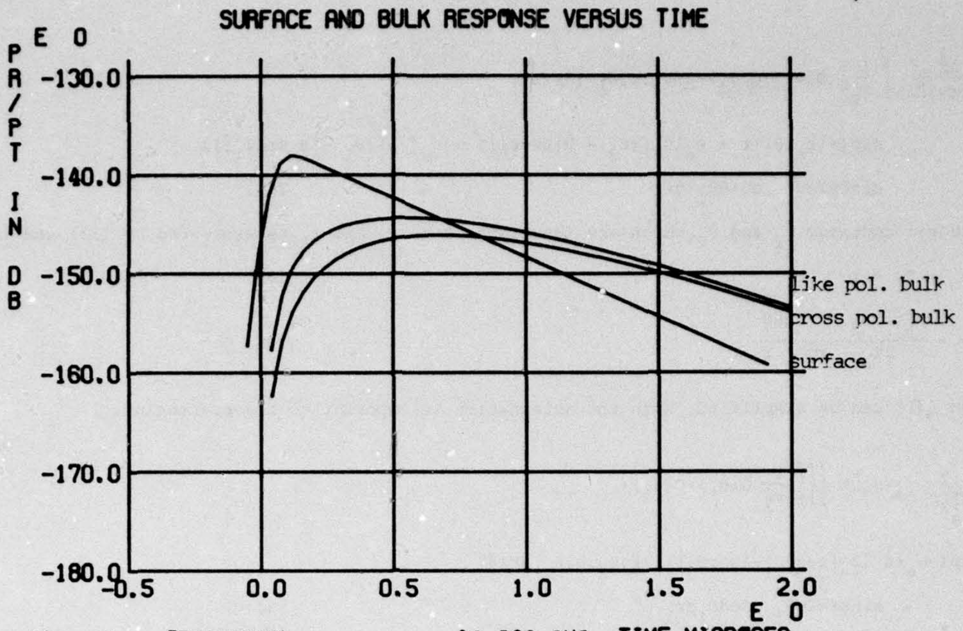

Figure 6

FREQUENCY	:	13.900 GHZ
ANTENNA GAIN	:	40.60 DB
PULSWIDTH	:	100. NSEC
HEIGHT	:	435.50 KM
SURFACE PARAMETERS :		
SIGMA	:	0.0200 M
TL	:	0.2000 M
TILT ANGLE	:	0.0 DEGREES
BULK PARAMETERS :		
L	:	0.0020 M
LP	:	0.0050 M
DELTA	:	0.1000E-03
KA	:	0.0100 M**-1
REL. E	:	1.80

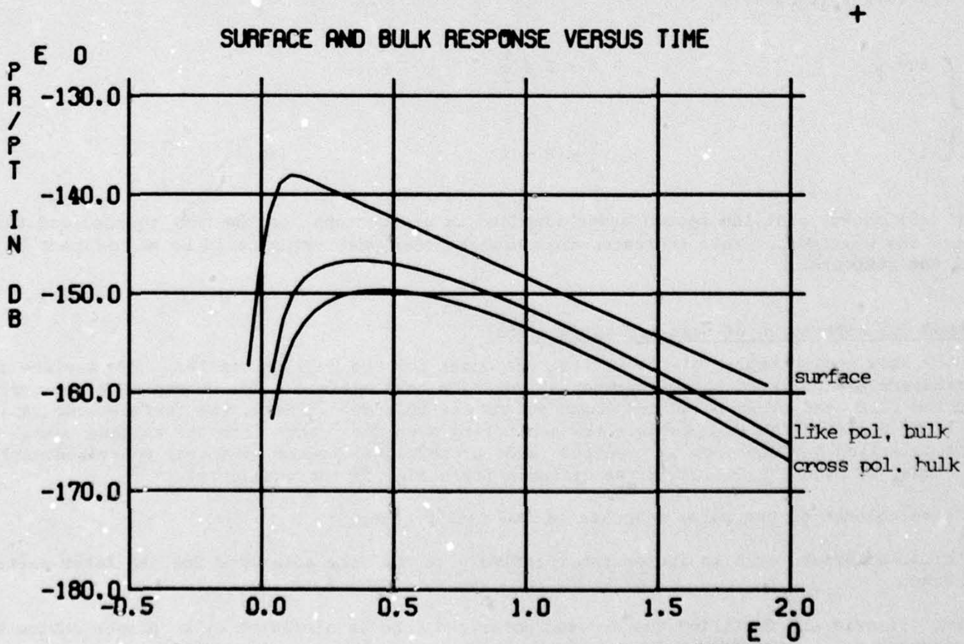

Figure 7

FREQUENCY	:	13.900 GHZ
ANTENNA GAIN	:	40.60 DB
PULSWIDTH	:	100. NSEC
HEIGHT	:	435.50 KM
SURFACE PARAMETERS :		
SIGMA	:	0.0200 M
TL	:	0.2000 M
TILT ANGLE	:	0.0 DEGREES
BULK PARAMETERS :		
L	:	0.0020 M
LP	:	0.0050 M
DELTA	:	0.1000E-03
KA	:	0.0150 M**-1
REL. E	:	1.80

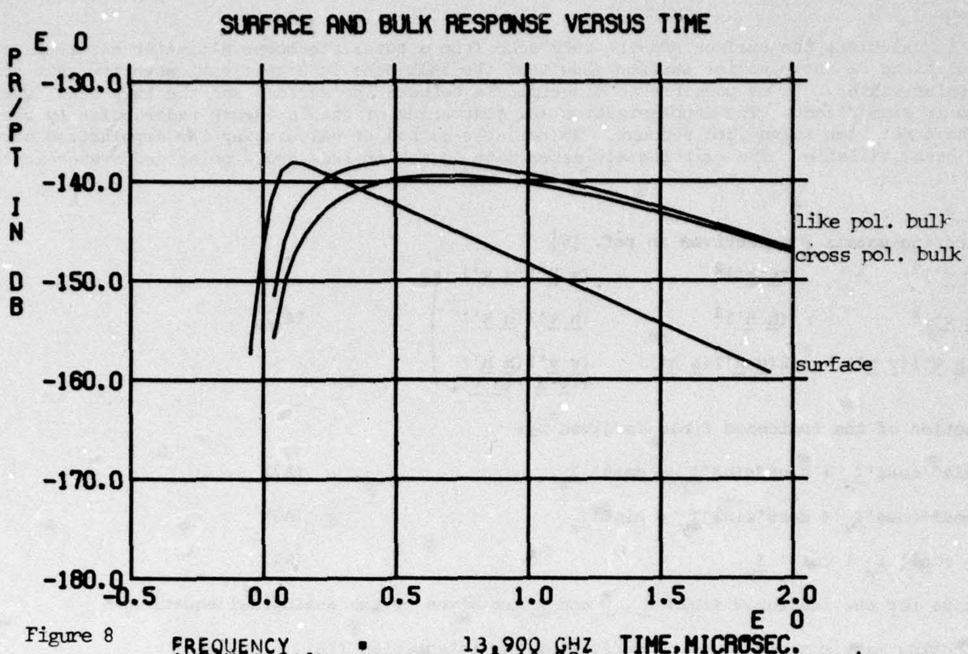

Figure 8

```
FREQUENCY          :        13.900 GHZ
ANTENNA GAIN       :         40.60 DB
PULSWIDTH          :         100.  NSEC
HEIGHT             :        435.50 KM
SURFACE PARAMETERS :
SIGMA              :        0.0200 M
IL                 :        0.2000 M
TILT ANGLE         :        0.0    DEGREES
BULK PARAMETERS    :
L                  :        0.0020 M
LP                 :        0.0100 M
DELTA              :    0.1000E-03
KA                 :        0.0100 M**-1
REL. E             :          1.80
```

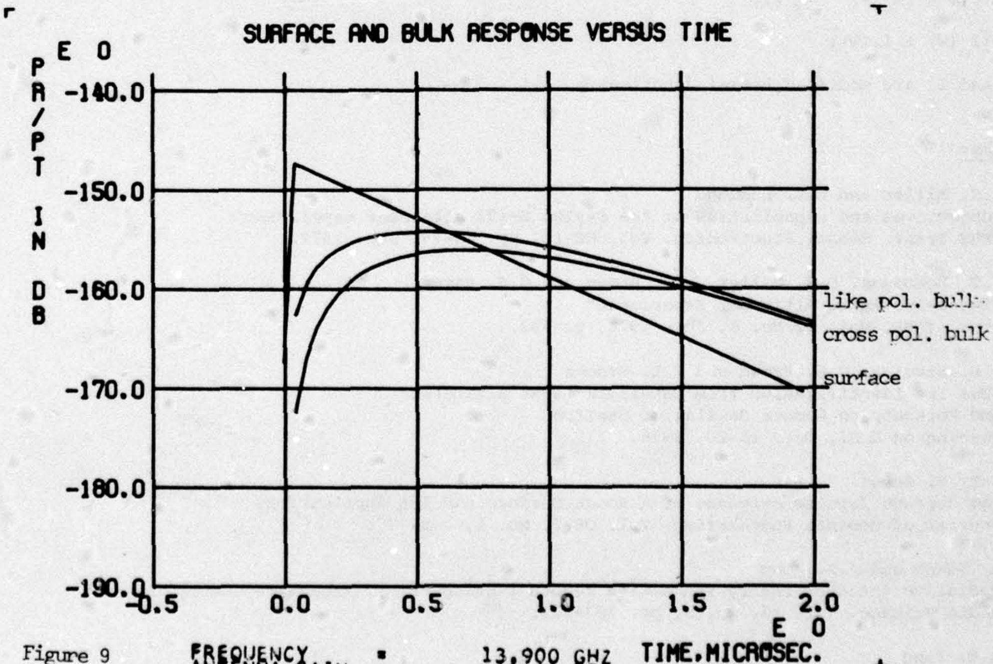

Figure 9

```
FREQUENCY          :        13.900 GHZ
ANTENNA GAIN       :         40.60 DB
PULSWIDTH          :          10.  NSEC
HEIGHT             :        435.50 KM
SURFACE PARAMETERS :
SIGMA              :        0.0200 M
IL                 :        0.2000 M
TILT ANGLE         :        0.0    DEGREES
BULK PARAMETERS    :
L                  :        0.0020 M
LP                 :        0.0050 M
DELTA              :    0.1000E-03
KA                 :        0.0100 M**-1
REL. E             :          1.80
```

Conclusion

A method to calculate the surface and the bulk echo from a satellite-borne altimeter has been developed. The calculations on snow and ice surface show that the bulk echo is significant when the skin depth is several pulse widths. It is possible to discriminate between the surface and the bulk echo, when the bulk echo is significant. The depolarization and scattering of the incidence radar pulse by the rough surface have not been taken into account. No reliable method of calculating the depolarized surface echo has been available. The existing altimeter data do not include cross polarized measurements.

Appendix A

The scattering matrix $\underline{\underline{p}}$ as derived in ref. |5|

$$\underline{\underline{p}} = \begin{pmatrix} (\underline{v}\ \underline{v}')^2 & (\underline{v}\ \underline{h}')^2 & (\underline{v}\ \underline{h}')(\underline{v}\ \underline{v}') \\ (\underline{h}\ \underline{v}')^2 & (\underline{h}\ \underline{h}')^2 & (\underline{h}\ \underline{v}')(\underline{h}\ \underline{h}') \\ 2(\underline{h}\ \underline{v}')(\underline{v}\ \underline{v}') & 2(\underline{v}\ \underline{h}')(\underline{h}\ \underline{h}') & (\underline{v}\ \underline{v}')(\underline{h}\ \underline{h}') + (\underline{v}\ \underline{h}')(\underline{h}\ \underline{v}') \end{pmatrix} \quad \text{(A1)}$$

The direction of the indicence field is given by:

$$\underline{I}_{k'} = \sin\theta'\cos\phi'\underline{I}_x + \sin\theta'\sin\phi'\underline{I}_y + \cos\theta'\ \underline{I}_z \quad \text{(A2)}$$

$$\underline{v}' = \cos\theta'\cos\phi'\underline{I}_x + \cos\theta'\sin\phi'\underline{I}_y - \sin\theta'\underline{I}_z \quad \text{(A3)}$$

$$\underline{h}' = -\sin\theta'\ \underline{I}_x + \cos\phi'\ \underline{I}_y \quad \text{(A4)}$$

The vectors for the scattered field $\underline{I}_k$, $\underline{v}$ and $\underline{h}$ are given by the analogical equations.

The scattering matrix $\underline{\underline{q}}$ is found by performing the integration (16)

$$q_{11} = (\sin^2\theta\cdot\sin^2\theta' + \tfrac{1}{2}\cos^2\theta\cdot\cos^2\theta')\ I_o(w) \quad \text{(A5)}$$

$$+ 2\sin\theta\cdot\sin\theta'\cos\theta\cos\theta'\quad I_1(w)$$

$$\tfrac{1}{2}\cos^2\theta\cdot\cos^2\theta'\quad I_2(w)$$

$$w = \tfrac{1}{2}\ k^2\ell_p^2\cdot\sin\theta'\cdot\sin\theta \quad \text{(A6)}$$

$$q_{12} = \tfrac{1}{2}\cos^2\theta\left[I_o(w) - I_2(w)\right] \quad \text{(A7)}$$

$$q_{21} = \tfrac{1}{2}\cos^2\theta'\left[I_o(w) - I_2(w)\right] \quad \text{(A8)}$$

$$q_{22} = \tfrac{1}{2}\left[I_o(w) + I_2(w)\right] \quad \text{(A9)}$$

I_o, I_1 and I_2 are modified Bessel functions.

References

|1| L.S. Miller and D.L. Hammond
"Objectives and capabilities of the Skylab S-193 altimeter experiment"
IEEE Trans. Geosci.Electronics, Vol. GE-10, pp. 73-79, Jan. 1972.

|2| J.T. McGoogan, L.S. Miller, G.S. Brown and G.S. Hayne
"The S-193 Radio Altimeter Experiment"
Proc. IEEE, Vol. 62 No. 6, June 1974, p. 793.

|3| R.H. Stanley, G.S. Brown and R.L. Brooks
"Sea ice identification from satellite radar altimeter"
WMO Workshop on Remote Sensing of Sea Ice
Washington D.C., Oct. 16-20, 1978.

|4| Gary S. Brown
The Average Impulse Response of a Rough Surface and Its Applications
Journal of Oceanic Engineering, Vol. OE-2, No. 1, Jan. 77.

|5| L. Tsang and J.A. Kong
Radiative transfer theory for active remote sensing of half-space random media
Radio Science, Vol. 13, No. 5, pp. 763-773.

|6| A.K. Fung
Theory of cross-polarized power returned from a random surface
Appl. Sci. Res., 18, 50-60, 1967.

|7| G.R. Valenzuela
Depolarisation of EM waves by a slightly rough surface
IEEE Trans. Ant and Prop., AP 15, pp. 552-557, 1967.

|8| L. Gray, J. Cihlar and S. Parashar
Scatterometer results from shorefast and floating sea ice
Canada Centre for Remote Sensing, Ottawa, Canada

|9| Robert G. Onstott and Richard K. More
Surface-based scatterometer results of Arctic Sea Ice
University of Kansas Center for Research

|10| A.L. Gray, R.O. Ramseier and W.J. Cambell
Scatterometer and SLAR results obtained over Arctic sea-ice and their relevance to the problems of Arctic ice reconnaissance
Canada Centre for Remote Sensing

|11| Georg T. Ruck, D.E. Barrick, W.D. Stuart and C.K. Krichbaum
Radar cross section Handbook
Plenum Press, 1970

|12| L. Tsang and J.A. Kong
Thermal microwave emission from half-space random media
Radio Science, Vol. 11, No. 7, pp. 599-609, Jul. 1976.

A LASER PROFILOMETER FOR DIGITAL TERRAIN MAPPING

BERNARD RUBIN
NASA Headquarters
Washington, DC 20546

MICHAEL W. FITZMAURICE
NASA, Goddard Space Flight Center
Greenbelt, MD 20771

I. Introduction

The development of ground-based laser ranging systems within the National Aeronautics and Space Administration (NASA) started in the early 1960's, soon after the invention of the laser. This program has grown substantially in the intervening years, and has produced important achievements in the areas of precision-orbit determination, polar motion, gravity-field determination, and Earth tides. In addition, work has progressed substantially so that laser ranging is expected to produce in the near future some unique results from measurements of crustal motions of the Earth, soil subsidence, ice-cap thickness changes as well as surface velocity, atmosphere aerosol distribution, cloud-top elevation and volcanic structure temporal changes.

With the advent of the Space Shuttle era, a preliminary design of a space-based decimeter accuracy ranging instrument was initiated and has now been completed. The instrument was originally designed to measure ranges with a precision of ±10 cm from the orbiting platform to a network of optical reflectors on the ground for the purpose of detecting crustal motions which occur before and after earthquakes. Sufficient link margin has been designed into the system so that it is also possible to operate in a profilometer mode. In this case, the instrument uses an internal pointing assembly under 3-axis gyro control to insure nadir pointing, and measures range using the laser signal reflected off the earth's solid or ocean surface.

It is the purpose of this paper to describe the instrument along with the ranging subsystem, the pointing subsystem and attitude reference, to define the measurement capabilities including ranging accuracy, the signal-to-noise ratio for water, ice, and solid-earth, footprint size, and atmospheric effects and then to summarize the overall system with its advantages and disadvantages.

II. Description of the Instrument

A. Functional Overview

This instrument is, in essence, a very precise distance measuring device. It accomplishes this by 1. transmitting a short pulse of very intense laser radiation and 2. measuring the round-trip transit time of this pulse to the target. A simplified system functional diagram is shown in Fig. 1. The ranging subsystem includes a Nd:YAG laser which generates a 50 mJ, 5 ns pulse of 0.53 micrometer wavelength radiation. A small portion of this signal is diverted to an optical detector and serves to start the time of flight measurement. The remainder of the signal is directed to a mirror within a 2-axis pointing system which steers the laser pulse at the target. A small portion of the energy reflected by the target is captured by this same mirror and is delivered to the optical detector within the ranging subsystem to terminate the time of flight measurement. Measurement accuracies of 0.3 to 0.6 ns (5 to 10 cm) are typical. If the pulse is to illuminate the target, the error in the pointing system must not exceed 1/2 the transmitter beam width which, in this case, is 50 microradians. Three pieces of information must be supplied to the system minicomputer: 1. the location of the instrument in three dimensional space (i.e., spacecraft ephemeris), 2. the attitude of the instrument, and 3. the location of the target. The location of the instrument is obtained from a Global Positioning Satellite (GPS) receiver on board the Shuttle with an expected accuracy of 10-15 meters. Instrument attitude is obtained from a NASA standard attitude reference system composed of a star tracker and a 3-axis gyro package. Accuracies of 2-5 arc-seconds are expected.[1] The target may be either a small array of optical cube corners, or a specific region of the earth's surface. If cube corners are used, their location must be known to about 25 meters. For profiling or altimetry, the nadir direction must be defined with an accuracy of at least 1/2 the transmitter beam width. The necessary information is implicit in the spacecraft ephemeris. Ephemeris accuracy of about 350 meters is required to satisfy this condition. Detailed analyses of the pointing system have been carried out by TRW.[1] The conclusion is that reliable pointing of a ±50 microradians (μr) beamwidth laser from the Space Shuttle is entirely possible.

B. Ranging Subsystem

The operation of the laser ranging portion of the instrument is described using the functional diagram and numbering sequence shown in Fig. 2.

1. The system minicomputer generates the desired pointing angles for the two axis gimbal assembly and also monitors the actual pointing direction as indicated by the angle encoders. When the commanded and actual pointing angles agree to within 10 arc-seconds, a "laser enable" signal is generated by the computer.

2. A digital "and" gate receives the "laser enable" as well as a 10 pps timing signal, and this gate generates the "laser firing pulse."

3. The "laser firing pulse" triggers high current pulse circuitry which drives the flash lamp within the laser cavity. The laser pulse exits the laser cavity about a millisecond after the flash lamp fires. The laser beam is collimated so that the total beam divergence is about 0.1 milliradians (mr). After collimation, the beam will be about 5 cm in diameter.

4. The beam is directed by a series of flat mirrors to the "beam sampler" unit. This device diverts a small percentage (less than 1%) of the beam into the receiver to serve as a start pulse for the time of flight measurement.

5. The remainder of the beam is directed to the "two-axis gimbaled mirror" which is pointed at the ground target. The transmitted pulse traverses the atmosphere, is incident on the ground and is reflected back to the flight instrument.

6. A small portion of the return signal is lost due to the obscuration caused by element 4, but about 90% of the return is collected by the "receiver optics" and is focused onto a pair of optical detectors. The first detector is the range measurement photomultiplier; the second detector is an angle-of-arrival detector which is used for "locking onto" return signals from cube corner targets.

7. The angle tracker receives about 15% of the return signal with the remaining 85% directed onto the photomultiplier. The angle tracker is a quadrant photodetector with a field of view of about 0.1 mr full angle. The signal received from cube corner arrays is imaged with an angular spot size of about .01 mr. The device therefore functions as a null seeking error sensor. The angle tracker is not used when making profilometer measurements.

8. The time-of-flight "photomultiplier" is an electrostatic photomultiplier tube with a rise time of about 1 ns and a current gain of 10^6. This unit detects both the start pulse, and about 5 ms later, the return signal from the ground target.

9. Both pulses are processed by a "realtime correlator" which is implemented using an 8-10 element tapped delay line.

10. The time of occurrence of the maximum of the correlation function is measured by the "peak detector."

11. In order to minimize false alarm probabilities, both the start and stop laser pulses are time-gated.

12. The time-gate for the start pulse is furnished by a "photodiode" which detects a portion of the transmitted pulse through an independent optical train. The time gate for the return signal is generated by the system minicomputer using predicted range information.

13. The epochs associated with both the start and stop pulses are generated by the "event timer" and sent to the system computer for formatting prior to entering the Shuttle telemetry system.

The ranging subsystem has been configured such that the "start" and "stop" laser pulses use the same photodetector and post-detection signal processor. This minimizes the possibilities of bias errors occurring in the range measurements since any delay time variations which occur in the receiver will alter the "start" and "stop" times by precisely the same amount, and these times are differenced to derive the range measurement. The initial calibration (or "zero set") for the system is implemented in the standard manner, i.e., by ranging to a target at a known distance.

C. Engineering Characteristics

A definition study of this instrument has recently been completed.[2] The instrument concept which has resulted is shown in Fig. 3. Components are mounted on both the top and bottom of the optical bench. The 2-axis pointing assembly has 60° coverage on the inner axis and 170° on the other axis. The telescope is an f/6 Ritchey-Chretien configuration with a focal length of 1.17 meters. Fig. 4 shows the components mounted on the underside of the optical bench. The principal underside components are the inertial reference unit (DRIRU II, three axis gyro) and the laser. A 10 pps frequency-doubled Nd:YAG laser of the type produced by Westinghouse for target designator applications has been baselined for the instrument.

The electronics required for instrument control and data processing are placed remotely from the optical bench to minimize thermal coupling. Fig. 5 shows a full scale model of the instrument mounted in a single 2-meter Spacelab pallet. The instrument electronics are on a shelf underneath the optical bench. The instrument, as designed for Spacelab weighs about 225 kg and requires about 800 watts during laser operations. The quiescent power requirement is about 75 watts.

III. Application to Geodynamics

A. Mission Scenario

The initial motivation for designing a very accurate laser ranging instrument for use in space was supplied by the geodynamics community in connection with earthquake prediction studies. The mission scenario is illustrated in Fig. 6. Small optical cube corner arrays are deployed on the ground in seismically active regions. Regions of scale 150 km to 1500 km are of principal interest. The laser ranging instrument is on the spacecraft, and as the spacecraft reaches 20° elevation angle (as seen from the nearest ground target), the laser beam is pointed at the target and ranging measurements collected at a 10 pps rate. After a short period of time (typically 2-3 seconds), the beam is directed to the next target and a similar set of measurements is collected. The procedure continues in a sequential manner until the entire network of targets has been covered. Dwell times per target and measurement rate for a particular mission are selected so that the entire network can be "mapped" three times per satellite pass; the first time occurs when the satellite is at low elevation angles and rising; the second time is when the satellite is at high eleveation angles; and a third time when the satellite is at low elevation angles near the end of the pass. A typical cube corner array for a ground target is shown in Fig. 7. The array is composed of 9 cube corners, is about 25 cm in diameter, and would cost about $800 per copy. Extensive mission simulations have been carried out at NASA/Goddard on the ability of this system to measure the cm level crustal deformations which are thought to precede large earthquakes. A map of the region considered in the simulation and typical simulation results are shown in Fig. 8.

B. Expected Results

In this simulation a network of ground targets was assumed to be deployed over the state of California. The total number of targets was 150, and they were deployed with a nominal separation of 50 km. The host spececraft was assumed to be in a 50° inclination orbit at an altitude of 1000 km. Ranging measurements were attempted on all passes over the network, but it was assumed that a data outage of 50% existed because of cloud cover. The simulation also incorporated errors due to gravity field uncertainties, atmospheric drag and radiation pressure uncertainties, and laser system noise and biases. Under these conditions, the simulation shows that in one week the system is able to measure horizontal position shifts throughout the network with cm precision. Specific results are listed in Fig. 8. Position shifts in vertical are also detectable, but a reduction of 2-3 in sensitivity can be expected (due principally to gravity field uncertainties). The capability to measure cm level deformations over such a large area (200 km by 1300 km) in such a short period (1 week) may have a very positive impact on the ability of geophysicists to understand and eventially predict earthquake events; for this reason the system is now being considered for space flight tests in the mid-to-late 1980's.

IV. Application to Profilometry

A. Link Analysis

In this operating mode the instrument does not receive reflections from optical cube corners, but rather it detects the signal reflected from the surface of the earth. Using ephemeris data from an on-board GPS receiver and attitude information from an instrument mounted gyro package (as discussed in II), the pointing system directs the laser pulse in the nadir direction. Under these conditions the received energy (E_r) is given by

$$E_r = E_t \sigma^\circ A_r T_t T_r T_a^2/4\pi R^2 \quad (1)$$

where

E_t = transmitter energy per pulse

σ° = target cross-section per unit area

A_r = area of receiver optics

T_t = transmission of transmitter optical system

T_r = transmission of receiver optical system

T_a = transmission of the atmosphere at zenith

R = range from spacecraft to ground (nominally the same as orbit height)

The σ° term is in essence the product of the reflectivity of the surface and the directional characteristic of the reflected signal (e.g. for a Lambertian surface σ° = 4 x reflectivity). The optical detector in the instrument converts received photons to electrons; these electrons, flowing in a short time period, constitute the electrical signal which is amplified and detected. The magnitude of the electron pulse which is detected is given by

$$N_e = E_r \eta/h\nu \quad (2)$$

where

N_e = average number of electrons per received optical pulse

E_r = energy of the received optical pulse

η = detector photon-to-electron conversion efficiency

h = Planck's constant

ν = frequency of the laser radiation

Combining eqs. (1) and (2), one can evaluate the radar link for various sets of conditions. The results for this laser system are shown in Fig. 9. The relevant system parameters are:

E_t = .05 Joules	η = .25
T_t = .88	$h\nu = 3.7 \times 10^{-19}$ Joules
T_r = .43	σ° = variable, 0.2 to 2.4
T_a = .8	R = variable, 200 km to 700 km
$A_r = 2.28 \times 10^{-2}$ m^2	

The orbit height span (200 km – 700 km) is typical of what can be expected on most Shuttle flights. The σ° value of 2.4 (snow or ice) assumes a reflectivity[3] of 0.6 and a Lambertian direction characteristic (gain = 4) on the reflected signal. The ocean σ° of 0.2 is based on the measurements of Jelalian,[4] which showed that typical ocean reflections at 1.06 micrometers have a modest specular component. For comparison purposes, a Lambertian ocean reflectance would make σ° equal to 0.08.

The receiver system can detect signals as low as 1 photoelectron per pulse. Therefore, in the absence of noise, all return optical pulses which generate at least a single photoelectron can be detected. However, during daytime operations, significant amounts of sunlight (from atmospheric backscatter and the earth's albedo) impinge on the receiver optical system. A small, but still significant, portion of this is transmitted through the optical filter and ultimately becomes the dominant noise source in the receiver. In order to maintain the false alarm probability at an acceptably low level (typically 10^{-2}), a post-detection electronic threshold is built into the receiver signal processor. In this case, assuming a 10 Å optical bandpass and a 10^{-4} radian field of view, a threshold level of 3 photoelectrons is sufficient to achieve the 10^{-2} probability of false alarm.

B. Instrument Accuracy

There are several factors which must be considered when assessing the accuracy of this instrument in the profilometry mode. The most important factors are:

1. receiver signal-to-noise ratio,
2. instrument systematic error sources,

3. atmospheric propagation delay, and
4. pulse spreading due to surface roughness.

1. Receiver signal-to-noise ratio

The accuracy with which the arrival time of an optical pulse can be estimated is proportional to the width of the pulse and inversely proportional to the square root of the average number of photoelectrons. After inclusion of the appropriate scaling factors,[5] the rms single measurement ranging accuracy is as shown in Fig. 10. The lower curve gives the performance of the classical maximum likelihood receiver; the upper curve gives our estimate for the performance of this instrument's receiver configuration. At accuracies of 10 cm, the difference is about 3 dB; this difference increases at higher accuracies with a limiting accuracy of about 3-4 cm. Using the link analysis results shown in Fig. 9, the nominal accuracy of this instrument using signals reflected from snow-ice-land-ocean can be estimated and is as shown in Fig. 10.

2. Instrument systematic error sources

There are several potential sources of systematic (i.e. bias) errors. These errors are particularly serious since they are not reducible through data averaging. These are:

a. Receiver clock

If the frequency standard which controls the time-of-flight measurement drifts off frequency, errors result. However, with a measurement time interval of about 10^{-2} sec and an accuracy requirement of about 10^{-10} sec, only one part in 10^8 is required. This requirement is not difficult to satisfy.

b. Time delay variations in receiver

This error source is reduced to a negligible level by using the same photodetector and signal processor for both the transmit and receive optical pulses. Delay variations affect both pulses to the same degree, and since the epochs of the two pulses are differenced to determine range, this error source can be neglected.

c. Amplitude dependent timing errors

Because of space-charge effects which vary transit time through high-gain electron multipliers, range errors of many cms can occur when the received signal level varies over 20-30 dB. (Such signal fluctuations are possible due to atmospheric fading). The magnitude of this error can be reduced by measuring the amplitude of each return pulse and modeling the delay variations.

3. Atmospheric propagation delay

The velocity with which light propagates through the earth's atmosphere is somewhat less than its free space value. Therefore, distance measurements based on transit time can have significant errors if this effect is not properly modeled. Models which are accurate to better than 1 cm have been developed[6] and are used routinely in the NASA laser ranging network.[7] However, these models require as inputs pressure, temperature, and humidity at the surface of the earth. Inaccuracies in this information will lead to errors in the estimate of the atmospheric propagation delay. The magnitude of the errors is shown in Fig. 11.[8] An elevation angle of 90° (nadir) is of principal interest. It is clear that pressure errors are the dominant concern. A pressure error of 10-20 mbar will cause range measurement errors of 2.3-4.6 cm. For some profiling systems, relative rather than absolute accuracies may be required. In this case, static errors in the estimate of surface pressure are not of consequence; only variations in the errors of the estimate are relevant. Reducing errors in this quantity to 10 mbar appears feasible.

4. Pulse spreading due to surface roughness

The post-detection signal processor used in this type of instrument would typically use a centroid detection algorithm. This procedure is equivalent to measuring the surface elevation averaged over the "footprint." For a typical orbit height (500 km), a 0.1 mr transmitter divergence will provide a 50 meter diameter "footprint." Surface undulations of 1 meter over this "footprint" will produce a spreading of the return signal of about 6 ns. Convolving this surface signature with the transmitter waveform will produce a detected waveform which is spread significantly. This broadening of the pulse (without any change in the total received energy) will result in a reduction in system accuracy as discussed earlier. The importance of this effect is critically dependent on the type of surface being profiled. For ice or snow, 1 m undulations over 50 m are not likely;[9] for sea surface profiling, such spreading is quite likely.

C. Unique Characteristics

A laser system similar to that described in this paper is being considered for an Ice Processes Satellite now under study by NASA. Included in the satellite instrument payload would be a radio frequency (RF) altimeter similar to that flown on SEASAT. The laser instrument would complement the RF altimeter by providing: high spatial resolution (i.e. smaller footprints) over selected areas, very high accuracy measurement data which would be used to calibrate the RF instrument, and on board, high accuracy orbit determination over limited access regions (such as the polar ice caps).

An RF altimeter such as flown on SEASAT (1 m diameter antenna, K_u band) would provide a spatial "footprint" of about 10 km. However, if a transmitter pulse width of 10 ns is used, the instrument will operate in the pulse-limited mode and, from a 700 km orbit height, will provide 3 km resolution. By contrast, the laser instrument will provide a resolution of 0.07 km.

The distance measurement from the satellite at optical frequencies is unaffected by the earth's ionosphere or by the amount of water vapor in the earth's atmosphere. As measurement requirements edge toward the 5-10 cm accuracy level, these are potentially serious error sources for RF altimeters and profilometers. Coupling periodic laser measurements with the RF data will provide a technique for reducing these errors.

Full utilization of 5-10 cm profilometry data will require that spacecraft orbits be determined to comparable accuracy. For previous space-based altimetry systems (GEOS III, SEASAT), this was accomplished by placing laser reflectors on the satellites and deploying ground-based laser tracking systems in the area where high accuracy data was needed. For missions such as the Ice Processes Satellite, this is not feasible due to the severity of the Arctic and Antarctic environments. However, it does appear that high accuracy orbit determination is possible if laser reflectors are deployed at a few dozen known locations along the satellite ground track. Periodic range measurements from the satellite-based laser instrument to these reflectors can provide the data needed for the high accuracy orbit determination. Simulations are currently underway to determine the required number and distribution of ground reflectors.

V. Summary

A space-based laser optical system for ranging to the earth's surface with an accuracy of ±5-10 cm is described, and application of this system for profiling terrain is presented.

It is shown that from a 700 km orbit, the optical system results in a spatial resolution of 0.07 km compared to 3 km for the RF system. Further advantages of the laser technique are that distance measurements from the satellite at optical frequencies are unaffected by the earth's ionosphere or by the amount of water vapor in the earth's atmosphere.

It is recommended that the use of a laser ranging system in conjunction with an RF system will provide a technique for optimizing the accuracy of terrain profiling from space.

REFERENCES

1. SGRS Pointing System Study, Vol. I, II, TRW Report No. 33394-6001-RU-00, November 1978.

2. Spacelab Geodynamics Ranging System Optical/Mechanical/Thermal Conceptual Design Study, Vol. I, II, General Electric Report No. GE 78SDS4242, October 1978.

3. O'Brien, H. W. and Munis, R. H., "Red and Near-Infrared Reflectance of Snow," U.S. Army Cold Regions Research and Engineering Laboratory (USACRREL) Research Report 332, 1975.

4. Jelalian, A. V., "Sea Echo at Laser Wavelengths," Proc. IEEE, 56, May 1968.

5. Abshire, J. B., "A Comparative Study of Optimum and Suboptimum Direct Detection Laser Ranging Receivers," NASA TP-1315, September 1978.

6. Marini, J. J. and Murray, C. W., "Correction of Laser Range Tracking Data for Atmospheric Refraction at Elevations Above 10 Degrees," NASA X-591-73-351, November 1973.

7. McGunigal, T. E. et al, "Workshop on Laser Ranging Instrumentation – III," NASA X-723-78-22, July 1978.

8. Gardner, C. S., "Statistics of the Residual Refraction Errors in Laser Ranging Data," U. of Ill. Report RRL 481, Jan. 1977.

9. De Q. Robin, G., "Mapping the Antarctic Ice Sheet by Satellite Altimetry," Canadian Journal of Earth Sciences, Vol. 3, 1966.

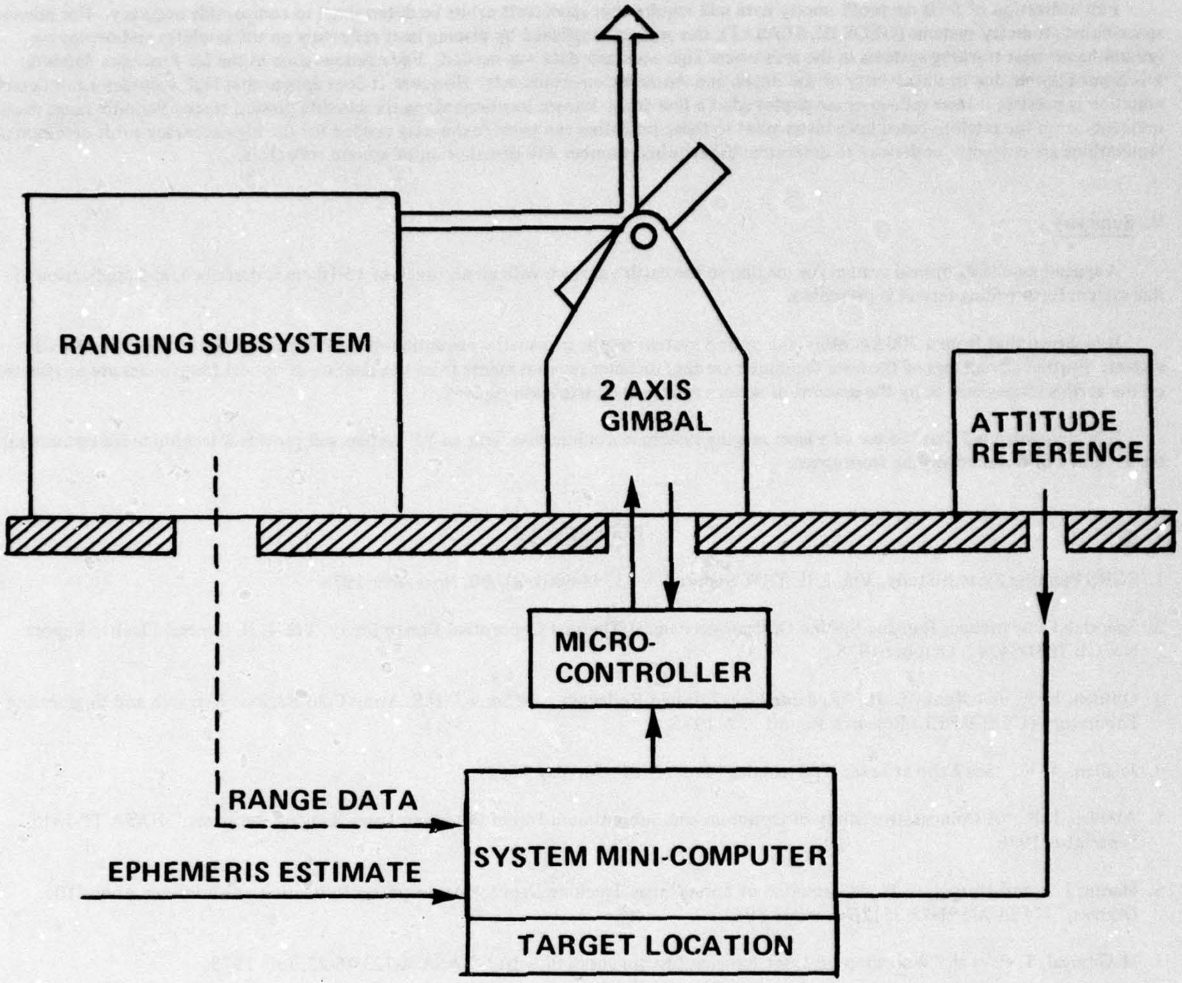

Fig.1 Spaceborne laser ranging system functional diagram

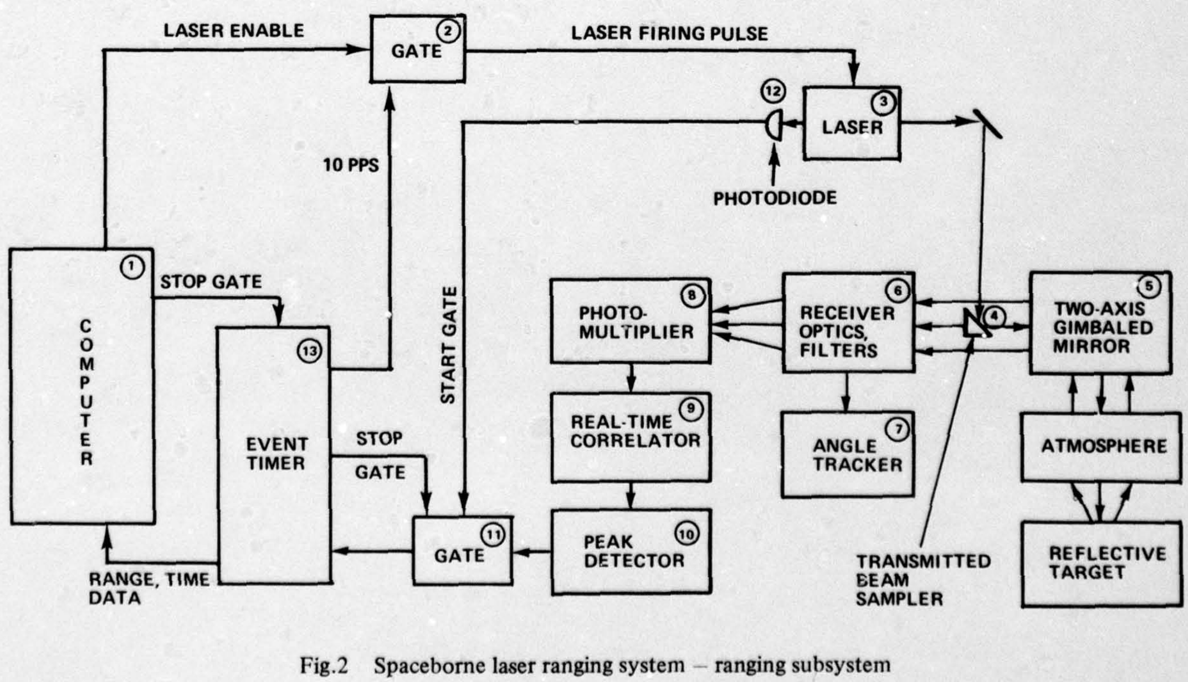

Fig.2 Spaceborne laser ranging system – ranging subsystem

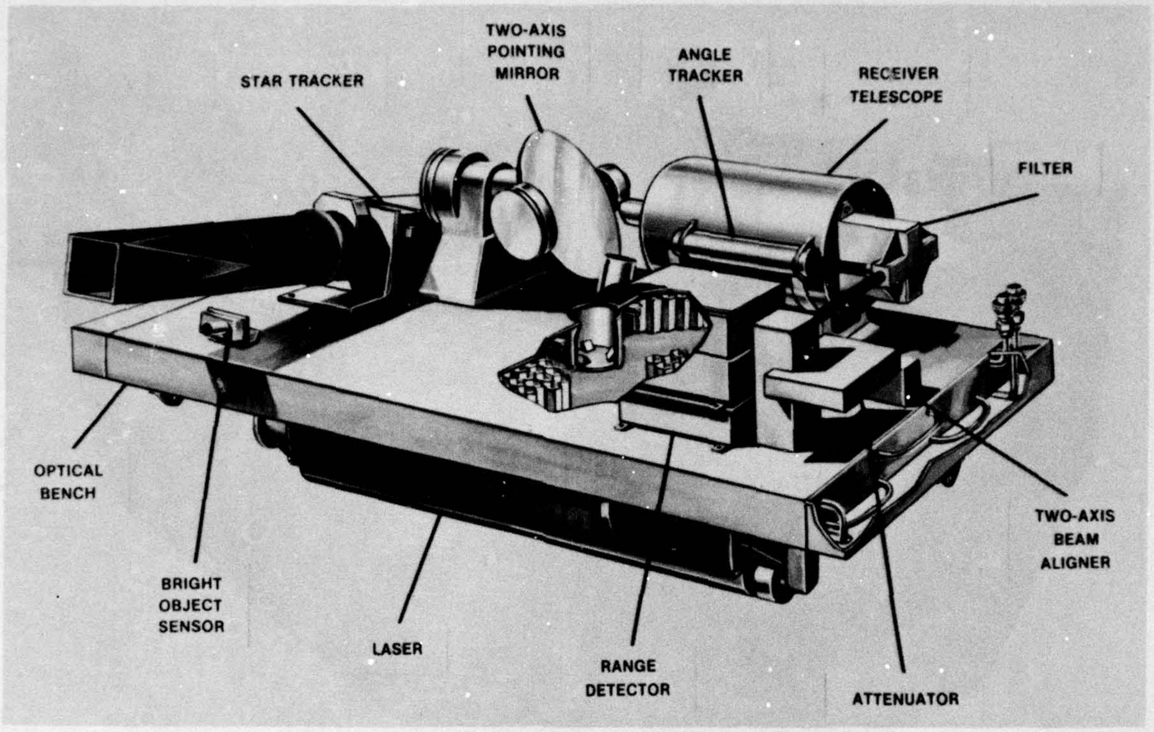

Fig.3 Spaceborne laser ranging system instrument concept

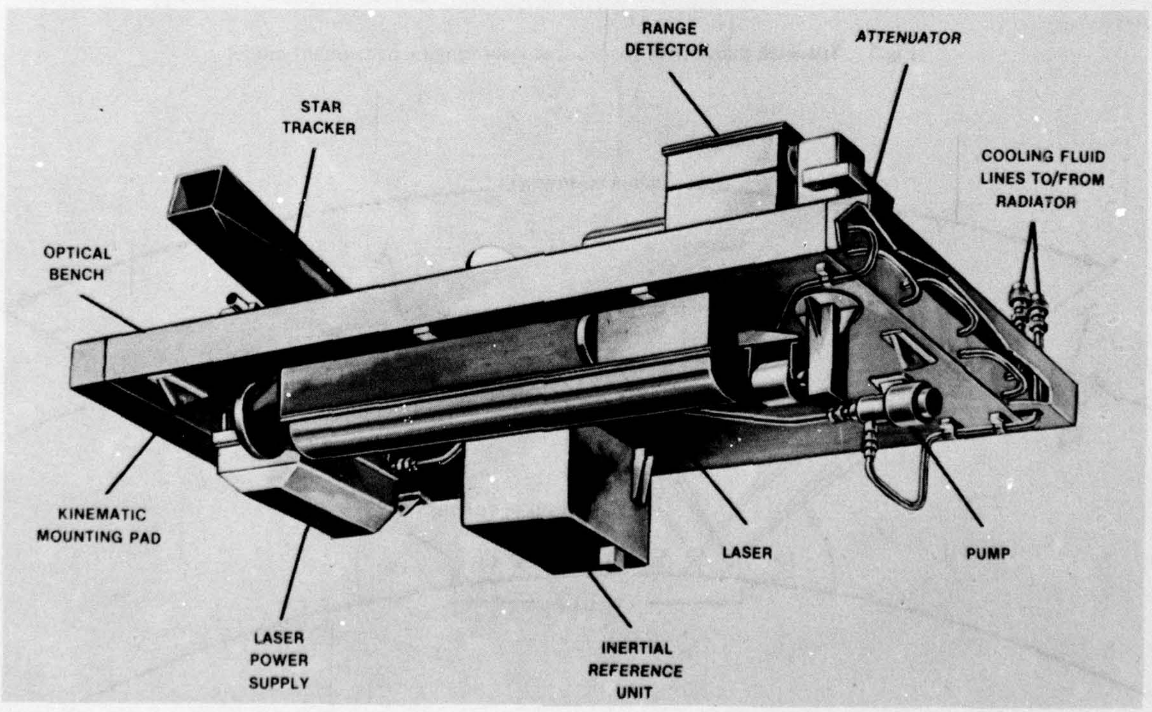

Fig.4 Spaceborne laser ranging system – underside

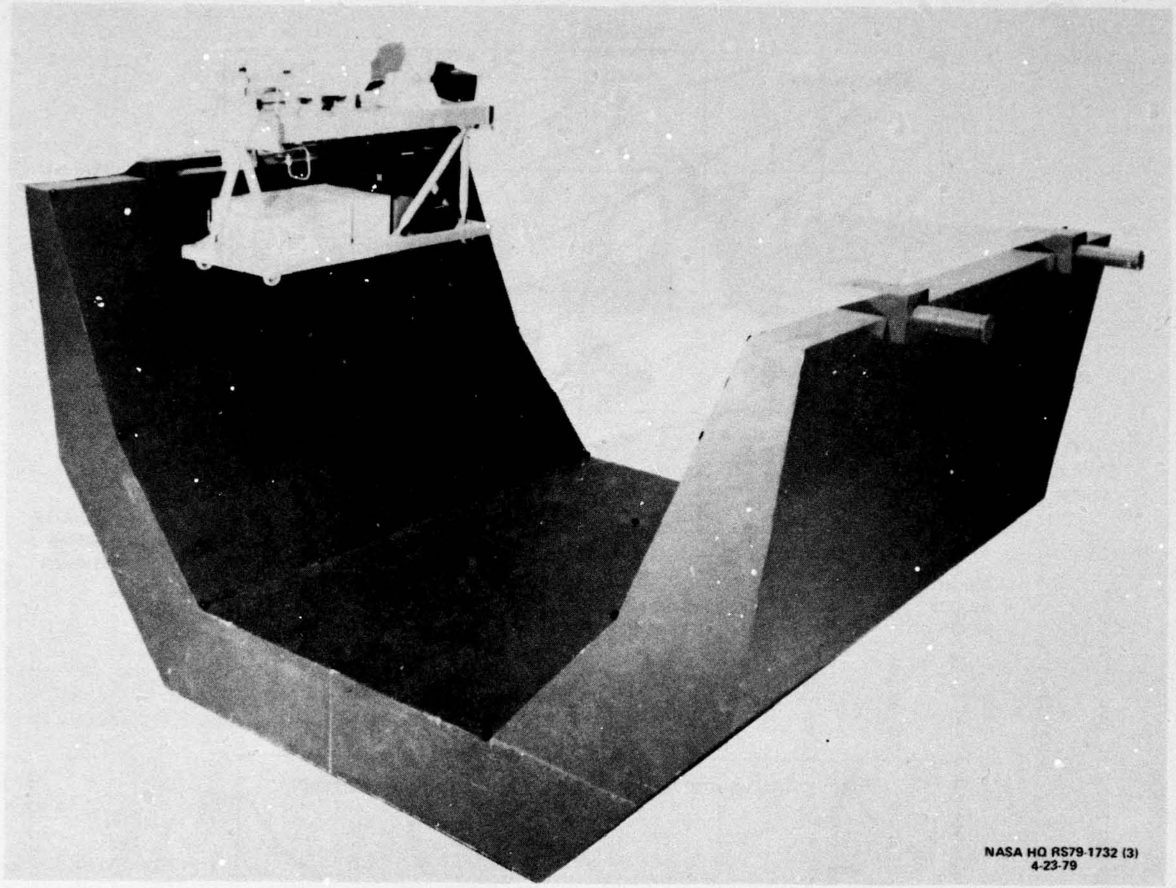

Fig.5 Spacelab pallet with spaceborne laser ranging instrument model

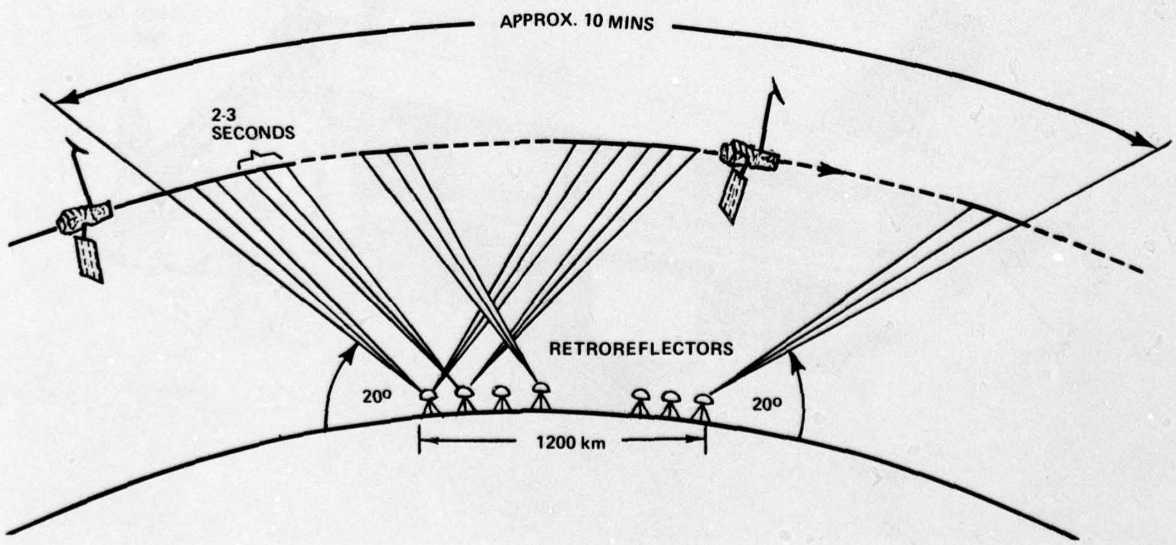

Fig.6 Spaceborne ranging system

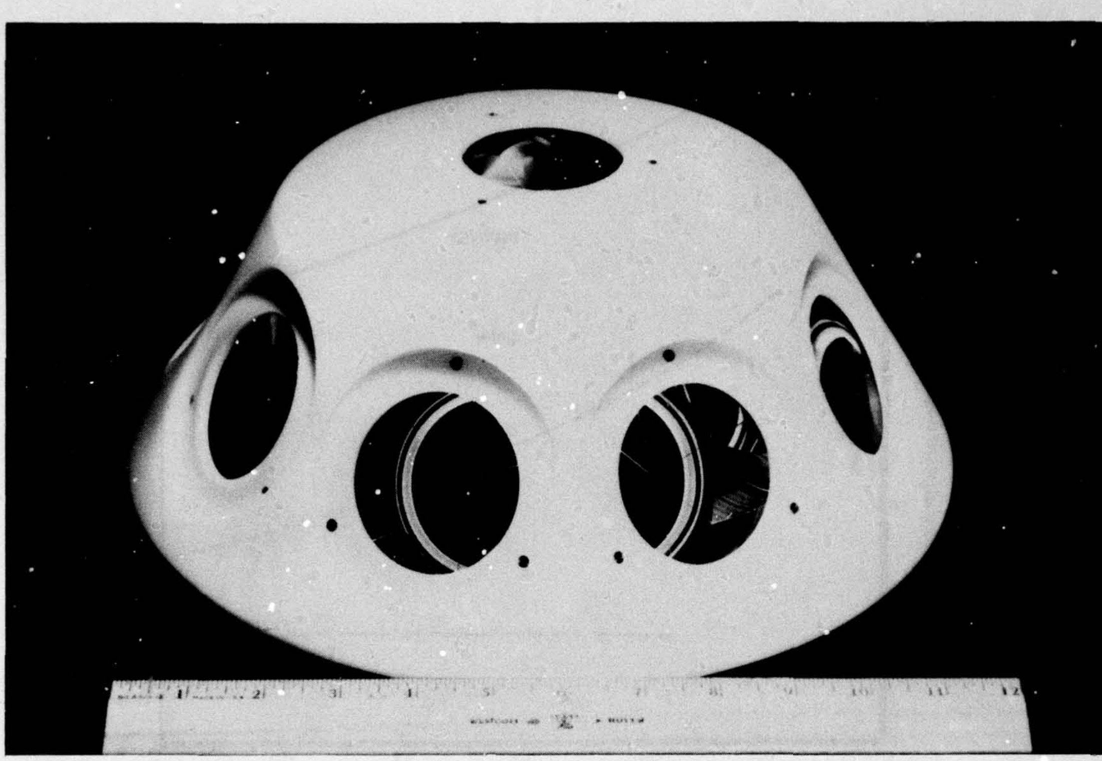

Fig.7 Ground target corner array

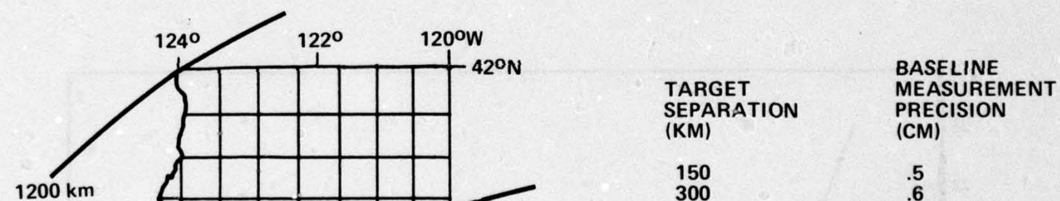

Fig.8 Distribution of ground targets for California simulation (spacing approx. 50 km)

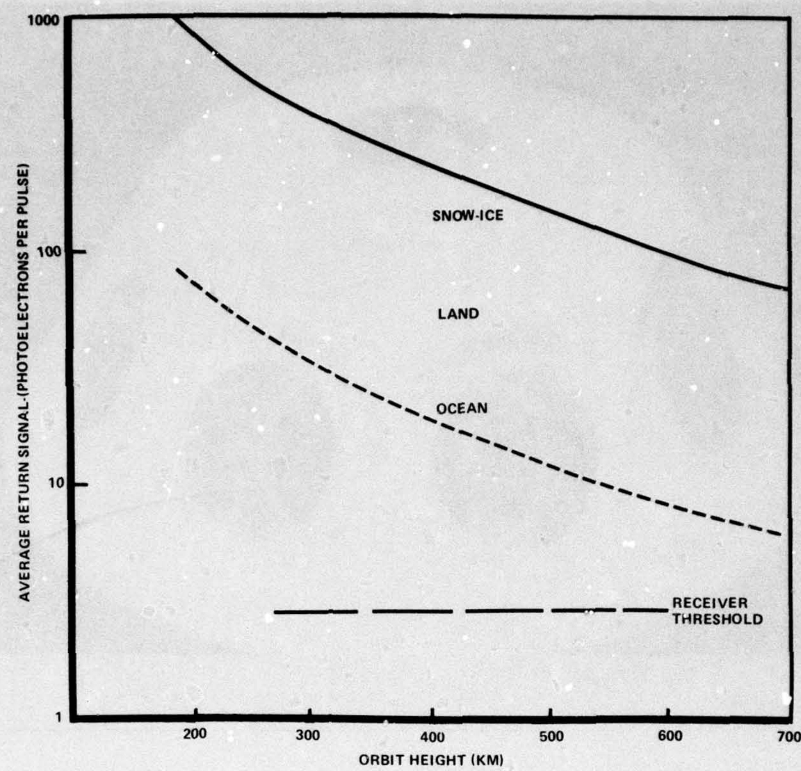

Fig.9 Return signal strength vs orbit height

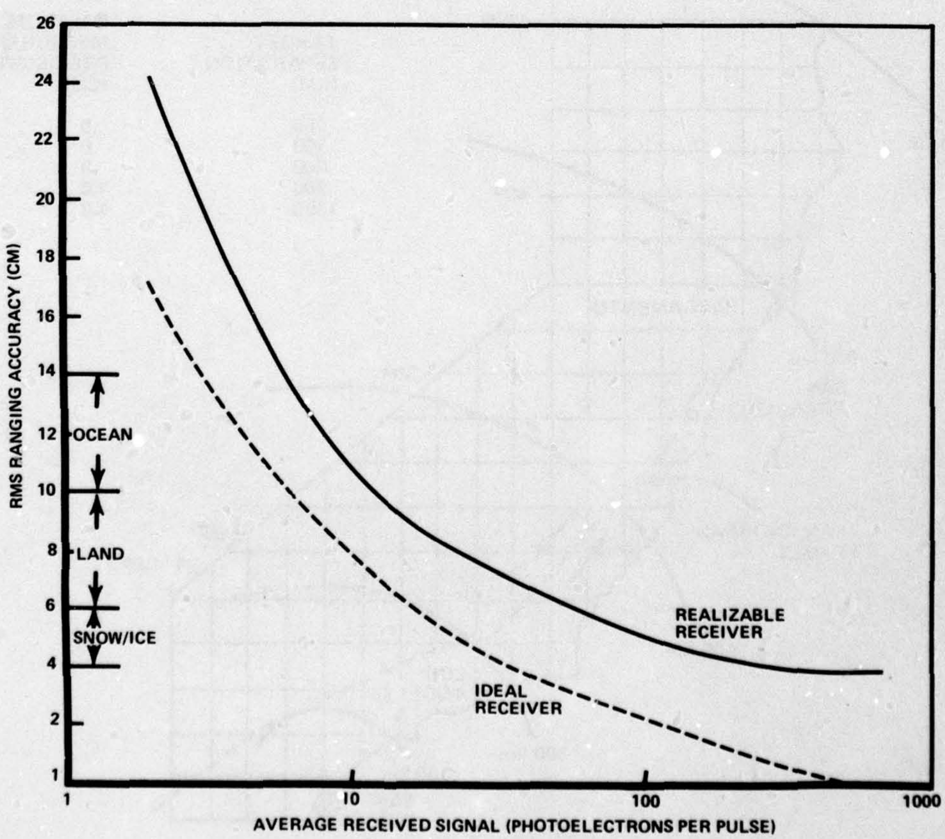

Fig.10 Instrument accuracy

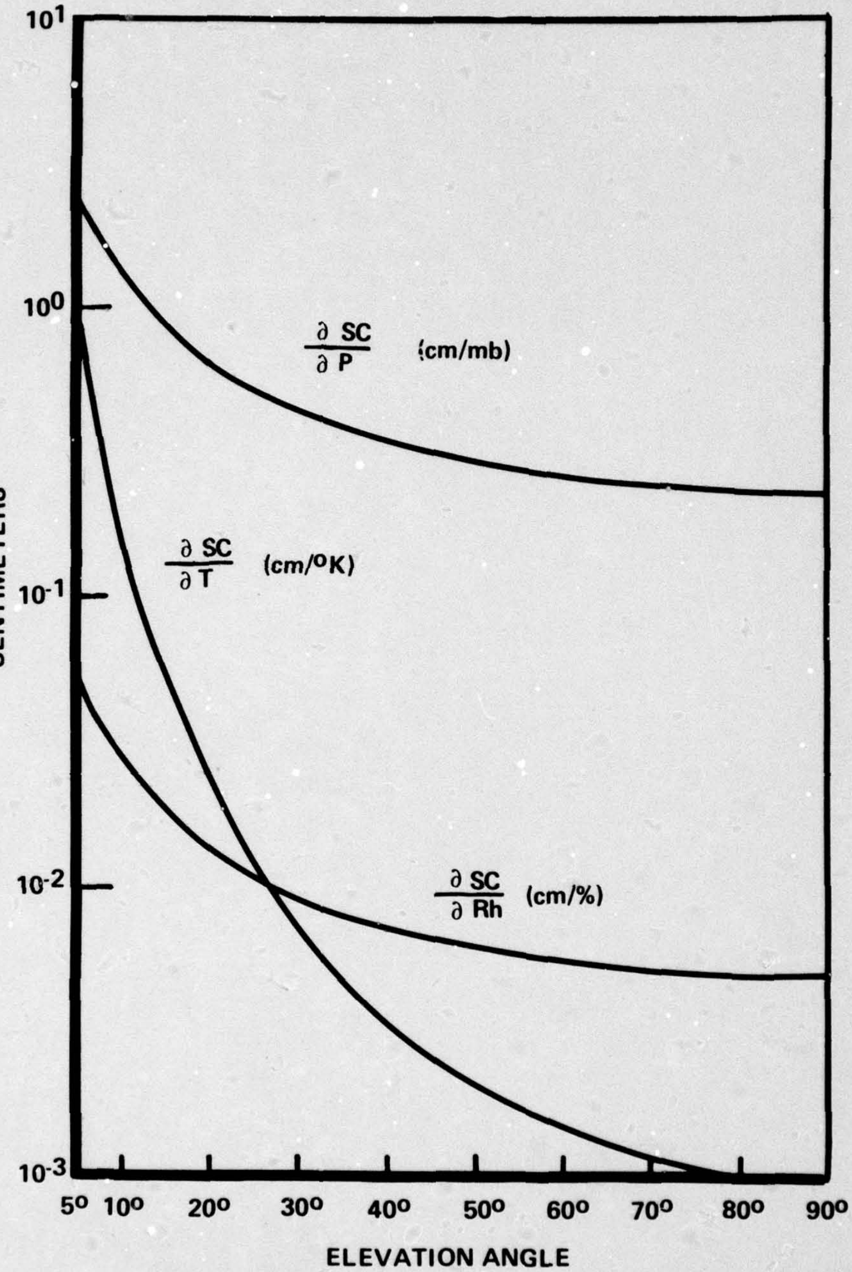

Fig.11 Variation of the atmospheric correction formula with respect to pressure, temperature and relative humidity

AN EXPERIMENTAL INVESTIGATION OF MULTI-PATH SCATTERING AT L-BAND

P. Lewis

formerly of Dept of Electronic & Electrical Engineering, University of Birmingham, England

now with

Standard Elektrik Lorenz AG (ITT), Ostendstrasse 3, 7530 Pforzheim, Federal Republic of Germany

SUMMARY

An investigation is described of the scattering effect responsible for large errors in the azimuth bearing measurements obtained with a 1 GHz monopulse receiver on a particular site when the source occupied different positions near the top of a distant hill. The received field distribution on a horizontal line of length 32 m directly in front of the monopulse antenna was sampled by a travelling probe antenna and recorded holographically. Computer processing of the hologram realised essentially a series of filtering operations to reconstruct sections of the field distribution (assuming 2-dimensional propagation in empty space) at different distances in front of the receiver, which were printed out as amplitude and phase plots. These images revealed the scattering mechanism, which included a ground reflected wave diffracted between two buildings. The reflection coefficient was in reasonable agreement with theoretical predictions. A computer model of the scattering mechanism served both to confirm the interpretation of the experimental data and to investigate the effects of different components of the multi-path field on the monopulse receiver. Maximum bearing errors to the order of 0.2 beamwidths were found.

1. INTRODUCTION

Some experiments to assess the azimuth bearing accuracy of a monopulse secondary radar revealed large errors in the case of a certain line of sight propagation path. For this path the test source occupied different positions near the top of a hill 17.5 km from the radar, subtending an elevation of 0.65°. The radar received at 1090 MHz, employed amplitude comparison processing, and the antenna consisted essentially of two side-by-side horizontal linear arrays of dipoles, against a reflecting screen to provide uni-directional patterns. As accurate bearings were measured over other transmission paths it appeared likely that the errors arose through scattering from terrain or artefacts near this particular path, although even at low elevation angles terrain reflections are not usually considered to cause large azimuth errors (cf. BARTON, D.K.,1974).

Figure 1 is a view from the radar at Malvern looking eastwards out to the transmitting sites on Bredon Hill. An elevation profile of terrain under the radio path was drawn up using contour maps, applying adjustments for standard atmospheric refraction. First Fresnel zone clearance obtained over the whole path, and the thickly wooded hill at a range of 1.4 km seen in Fig. 1 screened the receiver from any possible strong ground reflection occurring at a greater range. The immediate foreground of Fig. 1 is part of Malvern Common. On the far side of the Common, to the north of the radio path stood a Church, and to the south a house (labelled H3). The front of the Church was 300 m from the receiver, and for the most northerly transmitter position the line of sight to the centre of the northern half of the monopulse aperture cleared the belfry by about 9 m, equal to the first Fresnel zone radius at this range. The house was at a range of 330 m, and for points in the southern half of the monopulse aperture the line of sight ran 9 m above its roof ridge, compared with a first Fresnel zone radius of 9.5 m.

In such problems the delays (relative to the direct wave) of multi-path signals received with a directional antenna are very short, often to the order of one period of the carrier, so that no useful resolution can be obtained by a pulse transmission. A number of experimental investigations have been based upon height-gain measurements (BECKMANN, P. and SPIZZICHINO, A.,1963a) in which a continuous wave is radiated and the intensity of the received signal recorded as transmitter or receiver undergoes controlled displacements in a vertical line. The results have in some cases enabled the identification of regions of terrain producing strong quasi-specular reflections or knife-edge diffraction (TOMLINSON, H.T. and STRAITON, A.W.,1959) and of reflecting layers in the troposphere (JA, Y.H.,1976). The experiments to be described also employed a CW transmission, but the received field was measured on a horizontal line in front of the radar aperture on the site under investigation. In order to recover the complex amplitude distribution of the field without ambiguity, a travelling probe antenna provided with a phase-stable RF connection was used together with a fixed reference antenna. Imaging techniques were developed that revealed the scattering mechanism.

2. THE EXPERIMENT

Figure 2 shows the travelling antenna, the main component of the synthetic aperture receiving system. This antenna was a half-wave dipole against a wire mesh screen to cut out reflections from objects behind the synthetic aperture. It was mounted on a carriage of light alloy tube, drawn along steel straining cables by an electrical drive system. The cables were supported 8.5 m above ground level between lattice towers 34 m apart, making available an aperture of about 32 m. Support cables, drive cables and the RF feeder were all tensioned by hanging weights. One traverse of the aperture took 6.5 mins, the scanning speed being sufficiently slow that any spurious phase modulation products caused by mechanical oscillations of the antenna would fall outside the recorded signal band.

RF coupling to the travelling antenna was by means of a non-contacting coupler sliding on a fixed span of twin feeder (a two-wire transmission line embedded in a polythene ribbon). A second coupler at one end of the

aperture picked off the signal. The changing effective length of feeder with position of the antenna made it convenient to record the field as an off-axis (or single sideband) hologram, avoiding the need for matched in-phase and quadrature receiver channels. A small corner reflector antenna pointed at the transmitter provided the reference wave. Signals from travelling and reference antennas were brought to interference in a hybrid circuit at the front of a receiver with linear IF amplifiers, whose square-law detected output in a band 0.04 - 0.64 Hz represented the field distribution in the synthetic aperture. This signal took the form of a low frequency carrier contributed by the direct wave, with amplitude and phase modulations corresponding to the multi-path fields. It was filtered, A to D converted and punched on paper tape, samples being commanded by a photo-tachometer incorporated in the carriage drive system.

As in the original monopulse bearing measurements a frequency of 1090 MHz (λ =27.5 cm) and vertical polarisation were used. In a few cases the travelling antenna was set to receive horizontal polarisation but the results revealed no strong cross-polarised field. Measurements were made with the synthetic aperture at two positions in the same line, northerly and southerly. These partially overlapped each other, but only in the northerly position was the radar aperture completely covered. Bredon Hill transmitter sites lay about 7° off the aperture normal. Each experiment using a particular site was allocated a serial number. Two or four repeated runs were made, traversing the carriage to and fro across the synthetic aperture, in order to assess the short-term stability of the received field.

3. DATA PROCESSING AND IMAGING

Computer processing of the holograms was carried out in a series of stages, using files to store the partially processed data. Initial adjustments were subtraction of the average intensity, compensation for the variable attenuation associated with the twin feeder (a maximum of 3.6 dB), and collation of the repeated runs. The holograms were then filtered by means of an FFT routine: the spectral band corresponding to directions within ± 30° of the aperture normal was isolated, equalised for the transfer function of the video filter in the receiver, then re-transformed. Thus field distributions in the synthetic aperture were recovered in the form of complex samples spaced λ apart.

Images that revealed the scattering mechanism were formed by programming the computer to reverse the propagation of this wave intercepted by the receiver, sending it back into the region containing the scatterers. Such reconstructed fields differ from those existing in the actual system at the time of the recording for a number of reasons: the calculation assumes free-space propagation; the image is only 2-dimensional (in this case of a line measuring aperture); and the aperture has finite extent. Allowance can be made for all these factors in the interpretation of the results. The computation was cast as a filtering operation. To obtain an image section at a particular distance from the receiver, the Fourier transform of the aperture distribution was weighted with an appropriate "circular-phase" transfer function and re-transformed. Sections compensated for the phase gradient corresponding to the transmitter direction and centred on the line of sight were printed out as amplitude and phase plots.

A necessary development of the imaging technique involved processing each field section reconstructed from the experimental data with a "reference field" calculated by the same method from a theoretical aperture distribution that would have been produced by the transmitter radiating from its known position but in empty space. For constant amplitude, quadratic phase aperture distributions the reference field sections took the form of Fresnel diffraction patterns of a slit. "Quotient" and "subtraction" images produced in this way will be described in §4.

The resolution of the image is determined by the synthetic aperture dimension, D (except for ranges less than about D, where the spatial filtering of the recorded field distribution takes over). For range r the lateral resolution is given by:

$$\Delta x = \lambda r / D \tag{1}$$

and a measure of the range resolution at positions well inside the near zone is:

$$\Delta r = 4 \lambda r^2 / D^2 . \tag{2}$$

According to (1) the lateral resolution becomes equal to the aperture width at range D^2/λ, defined as the boundary of the near and far zones. For D = 32 m and λ = 27.5 cm this boundary was 3.7 km from the receiver. The significant scattering effects occurred well within the near zone.

To assist evaluation of the images they were marked with the calculated positions of possible scatterers. The calculations were based upon high quality photographs taken from known positions in the synthetic aperture, supplemented by theodolite measurements and large scale maps.

4. RESULTS

The reconstructed field images all have formats similar to that of Figure 3, which is a distribution in the synthetic aperture. The left hand column of figures represents distance measured in wavelengths from the northern edge. This aperture had a width of 117 λ (32.2 m). Amplitude and phase distributions of the field on two repeat runs are plotted by the characters '1' and '2', an 'X' being entered where both plots fall on the same space. The scales are -30 dB to +10 dB and -180° to +180°. Amplitude and phase of the average of the two fields are also tabulated.

Fig. 3 is a quotient image, the measured field distribution having been divided by its reference field distribution, which in the aperture simply removes the slight wavefront curvature. These fields were recorded with the mobile transmitter at a range of 7.7 km on a site for which accurate monopulse bearing measurements had been obtained. The two runs show good stability, and apart from a -3.5 dB shadow near the northerly edge of the aperture the field is practically constant. At the left of Fig. 3 the interval CC' indicates the

projected position of the monopulse radar aperture. Three-quarters of the included amplitudes fall inside a range of ± 1 dB, and three-quarters of the phases in a 10° interval — a degree of uniformity consistent with the high accuracy of the bearing measurements over this transmission path.

4.1. Transmission path Bredon Hill - southerly synthetic aperture

Figure 4 is a result for one of the Bredon Hill transmitter sites, measured with the synthetic aperture in the more southerly of its two positions. This is also a quotient image for zero range, but shows greater amplitude and phase variations than Fig. 3. The position of the house H3, projected along the line of sight, is indicated at the left of the distance scale. Field amplitudes in this region tend to be about 5 dB greater than to the south.

Figure 5 shows the corresponding image section at 330 m, the range of H3. The section is the width of the aperture and centred on the line of sight. Division of the reconstructed field distribution by the reference field in this case raises the amplitude near the edges by about 6 dB. Eq. 1 gives the lateral resolution as 10.3λ (2.8 m). The significant feature of this image is the nearly constant complex amplitude over the calculated position of H3, whose northern and southern limits are denoted by H3N and H3S. As will become clear the dominant scattering mechanism was a quasi-specular ground reflection from the Common, shadowed by the house. The first approach was to assume that the field over the position of H3 corresponds exactly to the wave propagating directly from the transmitter, which comes to interference with the ground reflection in the remainder of the image. The relevant elevation geometry and a refinement of the model are considered in §5.

Accordingly the complex amplitude of the direct wave was estimated by an average of 20 points in the centre of the calculated position of H3 in Fig. 5. The reference field distribution, weighted by this complex amplitude, was then subtracted from the reconstructed field distribution. The resulting subtraction image, Figure 6a, is therefore an approximation to the "scattered" field ≠. It contains a focussed shadow image of the house formed by the ground reflected wave, and differs quite strikingly from the bland appearance of the original data (Fig. 4). Further adjustments of Fig. 6a were averaging of the two repeated runs, smoothing the complex field distribution with a 1:2:2:1 weighting function, and final division by the reference field distribution. The last measure enabled a better estimate of the apparent reflection coefficient to be obtained. An approximate average over the amplitude and phase variations to the south of H3S is -7.2 dB, $\underline{/180°}$.

In other measurements with this synthetic aperture the transmitter occupied positions on different bearings near the summit of the Hill. The calculated position of H3 in the format (referred to the line of sight) shifted over an interval of about 20λ. Although there was some variation in the quality of the images, and the clearest has been chosen for the purpose of illustration, in more than half the cases the subtraction image for range 330 m contained a shadow of contrast 15-20 dB within about 1 m of the predicted lateral position of the house. In view of the low elevation angle of the line of sight path, it seems possible that some differences among the images were caused by atmospheric refraction. An estimate of the apparent reflection coefficient for the ground reflection occurring to the south of the shadow of H3, obtained by averaging 5 results, was -8.1 dB, $\underline{/180°}$.

Evaluation of the images was supported in part by simulations based on 2-dimensional models of the scattering mechanism. These were performed in two stages, using the same computer program that calculated the reconstructed fields. Figure 6b is the result of such a simulation of the ground reflected wave screened by H3, for comparison with Fig. 6a. Here the input was a wavefront of curvature appropriate to the range of the transmitter, scaled by the measured reflection coefficient, and set to zero over a 37λ interval to represent screening by the obstacle. The first stage was to calculate the corresponding diffraction pattern 330 m away at the position of the synthetic aperture. This field distribution was then processed as if it had been measured data (except that no subtraction was necessary). Whereas in the first stage the aperture field was calculated in such a way as to avoid diffraction by the edges of the format, the reconstruction properly includes truncation by the finite synthetic aperture, and shows the resulting distortions of the image under otherwise ideal conditions. In the southerly part of Fig. 6b the complex amplitude is very close to the set-in value of -8.1 dB, $\underline{/180°}$, showing that the final division of the subtraction image by its reference field in this case enables the reflection coefficient to be estimated without bias.

4.2. Transmission path Bredon Hill - northerly synthetic aperture

Measurements in the northerly synthetic aperture enabled the more complicated scattering mechanism affecting the monopulse receiver to be investigated. Two sets of measurements (Serials 2-6 and Serials 9-15) made on different occaisions employed two sets of transmitter sites, both near the summit of Bredon Hill. Results of one experiment of each set will be considered.

Figure 7a is a quotient image of the aperture field measured in Serial 2. Indicated at the left are the projected positions of the southern end of the Church (CS), the centre of the belfry (B), and P1, the most southerly of a row of 4 tall pine trees (cf. Fig. 1). The position of the monopulse aperture (CC') differs slightly from that in Fig. 3 owing to rotation of the antenna. Comparing the positions of H3N in Figs 7a and 4 gives an impression of how the two synthetic apertures overlapped (although the projections are for somewhat different transmitter bearings). Near the northern edge of the aperture, where the line of sight was obstructed by the belfry, Fig. 7a shows a 5-10 dB shadow, typical of measurements of the first set. Greater attenuations of 10-20 dB occurred in the second set. All the records showed a dip in amplitude near a lateral position 65-70 λ , and in Fig. 7a this feature forms part of a pattern in which the field strength

---

≠ In its general sense this term describes any modification of the incident field (represented here by the direct wave) owing to the presence of a material object, which may for example be a mirror or an absorbing screen.

over the northern half of the monopulse aperture averages about 3 dB less than over the southern half. Figure 7b is a simulation result that will be considered presently.

Quotient images for 330 m range again helped to set up subtraction images representing the scattered field. Reconstructed fields were calculated in a 300 λ wide format extending to both sides of the geometrically illuminated swath between transmitter and synthetic aperture. Outside this swath the decreasing magnitude of the reference field forming the divisor sets a limit to the usefulness of the quotient image. Nevertheless complex amplitude distributions were obtained sufficiently constant over the calculated position of H3 to provide estimates of the direct wave.

Figure 8a is a subtraction image of Serial 2 for range 315 m, chosen to show the ground reflected wave in the diffraction window formed between CS (range 300 m) and H3N (range 330 m). The interval 121-233 λ of this section corresponds to the swath passing through the aperture. In these subtraction images there was no final division by the reference field. An estimate of the reflection coefficient, indicated by the lines ruled on the Figure, is -10.5 dB, $\underline{/-157°}$.

The corresponding result for Serial 11 is Figure 8b, implying a similar reflection coefficient of -9 dB, $\underline{/180°}$. An average of 5 such measurements was -9.7 dB, $\underline{/-177°}$. In the region where the Church belfry obstructed the line of sight, Fig. 8b shows a strong scattered field approximately in anti-phase with the direct wave. In Fig. 8a similar values of the field occur about 12 λ north of the calculated position of B, and the difference in this part of the image is characteristic of the two sets of results.

The simulation constructed for comparison with these results is based on the model of Figure 9. It includes the ground reflection obstructed by the Church and H3, edge diffraction over H3 (considered in §5), and screening of the direct wave by the Church and 4 pine trees. Figures 10 and 11 give two of the scattered field distributions at the position of the synthetic aperture as calculated in the first stage of the simulation.

Fig. 10 is the contribution of the ground reflected wave windowed by CS-H3N, a Fresnel diffraction pattern. The maximum amplitude is 2.2 dB above the amplitude of the set-in reflection coefficient, -9.7 dB. (The greatest possible gain of 2.6 dB, corresponding to the longest chord of the Cornu spiral, occurred 85 m in front of the receiver.) Over the position of the monopulse aperture this component is practically in anti-phase with the direct wave. The amplitude profile is such that it will produce stronger interference in the northern half of the aperture than in the southern half, largely accounting for the average variation of field strength in the same region of the measured distributions.

The 2-dimensional model for screening of the direct wave by the Church was an opaque bar of width 15 λ, chosen to produce a -3 dB shadow in the synthetic aperture, the same as a 3-dimensional model in which the Fresnel zone pattern is obstructed over a 100° sector (cf. Fig. 9). Figure 11 shows the scattered field contribution in the aperture. For transmitter sites to the north of that assumed in the simulation this field distribution shifts to the south by up to 11 λ-units. The amplitude profile suggests that the greatest effect on the monopulse measurement would occur for these more northerly transmission paths. A possible scattered field contribution owing to screening of the direct wave by the four pine trees, represented in the model by four 5 λ-wide bars, was also calculated.

In the synthetic reconstructions, field distributions graphed by the character '3' and tabulated represent the sum of all components of the scattering model (including the direct wave where appropriate), and distributions graphed by the character '4', the sum of all components except the last mentioned. Figure 7b is the resulting quotient image in the aperture, for comparison with Fig. 7a. Both curves of the simulation reproduce quite well the actual behaviour of the field in the southern half of the image — the dip and gradual rise in amplitude — and the attenuation near the northern edge of the aperture. The -10 dB minimum of curve '3' at a lateral position of 34 λ had no counterpart in the experimental results however. Figure 8c is the simulated subtraction image for range 315 m, to be compared with Figs 8a and 8b. Over the interval shown curves '3' and '4' are close together, and reconstruct the ground reflection in the CS-H3N window as well as a strong scattered field in the region where the Church obstructed the line of sight. Agreement with the experimental image is particularly good in the case of Serial 11 (Fig. 8b). For range 340 m in the northern part of the extended format, curve '3' of the simulation produced distinct images of the bars representing pine trees P2-P4. The corresponding experimental results contained no such well defined maxima, and amplitude levels were about mid-way between the two curves of the simulation. Fig. 1 suggests that regions of locally high density of the foliage were widely distributed, which would account for diffuse images, but no firm conclusion was possible as to whether screening of the direct wave by these pine trees contributed to the measured fields.

Finally it should be noted that the simulation represents an approximate solution of a simple 2-dimensional scattering model, whereas an experimental image is a 2-dimensional reconstruction from a line sample of fields scattered by complex 3-dimensional objects. The measure of agreement obtained between experiment and simulation was therefore considered satisfactory.

5. THE GROUND REFLECTION

A study of the elevation geometry corroborated the interpretation of the 2-dimensional images. For comparison with the measured values, calculations were made of the "apparent reflection coefficient" — the complex amplitude of the ground reflected wave relative to the direct wave at the receiver after compensation for diffraction effects in the horizontal dimension. It was also possible to correct the measured reflection coefficients for the effect of straight-edge diffraction by H3.

Figs. 12 and 13 are elevation profiles of the Common constructed from clinometer measurements every 10 m; in view of the integration of errors inherent in such a process they cannot be regarded as very accurate. The profile of Fig. 12 was measured under a line of sight running to the south of the shadow of H3, and Fig. 13 under a line passing through the CS-H3N window. Both have the form of flattened hills sloping up

towards the receiver. The average gradients are close to the value of 0.7° at which a flat surface in this position would have produced a specular reflection, under a grazing angle of incidence of 1.4°. Quasi-specular reflections in fact occurred. The grass was short from being mown and grazed, and for this angle of incidence the intrinsic reflection coefficient of the ground could be assumed equal to -1. The profile of Fig. 12 was modelled by a flat mean surface with random roughness, centred at a range of 220 m from the receiver. For Fig. 13 the model was a smooth convex cylinder with the geometrical reflection point at a range of 240 m. The transverse profile appeared to play no significant role. For transmission from the position of the receiver, the ground reflection would be obstructed by H3 to a height 2.3 m above the ray path.

In §4 we gave a first estimate of the coefficient for the ground reflection to the south of H3. It was obtained from subtraction images such as Fig. 6a, calculated on the basis that the house completely blocks the reflection without affecting the direct wave. To correct this estimate we now remove both assumptions and allow for diffraction by H3 in the vertical dimension. The image sections are already focussed in the horizontal dimension, and the Fresnel approximation for straight-edge diffraction can be applied (cf. BECKER, J.E. and SUREAU, J.-C., 1966). For the direct wave the line of sight cleared the roof ridge by 9 m and the first Fresnel zone radius was 9.5 m. The Cornu spiral gives the effect of diffraction as contributing an extra field component over the position of H3 in the quotient image with complex amplitude 0.16-j.0.05 referred to the direct wave. For the ground reflection a similar calculation gives the component (0.15-j.0.24)R, where R denotes the true value of the apparent reflection coefficient. The quotient image over H3 therefore contained the contribution from straight-edge diffraction:

$$U = 0.16 - j.0.05 + (0.15 - j.0.24)R \qquad (3)$$

in addition to the direct wave with amplitude 1+j.0. Now the first estimate of the reflection coefficient is expressed in terms of R and U by:

$$R' = R - U. \qquad (4)$$

Substitution of the average experimental value R'= -8.1 dB, $\underline{/180°}$ or -0.39+j.0 leads to the solution:

$$U = 0.12 + j.0.016$$
$$R = -0.27 + j.0.016 \quad \text{or} \quad -11.4\text{ dB}, \underline{/177°}.$$

The corrected estimate of the coefficient for this ground reflection is thus about 3 dB smaller than the first estimate. In calculating subtraction images for the northerly synthetic aperture, the above determined value of U was applied to correct the estimate of the direct wave, so no further adjustment of the reflection coefficient was necessary.

A theoretical calculation for the reflection from the ground profile of Fig. 12 was based on specular reflection at a flat surface of length L = 134 m in the direction of propagation. The amplitude of the apparent reflection coefficient is given by the physical optics formula:

$$\frac{r_0 L \sin\gamma}{r_1 \sqrt{r_2 \lambda}} \qquad (5)$$

where γ represents the grazing angle of incidence (1.4°), r_0 is the length of the direct path (17.5 km), and r_1 and r_2 are the distances from the reflector to transmitter and receiver (17.3 km and 220 m). In this region the surface had appreciable small-scale roughness with an estimated rms height of 30 cm. A standard formula derived for a gaussian random surface (BECKMANN, P. and SPIZZICHINO, A.,1963b) gave the effect of roughness as reducing the average strength of the reflection by 0.5 dB. Thus a value of -7.9 dB was obtained for comparison with the amplitude of the measured reflection coefficient. The total phase shift associated with this specular reflection is $-3\pi/4$, including a $\pi/4$ advance owing to diffraction.

The profile of Fig. 13 was modelled by a convex curved surface. The radius of curvature, calculated by plotting the measured gradients against distance and finding the slope of the best straight line fit, was 1270 m. Application of a standard geometrical optics formula (BECKMANN, P. and SPIZZICHINO, A.,1963c) then gives the strength of the reflection at the receiver as -12.2 dB. The phase shift of this reflection is π.

To permit comparison with the measured reflection coefficients these theoretical values must be phase shifted to allow for the extra path length of the ground reflection relative to the direct wave. The geometry gave path differences of 25.3 cm and 27.5 cm respectively for the southerly and northerly sections. Since λ = 27.5 cm the corresponding compensations are +29° and zero. Theoretical and experimental values of the apparent reflection coefficient are therefore summarised as follows:

	South of H3		North of H3	
	theory	expt	theory	expt
dB	-7.9	-11.4	-12.2	-9.7
deg.	-106	177	180	-177

The measured values are close together and near the theoretical value for the curved profile; the flat surface model shows a phase discrepancy of 77°. In view of the simplifications and approximations involved, considerably greater differences would not have been surprising.

6. MONOPULSE BEARING ERRORS

In discussing the measured and simulated aperture field distributions of Figure 7, attention was directed to amplitude variations over positions corresponding to the radar aperture. To complete the study some calculations were made of the bearing errors that would occur in an amplitude comparison monopulse receiver. The signals delivered by the two halves of the monopulse antenna were obtained by integrating the aperture fields over appropriate intervals. Uniform weighting of the monopulse apertures was assumed, and phase tilts applied to incline the (sin x)/x beams outwards, crossing at the -3 dB level. For each 20 λ aperture the -3 dB beamwidth was 2.54°; the boundary of the near zone occurred at a range of 110 m, so significant scatterers were in the far zone. The error curve of the assumed processer was applied to convert the amplitude unbalance of signals from the northerly and southerly halves of the antenna to errors in the bearings indicated with the antenna boresighted.

Such amplitude ratios and corresponding bearing errors are given in Figure 14 for different directions of the transmitter. The horizontal scales show transmitter bearing and the projected position of H3N in the synthetic aperture. The diffraction pattern of the window CS-H3N had its maximum amplitude 25 λ north of this position. For the measured aperture fields the integrations were performed over intervals 65-84 λ and 85-104 λ, corresponding to the position of the monopulse antenna. The simulated aperture distributions had been calculated for a particular transmitter site, but since all the diffracting obstacles were at about the same distance from the receiver (near 315 m), different source directions could be simulated by shifting the integration intervals.

Some differences between the results of Serials 2-6 and those of Serials 9-15 have already been noted, and these are grouped separately in Fig. 14. The two sets form similar patterns with maxima of 4.7 dB and 7 dB unbalance for transmitter directions placing the H3N geometrical shadow boundary 2 λ and 6 λ inside the southerly edge of the monopulse aperture. The continuous curve corresponds to the simulated aperture distribution of Fig. 7b. A 5.3 dB maximum unbalance occurs for the same transmitter direction as in Serials 9-15, and the simulation reproduces quite well the bimodal pattern of the experimental results. All the indicated bearings would be to the south of the true bearing, with worst errors to the order of 0.2 beamwidths.

Figure 15, to the same scales, gives a view of the contributions of different components of the simulation. The diffracted and ground reflected wave interferes with the direct wave, attenuating the field more strongly over the northern half of the monopulse aperture as already shown. The corresponding curve of amplitude unbalance takes the form of a single broad peak, whose 2.8 dB maximum occurs for a transmitter direction placing the shadow of H3N near the centre of the southern half of the aperture, and the maximum of the diffraction pattern 5 λ inside the northern edge of the aperture. Inclusion of the component representing diffraction effects of H3 in the vertical dimension and the ground reflection to the south gives a somewhat greater maximum unbalance of 4 dB shifted towards more southerly transmitter directions. The remaining contributions have more rapid phase variations over the monopulse aperture, and their inclusion produces sharper fluctuations of the amplitude unbalance with changing transmitter bearing. The scattered field contribution to account for screening of the direct wave by the Church (Fig. 11) enters the beam of the northern monopulse aperture near the -4 dB point. Adding in this component gives a maximum of 5 dB unbalance for a more northerly transmitter site. Finally, inclusion of the component representing screening by the pine trees brings the minor peak near 88 λ. The complete simulation agrees best with the experimental results.

7. CONCLUSION

Results have been given of an investigation of the scattered fields affecting a certain radio propagation path. Field distributions measured on the receiving site were computer processed to form images that revealed the origins of the multi-path components. A computer simulation based on a 2-dimensional model provided further insight of the scattering mechanism. The occurrence of large errors in direction-finding measurements with a monopulse receiver on the same site was explained. It should therefore be attempted to place these detailed findings for a specific case in a more general perspective.

There were two main contributors to the greatest bearing error. The ground reflection had an amplitude of -10 dB referred to the direct wave. It was produced by a surface of sufficient extent (in relation to its distance from the receiver) whose small effective roughness, negligible vegetation cover and suitable average slope ensured a quasi-specular reflection. The diffraction of this wave between two buildings to form a field pattern with 2.2 dB gain and a strong amplitude variation across the monopulse aperture was a coincidence of (primarily) the plan geometry. Likewise, that the contribution should be nearly in anti-phase with the direct wave, causing maximum error in the amplitude comparator, was a coincidence of the elevation geometry. An 0.33° change in the elevation of the transmitter would have shifted the relative phase of the ground reflection by 90°, practically eliminating this source of error. Near maximum error would then occur in a phase comparison system with the antenna in the same position. The other significant scattered field was that associated with screening of the direct wave by the Church. Its contribution to the monopulse signals varied in both amplitude and phase with changing transmitter bearing. The resultant pattern of errors had a peak with values (according to the simulation) between 0.15 and 0.2 beamwidths over a 0.3° interval of azimuths.

It therefore appears that while similar sources of multi-path fields are present around many sites, the worst effects on bearing measurements are likely to be confined to relatively few specific narrow intervals of direction (azimuth x elevation). That such an unfavourable combination of circumstances occurred for the test site when transmitting from Bredon Hill was a matter of chance. For target elevations above a few degrees, even though the ground is still illuminated the reflection will be weaker, owing to the reduced amplitude of the intrinsic reflection coefficient (with vertical polarisation) and the increasing tendency of surface roughness to diffuse the reflected wave. Provided there are no obstacles near the direct path, large errors from these sources are less probable.

The results also show up a disadvantage of the amplitude comparison monopulse system as against a phase comparator: the offset beams reduce sensitivity to the direct wave while increasing it to scattered waves from neighbouring directions. In an amplitude comparison system however both beams may have the same phase centre, and where possible each should be formed from the full aperture. The narrower beams will receive scattered waves over smaller intervals of direction, and both will be affected equally by differential shadowing across the aperture, such as accompanied the ground reflection.

Experiments of the kind described, supported by models of the scattering mechanism, can improve our understanding of site effects, and provide a realistic basis for comparing the performance of different direction-finding systems.

ACKNOWLEDGEMENTS

This work has been carried out with the support of the Procurement Executive, U.K. Ministry of Defence. The assistance of staff of the Royal Signals & Radar Establishment is gratefully acknowledged.

REFERENCES

BARTON, D.K.,1974, "Low angle radar tracking", Proc. IEEE 62 6 687-704.

BECKER, J.E. and SUREAU, J.-C.,1966, "Control of radar site environment by use of fences", IEEE Trans. AP-14 6 768-773.

BECKMANN, P. and SPIZZICHINO, A.,1963a, "The scattering of electromagnetic waves from rough surfaces", Pergamon Press, Chapter 13.

ibid.,1963b, §5.3.

ibid.,1963c, §11.2, Eq. 7. The term 2/b should be replaced by (2 sin γ)/b.

JA, Y.H.,1976, "Holographic reconstructions of source distributions from microwave height-gain curves", IEEE Trans. AP-24 1 1-5.

TOMLINSON, H.T. and STRAITON, A.W.,1959, "Analysis of 3-cm radio height-gain curves taken over rough terrain", IRE Trans. AP-7, 405-413.

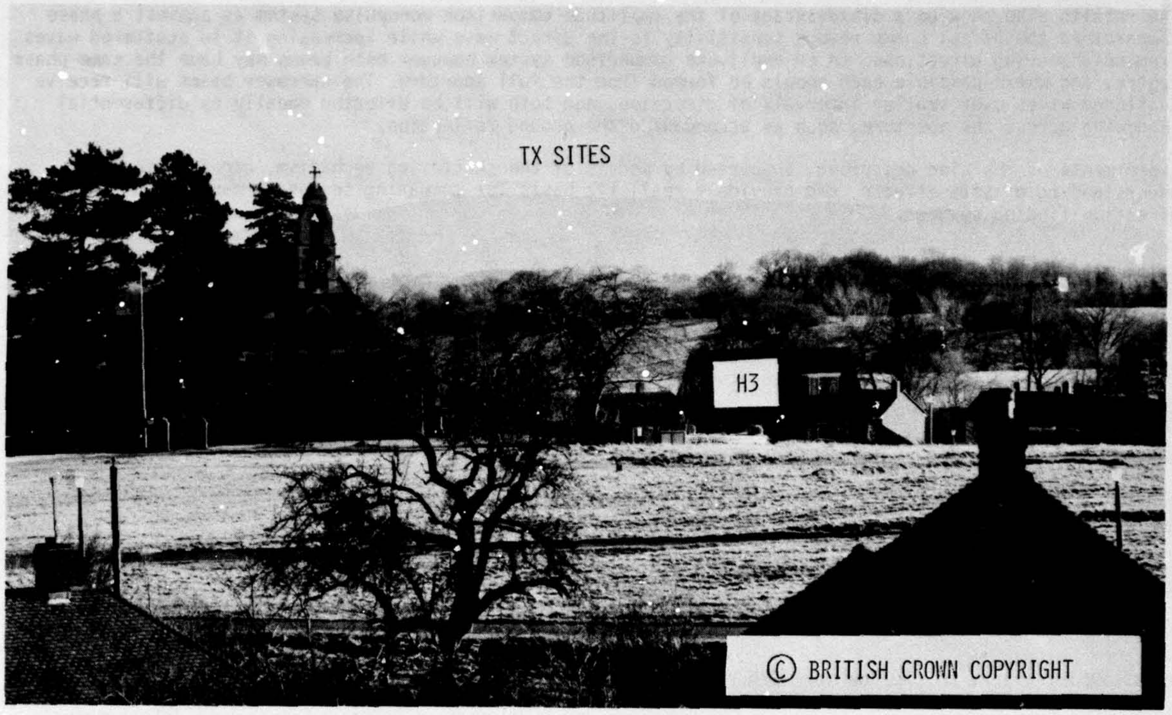

Fig. 1: View of the radio path.

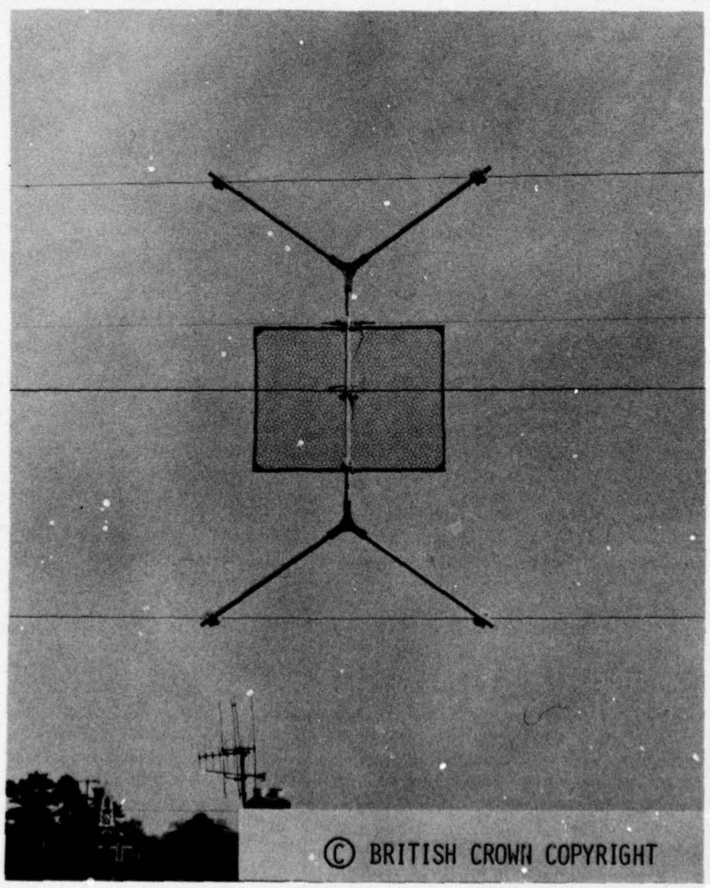

Fig. 2: The travelling antenna.

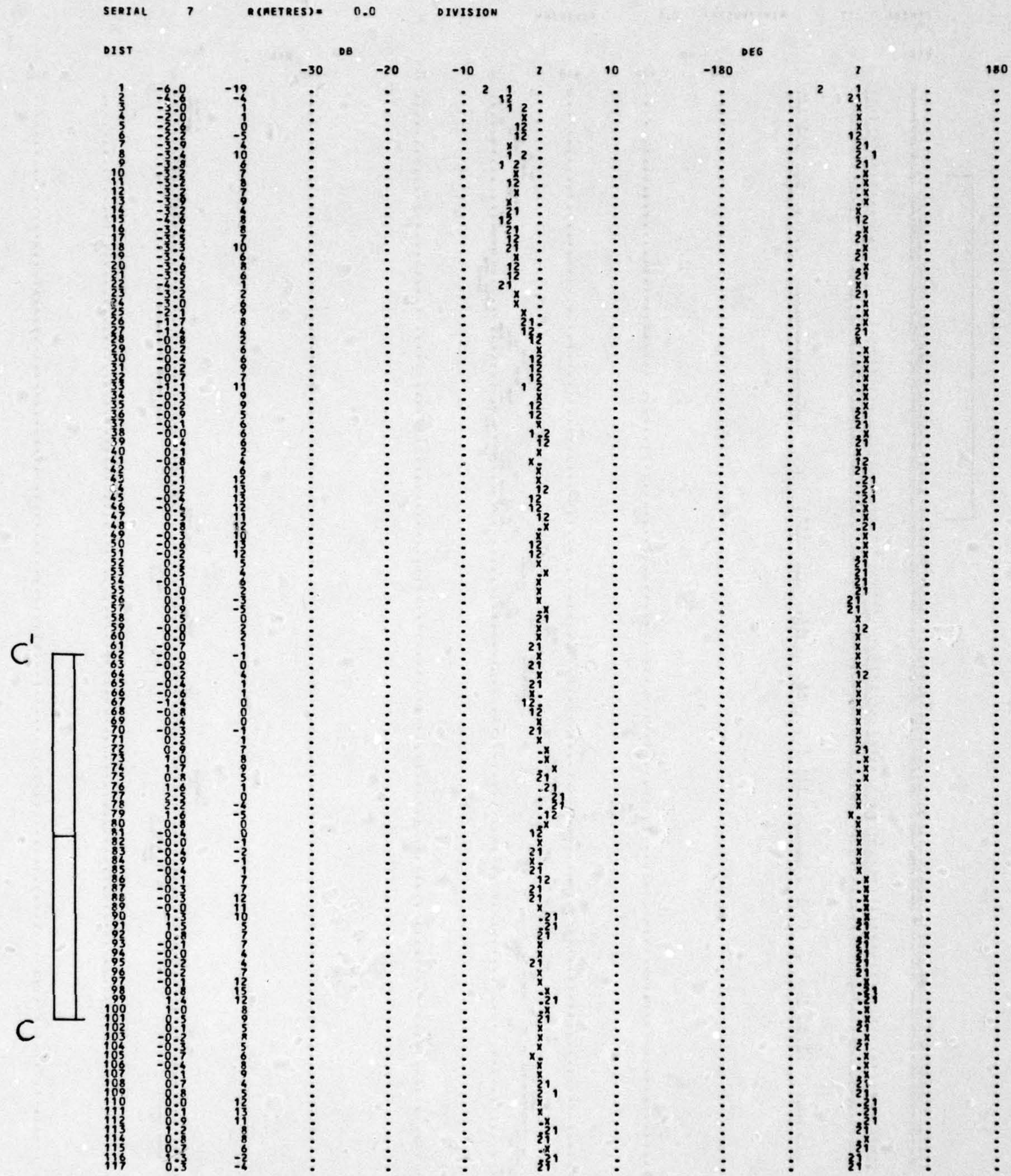

Fig. 3: Quotient image, range = 0. (Serial 7, tx bearing = 90.51°.)

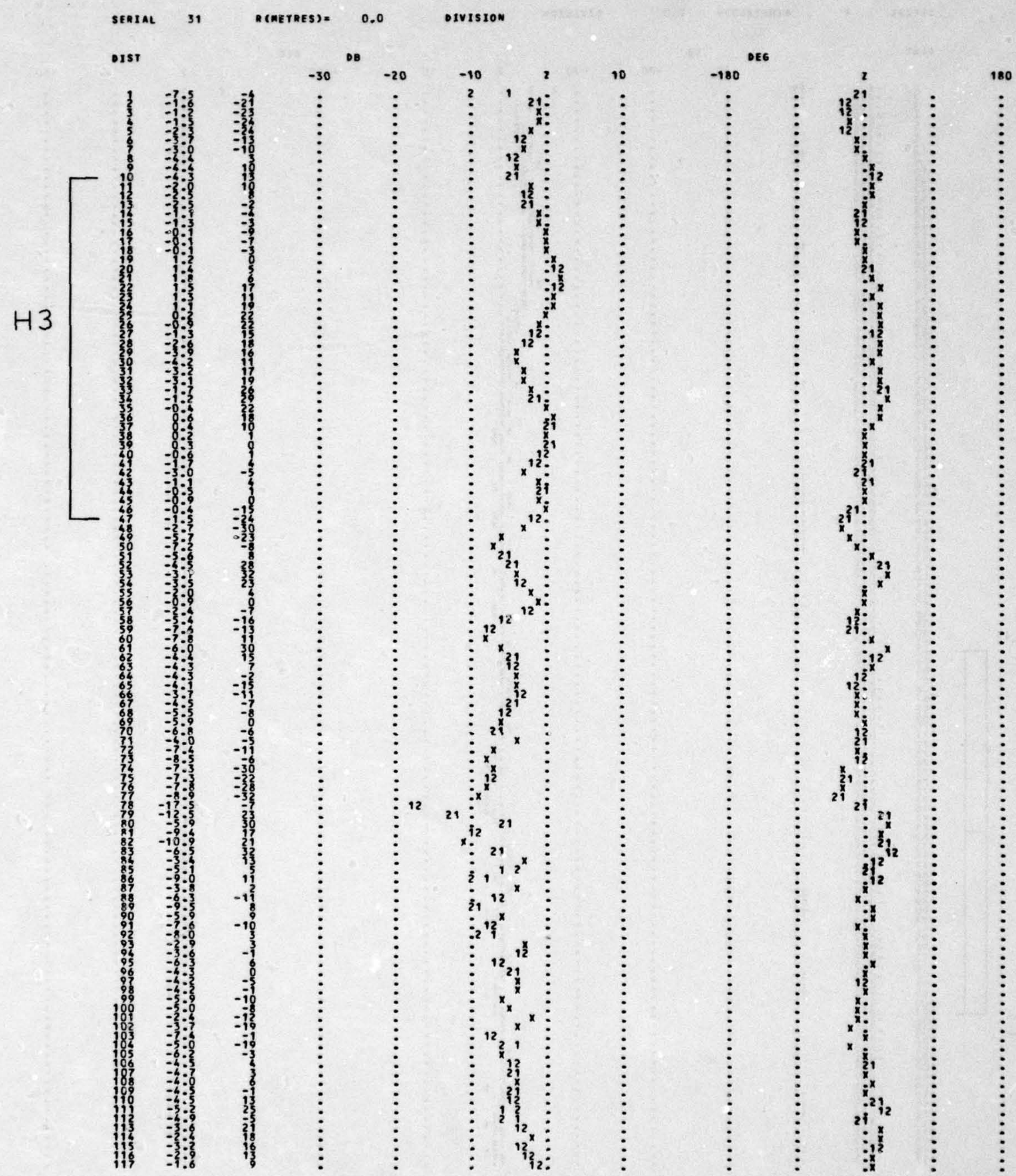

Fig. 4: Quotient image, range = 0. (Serial 31, tx bearing = 105.15°.)

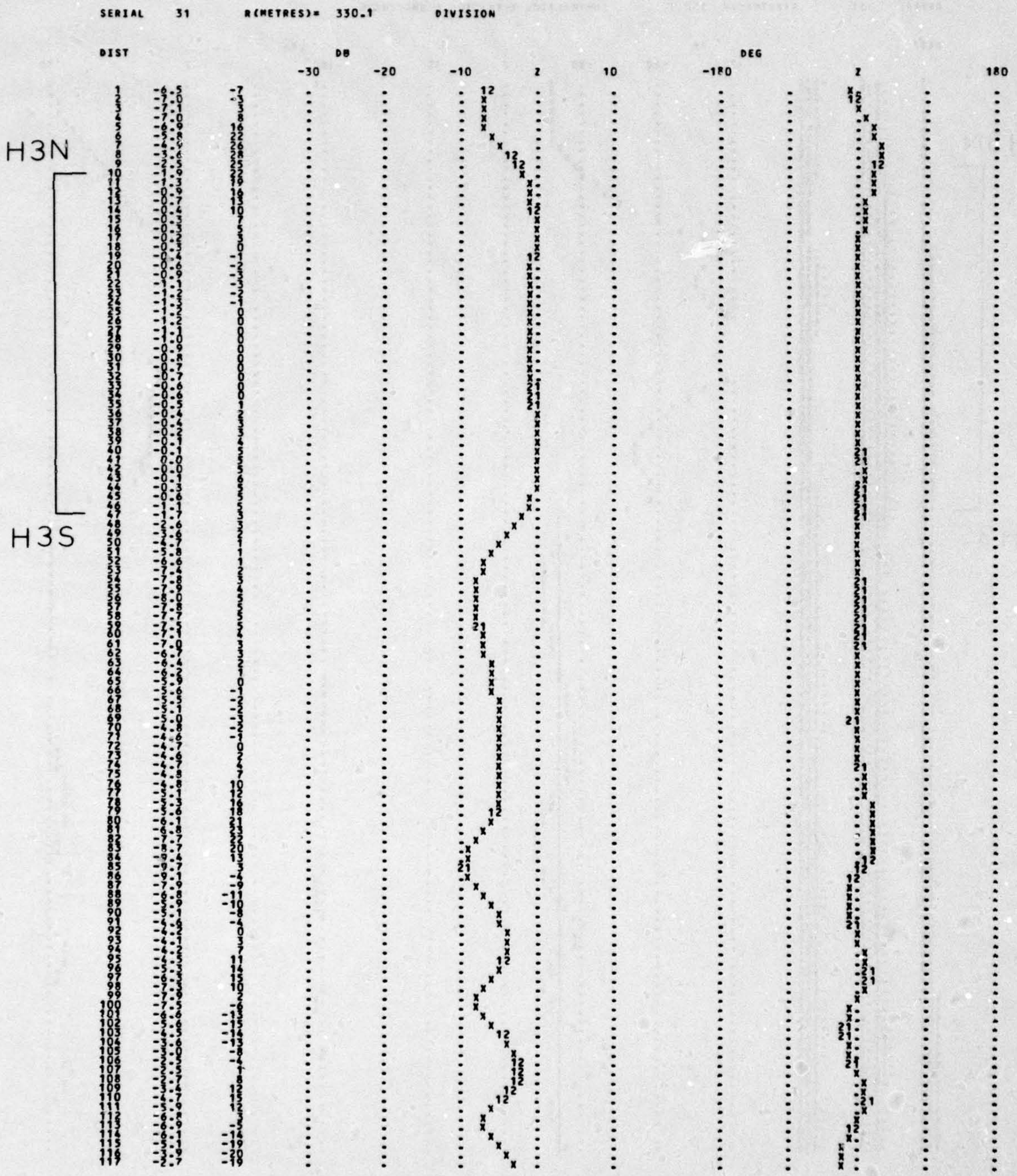

Fig. 5: Quotient image, range = 330 m. (Serial 31)

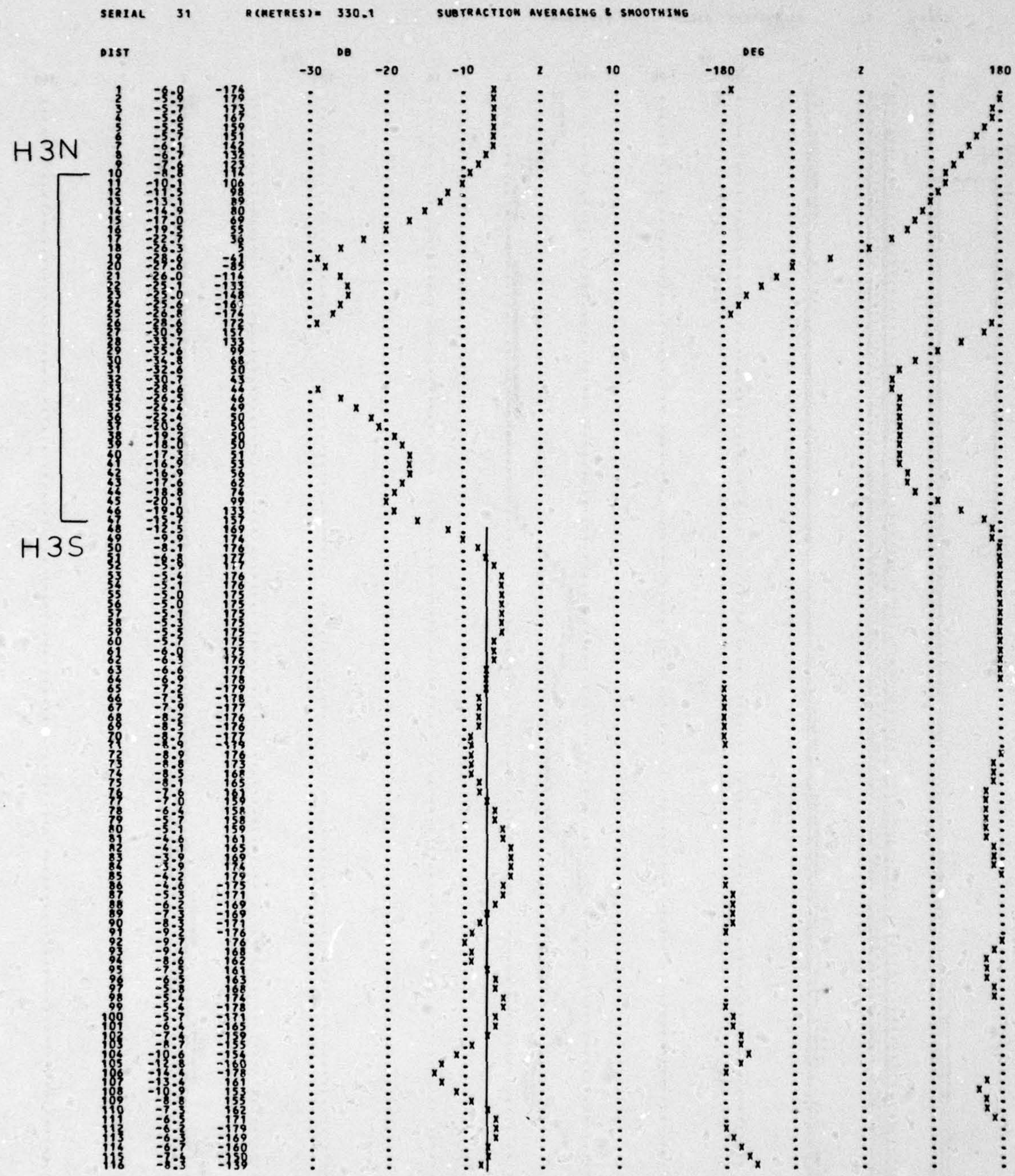

Fig. 6a: Subtraction image, range = 330 m. (Serial 31)

RESIM. R(METRES)= 330.0

DIST		
1	-10.5	173
2	-10.3	174
3	-9.9	175
4	-9.5	174
5	-9.0	171
6	-8.6	168
7	-8.3	162
8	-8.3	156
9	-8.5	148
10	-9.1	141
11	-10.0	134
12	-11.2	129
13	-12.4	126
14	-13.7	124
15	-14.9	123
16	-16.2	123
17	-17.6	123
18	-19.1	125
19	-20.8	128
20	-22.6	135
21	-24.0	146
22	-24.4	160
23	-24.2	170
24	-23.7	176
25	-23.5	178
26	-23.6	179
27	-24.1	179
28	-24.9	-179
29	-26.3	-177
30	-28.0	-172
31	-30.2	-161
32	-31.5	-140
33	-31.1	-115
34	-29.4	-102
35	-28.1	-96
36	-27.5	-95
37	-27.6	-93
38	-28.4	-92
39	-30.0	-87
40	-32.6	-80
41	-36.2	-61
42	-41.0	-24
43	-40.7	39
44	-37.2	91
45	-32.8	124
46	-27.8	150
47	-23.4	166
48	-19.4	175
49	-16.3	-179
50	-13.8	-177
51	-11.9	-176
52	-10.5	-176
53	-9.5	-177
54	-8.8	-177
55	-8.3	-178
56	-8.0	-179
57	-7.8	-179
58	-7.8	179
59	-7.7	179
60	-7.7	179
61	-7.8	178
62	-7.9	178
63	-7.9	178
64	-8.0	178
65	-8.1	178
66	-8.2	178
67	-8.2	178
68	-8.3	179
69	-8.3	179
70	[illegible]	179
71	-8.2	-179
72	-8.2	-179
73	-8.2	-178
74	-8.2	-178
75	-8.1	-178
76	-8.1	-178
77	-8.1	-178
78	-8.1	-179
79	-8.1	-179
80	-8.1	-179
81	-8.0	179
82	-8.0	179
83	-8.0	179
84	-7.9	179
85	-7.9	179
86	-7.9	179
87	-8.0	-179
88	-8.0	-179
89	-8.0	-179
90	-8.1	-179
91	-8.1	179
92	-8.1	179
93	-8.1	179
94	-8.1	179
95	-8.1	178
96	-8.0	178
97	-8.0	179
98	-8.0	179
99	-8.0	179
100	-8.1	179
101	-8.1	-179
102	-8.2	-179
103	-8.2	179
104	-8.2	179
105	-8.2	179
106	-8.2	178
107	-8.2	178
108	-8.1	178
109	-8.1	179
110	-8.0	179
111	-8.1	-179
112	-8.1	-179
113	-8.2	-179
114	-8.3	-179
115	-8.3	179
116	-8.3	179
117	-8.3	179

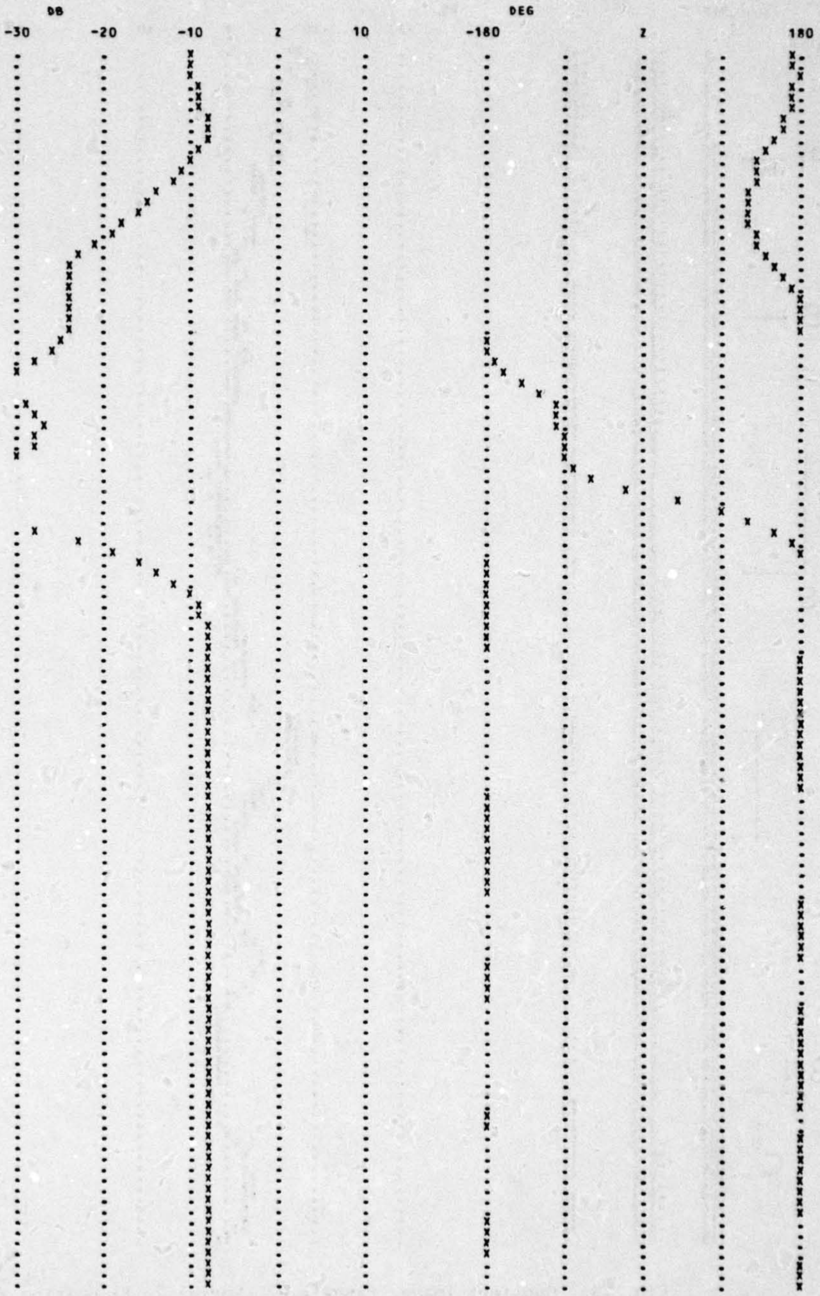

Fig. 6b: Simulation: subtraction image, range = 330 m.

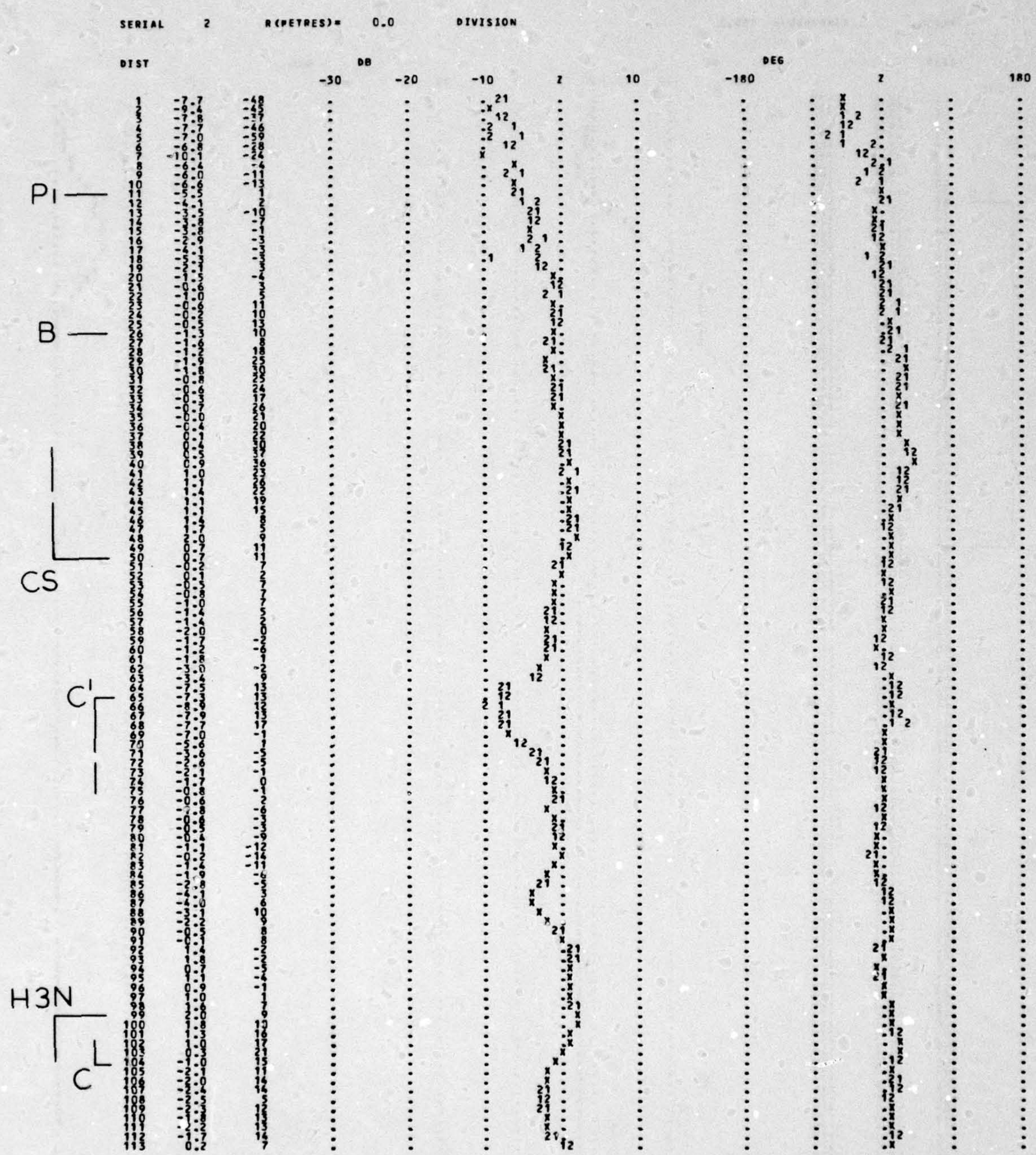

Fig. 7a: Quotient image, range = 0. (Serial 2, tx bearing = 104.68°.)

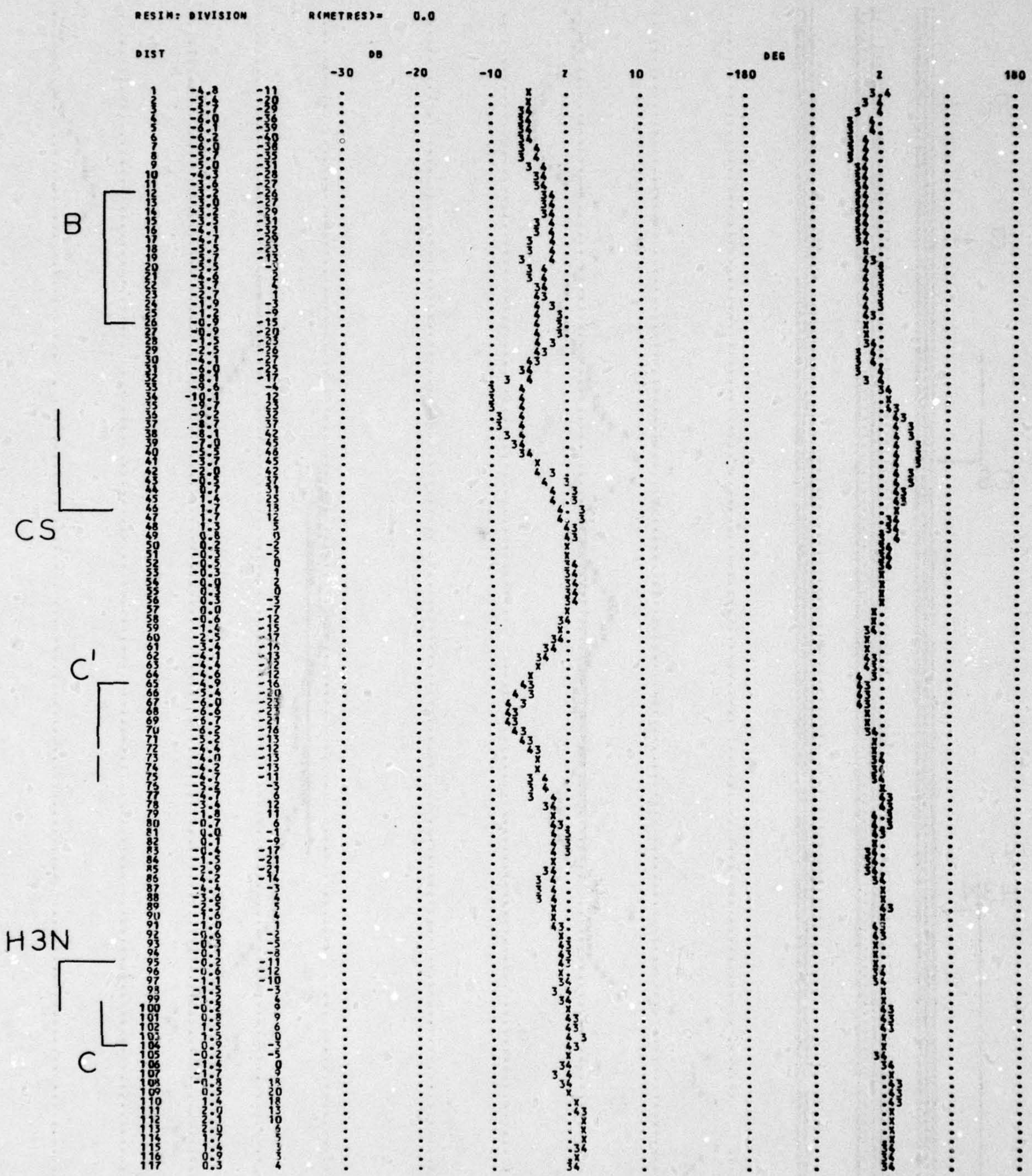

Fig. 7b: Simulation: quotient image, range = 0.

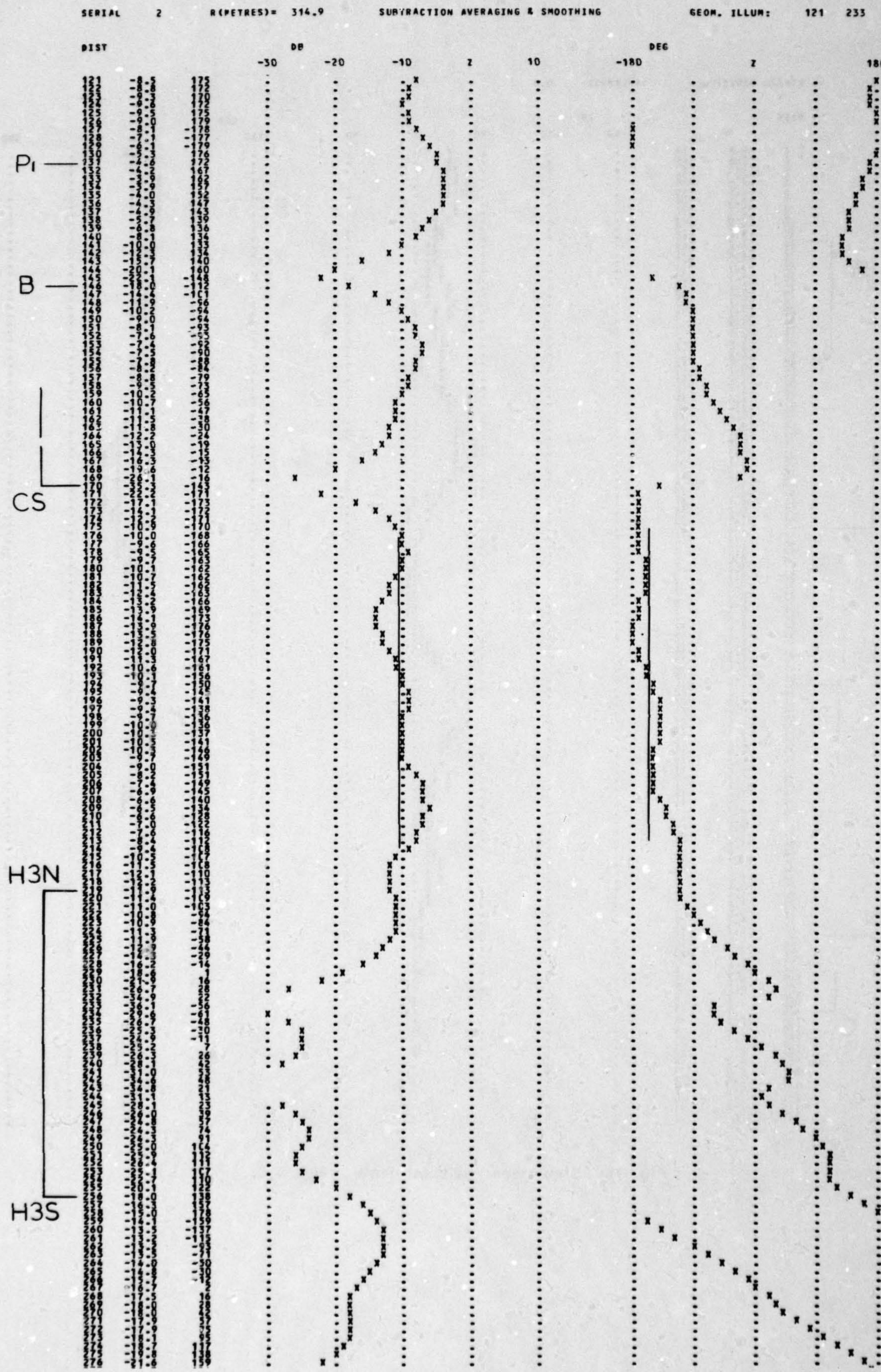

Fig. 8a: Subtraction image, range = 315 m. (Serial 2)

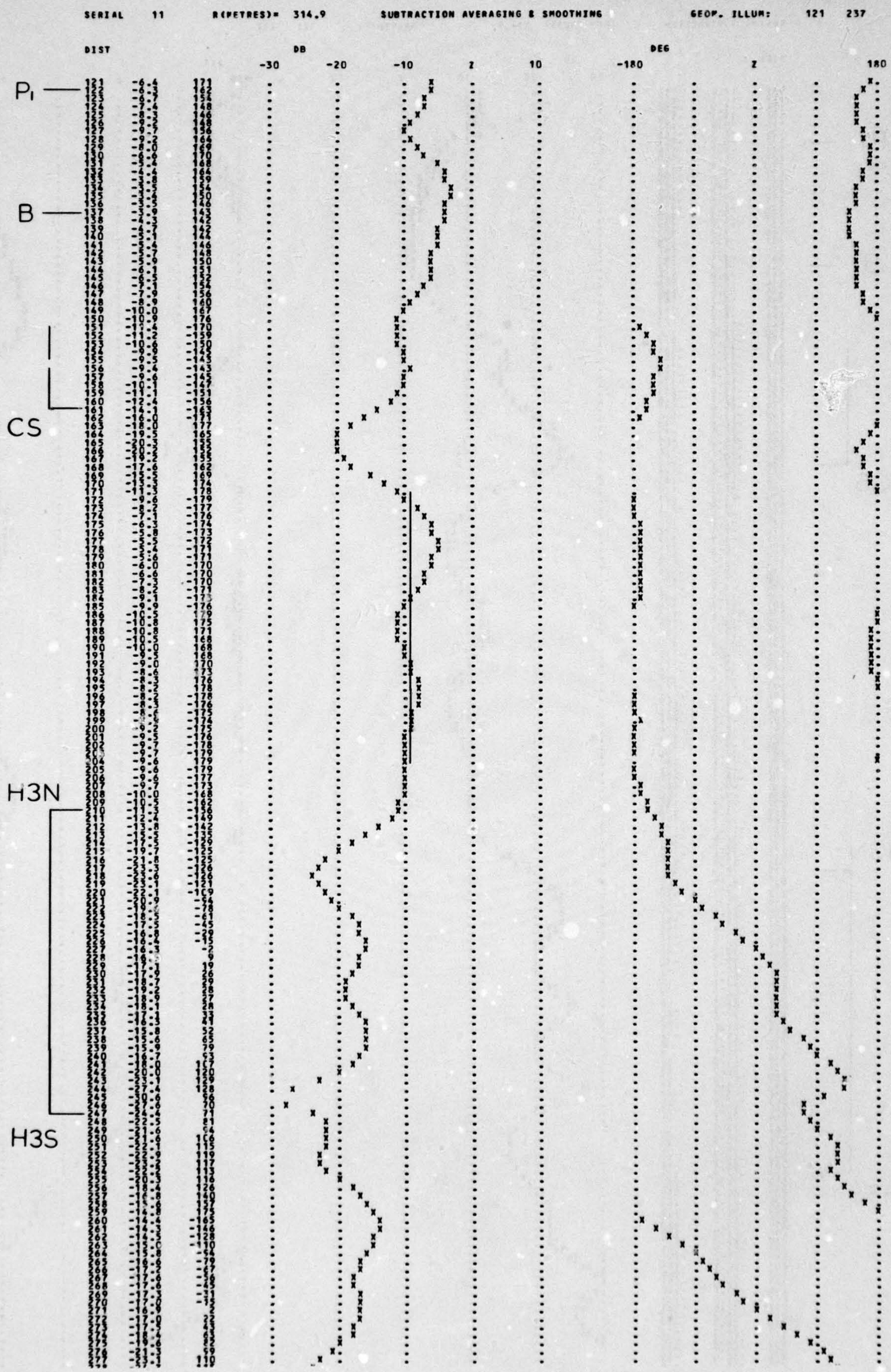

Fig. 8b: Subtraction image, range = 315 m. (Serial 11, tx bearing = 105.15°.)

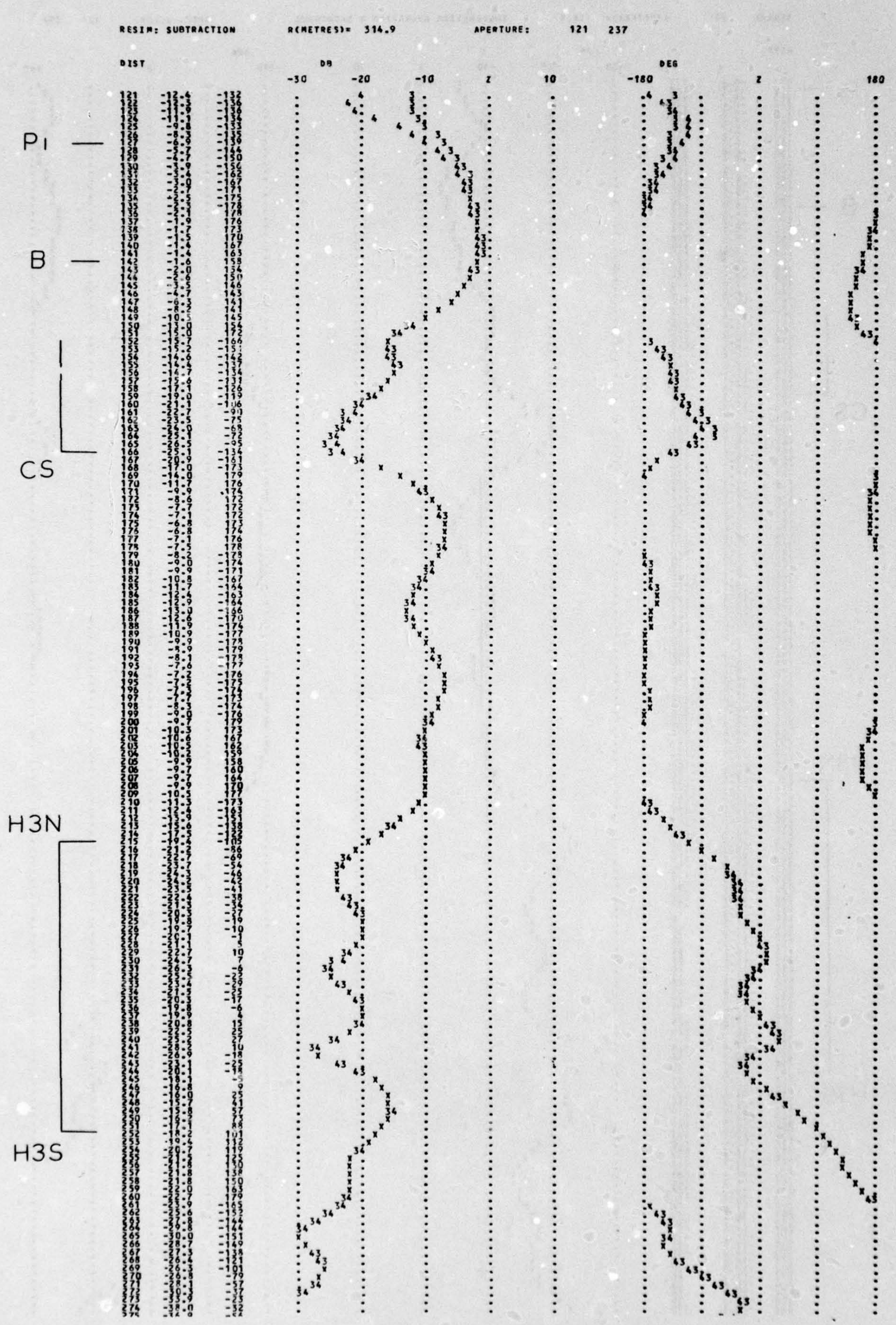

Fig. 8c: Simulation: subtraction image, range = 315 m.

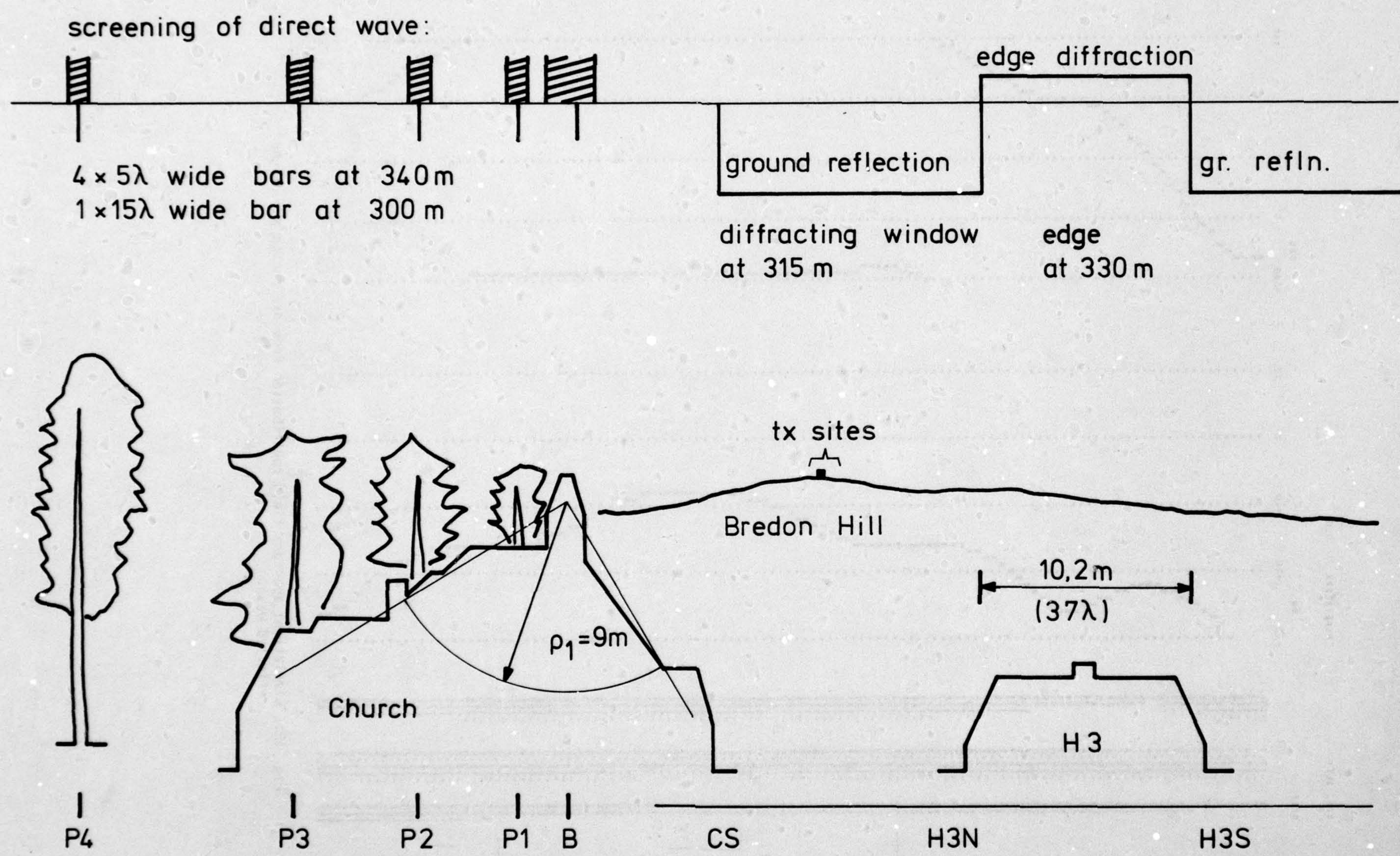

Fig. 9: Model of the scattering mechanism.

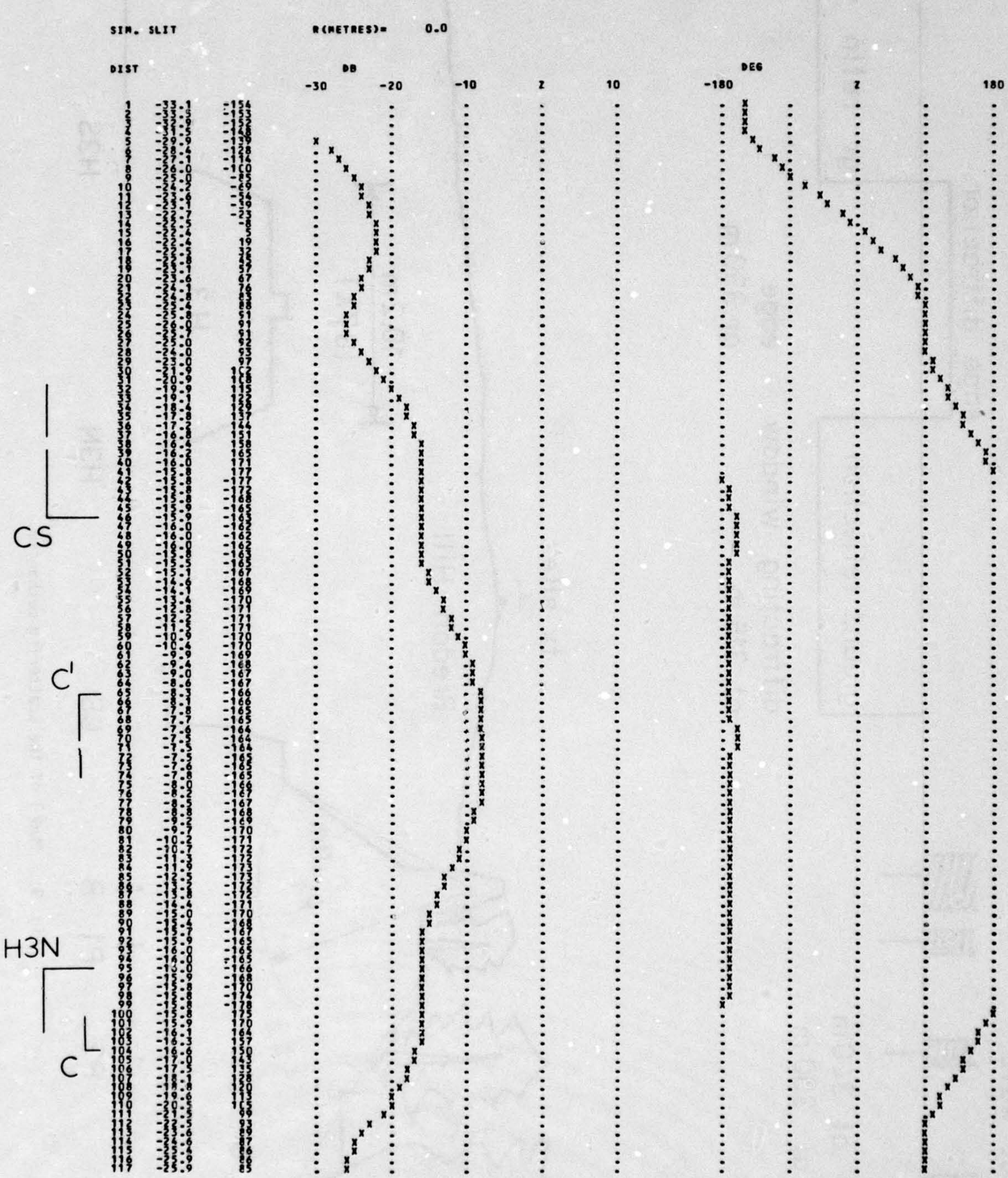

Fig. 10: Simulation: aperture field contribution from diffracted and ground reflected wave.

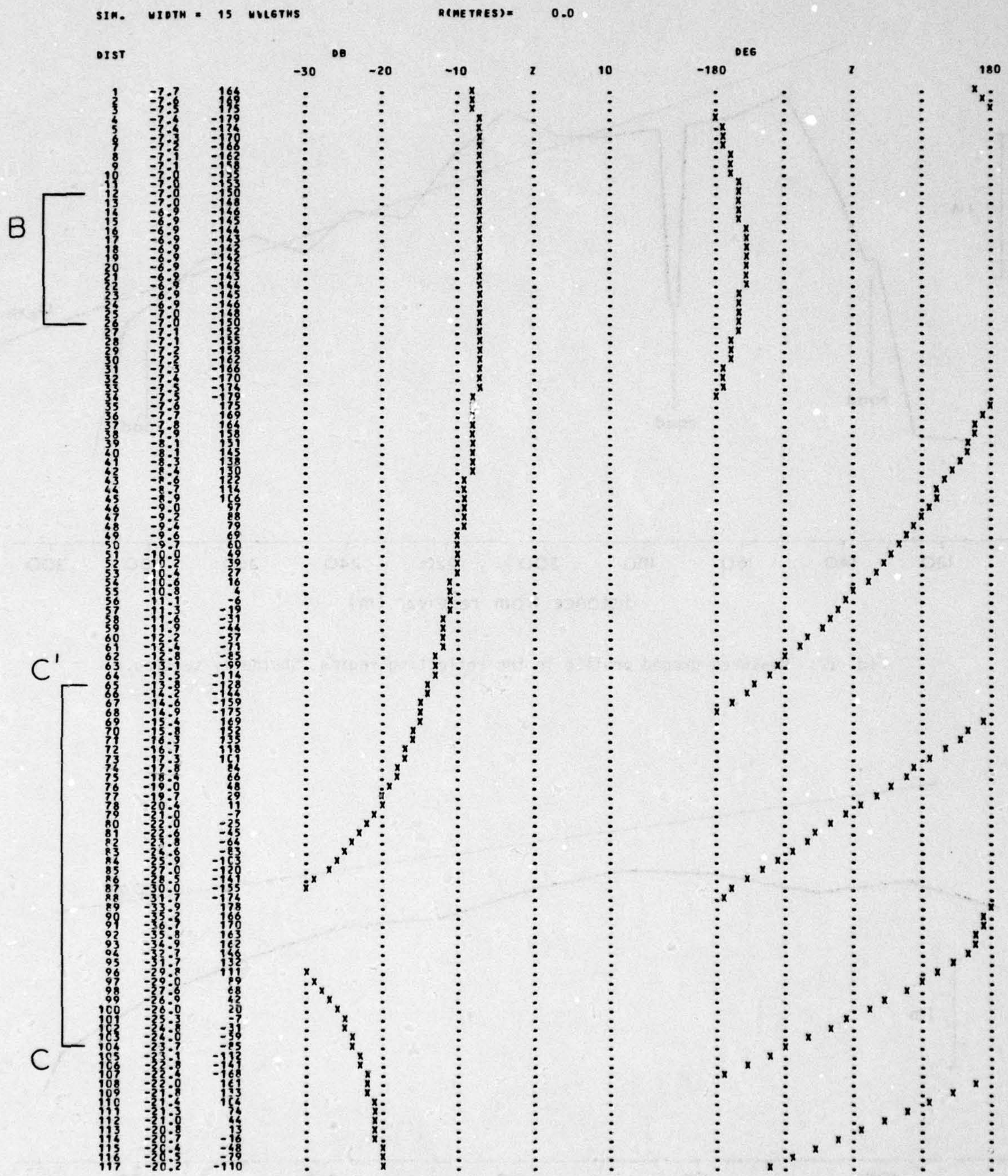

Fig. 11: Simulation: aperture field contribution owing to screening of direct wave by the Church.

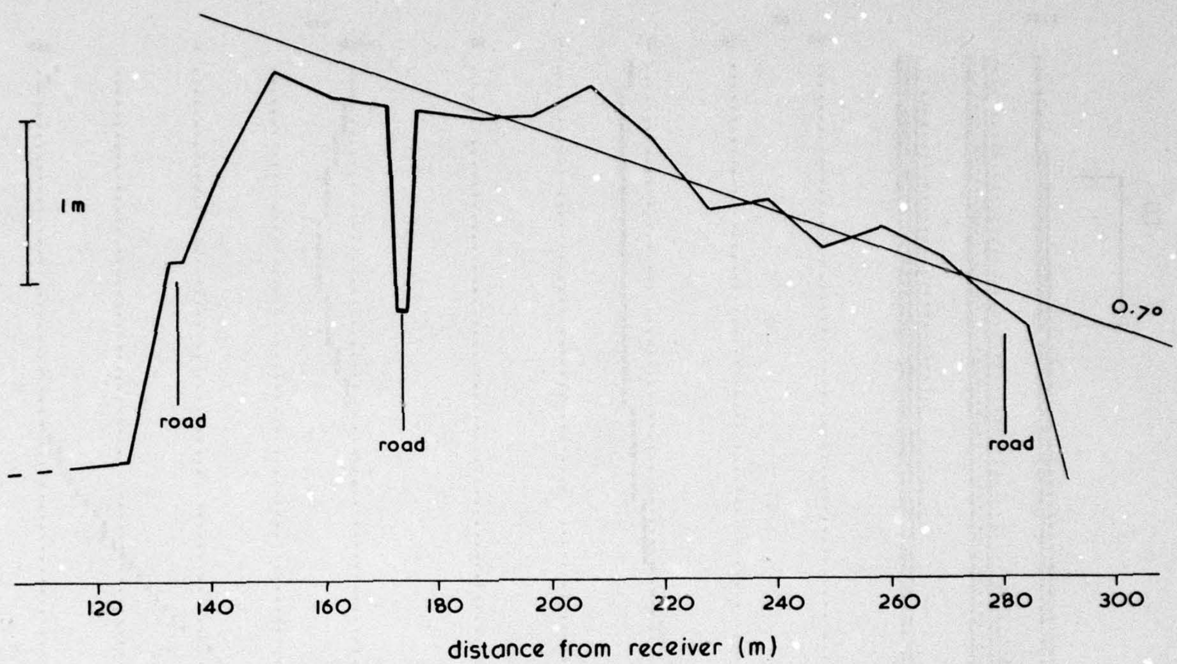

Fig. 12: Measured ground profile in the reflecting region. Southerly section.

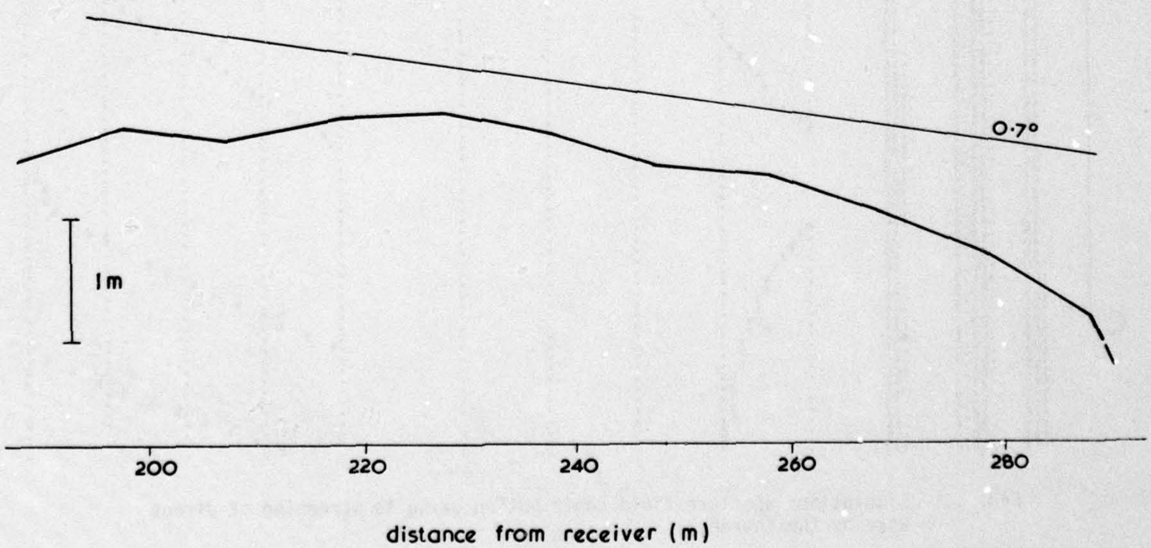

Fig. 13: Measured ground profile in the reflecting region. Northerly section.

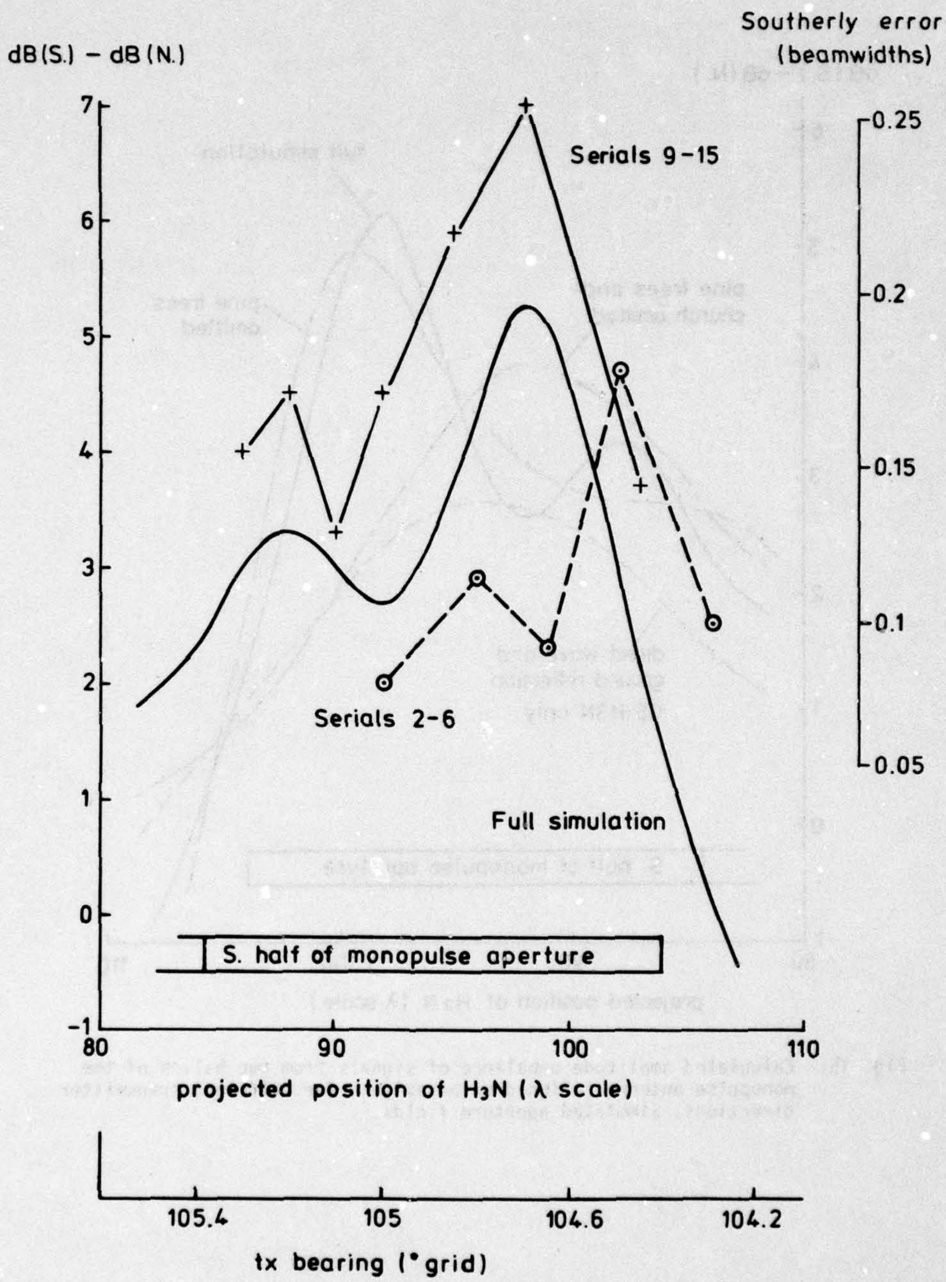

Fig. 14: Calculated amplitude unbalance of signals from two halves of the monopulse antenna (aligned on boresight) and corresponding bearing errors for different transmitter directions. Measured and simulated aperture fields.

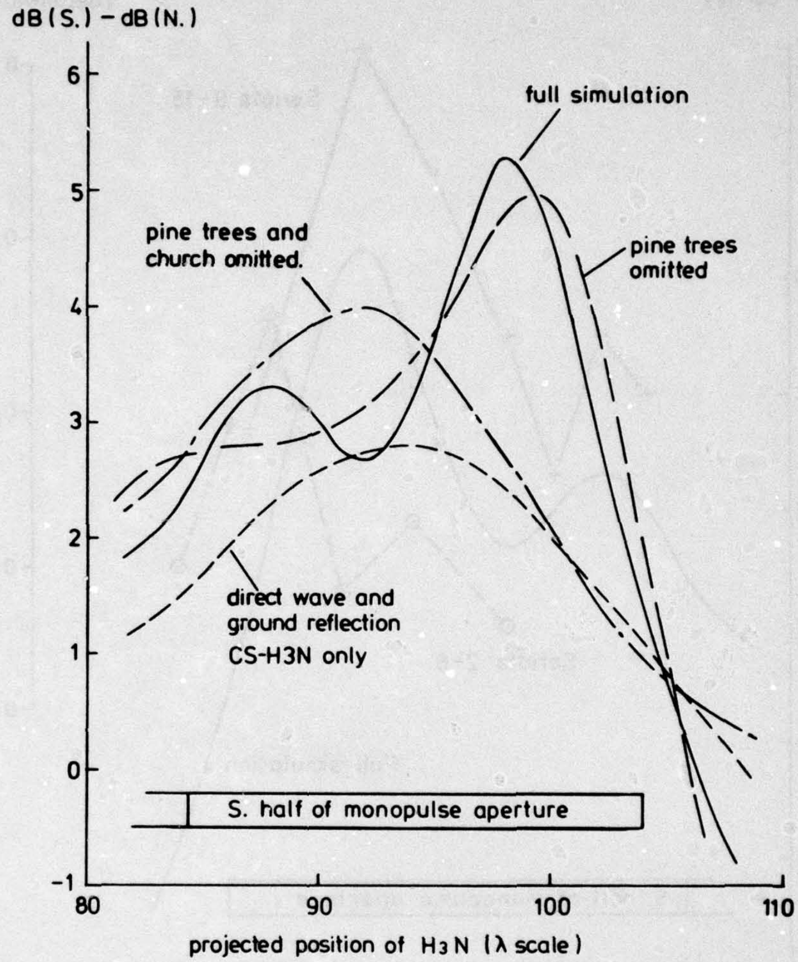

Fig. 15: Calculated amplitude unbalance of signals from two halves of the monopulse antenna (aligned on boresight) for different transmitter directions. Simulated aperture fields.

DIFFRACTION PHENOMENA DURING MULTIPATH FADING

by

H.G. Giloi

Research Institute of the Deutsche Bundespost
Darmstadt, Federal Republic of Germany

SUMMARY

The fast and deep fading on line-of-sight radio-relay links is caused by multipath propagation. The partial waves do not reach the receiving station only via the direct path, but also by reflection and refraction in a layered atmosphere, which gives rise to phase interference. In the particular case of two-path propagation, the electrical field strength profile is periodical with height, if the influence of the ground may be neglected. If the diffracting edge of an obstacle is located near the receiving station, Kirchhoff's formula can be applied to two coherent point sources, which are associated with the partial waves. In this case, fading in certain height ranges becomes much deeper than for the same ratio of amplitudes, but without diffraction.

Using this theory, it was possible to verify the measured electrical field strength height profiles at a receiving station located near a forest. The experiments were performed on a 40-km link operated at 9 GHz. The receiving aerial was set up on an elevator which moved up and down a 40-m tower. Electrical field strength height profiles were recorded with fade depths up to 26 dB.

1. Introduction

The large short-term variations of the field strength on line-of-sight radio relay links are caused by multipath propagation in a layered atmosphere. This type of fading is of particular importance in the frequency range below 10 GHz (Abel, N., 1978). Usually, fading is investigated by means of a stationary aerial. The phase interference of the partial waves does not only cause variations of the field strength with time, but also with height. The height profiles were investigated by an aerial mounted on an elevator moving up and down a tower. The interference patterns allow conclusions to be drawn on the related propagation phenomena, in general, and on the position of the reflecting tropospheric layers, in particular.

Electrical field strength height profiles, which are recorded with the aid of moving aerials, are described by several authors. These height profiles are not only attributed to reflections by atmospheric layers, but also by water surfaces and the ground (Fehlhaber, L., 1971, Fischer, K.E., 1974, Trolese, L.G., 1952). Measurements in periods without fading were made to find out the optimum height of the aerial on a given link (Czigany, S., 1976). The experiments show the electrical field strength patterns caused by diffraction at structures in the terrain.

In our experiments, the lower part of the elevator path was shadowed out by a forest in the vicinity of the receiving station. In periods without fading, the diffraction patterns closely resembled those of a knife edge. A part of the profiles of the fading periods showed also effects of scintillation and rain. The investigations were concentrated on multipath propagation. The period, during which the measurements were made, was relatively poor in fading. Only few events with rather deep fades were recorded. But it was possible to explain these events with the aid of a theory of diffraction in the case of two-path propagation.

2. Radio link and experimental set-up

The measurements were carried out on an experimental link in the Rhine valley from Mannheim to Wolfskehlen. The frequency was 9.3 GHz and the path length 39.7 km. At the receiving station, one aerial moved up and down between 2.5 and 38.6 m, a second one was fixed at 39.3 m. As is evident from the path profile (Fig. 1), the lower part of the receiving station tower is shadowed out by a deciduous forest at a distance of 640 to 950 m. In the case of an effective earth radius factor of $k = 1.33$, optical sight exists above a height of 28 m above ground. The first Fresnel zone is free above 33 m. If the reflecting atmospherical layers extend horizontally, they must be located either below the receiving aerial and closer than 13 km to the receiving station or above the transmitting aerial and close to the transmitter station.

At the 40-m tower of the receiving station, an elevator was mounted. It ran on rails to prevent the aerial from shaking. The elevator moved at two different velocities (.14 and .28 m/s) and was manually controlled. For this reason, the events of interest were only recorded during the presence of our staff at the normally unattended station. For safety reasons, it was not possible to install an automatic control.

3. Theoretical field strength profiles

3.1 Two-path propagation

The simplest model used to explain interference fading is that of two-path propagation. The attenuation A as a function of height is given by

$$A = -10\lg(1 + 2r\cos\psi + r^2) \qquad (1)$$

(Fehlhaber, L., 1970). Here, r ist the ratio of amplitudes of the partial waves, ψ is their phase difference

$$\psi = -\frac{2\pi\gamma}{\lambda} z + \psi_0 \qquad (2)$$

γ is the angle between the direct and the indirect rays at the receiving station, z is the height, λ the wave length and ψ_0 a phase constant. The fading has the height period

$$z_p = \frac{\lambda}{|\gamma|} \qquad (3)$$

Fig. 2 shows two examples of height profiles according to Eq. (1), where z_{max} is the coordinate of a field strength maximum. If this equation is valid, it is very simple to get r and z_p of a measured profile.

3.2 Diffraction at a knife edge

Eq. (1) is only valid, when the ray from the transmitter to the receiver is far away from buildings, mountains, and forests. The obstacle involving the simplest calculations is a knife edge. In periods of normal propagation, it causes the diffraction pattern depicted in Fig. 3. The attenuation is computed as follows:

$$A = -10\lg\left(\frac{1}{2}\left(\left(\frac{1}{2} + C(v)\right)^2 + \left(\frac{1}{2} + S(v)\right)^2\right)\right) \qquad (4)$$

with Fresnel's integrals

$$C(v) = \int_0^v \cos\frac{\pi}{2}\xi^2 \, d\xi \qquad S(v) = \int_0^v \sin\frac{\pi}{2}\xi^2 \, d\xi \qquad (5)$$

and

$$v = s\sqrt{\frac{2(d_1 + d_2)}{\lambda d_1 d_2}} \qquad (6)$$

The meaning of d_1, d_2 and s is evident from Fig. 3. Consequently, the distance of the transmitter from the receiver is

$$d = d_1 + d_2 \qquad (7)$$

3.3 Diffraction at a knife edge in periods of two-path propagation

Propagation on the radio-relay link shown in Fig. 4 will be discussed in the following. A reflecting layer causes a partial wave, which is diffracted at a knife edge together with the direct wave. This occurs on radio-relay links, where the knife edge is close to the receiving station. In the opposite case, reflection may also occur after diffraction; and if there is more than one obstacle, the problem may become very complicated.

Applying Kirchhoff's formula

$$u_p = \frac{1}{4\pi} \oint_F \left(\frac{e^{-\frac{2\pi i R}{\lambda}}}{R} \operatorname{grad} u - u \operatorname{grad} \frac{e^{-\frac{2\pi i R}{\lambda}}}{R} \right) d\vec{f} \qquad (8)$$

to two point sources with

$$u_1 = \frac{e^{-\frac{2\pi i R_1}{\lambda}}}{R_1} \qquad u_2 = r_0 \frac{e^{-\frac{2\pi i R_2}{\lambda}}}{R_2} \qquad (9)$$

which are related to the direct and the indirect rays, one gets

$$\begin{aligned} A = -10\lg\Big(\frac{1}{2}\Big(&\left(\frac{1}{2} + C(v)\right)^2 + \left(\frac{1}{2} + S(v)\right)^2 + r^2\left(\left(\frac{1}{2} + C(w)\right)^2 + \left(\frac{1}{2} + S(w)\right)^2\right) \\ &+ 2r\cos\psi\left(\left(\frac{1}{2} + C(v)\right)\left(\frac{1}{2} + C(w)\right) + \left(\frac{1}{2} + S(v)\right)\left(\frac{1}{2} + S(w)\right)\right) \\ &+ 2r\sin\psi\left(\left(\frac{1}{2} + C(w)\right)\left(\frac{1}{2} + S(v)\right) - \left(\frac{1}{2} + C(v)\right)\left(\frac{1}{2} + S(w)\right)\right)\Big)\Big) \end{aligned} \qquad (10)$$

where

$$v = z\sqrt{\frac{2(d - d_2)}{\lambda d d_2}} \qquad (11) \qquad\qquad w_0 = \gamma\sqrt{\frac{2 d d_2}{\lambda(d - d_2)}} \qquad (13)$$

$$w = v - w_0 \qquad (12) \qquad\qquad \psi = -\pi w_0 \cdot v + \psi_0 \qquad (14)$$

The coordinate z is the height of the receiving aerial above the end of the shadow. When the distances and the frequency are fixed, the parameters of the attenuation pattern (Eq. (10)) are: the ratio of the amplitudes r, the angle γ between the rays, and the phase-constant ψ_o. Assuming $r = 0$ in Eq. (10), one gets Eq. (4) for the simple knife edge diffraction. In the case of heights far above the shadow, i.e. with great values of z, Eq. (10) becomes the simple two-path propagation Eq. (1). Fig. 5 shows attenuation patterns varying with the parameter ψ_o, where $r = .8$ and $w_o = .4$. Both the position and the size of the attenuation maxima vary with ψ_o. For $r = .8$, Eq. (1) for the simple two-path propagation yields a maximum increase in field strength of 5.1 dB and a maximum attenuation of 14 dB. Near the shadow, these values are exceeded by far. The largest attenuation maxima are found where they coincide with maxima of the simple knife edge diffraction. Assuming aerials located at the corresponding heights, the large maximum at $v = 1.87$ is caused by an obstacle inside the 2nd Fresnel zone and an other one at $v = 2.74$ by an obstacle inside the 4th Fresnel zone. The definition of the protected zone claimed for line-of-sight links is normally based on the 1st Fresnel zone. As it is seen here, an obstacle outside this zone may strongly influence the fading. Fig. 6 shows how the attenuation pattern varies with r. The maximum of two-path propagation attenuation coincides with a maximum (Fig. 6a) and a minimum (Fig. 6b) of knife edge diffraction attenuation. It can be seen that there are unfavourable heights for the aerial. But these heights vary with the refractive index profile of the atmosphere, especially in fading periods. A comparison of Fig. 5 and Fig. 6 with Fig. 3 shows that during multipath propagation the field strength may rise at heights where normally shadowing effects become noticeable.

4. Measurements

The experiments were carried out from December 1977 to July 1978. Unfortunately, in June and July of that year less fading was found than in the years before. As a consequence, only few experiments with the elevator yielded informative results. During the whole experimental period, about 600 field strength profiles were recorded.

4.1 Periods without fading

The field strength profiles recorded in periods without fading are attributed to diffraction at a knife edge. The heights h of the maxima and minima of the measured curves were associated with the corresponding values of v of the theoretical curve (Fig. 3). Then the equation

$$z = h - h_o = c\,v \qquad (15)$$

was solved by *linear regression*. Here, h_o is the height of the shadow and c a quantity resulting from Eq. (11)

$$c = \sqrt{\frac{\lambda d d_2}{2(d-d_2)}} \qquad (16)$$

Since d and λ are known, there is a possibility to compute d_2, the distance of the knife edge from the receiving station. Fig. 7 shows some examples of measured field strength profiles. For clarity's sake, they are separated in this figure by 2 or 5 dB. The curves vary with the season. In winter there are four weak maxima in the height range of the elevator, in March and April three, and in summer two, which are clearly visible. A total of 140 such profiles were evaluated. The results are

Tab. 1

	h_o	d_2
Dec. - Feb.	26.9 m	500 m
Mar. - Apr.	27.6 m	530 m
June - July	28.2 m	860 m

In June and July, the knife edge is found in the area of the forest near the receiving station. In the other seasons, d_2 is too short compared to the geometrical distance. In addition, the maxima and minima of the field strength do not assume the theoretically expected values. Both facts show that the forest can only approximately be regarded as a knife edge. In the months during which the trees had no leaves the shadow was less high than in summer.

4.2 Scintillation fading and rain attenuation

Fig. 8 shows an example of scintillation fading. The curves are separated by 2 dB. This type of fading is caused by small-space inhomogeneities of the refractive index in a turbulent atmosphere. In Fig. 8 the field strength varies noticeably with small changes in height and within short periods. The attenuation does not exceed 5 dB above the height of the shadow. These events cannot be explained by the theory formulated in section 3. Profiles which are only slightly superimposed by this type of fading (see one of the examples in Fig. 7) were also analyzed.

During the recordings shown in Fig. 9, rain was observed. The diffraction pattern

becomes blurred. Only the first maximum above the shadow is recognizable.

4.3 Multipath propagation

With the movable aerial it was possible to observe the development of a fading event by means of field strength profiles recorded at time intervals of a few minutes. In some cases, curves according to Eq. (10) were found, which corresponded to measured profiles. The accuracy is limited by the facts that the field strength profile varies during the recording and that the forest is not a perfect knife edge. The curves were determined by the parameters r, w_o and ψ_o in Eqs. (12) and (14). The height of the shadow and the distance from the knife edge were computed with Eqs. (15) and (16). Then, γ was calculated, using Eq. (13) and z_p using Eq. (3). The measured profiles differ from the computed ones in a height-independent attenuation portion which is attributable to defocusing effects (Fehlhaber, L., 1976).

An event with a 26-dB fade was recorded on Dec. 8, 1977 from 12.50 h - 14.30 h. The attenuation relative to free space at the fixed aerial varied from -2 to +9 dB during this period. Some of the field strength profiles, which were recorded with the movable aerial, are shown in Fig. 10. A fade of 9 dB at a height of 33.5 m rose in 13 minutes to 20 dB and shifted to 32 m. A minute later, it was found with the highest recorded attenuation of 26 dB at 34 m and 3 minutes later with only 9 dB at a height of 36 m. The parameters of the profiles of 13.45 h, 13.51 h and 13.58 h were evaluated (see Tab. 2). Besides this event, two others - observed in June and July 1978 - were analysed. In these cases, the fades rose to 17 and 15 dB, respectively. The attenuation at the fixed aerial varied from 2 to 10 or 13 dB. All measured profiles were explained by reflection at ground-based layers, that means with $w_o > o$. This assumption, however, is not necessarily conclusive. The profiles measured on June 19, 1978 in Fig. 11 were also explained by reflection at a layer above the height of the transmitter aerial (Fig. 12). The corresponding values in Tab. 2 differ considerably from each other, but they do not show clearly which of both models is the correct one.

The distances d_2 from the receiving station to the knife edge are similar to those of periods without fading in Tab. 1. The values of December 8, 1977 are too small on the average, those of June 19 and July 25, 1978 are in the vicinity of the neighbouring forest. Assuming $w_o < o$, the resulting values are a little too great.

Tab. 2

Results of the analyzed fading events

date	hour	r	w_o	ψ_o	d_2 m	h_o m	γ mrad	z_p m	A_D dB
Dec. 8, 77	13.45	.45	.40	-12.2°	850	25.6	1.72	18.7	5.1
	13.51	.31	.46	-2.8°	620	26.2	2.33	13.8	5.0
	13.58	.78	.40	7.2°	450	24.8	2.36	13.6	7.6
June 19, 78	0.32	.46	.35	-78.0°	960	26.2	1.41	22.7	2.6
	0.35	.64	.35	-76.0°	850	26.9	1.50	21.4	3.3
	0.39	.40	.40	-38.6°	1000	26.2	1.57	20.4	3.7
June 19, 78	0.32	.60	-.37	114.0°	1070	30.3	-1.41	22.7	-.3
*)	0.35	.67	-.40	117.0°	1340	29.9	-1.36	23.6	1.6
	0.39	.65	-.40	96.0°	1330	29.6	-1.37	23.5	.5
July 25, 78	6.03	.70	.35	-38.0°	760	28.4	1.59	20.2	2.2
	6.06	.70	.35	-58.1°	670	28.3	1.61	20.2	1.3
	6.10	.33	.40	-45.0°	950	27.4	1.61	20.0	1.9
July 25, 78	6.33	.2	.35	-36.0°	900	28.7	1.47	22.0	6.5
	6.36	.2	.35	-36.0°	900	28.7	1.47	22.0	0.1

*) The field strength profiles of June 19 were explained by a reflecting layer below and above the direct ray.

On July 25, the end of the shadow was approximately at the height found for periods without fading (see Tab. 1). On December 8, 1977 and June 19, 1978, the height h_o was below normal, supposing $w_o > o$. Assuming $w_o < o$ for the fading event of June 19, h_o was higher than normal. The shifting of the shadow end may be explained by anomalous refractive index profiles and can be represented by the k factor (Fehlhaber, L., 76). Swingler (Swingler, P.N., 1977) calculated k from measurements made at a knife edge. Our experiments only allowed the order of magnitude of k to be determined. Assuming $w_o > o$, one obtains values for the events of December 8 and June 19 which are large compared to 4/3 or which are even negative, and for the event of July 25, a value around 4/3. Supposing $w_o < o$ for the event of June 19, one finds a value markedly below 4/3.

No matter which one of both explanations is correct, there is still the fact that the steep slope of the field strength began at a lower height than in periods without fading (compare Fig. 11 with Fig. 7) and that the first maximum of the field strength

was located 2.3 to 2.8 m below the normal height. The values for the other fading events are 3.4 to 4.1 m on December 8 and 1.1 to 1.7 m on July 25. For the field strength profiles recorded in July 1978, the statistical distribution of the height and the attenuation of the first maximum was computed and drawn in Fig. 13. In more than 80 per cent of the profiles, the maximum was found at a smaller height and in more than 45 per cent the field strength was higher than in periods without fading. These results agree with those obtained by Großkopf and Fehlhaber (Großkopf, J., 1963) and also by Vigants (Vigants, A., 1975) who report on good results of space diversity experiments, in which the lower aerial was shadowed out.

The height periods in Tab. 2 are 13 to 19 m on December 8, 1978 and 20 to 24 m on the summer days. They are greater than the height space of the elevator above the shadow. Using the values of γ, it is possible to estimate the position of the reflecting layer in Fig. 1. Assuming a ground-based layer, one obtains a position on the border of the first or third Fresnel ellipse computed for an aerial at the height of the attenuation maximum. For high layers a position of about 50 m above the direct ray is estimated. No events with deep fading were observed, from which one could infer greater angles γ or smaller height periods z_p.

The defocusing attenuation A_D rose to 8 dB on December 8, 1977. An event with clearly recognizable defocusing effects is shown in Fig. 14. In Tab. 2, the two curves of July 25 (6.33 h and 6.36 h) have the same parameters r , w_o and ψ_o. They only differ in A_D by 6 dB. The size of A_D depends on whether the fading is attributed to reflection at a ground-based or a high layer (compare the parameters of June 19, 1978 in Tab. 2).

5. Continuation of the experiments

The aerial mounted on an elevator is suitable for recording single field strength height profiles. The continuous recording shows the curves with all details. It was possible to explain the curves obtained in this experiment qualitatively and, in part, quantitatively by means of the two-path model.

The operation and maintenance of the equipment and the evaluation of the measurements were very time-consuming. Therefore, this procedure is unsuitable for gaining statistical data for applications of diversity reception. Consequently, in future investigations an array of aerials will be used and the measured values will be recorded digitally.

References

ABEL, N.,1978, "Statistics of multipath fading and rain attenuation on terrestrial radio links in the 7 to 15 GHz range", IEE Conference Publication No. 169

CZIGANY, S. KÜHN, U., REISSMANN, H., 1976, "Über einige Erfahrungen bei der Planung und beim Betrieb von Richtfunkstrecken", Technische Mitteilungen der RFZ, 20. Jahrgang, Heft 1

FEHLHABER, L., 1970, "Zweiwegeausbreitung im Richtfunk auf Funkfeldern mit direkter Sicht und freier erster Fresnelzone", Techn. Bericht des Forschungsinstituts der Deutschen Bundespost beim FTZ A 455 TBr 27

FEHLHABER, L., 1971, "Interferenzschwund auf Sichtstrecken im cm-Wellenbereich", Kleinheubacher Bericht Nr. 14

FEHLHABER, L., GILOI, H.G., 1976, "Effects of Nocturnal Ground-Based Temperature Inversion Layers on Line-of-Sight Radio Links", AGARD Conference Proc. No. 208

FISCHER, K.E., 1974, "Einflüsse von freien Inversionen des modifizierten Brechungsindex in der Troposphäre auf die Ausbreitung von cm-Wellen über See innerhalb des radiooptischen Horizonts", Bericht des Instituts für Radiometeorologie und maritime Meteorologie an der Universität Hamburg, Nr. 27

GROSSKOPF, J., FEHLHABER, L, 1963, "Feldstärke und Schwundbeobachtungen auf Landstrecken mit optischer Sicht im dm- und cm-Wellenbereich", Techn. Ber. des Fernmeldetechnischen Zentralamtes der Deutschen Bundespost Nr. 5577

SWINGLER, D.N., 1977, "Holographic Measurements of k Factor on Line-of-Sight Microwave Routes Containing Knife Edge Obstacles", IEEE Transaction Ant. Prop. 25

TROLESE, L.G.,DAY, J.P., HOPKINS, R.U.F., 1952, "Propagation Characteristics of Microwave Optical Links", Trans. of the IRE, PGAP-4

VIGANTS, A., 1975, "Space-Diversity Engineering", Bell System Techn. Journal, Vol. 54, No. 1

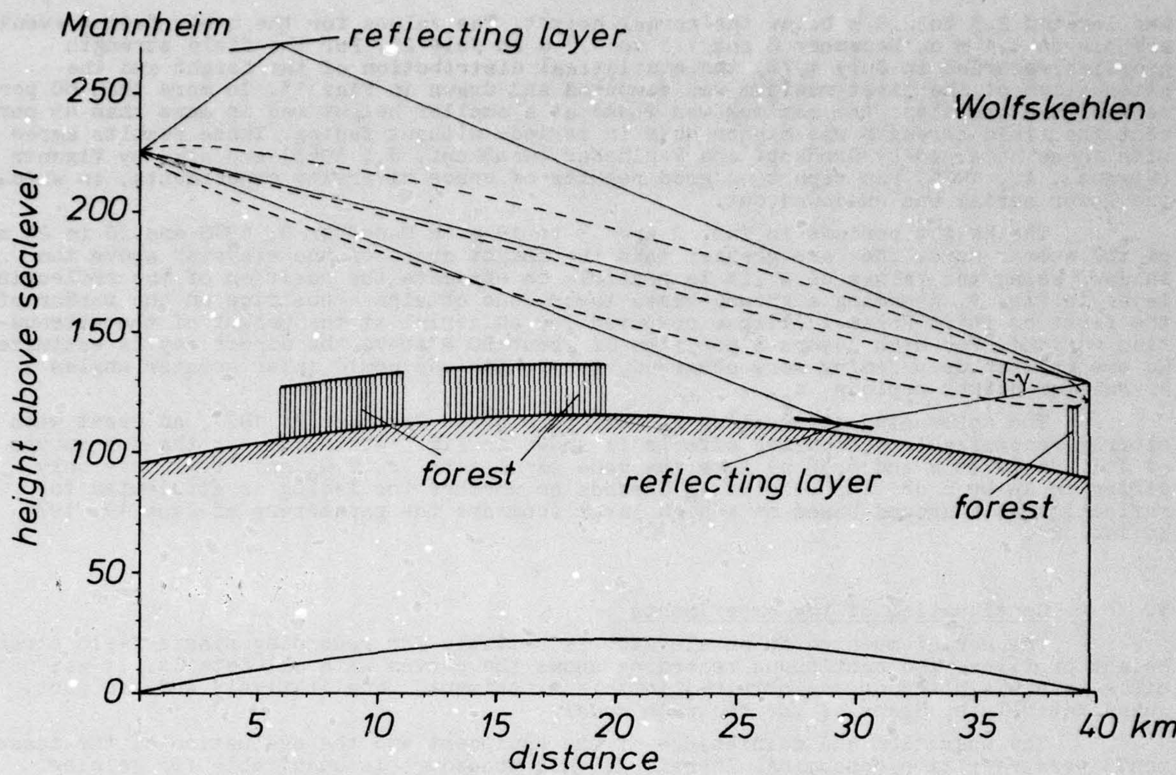

Fig.1 Path profile Mannheim – Wolfskehlen with the effective earth radius $k \cdot r_e = 8500$ km
– – – – – ray to the movable receiving aerial at the height, where the first Fresnel zone is free from obstacles
——— direct and reflected rays to the fixed receiving aerial

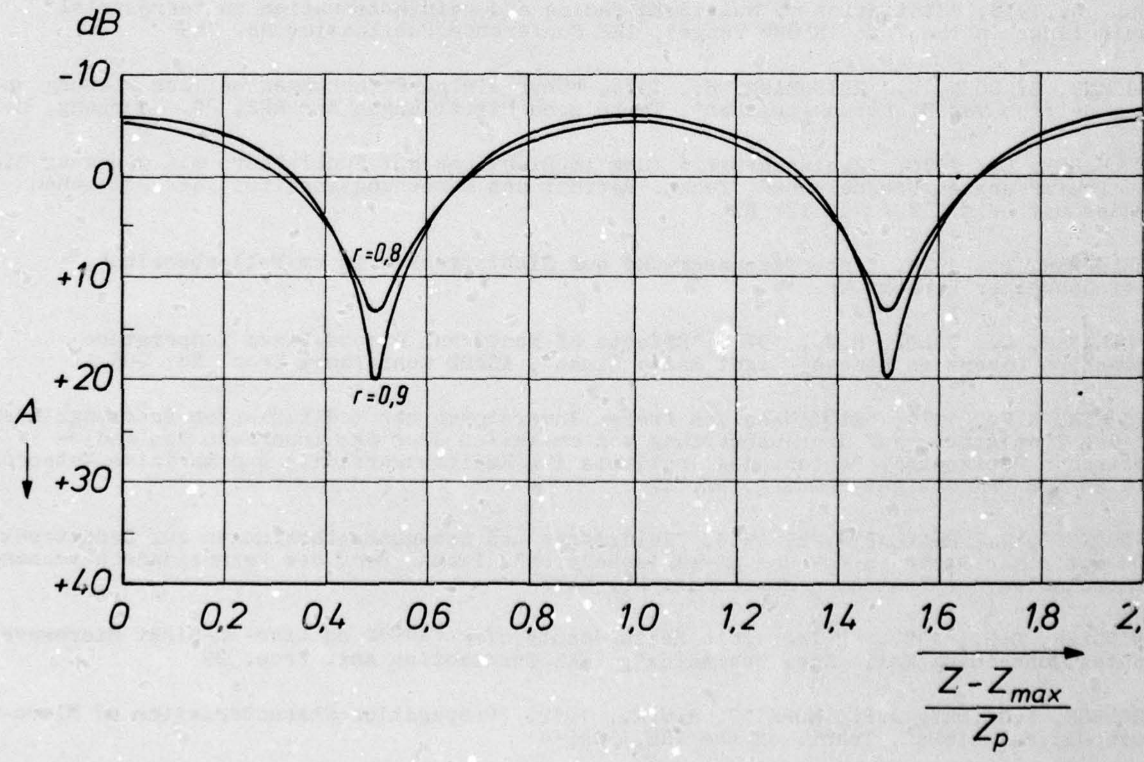

Fig.2 Theoretical attenuation-height profiles for two-path propagation

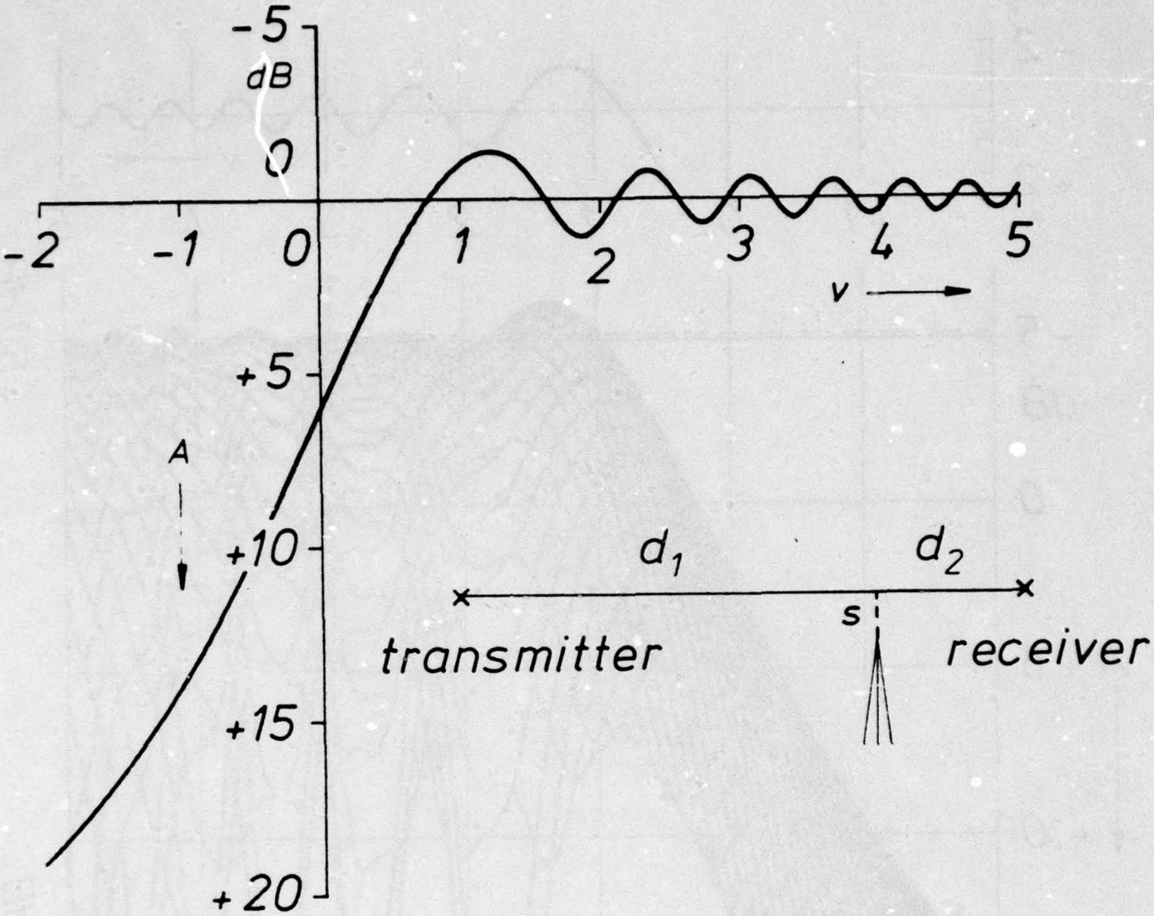

Fig.3 Geometrical arrangement and attenuation-height profile in the case of knife edge diffraction

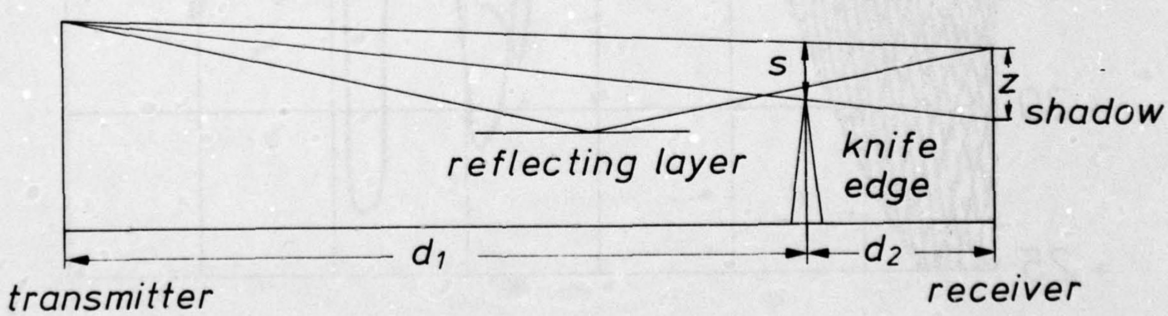

Fig.4 Geometrical arrangment for two-path propagation with diffraction at knife edge

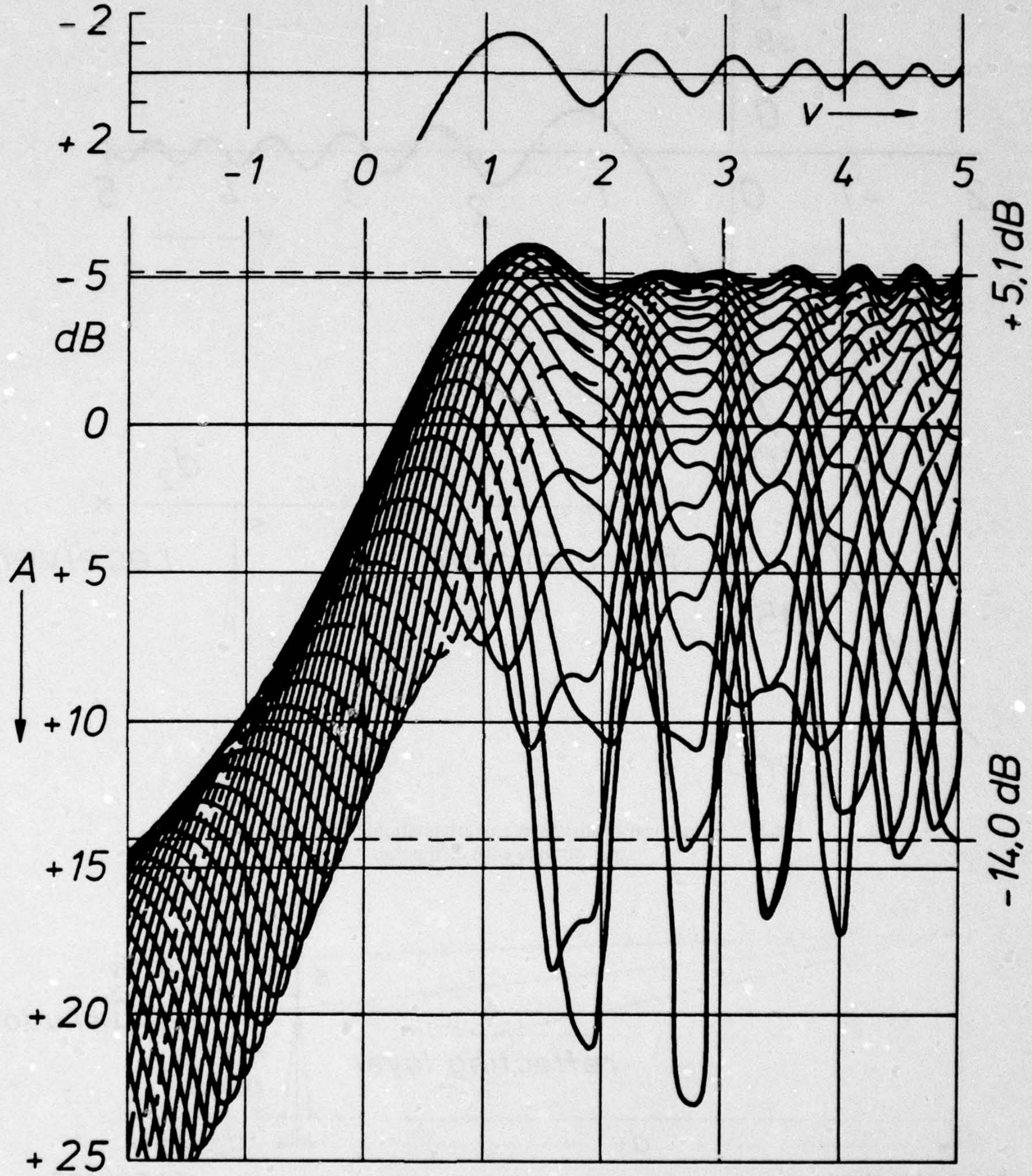

Fig.5 Knife edge diffraction patterns for two-path propagation
$r = .8$, $w_o = .4$, $\psi_o = -165°, -150°, -135°, \dots 180°$

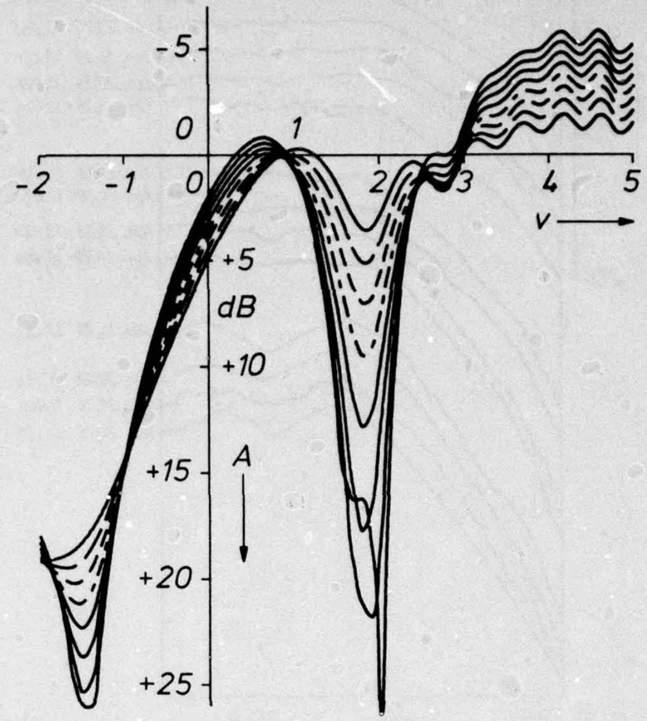

(a)

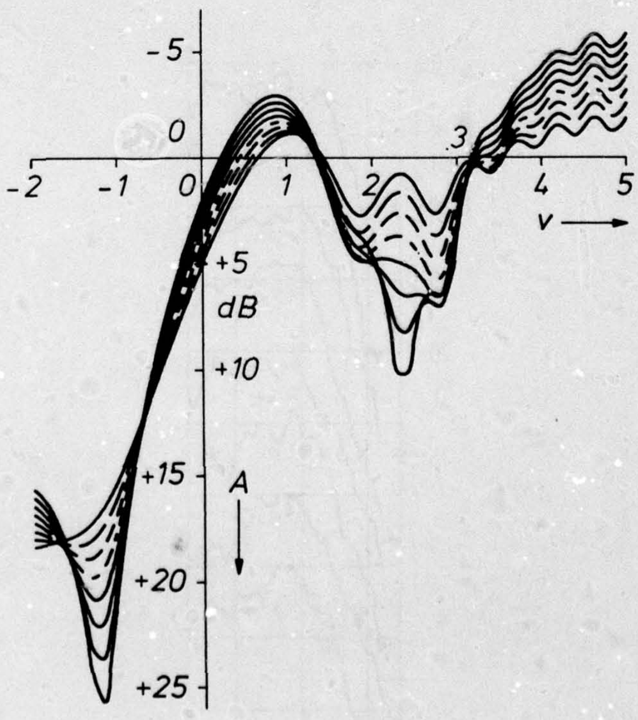

(b)

Fig.6 Knife edge diffraction patterns for two-path propagation
r = .2, .3, .4, ...9, $w_o = .4$
(a) $\psi_o = -45.4°$ (b) $\psi_o = -10.8°$

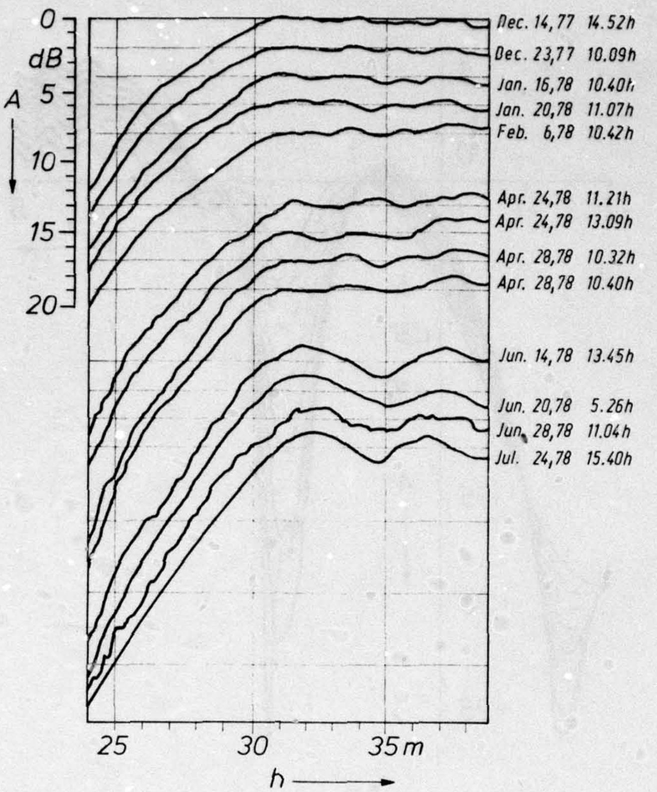

Fig.7 Measured electrical field strength height profiles during periods without fading. The curves are separated by 2 or 5 dB

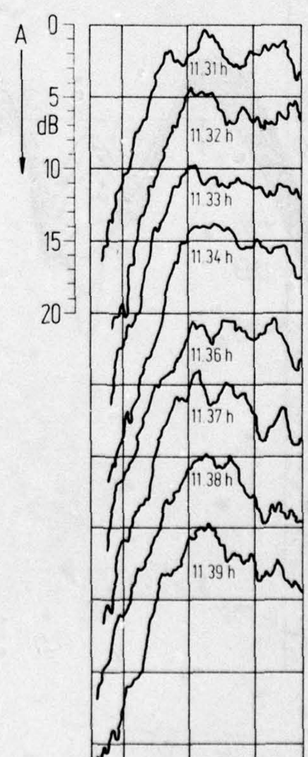

Fig.8 Electrical field strength height profiles during scintillation fading

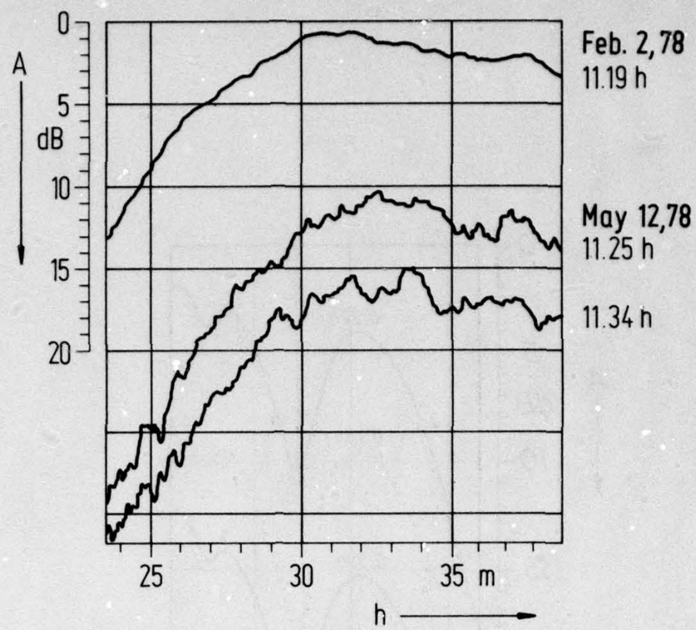

Fig.9 Electrical field strength height profiles during rain

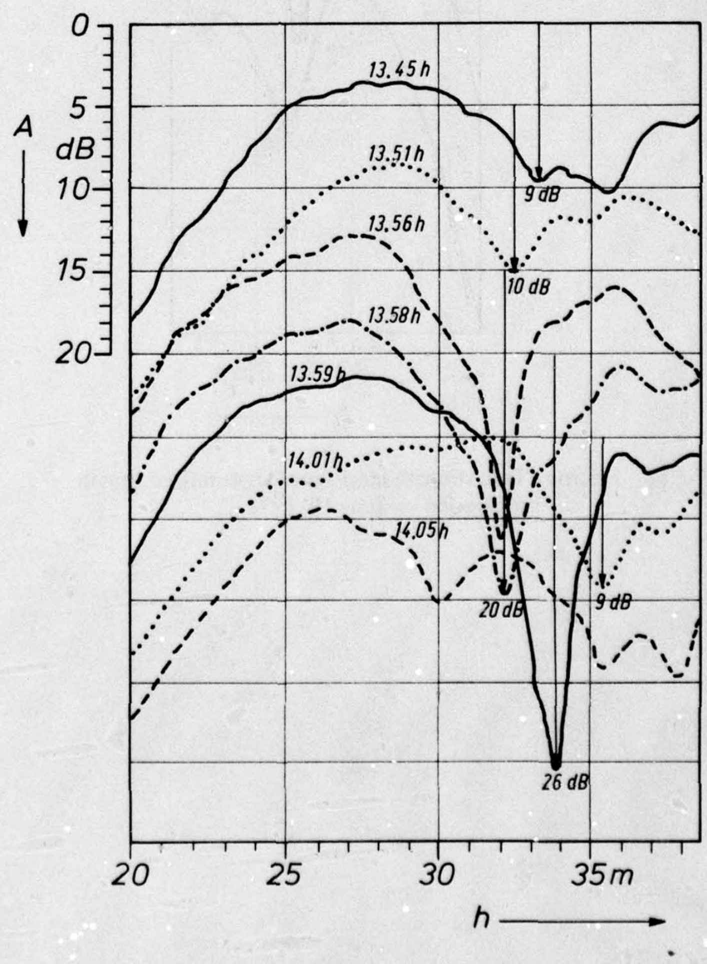

Fig.10 Electrical field strength height profiles during multipath propagation on December 8, 1977

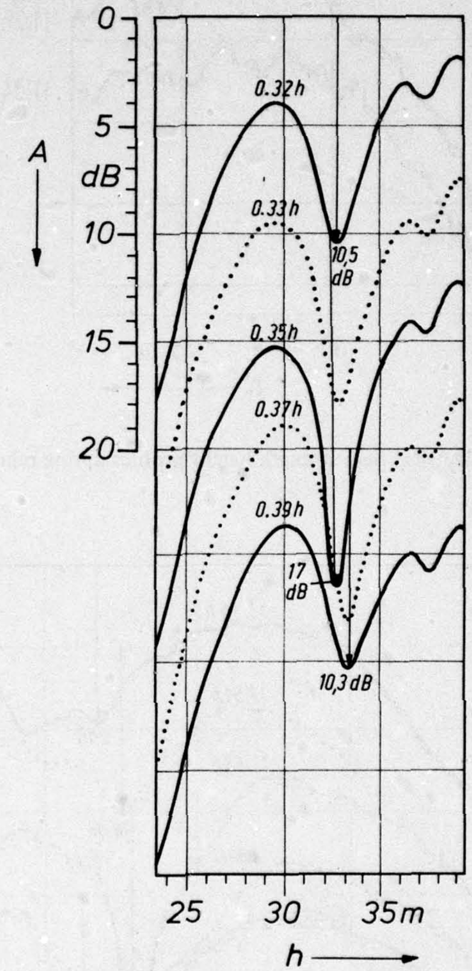

Fig.11 Electrical field strength height profiles during multipath propagation on June 19, 1978

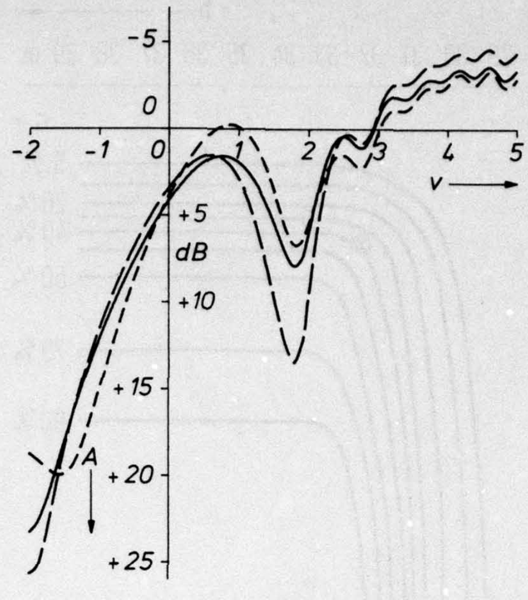

(a)

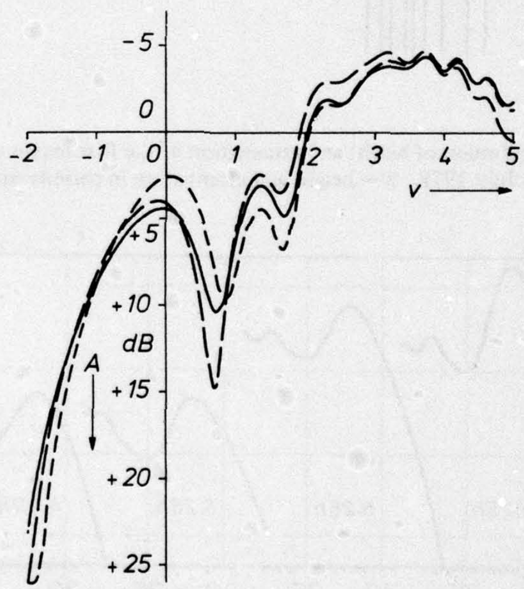

(b)

Fig.12 Attenuation-height profiles computed for the experiment of June 19, 1978

(a) attributed to reflection at a ground-based layer

	————	— — —	- - - - -
hour	0.32	0.35	0.39
r	.46	.64	.40
w_o	.35	.35	.40
ψ_o	−78.0°	−76.0°	−36.6°

(b) attributed to reflection at a higher layer

	————	— — —	- - - - -
hour	0.32	0.35	0.39
r	.60	.67	.65
w_o	− .37	− .40	− .40
ψ_o	114.0°	117.0°	96.0°

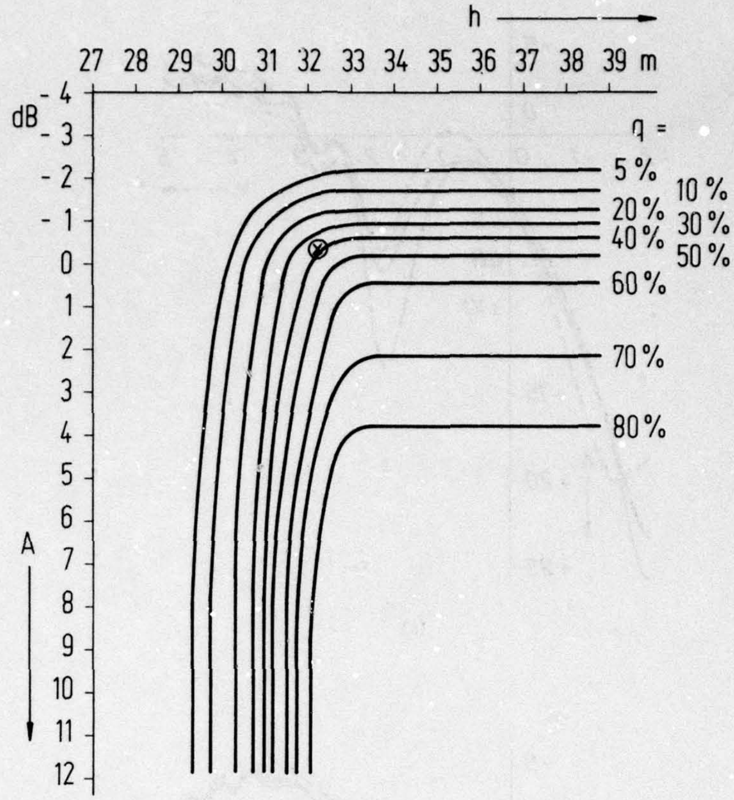

Fig.13 Statistical distribution of height and attenuation of the first maximum of the field strength recorded in July 1978. ⊗ = height and attenuation in periods without fading

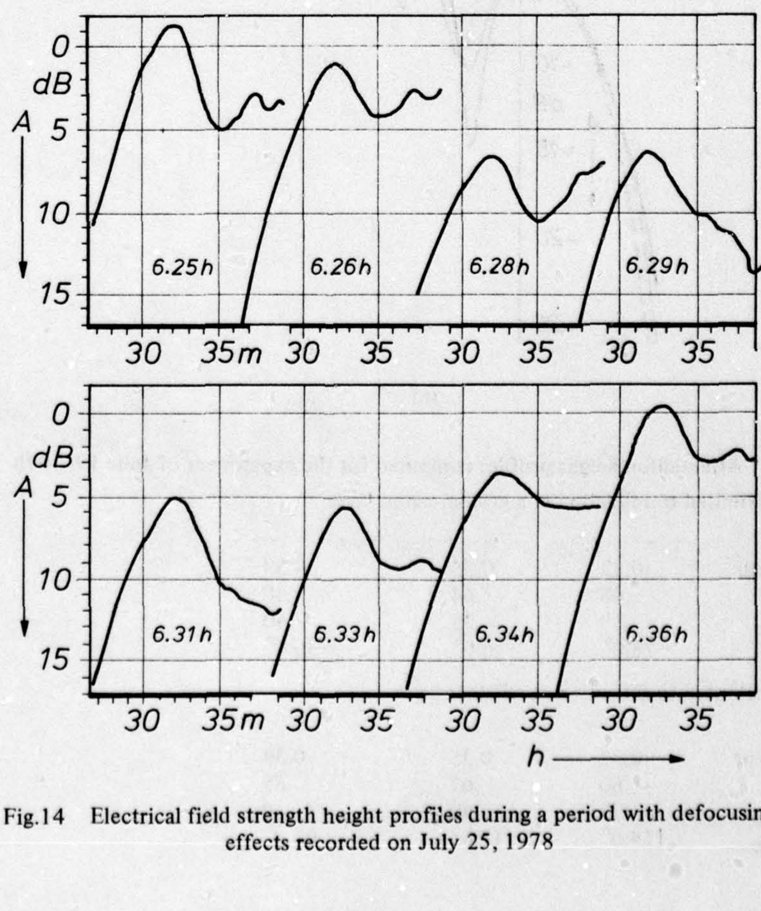

Fig.14 Electrical field strength height profiles during a period with defocusing effects recorded on July 25, 1978

APPENDIX A

QUESTIONS AND COMMENTS ON PAPERS

SESSION I

Paper No. 1

L. B. Felsen (U.S.): One of your slides shows an elevation of only 0.001 wavelength above the ground. It seems questionable to use the reflection coefficient approximation for such small elevations. Could you comment on that?

A. Hizal (Turkey): At the lower end of the antenna, the current is zero. When the antenna feed locations are not very close to the lower end of the antenna, the contributions of the currents in this region to the antenna field will be small in comparison with those of the currents at the upper end of the antenna. Thus, it is expected that incorrect contributions, resulting from inaccuracies of the reflection coefficient approximation, are not very significant.

L. B. Felsen (U.S.): What do you use as a reference solution for assuming the validity of the reflection coefficient approximation?

A. Hizal (Turkey): The current distributions were calculated for half wave vertical dipoles just above the ground with an exact Sommerfeld approach by D. C. Chang and J. R. Wait. We verified the accuracy of our calculated reflection coefficient approximation with their calculations. It was observed that the two current distributions were in good agreement. The agreement between the real parts of the current distributions was better than that of the imaginary parts.

K. J. Langenberg (FRG): I do not understand your symmetric current distribution in Fig. 2 for a half wave dipole above moist earth. I would expect the current maximum to be shifted a little more towards the earth.

A. Hizal (Turkey): The proximity effect, where the current increases in regions of the antenna near the ground, depends upon various factors such as antenna radius, feed location, ground parameters, and antenna length. It was found that this effect becomes less pronounced for thin antennas, especially for center feed antennas (A. Hizal, Int. J. of Electronics, vol. 37, 1974).

K. J. Langenberg (FRG): What are your shape parameters?

A. Hizal (Turkey): The radius of the antenna is about one tenth of the wavelength. The thin wire approximation is applicable.

K. J. Langenberg (FRG): Did you use the thin wire approximation in the Green's function, avoiding the ϕ integration?

A. Hizal (Turkey): Yes, I avoided the ϕ integration around the antenna diameter.

Paper No. 2

K.J. Hortenbach (FRG): How did you model the ground constants of the real ground?

J. S. Belrose (Canada): We did not model the ground constants. The numerical modelling to date has assumed a perfectly conducting ground plane, and we were comparing this in detail with the model measurements. The twenty foot diameter turntable, described in my paper, was a copper sheet.

A. W. Biggs (U.S.): When you modelled the buildings, was it desirable to model the distribution of conductors within buildings, or did you you treat the building as a uniform imperfect conductor?

J. S. Belrose (Canada): In my presentation this morning, I have not really rigorously modelled buildings, since the calculations were only for thin monopoles, which do not resemble buildings. However we have done some preliminary work, treating buildings in the same way as with power lines. Power lines are modelled with wire grids, and wire grids will probably closely approximate high rise buildings which are currently in use. High rise buildings look like ribbed structures. The structural steel forms that structure. All power lines for electric lights have ground wires and those also form a grid structure. I believe that buildings look like the square structures in our model. The uncertainty with buildings is the uncertainty of connections of the masses of steel, wire grid systems, and water lines to the actual earth. The building is uncertainly connected to a finite conducting earth, and that is a major difficulty which must be considered. We must measure parameters of real buildings. You cannot estimate them.

Paper No. 4

L. B. Felson(U.S.): To what extent is the surface impedance model justified when media are multilayered and poorly conducting so that multilayer effects are noticeable?

R. J. King (U.S.): This is not the situation in the cases considered in our paper, but I will attempt to answer your question. Aside from the possible existence of leaky waves which may exist near a source or where there is a local change in layering, the well-known surface impedance corresponding to a plane wave obliquely incident on the stratified media should suffice. It includes the angle of incidence, the effect of possible internal resonances, and is obtained by satisfying the boundary conditions at each interface. If one tries to use this impedance in situations where the fields vary rapidly (e.g., near a source), the index of refraction of each of the layers

must be sufficiently large that the angle dependence drops out. Essentially, this means that the fields in each of the layers must be plane (although inhomogeneous and with standing waves). In terms of Snell's law, the refracted waves must essentially propagate normal to the boundaries.

If the surface wave impedance was known exactly, its use in our formulation would give the effect of these additional complex waves. However one is forced to use an approximate impedance such as that for a plane wave at oblique incidence, or that which is a solution of the transverse resonance condition. Neither accounts for the presence of the source, and so they do not account for any additional leaky waves. If such waves are strongly excited and guided, they couple energy into the radiation field at some characteristic angle other than the specular or grazing angles. For rapid leakage along the surface this additional radiation appears near the zenith. In such cases, the radiation pattern calculated using the surface impedance should be accurate at the lower angles near the horizon.

Excitation of these troublesome fields depends on the type of source, and on the structure and losses of the multilayer media beneath the source. For example, it is known that transverse magnetic (TM) waves are weakly excited when a magnetic line source or a vertical electric dipole is located above a grounded dielectric slab if the slab is thin enough to support only one surface wave mode (Barone and Hessel, R-698-58, Polytechnic Inst. of Brooklyn). We have tested this in a series of microwave, 4.8 GHz, experiments using various thicknesses of Plexiglass laid on a metal sheet, and found no evidence of the presence of significant leaky waves near the source. We did, however,find that small airgaps between the Plexiglass amd metal caused leakage of the guided surface wave. Moreover, no evidence of leaky waves of any kind was found when the metal was replaced with water, which has a very large index of refraction and losses (King et al, Radio Science, vol. 8, 1973).

For simple geometries, one can use existing theories to predict the presence of leaky waves. For more complex geometries, such as a radial wire system over a low-loss stratified medium. this question needs to be considered seriously. Probably the simplest way would be to conduct microwave experiments using laboratory models where conditions and geometries can be carefully controlled. Such experiments can point out deficiences in the theory or prove its sufficiency and establish confidence in applying it to practical real world problems.

L. B. Felsen (U.S.): If you have a dielectric slab that isn't very lossy, to what extent can you model one slab or several layers?

R. J. King (U.S.): In the laboratory, you can model these within about a wavelength from the source. It behaves like the surface impedance that we suggested. When you have a dielectric slab on a perfect conductor and are more than a wavelength away from the source, the model is like the surface impedance that can be calculated. However this is a laboratory model, and it really works.

L. B. Felsen (U.S): For cases of small screens, you have significant edge diffraction and generation of side lobes. Could you use a more efficient way to calculate these effects, such as the geometrical theory of diffraction, instead of the integral equation?

R. J. King (U.S.): Perhaps GTD could be used; we have not done it. But remember that the surface is radially nonuniform and the fields which are incident on the edges must be found first. Moreover, the surface fields are radiating, and scattering from the edges is only one part of the radiated field. The integral formulation is a convenient means of simultaneously accounting for the nonuniform surface and edge scattering. However, it should be mentioned that the *surface* field used in (4) does not include edge reflections, i.e., waves which are reflected from the edges and propagate back toward the source (see Sec.3). These reflections are normally quite small.

L. B. Felsen (U.S.): How many radial wires must be packed per wavelength in order to validate the surface impedance model for a wire screen?

R.J.King (U.S.): That depends on how many terms one uses in the series for Δ_f in (25), as derived by Wait [1962], and on the refractive index of the underlying earth. If only the leading term is used, the spacing d should satisfy $d/\lambda < (2\pi|n|)^{-1}$ where $|n| = |\epsilon - j\,\sigma/\omega\epsilon_0|^{1/2}$. As the systems discussed here extend to radii as large as 10λ, we found 30 terms to be sufficient.

SESSION II

Paper No. 6

L. B. Felsen (U.S.): You did point out some discrepancies in the surface impedance concept, but you did not clarify any of them. The use of surface impedances requires a good deal of attention because it enters into most of the theoretical models that are being presented. Do you have something very brief to say about it now?

R. H. Ott (U.S.): No, because I did not have enough time to study it. It is a very difficult problem.

E. Bahar (U.S.): Even if the surface is flat, the impedance boundary condition is still not exact. In your expressions, if you let the radius of curvature go to infinity, you indicated the surface impedance was valid. However, if you let the radius go to infinity, everything washed out on the right hand side.

R. H. Ott (U.S.): I don't agree with Bahar's atatement.

Paper No. 7

L. Boithias (France): Votre méthode peut-elle être utilisé pour calculer l'influence d'un conduit troposphérique? Un travail a-t-il été commencé à ce sujet?

Translation:

Can your method be used to calculate the influence of an obstacle within a tropospheric duct? Has any work been undertaken in this respect?

L. B. Felsen (U.S.): We are now in the process of applying the method to tropospheric propagation. We have obtained results for elevated tropospheric ducts with sources and points of observation located inside and outside the duct. We are now adapting the model to perform calculations when there are obstacles in the duct. Although this is one of our current programs, we do not have results at the present time. However, the method is applicable to obstacles in the duct. Results on tropospheric propagation were presented at the recent AGARD meeting in Lisbon, Portugal.

E. Bahar (U.S.): Is this method applicable to ducts that change laterally along the path of propagation?

L. B. Felsen (U.S.): We have strong hopes for applying the method to laterally varying ducts, but have not yet done this. When we do apply it, we intend to use local modes with possible mode coupling. For the ray portion, lateral inhomogeneities can be accounted for in a straight-forward manner if the scale of variation is reasonably slow. Ray tracing in inhomogeneous ducts can be done under more general conditions, and one of our principal goals will be to do this. We have already planned to do this for some studies that are associated with underwater acoustic propagation. This is a problem, not only in electromagnetic propagation, but also in underwater acoustics.

There are many sophisticated computer programs for ducts that have almost arbitrary transverse inhomogeneities, but are laterally uniform. When lateral inhomogeneities are present, one must explore all possible techniques to resolve them. However, computers have limited capacities, and even large computers run out of space with lateral and longitudinal inhomogeneities at a fairly fast rate.

Paper No. 8

L. B. Felsen (U.S.): Can I ask to what extent are the ridge effects included in the integral equation? What do you introduce when you have knife edge effects?

R. H. Ott (U.S.): There is no knife edge diffraction Fresnel type diffraction effect included in the integral equation explicitly. When you come to a ridge, you continue up to it and then over it. The two things that are needed in this piecewise linear approximation of the terrain are the height of the terrain and its slope.

L. B. Felsen (U.S.): Is not the slope discontinuity a problem?

R. H. Ott (U.S.): That is an interesting point. I formulated the integral equation in a form that excluded any discontinuities.

L. B. Felsen (U.S.): Do you have smooth bumps instead of sharp ridges?

R. H. Ott (U.S.): Yes, we have smooth bumps.

L. B. Felsen (U.S.): How do you respond to a real ridge?

R. H. Ott (U.S.): If it was a true disconituity, my method would not resolve it.

E. Bahar (U.S.): You presented data for both source and receiver on the surface of the interface. When both of them are far from the surface, could you apply your method?

R. H. Ott (U.S.): The formulation is able to accomodate sources located above or on the surface, with no increase in computer time. However, if you want to obtain a height gain pattern by moving the

point of observation up and down, this introduces a problem in this method. This occurs because, for each location of the observer,the surface fields must be recomputed. The integral equation must be redone each time for each point of observation.

L. B. Felsen (U.S.): This is one of the reasons, mentioned by Dr. Bahar, that you have insufficient computer space. This occurs with laterally inhomogeneous ducts because you must solve it in two dimensions. As long as the source and point of observation are on the surface of the earth, you can find adequate solutions. Otherwise you have some difficulties.

R. H. Ott (U.S.): This is a limitation to its applicability, but in many radio propagation problems, we are only interested in two locations.

L. B. Felsen (U.S.): That is the reason for the inability of this kind of method in solving true ducting problems, and that is where open problems are located.

J. Aarons (U.S.): How well do most high frequency (3 to 30 MHz) observations agree with calculations done by this method?

R. H. Ott (U.S.): All of the observations agreed with calculations by this method except for one set of results at 20 MHz, where it did not work well. This was based on my definition of exceeding my criteria of 15 minutes of computer time. If the time had been extennded for one or two hours, it might have produced results. The poor result was over very rough terrain,with very large slopes in the Colorado mountains. I do not know of any techniques that would work for that particular example. In general, I believe that this program or algorithm will be suitable in almost all cases for frequencies up to 30 MHz.

L. B. Felsen (U.S.): Any method will produce results if you make a fine enough grid and model it in range. In principle, solutions can be found, but your computer time becomes excessive.

Paper No. 9

E. Bahar (U.S.): You had an expression that varied inversely with the susceptibility. When does that expression collapse? How small can the susceptibility become before your expression is no longer valid?

R. J. King (U.S.): In that expression, it was assumed that the angle of incidence approaches 90^o so that the cosine of the angle of incidence was much less than the susceptibility. In other words, the angle approaches 90^o so that the cosine of the angle of incidence is going to zero faster than the susceptibility is going to zero. You must be very close to the surface. Since that expression referred to launching a surface wave, one must have a source close to the surface. As the index of refraction of the medium approaches unity, the closer to the surface you must go to excite the surface wave.

R. H. Ott (U.S.): Why do you not plot predicted results with measured results for curves of field strength versus location of thesource?

R. J. King (U.S.): We did not have enough time. These comparisons will be published in the immediate future.

R. H. Ott (U.S.): The breakdown into the Norton wave,the space wave, the reflected wave, and all of the other waves are in one of J. R. Wait's papers in a recent book.

When you obtained positive values for "h" on the vertical polarization slide, it increases by -3 dB.

R. J. King (U.S.): The scale is arbitrary. It might be expected to be on the order of 4 1/2 to 5 dB.

R. H. Ott (U.S.): I just do not understand the oscillatory behavior there from the region 50 to 70 meters above (source location). I expected one broad lobe as the source gets higher.

R. J. King (U.S.): There may be some subsurface reflections because the source is fairly high, and this would cause them. As the source is lowered, the reflections diminish.

L. B. Felsen (U.S.): Your system looks like a fairly massive experimental structure. If you find that the experimental results agree with the theory, it would be interesting to do this work on a curved surface.

R. J. King (U.S.): The next part of this project will involve some material that is sufficiently lossy to that the direct field can be absorbed. The lateral wave can then be observed. Then we can make a curved surface.

L. B. Felsen (U.S.): The various waves will be very interesting on a curved surface.

Paper No. 10

L. B. Felsen (U.S.): I believe that this model can be used in ranges where the integral equation of Ott cannot be used,namely, where you are dealing with rough surfaces that are fairly large in terms of a wavelength. One may apply this method, where the other method, based on the integral equation and the compensation theorem, will fail. Dr. Peter Christiansen, at the Technical University in Denmark, has obtained results for wedges for impedance boundary conditions,which are, to the best of my knowledge, the most extensive available.

Paper No. 11

R.H. Ott (U.S.): I do not understand the spectrum of diffuse power spectral density in Fig. 8. It decreases inversely with the square of frequency, and then has a large spike in the vicinity of 0.75 Hz. What causes this spike?

A.L. Johnson (U.S.): The cause is the specular energy in the one Hz per second fade rate (approximate).

R.H. Ott (U.S.): Does it result from the specular or reflected wave from the ground? The Fourier transform of a spike in the time domain would be a very broad frequency response, would it not?

A.L. Johnson (U.S.): We are seeing a fade at one cycle per second, resulting from a combination of the direct and reflected waves. It is not only the specular reflected signal. When you take the Fourier transform of the resultant fade, you will find a one Hz component in the resulting spectrum.

R.H. Ott (U.S.): Why do the direct and reflected rays interfere at this approximately one Hz wave?

A.L. Johnson (U.S.): The interference results from the geometry. The airplane is flying towards the satellite, and the path difference is decreasing at a different rate for the reflected wave than for the direct wave. The two waves are in and out of phase as the geometry of the path fluctuates.

K.J. Hortenbach (FRG): I understand that the multipath fading the peak in the signal spectrum originates from changes in path geometry during constant altitude flight. This is equivalent to slow changes of the elevation angle when the aircraft moves towards the satellite. How can you exclude changes in flight altitude as a reason, when relatively small changes in altitude create correspondingly large fading effects?

A.L. Johnson (U.S.): The periodic multipath that we observe is caused by the difference in the rate of change of the direct and reflected wave path lengths as the airplane flies toward the satellite. Changes in airplane altitude during level flight introduce random and nonvarying fading, which may explain some of the nonperiodic fading in Fig. 7 of my paper.

K.J. Hortenbach (FRG): At which altitudes did you carry on your experiments? Did you observe any changes in signal characteristics at different elevations, especially at very low altitudes?

A.L. Johnson (U.S.): Our experiments were carried out at approximately 30,000 feet altitudes. Some limited testing was done at altitudes of 10,000 feet and 20,000 feet, and we observed no significant difference in the reflected signal structure. We have not done any tests at very low altitudes.

H. Soicher (U.S.): How was the effect of possible fading due to ionospheric irregularities (scintillations) separated from fadings due to multipath effects?

A.L. Johnson (U.S.): The fading from ionospheric irregularities of VHF signals tends to be random and nonperiodic, while the earth multipath fading tends to be periodic. Secondly, if one looks at two frequencies separated by approximately 100 kHz, the ionospheric fading shows no frequency dependence (both fade simultaneously), while the earth multipath fading is very frequency dependent (fades are out of phase on the two frequencies).

R.J. King (U.S.): Have you measured the narrow angular range where the phase reversal occurs at the pseudo Brewster angle of rough sea water for vertically polarized waves?

A.L. Johnson (U.S.): No. We have calculated the phase change with elevation angle from the complex reflection coefficient expression in my paper. As you suggested, the phase reversal of the vertically polarized wave is very rapid near the Brewster angle.

SESSION III

Paper No. 12

L.B. Felsen (U.S.): You have discussed an interface between two media. I do not understand your simultaneous use of lateral and surface waves in your representation. Where does the surface wave originate?

E. Bahar (U.S.): If you apply a Fourier expansion of the fields, you can start at this point. Then you adapt contour integration around the two branch cuts, associated with k_0 and k_1, and obtain the contributions of the radiation fields and the lateral waves. There is also a singularity contributed by the pole of the reflection coefficient. This singularity is the source of the surface wave.

L.B. Felsen (U.S.): This singularity usually lies on the wrong Riemann sheet when you conduct your contour integration correctly. I do not understand your results.

E. Bahar (U.S.): It depends upon the wave polarization and the two media. There are no surface waves with horizontally polarized waves and when both media are dielectrics. The pole is on the wrong Riemann sheet. However, when permeability and dielectric constant vary with location, you can obtain surface waves for both horizontal and vertical polarizations.

L.B. Felsen (U.S.): If we were to compare this procedure with that described by R.H. Ott, how would you respond in performing numerical calculations with both procedures? What is the relative complexities in obtaining results?

E. Bahar (U.S.): I can calculate the scattered field at a given location in less than a minute. I can obtain the entire radiation pattern within the reasonable time (under 15 minutes) described by R.H. Ott.

L.B. Felsen (U.S.): How successful are your results for the field along the surface? This field is equivalent to the ground wave.

E. Bahar (U.S.): If you are talking about grazing incidence waves, or the ground wave, you can use the radiation field to describe them. When the transmitting and receiving antennas are both on the surface, and the surface is irregular, the coupling of the radiation field into the surface and lateral waves must be included. I have written a paper, listed in references of my paper presented at this meeting, describing these surface and lateral waves. Since the radiation fields tend to vanish near the surface, their energy reappears in these waves. The surface and lateral waves are the most important components at the surface.

L.B. Felsen (U.S.): What ranges are covered by your lateral and surface wave calculations? Do you have computations for large separations of transmitter and receiver?

E. Bahar (U.S.): Yes.

R.H. Ott (U.S.): Have calculations of the ground wave field (source and observer on the surface) for a given frequency and set of ground constants for a large range of terrain irregularities (slopes and heights) and different locations of the observer been made? I would like to compare computer times for a given problem.

E. Bahar (U.S.): As described in my paper, when the source and/or observer are near the earth's surface, it is necessary to account for the lateral and surface wave contributions to the total field. In a recent paper (1977), I have accounted for the coupling between the radiation fields, the lateral waves, and the surface waves. In that paper I presented analytical solutions and several numerical computations. These computations have taken less than 10 minutes on an IBM 650/65 computer.

Paper No. 13

L.B. Felsen (U.S.): If you want to find the results for a multipole, you can differentiate the expressions for these fields with respect to source coordinates or time. Why did you solve this problem?

M. Döbrich (FRG): We wanted to study more complicated sources. The first step was with multipoles.

J. Blythe (U.K.): Mr. Döbrich stated in his paper that he has also a computer program. I think this is part of the preliminary phase to developing a computer program.

R.H. Ott (U.S.): Some complementary work appeared in papers by David Hill, who developed an impulse response for the Sommerfeld program.

Paper No. 17

L. Boithias (France): Le problème des liaisons mobiles est très difficile à cause de la statistique qui doit porter non seulement sur le temps mais aussi sur les emplacements des récepteurs qu'on ne connaît pas. Cela dépend du type de service considéré. Au CCIR, par exemple, on a considéré longtemps que les statistiques pour les services mobiles et la radiodiffusion étaient les mêmes. On fait maintenant une séparation entre ces deux types de service qui ont chacun leur texte propre. La raison en est que les récepteurs de radiodiffusion peuvent être situés un peu n'importe où alors que les services mobiles terrestres sont en général des voitures sur routes. Ceci peut modifier considérablement les statistiques des emplacements et l'on peut avoir des courbes très différentes pour les radiodiffusions et pour les mobiles. Ce problème de pondération des valeurs des emplacements a-t-il été pris en considération: c'est à dire, avez-vous envisagé une pondération des emplacements ou les emplacements ont-ils été statistiquement traités de la même façon?

Translation: Mobile links raise a very difficult problem due to the fact that statistics must deal not only with time, but also with the locations of unknown receivers. This depends on the type of service considered. At CCIR, for instance, it was believed for a long time that statistics for mobile links and radio broadcasting were the same. A distinction is now made between these two types of services, which have each their own regulations. The reason for this is that radio broadcasting receivers can be located almost anywhere, whereas mobile land services generally consist of vehicles on roads. This can modify considerably location statistics, and the curves obtained for radio broadcasting and mobile services can be very different. Was this problem of the weighting of location values taken into account, that is to say, did you consider weighting locations, or were the same statistics applied to locations?

R.W. Lorenz (FRG): There are two questions included in your discussion. The first relates to the relative importance of spatial dependence and time dependence. Since we want a large number of subscribers in our mobile radio system, such as 100,000 or 200,000, we must use very small radio terminals. This is the reason for the use of a very low transmitted power, approximately 10 watts, and therefore the areal coverage is limited to 15 or 20 km. The time dependence is almost negligible except for trans-horizon propagation, which represents unwanted signals in our radio mobile service. Thus we consider time dependence only for unwanted signals.

In the other part of the question, the major difference between radio communication and the mobile radios is the antenna height. Another difference is that mobile systems are located only on streets, so that our measurements are made only on these streets. We have been assigned a frequency band and with a low mobile antenna height, fluctuations of radio signals are larger than those at the top of the measuring loop (10 meters above the ground). These were considered in our measurements.

R. Ott (U.S.): Have you observed the angle of arrival statistics for multipath propagation in city environment?

Are you computing power spectra for your observed time series? Bill Jakes, with Bell Telephone Laboratories, has investigated this problem.

R.W. Lorenz (FRG): I first planned to include Doppler spectra in my paper, as you may have seen in the first announcement of this AGARD meeting. Doppler spectra contain the angle of arrival statistics. Due to experimental problems, we could not finish this work in time. I had to exclude it from my paper and present only the amplitude statistics. I know about the work of Dr. Jakes in this area from papers published in his book and in the Bell System Technical Journal. Qualitatively we found similar results. In connection with multipath fading simulation, however, we had some additional ideas. If they result in interesting and practical relevant conclusions, I would be happy to report them later.

J.H. Blythe (U.K.): Have you considered the use of diversity in radio telephone systems?

R.W. Lorenz (FRG): We planned to do this work because it seemed to be worthwhile. Unfortunately our maintenance department did not support this work because subscribers do not complicated antenna structures on the roofs of their houses. That is why we gave no priority on this work, and just used a simple monopole like those found in actual mobiles.

Paper No. 18

R.H. Ott (U.S.): Does the observed spectra have an f^{-p} dependence with p equal to about 2?

K.J. Hortenbach (FRG): The spectrum of the demodulated signal depends on the slope of the input spectrum and the transfer characteristics of the rectifying device (linear demodulator in this case). The shape of the input spectrum is a function of the fine structure of the effective scattering area and the velocity vector with respect to it. A f^{-2} dependence would therefore be accidental.

J.H. Blythe (U.K.): Again, referring to that last slide, can you comment on the shape of the measured spectrum near the origin? There appeared to be a large increase of the measured spectrum relative to the theoretical spectrum. Is this a result of your assumption of a linear detector?

K.J. Hortenbach (FRG): Yes, this is an effect of the demodulation process.

Paper No. 19

F. Thomsen (Denmark): In some of your first slides, you have a high value of permittivity and thus a great scattering. How many iterations were necessary to perform the modelling?

J.A. Kong (U.S.): Are you asking about the background dielectric constant? In theory, the background dielectric constant is not crucial. You made a very good observation from my first few graphs. The match was done in a very historical manner. At that time, the background dielectric constant was chosen to be 1.4. If we calculate the background dielectric constant for vegetation, it is substantially smaller than that. However, at that time we did not have ground truth. Now we pay more attention, and in the later matches, used a smaller dielectric constant. Since the data available are of a limited set, we can match them with 1.4, 1.2, or 1.1 by adjusting other parameters.

When we have redundant data to the extent of 10 sets, the parameters chosen to match the set will be restricted. If I have only one curve, then I can match it with a hundred sets of parameters. However, if I have one more curve, then I can match it with one set of parameters. The answer is involved because we have real values, so there is a practicability range for the parameters used, and 1.4 is slightly high but reasonable. In the Born series approximation for the like polarization return, they correlate because the same set was matched for depolarization. Thus the second or third order terms are very small.

D.W.S. Lodge (U.K.): Do you have any data showing the differences between fresh snow and refrozen or compacted snow?

J.A. Kong (U.S.): Yes. In my paper, data shown in Figs. 4 and 5 (pages 19-6 and 19-7) are for more compacted snow than those shown in Figs. 6 and 7 (pages 19-7 and 19-8). For more passive remote sensing data, please refer to the second reference by Kong et al., which will appear in the JG R.

DISCUSSION OF SESSION III

J.H. Blythe (U.K.): In order to give some structure to the discussion, I would like to pursue two themes. One is the theme suggested in the earlier discussion on boundary conditions. The second arises from a number of papers which have computer programs, which enable scattering computations to be made from profiles or slope distributions. It is worth pursuing a comparison of the powers and limitations of these programs.

Therefore, I would like to discuss boundary conditions under the first theme. None of the five papers mentioned the dreaded words, "Leontovich boundary condition" or "surface impedance". I suspect that the reason is that the first four papers were not concerned with subsurface media. Under these conditions, that boundary condition or an equivalent one is entirely valid. Since Dr. Kong, who has layers very much in mind, made no use of such boundary conditions, I think that Dr. Felsen would consider his treatment impeccable. I will ask the authors to comment on the treatment of boundary conditions in their papers. I'll begin with Dr. Bahar, who has an interesting comparison to make with the assumptions and results of Beckmann and Spizzachino.

E. Bahar (U.S.): I made a previous analysis with an impedance boundary condition. Later I removed that approximation from the theoretical analysis, and then applied the two media rigorous boundary conditions in my solution. I did not find it necessary to use the impedance boundary condition in my analysis. The results were not in a simpler form with the impedance boundary condition. Therefore, from that time I have not returned to the impedance boundary condition for two media problems. In order to resolve this question, I made numerical comparisons between analyses made with the impedance and rigorous boundary conditions. I have shown that when the parameter "delta", the normalized surface impedance, is about 0.1, the impedance boundary condition is reasonably good. When delta (used by some of the authors here) is not very small, you encounter some discrepancies between the impedance and rigorous boundary conditions.

My experience indicates that the impedance boundary condition is suitable when the angle of incidence of the waves in the lower medium is independent of the angle of incidence of the waves in the upper medium. This occurs when there is a very strong contrast between the refractive indices of free space (above) and ground (below). Since I do not see any sizable benefits from using the impedance boundary condition in my problem, I used the rigorous two media boundary condition.

L.B. Felsen (U.S.): Your statement is correct, but it is incomplete. It also depends on the scale of the irregularities. If the irregularities are small, then even though the contrast is large, there are difficulties with the impedance boundary condition. The normal at the surface will oscillate too rapidly.

R.W. Lorenz (FRG): The impedance boundary condition is beyond the scope of my paper. I used the rough classification of terrain such as cities or forests, so that it would not be a sufficiently practical solution to take special cases such as one high house or something similar. Instead I took many measurements and converted them into a statistical base.

K.J. Hortenbach (FRG): In my paper, I did not consider this problem. I used results from physical optics and from the specular point theory. These are valid only in the high frequency limit. I limited my study to large scale roughness.

J.H. Blythe (U.K.): Another matter raised yesterday was the comparison between Ott's and Bahar's computer programs. There are several authors with computer programs, which take profiles as inputs and produce backscatter information as outputs. There are several differences between these programs. I am not convinced that they are computing the same problem.

One difference in Ott's program is the necessity to specify the profile or terrain height to a fraction of a wavelength because he is interested in exact phase. (At this point, Ott tells me that this assumption is incorrect).

Perhaps your programs are only concerned with a power integration of scattered power. This represents a loss of phase information. Ott just indicated that he did not lose phase (no pun intended). It might be better to ask the authors to describe their programs and to indicate those circumstances where it will be inappropriate to use their programs. I will begin again with Dr. Bahar.

E. Bahar (U.S.): This is a good starting point for our discussion. I have conducted my analysis in an absolutely rigorous manner. Maxwell's equations were converted into another set of equations with a complete expansion of the fields. This was done with imposition of exact boundary conditions and use of proper analytical techniques that do not involve differentiation of the expansions. The result is a rigorous set of first order coupled equations for wave amplitudes.

The first order coupled equations resemble those found in irregular waveguide problems. The only difference is the inclusion of a continuous spectrum of waves. These involve the radiation field and lateral waves in addition to the discrete spectrum of modes present in guided wave problems.

I tested these equations with different complete expansions. Simple algorithms were applied to integrate these rigorously. Different expansions yielded different solutions for the wave amplitudes. Although

the amplitudes are different for each mode, the same scattered field is obtained. The total fields are also the same when I used irregular waveguides. I found that, if one uses modes which closely fit the waveguide features, the expansion based on these modes will yield fewer modes. Even a simple iterative approach gives accurate results. On the other hand, when you use cylindrical modes (for example) that do not fit the geometry as well, many more modes are needed. Simple iterative solutions do not give correct results in this case.

I could have, as with waveguide modes, applied various techniques at this point. Two forms applied were the perturbational form of Rice, where small slopes are assumed, and the physical optics form of Beckmann and Spizzachino. This is the reason that I did not say that I have simple first order differential equations with numerically integrable scalar functions.

The next few steps are summarized below. A second order iterative approach was applied to three equations, where the primary fields were assumed to be almost the same as the unperturbed fields. This assumption assumes small perturbations. The final step removes the small slopes which uses the transformation to local coordinates. The scattered field is the accumulation of scattered fields from elementary strips. The final form is an integral (but not an integral equation).

The only information necessary to fit a profile and get results is the profile itself. My algorithm can then be applied for very suitable results. Other programs may also be found to evaluate integrals. My method may include a region of several wavelengths, but this does not affect the number of points in the integration.

After obtaining these forms, I found different kernals than those found with the methods of Beckmann and Spizzachino or Rice. When I assume very small slopes at the end of my method, I obtain the Rice perturbation theory solutions. When I assume that the frequency is very large, and that most of the scattering is specular, the Beckmann and Spizzachino solution is obtained. My theory covers regions which are not covered by either Rice's or Beckmann and Spizzachino's theory. Although restricting myself to the radiation field here, I included coupling into lateral and surface waves elsewhere.

The lateral and surface wave expressions are important only when your transmitter and receiver are near the surface. When you are far away, the radiation field expressions are sufficient.

J.H. Blythe (U.K.): I would like to return to a question raised yesterday regarding computer time. Perhaps you can comment on this?

E. Bahar (U.S.): At the University of Nebraska, we are alloted three hours per year of free computing time. If I use up three hours at once, then I would have no more computing time for the rest of the year. Therefore, I develop my algorithms sufficiently efficient to obtain entire radiation patterns for all angles of scatter. These can be executed within Ott's 15 minute limit.

L.B. Felsen (U.S.): What lengths or irregularities are covered by these short computer times? In your sketches, your irregularities are confined to a distance L.

E. Bahar (U.S.): The computer algorithm is absolutely insensitive to the length L. The length L may be hundreds or thousands of wavelengths. The algorithm is only sensitive to roughness and surface heights.

R.H. Ott (U.S.): I would like to correct a statement by John Blythe. However, we should compare my solution with that of Bahar for a given profile before continuing this discussion. The lateral and surface waves should be computed for a given profile by Bahar so that they can be compared with my integral equation solution. Then we can discuss comparisons of computational time. Until then, there is no point in discussing relative efficiencies of the two methods.

I will not correct John Blythe's statement on the number of points in a wavelength. The terrain profile can be defined as accurately as the increments available on the topographic map. If maps provide data at 10 meter intervals, then these are used to define Y(X). If the interval is 50 meters, that increment is used. It is not related to wavelength. The interval in my paper was 100 meters except in the mountains of Colorado (US), where it was 10 meters.

L.B. Felsen (U.S.): Now that computer programs and analytical models are available, it is important to design a test situation to compare them. Otherwise it is analogous to comparisons of potatoes and oranges. We can now compare efficiencies of different programs. We have had interesting comparisons of numerical results with actual data. The next step is to standardize these so that a common ground can be reached.

J.H. Blythe (U.K.): The two themes suggested by me have been discussed sufficiently. Are there other comments regarding these papers?

K.J. Langenberg (FRG): Dr. Bahar, if you want to derive transient results with your method, can it be done only with direct Fourier inversion? Can you derive it directly in the time domain with generalized telegraphists' equations?

E. Bahar (U.S.): In a recent study I assumed the transient pulse to be a L oran type, or bell shaped envelope, as the signal. Numerical data was obtained on the response to such a signal. I have used both numerical Fast Fourier Transform (FFT) and some analytical techniques to derive the solutions. I found that the analytical techniques, which are easier to apply than the FFT, are more than one or two half cycles away from the beginning of the pulse.

L.B. Felsen (U.S.): That is an interesting statement. If the problem can be solved without the Fourier inversion, this would be a worthwhile approach. It is better to resolve a pulse directly in the time domain, and then do the time domain scattering of the irregularities. This is done with seismic propagation in layers. An iterative Cagniard technique is used. It would be worthwhile to see if this can

also be done for irregularities without first doing the harmonic analyses and then transforming back again.

J.H. Blythe (U.K.): Does anybody have any views on the theoretical distributions introduced by Dr. Lorenz for comparisons with his data? I expected to find some enthusiastic supporter for the Weibull distribution.

L. Boithias (France): Il semble que l'on essaie un peu au hasard de trouver la distribution la plus convenable sans s'efforcer de trouver les raisons physiques pour lesquelles une distribution est plus adaptée qu'une autre. N'y aurait-il pas des raisons physiques pour que telle distribution soit mieux adaptée que telle autre?

A l'influence du sol s'ajoute l'influence de l'atmosphère qui peut créer des variations du champ, représentées par des lois du même type. Peut-on séparer l'influence du sol de celle de l'atmosphère?

Translation: It seems that the attempts at determining the most suitable distribution are made somewhat empirically, without endeavouring to find out the physical reasons for which a given distribution is more suitable than another. Are there no physical reasons for which a distribution is more suitable than another?

To the influence of the ground can be added the influence of the atmosphere which may create field variations, represented by laws of the same type. Can the influence of the ground be separated from that of the atmosphere?

R.W. Lorenz (FRG): There were some physical reasons. The first physical reason is that, if you have no free line of sight, then you have a Rayleigh distribution. We often made measurements when the surroundings did not change in a microscopic manner. For instance, if we drove through a forest, then we had a very good Rayleigh distribution.

The overlay of the Rayleigh and log-normal distributions of this microscopic scope seems to also have a physical foundation. I am very happy that this distribution, which has been statistically averaged and found without a line of sight, has been this mixed distribution. If it, for instance, had been the Weibull distribution, then there would be a lack of physical explanation.

It seems to me that if you had a free line of sight, the Nakagami distribution or the Rice distribution were favored by our measurements. It seems to me that this also is a physical reason.

Your second question is very important. There are some difficulties encountered with distinguishing between atmospheric and terrain reflections.

You can never reproduce your measurements exactly. For instance, the traffic in the streets is a very fixed factor which adds scattered waves to your received signal. If there are large lorries (motor trucks) in the street, the situation is completely different from that found on a quiet Surday afternoon. Another comparison may be made with "rush-hour" traffic and late evening traffic in London.

I think that Dr. Palmer's paper has an approach which adds the local variations in time. This is the only way to treat these measurements. Our measurements were made over very short distances, up to a maximum of 40 to 45 km. In this region, the time dependence is very small. With co-channel distances, and where the ratio of wanted to unwanted signals are considered, it is a very important question.

SESSION IV

Paper No. 20

L. Boithias: Pour quel service et dans quel but cette modelisation est-elle faite? (Service Mobile Terrestre, Radiodiffusion, Service Fixe, détermination de la Zone de Service ou des brouillages à grande distance, etc?)

G.B. Thersby: The uses of these terrain models have included all of those suggested over a wide range of frequencies. The normal use is more often for mobile systems than static, generally in an EMC environment.

R.W. Lorenz: In facsimile transmission of black and white drawings a method called "Run Length Coding" has been created, to save transmission time. The picture is scanned line by line and the lengths between two changes from black to white and vice versa are transmitted by a code. Thus the transmission time for one line is somehow proportional to the content of information in this line. Do you think a similar approach for the organisation of a topographical data base could be used to minimize storage and processing time?

G.B. Thersby: With suitable organisation of the raw terrain data, I would think that this type of approach could be adapted to provide compact storage and fast access. I am not certain that the data processing would remain fast if many "levels" of data were used to construct the terrain model.

L. Hoivik: I am concerned about the numbers for used storage area which were given. It is not obvious to me that digitizing a map according to contours will require four times as much storage area as digitizing it in a grid faschion. Terrain data required 93 K words, and in a grid fashion 18 kilowords I would think you could store more data in a smaller area by using a contour method. The reason being, in a contour fashion when terrain is flat you can allow large distances between points and still maintain all information, the only way out which could reduce the amount of data in a grid fashion would be to scale the density of the grid according to the map, which would be an enormous task.

G.B. Thersby: The comparison figures were misleading in that the mesh data would not achieve the same degree of accuracy as the co-ordinate strings. To compare the storage of the two methods for identical accuracy it would be necessary to consider a 50m mesh; this would require 80k words approximately.

If linear interpolation is used with the co-ordinate strings then very flat regions require little data storage. For non-linear interpolation to produce a significant improvement in height estimation it is often necessary to insert spot heights in flat areas to avoid the odd cases where the extrapolation of actual data could lead to anomalous height estimates.

F.H. Palmer: It is not practical or economic to store the locations of individual trees and building in a large data base. In my view, the way in which surface cover is handled by a program depends upon the use to which the final results are put. In many broadcast and mobile systems it is sufficient to know the average effect of terrain cover over, say, one data base cell. Such effects can be derived from a simple "terrain cover code" which has very modest storage requirements. For point-to-point systems on the other hand, we feel that it is reasonable to ask the user for details of the local transmitting and receiving antenna environments.

G.B. Thersby: This in fact is the way in which we often use our terrain model. Unfortunately it is often impossible for the user to supply additional information on local environment and it is in these cases that a more detailed data base could be useful.

Paper No. 22

C. J. Samwell (U.K.): In your paper, you stated that you used the difference correlation method to obtain a horizon comparison. Did you consider any other correlation methods, such as product correlation? If you did, how do they compare?

G. E. Carlson (U.S.): In initial studies we compared difference correlation with minimum mean square and product correlation. These studies were all for flights through valleys. Essentially no performance difference was noted for difference and mean square comparison. Product correlation did not appear to perform as well. It appeared that this may have been due to the valley flight characteristics.

Due to the lack of performance difference and the simplicity of the difference correlation method, it was used with an adaptive threshold to reduce computation time. Similar comparisons of methods have been noted by other investigators. I refer to a paper by Pope et al of McDonald Douglas, St. Louis, Missouri, (U.S.)

F. Klinker (Netherlands): Can you comment on the influence of aircraft velocity upon the accuracy of horizon correlation?

G. E. Carlson (U.S.): Most of our studies were done for fixed viewing locations for simplicity. We did investigate a few cases where we included aircraft motion in the simulation. The results indicate that similar performance can be achieved in this case if reference horizons are generated including the planned aircraft velocity and motion. Comparisons degrade significantly if this motion is not included in the generation of reference horizons.

Paper No. 24

Comments and questions on this paper appear in Session V.

Paper No. 25

L.B.Felsen: Have any measurements been made to check the predictions, and if so, what has been the quality of the comparison?

C.E.Dadson: At the initial stages of the introduction of this technique, the predictions were tested and an RMS value of 6dB was obtained. Since then improvements have been made to the programs and measurements have been taken, but these are not available in a suitable form for me to comment sufficiently precisely.
However, I propose to rectify this, and I will send you the results when they are available.

R.W.Lorenz: In digitalizing the terrain data you used very sophisticated methods to describe peaks, basins etc. and you even moved some points a little in order to store the most relevant information of the terrain. Compared to this the German data base is rather primitive, as it only contains the maximal height within one area element. But even then lots of errors are contained, originating from bad prints of figures in the maps or just from a bad monday, when it was digitalized. Do you have also this type of error? If not, how did you manage to employ so clever and skillful girls to gather the data in such a sophisticated way?

C.E.Dadson: I do not think that I would describe our method of terrain map analysis as sophisticated, but I do agree that skilled operators were used to apply the rules which are described in my paper.

The people employed in this work were of little above-average intelligence with an aptitude for map reading and an interest in the project. They were employed for only four hours per day for the duration of the contract, which was in the hands of the company named in the paper. It was found that four hours at a time was sufficient for this kind of concentrated activity.

The process used was for an operator to encode a map, and the same map would then be encoded again by another operator who would not know how the map had been previously treated. A superviser then compared the two results and adjudicated on any discrepancies between the two. The adjudicated results were then entered into the computer by a punched card process and a verification routine checked the validity of the entry against the original encoding.

Of the 880,000 data entries, only two or three errors have appeared.

R.H. Ott: Does the model work at VF or MF frequencies?
How do you account for multiple knife-edge diffraction?

C.E. Dadson: The model uses theories developed by Rock (See References) as described in Section 4.3. These are for free-space and plane earth propagation between half-wave dipole antennas. The model has not been tested for VF amd MF conditions, for which other equations would need to be used.

Multiple knife-edge diffraction losses are treated in a manner suggested by Bullington (see References) as described in detail by Edwards and Durkin (see References).

L. Boithias: Votre étude concerne les services mobiles, mais une phrase du sommaire indique qu'un programme semblable existe pour les liaisons point à point. Peut-on avoir des détails sur la précision obtenue dans ce dernier cas?

C.E. Dadson: I regret taht at the present time I cannot quantify the accuracy of these predictions. In all the cases for which calculations have been made, they fall within "acceptable limits". However, it is intended to rectify this and I will make the results available to you.

Paper No. 26

L.Boithias: Le detail de vos calculs est il exposé dans un document?

F.H.Palmer: No. This is the first time that I have described the types of corrections or modifications which it is necessary to make to the standard Deygout procedure. It is hoped that the details of these modifications will be published in the future.

R.W.Lorenz: If I look at the development of your work historically, I remark that you started with theoretical approaches of path loss calculations and ended up in a more empirical way. Did you compare your method with that of OKUMURA, who also uses an empirical method based on a large quantity of measurements?

F.H.Palmer: There are some similarities and many differences between our approach and that of OKUMURA. We have not made any detailed comparisons of the two methods but have concentrated until now on comparing our predictions with our own, and other, experimental data.

L.Hoivik: How frequent do interactions between peaks (knife-edges) occur in the terrain you have studied?

F.H.Palmer: Much of our experimental data has been collected over terrain which is gently rolling to hilly. In order to make the predictions adequately match the experimental results over such terrain it is mandatory to take into account the interactions between obstacles.

ROUND TABLE ON DIGITAL TERRAIN MAPPING

H. Albrecht (FRG): The members of the round table are Dr. Palmer, Dr. Belrose, Dr. Høivik, Professor Felsen, and myself. We will start with a brief discussion on the state of the art on data selection and methods of data collection.

L. Høivik (Norway): Let us go back slightly and review the map material currently in existence. We have many digitized maps available at the present time. Most of these digitized maps are made with data from stereo photographs and older conventional maps. They do not always meet the standards desired for our studies. At the present time, the state of the art on collecting data or selecting data for maps is similar at several locations in Europe and in the United States. Methods and machines have become available that are designed to generate digital maps in an automatic or a semi-automatic format. Most of these methods and machines use conventional maps. One method is a line following scheme where an automatic laser system is following lines on conventional maps and digitizing them automatically. You start the system and in ten minutes you receive digital maps with all of the errors and mistakes of the original maps.

Other methods of digitizing maps involve slow and tedious manual labor, or just "slave labor". Not every country has beautiful young ladies without much to do (reference to Dadson), but we really want to be able to approach this problem in a direct manner. One method involves going directly into stereo photographs and digitizing them directly, and then processing and compensating for projection errors and parallax.

A better method involves mounting a radar on an airplane and then simply record data on tape as you fly over the terrain. This last method is one toward which we are working. We hope that it will soon be realizable.

F.H. Palmer (Canada): I cannot add very many comments to that. The situation is almost identical in Canada. In order to obtain a usable data base at this time, we must use "slave labor" (unskilled workers with tedious and dull assignments) methods. These methods generate inherent errors which may be removed by doing the work a second time. If both results are identical, the data base is verified. This has been done in the past because there was no alternative. I agree, in the future that some groups are considering automated techniques for looking directly at stereo photographs or line following devices for contour maps.

Our group is not considering either method because of the high cost associated with it. These are very expensive methods. We were very fortunate in being able to obtain manpower at almost nc cost. Even when we must pay for this work, the cost of manual techniques was much less than the cost of equipment which eventually will be used. However, I agree that these automatic methods are the ways to digitize large areas more accurately.

J.R. Delaney (U.S.): I have been using the products of some of these automatic and semi-automatic devices. They include line followers and stereo imagery systems. I have also read reports which utilize the data from stereo images. It is not Utopia. You may not have somebody making mistakes on Monday morning by selecting incorrect data. However, you may have machine errors which are equally unsystematic. You may have other problems with techniques used in going from the contours, picked up by line followers, to mesh together. The interpolation schemes there can lose much useful information.

H. Albrecht (FRG): We should not forget one particular area which has been carefully indicated. This area is the reliability of the data collected as a function of time.

I refer to vegetation. In the situation indicated in an earlier paper, the farmers will not tell you what usage they will make of the land in many cases. Therefore you cannot predict how your digital map will change because of the vegetation changes.

F.H. Palmer (Canada): We realize that there is a problem in maintaining these maps. I do not see an easy way to resolve it. If you classify a terrain as tree covered, then two years later it is either house or apartment covered. It is very time consuming to change a data base.

L. Høivik (Norway): In one month from now, part of this country will be covered with snow. The depths of snow cover vary from a few centimeters to 10 meters. The snow cover changes continuously during the year. It also changes from year to year. When spring arrives, vegetation appears and different changes are seen.

F.H. Palmer (Canada): Maybe one should consider different applications for his data base. At low frequencies such as VHF, one is not as concerned with snow depth as at higher frequencies such as UHF and microwave. In my area, which is mobile broadcast coverage, you are not interested in the location of each tree and house. These are only of interest on specific point-to-point paths. It would be useful to block off different areas of application. One could then decide costs and tradeoffs in updating data bases for each area.

H.J. Albrecht (FRG): Would it be possible at this part of our discussion to set some categories of reliability with respect to the service used?

This is not in reference to the propagation mechanism, but service such as mobile, point-to-point, fixed, many-to-many, one-to-many, or one-to-one.

L. Boithias (France): Il ne faut pas essayer de résoudre les problèmes qui ne se posent pas. Ceux qui se posent suffisent. Le but des études effectuées est généralement de déterminer les zones de couverture d'un émetteur de radiodiffusion ou d'un émetteur central de service mobile. Pour cela, la valeur exacte du champ n'a pas tellement d'importance. Il suffit de savoir s'il est supérieur à un certain nombre de microvolts ou non. D'autre part, il faut distinguer le problème des villes de celui de la campagne. Ceci est surtout vrai pour la radiodiffusion, un peu moins pour les services mobiles parce qu'il y a plus de voitures à l'intérieur des ville que sur les routes de campagne. Pour les services de radiodiffusion, le problème des maisons se pose très peu étant donné que, sur le plan TV, les antennes sont en général situées sur les toits; qu'il s'agisse des villes ou de la campagne, la différence est moindre que pour le service mobile. Les services de radiodiffusion avaient essayé en France une autre méthode dont j'ignore si elle a été généralisée: elle consistait à utiliser une carte en relief, à simuler l'émetteur par une petite ampoule électrique et à prendre une photo de la partie éclairée par cette ampoule. Moyennant quelques précautions (temps de pose, etc.) les résultats obtenus sur la zone de couverture étaient très bons. Il s'agit là d'une méthode qui n'a pas été décrite ici. Pour en revenir aux cartes, j'ai vu qu'on avait pris un pas de 500 m. Cette valeur, que j'ai entendu citer à l'exclusion de toute autre, peut-elle être considérée comme normalisée et définitive? Est-elle parfaitement convenable?

Translation: There is no point in solving problems with which we are not faced. Those with which we are faced are sufficient. The purpose of the studies performed is usually to determine the coverage areas of a radio broadcasting transmitter or of the central transmitter of a mobile service. For this purpose, the exact value of the field is not of great importance. It suffices to know whether it exceeds a given number of microvolts or not. In addition, the problem is different according as towns or the countryside are considered. This applies especially to broadcasting, and a little less to mobile services since there are more cars in towns than on country roads. For radio broadcasting services, the problem related to houses hardly exists since, as regards TV, aerials are generally located on roofs. Whether towns or the countryside are concerned, the difference is smaller than for mobile services. French radio broadcasting services tried another method. I don't know whether its application was generalized. It consisted in using a relief map, simulating the transmitter by a small electric bulb, and taking a photograph of the area lighted by this bulb. Provided certain precautions were taken (exposure time, etc.), the information provided on the coverage area was quite good. This method has not been described here. To come back to the subject of maps, I noticed that the interval chosen was 500 m. I heard this value quoted, to the exclusion of any other values. Can it be regarded as standardized and final?

L. Høivik (Norway): We have been talking about communications and broadcast. When we go into higher frequency ranges, we refer to radar and its applications.

Then we will consider more accuracy and resolution in meters.

F.H. Palmer (Canada): When I mentioned data base resolution, I refer to the original data base constructed around the immediate Ottawa (Canada) area.

This data base had a one km resolution. It provided essentially the same results as those from the 500 m resolution data base. The 500 m resolution was chosen because there are some areas that could not be adequately modelled with a one kilometer resolution. Also, the manpower available was sufficient to scale the area at a 500 m resolution.

One is better off when he can structure the data base to utilize a resolution that varies with the terrain category. In flat terrain, one can use one km or five km, or even more, for the VHF and UHF bands. As the terrain becomes very jagged, this can be reduced to a hundred m. One can save much storage by following this procedure.

H. Albrecht (FRG): While discussing data selection and data collection, we should not forget that these data bases are constructed for other groups in addition to those working in propagation and communication. These include military applications, road construction, oil exploration, and related areas.

This may indicate that, whatever digital map is made, it is compromised from its inception.

I want to know if there is any improvement with real time updating. It has been indicated with mapping by radar imagers. With real time updating, would we benefit from changes indicated such as snow or cultural use of the land?

J.R. Delaney (U.S.): The difficulty with real time updating is that, at least for cultural information and vegetation and snow cover, the automated techniques are not very suitable.

The only method to perform this updating, for the next 10-20 years, is manually. The number of people willing to perform this work for more than a few successive years is very small.

It will probably be extremely difficult to do this work on a real time basis with even a small area of the earth.

G.E. Carlson (U.S.): One of the improvement areas that must be considered from the radar standpoint is a better knowledge of terrain backscatter.

Many people have investigated radar backscatter from various types of terrain, but most of this data is not standardized and not comparable. There is a real need, as you assemble data bases, to include some studies to improve that aspect.

We will not be able to improve our capabilities to map terrain with radar if we cannot relate it to what is expected when the terrain is illuminated by the radar.

H. Albrecht (FRG): Can we assess any numbers to the accuracy? Perhaps we cannot do this unless we know the application.

F.H. Palmer (Canada): As I mentioned earlier, as far as VHF and UHF are concerned, a data base with a variable resolution would probably be most useful. Not much work has been conducted with respect to the resolution which is most useful for a specific area. Some studies should be conducted here. This was the same need described by Dr. Carlson.

If you have a series of measurements, and then make calculations for different resolutions of data bases, you can see how the results compare. This comparison determines the minimum measurements necessary for any given degree of reliability desired. The results can be taken to a given area under study, and then some numbers are assigned to it.

The reason for our selection of 500 meter squares was that we knew somebody else chosen it. The 500 meter square was a good number. The order of 0.5 to 1.0 kilometer was within our manpower available.

We made some very short term comparisons with 0.5 and 1.0 kilometer in some areas. We had some concepts about optimum resolution, but this was not done in any rigorous manner. An optimisation program could be developed from a propagation approach.

L. Høivik (Norway): One limitation on our resolution studies was manpower to perform the digitizing. Another limitation was the computer's capacity to accommodate our data. As the information rate into the data base increased, the processing time also increased.

I believe that the great advantage of automatic digitizing of data will occur when we perform integrated optics and actually store data in the form of images. It may be Utopia and more than 20 years away, but existing methods are also very expensive.

H. Albrecht (FRG): The first part of the discussion may be summarized in saying the value of digital data selection and collection methods is questionable in some applications in the propagation field.

The value of these methods has been worthwhile in other applications, and its usefulness is indicated in general planning activities. We can now look at the applications area, because the question of value is interlaced with applications.

L.B. Felsen (U.S.): I will commence with a cultural comment regarding data collection by attractive young women with nothing to do. This remark would be very prejudicial by feminists in the U.S., and would be subject to lawsuits by ugly old men who would like to compete for these positions.

I find myself in a dilemma with respect to some parts of the application area and to some of the theoretical questions. I would like to divide my response into three parts. First, I respond to theoretical questions as a theoretician. Second, I try to accommodate implementations of theoretical results on computers. Third, I really think that this meeting will contribute something in seeing how one translates results of the theoretician into real needs.

I will start with the first part on theoretical questions. Dr. Albrecht had an excellent plan of action when he distributed comments, made at a similar meeting three years ago, to members of the round table. Very few changes have occurred with the purely theoretical aspects of this area.

At that time we were debating the validity (or lack thereof) of the surface impedance condition. We are continuing to debate the same subject. When surface impedance is applicable, it is a fine concept. However, it must be applicable and cautiously applied.

The third part, relating theoretical results to real world needs, will become a purely academic matter which I will discuss later.

As long as one has a model, it should be reasonably justified. We have heard several contributions with different theoretical models. There was an integral equation model based on the compensation theorem from Dr. Ott. There was a model developed from local modal expansions and asymptotic series evaluations from Dr. Bahar. There was a model using a geometrical theory of diffraction (GTD) approach with piecewise planar surfaces from Dr. Breien.

All of these theoretical models appear to be feasible under various circumstances. Some of these will be complementary. Dr. Breien's model is complementary to Dr. Ott's model because Dr. Ott's model has difficulties at high frequencies and long distances. He must divide regions into an excessive number of intervals, where the GTD model should be very suitable under those conditions. Dr. Bahar concentrated on both source and observer being away from the surface. He may be able to adapt his model to allow them on the surface. We have seen these three theoretical models, each with advantages and disadvantages.

If we now consider implementation of these models, one important development has happened since a similar discussion in Ankara three years ago. Workable computer programs have been developed. Drs. Ott, Breien, and Bahar have working computer programs. It is now necessary to compare efficiencies of these computer programs. It does not refer to comparisons of 14 versus 13 minutes, but rather "ball park" computer times.

The most difficult question for the theoretician, who has a suitable theory and a working computer program, is "what do you do with it now?" If you want to compute the path loss over realistic terrain, what do you feed to the computer?

Any chain of calculations, or any type of a systems approach, which this clearly must be, is as good as the poorest data fed to the computer. When the data is poor, you should not use highly sophisticated theoretical models and good computer programs. Results are not sufficiently meaningful.

It is not sufficient to have a computer program by itself. You must have an estimate of the relative value of the program. This can be measured with an error analysis. An error estimate is necessary if the computer results are used as references.

How does one collect the digital type of data that have been presented? I did not know much about this area until this meeting. It is a fascinating way of collecting data. There should be a method for coupling that into the computer programs. The question again arises, "How good should the theory be in order to have compatibility with the data?"

In order to make progress in this area, some form of standardization is necessary. It will involve a meeting of people who collect terrain data, make theoretical models, and make computer programs to fit these models. The outcome will be a set of realistic test problems to be tried by the various techniques.

Realistic test problems must correspond to reality. If data is sampled once over each 50 km interval, a sophisticated computer model based on a much finer grid (1 or 5 km) should not be used.

On the other hand, gross effects such as double knife edges do not look like two rounded humps. There are simpler approaches for these things. A workshop, where one delineates a series of test problems, would provide a mechanism where various techniques can be applied. Then one would have an evaluation of the efficiency of each technique.

H. Albrecht (FRG): Your reference to our meeting three years ago is appropriate. Among the people around the table are Professor Felsen, Dr. Belrose, and myself, who were in a similar group in Istanbul. The topic, "Electromagnetic Propagation Characteristics of Surface Materials and Interface Aspects," was very similar. Dr. Belrose also indicated that he has not seen much progress.

J.S. Belrose (Canada): I made a mistake in referring to Ankara instead of Istanbul. Dr. Felsen said that incorrect literature references propagate in a similar way. They propagate continuously.

I would like to preface my comments by referring to an comment made earlier by M. Boithias and Dr. Palmer on Mrs. Thersby's paper. They asked what application she was considering when she spoke of digital mapping.

If one is predicting the far fields for FM, television, or radar coverage, he needs a specific form of digital terrain mapping. If he is predicting near field effects due to high rise buildings, power lines and towers, or finding local terrain effects on ILS in airplanes, the digital terrain mapping has a different form than that for the far field predictions.

Digital terrain mapping, in my interpretation, refers to our round table discussion. You take a map and digitize it by dividing it with grids and assigning numbers to each grid element. The result is a digital terrain map. The near field problem mentioned previously is not included in this form of digital map. It is part of another form of digital map.

When you are interested in the near field problem, you want to know the exact location of things. You do not use a grid. The points fed into your digital data base are exact corners of buildings, its height and shape, and exact locations of power lines, heights of power lines, and the exact location of each tower, etc. However, it is also digital mapping, but it is not really conventional mapping. There is a difference, but I do not know how to express it. I spoke of wire grid modelling and method of moment calculations. The example in my paper related to calculations for a power line and the effects of that power line on antenna patterns.

The basic program is wire grid modelling. We mentioned briefly in these discussions that one can analyze buildings. If there is a high rise building, it can be analyzed with effects on antenna patterns by the wire grid program. The building sits on a flat earth, which is also a wire grid. The flat earth can be curved by curving the wire grid. Hills and terrain effects can be formed by the same wire grid.

When you have a long power line, many towers are needed. A flat structure is assumed because of most of the large number of points are needed for the towers. When losses are introduced, the computer times are increased. The losses relate to the real world.

In other words, can one consider a monopole antenna on a radial ground screen sitting on top of a lossy earth with contours? The problem becomes horrendous. But these are the situations which must be resolved if we relate to pattern distortion due to objects sitting on a finitely conducting earth with hills.

L. Høivik (Norway): Now we will talk about near field problems. One takes a digitized map and puts all of the formulas into the computer. He then turns a crank and, with much success, tells himself that it is better than the far field problem.

One does not verify the far field problem. It cannot be truly verified. An overlooked problem is that most of our maps are usually projections. You cannot join maps side by side or top to bottom.

If you look at a radar beam as it propagates through space to create an image map, it follows a curved path in the image. The image created map kinks at the edges because of propagation errors.

It is necessary to know these facts when using computers. A friend once told me, after I turned in some computer results, "Computers are like trash amplifiers. A tiny amount of trash in creates an enormous amount of trash out."

R.W. Lorenz (FRG): One difference between the German data base and other data bases mentioned here is that the German data base is derived from spherical coordinates. Our elements are 5 seconds in arc instead of 500 meters in length. We do not have this problem. It is easier to calculate in spherical coordinates.

L. Høivik (Norway): We did some work in this area, and found it necessary to transform all of the information into geographical coordinates. Norway is very stretched, and, as it approaches the North Pole, it converges to a point. We could not use the rectangular representation on the map.

L. Boithias (France): Il serait peut-être intéressant de dresser un tableau, dans les colonnes duquel on porterait les services intéressés par ces problèmes de cartes mises sur ordinateur, la bande de fréquence en question, la précision demandée, etc. ainsi que l'étendue de la zone. Chaque fois que j'ai entendu parler de ces problèmes de cartes, c'était pour des fréquences de la bande métrique ou plus courte et pratiquement jamais en dessous. On a parlé aussi des couvertures radar, sur des fréquences encore plus hautes. Un autre problème devient de plus en plus important dans le domaine des communications. Pour le résoudre, la mise sur ordinateur des grandes étendues de terrain serait utile: il s'agit du problème de la coordination entre stations terriennes et stations de faisceaux hertziens qui travaillent dans les mêmes bandes de fréquence. La réglementation dans ce domaine est considérable. Quand on veut construire une station terrienne dans un pays, on doit faire une étude des brouillages possibles autour de cette station sur des distances allant de quelques centaines à quelques milliers de kms. A l'intérieur de cette zone de coordination, on doit s'assurer qu'il n'y a aucun brouillage possible avec tous les faisceaux hertziens existant déjà. C'est un travail considérable pour lequel on cherche des méthodes à base de calculateurs, au moins pour procéder à un travail d'élimination (éliminer les récepteurs dont on peut dire à priori qu'ils ne brouillent pas). Ceci nécessite une méthode très rapide. Peut-être ne restera-t-il ensuite que quelques récepteurs pour lesquels on devra faire appel à une méthode manuelle pour une étude complète. Dans ce cas, l'utilisation de cartes sur ordinateur serait très utile, mais les ordres de grandeur sont différents: au moins 1000 km de rayon, et des fréquences de quelques GHz.

Translation: It might be interesting to draw up a table, in the columns of which various data would be indicated, such as: services concerned with the problem of computerized maps, frequency band used, accuracy required, etc., as well as size of the area. Everytime I heard this map problem mentioned, it was in relation to frequencies of the order of some metres or somewhat shorter, but almost never in relation to frequencies under this order of magnitude. Radar coverages have also been mentioned, but this time at still higher frequencies. There is another problem which is becoming increasingly important with respect to transmissions. To solve it, the computerization of large expanses would be useful. It is the problem related to the coordination between ground-based stations and hertzian beam stations which operate within the same frequency bands. Regulations in this field are considerable. When planning to build a ground-based station in a country, it is necessary to investigate all the jamming possibilities around this station, within ranges up to a few hundreds or even a few thousands of kms. It must be established that there is no possible jamming from all the hertzian beams already existing in this area. This involves a considerable amount of work for which computer aided methods are sought, at least to carry out an elimination process (eliminate the receivers which are known not to create jamming). This process necessitates a very quick method. Then, maybe a few receivers will remain, a complete study of which will require a manual method. In such a case, the use of computerized maps would be quite worthwhile, although the orders of magnitude are different: radii of at least 1000 km and frequencies of some GHz.

H. Albrecht (FRG): One of your ideas, an attempt to assess the needs, requirements, and required accuracies as a function of services, frequencies, and other parameters, is what we tried to derive from the start of this round table. This is to assess critically the actual accuracies obtained, and then try to apply the data maps in the proper way. This is wanted instead of making data maps, and then trying to apply them and make comparisons. When you make measurements over the same link before and after a passage of time with the same data map, and have 10 meters of snow cover in the interim, you will find different values. Then you question the value of digital data maps.

L.B. Felsen (U.S.): I pointed out the dichotomy between the theoretician's creation and the practitioner's real needs. The overall evaluation is no better than the weakest link.

Certain theoretical models have been developed so that numerical calculations can be made with computer programs efficiently. Better data is needed now.

J.A. Kong (U.S.): The issues here have an impact on model development. I would like to classify the problems into categories based on sensor altitudes.

The communications problems of line of sight and mobile communications are affected by ground wave effects, surface wave effects, and diffraction. These are transmission problems at low altitudes.

There are high altitude remote sensing problems where bounded waves at the surface are not crucial to experimental or analytical results. There are intermediate remote sensing problems, classified as radar scattering and communication problems.

I would like a digital map for high altitude remote sensing. This would include slopes, heights, and resolution for sensors. It could be used for vegetation cover predictions. Updating with overflights would include changes due to snows and harvests. Based on theoretical models, maps could be extended to other areas.

P.F. Checcacci (Italy): There was very little information on the scattered energy in many papers. This may be very important in the future. With the increasing number of transmitting links, the selection criteria will not be the path loss. It will be the backscattered energy from one link to another link.

C.E. Dadson: I shall probably be remembered as the bloke who employed the dolly birds to do his jolly graphs for him.

In the end, the users of our data base and computer programs only want the output in plotted form. This was in terms of good, bad, and indifferent.

Our users are not interested in signal levels and field strengths which are expressed with 15 decimal places or even 2 significant figures. They are interested only if their signals will be good, bad or if something should be done to a particular corner to improve their reception.

I often wonder if we are becoming too sophisticated for actual use of our results.

L.B. Felsen (U.S.): Dr. Dadson's comments are certainly applicable in terms of user needs. If you are using radio waves for navigation, your information must be more accurate. Some applications require very sophisticated methods. Others require very simple methods.

H. Albrecht (FRG): We will end with a few concluding remarks.

L. Høivik (Norway): Independently of our feelings about them, digital maps will be used by other people in other places. Our job is to use these maps in the best possible way.

L.B. Felsen (U.S.): It is important to find the minimum data needed to generate critical information.

F.H. Palmer (Canada): Since data bases will be made, we must use them to the best of our ability, and to keep our user needs in mind. Some degraded data bases are more economical than the complete data base.

J. Belrose (Canada): Re-radiation may be more important than we think.

H. Albrecht (FRG): The applicability of digital data maps is possible in many applications. The value of the applicability may be summarized in a few words -- CUM GRANO SALIS(avec un grain du sal).

SESSION V

Paper No. 24

E. Bahar (U.S.): Did you say that you had a modified wave form for grazing incidence angles?

J.R. Delaney (U.S.): We originally concluded that we could neglect the dielectric mismatch between the air and ground. One of my co-authors later decided to introduce a correction for this effect.

E. Bahar (U.S.): Did you include the formulation by Beckmann and Spizzachino for grazing angles?

J.R. Delaney (U.S.): We are using it with a modification from results by Bruce Smith. It seems to have good experimental justification.

L. Boithias (France): Je voudrais une premiere information, qu'elle est la fréquence versée (UHF), que à était écrit mais que je n'ai pas vu, et d'autre par, est ce qu'un vient à chèf d'une vuance de la polarisation ça vent dire, soit verticale, horizontal, soit circulaire.

Translation: I would like to know your signal frequency. It was written, but I could not see it. What was your polarization? Was it vertical, horizontal, or circular?

J.R. Delaney (U.S.): The VHF frequency is 150 MHz. When we do the modification to include the dielectric coefficient of the ground in our calculation, the use of horizontal or vertical polarization produces different results.

The experiment was performed with vertically polarized waves. In general our model neglects polarization because it assumes very low grazing angles.

Paper No. 27

L. Høivik (Norway): What type of communication is this model considering? If it is designed for use in conjunction with submarines, how do you make an efficient antenna?

A.W. Biggs (U.S.): This model can be used for communication with submerged submarines and with miners in deep rock mines. In both modes, the attenuation decreases with frequency.

Since the refractive index is extremely large, a resonant antenna would have a wavelength of a few hundred meters in sea water.

Paper No. 29

D.W. Lodge (U.K.): I have some reservations about your assumptions in this paper. I would like to hear your comments on the seriousness of them. Each assumption seems to be valid in isolation, but some are virtually inconsistent.

(a) You describe a Space Shuttle payload and assume a nominal orbit of 1000 km altitude and an inclination angle of 50°. This is a higher altitude and inclination angle than the nominal Space Shuttle mission.

(b) You describe the use of the instrument over the Arctic and Antarctic regions. Neither region would be visible from either the nominal Space Shuttle orbit described.

These reservations do not affect the substance of your paper. However, more seriously:

(c) I question the validity of your assumption of 50% loss of data due to cloud cover. This may be legitimate over the state of California, but it is certainly not the situation over northern Europe. The sky of the north polar regions is free of clouds only for a very small proportion of the time.

B. Rubin (U.S.): (a) Equation (1), which defined the return signal in joules from a Space Shuttle, assumed an orbit height of 200-700 km. The 50° inclination of the spacecraft was used for the case where earthquake prediction was the object. In the case where profiling is to be accomplished, the laser is pointed in the nadir direction.

(b) The Space Shuttle is a manned vehicle whose orbit can be varied depending upon the experiment or mission. If there is a need for polar orbits, this can be achieved without any difficulty. Inclinations can be varied according to need.

(c) Over regions of the earth where cloud cover is greater than 50% of the time, it will be necessary to resort to RF techniques with the reduced spatial resolution of the method.

H. Soicher (U.S.): What is the order of the excess signal time delay? Of what is it a function?

B. Rubin (U.S.): Atmospheric time delay is due to the difference in the velocity of light in the earth's atmosphere compared with its free space value. The delay has been incorporated into models and results in an error of 1.0 cm in distance measurement.

Models require inputs of pressure, temperature, and humidity at the earth's surface, and pressure errors of 10-20 millibars cause errors of 2.3 to 4.6 cm.

L. Høivik (Norway): One of your graphs presented signal strength as a function of altitude. If the aspect angle of the reflective surface changes, how would this affect the strength of the echo?

B. Rubin (U.S.): The target cross section per unit area, $\sigma°$ (which was used to derive the graph that you mention), is the product of the reflectivity of the surface and the directional characteristic of the reflected signal. $\sigma°$ can vary from 0.2 to 0.4, depending on the medium (snow, ice, water, etc.) and on the directional characteristics of the reflected signal.

Paper No. 32

J.H. Blythe (U.K.): The rapid time variation of fading, when deep nulls occur, suggests that the high level layers are important. Another indication can be found from the general weather conditions, which are expected to be stable (autocyclonic) during periods of deep fading. Have you examined this?

H.G. Giloi (FRG): According to the theory of Fehlhaber, in whose research group I have been, deep fading is caused by ground based inversion layers.

I know that many people believe that high altitude layers cause this fading. Therefore I attempted to explain some of the field strength versus height profiles in this paper with a ground based layer and a high level layer. Results did not indicate that one of these layers could be excluded.

In another experiment a very stable layer, causing deep fading for several days, was found below the heights of the transmitter and the receiver by aerological balloon ascents.

Nevertheless I am not sure that these layers are always below the direct path. In experiments with antenna arrays described at the end of my paper, we will measure the phase differences between antennas as well as the amplitudes. This technique will enable us to find which waves come from above or from below the direct path.

P. Lewis (FRG): In your new experiments using a vertical array, do you intend to measure the phase as well as the amplitude of the received field? This enables a scattered wave to be positively identified as coming from above the line of sight rather than from below, and conversely.

H.G. Giloi (FRG): We intend to measure not only the amplitudes, but also the phase differences between the antennas. We shall use two oscillators of high stability, which are a little different in frequency. One will be located at the transmitter station, and the other one in a supplementary transmitter near the receiver station.

With the model described here, I computed the amplitudes and phase differences of the array and used them to successfully reconstruct the two sources.

L. Boithias (France): (1) Quels etaient les gains des antennes utilises?

(2) Aves-vous prevu d'utiliser les pylône pour effectuer des mesures de pression, température, et humidité, ce pour permet d'interpréter certaines mesures?

Translation: (1) What were the gains of the antennas used?

(2) Have you contemplated the use of the pylon pole for pressure, temperature, and humidity, which permit the interpretation of certain measurements?

H.G. Giloi (FRG): We used parabolic antennas, which have a diameter of 60 cm. The gain was about 35 dB.

(2) I think that I should measure temperature, humidity, and pressure at the location where reflecting layers are expected. We made similar experiments on another link, but the evaluation is not yet ready.

L. Boithias (France): (1) Etes-vous certain que l'antenne naissait ou descendait sans le moins de mouvement horizontal provoquant un depintage parasite?

(2) Le modelage par une lame de couteau ne semble pas bien adaptée au profil de la liaison.

(3) Avez vous mesure (ou pensez-vous mesurer) le retard du trajet refleche par rapport au trajet direct?

Translation: (1) Are you sure that the antenna went up and down without the slightest horizontal motion creating fading?

(2) The knife edge modelling does not seem to be well suited to the link profile.

(3) Did you measure (or do you intend to measure) the reflected path delay in relation to the direct path?

H.G. Giloi (FRG): (1) The elevator was very solid and it ran on rails. I am sure that the antenna did not shake, at least not to an extent where variations of the gain became noticeable.

(2) The knife edge was chosen because it is a very simple model. In the summer, when the trees have leaves, the knife profile did not deviate much from the theoretical curves in periods of normal propagation. In the winter a good model of the forest, with the branch density varying with height, would be very complicated.

(3) The measurements were carried out with CW transmission. Measurements with modulated waves were performed on another link of 180 km. The average per month, of the time delay, was 2-4 nanoseconds.

DISCUSSION OF SESSION V

L. Høivik (Norway): I would like to ask the authors of papers in this session if they have some questions or comments about another author's paper. I have a question for Dr. Delaney. In your paper, you had several pictures which described the diffraction region. Have you made any similar studies of the diffraction region over coastal waters (along the ocean shore)?

J.R. Delaney (U.S.): We have not made similar studies along coastal waters. The areas of greatest interest are inland areas. We realize that the coastal and the over water situations are very different. We have been intentionally avoiding it for simplicity purposes.

A.W. Biggs (U.S.): I would like to know what sensitivity your altimeter has above snow or ice. In previous years we have had some difficulties when the snow or ice layer had a low dielectric constant. The altimeter often followed the land-ice interface instead of the ice-air interface.

F. Thomsen (Denmark): It is difficult to provide an exact number for the resolution capability. It depends upon whether you are able to measure the like polarized and cross polarized response of the altimeter. At the present time I cannot give a more precise answer.

L. Høivik (Norway): I have a question for Mr. Thomsen. How much progress have you made in experimental verifications?

F. Thomsen (Denmark): The existing measurements only include like polarizations. We do not have measurements of cross polarizations. That leaves a large ambiguity, especially with respect to the subsurface parameters.

R.W. Lorenz (FRG): I would like to ask Dr. Lewis a question. The mechanical stability of your experimental setup should have been very high, since 10 mm vibration amplitude gives an error of about 10° at one GHz. How did you remove this problem?

P. Lewis (FRG): Mechanical oscillations of the travelling antenna and deformation of the synthetic aperture by wind loading were considered in the mechanical design. When the carriage was at the center of the aperture, the pendulum frequency (determined by the sag) was 1.5 Hz.

The chosen scanning speed of 0.3λ per second ensured that spurious sidebands, produced by mechanical oscillations at this frequency or a higher frequency, would be well separated from the desired spectrum. Such components were filtered out by the filter preceding to A to D (analog to digital) converter. Oscillations with amplitudes up to about 20 mm could be tolerated. In practice most measurements were made in conditions of calm or light wind. No difficulties were experienced.

P.F. Checcacci (Italy): I refer to the paper by Dr. Lewis, describing experiments which located the position of scatterers causing multipath propagation. My opinion is that this problem is more easily solved with a pulse coded or frequency sweeped emission instead of a CW emission.

From the measurements of time delays and beat frequencies at the receiving site, the surfaces of constant delay can be determined. The frequency sweep (or chirp) method seems, assuming a high frequency sweep rate, to be the most suitable for short delays.

P. Lewis (FRG): I do not see very much difference between the two techniques which you described. My technique was different, where a constant frequency was radiated and the spatial distribution of the field was measured. It was used to calculate images.

As far as the two techniques described by you are concerned, these work very well as long as the scattered waves have different delays, relative to the direct wave.

In my studies, scattered fields were received by a strongly directional antenna. They arrived with very short time delays after the arrival of the direct wave. The ground reflection, which I described in my paper, had a path difference of one wavelength with respect to the direct wave. This came from the system geometry. In that case the time domain techniques are not so applicable.

P.F. Checcacci (Italy): I agree, but if you use a frequency shift with your system, you would have a one cycle bit for one wavelength.

P. Lewis (FRG): If you want to resolve a one cycle frequency difference, or a one wavelength difference, you must have a very large bandwidth in your receiver.

P.F. Checcacci (Italy): You must simply have a very fast sweeping rate on the frequency modulation.

P. Lewis (FRG): It is not possible unless you radiated something near a delta function.

P.F. Checcacci (Italy): Why? The well known FM radar can resolve one meter of length.

P. Lewis (FRG): This is not the same problem.

A.L. Johnson (U.S.): Does the satellite radar altimeter described by you (F. Thomsen) complement Professor P.E. Gudmandsen's measurements of the Greenland ice cap?

F. Thomsen (Denmark): The radio echo sounding performed by Professor P.E. Gudmandsen maps the bedrock and the ice layers above it.

Satellite altimeter measurements can only be used to measure the stratification of the upper few hundred meters of the glacial ice sheet.

J.S. Belrose (Canada): I would like to present a question to the authors of papers presented during this session and also to members of the audience. When one considers ionospheric physics, he takes radio propagation data and tries to determine the ionospheric layer structure. He can also determine these characteristics in another route. If he knows the density height profile and the collision frequency height profile, he can calculate the amplitude of the downcoming wave.

In this situation, when you include the terrain, the ionospheric problem is very difficult and the tropospheric problem is probably impossible to solve. The reasons for the tropospheric problem being "almost impossible" were discussed earlier. Propagation over curved hills, tree covered hills, knife edges, and man made structures contribute to these difficulties. Is there any hope for the measurement of terrain parameters by the experiments described by the participants here?

H.G. Giloi (FRG): My results were applicable to some special situations.

H. Albrecht (FRG): Our terrain is not on the moon or in similar areas where there is no atmosphere. Therefore I believe that the troposphere, bordering the planet's surface, has a very important effect on terrain measurements. Although it is not a measurement of the terrain, terrain measurements can be interpreted better by knowledge of tropospheric behavior.

L. Høivik (Norway): One should look at terrain parameter measurements in a wider sense. He must not only look underneath him in terms of the earth. When we use digitized data, we encounter problems generated by waves propagating through the different media.

L. Boithias (France): Au sujet du dernier exposé, quel était le gain de l'antenne; ce point est très important pour fixer la zone de terrain qui est illuminée par l'antenne. Je pense que le gain devait être assez élevé, ce qui élimine certaines zones du terrain qui ne peuvent être illuminées par l'onde. D'autre part, pour cette expérience, il faut connaître le profil exact; or le profil représenté ici me semble un peu trop schématique pour être exact. Cette expérience me semble très intéressante, mais à peine commencée. Il manque trop d'éléments pour pouvoir en tirer des renseignements. Comme il me semble que des sommes importantes aient déjà été engagées, ce serait dommage de ne pas en tirer tout le parti possible. Il faudrait connaître exactement: 1) l'illumination du sol, donc le gain des antennes; 2) le profil rigoureusement exact du terrain pour toutes les valeurs du facteur k; 3) l'atmosphère (ceci est facile car on peut installer sur le même chariot que l'antenne un petit dispositif mesurant simplement la pression, la température et l'humidité, ou directement l'indice de réfraction, ce qui permet d'interpréter les résultats et de savoir s'il y a des couches réfléchissantes ou pas. En conclusion, la base de cette étude est très intéressante, mais elle demande à être complétée.

Translation: As regards the last paper, what was the antenna gain? This is very important to know in order to determine which part of the zone is illuminated by the antenna. I think the gain was probably rather high, which eliminates certain parts of the zone which cannot be illuminated by the wave. In addition, this experiment requires that the exact profile should be known. Now, the profile represented here appears too simplified to be accurate. Therefore, this experiment, which otherwise looks very interesting, seems to me to be still in its initial stage. Too many elements are missing for information to be derived. As it appears that considerable funds have already been spent on this study, it would be regrettable if the maximum benefit could not be derived from it. We need to know exactly: 1) the ground illumination, that is the antenna gain; 2) the accurate terrain profile for all the values of the factor k; 3) the nature of the atmosphere (this is easy, since a small device can be fitted on the same carriage as the antenna, to measure pressure, temperature and humidity, or directly the refraction index, which would make it possible to analyze the results obtained and to know whether there are any reflecting layers). In conclusion, the basis of this study is most interesting, but complementary work is needed.

H.G. Giloi (FRG): The antenna gain was about 30 dB. It was not a high gain antenna. The antenna is the wrong place to measure temperature and humidity because reflections do not occur there.

I had a list of parameters to measure at the place where I expected to find reflections. This place is about 13 km from the receiver, in the direction toward the transmitter.

On another link I made similar experiments. I am not yet ready to evaluate the results. I calculated the whole profile with many k-factors. The results were not very conclusive.

L. Høivik (Norway): Dr. Rubin, what is the price of your instrument?

B. Rubin (U.S.): The entire system, including the laser, the emitter, the receiver, the minicomputer, etc., represent an investment exceeding $1 million. This covers studies done, a flight qualified laser, and a half built receiver. Flight qualified costs will be about $3 million.

The advantages of high spatial resolution and operational capability may pay for the cost.

J.A. Kong (U.S.): Dr. Rubin, your viewgraph differentiates between the backscatter return from ground, snow, and sea surfaces. The snow return was highest, and the sea return was lowest. At what angle are you looking at the ground?

B. Rubin (U.S.): That graph was for looking straight down with an elevation angle equal to 90° (or 0° angle of incidence).

J.A. Kong (U.S.): I do not understand why the snow return was higher than the sea return.

B. Rubin (U.S.): I think that it was because the reflectivity of snow is higher than that of land or water at that angle.

J.A. Kong (U.S.): The reflectivity of snow has a dielectric constant equal to 1.8, and the sea surface

has a reflectivity corresponding to a much higher dielectric constant.

B. Rubin (U.S.): At the system's wavelength, the snow reflectivity was higher.

J.A. Kong (U.S.): Was it due to scattering of the snow?

B. Rubin (U.S.): That is possible. Dr. Biggs told me that it was space qualified. This increases the price to a much higher figure.

Data reduction is more expensive than data collection. Only one percent of the Landsat data has been reduced. We are hoping to reduce this cost with data reduction on the spacecraft.

L. Boithias (France): Remarque sur la comparaison entre la neige et la mer. Il ne faut pas oublier que, dans les ondes radio, l'indice de réfraction de l'eau est supérieur à celui de la neige, mais pas dans les ondes lumineuses. Or ici il s'agit d'ondes limineuses.

<u>Translation</u>: Remark on the comparison between the snow and the sea. One should bear in mind that, with radio waves, the refraction index of the water is higher than that of the snow. However, this remark does not apply to light waves. Now, it is light waves that are considered here.

APPENDIX B

LIST OF ATTENDEES

Number in parenthesis indicate author of paper presented

Aarons, J.	AFGL/PHP, Hanscom AFB, Mass.,01731, USA
Albrecht, H.J.	Forschungsinstitut für Hochfrequenzphysik, Königstrasse 2, D-5307 Wachtberg-Werthoven, Germany
Assis, M.S.	Senior Researcher, Centro de Tecnologia PROMONCTP, Praia do Flamengo, 154-12 (º) Andar, 22210 Rio de Janeiro, Brazil
Bahar, E. (12)	Electrical Engineering Dept., University of Nebraska, Lincoln, Nebraska 68588, USA
Becker, K.D.	Fachrichtung 122 Elektrotechnik, Universität des Saarlandes, D-6600 Saarbrücken, Germany
Belrose, J.S. (2)	Communications Research Centre, P O Box 11490, Station H, Ottawa, KZH 852, Canada
Berner, H.	Fa.SEL.Dept. CNS/KSO, Hellmuth Hirth Strasse 42, D-7000 Stuttgart, 40, Germany
Biggs, A.W.	Space Technology Center, Raymond Nichols Hall, University of Kansas, Lawrence, Kansas 66045, USA
Blythe, J.H.	GEC-Marconi, Great Baddow Research Lab., Great Baddow, Chelmsford, CM2 8HN, England
Boithias, L.	CNET, 38, 40 rue de Général Leclerc, 92131, Issy-les-Moulineaux, France
Brandsaeter, O.	Geographical Survey of Norway, P O Box 8153, Oslo Departemnt, Oslo 1, Norway
Breien, T. (10)	Norsk Marconi A/S, Ryensvingen 5, Norway
Calamia, M.	Istituto di Elettronica Facolta di Ingegneria, Via S. Maria 2,50139 Firenze, Italy
Carlson, G.E. (22)	Electrical Engineering Dept., University of Missouri-Rolla, Rolla, Missouri 65401, USA
Checcacci, P.F.	Istituto Ricerca Onde Elettromagnetiche, Via Panciatichi, 64, 50127, Firenze, Italy
Consentino, A.	CISET, SpA Via Salaria 1027, 00138 Roma, Italy
Coyne, V.J.	RADC(AFSC), Griffiss AFB, NY 13441, USA
Dadson, C.E. (25)	Electricity Council, 30 Millbank, London WC1A 1HE, England
Darnell, M.	Room 431, Prospect House, 100 New Oxford Street, London WC1A 1HE, England
D'Auria, G.	Istituto di Elletronica, Universita di Roma, Via Eudossiana 18,00184, Roma, Italy
Davies, K.	Environmental Research Lab., NOAA, Boulder, Colorado 80302, USA
Delaney, J.R. (24)	Group 38, Lincoln Lab., P O Box 79, MIT, Lexington, Mass. 02173, USA
DeVries, B.	KLM, Aerocarta B.V. Princess Beatrixlaan 7, P O Box 95306, 2509 CH The Hague, Netherlands
Döbrich, M. (13)	Fachvichtung 122, Elektrotechnik Universität des Saarlandes, D-6600 Saarbrüchen, Germany
Drummeter, L.F., Jr	Optical Sciences Division, US Naval Research Lab., Washington, DC 20390, USA
Eggestad, M.	NDRE, P O Box 25, N-2007 Kjeller, Norway
Felsen, L.B. (7)	Electrical Engineering Dept., Polytechnic Institute of New York, Route 110, Farmingdale, NY 11735, USA
Finnie, J.S.	Directorate of Radio Technology, Waterloo Bridge House, Waterloo Road, London, England
Giloi, H.G. (32)	Forschungsinstitut der DBP beim FTZ, F1 32 C, Postfach 5000, 6100 Darmstadt, Germany
Henriksen, R.	Geographical Survey of Norway, P O Box 8153, Oslo, Dept. Oslo 1, Norway
Hansen, N.K.	Danish Defence Research Est., 2100 Copenhagen, Denmark

Hizal, A.	Electrical Engineering Dept., Middle East Technical University (Orta Doğu Teknik Universitesi), Inönu Bulvari, Ankara, Turkey
Hodara, H.	Tetra Tech., 630 N. Rosemead Blvd., Pasadena, California 91107, USA
Høivik, L.	NDRE, P O Box 25, N-2007 Kjeller, Norway
Hortenbach, K.J. (18)	Deutsche Welle, Postfach 10 04 44, 5000 Köhn 1, Germany
Johnson, A.L. (11)	USAF Avionics Lab., Wright Patterson AFB, Ohio 45433, USA
King, R.J. (4), (9)	Electrical Engineering Dept., University of Wisconsin, Madison, WI 53706, USA
Kjaerstad, O.	A/S Kongsberg Vapenfabrik, Defense Products Division (FBA), 3600 Kongsberg, Norway
Klinker, F.	NLR, P O Box 153, 8300 AD, EMMELOORD, Netherlands
Kong, J.A. (19)	Electrical Engineering Dept., MIT, Cambridge, MA 02139, USA
Kusters, E.R. (23)	AMT für Wehrgeophysik, Mont Royal, D5580 Traben-Trarbach, Germany
Ladell, L.	Senior Scientist, NDRI, P O Box 1165, S-581, 11 Linkoping, Sweden
Lampert, E.	Siemens AF,NW$_V$ZL, Postfach 70 00 77, 8000 München, Germany
Lange-Hesse, G.	Max Planck Institut für Aeronomie, Postfach 20.D – 3411 Katlenberg-Lindau 3, Germany
Langenberg, K.J. (5), (13)	Fachrichtung 122, Elecktrotechnik Universität des Saarlandes, D-6600 Saarbrüchen, Germany
Larsen, T.R.	NDRE, P O Box 25, 2007 Kjeller, Norway
Lewis, P. (30)	Standard Elektrik Lorenz, CFP/LG Ostendstrasse 3, 753 Pforzheim, Germany
Loforti, R.	Elettronica S.p.a. Via Tiburtina Valeria, Km 13700,00131, Roma, Italy
Lodge, D.W.S.	Procurement Executive, MOD, Royal Aircraft Establishment, Farnborough, Hants, England
Low, A.J.	Smith Associates, 20 Queens Road, Weybridge, Surrey KT13 9UZ, England
Lorenz, R.W. (17)	Forschunginstitut der DBP beim FTZ, FI 32 C, Postfach 5000,6100 Darmstadt, Germany
Mendes, A.S.	Instituto Nacional de Meteorologia e Geofisica, Rua C, Aeroporto de Lisboa, 1700 Lisboa, Portugal
Mortensen, E.T.	Post Telegraphs, Radio Engr. Service, Nørrebrogade 10, DK2200, Copenhagen Denmark
Ott, R.H. (6), (8)	ITS/NTIA, US Dept. of Commerce, Boulder, CO 80309, USA
Palmer, F.H. (26)	Communications Research Center, P O Box 11490, Station H, Ottawa, Ontario K2H 852 Canada
Piefke, G.	Theoretische Elektrotechnik, Technische Hochscule, Schlossgartenstrasse 8, D-6100 Darmstadt, Germany
Pronk, P.	DMKL-MVA2, Building 33, Van de Burchlaan 31, 2597 PC The Hague, Netherlands
Rech, K.D. (5)	Fachbereich 122, Universität des Saarlandes, D-6600 Saarbrüchen, Germany
Rocco, F.	CISET, spA, Via Salaria 1027, 00138, Roma, Italy
Rønning, A.	Harens Forsyningskommando, Lorenseien 36, Oslo MIL/Loren, Oslo 1, Norway
Rubin, B. (29)	NASA Hqs. Mail Code RSI–4, Washington, DC 20546, USA
Saethermoen, N.A.	NDRE P O Box 25, N-2007 Kjeller, Norway
Samwell, C.J.	Sperry Gyroscope Ltd., Downshire Way, Bracknell, Berks, RG 12 1QL, England
Skarstein, A.	Geographical Survey of Norway, P O Box 8153, Oslo Dept., Oslo 1, Norway
Soicher, H.	DRDCO-COM-RF-5, Fort Monmouth, NJ 07703, USA
Soldani, A.	CISET, spA, Via Salaria 1027, 00138, Roma, Italy
Sprenkels, C.	Quartier Reine Elisabeth, Rue d'Evere, 1140 Brussels, Belgium
Stork, C.F.	KLM, Aerocarto B.V. Princess Beatrixlaan 7, P O Box 95306, 2509 CH The Hague Netherlands
Thomsen, F. (28)	Electromagnetics Institute, Technical University of Denmark, 2800 Lyngby, Denmark
Thorvaldsen, T.	NDRE P O Box 25, N-2007 Kjeller, Norway
Tsoukias, J.	HAFGS/KETA, Delta Falirou, Holargos, Athens, Greece
Uebelhor, W.	Messerschmitt-Bolkow-Blohm, UA-AE212, Postfach 80 11 49, 800 München 80, Germany

Vaizan, Mr	ONERA, 29, Avenue de la Division Leclerc, 92320, Chatillon-sous-Bagneux, France
Van Buuren, J.A.	DMKL–MBAI Building 238, Van de Burchlaan 31, 2597 PC The Hague, Netherlands
Van der Scheur, M.J.	Physics Lab., TNO, P O Box 96864, 2509 PC, The Hague, Netherlands
Vissinga, H.	Physics Lab., NDRO, P O Box 96864, 2509 PC, The Hague, Netherlands
Wang, G.	Division for Electronics NDRE, Kjeller, Norway
Woerrlein, H.H.	MBB, Abteilung AE212, Postfach 80 11 49, D-8000 Müchen 80, Germany

AGARD Staff

Bramsen, M.B		Interpreter
Brown, B.	SHAPE, Belgium	Technician
Catiller, J.B.	AGARD, France	EWPP Executive
DeLiffiac, T.		Interpreter
Gause, C.	SHAPE, Belguim	Technician
Gillman, R.		Interpreter
Tessier, M.	AGARD, France	Secretary

REPORT DOCUMENTATION PAGE

1. Recipient's Reference	2. Originator's Reference	3. Further Reference	4. Security Classification of Document
	AGARD-CP-269	ISBN 92-835-1345-2	UNCLASSIFIED

5. Originator	Advisory Group for Aerospace Research and Development North Atlantic Treaty Organization 7 rue Ancelle, 92200 Neuilly sur Seine, France
6. Title	TERRAIN PROFILES AND CONTOURS IN ELECTROMAGNETIC WAVE PROPAGATION
7. Presented at	the Specialists' Meeting of the Electromagnetic Wave Propagation Panel held in Spåtind, Norway, 10–14 September 1979.

8. Author(s)/Editor(s)		9. Date
Various	Edited by A.W.Biggs	December 1979

10. Author's/Editor's Address		11. Pages
Various	University of Kansas Lawrence Kansas 66045, USA	392

12. Distribution Statement	This document is distributed in accordance with AGARD policies and regulations, which are outlined on the Outside Back Covers of all AGARD publications.

13. Keywords/Descriptors

Terrain
Electromagnetic wave transmission
Mapping
Antennas
Antenna radiation patterns
Electromagnetic interference
Telecommunication

14. Abstract

The Meeting explored propagation problems associated with terrain profiles and contours. Specifically examined were theoretical aspects, methods of digital terrain mapping, and terrain effects on antenna characteristics.

Future communication and data transmission will make extensive use of digital terrain maps. Characteristics of terrain near terminals or communication links may provide protection against interference from other sources. Experimental data interpretation requires understanding of sensors and antennas. Theoretical contributions include cw and transient scattering from statistically rough and smoothly varying terrain. Analytical methods include full wave solutions, ray techniques, and modal techniques.

The program of the Meeting consisted of five sessions covering the following main topics: (1) Terrain effects on antenna characteristics; (2) Propagation effects in terrain mapping; (3) Theoretical aspects of scattering and emission from terrain; (4) Methods of digital terrain mapping; (5) Measurement of terrain parameters.

A round table discussion was concerned with the current and future trends in the areas covered by the above sessions.

AGARD Conference Proceedings No.269
Advisory Group for Aerospace Research and Development, NATO
TERRAIN PROFILES AND CONTOURS IN ELECTROMAGNETIC WAVE PROPAGATION
Edited by A.W.Biggs
Published December 1979
392 pages

The Meeting explored propagation problems associated with terrain profiles and contours. Specifically examined were theoretical aspects, methods of digital terrain mapping, and terrain effects on antenna characteristics.

Future communication and data transmission will make extensive use of digital terrain maps. Characteristics of

P.T.O.

AGARD-CP-269

Terrain
Electromagnetic wave transmission
Mapping
Antennas
Antenna radiation patterns
Electromagnetic interference
Telecommunication

AGARD Conference Proceedings No.269
Advisory Group for Aerospace Research and Development, NATO
TERRAIN PROFILES AND CONTOURS IN ELECTROMAGNETIC WAVE PROPAGATION
Edited by A.W.Biggs
Published December 1979
392 pages

The Meeting explored propagation problems associated with terrain profiles and contours. Specifically examined were theoretical aspects, methods of digital terrain mapping, and terrain effects on antenna characteristics.

Future communication and data transmission will make extensive use of digital terrain maps. Characteristics of

P.T.O.

AGARD-CP-269

Terrain
Electromagnetic wave transmission
Mapping
Antennas
Antenna radiation patterns
Electromagnetic interference
Telecommunication

AGARD Conference Proceedings No.269
Advisory Group for Aerospace Research and Development, NATO
TERRAIN PROFILES AND CONTOURS IN ELECTROMAGNETIC WAVE PROPAGATION
Edited by A.W.Biggs
Published December 1979
392 pages

The Meeting explored propagation problems associated with terrain profiles and contours. Specifically examined were theoretical aspects, methods of digital terrain mapping, and terrain effects on antenna characteristics.

Future communication and data transmission will make extensive use of digital terrain maps. Characteristics of

P.T.O.

AGARD-CP-269

Terrain
Electromagnetic wave transmission
Mapping
Antennas
Antenna radiation patterns
Electromagnetic interference
Telecommunication

AGARD Conference Proceedings No.269
Advisory Group for Aerospace Research and Development, NATO
TERRAIN PROFILES AND CONTOURS IN ELECTROMAGNETIC WAVE PROPAGATION
Edited by A.W.Biggs
Published December 1979
392 pages

The Meeting explored propagation problems associated with terrain profiles and contours. Specifically examined were theoretical aspects, methods of digital terrain mapping, and terrain effects on antenna characteristics.

Future communication and data transmission will make extensive use of digital terrain maps. Characteristics of

P.T.O.

AGARD-CP-269

Terrain
Electromagnetic wave transmission
Mapping
Antennas
Antenna radiation patterns
Electromagnetic interference
Telecommunication

terrain near terminals or communication links may provide protection against interference from other sources. Experimental data interpretation requires understanding of sensors and antennas. Theoretical contributions include cw and transient scattering from statistically rough and smoothly varying terrain. Analytical methods include full wave solutions, ray techniques, and modal techniques.

The program of the Meeting consisted of five sessions covering the following main topics: 1. Terrain effects on antenna characteristics; 2. Propagation effects in terrain mapping; 3. Theoretical aspects of scattering and emission from terrain; 4. Methods of digital terrain mapping; 5. Measurement of terrain parameters.

A round table discussion was concerned with the current and future trends in the areas covered by the above sessions.

Papers and Discussions presented at the Specialists Meeting of the Electromagnetic Wave Propagation Panel held in Spåtind, Norway, 10–14 September 1979.

ISBN 92-835-1345-2

terrain near terminals or communication links may provide protection against interference from other sources. Experimental data interpretation requires understanding of sensors and antennas. Theoretical contributions include cw and transient scattering from statistically rough and smoothly varying terrain. Analytical methods include full wave solutions, ray techniques, and modal techniques.

The program of the Meeting consisted of five sessions covering the following main topics: 1. Terrain effects on antenna characteristics; 2. Propagation effects in terrain mapping; 3. Theoretical aspects of scattering and emission from terrain; 4. Methods of digital terrain mapping; 5. Measurement of terrain parameters.

A round table discussion was concerned with the current and future trends in the areas covered by the above sessions.

Papers and Discussions presented at the Specialists Meeting of the Electromagnetic Wave Propagation Panel held in Spåtind, Norway, 10–14 September 1979.

ISBN 92-835-1345-2

terrain near terminals or communication links may provide protection against interference from other sources. Experimental data interpretation requires understanding of sensors and antennas. Theoretical contributions include cw and transient scattering from statistically rough and smoothly varying terrain. Analytical methods include full wave solutions, ray techniques, and modal techniques.

The program of the Meeting consisted of five sessions covering the following main topics: 1. Terrain effects on antenna characteristics; 2. Propagation effects in terrain mapping; 3. Theoretical aspects of scattering and emission from terrain; 4. Methods of digital terrain mapping; 5. Measurement of terrain parameters.

A round table discussion was concerned with the current and future trends in the areas covered by the above sessions.

Papers and Discussions presented at the Specialists Meeting of the Electromagnetic Wave Propagation Panel held in Spåtind, Norway, 10–14 September 1979.

ISBN 92-835-1345-2

terrain near terminals or communication links may provide protection against interference from other sources. Experimental data interpretation requires understanding of sensors and antennas. Theoretical contributions include cw and transient scattering from statistically rough and smoothly varying terrain. Analytical methods include full wave solutions, ray techniques, and modal techniques.

The program of the Meeting consisted of five sessions covering the following main topics: 1. Terrain effects on antenna characteristics; 2. Propagation effects in terrain mapping; 3. Theoretical aspects of scattering and emission from terrain; 4. Methods of digital terrain mapping; 5. Measurement of terrain parameters.

A round table discussion was concerned with the current and future trends in the areas covered by the above sessions.

Papers and Discussions presented at the Specialists Meeting of the Electromagnetic Wave Propagation Panel held in Spåtind, Norway, 10–14 September 1979.

ISBN 92-835-1345-2

DAT

FILM

4 –